

# **Quantitative Nanohistology: Collagen Disorders of Connective and Mineralised Tissues**

Adam Philip Strange

*Accepted for the degree of Doctor of Philosophy*

*University College London*

Eastman Dental Institute

April 2019

# Abstract

---

This thesis explores the behaviour of collagen; both as a biomaterial and as a tissue vulnerable to disease. It aims to develop a novel, scalable, and multimodal system for recognising and characterising collagen abnormalities.

Initially, collagen implants were characterised using Scanning Electron Microscopy (SEM), before a more detailed analysis using Atomic Force Microscopy (AFM) and Optical Coherence Tomography (OCT) gave an overview of the mechanical properties and degradation rates. The rates agreed with previously established models, but imaging analysis led to new developments in the manufacturing process. Using an AFM bead functionalised with fibroblasts and characterising *ex vivo* implants from mice, helped monitor the behaviour and lifespan of the implants.

Moving from an engineering biomaterial to *ex vivo* tissue, mice tendons were obtained. The tendons were induced with a model of the terminal condition ARC syndrome. SEM of ARC syndrome tendons showed disorder throughout the hierarchy, and nanoscale imaging revealed a previously unreported swelling of the D-band in collagen, these findings were highly indicative of disorder. Having confirmed the D-banding swelling, a significant decrease of the Young's modulus of the tendons was found using AFM nanomechanics.

Having confirmed the suitability of AFM on tendons, healthy human skin biopsies were obtained. These were used to form a baseline for healthy skin

behaviour at the nanoscale. The addition of histological microscopy using picro sirus red stain allowed for more reproducible AFM measurements. Data analysis of the AFM images was significantly improved through the development of an image quantification protocol. This protocol allowed for rapid comparison of images based on a four-point dominant feature system.

Finally, this enhanced imaging and mechanical analysis system, termed Quantitative Nanomechanics (QNM), was applied to three patients with the fibrotic disorder scleroderma and matched healthy donors. Significant changes to the morphology of scleroderma collagen, along with an increase in Young's modulus was reported.

# Impact Statement

---

This work in this thesis has been presented in approximately a dozen conferences, seminars and away days, and published as nine articles.

The work in Chapters 3 and 5 were part of paid external corporate consultancies. The first consultancy was to investigate the effects of the manufacturing processes on collagen membranes, both on membranes currently produced (presented in this thesis) and prototypes (non-disclosure agreement, NDA). The second consultancy investigated the differences in ethnicity and age in different skin types. The protocol is presented, but the data is under an NDA.

Ethical approval for a clinical study into debrided surgical tissues from patients with Ehlers-Danlos syndrome (EDS) was written and approved. An honorary research fellowship at UCLH was obtained, and several patient-engagement and awareness day talks were given, mostly on the joint and soft tissue behaviour. This ethical approval has been duplicated at the University of Toronto, where patient recruitment is ongoing. The implications of the work to be performed on EDS has formed a part of the updated clinical classifications.

Other work was presented on scleroderma (Chapter 5) at patient-engagement events. Further information obtained from this work could be used in future patient literature. Work on the effects of dentinogenesis imperfecta has been turned into patient information leaflets, to help educate and raise awareness.

Training formed a large part of this research, with regular training on the AFM for group members. This culminated in an invited visit to the University of Toronto to help setup and train for their new AFM imaging suite.



## Scientific Publications

---

1. Aguayo, S., A. Strange, N. Gadegaard, M. J. Dalby, and L. Bozec. 2016. "Influence of Biomaterial Nanotopography on the Adhesive and Elastic Properties of Staphylococcus Aureus Cells." *RSC Advances* 6 (92): 89347–55.
2. Al-Azri, Khalifa, Lucia N. Melita, Adam P. Strange, Frederic Festy, Maisoon Al-Jawad, Richard Cook, Susan Parekh, and Laurent Bozec. 2016. "Optical Coherence Tomography Use in the Diagnosis of Enamel Defects." *Journal of Biomedical Optics* 21 (3): 036004.
3. Banushi, Blerida, Federico Forneris, Anna Straatman-Iwanowska, Adam Strange, Anne Marie Lyne, Clare Rogerson, Jemima J. Burden, et al. 2016. "Regulation of Post-Golgi LH3 Trafficking Is Essential for Collagen Homeostasis." *Nature Communications* 7 (July): 12111.
4. Calciolari, E., F. Ravanetti, A. Strange, N. Mardas, L. Bozec, A. Cacchioli, N. Kostomitsopoulos, and N. Donos. 2018. "Degradation Pattern of a Porcine Collagen Membrane in an in Vivo Model of Guided Bone Regeneration." *Journal of Periodontal Research* 53 (3): 430–39.
5. Loaiza, Sandra, Silvia A. Ferreira, Tamara M. Chinn, Alex Kirby, Elena Tsolaki, Camilla Dondi, Katarzyna Parzych, et al. 2018. "An Engineered, Quantifiable in Vitro Model for Analysing the Effect of Proteostasis-Targeting Drugs on Tissue Physical Properties." *Biomaterials* 183 (August): 102–13.
6. Lopez, H, B Abdi Ahmed, David Abraham, L. Bozec, Christopher Denton, Adam P. Strange, G Martin, and Richard Stratton. 2018. "Role of the Prolyl 3-Hydroxylase Leprel1 in Fibrosis." *Annals of Rheumatic Diseases* 77 (2).
7. Neel, Ensanya Ali Abou, A Aljabo, Adam P. Strange, S Ibrahim, M Coathup, AM Young, Laurent Bozec, and Vivek Mudera. 2016. "Demineralization–remineralization Dynamics in Teeth and Bone." *International Journal of Nanomedicine* 11: 4743–63. <https://doi.org/10.2147/IJN.S107624>.
8. Redha, O, Adam P. Strange, A Maeva, R Sambrook, N Mordan, A Mcdonald, and L Bozec. 2019. "Impact of Carbamide Peroxide Whitening Agent on Dentinal Collagen." *Journal of Dental Research*, 1–7. <https://doi.org/10.1177/0022034518822826>.
9. Strange, Adam P., Sebastian Aguayo, Tarek Ahmed, Nicola Mordan, Richard Stratton, Stephen R. Porter, Susan Parekh, and Laurent Bozec. 2017. "Quantitative Nanohistological Investigation of Scleroderma: An Atomic Force Microscopy-Based Approach to Disease Characterization." *International Journal of Nanomedicine* 12: 411–20.

# Declaration

---

I confirm that the work presented in this thesis is my own original work. When information has been derived from published work, it has been cited when appropriate. Results that have been published by my colleagues and me, or are pending publication, are also indicated. Samples obtained as a result of collaborations have been noted. External funding, and in particular commercial external funding, has been recognised in the acknowledgements section and at the start of every relevant chapter

Adam Philip Strange

# Acknowledgements

---

Firstly, I must extend my gratitude to my two supervisors, Dr Laurent Bozec and Dr Susan Parekh for their continued advice and support during the PhD. Without their support this thesis would not be where it is today; their consideration allowed me to pursue the varied topics found in this thesis.

Help was always given easily at the Eastman. Particularly, Dr Nicky Mordan, Dr George Georgiou and Dr Graham Palmer were constantly on hand to offer me technical advice, provide a view on my work from another angle or otherwise being friendly faces during my time. Dr Richard Thorogate at the LCN provided constant support for all of the AFM work performed.

Of course, peer help is invaluable. The members of the wider group could always be counted on for assistance – they made my journey much easier, whether in the lab or the office. Thank you to Alex, Angelica, Anna, Jacob, Lucia, Michael, Samera, Sebastian, Tarek, and Yingqi. There are many more people throughout the Eastman, UCL and London who provided their help.

No research is done in isolation: collaborations during my PhD came from the groups of Prof Paul Gissen, Prof Nikolaos Donos, Dr Eileen Gentleman and Dr Richard Stratton. Funded collaborations with Dr Hervé Pagon (L'Oréal), Dr Paul Buxton and Marco Mehr (Geistlich), as well as additional funding from the British Society for Oral and Dental Research (BSODR) and the Osteology Foundation. The main body of my funding came from the Paediatrics department of the Eastman Dental Hospital, with additional funding from Prof Stephen Porter and the Eastman Dental Institute.

Lastly, I have to thank my non-university friends who must have been baffled why I was still at university, and my family. My fiancée, dad, sister and all my family constantly gave me love and support. And, finally, to my mum, who would have been so happy to see this project finished.

# Table of Contents

---

<b>ABSTRACT .....</b>	<b>2</b>
<b>IMPACT STATEMENT .....</b>	<b>4</b>
<b>SCIENTIFIC PUBLICATIONS .....</b>	<b>5</b>
<b>DECLARATION .....</b>	<b>6</b>
<b>ACKNOWLEDGEMENTS .....</b>	<b>7</b>
<b>TABLE OF CONTENTS .....</b>	<b>8</b>
<b>TABLE OF FIGURES .....</b>	<b>11</b>
<b>LIST OF ABBREVIATIONS.....</b>	<b>15</b>
<b>1 INTRODUCTION.....</b>	<b>17</b>
1.1 COLLAGEN SYNTHESIS AND BEHAVIOUR .....	17
1.2 CLINICAL SIGNIFICANCE OF COLLAGEN .....	26
1.3 MEDICINE AT THE NANOSCALE .....	43
1.4 METHODOLOGY – PRACTICAL CONSIDERATIONS IN AFM USE .....	56
<b>2 AIMS AND OBJECTIVES OF THE THESIS.....</b>	<b>75</b>
2.1 RESEARCH QUESTION.....	75
2.2 THESIS OBJECTIVES .....	75
<b>3 MULTIMODAL CHARACTERISATION OF COLLAGEN SCAFFOLDS: TOWARDS A CLINICAL APPLICATION .....</b>	<b>76</b>

3.1	INTRODUCTION .....	76
3.2	AIM .....	77
3.3	OBJECTIVES.....	77
3.4	MATERIALS AND METHODS .....	78
3.5	PART A – COLLAGEN MEMBRANES.....	84
3.6	PART B <i>Ex-Vivo</i> ANIMAL MODEL .....	114
3.7	CHAPTER SUMMARY .....	129
<b>4</b>	<b>COLLAGEN DISEASE MODEL IN MICE .....</b>	<b>131</b>
4.1	INTRODUCTION .....	131
4.2	AIM .....	132
4.3	OBJECTIVES.....	132
4.4	MATERIALS AND METHODS .....	132
4.5	RESULTS AND DISCUSSION.....	135
<b>5</b>	<b>DEVELOPING QUANTITATIVE NANOHIOTOLOGY IN SKIN &amp; CASE</b>	
	<b>STUDIES OF SCLERODERMA .....</b>	<b>161</b>
5.1	INTRODUCTION .....	161
5.2	AIM .....	162
5.3	OBJECTIVES.....	162
5.4	MATERIALS AND METHODS .....	163
5.5	BLIND AFM IMAGING AND MECHANICS .....	169
5.6	LM-GUIDED QNH PROTOCOL .....	177
5.7	PART B - SSC CASE STUDIES.....	190
5.8	CHAPTER SUMMARY .....	224

<b>6</b>	<b>CONCLUSIONS AND FUTURE DEVELOPMENTS .....</b>	<b>226</b>
6.1	MULTIMODAL APPROACH.....	226
6.2	TENDON HIERARCHY AFFECTED BY INTERFIBRILLAR CROSSLINKS.....	228
6.3	TOWARDS QUANTITATIVE NANOHIOTOLOGY .....	229
6.4	FUTURE DEVELOPMENTS .....	231
6.5	SUMMARY .....	232
<b>7</b>	<b>BIBLIOGRAPHY .....</b>	<b>234</b>
	<b>APPENDICES.....</b>	<b>268</b>
	A.Optical Coherence Tomography .....	268
	B. Morphology And Mechanics Of Mice Tendons.....	278
	C. Bone Fragility Of Arc Syndrome Mice .....	284
	D. Mouse Model Of Scleroderma .....	293
	E. An Engineered, Quantifiable In Vitro Model For Analysing The Effect Of Proteostasis-Targeting Drugs On Tissue Physical Properties .....	301
	F. Impact Of Carbamide Peroxide Whitening Agent On Dentinal Collagen .....	311
	G. Influence Of Biomaterial Nanotopography On Adhesive And Elastic Properties Of Staphylococcus Aureus Cells.....	317
	H. Optical Coherence Tomography Use In The Diagnosis Of Enamel Defects .....	325
	I. Demineralisation-Remineralisation Dynamics In Teeth And Bone ...	336

# Table of Figures

Figure 1-1 Schematic representation of the main stages of collagen synthesis	20
Figure 1-2 Collagen fibril representation showing gap-overlap D-band structure	22
Figure 1-3 Structure of tendons showing the hierarchical organisation of collagen across length scales	25
Figure 1-4 Schematic representation of the skin layers.	28
Figure 1-5 Histology of the major skin layers.	29
Figure 1-6 TEM of collagen showing 'cauliflower' or 'galaxy' structures in EDS	35
Figure 1-7 Summary of the origin and effects of collagen diseases	40
Figure 1-8 Simplified representation of an AFM	58
Figure 1-9 Optimised gains for imaging from Bruker Nanoscope	62
Figure 1-10 Movement of the cantilever during indentation	66
Figure 1-11 AFM setup for indentation on JPK Nanowizard 1	67
Figure 1-12 Comparison between mechanics models	71
Figure 3-1 LM of AFM cantilevers	80
Figure 3-2 AFM cantilever functionalisation	81
Figure 3-3 Representative SEM images of collagen membrane BG showing typical surface features	85
Figure 3-4 Representative SEM images of collagen membrane MG showing typical surface features	86
Figure 3-5 Representative SEM images of bone substitute BO showing typical surface features	87
Figure 3-6 Representative SEM images of soft tissue substitute FG showing typical surface features	89
Figure 3-7 AFM surface images of BG in different locations	93
Figure 3-8 AFM mechanics for Young's modulus of BG in air	94
Figure 3-9 AFM mechanics for Young's modulus of BG in liquid	95
Figure 3-10 AFM surface images of MG in different locations.	96
Figure 3-11 AFM mechanics for Young's modulus of MG in air	97
Figure 3-12 AFM mechanics for Young's modulus of MG in liquid	98

Figure 3-13 (A) Adhesion force and (B) energy of BG when probed with MG-63 cells. _____	101
Figure 3-14 (A) Adhesion force and (B) energy of MG when probed with MG-63 cells. _____	103
Figure 3-15 Box plot summaries of (A) adhesion force and (B) adhesion energy	104
Figure 3-16 Left: B-scan images during degradation of BG, 0-80 minutes. Right: B-scans of the Density is measured by the red line, porosity on the green box and surface behaviour in blue _____	107
Figure 3-17 B-scan images during degradation of MG, 0-100 minutes. Density in red, porosity in green, surface in blue and surface compliance in purple _____	110
Figure 3-18 Light and dark field LM of the clavicular defect after 7 days of healing _____	115
Figure 3-19 SEM images of the membrane after 7 days of healing. _____	116
Figure 3-20 AFM of the membrane after 7 days of healing _____	117
Figure 3-21 Light and dark field LM of the clavicular defect after 14 days of healing _____	118
Figure 3-22 SEM images of the membrane after 14 days of healing _____	119
Figure 3-23 AFM of the membrane after 14 days of healing _____	121
Figure 3-24 Light and dark field LM of the clavicular defect after 30 days of healing _____	123
Figure 3-25 SEM images of the membrane after 30 days of healing. _____	124
Figure 3-26 AFM of the membrane after 30 days of healing in the red area _____	125
Figure 4-1 SEM of WT mouse tendon showing fascicle alignment _____	136
Figure 4-2 SEM of VIPAR mouse tendon showing some fascicle alignment _____	138
Figure 4-3 SEM of VPS33B mouse tendon showing disordered fascicles. _____	140
Figure 4-4 AFM of WT mouse tendon showing aligned fibrils in sheets _____	145
Figure 4-5 AFM of VIPAR mouse tendon on the glass surface _____	147
Figure 4-6 AFM of VPS33B mouse tendon on the glass surface _____	149
Figure 4-7 shows the D-band line profile analysis. _____	150
Figure 4-8 Young's modulus of WT tendon showing some bimodal distribution _	155
Figure 4-9 Young's modulus of VIPAR tendon _____	155



Figure 4-10 Young's modulus of VPS33B tendon _____	156
Figure 4-11 Young's modulus of all tendon samples showing comparisons ____	157
Figure 5-1 Image quantification examples _____	167
Figure 5-2 Image quantification graphs _____	168
Figure 5-3 Morphology of four locations of Patient 1 _____	170
Figure 5-4 Young's modulus of four locations of Patient 1 _____	172
Figure 5-5 Morphology of four locations of Patient 2 _____	173
Figure 5-6 Young's modulus of four locations of Patient 2 _____	175
Figure 5-7 LM of the section of Pt 3, 20x magnification _____	178
Figure 5-8 Morphology of four locations of Patient 3 _____	179
Figure 5-9 Image quantification damage markers of Patient 3 _____	180
Figure 5-10 Young's modulus of four locations of Patient 3 _____	181
Figure 5-11 LM of the section of Pt 4, 20x magnification _____	182
Figure 5-12 Morphology of four locations of Patient 4 _____	183
Figure 5-13 Image quantification damage markers of Patient 4 _____	184
Figure 5-14 Young's modulus of four locations of Patient 4 _____	185
Figure 5-15 LM of reticular dermis of NK (healthy) _____	191
Figure 5-16 SEM of NK _____	192
Figure 5-17 AFM of NK _____	193
Figure 5-18 Image quantification damage markers of NK _____	195
Figure 5-19 Young's modulus of NK _____	196
Figure 5-20 LM of reticular dermis of NR (SSc) _____	197
Figure 5-21 SEM of NR _____	198
Figure 5-22 AFM of NR _____	199
Figure 5-23 Image quantification damage markers of NR _____	200
Figure 5-24 Young's modulus of NR _____	202
Figure 5-25 Image quantification damage markers of LG _____	204
Figure 5-26 Young's modulus of LG _____	205
Figure 5-27 Image quantification damage markers of MA _____	206
Figure 5-28 Young's modulus of MA _____	207
Figure 5-29 Image quantification damage markers of FM _____	208

Figure 5-30 Young's modulus of FM _____	209
Figure 5-31 Image quantification damage markers of RT _____	210
Figure 5-32 Young's modulus of RT _____	211
Figure 5-33 Comparative green regions of healthy and SSc patients. _____	212
Figure 5-34 Comparative yellow regions of healthy and SSc patients. _____	213
Figure 5-35 Comparative red regions of healthy and SSc patients. _____	214
Figure 5-36 Combined damage markers of the red region _____	215
Figure A-1 en-face and B-scan during collagen degradation at T0 on BG _____	268
Figure A-2 en-face and B-scan during collagen degradation at T20 on BG _____	269
Figure A-3 en-face and B-scan during collagen degradation at T40 on BG _____	270
Figure A-4 en-face and B-scan during collagen degradation at T60 on BG _____	270
Figure A-5 en-face and B-scan during collagen degradation at T80 on BG _____	271
Figure A-6 en-face and B-scan during collagen degradation at T0 on MG _____	272
Figure A-7 en-face and B-scan during collagen degradation at T20 on MG _____	273
Figure A-8 en-face and B-scan during collagen degradation at T40 on MG _____	274
Figure A-9 en-face and B-scan during collagen degradation at T60 on MG _____	275
Figure A-10 en-face and B-scan during collagen degradation at T80 on MG _____	276
Figure A-11 en-face and B-scan during collagen degradation at T100 on MG _____	277
Figure C-1 SEM of control mouse skin showing surface features and fibrils within surface cracks _____	279
Figure C-2 AFM of control mouse tendon. _____	281
Figure C-3 AFM mechanics of control mouse tendon _____	283
Figure D-1 Graph showing compressive load through indentation _____	286
Figure D-2 Graph showing the yield stress through indentation _____	287
Figure D-3 Graph showing Young's modulus through indentation _____	288
Figure D-4 shows $\tan \delta$ of mouse bones _____	289
Figure E-1 Light field LM of the fibroblast KOs after purification _____	294
Figure E-2 SEM of fibroblast cells on glass slides _____	295
Figure E-3 AFM of proteins after precipitation _____	296
Figure E-4 Young's modulus of WT, SKO and DKO showing unimodal distribution _____	297

# **List of Abbreviations**

---

AFM – Atomic Force Microscopy

AGE – Advanced Glycation Endproducts

ARC – Arthrogryposis, Renal failure, and Cholestasis syndrome

BG - Bio-Gide membrane

BO – Bio-Oss

DI– Dentinogenesis Imperfecta

DMT - Derjaguin-Muller-Toporov model

ECM – Extracellular Matrix

EDS – Ehlers-Danlos Syndrome

ER – Endoplasmic Reticulum

FG – Fibro-Gide

JKR - Johnson-Kendall-Roberts model

KO/SKO/DKO – Knock Out/ Single/Double Knock Out

LM – Light Microscopy

MG - Mucograft

OCT – Optical Coherence Tomography

OI – Osteogenesis Imperfecta

PS – PicroSirus Red

QNH – Quantitative Nanohistology

SEM – Scanning Electron Microscopy

SSc – Systemic Sclerosis

TEM – Transmission Electron Microscopy

VIPAR - VPS33B Interacting Protein, Apical-basolateral polarity Regular

VPS33B - Vacuolar Protein Sorting-associated protein 33B

WT – Wild Type

# 1 Introduction

---

Few proteins are as essential to animal life as collagen. This family are ubiquitous in the animal kingdom, having crucial and wide-ranging functions throughout the body <sup>1,2</sup>. As a part of the scleroprotein family, these functions are mostly structural, such as in tendons, bones and cartilage; at the cellular level, collagen provides support for cell attachment and adhesion, as well as communication through mechanotransduction <sup>1,3–6</sup>. Less common uses include functions as transport co-proteins, and modification through the addition of glycoproteins further the many applications of collagen <sup>7,8</sup>. Defects, diseases and disorders of collagen can be life-threatening and pervasive <sup>9–11</sup>. These diseases are chronic and progressive with difficulties in diagnosis. Diseases of collagen are often hereditary or progressive conditions, with limited treatment options available <sup>9,12–15</sup>.

## 1.1 Collagen Synthesis and Behaviour

### 1.1.1 Intracellular Activity

All collagens consist of polypeptide chains with a triple helix structure <sup>2,16–18</sup>. Type I collagen is synthesised from the transcription of *COL1A1* and *COL1A2* genes<sup>19,20</sup>. Recently-transcribed mRNA moves to the cytoplasm and is translated at the cytoplasm. Transcription of type I collagen has been well characterised and forms the basis of much of what is understood in collagen formation <sup>1</sup>. Chains  $\alpha_1(\text{I})$  and  $\alpha_1(\text{II})$ , are coordinately regulated in a stochastic ratio of 2:1 to form a heterotrimer

<sup>13,21,22</sup>. At this stage, the molecules are referred to as pre-pro-polypeptides, which are sent to the endoplasmic reticulum (ER) for further modification <sup>23–25</sup>.

Post-translational modification begins at the ER <sup>26,27</sup>. Though most of the enzymatic reactions are complex and occur throughout the process of collagen synthesis, three essential modifications are made at this stage <sup>5</sup>. Initially, the N-terminal signal peptide is removed and returned to the ribosomes, acting as a negative feedback loop <sup>28–30</sup>. Secondly, amino acids lysine and proline are hydroxylated, using hydroxylase enzymes with ascorbic acid as the cofactor <sup>12,16,22,31,32</sup>. Thirdly, the hydroxylated lysine is glycosylated by glycosyltransferases with glucose and galactose <sup>33–35</sup>. At the end of this third stage, the molecule is referred to as pro-collagen. Three of the modified chains with a left-handed twist combine in a zipper-folding to form a right-handed triple helix, at the step known as registration <sup>18,36,37</sup>. The pro-collagen fibrils can only wind in this specific arrangement due to the presence of the glycine; the small amino acid sits inside the helical structure, with the other amino acids taking positions on the outside of the chain<sup>9,38,39</sup>.

After registration, the pro-collagen is sent to the Golgi body, an organelle with distributive and extra-cellular transport functions <sup>25,40</sup>. Pro-collagen is packaged at the Golgi body where it is further modified with oligosaccharides <sup>40,41</sup>. Membrane transport proteins actively transport the peptides to the extracellular environment <sup>41</sup>.

### 1.1.2 Extracellular Interactions

Additionally, alterations to procollagen occur extracellularly, as proteinases are required to cleave the N- and C-terminals, found at the termini of the pro-collagen

molecule <sup>20,22,42,43</sup>. Collagen peptidases are used to scission the end groups of the pro-collagen molecule, with the end groups returning to the fibroblasts <sup>16</sup>. These scissioned end groups act as a negative feedback system, with excess end groups signalling that sufficient collagen has been secreted <sup>16</sup>. As collagen is a biopolymer, the terminal ends also prevent pro-collagen from polymerising intracellularly <sup>1,44</sup>. Extracellularly, these ends are cleaved, reabsorbed into the cell, and the procollagen is allowed to form the long chain collagen molecules in the extracellular space <sup>22,45</sup>. At this stage, the molecule is known as tropocollagen.

The final stage of collagen synthesis is fibrillogenesis. Two key enzymes are copper-dependent lysyl oxidase and lysyl hydroxylase, which catalyse lysine and hydroxylysine to form intermolecular covalent cross-links <sup>1,16,46</sup>. These cross-links pull the collagen into a head-to-tail arrangement, which is essential in giving collagen strong mechanical properties in that direction <sup>7,47</sup>. Glycine contains a single hydrogen molecule as its side-chain, providing a small internal space to allow for the tight winding of the collagen fibril <sup>48-50</sup>. Depending on the function of the collagen, at this stage fibrils will form a distinct hierarchy, bundling into larger collagen units of fibrils and fibres <sup>51</sup>.

### 1.1.3 Collagen Cross-Linking

As tropocollagen molecules assemble into fibrils, stabilisation is performed by weak van der Waals forces and hydrogen bonds <sup>25,52</sup>. Enzyme-mediated bonds are required for further long-term stabilisation, and the reactions of lysyl oxidase (and the essential role this enzyme plays in collagen) have been mentioned above. However,

not all cross-links and interactions with collagen have an enzymatic component. Collagen undergoes a high level of hydroxylation and glycosylation, using ascorbic acid, manganese and iron as various cofactors <sup>1,16</sup>. The nature of this process is still debated, although the degree of glycosylation increases with ageing, forming advanced glycation end-products (AGE) <sup>53–56</sup>. These AGE products are currently believed to be directly responsible for the majority of non-enzymatic crosslinking <sup>57–59</sup>. It has been further observed that patients with diabetes have an increased glycosylation level than their age would suggest, so it is reasonable to assume that higher levels of circulatory glucose (and its poor systemic control) increases glycosylation <sup>54,58,60</sup>. In this way, collagen molecules undergo continuous and varied modifications at several stages, and this is also linked to the age and morbidities of the individual.

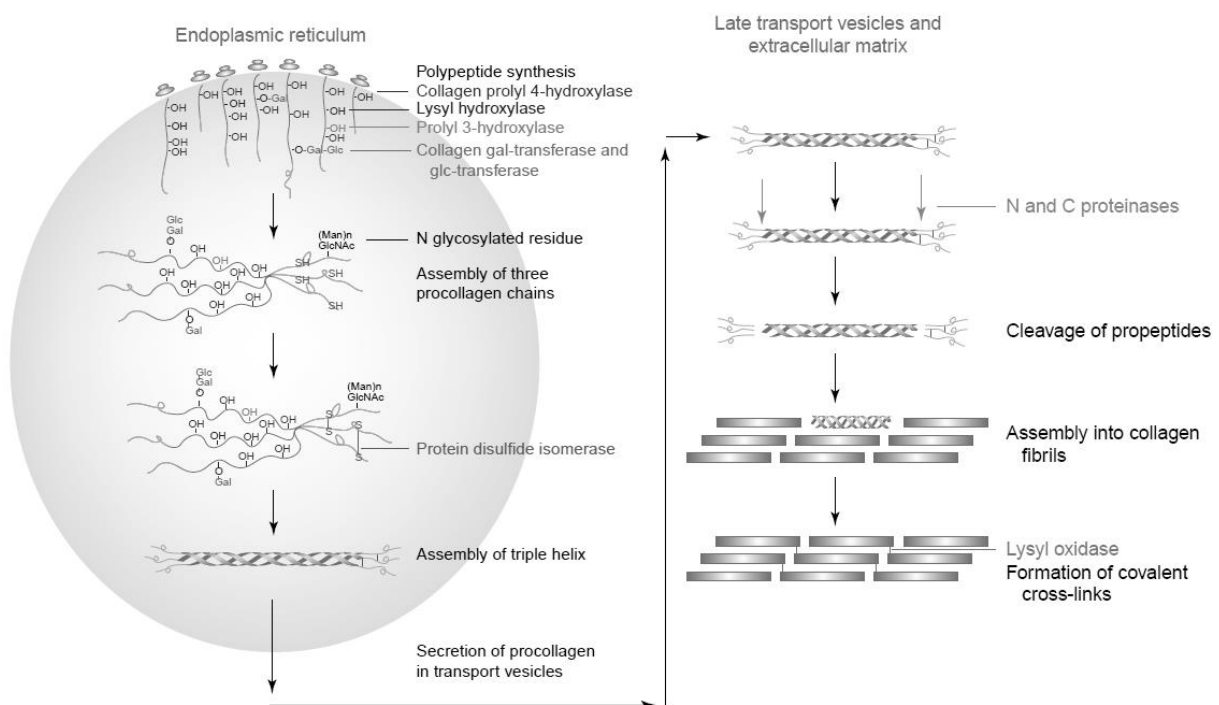


**Figure 1-1 Schematic representation of the main stages of collagen synthesis**<sup>25</sup>



#### 1.1.4 Collagen Ultrastructure

Several models have been suggested to explain the 3D structure of collagen fibrils<sup>53</sup>. Historically, a simplified stacking model of collagen was promulgated, with amino acids, residues found periodically along the tropocollagen molecule<sup>61,62</sup>. This was proposed as Hodge and Petruska's quarter-staggered end overlap, which has four tropocollagen molecules crossing each gap and overlap region<sup>62</sup>. Advances in the use of X-ray diffraction confirmed this stacking system in 1D space<sup>63</sup>. The stacking in fibrillar collagens gives rise to a phenomenon known as the D-band<sup>1</sup>. The overlap occurs every 67 nm irrespective of fibril diameter, allowing unambiguous identification of a dark annular area on collagen fibres<sup>12,19,64-66</sup>. The D-band period is made by four and a half collagen molecules, as the length of the collagen molecule is 300 nm, and the D-band staggered distance is 67 nm<sup>67</sup>. The 2D model is represented in Figure 1-2. This unique structure allows for identification of collagen when using high powered microscopy such as SEM, TEM or AFM, as the repeated structure can be readily seen<sup>68,69</sup>. This identification, however, is predicated on ordered fibrillogenesis; changes to collagen formation could disrupt or remove the D-band entirely<sup>65,69,70</sup>. In terms of gap to overlap proportion of the D band, the gap region represents 60% of the repeating pattern, with the overlap taking the remaining 40%<sup>71</sup>.

Simplistic, this model caused several issues arising from the fact that collagen was only modelled as a flat molecule in one dimension, and that contemporary imaging only allowed for 1D or 2D geometric reconstructions in Transmission

Electron Microscopy (TEM), instead of a complex 3D structure <sup>53,72,73</sup>. However this 2D model cannot be fully realised in 3D, as the tight molecular packing does not allow for all of the molecules to occupy the available space <sup>51,74,75</sup>. Finally reconciling the contradictions of Hodge and Petruska's model, Smith suggested that there was a hollow pentagonal microfibril being formed by collagen <sup>69,76,77</sup>.

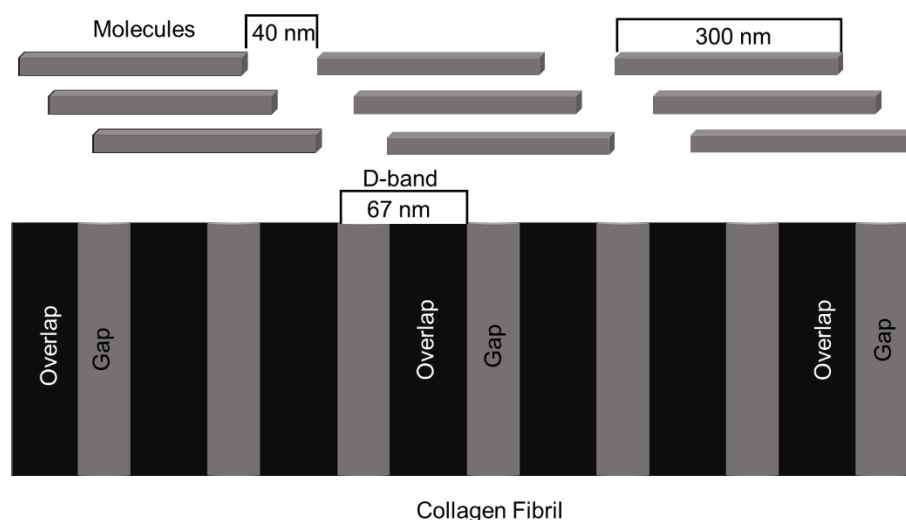


**Figure 1-2 Collagen fibril representation showing the gap-overlap D-band structure**

Intermediary work was performed by several groups, theorising that the five tropocollagen molecules were in a crystalline lattice, forming a hexagon <sup>78</sup>. This was improved by suggesting that the overlap (banded) collagen zone is hexagonal crystalline in nature, but the gap zones are highly disordered <sup>66,79</sup>. Combining the model improvements, Orgel proposed that five tropocollagen molecules are staggered and discontinuous, but form a “quasi-hexagonal” packed structure, which can easily interact with other tropocollagen in the microfibril, which has a right-handed twist for the whole molecule <sup>78,80,81</sup>. Orgel included the latest discoveries in collagen modelling, and allows for a simplified system to explain collagen behaviour,

as further supported with recent work <sup>4,59,67,81,82</sup>. While imperfect however, the model presented by Hodge and Petruska remains valid as a visualisation concept for flattened 2D projections (such as in Figure 1-2), which are often used for imaging <sup>83–87</sup>.

#### 1.1.5 Collagen Types

Twenty-nine (I – XIX) different types of collagen in humans have been identified and catalogued in humans <sup>12,16,17</sup>. In terms of broad categorisation, collagen can be separated into three distinct groups, fibril-associated collagens with interrupted triple helices (FACITs), fibrillar and non-fibrillar collagens. This is based on how the collagens form their supramolecular arrangements, and often determines where the collagens will be found *in vivo* <sup>7,17</sup>. FACITs are the smallest group of collagens, and can be found on their own, or combined with other collagen fibrils, but regardless of location, they tend to provide elastic and compression support <sup>7,41,88</sup>. Non-fibrillar collagens perform other supportive or communicative functions throughout the body, either as long-chain molecules or single molecules. Collagen IV is the most prevalent non-fibrillar collagen and forms mesh networks on the basement membranes and basal laminae of most cells <sup>16,46</sup>. However, this support is not considered to extend to mechanical support for the extra-cellular matrix (ECM), and rather acts as a filtration network <sup>1</sup>. Mechanical support is provided by the final class of collagens, the fibrillar collagens. These fibrillar collagens will be of particular interest in this thesis.

#### 1.1.6 Fibrillar

Fibrillar collagens are comprised of types I, II, III, V, XI, XXIV and XXVII, and are the most abundant type in the body <sup>2,78,89</sup>. The fibrous nature of these collagens allows for anisotropic tensile strength along the fibre axis <sup>1,12</sup>. Fibrillar collagens are secreted with varying length scales; the lengths homogenise in healthy adults for most tissues <sup>1</sup>. Fibrillar collagens contain thousands of amino acid residues in long chains, increasing the strength of the fibres <sup>1,16</sup>. These binding sites allow for intramolecular cross-linking, which stabilises the collagen molecule and helps to give fibrillar collagen an increased level of mechanical properties <sup>46</sup>. The hierarchical structure of collagen tissues functions to improve and maintain the mechanical properties <sup>90–92</sup>. This can be seen in a tissue such as a tendon, which has increasing levels of structural complexity from nanometres to centimetres (Figure 1-3). However, out of all of the collagens, only type I has been shown to form the D-band periodicity structure <sup>36,93,94</sup>. The presence of D-banding provides an effective means of identification for fibrillar collagens under high powered microscopy in skin, tendons and ligaments <sup>70,95–97</sup>.

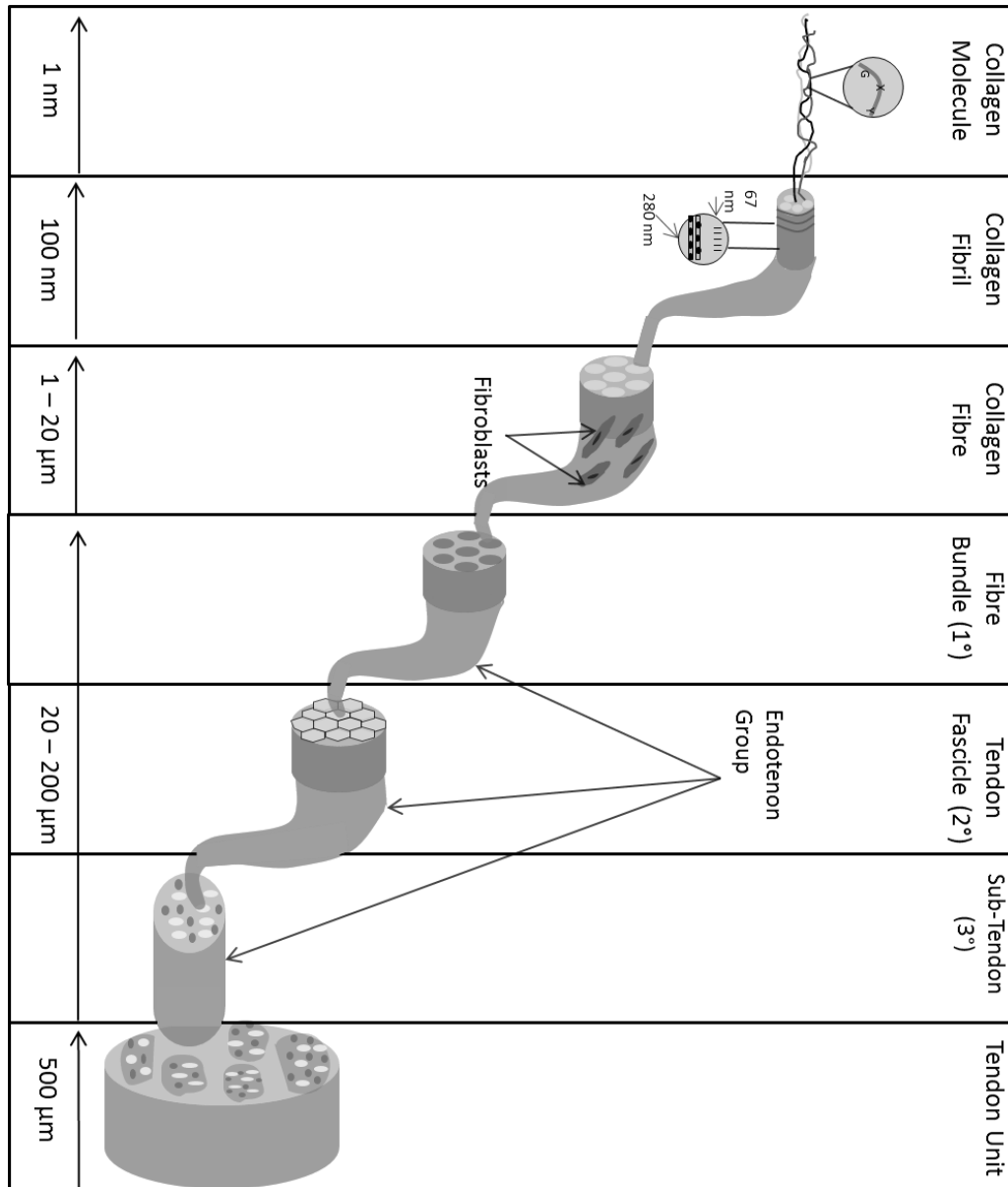


**Figure 1-3 Structure of tendons showing the hierarchical organisation of collagen across length scales**

## 1.2 Clinical Significance of Collagen

The importance of all collagen types in the healthy functioning of the body is well understood. Diseases and disorders of collagen can occur at every stage of collagen synthesis, and throughout the ageing process of collagen <sup>12,98–101</sup>. Several disorders will be investigated in detail throughout this thesis; those diseases have their own sub-sections background information. Most collagen diseases are found predominantly or exclusively in the skin. An understanding of the organisation of the skin, therefore, is essential.

### **1.2.1.1 Skin Structure**

The functions of the skin are numerous; however, they can generally be grouped into four main categories: barrier protection, sensation, thermoregulation and metabolic functions. For the purpose of this thesis, it is the barrier protection through support of the underlying tissues that are of interest. The histology of skin is also complex, comprising three main layers, the epidermis, dermis and hypodermis. Two images of skin anatomy, one as a schematic and the other as a histology image are presented in Figure 1-4 and Figure 1-5.

The epidermis is the external layer of the skin, closest to the outside world. This is also the thinnest layer and acts to protect the deeper layers of the skin <sup>102</sup>. Thin skin, which is found across most of the body) has four layers of cells in the epidermis. Apart from the basal layer (stratum basale), these cells do not divide and have minimal cellular activity <sup>102</sup>. The basal layer is also responsible for excreting collagen type IV to form the basement membrane, anchoring the epidermis and dermis. The

final surface layer is often the most visible at low power under histology and is known as the stratum corneum <sup>103</sup>. This layer is comprised of thick layers of dead cells which are highly keratinised <sup>104</sup>. The integrity of the stratum corneum is an indicator of the health of the epidermis layer; cells are replaced after 14-28 days so any change to the basal layer can be rapidly noticed at the stratum corneum <sup>105,106</sup>.

The dermis is the middle layer of the skin, and the main focus of the skin samples taken for this thesis. This is comprised of three major cell types, adipocytes, macrophages and collagen-producing fibroblasts <sup>107,108</sup>. The extracellular matrix of the dermis is dominated by collagen, although elastin, glycosaminoglycans, proteoglycans and glycoproteins make up the non-collagenous material present <sup>75,109</sup>. The dermis is itself split into two main layers. The upper layer is the papillary dermis, where loosely arranged collagen fibres and loose connective tissues are found <sup>32</sup>. Dermal papillae, small extensions of the dermis into the epidermis, responsible for fingerprints, also originate here <sup>110</sup>. The much larger lower layer is the reticular dermis, containing dense irregular connective tissue and densely packed collagen <sup>32</sup>. The alignment of the collagen changes throughout the body, with Langer's lines, shows the direction of tension in the particular area <sup>111</sup>. Hair follicles, sebaceous glands and vasculature are also present <sup>102</sup>.

The hypodermis is the lowest layer of the skin <sup>112</sup>. This is the subcutaneous region, predominantly made of lipid lobules and some loose connective tissue with collagen similar to the epidermis <sup>113</sup>. Adipose cells are found in the highest concentration here, and the largest blood vessels and nerves of the skin are connected in this layer, to serve the rest of the skin <sup>102</sup>. The primary immune and

glandular responses of skin are focused on the hypodermis <sup>114,115</sup>. While it plays an essential role in the coordination and nourishment of the other two skin layers, the high percentage of subcutaneous fat makes the analysis of the other components in this region difficult <sup>116,117</sup>.

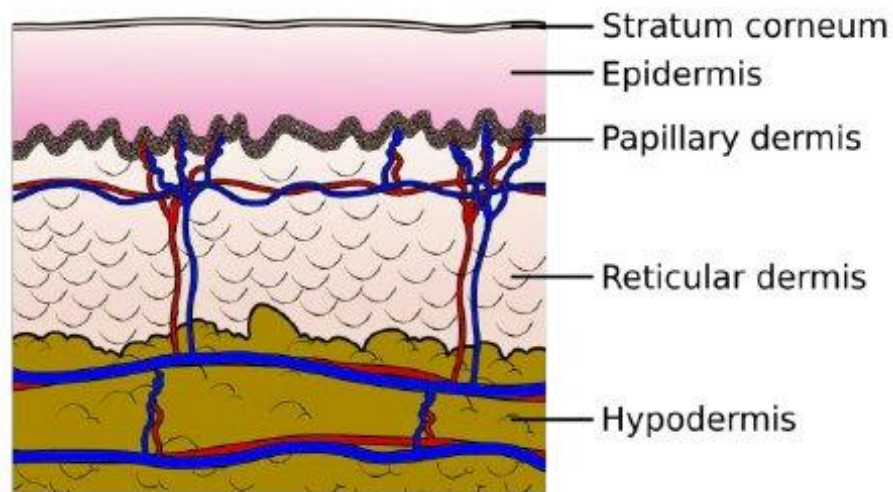


**Figure 1-4 Schematic representation of the skin layers. From <sup>118</sup>**



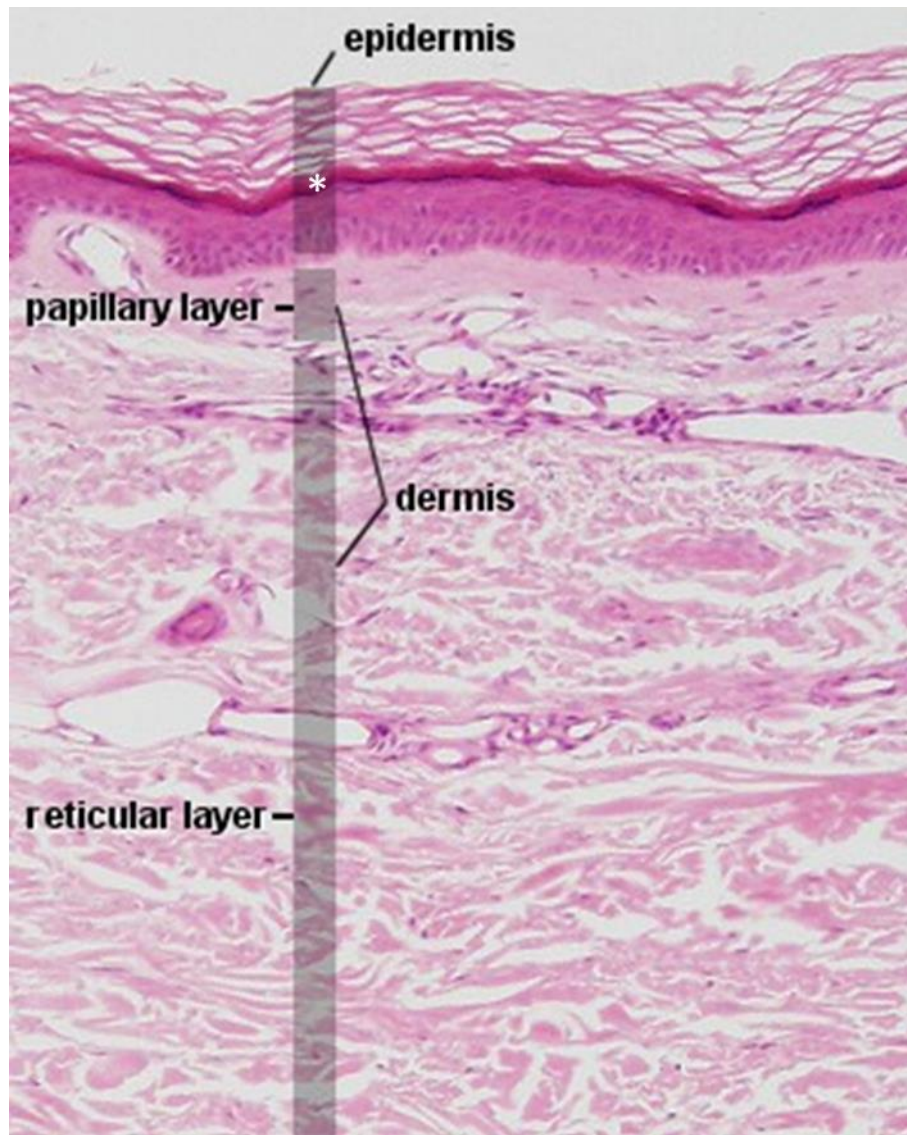


Figure 1-5 Histology of the major skin layers. The stratum corneum is labelled with an asterisk, with layers of stratum corneum seen peeling off the surface

#### **1.2.1.2 Diseases Linked to Collagen**

The role of vitamin C/ascorbic acid as a cofactor in intracellular hydroxylation has already been discussed <sup>31,32</sup>. A deficiency in water-soluble ascorbic acid is most commonly associated with the disease scurvy, although the role of the vitamin in the immune system, wound repair and as an antioxidant is well established <sup>119–121</sup>. As there is limited ascorbic acid available to act as a cofactor, patients initially present

with fatigue, weakness, and impaired wound healing <sup>119</sup>. While often thought of as a historical disease, it is becoming more common in the developed world due to inadequate nutritional intake <sup>122</sup>.

Diabetes has been previously discussed as leading to a change in collagen behaviour due to the relatively rapid formation of AGEs <sup>55,123</sup>. However, senescence itself plays a role in the changing properties of collagen <sup>124,125</sup>. Changes to the water retention of the stratum corneum, transepidermal water loss, skin pH and sebum content are all known to be caused due to the ageing of the skin, which can influence the behaviour of the skin at the nanoscale <sup>59,126</sup>. However, this ageing process is not solely due to chronological senesce, as premature ageing of the skin can occur. Most often this is to ultraviolet radiation from excess sun exposure, with malignancy a more severe threat <sup>114,124,127</sup>.

More rarely, Alport and Goodpasture syndromes are described in terms of their effects on the secondary and tertiary structure of collagen <sup>49</sup>. Other diseases, such as rheumatoid arthritis, systemic lupus and Menkes' disease can interfere with collagen at any stage of its synthesis, although most diseases impacts procollagen before secretion into the extracellular space, and before fibrillogenesis begins<sup>11,128,129</sup>.

### 1.2.2 Osteogenesis Imperfecta (OI)

While many collagen diseases often associated with the skin, there are other collagen disorders where the skin is not the focus of the main symptoms.

Referred to as ‘brittle bone disease’, osteogenesis imperfecta (OI) is another heterogeneous collagen disorder, linked to a genetic defect in type I collagen <sup>130,131</sup>. The main symptoms are bone fragility and low bone mass. Some skin hyperelasticity and joint hypermobility are recorded, but blue coloured sclerae, potential dental abnormalities and congenital hearing loss can help to distinguish it from the much greater elasticity experienced in EDS <sup>132</sup>. Eleven different variations of OI are recognised, with some giving a mild phenotype (type I) others a degenerative phenotype (III, IX, XI) and others still being severe (VII, VIII) or lethal (II, VII) <sup>131,133</sup>.

The variation in phenotypes is predominantly linked to defects in *COL1A1* and *COL1A2* <sup>1,134</sup>. Again, however, mutations in genes related to the activity of lysyl oxidase in some types implicate pathological post-translational modification cross-linking as a cause <sup>134–136</sup>. The diagnosis of OI is primarily differential, based on the signs and symptoms previously stated. Current indications suggest that upwards of 90% of type I collagen defects can be tested with genetic testing, but several types of OI are not linked to *COL1A1/2* mutations <sup>131</sup>. The presence of blue sclerae is often a significant sign of OI and is a recommended investigation for all paediatric patients presenting with suspicious fractures. Other objective diagnostic tools are dual-energy x-ray absorptiometry and computed tomography to indicate widespread changes to bone density and activity <sup>99,137</sup>.

OI was initially associated with abnormalities in the structure and synthesis of type I collagen. As most of the models of type I collagen formation have been made in fibroblasts, it should be noted that collagen synthesis in bone takes place in osteoblasts, which are suggested to have a different post-translational modification

pathway than fibroblasts <sup>138</sup>. The importance of glycine in fibrillogenesis has already been discussed; glycine in every third position on an alpha polypeptide chain allows for tight winding of the fibril <sup>48,139</sup>. The most common *COL1A1* and *COL1A2* mutations alter the ratio and position of the glycine residue. The severity of OI that occurs is dependent on which alpha chain is affected, the location of the amino acid substitution, and the amino acid substitution that occurs <sup>140</sup>. Often the mutations are not homogenous, and a mixture of typical and atypical collagen will be produced if the mutation is not lethal. Other mutations of the genes include a premature stop codon or non-sense mediated mRNA error <sup>141</sup>. This generally does not allow for abnormal collagen to be formed, and would not prevent the formation of healthy collagen, but it is heavily reduced from the expected amounts <sup>142</sup>. When abnormal collagen is released, however, it is noted to be significantly weaker than normal collagen. This change in structural support of the collagen is indicated as a factor in the repeated bone fractures experienced by OI patients <sup>140,143</sup>.

### 1.2.3 Dentinogenesis Imperfecta (DI)

Dentinogenesis Imperfecta (DI) is related to OI, in that they are both collagen diseases that affect mineralised tissues. There are three types of DI. DI type I is co-morbid with OI (sometimes referred to as OIDI) and arises from the same mutations in *COL1A1* and *COL1A2* <sup>13,144</sup>. The clinical presentation of OIDI is also varied, affecting approximately 50% of children with OI Types I, II and IV <sup>145</sup>. The two other types are DI type II (not associated with OI) and DI type III (rare and also not

associated with OI, and found in certain ethnic groups) are caused by mutations in the dentine sialophosphoprotein (DSPP) gene <sup>146,147</sup>.

Whereas OI affects bone, all types of DI affect dentine in the teeth. Dentine is the mineralised matrix situated within the core of the tooth. Dentinal tubules run throughout the thickness of the dentine and contain the cytoplasmic extensions of odontoblasts, responsible for formation and maintenance of the dentine<sup>147–149</sup>. Although dentine is broadly similar to bone, both its creation and overall architecture present some key differences when compared to bone matrix <sup>150</sup>. Dentine is a calcified tissue formed through dentinogenesis, which results in the conversion of unmineralised pre-dentine into mineralised dentine <sup>151</sup>. At the end of dentinogenesis, 20% of the mass is fibrillar collagen. Similar to the bone, collagen fibres form a consistent distribution of interrupted striations and thinner fibrils, thus building an overall collagen network <sup>92</sup>.

While the effect of OI on bones has been well reported and studied, there is a lack of reported outcomes for OIDI in teeth. These teeth present an increased susceptibility to wear and fracture similar to the bones found in OI <sup>152</sup>. The primary dentition usually is more severely affected than the permanent teeth <sup>14</sup>. The enamel layer is regular, but spontaneous enamel chipping results in dentinal wear; which can be accompanied by periapical pathology in the more severe forms of OIDI. The failure rate of fillings has also been observed to be higher in patients with OIDI, yet the cause is not known. There is an apparent loss of mechanical strength in this collagen which affects the dentine and the teeth; however, this has yet to be fully quantified <sup>14</sup>.

#### 1.2.4 Ehlers-Danlos Syndrome (EDS)

Ehlers-Danlos Syndrome (EDS) is a collection of heterogeneous, rare connective tissue characterised by abnormal skin elasticity and abnormal joint mobility and forms a part of a class of diseases known as hypermobility disorders <sup>100</sup>. The exact number of patients with a hypermobility disorder is hard to ascertain due to the complex and varied nature of symptoms, but estimates have ranged from 2% of the population to 0.2%, without apparent distinction of race or gender <sup>100,153,154</sup>. Most patients can be diagnosed in the clinic, with EDS described as being a “diagnosis of exclusion;” where possible complex cases can be sent for genetic or, rarely electron microscopy analysis (Figure 1-6) <sup>155–158</sup>. Recent attempts to reclassify the disease led to the suggestion that EDS should be renamed “the Ehlers-Danlos Syndromes” as the variability between the EDS types makes diagnosis and treatment complicated and balancing acts. Some of the rarest types of EDS have very few reported patients, sometimes a rare as symptoms being identified in a single family or individual <sup>159–163</sup>.

Clinically, patients with classic or hypermobility EDS may start to manifest symptoms between 4-6 years of age <sup>158,164</sup>. Often, these are ease of bruising, skin hyperextensibility, joint hypermobility, atrophic scarring and a generalised fragility of connective tissues <sup>165,166</sup>. As with most collagen-based disorders, it is the dermatological symptoms that are likely to be detected early. After further investigation, the presence of calcified spheroids and piezogenic papules may be recognised on the limbs and especially at the base of the foot <sup>167</sup>. On taking a history

recurrent joint dislocations and slow healing from scrapes to the knees and arms are frequently reported for various types of EDS. Symptoms of classic EDS but with the addition of tooth loss and periodontal weakness may suggest periodontal EDS <sup>168,169</sup>. A family history of unexpected heart attacks and sudden deaths are often indicators of the life-threatening type, vascular EDS <sup>165,166,170</sup>.

Testing for the vascular type usually is also confirmed through genetic tests, mostly from an abundance of caution <sup>170</sup>. There is an advantage in that mutations in intron 14 of *COL3A1* has been linked solely to vascular EDS, whilst experimental diagnostic techniques such as siRNA analysis have been seen to discriminate between normal *COL3A1* and mutated *COL3A* <sup>38,171,172</sup>.

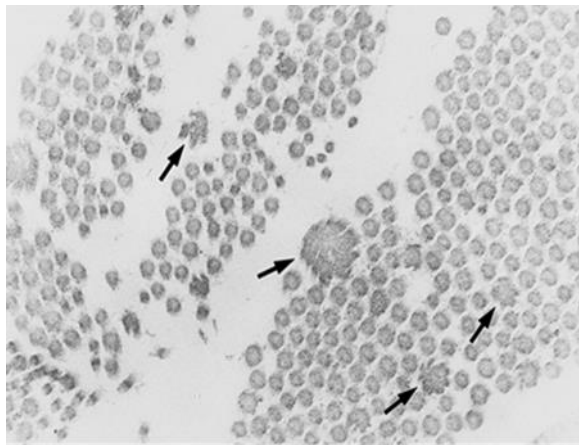


**Figure 1-6 TEM of collagen showing 'cauliflower' or 'galaxy' structures in classic EDS** <sup>173</sup>

The most well-reported mutations in collagen for EDS are in the genes *COL3* and *COL5* <sup>156,171</sup>. Other mutations causing the misplacement of a stop codon in *COL5A1* is thought to be at least partially responsible for *COL5A1*-linked mutations in type I, III, and V collagen<sup>156</sup>. Experimental techniques such as the addition of siRNA in vascular EDS patients can show the reversion of the mutation;

conformational changes in collagen which resulted in the collagen appearing to take on a typical structure as if it were coded for by a correct version *COL3A1* <sup>171,172</sup>. However, it is not always possible to obtain a diagnosis through genetic or clinical testing. Hypermobility EDS (type III) has no identified collagen mutation, with the characteristic symptoms of hypermobility and classic EDS often masked <sup>164,174,175</sup>. Further speculation suggests that the deletion or skipping of exons in *COL5A1*, is a leading cause of EDS, as glycine is not as prevalent in the collagen <sup>164</sup>.

Very little work has been performed in terms of cellular mutations and mechanics, but fibroblasts have shown a reduced mRNA level of pro $\alpha$ 1(V) relative to the mRNA level for pro $\alpha$ 2(V) in coding for collagen V <sup>156</sup>. Lysyl oxidase PLOD1/LH1, essential in the post-translational modification of collagen, is mutated in some patients with kyphoscoliotic EDS <sup>176,177</sup>. There are also mutations which are linked to a tenascin-X on V1195M which can be found in EDS patients (tenascin-X linked EDS was not recognised in the Villefranche nosology), but minimal observed changes in the mechanical and thermochemical properties suggest that this is not a cause of hypermobility EDS <sup>3,159</sup>. Recent reclassifications have sought to include tenascin linked conditions as a subcategory of EDS <sup>163</sup>.

#### 1.2.5 Scleroderma (SSc)

Scleroderma, or systemic sclerosis (SSc), is a multi-systemic collagen disorder of indeterminate aetiology <sup>178,179</sup>. It can be characterised primarily by the severe fibrosis of skin and viscera, but widespread vasculopathy and a spectrum of other features can arise <sup>179</sup>. SSc can cause significant physical impairments, which are



often reported as reducing the patients' quality of life <sup>110,180</sup>. SSc occurs globally, with females significantly more frequently diagnosed than males but without a racial bias <sup>181</sup>. The precise cause of scleroderma remains unknown, although the most significant predictive factor remains the identification of an SSc diagnosed relative, suggesting a hereditary factor <sup>182,183</sup>. No conclusive genetic or biomarkers have been identified for the diagnosis of SSc <sup>184</sup>. There are two broad types of SSc, denoted as limited and diffuse cutaneous SSc <sup>185–187</sup>. Limited cutaneous SSc primarily causes vasculopathy with slow fibrosis whereas diffuse cutaneous SSc is dominated by the rapid fibrosis of skin and organs <sup>188</sup>. Diffuse cutaneous SSc is often identified earlier than limited cutaneous SSc in clinic <sup>188</sup>.

The diagnosis of the disease is performed through clinical investigation via a differential diagnosis approach. Histological biopsies of the skin can prove useful in later-stage SSc, though after the disease has progressed a visual assessment in the clinic is often sufficient and avoids aggravating any skin lesions<sup>110,189</sup>. Biopsies of other commonly affected areas such as the liver, lungs or kidney can be taken to gain a complete diagnosis of the subtype, and have some usefulness in the prognosis of the disease <sup>190–192</sup>. There is a well-recognised need for earlier, faster and more diagnosis of SSc, as a late stage diagnosis severely limits treatment options <sup>180,183,193</sup>. Some methods have been tried to detect the early onset or spread of SSc. One such approach has been the use of optical coherence tomography (OCT). This has been used to limited effect in monitoring the blood flow in the fingers and the nail bed <sup>191,194</sup>. These studies did not appear to distinguish between the subtypes of SSc investigated; it is reasonable to assume however that by looking for vascular changes

that their focus was on limited cutaneous SSc. Irrespective of the investigations, however, current OCT research is as yet unable to distinguish between the density of healthy skin, keloid scar formation and an SSc lesion, limiting its use <sup>110</sup>.

SSc is often referred to as being a skin disorder, however it affects collagen throughout the body, and the effects of this should not be overlooked <sup>182,189,193</sup>. SSc is believed to be associated with an excess of collagen cross-linking from lysyl oxidase and other enzymes noted as possible causes <sup>195</sup>. It is important to note that other diseases in this thesis are congenital collagen disorders, while SSc is a developed and progressive condition with an average onset in middle age without any suggestive history previous to onset <sup>101,188,189</sup>. As has been observed in other crosslinking studies, excessive crosslinking within SSc lesions would likely confer both structural and mechanical abnormalities to collagen fibrils <sup>196–198</sup>. However, to date, outside of the published work in this thesis, there has been no research effort to investigate the biophysical properties of collagen in SSc patients. The limited amount of research that has been performed on laboratory cell models is decades old without further developments <sup>199</sup>.

Despite recent advances in disease management, 55% of patients are reported as dying within ten years of diagnosis <sup>189,200</sup>. As a consequence of its relative rarity and the absence of sensitive biomarkers, SSc may go undetected for several years after clinical onset, and thus opportunities to modify disease progress are lost. Improvements to clinical care and condition management have increased patient life expectancy. The rapid emergence of SSc combined with difficulties in early diagnosis

are considered as the likely reasons for the high mortality rate associated with this condition <sup>193</sup>.

#### 1.2.6 ARC Syndrome

ARC syndrome is a sporadic and fatal paediatric disease, primarily causing hepatic cholestasis <sup>201</sup>. The principal symptoms are arthrogryposis, renal tubular dysfunction and cholestasis with a low blood  $\gamma$ -glutamyl transpeptidase activity, with the additional inability of the patients to thrive and develop normally in all aspects <sup>8,202</sup>. It is often, but not exclusively, found in patients with consanguineous parents of Arab or South Asian origin <sup>203</sup>. There is no known cure, with life expectancy ranging from several weeks to 6 months with rarer cases approaching one year with the syndrome. The inability of the renal tubules to filter urine results in an unstable alteration to the blood chemistry. This then affects the rest of the organs, resulting in multi-system failure. Mutations in the gene *Vacuolar Protein Sorting 33B* (*VPS33B*) and related families have been mapped as the cause of the ARC syndrome <sup>98</sup>. Human *VPS33B* protein has not been sufficiently studied, although a bacterial homologue, *VPS33P*, has been shown to be instrumental in the formation of transport and secretory vesicles in yeast, and there are other analogues throughout nature <sup>98</sup>. However, mutations in these analogues in non-mammalian species produce different phenotypic variations than those seen in humans <sup>201,202</sup>. *VPS33B* has also been shown to interact with *VPS33B*-Interacting Protein Apical-basolateral polarity Regular (*VIPAR*), allowing for the formation of junctions crucial to secretory vesicles <sup>8</sup>. *In vitro* mutations in *VIPAR* have been seen to produce a phenotype with ARC

syndrome-like symptoms, even when *VPS33B* mutations were not present. VIPAR forms a functional complex with VPS33B in allowing cell transport of several proteins, essential for the formation of lysyl oxidase-mediated cross-links in collagen. The importance of these crosslinks has already been discussed at length in this thesis <sup>57</sup>.

Further markers of the disease are alterations to the platelet alpha granule proteins in the fibroblasts. This inhibits the ability of fibroblasts and platelets to respond to injury and damage within the body <sup>204,205</sup>. However despite several crucial developments, there is a need for further research into the genotype and phenotype of ARC syndrome, as there is little available knowledge on the disease <sup>206</sup>.

#### 1.2.7 Collagen Disease Summary

Disease	Origin	Primary Genes	Collagen Effect	Main Treatment
<b>EDS</b>	Genetic	<i>COL1A1</i> <i>Unknown</i>	1-5% fibrils weakened	Physiotherapy, surgery
<b>SSc</b>	Acquired	None	Fibrotic, increase stiffness	Immune suppressants
<b>OI</b>	Genetic	<i>COL1A1</i> <i>COL1A2</i>	Weakened, brittle	Bisphosphonates
<b>DI</b>	Genetic	<i>COL1A1</i>	Weakened, brittle	Conservative dentistry
<b>ARC Syndrome</b>	Genetic	VPS33B VIPAR	Poor cross-linking	None

**Figure 1-7 Summary of the origin and effects of collagen diseases**

#### 1.2.8 Collagen as a Biomaterial

Collagen also has a therapeutic use, in a broad range of biomaterials for surgical and therapeutic purposes which is an increasing trend in both medicine and dentistry worldwide <sup>207,208</sup>. The three main conditions for most implantable

biomaterials are that they are biocompatible, biodegradable and biomimetic, the '3Bs'<sup>209</sup>. Biocompatible means that the body should not reject the implanted membrane. If an immune response is provoked, this must be of a limited duration wherever possible. Fibrous encapsulation of long-term implanted devices is a common and low-level patient response, usually without impacting its function. Biodegradable is a subjective description. Metal-based devices, such as a hip replacement or dental wire, should not be expected to degrade over time. Depending on their function, dental wires can last for the patient's life, while hip replacements can wear out within 15-20 years. An implanted pacemaker may need its settings altered over time or require a change of battery. Both of these changes should be minimally invasive wherever possible. Biomimetic means that the device should seek to replace or enhance a function. Replacement mitral and atrial valves, for example, prevent blood back-flow in the heart, and collagen membranes in surgery allow for cell recovery and wound healing.

More specifically, biomaterial-based membranes are being used for procedures involving techniques such as guided bone regeneration (GBR) and guided tissue regeneration (GTR)<sup>210</sup>. In the case of GBR, these membranes prevent the invasion of soft tissue cells into bone defects, allowing osteoblast migration into the compromised area to promote optimal osseous tissue formation<sup>211,212</sup>. Therefore, biomaterials to be used as barrier membranes must fulfil specific favourable biological and mechanical parameters; and ideally have the ability to reabsorb and thus avoid the need of a subsequent removal surgery, which increases the risk of complications and infection<sup>213–215</sup>. In recent years several natural polymers such as

chitosan, alginate and collagen have been studied as potential barrier membrane materials, due to their high biocompatibility and mechanical stability after implantation<sup>216–218</sup>.

Within this context, the use of collagen as a biomaterial barrier in wound healing is becoming increasingly common, notably in oral surgery and dermatology<sup>219–221</sup>. Collagen membranes are usually derived from porcine, bovine, or de-cellularised human tissues, and are recognised as promoting a higher level of wound-free and scar-free healing<sup>220,221</sup>. As discussed previously, collagen type I has a significant structural and stabilising role in soft and mineralised tissues<sup>222</sup>. Collagen is also a key component of cell-matrix communication and has been shown to promote the attachment and proliferation of human osteoblasts and periodontal ligament fibroblasts<sup>223,224</sup>. Furthermore, collagen can be degraded due to the activity of enzymes such as metalloproteinases (MMPs)<sup>225</sup>, and therefore can be remodelled and resorbed by the body, preventing the need for a second surgical procedure for removal<sup>216,226</sup>.

While well-regulated and safe, little information is available regarding the behaviour and mechanics of collagen membranes during implantation and wound recovery<sup>221</sup>. Additionally, the adhesive interaction between cells and collagen membranes at the nanoscale is not fully understood; only that materials are generally biocompatible<sup>27,227</sup>.

### 1.3 Medicine at the Nanoscale

The use of medicine at the nanoscale seeks to combine two large cross-disciplinary fields; uniting physicists and physicians in an attempt to harness recent developments in science and translate these to clinical practice as safely and efficiently as possible. This section of the introduction will focus on the use of nanotechnology in diagnostic medicine, and an overview of the use of nanomedicine as clinical treatments.

#### 1.3.1 Nanotechnology in Diagnostics

Irrespective of their type, physiological diseases always have one or more bases in the nanoscale <sup>228</sup>. If these bases can be identified, then the behaviour and progression of a disease might, too, be identified <sup>229,230</sup>. The use of blood tests in diagnosis is an excellent example of this; changes in hormone levels in routine tests can give an early sign of sex hormone-dependent cancers <sup>231</sup>. However, understanding the underlying mechanisms of pathophysiology was initially limited without effective instrumentation.

The importance of diagnosis on *in vitro* (or *ex vivo*) samples has been well established. While blood tests are on one end of this spectrum, the other end seeks to diagnose diseases through cell cultures and biopsies <sup>232,233</sup>.

Single cells are a prime target for *in vitro* diagnosis <sup>234</sup>. Large numbers of primary cells can be taken from diseased tissue without the risk of donor site morbidity, due to the density of cells present <sup>235</sup>. Another benefit to single cell analysis

is that it limits any dilution of effects that could be lost in a tissue <sup>236,237</sup>. Biochemical identification methods often require large amounts of tissues, which act in a system. It can be difficult or impossible to separate each effect for identification <sup>237</sup>. In two examples, nanoparticle labelling techniques have been used to identify the endocytosis of a range of cancer cells, or the intercellular activity of prostate cancer cells <sup>235,238</sup>.

Biochips and microarrays have also been successfully used. Through the use of miniaturisation of test sites, the rapid identification of pathological features can be achieved <sup>239–241</sup>. Due to ease of access, this has seen particular success in dentistry with the analysis of saliva. Over 700 specific species of bacteria that cause oral infections can be identified within seconds using mRNA analysis <sup>240,242,243</sup>. Similar systems are also used to test the resistance of bacteria to specific antibiotics, decreasing treatment time and helping to prevent further antibiotic resistance <sup>244–246</sup>. Cancer detection, early signs of periodontitis and the progress of cardiovascular disease can also be obtained through the use of biochips with saliva samples <sup>247–250</sup>.

### 1.3.2 AFM as an Experimental Tool

In the results sections of this thesis, AFM will be explored as a diagnostic technique. Its current use in medical diagnosis is limited although it is widely used as a laboratory tool.

The first use of nanoscale imaging was established in 1982, through the use of scanning tunnelling microscopy, and later AFM <sup>251</sup>. Since then, developments in TEM and SEM have allowed for a variety of methods to image nanoscale features



alongside the co-localisation of other techniques such as light microscopy<sup>143,252–254</sup>. Though it remains a frequently used tool in materials science, manufacturing and physics, AFM has proven its use in analysing samples in diverse environments that would be applicable in diagnostic medicine.

The structure of DNA can be resolved in a liquid environment using AFM<sup>255,256</sup>. Studies have already shown the potential benefits of imaging and sizing DNA molecules using established techniques<sup>257</sup>. Protein folding and unfolding events have been observed using AFM, and monitoring of the behaviour of amyloids and atherosclerotic plaques indicate possible future clinical uses<sup>251,258–263</sup>. Individual cells have also been probed. Ranges of mechanical measurements on living cervical, breast and bladder cells, for example, have been published<sup>95,264–266</sup>. Similar studies have also been performed on bacteria and fungi<sup>267,268</sup>. Interactions between various cells and surfaces, as well as each other, have been reported<sup>95,269–271</sup>.

When used on soft structural materials like collagen, fibronectin or keratin structures, AFM has been used in liquid and dry conditions<sup>269,272–276</sup>. When looking at mechanical or other quantitative data, this could make inter-comparisons difficult, as differences between experimental setups and models give drastically varied results<sup>264,277,278</sup>. For example, the Young's modulus of collagen has been reported between 1-5 GPa using AFM in dry conditions, but this decreases to 1-5 MPa when measured in liquid<sup>93,279,280</sup>. D-banding, a crucial physical identifier of collagen, is often not seen in liquid environments, as the uptake of interstitial water causes fibril swelling which hides the banding<sup>65,70,279</sup>. Keratin and models of fibronectin have also

been shown to exhibit mechanical and topographical differences in a range of physiological and non-physiological conditions <sup>5,281–283</sup>.

### 1.3.3 AFM Uses in Medicine

AFM can also be used on models and complex *ex-vivo* samples. Data on the topography, stiffness, adhesion and surface energy are often reported. A selection of recent applications of AFM across several medical specialities are presented here.

#### 1.3.3.1 **Neurology**

There was limited information about the morphology of peripheral nerves in a liquid environment before imaging with AFM was performed <sup>284</sup>. Similarly, AFM has been used in comparisons between myelinated and demyelinated fibres. A loss of myelin protection around nerves is a symptom of multiple sclerosis <sup>285</sup>. AFM was shown to be crucial in the comparative mapping of the elastic modulus between myelinated and non-myelinated fibres, as well as producing morphological and topographical images <sup>286</sup>.

AFM has also been used in conjunction with fluorescent imaging to observe the changes of primary cell lines in complex 3D culture, mimics progression of the disease while also acting as an interrogative model for nerve repair <sup>287</sup>. Another model sought to use electrospun silk nanofibers doped with melanin to serve as a conduit for guided central nervous system repair. Here, AFM was used to confirm the doping and attachment of the cells <sup>288</sup>.

### **1.3.3.2 Ophthalmology**

Type VIII collagen is essential in the basement membrane of the cornea, known as Descemet's membrane <sup>7,289</sup>. Being thin, lacking in rigidity, and difficult to remove from the surrounding cell layers, the mechanics of Descemet's membrane was poorly understood as it was likely overestimated by the use of tensile stretching <sup>290</sup>. AFM was used to image the surface of the membrane in liquid; the presented image was poor in quality compared to other tissues, but the features were identifiable <sup>291</sup>. More successfully, adhesion measurements showed a previously unreported surface heterogeneity and minimal adhesion. The Young's modulus of the type VIII collagen in 'semi-dry' conditions was reported in the region of 0.23 to 2.6 kPa <sup>291</sup>. Taking a different approach, another collagenous ocular membrane, the Bowman's membrane of the anterior corneal surface was imaged using AFM. It was previously established that changes to the surface of Bowman's membrane were linked to rapid and irreversible sight loss, but the diagnosis was slow and imprecise <sup>292</sup>. Fractal image analysis of AFM images taken from post-mortem corneas confirmed the average roughness of the membrane, which was linked to case histories helping to understand the development of the condition <sup>293</sup>.

### **1.3.3.3 Cardiology and Haematology**

Erythrocytes (red blood cells) are essential in the transport of oxygen throughout the body. Erythrocytes are abnormal in that they do not have a cell nucleus or other organelles to maximise space for haemoglobin <sup>294</sup>. In order to transport oxygen more effectively, erythrocytes must be able to pass through narrow vessels which are less than half of their size, making deformation of erythrocytes a

key characteristic <sup>295</sup>. This deformation is dependent on the cell membrane of erythrocyte <sup>294</sup>. In one study AFM was used to indent across the surface of erythrocytes, to determine local changes in stiffness, along with any hydration-dependent effects. Consideration was given to AFM probe geometry, any conditions such as smoking which the donor may have had, and the use of glutaraldehyde as a fixative in the experimental setup <sup>296</sup>. The Hertzian model was also used, and it was recognised that the data presented would only have been relevant to this setup. However, a value of Young's modulus of 7.57 kPa was recorded, with local deformations up to 200 nm, despite the use of fixative <sup>296</sup>.

In another study, flow in blood vessels was modelled using AFM in an unusual experimental setup. The loose connective tissue of blood vessels, the adventitia, is similar to the loose connective tissue found in the papillary dermis <sup>32,297</sup>. It is a tissue layer rich in collagen and elastin <sup>32,297</sup>. A key difference, however, is in the fluid transport throughout the layered porous tissue <sup>298</sup>. The flow behaviour of these fluids is often non-Newtonian, and difficult to model effectively *in vivo* <sup>299</sup>. Having modelled the flow behaviour of fluid throughout the adventitia of a vena cava, one study used an AFM in intermittent contact mode as a replacement for cardiac rhythm in a flow chamber model, as well as colocation with TEM to confirm the fluid flow rate and channel pore size <sup>298</sup>.

Other uses, such as molecular recognition on binding sites, the behaviour of vascular endothelial cells and cardiomyocytes as models for hypertrophy have all been investigated <sup>300–303</sup>.

#### **1.3.3.4 Dentistry**

The use of AFM in dentistry is limited, and often appears incidental to the subject of analysis without much-dedicated research <sup>241</sup>.

The adhesion of bacteria to implant surfaces is a prominent feature of cross-disciplinary research, with a particular interest in the behaviour of implants in dentistry and orthopaedics <sup>209,304</sup>. Titanium is often used in dental implants and remains safe and effective, yet susceptible to bacterial infection <sup>304</sup>. In one article, measurements on the maximum adhesion and bond length were recorded using AFM. This approach used an AFM probe with a spherical bead to attach to the individual bacterium and probe surfaces, similar to previously published research as an accepted but specific and specialised application <sup>305,306</sup>. This approach allows the bacterium to function as the probe, allowing for effective interrogation of the surface-bacterium interactions <sup>307</sup>. An increase in adhesion of the bacteria to the surface as a function of time was predicted and found <sup>305</sup>. Counterintuitively, an increase in the adhesion of the bacteria was also observed with the use of an antimicrobial agent; this killed the infection but increased the risk of secondary colonisation without further effective care <sup>305</sup>.

Another adhesion study used AFM to monitor the colonisation of bacteria onto an enamel surface. Highly mineralised, enamel is susceptible to acidic secretions from oral bacteria that can lead to dental caries <sup>308–310</sup>. However, this surface is often etched through the presence of dietary acids as well as bacteria, and it has been well established that a rough surface can increase bacterial attachment <sup>311–313</sup>. The study found significant differences between the adhesion forces of different bacteria onto enamel; also it confirmed a time-dependent variable as bacterial would be more

strongly adhered onto the surface with increasing time <sup>314</sup>. Following that, a different study trailed the use of a self-assembled protective protein to prevent dental erosion. AFM images of the enamel were taken, and the mean roughness analysed to suggest a moderate protective effect <sup>315</sup>.

#### **1.3.3.5 Summary**

It is clear that AFM has been successfully translated from a materials science and physics technique into the biomedical field. Most of the applications of AFM are currently focused on *in vitro* models of tissue behaviour, with primary cells appearing to be the most generally used human samples <sup>316</sup>. There is an apparent disinclination to use human tissue as animal substitutes are often presented. This could be because of a lack of collaborations between scientists and clinicians, and the complexity of ethical approval required by countries and journals for publication could cause reluctance <sup>317–319</sup>. The use of human cell lines is still commonly accepted, although there is established recognition of the advantages of primary cells wherever possible.

There is however a need to establish consistent protocols when using AFM. Disparate results in similar tissues are the inevitable result of using different experimental procedures, and these differences in setups can make comparisons between published data meaningless. The use of glutaraldehyde as mentioned in one paper in section 1.3.3.3, for example, means that trying to use their data to compare the stiffnesses of erythrocytes to another publication is impossible <sup>296</sup>.

Other considerations include the lack of harmonisation of the modelling of AFM force data. This will be discussed in more detail in Section 1.4.5, but there are notable differences between the Hertzian and DMT models, and appropriate reasons to use each, yet papers claim that each is the correct one to analyse the same sample <sup>264,322</sup>. Fortunately, new methods of standardisation have been proposed and accepted by some groups of researchers, but these have also struggled to gain rapid and widespread acceptance <sup>323</sup>.

AFM is a powerful technique in analysing samples around the nanoscale; however, it has been shown that it cannot work in isolation. Through a combination of complementary methods, AFM could be used more effectively. AFM paired with SEM, TEM, light, confocal and fluorescent microscopy are all commonly used <sup>27,268,272,324,325</sup>. There are also widespread applications of the AFM as reported in this introduction. These range from the conventional (imaging and force-displacement), some more advanced operating methods (simultaneous force and imaging per pixel), innovative alterations of the AFM setup (bacterial adhesion) to the bizarre (intermittent contact as a replacement for the cardiac rhythm) <sup>268,298,326,327</sup>.

#### 1.3.4 AFM-Based Developments on Collagen

The core aims and objectives of this thesis centre around the use of AFM on mammalian, and eventually human, collagen. An overview of the use of AFM on human collagen is presented here, as are some recent publications on the broader topic collagen focusing on novel developments. Currently, publications focusing on

collagen come from a variety of medical fields, but predominantly within the fields of rheumatology and dermatology.

#### **1.3.4.1 Skin**

In dermatology, ethnicities are often presented as split into broad Fitzpatrick types, with type I the lightest (very pale, always burns, never tans) to type VI the darkest (highly pigmented, never burns) <sup>328</sup>. This system is used to determine the exact treatment needed, as variations between races are often reported <sup>329,330</sup>. One study investigated the importance of the stratum corneum in dermatitis, with a particular focus on comparisons between Fitzpatrick types II and VI. The change in natural moisturising factor between type II and type VI dermatitis was compared against matched controls. In all cases, dermatitis patients had a lower natural moisturising factor, with type VI having a higher moisturising factor than type II in all cases <sup>331</sup>. AFM was used to compare surface roughness and detect the presence of nanoparticles, indicative of the natural moisturising factor <sup>331,332</sup>.

One study looked at the effects of tattooing on the skin, in particular, the build-up of nanoparticles. In this study, sections of skin were taken from a single donor and examined using AFM imaging. The nanoparticles were readily visible within the fibril structure and appeared to cause a localised loss of fibril alignment <sup>333</sup>. In areas of the dermis where the nanoparticles were highly agglomerated, the collagen fibril structure could not be fully identified. The work also confirmed the cytotoxicity of the nanoparticles, which are also known to be carcinogenic <sup>333,334</sup>. An extension of that investigation highlighted that the nanoparticles could become embedded into the fibril



structure, in comparison to mineralised collagen where the particles remain on the surface<sup>137,335,336</sup>

#### **1.3.4.2 Ageing**

The effects of ageing of the skin are well-reported, but there has been a recent focus on these effects at the nanoscale using AFM. One study looked at the impact of diabetic crosslinking of skin and the links to the appearance of early ageing. The Young's modulus of the skin was increased in diabetes, as was the disorder observed in the collagen fibrils. These fibrils were described as appearing to be fragmented and disorganised and linked to an increase in matrix metalloproteinase activity in the dermis, and lysyl oxidase crosslinking<sup>337</sup>. Members of the same group excised skin from the buttocks of donors, treating it with retinol for one week. The use of this vitamin was reported to have anti-ageing effects by stimulating dermal fibroblasts into increasing ECM deposition. After AFM measurements were taken, the average surface roughness was found to decrease in the treated samples, with an increase in directional orientation being observed<sup>338</sup>. However, mechanical measurements were not taken, possibly because one week is insufficient to observe a turnover in collagen, and an impact in crosslinking to be detected.

The effect of photoaging on skin has also been investigated using different techniques. One approach repeated the previous studies by looking at changes to fibril order and Young's modulus<sup>339</sup>. Another study looked to examine the efficacy of sunscreens using AFM to determine average D-band length, extracting quantitative data from images<sup>340,341</sup>. Models of photoaging generated by the use of polychromatic light have also been presented. In these studies, the effects of low-

level red lasers on the ECM were studied. Collagen gels were made, and irradiated using the laser before being imaged using AFM. In gels where fibrils were found not to have repeatable D-banding, repeated short irradiations led to an increase in the percentage of D-banding present but a decrease in fibril width <sup>342</sup>. In gels where the fibril structure appeared to be regular, irradiation led to a moderate reduction in fibril width and a small increase in fibril height, altering the aspect ratio <sup>342</sup>. This also led to an increase in Young's modulus by almost 25% after repeated irradiations <sup>342,343</sup>. While taking different approaches, the studies in these sections all report similar results; when crosslinking is increased, a significant increase in Young's modulus and a decrease in fibril orientation is seen.

#### **1.3.4.3 Tendons**

Tendons are highly aligned tissues and comprised predominantly of collagen types I and III <sup>79,344,345</sup>. When damaged, they have poor regenerative abilities, and surgical outcomes can be low <sup>346,347</sup>. In one model, an increase in exercise was seen to lead to an increase in fibril diameter of the tendons, as well as an increase in Young's modulus but still within healthy ranges <sup>348</sup>. These two changes have been suggested as markers of tendon health and were believed to have a shielding effect from future tendon ruptures <sup>123,349,350</sup>. Other studies have shown that the physiological differences in the requirements of tendons led to different nanostructures, detectable with AFM. Tendons have two primary functions: energy storing and positional. The energy storing tendons act as springs, recovering stored energy with high efficiency, while the positional tendons move limbs into repeated patterns without positional change <sup>92,94,351</sup>. The energy storing tendons have been

shown to have high strain stiffening effects while maintaining molecular and fibril alignment, therefore increasing their energy storage efficiency <sup>352</sup>. Collagen fibrils were strained until failure, using an AFM setup similar to a bowstring. Predictably, the positional tendons failed at lower stress and strain values than the energy storing tendons <sup>352</sup>. The morphological changes between the two tendon types were more pronounced, however, with the failure of the positional tendon showing repeated kinks in the core collagen structure <sup>352</sup>. These kinks in the tendons appeared similar to collagen fibril unwinding, with the outer layers of the fibrils losing D-banding and appearing denatured <sup>64,352,353</sup>.

Another paper on tendon failure investigated the collagen kinking phenomenon at a higher hierarchical level. In this case, multiphoton imaging was analysed using Fourier transform to identify disorder in the orientation and structure of the tendon <sup>354</sup>. Once this was mapped, AFM mechanical mapping was used to compare the changes in ultrastructural mechanical behaviour in the kink and non-kink regions. Localised tissue did not show a difference in mechanical response despite topographical changes and reported denaturation of the collagen <sup>354</sup>. This finding contrasted heavily with what has been previously established in collagen degradation behaviour with a change in mechanical properties <sup>355,356</sup>. However, it is possible that the collagen was not fully degraded into gelatine. Additionally, the mechanical measurements did not appear to be linked to any imaging taken at the same scale; force-indentation curves would have been made without locational correlation.

## 1.4 Methodology – Practical Considerations in AFM Use

As well as investigating collagen, this thesis shows the development of a protocol. From the initial concept, as will be seen in Chapter 3 to a refined methodology in part B of Chapter 5, the use of every technique changes from chapter to chapter. For that reason, a separate materials and methods section will not be presented in this thesis. Instead, each iteration of the protocol will be listed in the materials and methods section of each chapter, along with commentary throughout the results and discussion sections.

The primary techniques that will be presented in this thesis are SEM, AFM and light microscopy (LM). This thesis will not present novel applications of SEM or LM, and protocols for their usage are well recognised and understood. However, the introduction has so far highlighted a wide disparity in AFM use. Differences in setups have been noted to change often from one experiment to another, making inter-experimental comparisons difficult.

In this section, explanations and justifications for the decisions about AFM will be presented, along with comparisons between different experiential conditions and the uses of more advanced mechanical modes. Additionally, there will be an overview and discussion about the use of mechanical models used in AFM research.

### 1.4.1 Fundamentals of AFM

#### 1.4.1.1 **Principle Components**

The AFM belongs to the family of scanning probe microscopes and allows for the analysis and characterisation of surface properties such as topography, mechanics, thermal response, electrical capacity, and magnetic interactions <sup>357</sup>. Irrespective of its designated use, all AFMs have a similar method of operation. A cantilever has a sharp tip on its front and has a laser focused on its back. The laser is emitted by the AFM, passes through several mirrors and lenses, bounces off the cantilever, and is directed onto a photodiode. The cantilever is moved into proximity to the sample, which is scanned. Broadly, there are two separate methods of scanning; either the sample remains stationary and is scanned by a moving cantilever, or the sample moves underneath a stationary cantilever. All the AFMs in this thesis use the tip-scanning method. Figure 1-8 shows a highly simplified diagram of the principal interactions of the AFM. The laser reflection from the cantilever onto the photodiode is indicated, and the movement of the cantilever with the resultant laser movement is easy to infer.

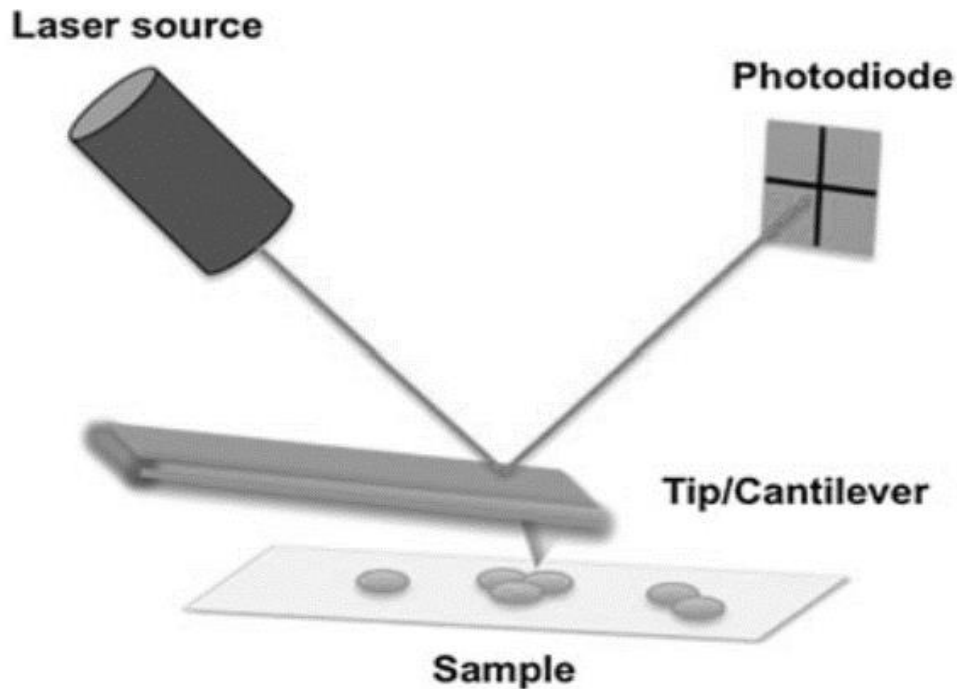


**Figure 1-8 Simplified representation of an AFM** <sup>271</sup>

As the samples are scanned in a raster scan pattern, attractive and repulsive forces, as well as physical interactions can cause a deflection of the cantilever. The deflection of the cantilever causes a sympathetic movement in the laser, which is then measured by a photodiode. This feedback is monitored by the AFM and is used to induce a movement in the scanner to keep the tip in contact with the surface. The topography or height image itself is generated by a sensor attached to the piezoceramic, as a function of the movement of the cantilever. The contrast in the data arises from the tip-sample separation and the material differences between both the tip and sample. Much of the contrast is obtained from very short range Born repulsions, occurring as a result of the overlaps of the electron orbitals between the tip and sample.

The movements of the AFM scanner, the cantilever and the sample are all potentially governed by a controller. Piezoelectric ceramics are used to control the fine movement of the AFM, which is the X Y Z movement of the cantilever as it scans the samples. Feedback from the piezo scanner aims to maintain a constant distance or height from the sample, preventing excessive drift.

#### **1.4.1.2 Cantilever Properties**

Regardless of the type of data collection mode used, the probe properties are paramount to a successful experiment. Tips used in this thesis were made from silicon or silicon nitride and were mounted on a reflective aluminium coated cantilever. The main reported features of a cantilever are its spring constant and resonance frequency. Both of these properties are a result of the manufacturing materials and dimensionality of the cantilevers.

At the correct spring constant for a sample, cantilevers are stiff enough to reliably track the surface of a sample without damaging or shredding it during a scan. Vibrations in the environment are less easily transferred to a cantilever with a higher resonance frequency. There are no set guidelines to pair cantilevers with samples; the choice of spring constant and resonance frequency depends on the sample, the scanning environment, experimental requirements, AFM type, and often user preferences.

The geometry of the cantilever and tip should also be considered. Two common cantilever geometries are rectangular and triangular. Predominantly in this thesis triangular cantilevers will be used for imaging, while stiffer rectangular cantilevers will

be used for mechanics. The principle tip properties are the angle of the tip and its shape; these are needed for mechanics modelling.

Most cantilevers are equipped with sharp tips (effectively a small tip angle), although the 'sharpness' will change with use. Cantilevers can also be functionalised for experimental use. Gold-thiol coating is commonly used to investigate the chemical properties of a sample. Cantilevers are sputter coated with gold before being exposed to thiols in a solvent solution and dried. Silane coatings are also used, depending on the functional groups required. The cantilever is made hydrophilic in strong acids, rapidly dehydrated before being exposed to silane in organic solvents. Both methods of coatings can be further modified with chemical groups as appropriate <sup>281</sup>. Chemically mediated cantilevers are generally susceptible to damage and must be used carefully.

Other cantilever modifications involve the attachment of colloidal probes. These probes are often smooth spheres made of glass, silica or polystyrene with a defined radius. A tip-less cantilever is dipped in adhesive and brought into contact with a sphere, and the adhesive sets. This is used in Chapter 3 in this thesis. These spheres can be further modified using the chemical processes above.

#### 1.4.2 Contact vs Intermittent Contact Modes

The two main methods of scanning a sample are by contact mode and intermittent contact ("tapping") mode. Additionally, there are other modes such as non-contact mode.

Contact mode is the most basic mode, and the tip is kept in constant contact with the sample utilising a continuous feedback signal. Cantilevers that are chosen



for contact mode often have low spring constants as this mode is susceptible to noise due to a static feedback signal. Stiffer cantilevers are more prone to cause damage to the samples in contact mode as the tip is dragged along the sample surface. Force interactions between the sample and cantilever are strong in this mode as the cantilever is in constant contact.

In intermittent contact mode, the interactive forces between the sample and the cantilever are minimised. The resonance frequency of the cantilever is measured. The drive frequency applied to the cantilever is close to the response frequency. The cantilever is rapidly raised and lowered or vibrated in a scanning pattern across the sample. As the tip approaches the sample surface, Van der Waals and dipole-dipole interactions occur, altering the movement of the cantilever. The AFM controller measures this movement. The amplitude and frequency of the driving signal are kept constant, resulting in stable movement of the cantilever. As the tip is not in continuous contact with the sample, lateral force interactions are mostly negated, so the sample is not “dragged” by the cantilever. Whilst slower than contact mode, intermittent contact mode greatly reduces the amount of sample-tip interaction that is needed.

### 1.4.3 Imaging

#### **1.4.3.1 Setup**

Imaging requires the least initial setup of AFM modes. In either contact or intermittent contact mode, the movement of the laser on the photodiode is recorded and interpreted as a topographic (height) image. Principle settings needed for imaging mode are the setpoint (applied force), feedback gains, scan size and scan rate. In imaging mode, the cantilever is often uncalibrated, so the setpoint is applied

in terms of volts. Feedback is controlled through the integral and proportional gains, depending on the mode. These settings work to track the movement of the cantilever accurately, keeping it close to the sample. When optimised, they reduce the amount of noise in the image. If the gains are too low, the AFM controller will not have time to register the fine movement of the cantilever across the sample so only the most significant features will be recorded. If the gains are too high, the controller will overcompensate, and add high-frequency noise, visible in the image and on the oscilloscope. Figure 1-9 shows the oscilloscope trace and retrace which indicate that the gains have been well optimised.

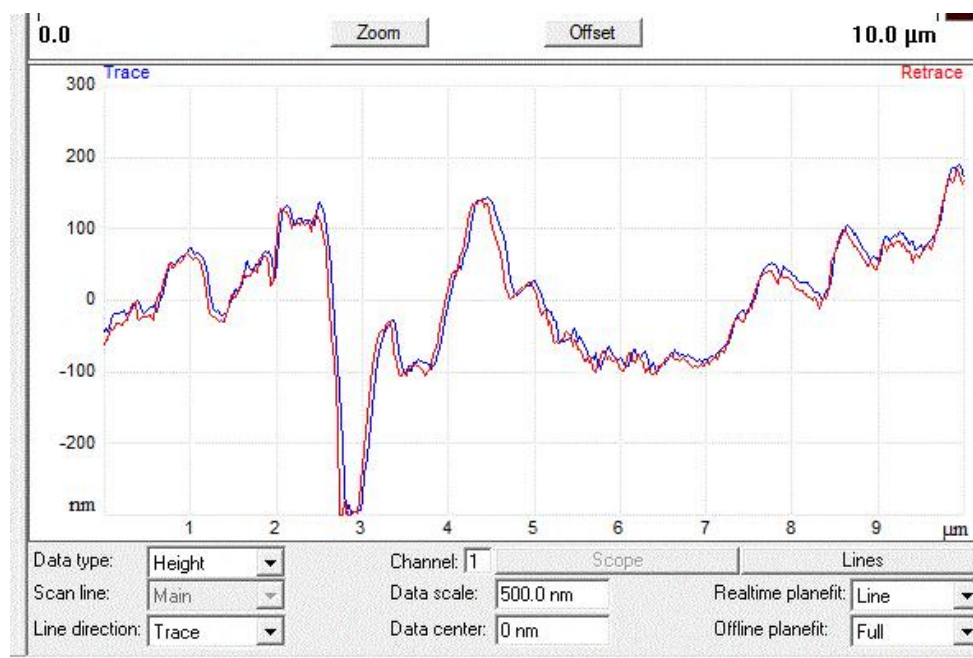


**Figure 1-9 Optimised gains for imaging from Bruker Nanoscope**

Generally, the imaging is run with as little setpoint as possible (to avoid sample damage and tip wear), with a high scan rate (to speed up the process) and with as high gains as possible (to ensure maximum data collection with minimum noise).

#### 1.4.4 Mechanical Analysis

##### 1.4.4.1 **Calibration**

The setup of an AFM differs in mechanical measurements from imaging in one crucial step; the requirement of cantilever calibration. In this step, the spring constant is calculated, having only been manufactured to an approximate value. This is required because mechanical measurements using AFM are dependent on the force applied to the sample from the tip. As movements of the cantilever are governed by a piezoelectric ceramic, which is liable to change over time, calibration is needed to determine the resultant force of an applied voltage <sup>358</sup>.

There are several approaches to cantilever calibration. The most fundamental is to calculate the spring constant mathematically by geometry. This is extremely difficult and unreliable due to the uncertainty in thickness and exact dimensionality of the cantilevers and is generally reserved for theoretical discussion and modelling <sup>359</sup>. A challenging but more widely used approach is to bring the cantilever in contact with a pre-calibrated reference lever. The deflection of the cantilever can be measured for any given movement of the piezo connected to the reference cantilever <sup>360</sup>. This tip-to-tip method is highly reliable but time-consuming and potentially challenging to execute <sup>359</sup>.

The final method is a reliable, straightforward and modern approach, and is generally considered to be user-friendly as it is used in most built-in AFM calibration methods <sup>323,361</sup>. The first step is to calibrate the sensitivity of the photodiode. Initially, a tip is used to attempt to indent a surface such as a microscope slide or sapphire glass. These surfaces are far harder than the tip, and therefore cause the cantilever

to deflect by a large amount, rather than the surface to be indented. The gradient of the approach force curve is calculated, which is also known as the deflection sensitivity (unit V/nm). Once photodiode is calibrated, the cantilever is withdrawn from the surface. The cantilever is then thermally actuated in order for it to oscillate at its natural resonance frequency. This method does not require the exact dimensions and physical properties of the cantilever to be known. The amplitude/frequency response of the cantilever is then fitted with a Lorentzian fit in order to calculate the value of the natural resonant frequency, which is in turn used to calculate the spring-constant of the cantilever<sup>277,359,362</sup>. This final method of spring constant calibration is the one that will be employed in the work of this thesis. Once calibrated by any method, the tip and cantilever are ready for use.

#### **1.4.4.2 Experimental Setup**

Indentation is the most used mechanical technique presented in this thesis. It is used primarily to determine the Young's elastic modulus of a sample. The Young's modulus is the relationship between stress and strain in a material in the linear elasticity regime of a uniaxial deformation. Having calibrated the cantilever previously, and making sure that samples are always mounted on a hard substrate, the resultant interactions of the sample can be measured.

The primary settings for experiments in indentation mode are the relative setpoint and the cantilever movement speeds. The relative setpoint is the force applied for indentation. This differs from the setpoint used in imaging mode, in that here the relative setpoint uses the cantilever calibration to ensure that the force applied remains constant. For a standard experiment, the setpoint should remain

constant, so a constant force is applied to the sample. The cantilever movement speeds control the speeds at which the cantilever and tip will: approach the surface, remain on the surface, withdraw from the surface and pause before the next measurement. For indentation in air, as the majority of the experiments in this thesis will be, no pausing is needed either on the sample surface or between measurements. The approach and withdraw speed should be identical and kept constant throughout the experiments.

The cantilever goes through a set movement to generate a force curve, as shown in Figure 1-10. A: the cantilever is 'infinitely' far from the surface, but is approaching the surface. B: the tip is in contact with the sample surface. The sharp drop in deflection is the snap of the tip to the surface, the interactions of the two water layers surrounding the tip and the sample, as well as any chemical interactions. C: maximum force is applied at the apex of the curve. D: the tip begins to withdraw from the surface. The gradient of this line is used to determine the Young's modulus. E: as the tip is about to withdraw from the surface, adhesion occurs. The adhesion can be measured as the integration of the area under the flat baseline. F: the adhesion has been overcome, and the cantilever is infinitely far away from the surface again.

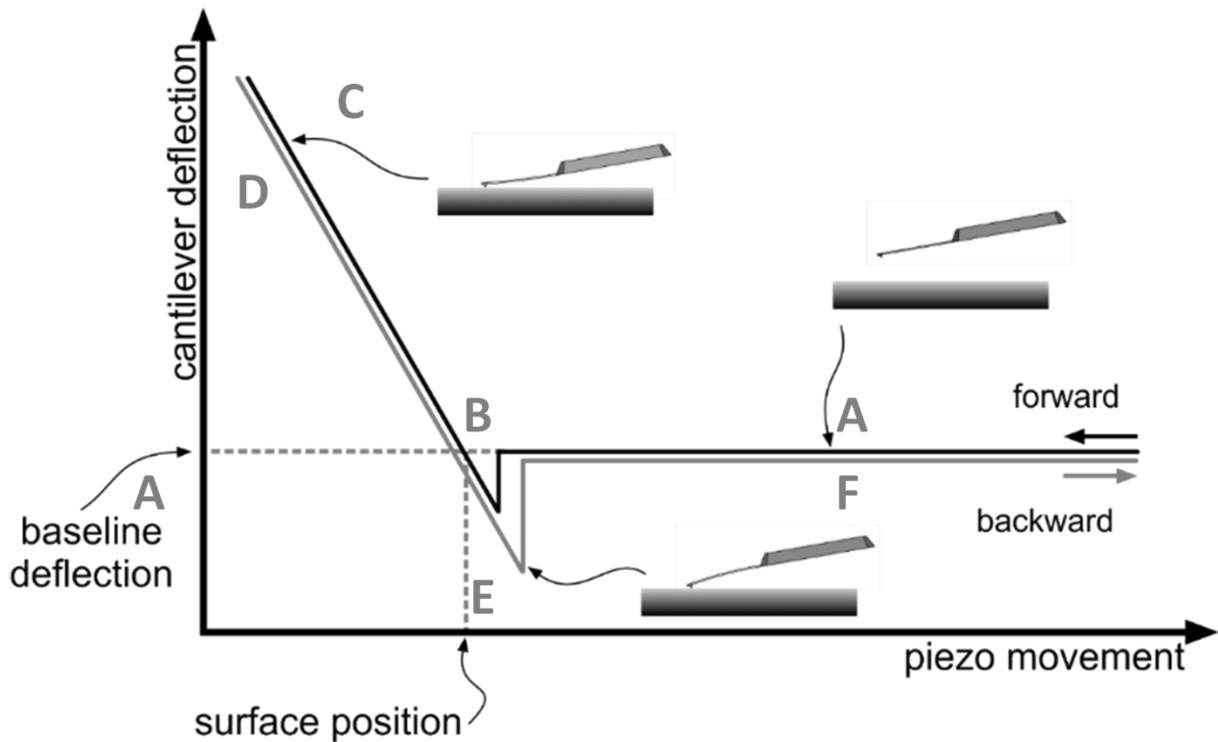


**Figure 1-10 Movement of the cantilever during indentation**

When analysing a homogenous layer such as a polymer film, indentation can be performed with a grid system to collect measurements, without the need to identify the surface <sup>326,363</sup>. However, when analysing a sample with distinct or important surface features, imaging is required before mechanical analysis can take place. This imaging is often carried out at a low resolution and fast line rate to get an overview of the surface. Once this image has been obtained, either exact locations can be selected for indentation, or a grid applied to a specific area of the image to take measurements.

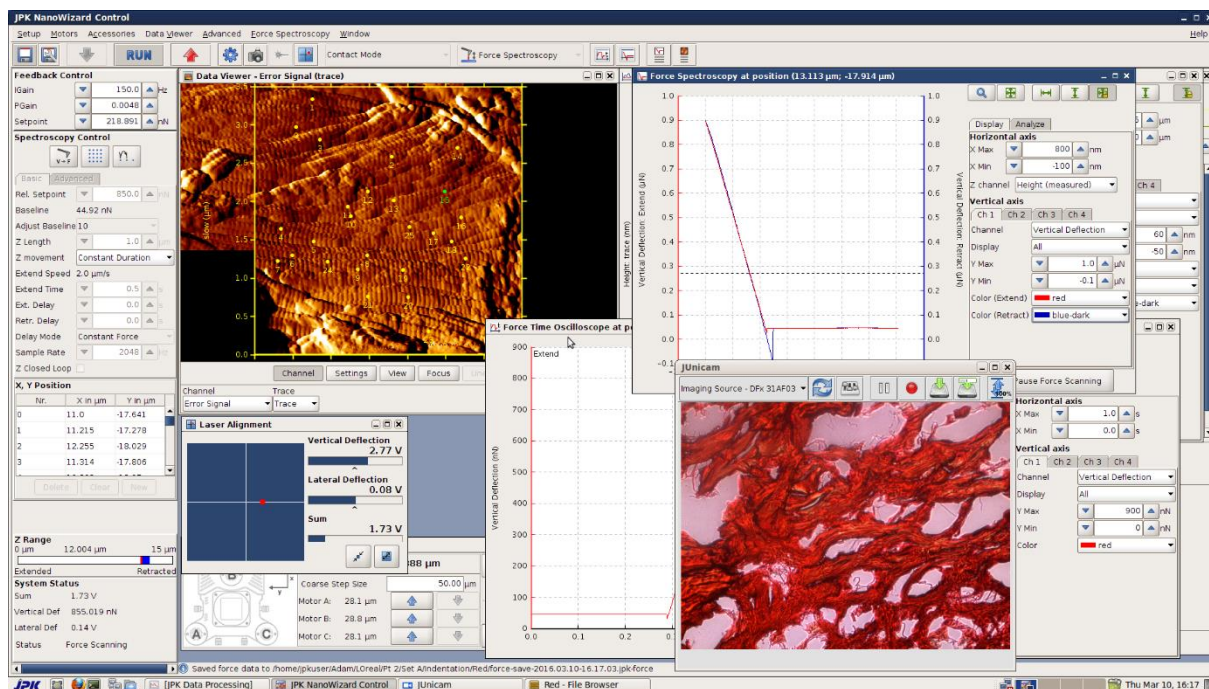


**Figure 1-11 AFM setup for indentation on JPK Nanowizard 1**

Figure 1-11 shows an indentation experiment in progress, as performed in this thesis. On the left-hand side is spectroscopy control. This indicates that the relative setpoint, Z-piezo length and movement, as well as the cantilever movements and delays. In the middle, the sample of collagen fibrils is coloured orange showing the ultrascale location. Numbered yellow dots indicate the sites to be probed, and these have been selected manually. On the right-hand side, at the top, the last force curve taken is displayed, and at the bottom, the live light microscopy image shows the sample area being scanned at the microscale.

Once the data has been collected, it can be batched processed and fitted according to several models.

#### 1.4.5 Data Analysis & Modelling

When a sample is indented with a set loading force for a specified duration, the surface of the sample will be deformed by a given amount. This is the fundamental stress-strain relationship and can be used to determine the stiffness of a sample. However, with the application of mechanical modelling, the Young's elastic modulus can be calculated. While the exact mathematical approaches are outside the interest of this thesis, an overview and justification for the use of specific models are presented.

##### **1.4.5.1 Hertzian Model**

In biological AFM use, the Hertzian model for spherical indentation has often been applied. This model is simple and is expressed as a relationship between force and indentation. However, this model assumes that there will not be any adhesive interaction between the AFM probe and the surface. Additionally, it assumes that the sample is infinitely thick and that the only indentation that will occur is on the surface sample. In biological AFM use, neither of these assumptions can be taken for granted<sup>322</sup>. Indeed, the opposite is often true, with the surfaces of mammalian and bacterial cells being compliant, even in air, and this extends further to tissues and collagen<sup>59,271,286,294</sup>. It is safe to assume, therefore, that a degree of deformation of the surface of any biological material could be occurring.

For a spherical probe, and assuming no adhesive interactions between the probe and the sample, the force-indentation relationship is modelled according to Hertz in Equation 1-1:



$$F_n = (KR)^{\frac{1}{2}} \delta^{\frac{3}{2}}$$

**Equation 1-1 The Hertzian Model**

Where:  $F_n$  the normal load,  $\delta$  the indentation depth,  $R$  the radius of the indenter, and  $K$  the normalised elastic modulus. The factor  $K$  (Equation 1-2) is itself derived from an equation and contains the Poisson's ratio of the material  $\nu$ , and the Young's modulus  $\epsilon$ :

$$K = \frac{4\epsilon}{3(1-\nu^2)}$$

**Equation 1-2 The factor  $K$  in the Hertzian model.**

While imprecise, the Poisson's ratio is typically assumed to be 0.5 for biological samples, making the factor  $K$  effectively equal to the Young's modulus when two spheres are interacting without adhesion <sup>264,364–366</sup>.

#### **1.4.5.2 JKR Model**

Further developments to the Hertzian model seek to calculate the missing adhesion. There have been two major approaches to this problem. The first is the Johnson-Kendall-Roberts (JKR) model. This is used for soft materials with high surface energy and for probes with a large contact radius. In this approach, the adhesive interactions between the probe and sample are considered to be the dominant reaction of the sample <sup>267,322,364</sup>. At contact, the probe is considered to be deeply embedded into the highly compliant sample. The JKR model could, therefore,

be reliably used in experiments using spherical probes and cells of similar sizes in a liquid environment. However, it is important to note that while functionalised beads on cantilevers tend to have a large radius relative to the size of the cell, the actual area that is indented by the bead will be far smaller than the total radius.

The equations for the JKR model are as follows:

$$\delta = \frac{\alpha_{JKR}^2}{R} - \frac{4}{3} \sqrt{\frac{\alpha_{JKR} F_{ad}}{RK}}$$

**Equation 1-3 The JKR model**

$$\alpha_{JKR} = \left(\frac{R}{K}\right) (\sqrt{F_{ad}} + \sqrt{F_n + F_{ad}})^{\frac{2}{3}}$$

**Equation 1-4 The factor  $\alpha_{JKR}$  for the JKR model**

$$F_{ad} = \frac{3\pi}{2} \gamma R$$

**Equation 1-5 The factor  $F_{ad}$  for the JKR model**

For Equation 1-3, the same notations as given in Equation 1-1 apply, with  $\alpha_{JKR}$  in Equation 1-4 the radius of the contact zone of the tip, and  $\gamma$  in Equation 1-5 the adhesion energy.

#### **1.4.5.3 DMT Model**

The other main approach to adhesion is the Derjaguin-Muller-Toporov (DMT) model. Conversely, this applies for samples with low surface energy and probes with a relatively small radius. In this model, adhesion is factored as an elastic response of the samples by the indentation of the probe, not the dominant factor<sup>364</sup>.

The equations for the DMT model are:

$$\delta = \left( \frac{F_n + F_{ad}}{KR^{\frac{1}{2}}} \right)^{\frac{2}{3}}$$

Equation 1-6 The DMT model

$$F_{ad} = 2\pi\gamma R$$

Equation 1-7 The factor  $F_{ad}$  for the DMT model

As in the JKR model, in Equation 1-7 the factor  $\gamma$  is the adhesion energy. The solution to Equation 1-6 can re-enter the rearranged Hertzian model (Equation 1-1) to calculate Young's modulus.

#### 1.4.5.4 Hertzian Summary

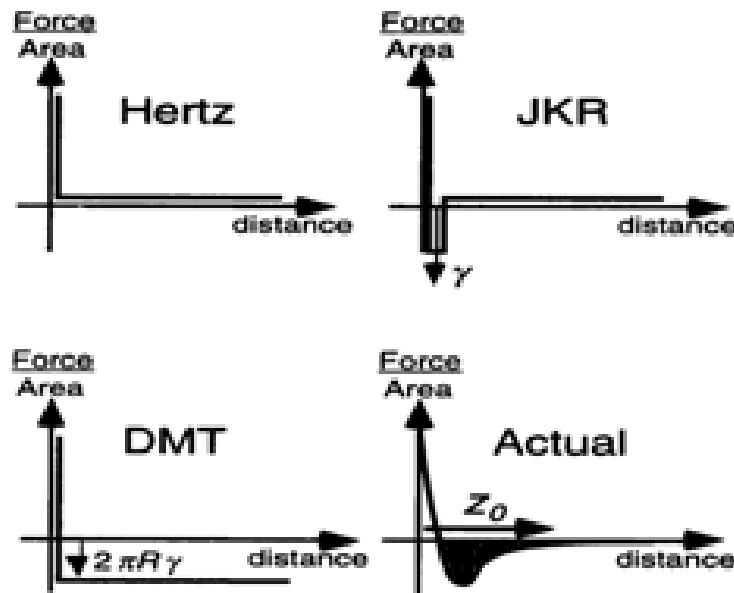


Figure 1-12 Comparison between mechanics models <sup>367</sup>

Figure 1-12 shows the comparison between the models. As has been discussed, the Hertzian model assumes no adhesion, while the JKR factors in a large

amount of adhesion with rapid detaching. The DMT model can be considered an extension of the Hertzian, by factoring in the detachment force below the baseline, but without accounting for adhesion. Consideration must also be given between the DMT and JKR models, with the transition point between the models being reported as notably small, and will depend more on experimental interest whether adhesion or indentation is given preference <sup>368</sup>.

#### **1.4.5.5 Sneddon Model**

The Hertzian, DMT and JKR models all assume spherical probe. Most 'sharp' tips sold currently have a conical indenter, and that the geometry of the tip itself is triangular or square-based pyramids <sup>369</sup>. This assumption is factored into another model, the Sneddon model, which is shown in Equation 1-8 in its generic form

$$^{364}.F_n = \frac{3}{2\pi} K \delta^2 \tan \theta$$

**Equation 1-8 The Sneddon model**

Crucial to the Sneddon model is the incorporation of the tip angle  $\theta$  which can be calculated during calibration, or a default value can be used from the manufacturers <sup>366</sup>. The Sneddon model recognises the importance of adhesion to the movement of the cantilever but calculates its effects proportional to the surface area of contact. It has also been further updated to account for a moderate amount of adhesion (such as in the DMT model) or a substantial contribution of behaviour from adhesion (such as JKR). The model is also enhanced by assuming that the indenter is small (such as JKR) yet still a cone or other indenter shape <sup>369</sup>. The tips used in

this thesis for indentation are pyramidal, so the modified Sneddon model is found in Equation 1-9 <sup>369</sup>:

$$F_n = \frac{3K \tan \theta}{\pi^{\frac{3}{2}}} \delta^2 - F_{ad}$$

**Equation 1-9 The Sneddon model for pyramidal tips**

$$F_{ad} = \frac{32\gamma \tan \theta}{\pi^3 \cos \theta} \delta$$

**Equation 1-10 The factor  $F_{ad}$  from the modified Sneddon model**

An assumption made in the Sneddon model is that the behaviour of the acquired force curves is linear. This is invariably incorrect, and the Oliver-Pharr model seeks to account for the variation in tip geometry and sample interaction in every force curve by way of a correction factor <sup>370,371</sup>. This approach, however, is laborious, and while generally recognised as providing a positive impact on the validity of data, has yet to be widely adopted by AFM manufacturers <sup>372,373</sup>. The complexity of the correction factor needed and the varied range of uses that AFM has currently has made an automatic calculation of the model difficult. Conversely, Bruker, the owner of the JPK and Nanoscope AFM brands, includes Hertz/DMT and Sneddon models, with easy modification to JKR if required. Asylum Research's Cypher AFM uses Hertz/Sneddon, JKR and DMT model, with Oliver-Pharr advertised as an additional model for nano-indenter devices only.

One individual model is not innately superior to another; each has its correct application for a specific experimental setup <sup>323,359</sup>. In this thesis, the indentation of collagen with sharp tips will be performed, along with some adhesion measurements

using spheres. The indentation will take place in air, on collagen, and in standard lab conditions. In these conditions, the indentation of collagen is expected to be around 4-8 nm deep, and some adhesion is assumed<sup>59,93,374,375</sup>. Furthermore, large data sets will be collected and compared, suggesting that bulk data analysis is crucial. Therefore, the Sneddon model will be used in this thesis, although research from the thesis has been published using the Oliver-Pharr model. The Sneddon model has three main advantages: it accounts for tip geometries at very small indentation depths, allows for the Young's modulus to be calculated from the full gradient of the force curve, and is widely accessible and validated.

## 2 Aims and Objectives of the Thesis

---

### 2.1 Research Question

*Can a novel AFM-based analysis be developed to characterise collagen in health and disease in connective tissues?*

### 2.2 Thesis Objectives

Each of the developments in the major results chapters helps to advance an answer to the research question, which will be tested at the end of the thesis

1. Initially, test nanoscale and mesoscale imaging and mechanics on commercially available collagen membranes with a multimodal approach
2. Evaluate the effect of a genetic disorder on mouse tendon hierarchy
3. Develop enhanced analysis suitable for use in characterising human skin, combining imaging and mechanics.
4. Evaluate a streamlined analysis series on a fibrotic skin disorder, moving towards a quantifiably descriptive approach.

# 3 Multimodal Characterisation of Collagen Scaffolds: Towards a Clinical Application

---

## 3.1 Introduction

The use of collagen as a clinical tool to promote wound healing is becoming increasingly common, notably in oral surgery and dermatology <sup>219–221,376</sup>. Collagen membranes have been shown to increase the recovery of tissues, and are recognised (and marketed) as allowing for a higher level of wound-free and scar-free healing than other, more simplified approaches <sup>220,221</sup>. While well-regulated and safe, little information is known about the behaviour and mechanisms of the collagen membrane during implantation and wound recovery <sup>221</sup>. Additionally, the response and behaviour of cells on membranes is not known; only that the materials are generally biocompatible <sup>27,227</sup>. In this part of the thesis, preliminary investigations into the collagen membrane were performed, laying the groundwork for a more detailed suite of tests to analyse collagen behaviour.

The work in this chapter in Part B has been published as “Degradation pattern of a porcine collagen membrane in an in vivo model of guided bone regeneration”<sup>220</sup>.

---

Membrane analysis formed part of a work in collaboration with Marco Mehr (Geistlich Pharma) who sponsored an extended version of this chapter. Cells were grown by Nazanin Owji (UCL) In-vivo work was performed alongside Dr Elena Calciolari (QMUL) and Prof Nikolaos Donos (QMUL).



Additionally, a paper comprising some of the data in Part A has been prepared for submission.

### 3.2 Aim

This investigation aimed to characterise commercially available collagen surgical membranes using multimodal qualitative and quantitative approaches, and apply that to an animal model.

### 3.3 Objectives Part A

1. Characterise the morphology of the membranes with a particular focus on the presence of porosity, collagen fibres and D-banding.
2. Evaluate the mechanical behaviour of the identified collagen fibres seen in dry and liquid environments.
3. Quantify the fibroblast-membrane interactions to identify the immediate cell response on implantation.
4. Measure the degradation process of the membranes *in vitro* when exposed to collagenase.

### Part B

5. Apply knowledge learnt in Part A to characterise the morphology of *ex-vivo* membranes

### 3.4 Materials and Methods

#### 3.4.1 Materials

All samples were obtained from Geistlich Pharma, Zurich, as either a part of a paid consultancy, or through commercial purchases. Two types of collagen membranes were obtained. The first was Bio-Guide (BG), a porcine-derived membrane and has been reported as the market leader in North America and Europe for oral tissue regeneration <sup>377</sup>. Previous studies have identified BG as having a bilayer structure, promoting wound healing while resorbing over time <sup>219,378</sup>. The second membrane was Mucograft (MG), a porcine-derived collagen/keratin composite membrane designed for soft tissue regeneration. Previous studies have identified MG as reducing the number of clinical visits for the patients, as well as reducing post-operative pain and increasing wound healing <sup>379</sup>. Additionally, the bone substitute Bio-Oss (BO) and collagen sponge Fibro-Gide (FG) were analysed solely for collagen morphology using SEM. BO is a bovine-derived tissue indicated for repairing bone loss, while FG is used as a spacing and cell recovery sponge.

Sample preparation focused on keeping the membranes intact wherever possible and minimising the amount of preparation needed to perform the experiments.

#### 3.4.2 Methodology

##### **3.4.2.1 Mesoscale Imaging**

For the soft membrane materials, a square approximately 2 cm<sup>2</sup> was cut and prepared. Mineralised sponges were cut where possible. For granular materials,

approximately 2g of the sample was used. All soft sheet materials were fixed for 10 minutes in 3% glutaraldehyde (Agar Scientific, Essex) in 0.1M sodium cacodylate solution. These samples were then dehydrated using an ethanol series over 20 minutes. All samples were mounted using carbon adhesive tabs to aluminium stubs (Agar Scientific, UK), and coated in Au/Pd. Imaging was performed using a Philips XL30 FEG-SEM (FEI, Eindhoven), with an accelerating voltage of 5 kV. Low, medium and high magnifications were chosen as appropriate for each sample. Images were taken in random locations (minimum of 3 per sample) or to display notable features.

#### **3.4.2.2 Nanoscale Imaging**

All previously cut or weighed materials were mounted on to clean glass slides using adhesive tape. For imaging, two AFMs were used depending on the requirements of the individual sample. A Nanowizard 4 (JPK, Berlin) AFM operated in contact mode in air was used to image most samples, equipped with MSNL (Bruker, Santa Barbara) cantilevers with  $k = 0.03\text{-}0.6\text{ N/m}$ . **Figure 3-1 A** shows the MSNL cantilevers and **B** the tips used predominantly for imaging. For samples that were not suitable for contact mode imaging, a Dimension Icon (Bruker, Santa Barbara) AFM in tapping mode in air was used, equipped with NSC-35 cantilevers (MikroMasch, Tallinn)  $k = 5.4\text{-}16\text{ N/m}$ . In liquid, the Nanowizard was used, as described previously. Drops of deionised water were applied to the surface until the materials were fully hydrated. These materials were left to stabilise for 10 minutes before measurements were taken. With all instruments and imaging modes, the setpoint, gains and scanning speed were optimised for each sample. Images were

taken in random locations across the sample, processed using proprietary JPK software, and representative images presented.

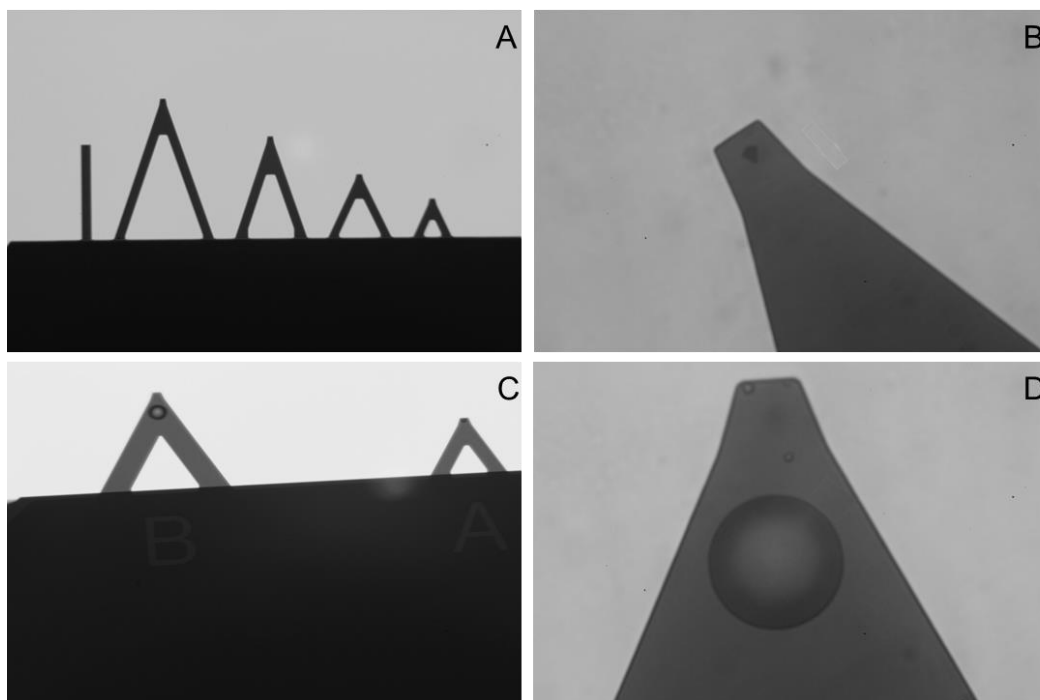


Figure 3-1 LM of AFM cantilevers. A & B) MSNL cantilevers with a magnification of the tip. C & D) NPO cantilevers modified with a silica bead. A, C 20x magnification, B, D, 100x magnification.

### 3.4.2.3 Nanoindentation

For mechanical measurements (indentation) the Nanowizard 4 was used. In air, calibrated RFESPA (Bruker, Santa Barbara) cantilevers,  $k = 3 \text{ N/m}$ , were employed to take 500 force-displacement measurements on the sample with an applied relative setpoint of 300 nN. For mechanical measurements (adhesion) in liquid, NP-O (Bruker, Santa Barbara) cantilevers,  $k = 0.175 \text{ N/m}$ , were modified with  $10 \mu\text{m}$  diameter silica beads. Drops of deionised water were applied to the surface until the materials were fully hydrated. These materials were left to stabilise for 10

minutes before measurements were taken at a relative setpoint of 0.5 nN. No more than 50 measurements were made in any one  $10\ \mu\text{m}^2$  location. The force-displacement curves were processed using proprietary JPK software and fitted according to the Sneddon model. This data was graphed, statistically analysed and presenting using OriginPro (Origin Corp, Massachusetts).

#### **3.4.2.4 Fibroblast-Membrane Mechanical Response**

For single-cell force spectroscopy, tip-less cantilevers were functionalised with a  $50\ \mu\text{m}$  diameter polystyrene bead, similar to **Figure 3-1 C**, with an ideal placement seen in image **D**. These beads were then functionalised with poly-L-lysine to promote the selective binding of MG-63 cells, using an already established methodology by the research group for bacterial investigations as shown in Figure 3-2.

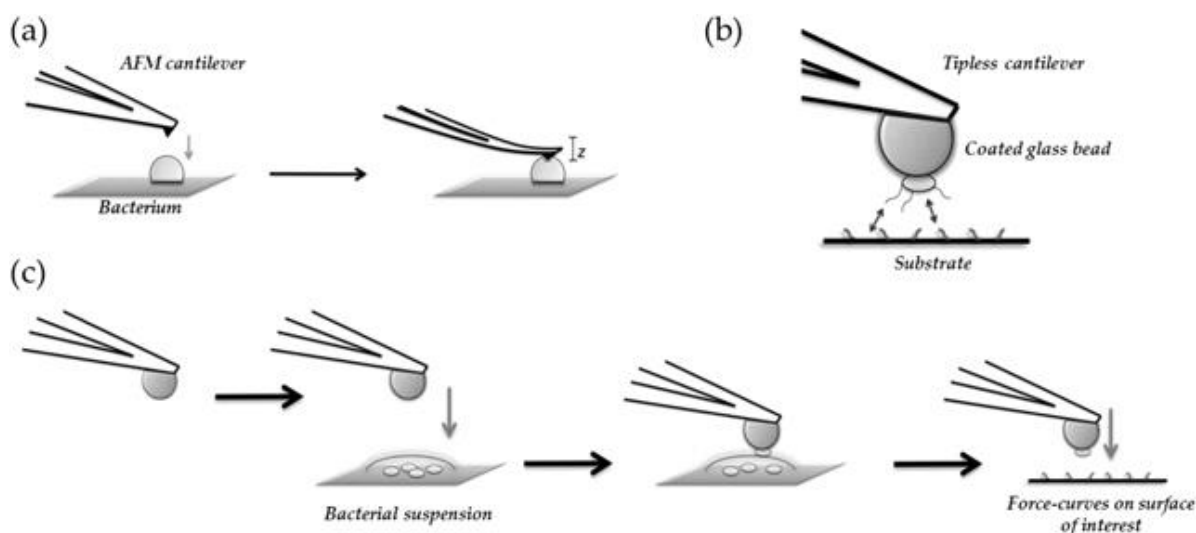


**Figure 3-2 AFM cantilever functionalisation, adapted from** <sup>271</sup>

Previously trypsinised cells were placed in buffer solution and placed under the AFM. The coated bead was slowly brought into contact with a cell, and left in contact for 2 minutes. After withdrawing the bead, an inverted optical microscope

was used to confirm the bead functionalisation through cell attachment. Cell-functionalised cantilevers were replaced every 45 minutes to ensure that the cell was kept alive. Adhesion measurements were carried out in PBS by applying a zero-contact force (0.5 nN) with a piezo Z-length of 7.5  $\mu\text{m}$  between the cell and the sample. A similar protocol to this has been published <sup>271,305</sup>.

#### **3.4.2.5 Digestion Study**

All materials were imaged using a VivoSight OCT scanner (Michelson Diagnostics, Kent) directly on the surface; no sample preparation was needed. This OCT has an optical resolution of less than 7.5  $\mu\text{m}$  laterally and less than 5  $\mu\text{m}$  axially. The image stack was made of 500 B-scans (cross-sectional image) separated by a distance of 10  $\mu\text{m}$  between each frame. Additionally, a smoothed curved enface image was recalculated from the B-scan stack to obtain a top view across the surface of the sample. All final acquired images were 6  $\text{mm}^2$  in the area and approximately 1.84 mm depth. The images were then exported from OCT software as 16-bit TIFF images and imported into ImageJ (NIH, USA). The A-scan (line profile) of each B-scan was extracted, and the gradients and shapes of the lines recorded.

#### **3.4.2.6 Ex-Vivo Animal Model**

Eighteen 10-month-old Wistar rats were used, in accordance with the EU Directive for animal experiments and the ARRIVE guidelines for animal research <sup>380</sup>. After 2 weeks of acclimatisation, the experimental guided bone regeneration surgery was

---

The animals in this subsection were reared by Dr Kostomitsopoulos (Laboratory Animal Facilities, Biomedical Research Foundation, Athens)

performed using an established research procedure <sup>381</sup>. A standardised 5-mm diameter critical size defect was created on each parietal bone by the use of a trephine burr. The collagen membrane BG was trimmed and adapted to the intracranial part of the defects, and then the bone substitute BO was loosely compacted into the defect and eventually covered by the second layer of BG. The flap was sutured in layers using Vicryl 5 (Ethicon, Cincinnati). Six rats were randomly sacrificed at 7, 14- and 30-days post-defect creation. One defect section was randomly chosen for decalcified histology. Samples were embedded in paraffin wax for histological sectioning, and stained using picro sirius (PS) red for collagen. When imaged using a polarised light microscope, the use of PS would show the presence and alignment of collagen <sup>382,383</sup>. Samples were de-waxed in paraffin before preparation for SEM and AFM as above.

### 3.5 Part A – Collagen Membranes

#### 3.5.1 Mesoscale Imaging

All of the products tested are marketed as having “microscopic” features which are crucial to their function. As collagen is a highly hierarchical material, a technique such as SEM would allow for mesoscale imaging of a range of features across varying length scales from millimetres to several microns. As a technique, SEM is a well-established and the fast image acquisition time allows the user to move between large areas, and varying magnifications so is well suited to this task. However, the standardised sample preparation protocol for SEM limits the type of data that can be obtained as samples must be wetted before imaging. Despite this small limitation, which must be considered during the analysis and succession of the results, SEM is the only suitable technique that will allow for the rapid acquisition of images across length scales. The use of SEM is intended to answer Objective 1 “*characterise the morphology of the membranes with a particular focus on the presence of porosity, collagen fibres and D-banding*”. The images that are presented here are representative of the sample taken at varying magnifications



### 3.5.1.1 BG Mesoscale Imaging

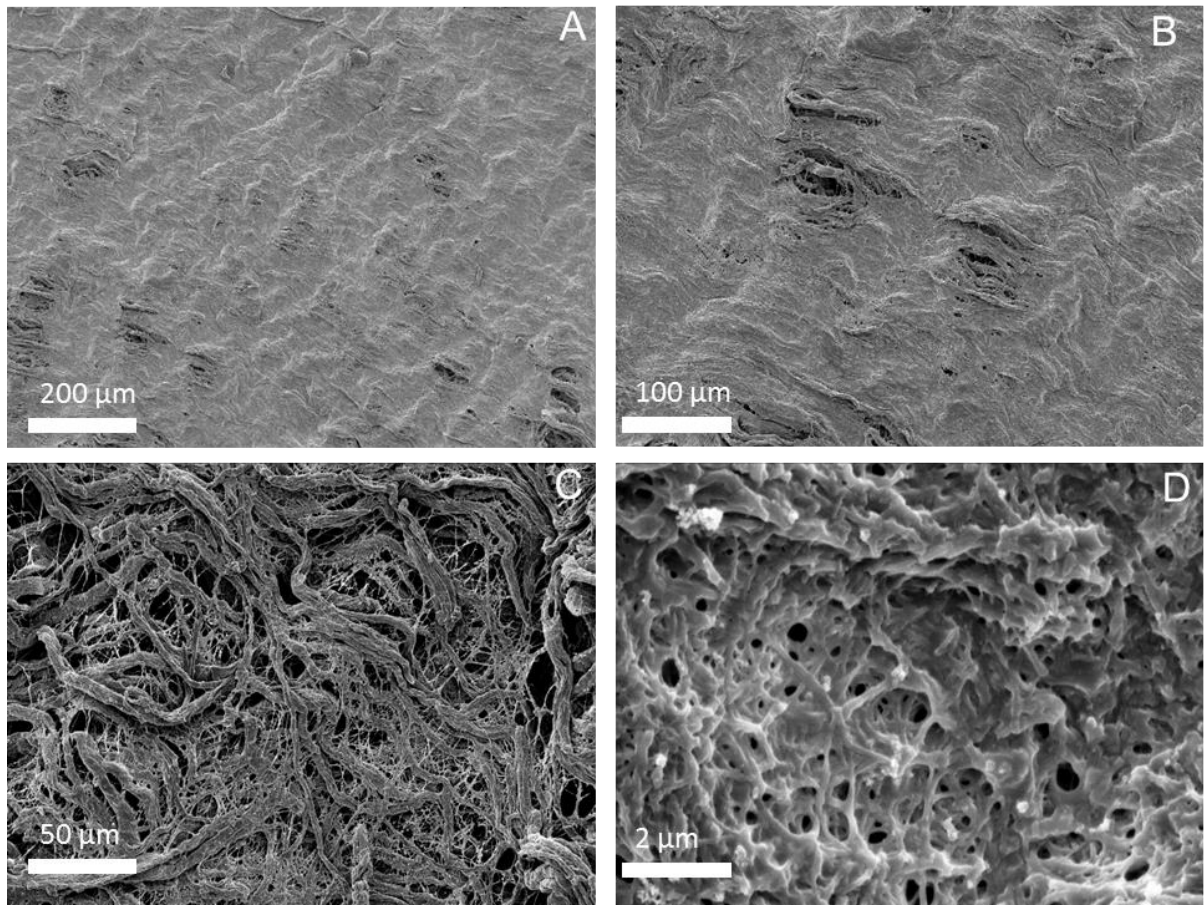


**Figure 3-3 Representative SEM images of collagen membrane BG showing typical surface features**

**A 100x, B 250x, C 500x, D10,000x magnification**

**Figure 3-3** shows the images taken of BG at different magnifications. The low magnification image **A** shows a homogenous ridged surface with only small imperfections in the ridges. Some imperfections, seen in **B**, are visible in the surface, where fibres can be seen. When magnified in **C**, the collagen network is apparent. The disordered alignment of collagen is not typical for skin. However, the formation of bundles with other smaller bundles interconnecting is seen in native skin tissue. At the highest magnification **D**, it can be seen that porosity is present. These pores were not

seen at other magnifications, and are small enough to prevent cell movement through them. At 10000x magnification, the collagen does not display D-banding but does show evidence of structural glassification, an early sign of denaturation of collagen into gelatine.

### **3.5.1.2 MG Mesoscale Imaging**

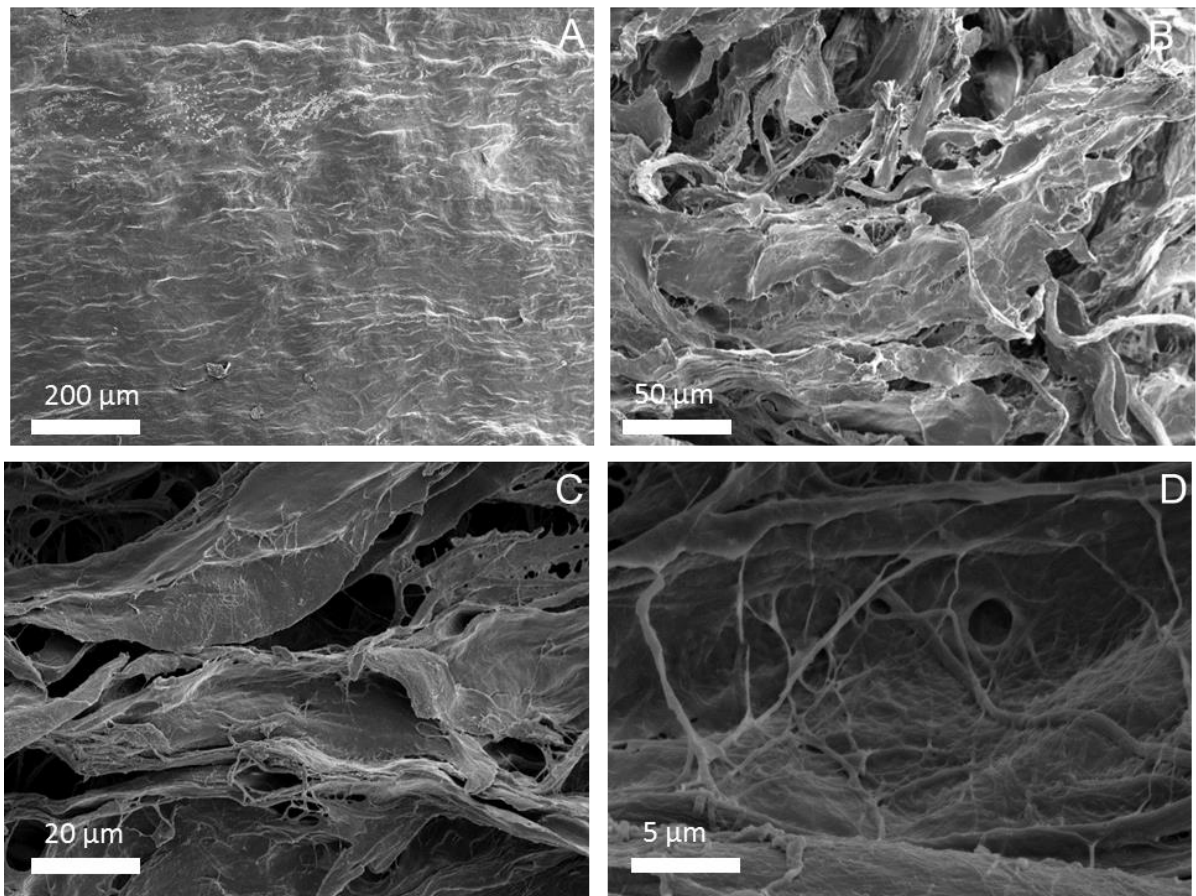


**Figure 3-4 Representative SEM images of collagen membrane MG showing typical surface features**

**A 100x, B 350x, C 500x, D 5000x magnification**

**Figure 3-4** shows the images taken of MG at different magnifications, with image **A** showing the lowest magnification. Initially, MG and BG appear to be very similar with both samples having a homogenous ridged surface. The imperfections in BG that

showed bundled fibres (Figure 1-1B) however are not present in MG when seen in image A. At medium magnification in images **B** and **C** the surface collagen shows large sheet structures without visible fibres. The highest magnification in image **D** shows bundles of fibres where individual fibres cannot be identified. Smaller fibrils link the larger bundles and form a thin spindle network. No banding is seen, and the only fibrils identifiable are in the spindle network.

### 3.5.1.3 BO

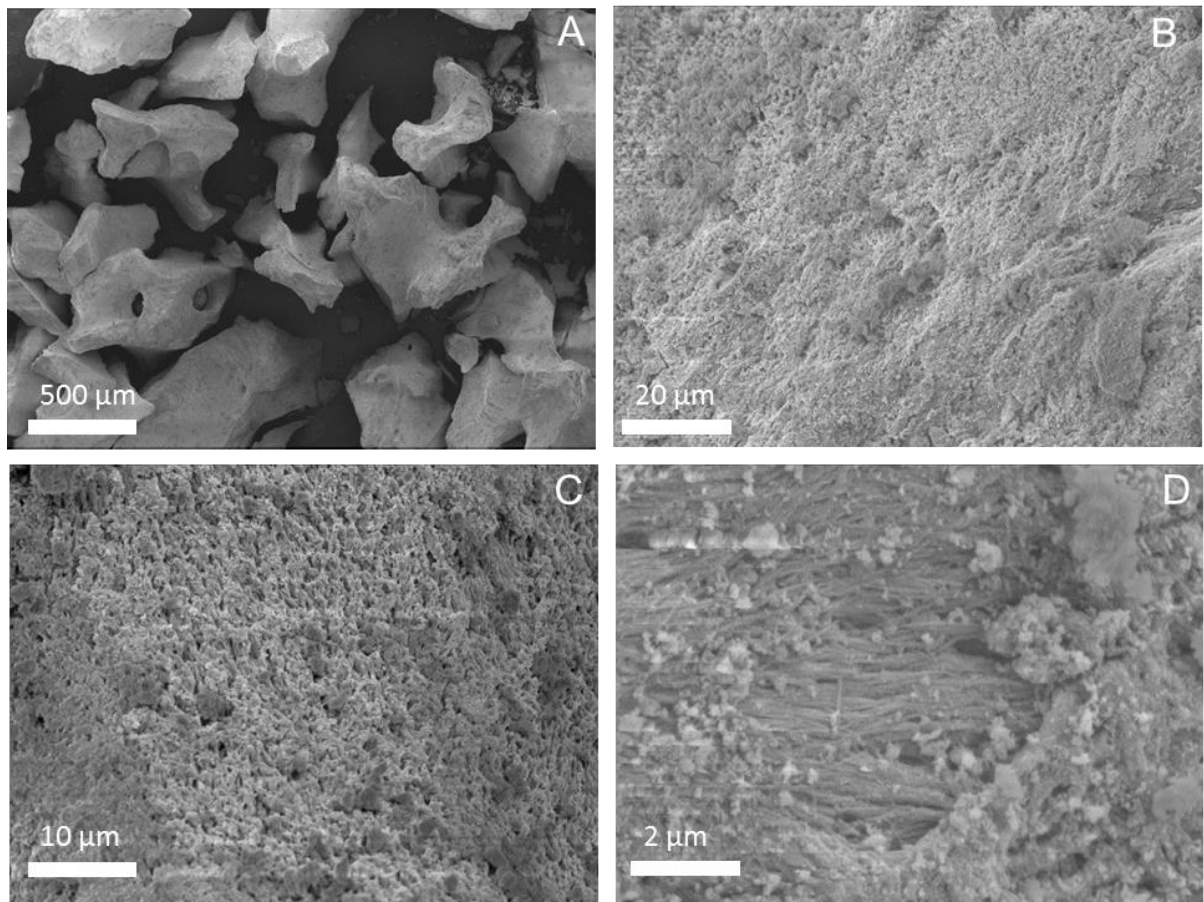
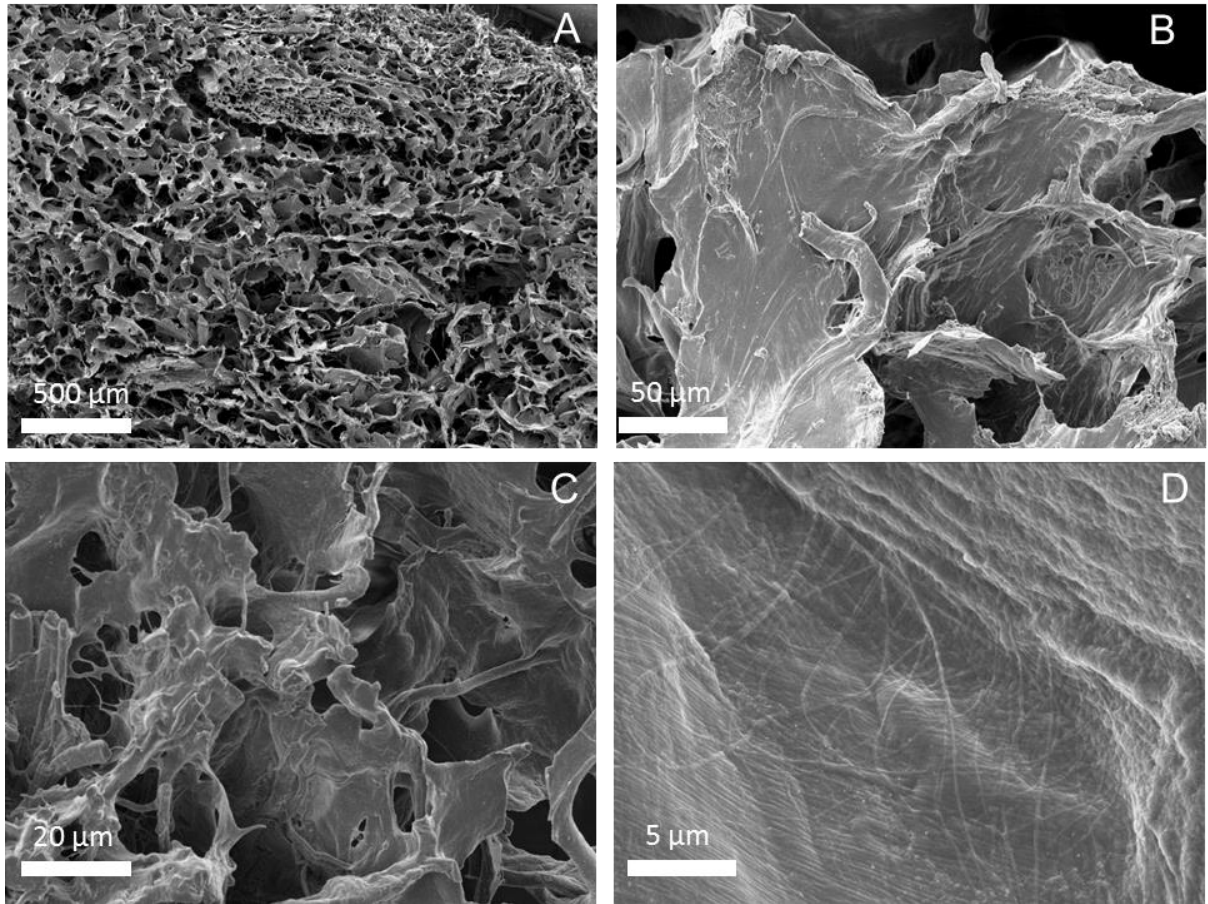


Figure 3-5 Representative SEM images of bone substitute BO showing typical surface features

A 35x, B 1500x, C 2000x, D 12,000x magnification

**Figure 3-5** shows images of the bone substitute BO. Image **A** shows clearly that the dimensions of the mineralised material are heterogeneous. A variation in surface roughness can also be seen with some individual granules having both rough and smooth surfaces. This is consistent with a manufacturing process that would both fracture and grind bones into smaller granules. Some holes in the mineral structure can be observed which appear to penetrate the material fully. Images **B** and **C** both show exposed mineral crystals, the two-tone colours have been shown previously to indicate acid etching and then the resultant remineralisation from mineral leaching. The rough surface in C also suggests acid etching, which is not seen in the smoother B image. At the highest magnification, image **D** collagen fibres can be easily identified. They are aligned, bundled and have a strong preferential orientation, and are decorated with particles resembling hydroxyapatite. While collagen is clearly present and can be readily identified, the rough nature of the sample prohibited further investigation.

#### 3.5.1.4 FG



**Figure 3-6 Representative SEM images of soft tissue substitute FG showing typical surface features**

**A 35x, B 500x, C 1000x, D 3500x magnification**

**Figure 3-6** shows all magnifications of FG. Highly porous and sponge-like, image **A** shows the high degree of pores, which extend throughout the depth of the material. Collagen sheets form a series of chambers which resemble a honeycomb structure. Most of the sheets are parallel to the imaging direction, so the surface area imaged is minimised, and the pore size maximised. The sheets themselves can be seen in **B** and **C**, and smooth glassy structures, probably altered by the SEM preparation process.

Some smaller fibrils can be seen around the edges of the sheets, and the sheets appear to overlap and are rounded. When looking at the sheets at the highest magnification in image **D**, a very fine fibril network can be seen in the sub-surface region. Clearly heavily processed and artificially altered, this material bears little resemblance to native tissues.

#### **3.5.1.5 Mesoscale Discussion**

Being a porcine-derived material, both BG and MG have similarities to native skin tissues. Both samples could be imaged without difficulty and showed some clear markers of collagen at every length scale. At low magnification (Figure 3-3 A, Figure 3-4 A), due to wetting from sample preparation, few features are visible, and a homogenous surface is seen. At medium magnification (Figure 3-3 B-C, Figure 3-4 B-C), the fibres of BG can be clearly seen, and this contrasts with the sheet-like structure of MG. Some fibres are preserved at high magnification in BG and MG (Figure 3-3 D, Figure 3-4 D), but glassification in BG and loss of banding in MG suggest that the collagen is not intact.

Passivation and sterilisation are essential for manufacturing collagen membranes from an animal source <sup>384–386</sup>. The first concern of passivation and/or sterilisation technique is that it must destroy or deactivate any reasonable pathogen or contamination, to prevent cross-species infection<sup>387–389</sup>. The exact preparation for the method of the membranes is not publicly available. However, several mechanisms could be used by the manufacturers. One such mechanism could be alkaline passivation with thermal shock; the exposure of collagen to a calcium hydroxide slurry before heating to a temperature to damage any remaining pathogens <sup>390</sup>. This is likely to cause some damage to the collagen, even when steps are taken to protect it from losing structural integrity <sup>390,391</sup>. If heating for an extended period, gelatinisation can occur. This would

be identified by the loss of D-banding and a shiny or glassy appearance of the collagen<sup>356,392</sup>. Acid treatment also causes gelatinisation and then further degradation of the protein. Methods such as autoclaving would give similar gelatinisation, as both heat and water exposure causes gelatine formation<sup>278</sup>. Irradiation, either with gamma rays or UV are likely to be too expensive and unstable, damaging collagen cross-links and potentially creating free-radicals<sup>343,389,393,394</sup>

From the evidence of the mesoscale imaging, it appears that thermal treatment has been used to passivate the membranes, alongside an alkaline bath. Both materials show clear evidence of collagen damage, through a lack of D-banding and clear fibril structures. However, it must be noted that imaging solely using SEM does not allow for a complete picture of the damage caused.

The spongy and highly porous nature of FG and the rough mineralised surface of BO confirmed that there was a significant amount of alterations from the native tissue occurring during manufacturing. As the focus of this section was to perform a multimodal characterisation of collagen, it was decided that the problematic surface behaviour of FG and BO meant that those two samples should not be analysed further. Therefore, the future sections will be focused on the two collagen membrane BG and MG, which have so far been shown to have the most native-like appearance.

The use of SEM was very effective in showing the porosity of the membranes. However, the D-banding and fibril structure could not be successfully resolved, so Objective 1 was not fully met in this section.

### 3.5.2 Nanoscale Imaging and Mechanics

In section 3.5.1 membranes BG and MG were imaged, and their mesoscale features were identified. Crucially, while there was definite evidence of collagen being present under SEM, there was evidence of disruption and damage to the collagen at the smallest length scales. Areas that appeared to be gelatinised were seen, as were fibrils. It was also not known how the sterilisation and passivation process had potentially damaged the collagen, as not all damage could be identified visually. Further investigations into the properties of the membranes were needed, and this would fully complete Objective 1: *“characterise the morphology of the membranes with a particular focus on the presence of porosity, collagen fibres and D-banding.”*

In order to image the samples at the smaller length scales and to quantify any potential damage caused by the manufacturing processes of the membranes, AFM was used. As a technique, AFM is very well suited to imaging features in the nanometer and small micrometre range in length and width. Regarding height, most AFMs are optimised to work in the range of hundreds of nanometers and at a maximum can image features that are in the single digit micrometre range. The Young's modulus of the samples, a value of the stiffness can also be measured using AFM. This would allow for the identification of both quantitative and qualitative assessment methods using a single instrument in two different modes, and finalise Objective 1 while comprehensively answering Objective 2: *“evaluate the mechanical behaviour of the identified collagen fibres seen in dry and liquid environments”*.



### 3.5.2.1 BG

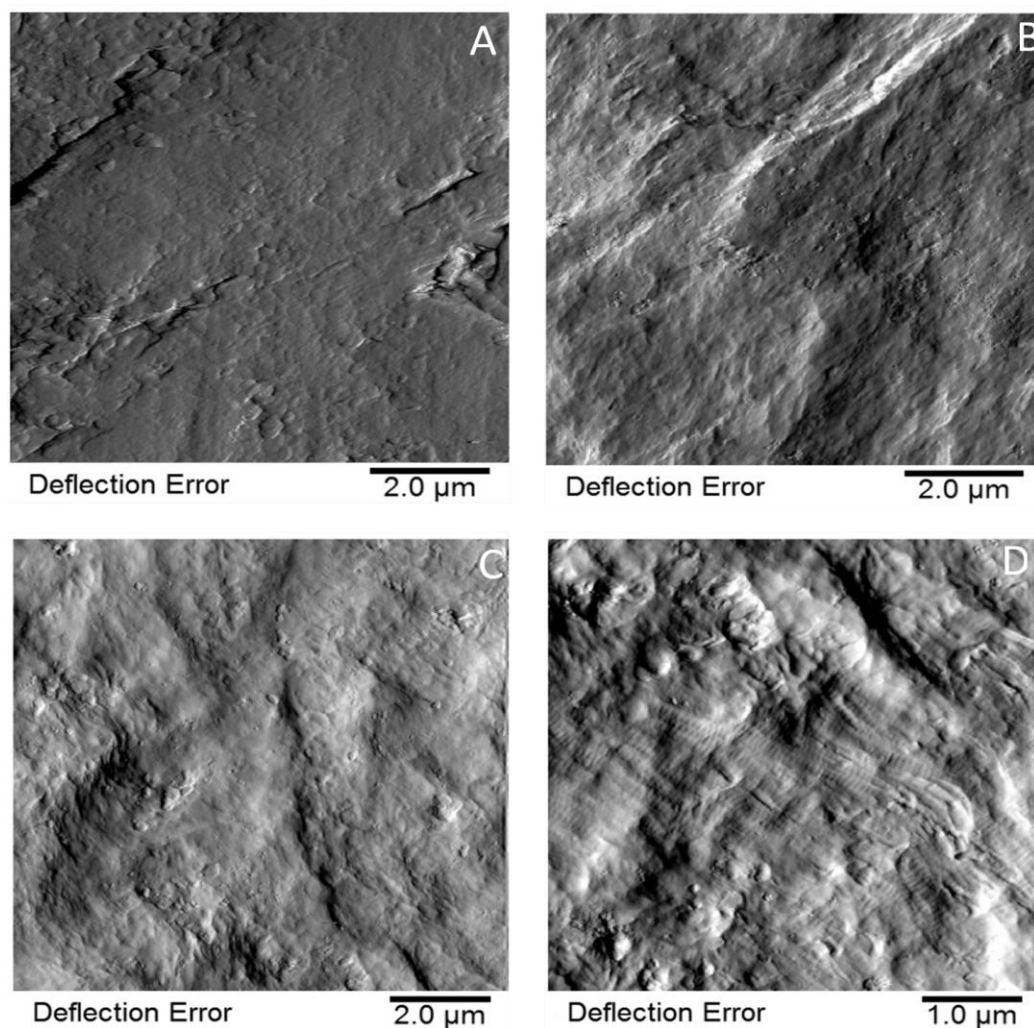
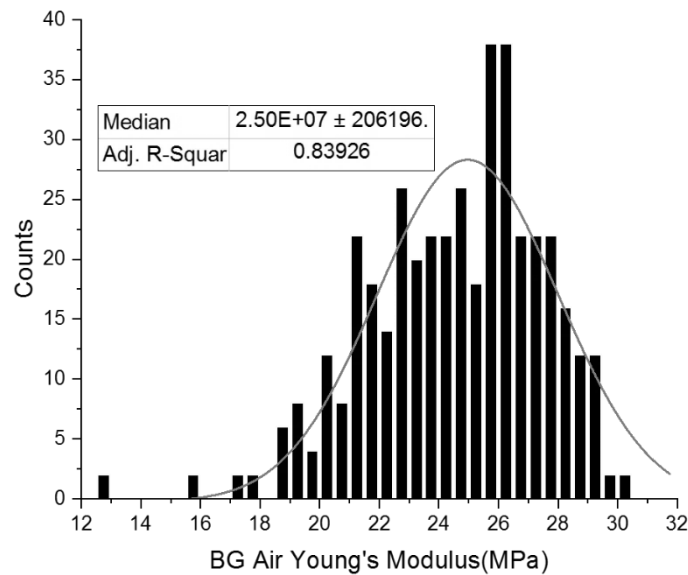


Figure 3-7 AFM surface images of BG in different locations

**Figure 3-7** shows the surface of BG as seen by AFM in different areas. Images **A** and **B** both show a homogenous surface, similar to what was shown under SEM. The smooth surface was suggested as being a side effect of the SEM preparation (Figure 3-3 A). For SEM preparation, the surface must be wetted, chemically fixed and dehydrated using ethanol. As the AFM sample preparation did not wet the sample, the presence of a smooth surface layer using SEM and AFM can be confirmed. Image **C**

shows similar smooth areas, but there are some definite locations where some sub-surface features are visible, as are some very small nodules or particles. These are likely a part of a loose surface layer. Image **D** shows a higher resolution image where collagen fibrils with D-banding is visible. These fibrils were aligned in register. An amount of the homogenous surface layer can still be seen on the edge of the image.



**Figure 3-8 AFM mechanics for Young's modulus of BG in air**

**Figure 3-8** shows Young's modulus of BG in air as calculated from force-distance curves. The graph shows a normal distribution, centred on  $24.97 \pm 0.2$  MPa. The range of values was small, typical of the behaviour of BG. This could be caused by the homogeneity seen under SEM and AFM (Figure 3-3 & Figure 3-7) which appeared to be a coating, and the presence of readily seen fibrils.

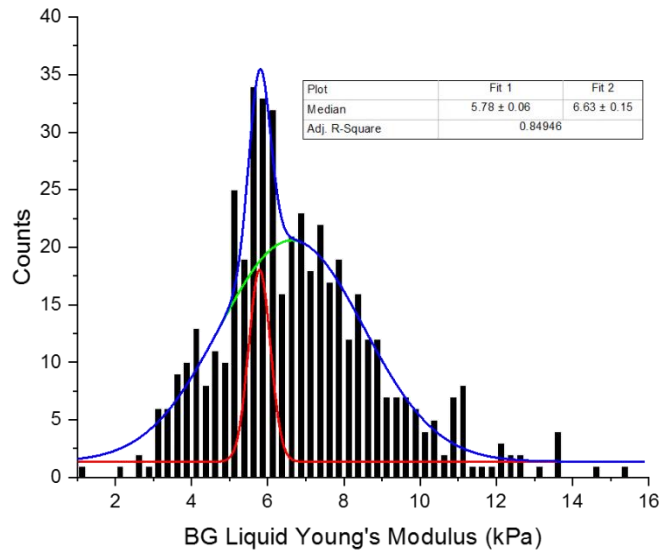


**Figure 3-9 AFM mechanics for Young's modulus of BG in liquid**

**Figure 3-9** shows Young's modulus of BG in liquid. This had a bimodal distribution of  $5.78 \pm 0.0$  as a very narrow peak and a much broader peak of  $6.62 \pm 0.2$  kPa. This could suggest that the swelling of the surface fibrils in water is slightly uneven, splitting the original normal distribution into a bimodal distribution. The difference between the distributions is narrow but present.

### 3.5.2.2 MG

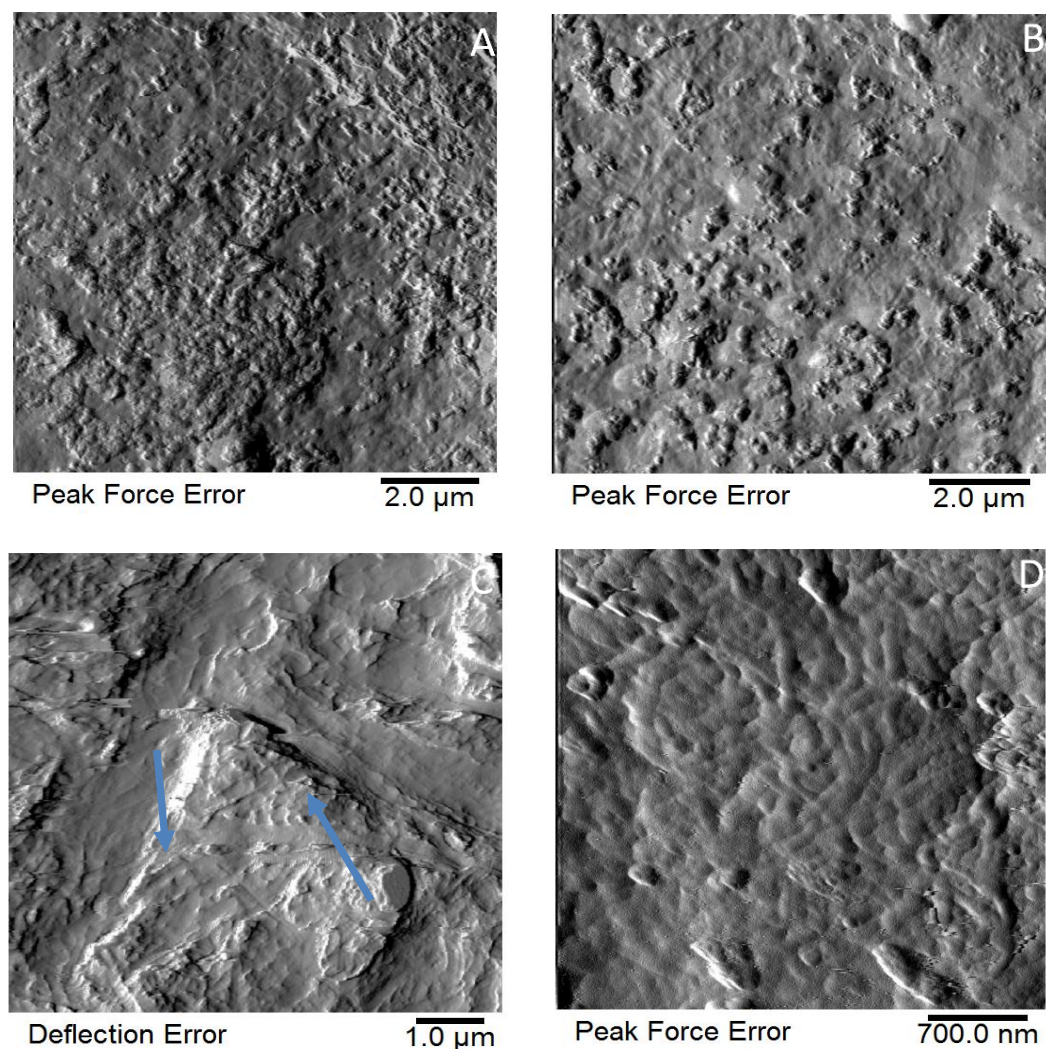


**Figure 3-10** AFM surface images of MG in different locations. Blue arrows show sub-surface fibrils

**Figure 3-10** shows AFM images of MG. Images **A** and **B** show similar features, with small particles or nodules on the surface of the sample. Similar nodules as a surface layer were seen in BG (Figure 3-7 C), but MG shows a much higher proportion of coverage, beneath which it was very difficult to determine conclusively any features. Image **C**, at higher resolution, shows areas which appear to have fibril imprints, but the fibrils can only be faintly seen in one or two areas (blue arrows). 3D-topography data

showed that these are below the plane of the image, with a thin surface covering the fibrils. Image **D** is at a higher resolution than the other images and shows degraded and swollen fibrils. No D-banding was seen on these fibrils, and they are not healthy or intact in appearance.

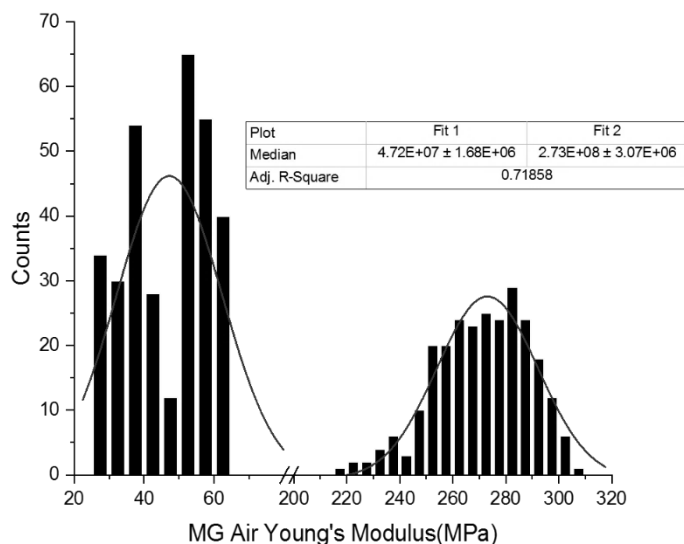


**Figure 3-11 AFM mechanics for Young's modulus of MG in air**

**Figure 3-11** shows Young's modulus of MG in air. This had a discrete bimodal distribution, with peaks seen at  $47.2 \pm 0.2$  and  $273.1 \pm 3.1$  MPa. This gave a wide distribution within the 95% confidence interval. The low value of 47.2 MPa is likely to be the small nodules seen on the surface using AFM (Figure 3-10 A & B). There is a broken scale until the bimodal distribution of stiffness. The high values of Young's modulus on this membrane are consistent with the visual appearance of the material as sold, which consists of a hard-outer shell with a softer sponge material inside.

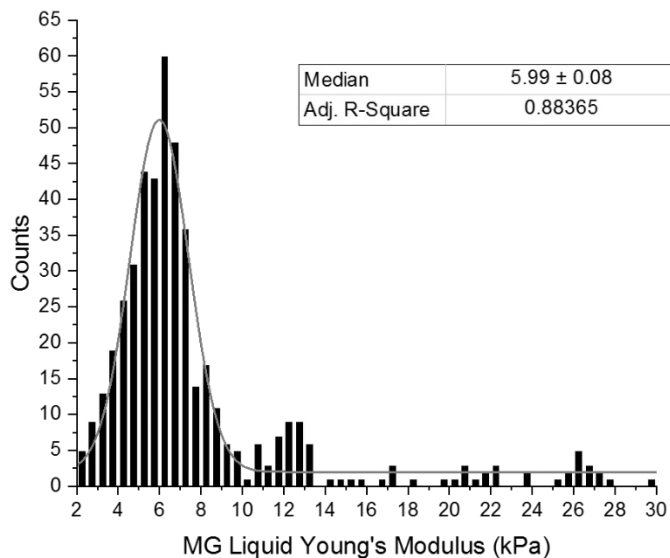


**Figure 3-12 AFM mechanics for Young's modulus of MG in liquid**

**Figure 3-12** shows Young's modulus of MG in liquid. Here, a normal distribution of  $5.99 \pm 0.1$  kPa can be observed, with a large tail towards 30 kPa. Small clusters, around 12-14 kPa and 26-28 kPa, were seen but were not statistically different. The median value matches the medians seen in BG (Figure 3-9), but without the bimodal distribution of BG.

### **3.5.2.3 Nanomechanics Discussion**

In air, both membranes have significantly lower Young's modulus than found in the literature for mammalian fibrillar collagen in a dry state. For dry collagen under AFM, values for collagen are distributed within the region of 0.5-20 GPa<sup>123,374,395</sup>. In a dry environment, the influence of water and the ability of molecules to retain water is paramount, achieved by chemical crosslinking<sup>59,123</sup>. This crosslinking supports the higher-order structures of collagen and can be both enzymatic and non-enzymatic<sup>396–398</sup>. Evidence obtained using mesoscale SEM imaging (section 3.5.1) suggested that thermal denaturing could be a factor in the passivation of the membranes. With the data

collected in this section, it is reasonable to assume that thermal denaturing is occurring, alongside an alkaline bath. If heating is involved in the manufacturing process, then the crucial crosslinking of collagen is likely to be destroyed or severely damaged. Previous studies have linked the lack of crosslinking to a decrease in mechanical properties of collagen, which could explain why the values seen here are several orders of magnitude lower than expected <sup>59,396</sup>. Additionally, the manufacturing processes may damage the collagen itself. Damage to the collagen, especially heat and acid attack, can cause gelatinisation <sup>356,392,399</sup>. This would cause a loss of D-banding and Young's modulus in the sample <sup>2,400–402</sup>.

#### **3.5.2.4 Section Summary**

AFM imaging was used to confirm the presence of collagen, and to confirm that there were several markers of intact, healthy collagen present. There were also areas that were obviously damaged and showed signs of degradation. These degraded areas were also found to be mechanically weaker than native collagen, further confirming their degradation and providing more clues to the manufacturing process of the membranes. Objectives 1 and 2 were fully answered. The mechanical behaviour of the collagen has been profiled, as has three key elements of its morphology. The behaviours and morphology of the two membranes have been compared to each other.

### 3.5.3 Fibroblast-Membrane Mechanical Response

Previously AFM (section 3.5.2) and SEM (section 3.5.1) confirmed the presence of intact collagen at the surface of the membrane. However, Young's modulus mechanical values of the membranes were much lower in both air and liquid than would be expected for intact healthy collagen. Additionally, imaging has confirmed that while there are areas of intact and ordered collagen, there are also many areas where there are signs of collagen degradation, up to gelatinisation.

When these membranes are used clinically, it is often at a trauma site. While it is unlikely that the wound would have been exposed to large changes in temperature or pH, it is likely that the wound site would not be perfectly intact and healthy. Clearly, the membranes must be usable in areas of trauma, but it was not known how cells would respond to the areas of disrupted and disordered collagen. While collagen may be a structural protein that is not sensitive to small changes in structure, unlike enzymes, it cannot be guaranteed that cells in the body will respond normally to the degraded collagen<sup>1,197</sup>. Objective 3 "*quantify the fibroblast-membrane interactions to identify the immediate cell response on implantation*" is examined here, to see if there is a change in cell behaviour for the membrane materials over time.

Here, MG-osteosarcoma cells with a fibroblast-like morphology were mounted alive on a functionalised probe and brought to rest on the membrane surface in PBS at 3 different contact times; 1, 2 and 5 seconds. This advanced use of the AFM as a single-cell spectroscope allow for the recording of the adhesion interactions between the cell



and the membrane as a function of contact time. Two sets of measurements were recorded simultaneously, adhesion force and adhesion energy.

### 3.5.3.1 BG

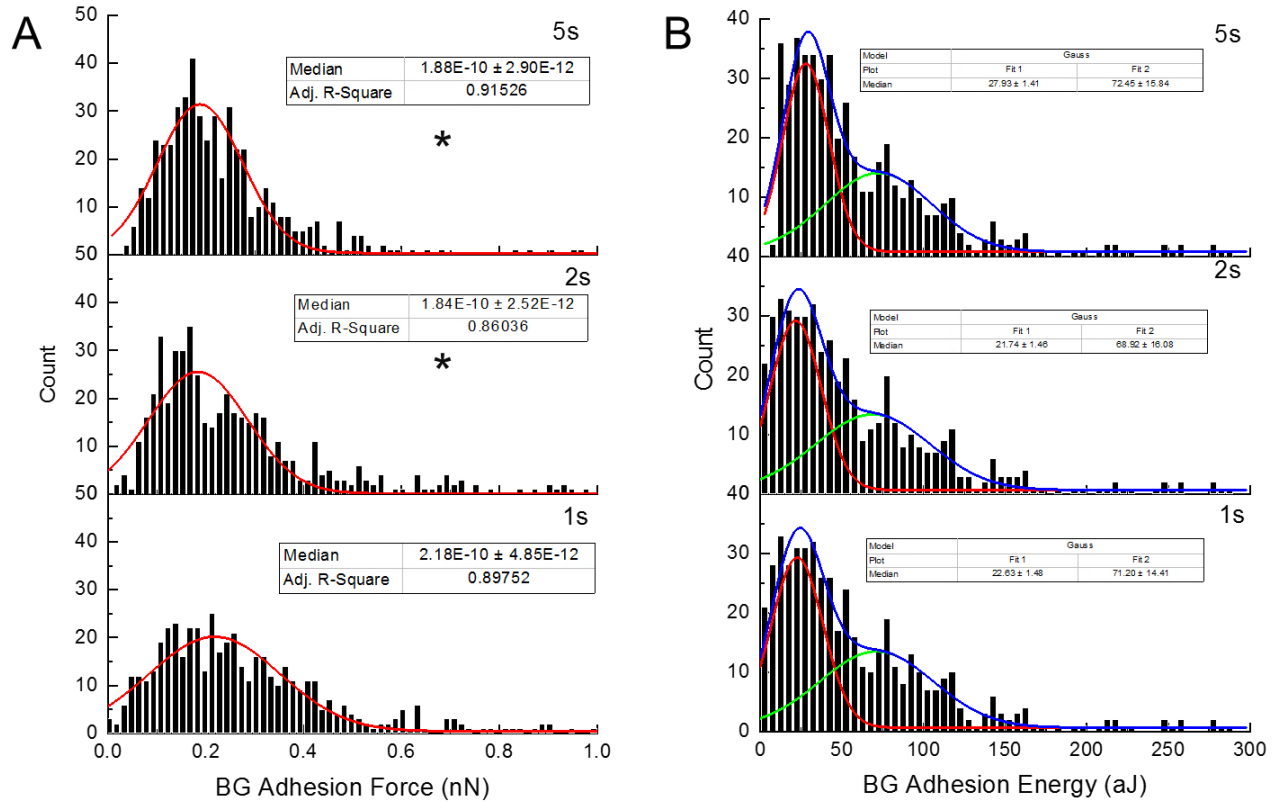


**Figure 3-13 (A) Adhesion force and (B) energy of BG when probed with MG-63 cells.**

**Figure 3-13** shows the adhesion force and energy for BG at all time points. Graph **A** shows the measured adhesion force. The initial force was  $218 \pm 4.9$  pN at 1 s, which changed over time to 2 s. A dwelling time of 2 s gave a distribution of  $184 \pm 0.3$  pN, a lower median than the median of 1 s. At 5 s dwelling time there was a distribution of  $118 \pm 0.3$  pN which was significantly different from the 1 s value, but not the 2 s value. The behaviour of the cells at 2 s and 5s suggests that these interactions are vital in adhering the cells to the membrane, but that these interactions require more than just transient

contact, several seconds is needed for the anchoring process. The interactions measured at 2 s appear to be a transition period between two different groups of adhesion molecules, with the combination allowing for attachment which did not change over time at 5 s. The adhesion force is a measurement of the individual protein binding events occurring as the cell binds to the surface. Change in surface properties will affect how the cell bind to the surface.

Graph **B** shows the measured adhesion energy. The initial energy had a bimodal distribution at 1 s of  $22.63 \pm 1.48$  aJ and  $71.2 \pm 14.41$  aJ. This bimodal distribution did not change at 2 s:  $21.74 \pm 1.46$  aJ and  $68.92 \pm 16.08$  aJ, nor at 5 s:  $27.93 \pm 1.41$  aJ and  $72.45 \pm 15.84$ . The adhesion energy is a measurement of the total energy needed to detach the cell from the membrane. This energy measurement includes the contribution from both the non-specific cell surface membrane to collagen membrane interactions as well as the specific, such as integrins through focal adhesions. While there was a change seen regarding force needed to detach the cell, the overall amount of energy for the entire interaction remained constant. This could suggest that the number of molecular detachment events changed over time; with a change in force needed to detach them, but a larger number of events to balance this out.

### 3.5.3.2 MG

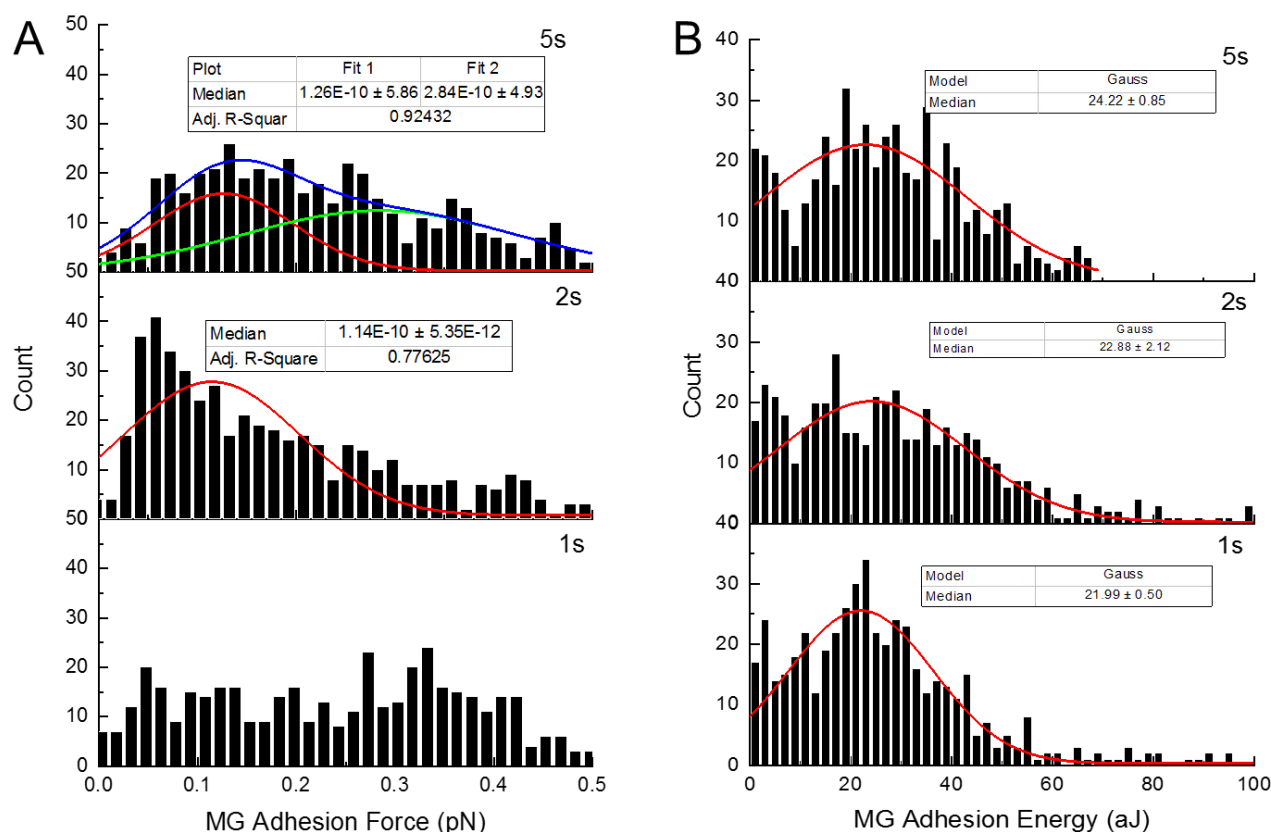


**Figure 3-14 (A) Adhesion force and (B) energy of MG when probed with MG-63 cells.**

**Figure 3-14** shows the adhesion force and energy for MG at all time points. Graph **A** shows the measured adhesion force. The initial force was found to be heterogeneously distributed, and a median could not be calculated. 2 s was calculated at  $114 \pm 5.4$  pN before rising at 5 s to a bimodal distribution centred on  $126 \pm 5.9$  and  $284 \pm 4.9$  pN. 5 s was the only 5 s cell response measurement that could be fitted to a bimodal distribution. The increase between 2 s and 5 s was significantly different when 2 s was compared against the high median of 5s. The 5 s high median was the same as the 5 s high median for BG (Figure 3-13). The change in adhesion force over time is

similar to BG. The pattern of behaviour over time was to decrease and then re-increase the adhesion force. This pattern of behaviour for the adhesion force suggests that the short and (relative) long timescale interactions are significant to catch and anchor cells on to the membrane, with the initial interaction being stronger than the latter interaction.

Graph **B** shows the measured adhesion energy. The initial energy was  $21.99 \pm 0.5$  aJ which did not change at 2 s ( $22.88 \pm 2.12$  aJ) or 5 s ( $24.22 \pm 0.85$  aJ). There was no significant difference seen despite the large changes in adhesion force. The median values for the adhesion energy were not significantly different from the lower medians found in BG (Figure 3-13) suggesting a similar cellular mechanism for adhesion.

### 3.5.3.3 Section Summary

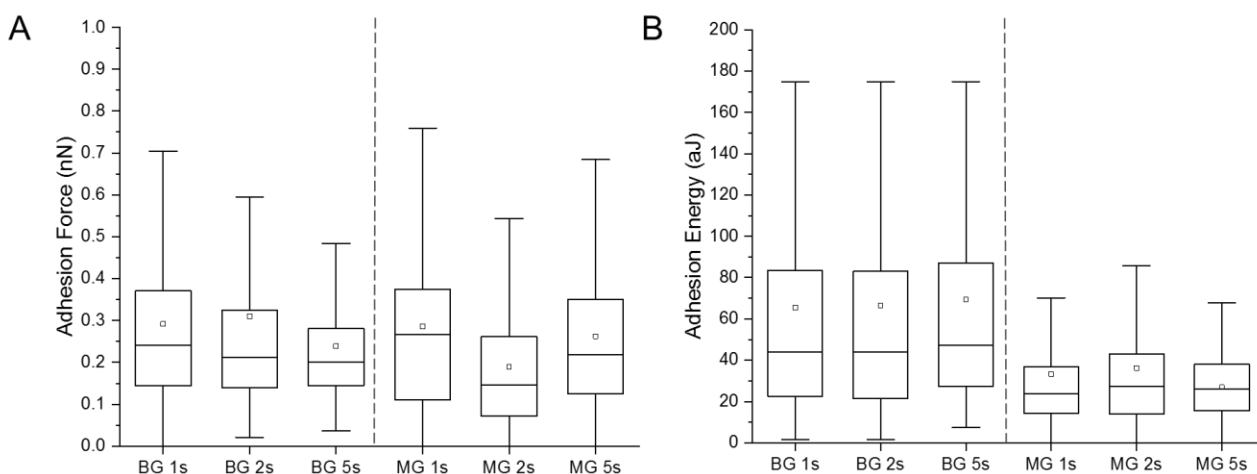


**Figure 3-15** Box plot summaries of (A) adhesion force and (B) adhesion energy

**Figure 3-15** is an overview of the adhesion force (A) and energy (B). The unimodal medians (box) and 95% confidence intervals (range of data shown) do not show the significance or detail of the individual time points.

Single cell force spectroscopy was successfully used to investigate the behaviour of the membranes with interacting with fibroblasts. The force and adhesion values were not found to be dependent on dwelling time for each membrane. Adhesion force is the amount of force needed to break the specific individual interactions as modelled using the worm-like chain model <sup>403</sup>. This was likely to be a time-dependent variable. The adhesion energy was calculated through the integrated area under the force-distance curve <sup>313</sup>. This measurement was likely to be dominated by the non-specific interactions between any two bodies in an environment.

For BG, the adhesion force increased after 1 s, but did not change between 2 s and 5 s. The adhesion energy did not increase over time and was bimodal. The opposite was seen for MG, where the adhesion force increased with time without a change in adhesion energy which was unimodal. There is little information published about the behaviour of cells on collagen membranes. While this study did not give information on whether the fibroblasts recognised the membranes as being made of intact collagen, the data does show that fibroblasts responded to the membranes and adhered to them, and additionally showed a difference in response to the two membranes.

Objective 3, *“quantify the fibroblast-membrane interactions to identify the immediate cell response on implantation”* has therefore been successfully completed. However, the mechanism of the interactions between the cells and the membranes have not yet been determined. One approach would be to stain the cells with alamarBlue to confirm cell viability, and an AFM approach has been previously used to analyse the structure of focal adhesions <sup>404</sup>. Other approaches have used a live cell imaging technique to observe the cells while placed under tension, or through the use of protein

expression assays <sup>405–407</sup>. However, none of these approaches would have been appropriate for this investigation. Firstly, the membranes and AFM probes are opaque, ruling out the use of light microscopy. Secondly, the short contact times that were used in this experiment would not be conducive to the focal adhesion investigations as described in literature. While some longer contact times have been used previously, this was not successful here, chiefly due to the inherent drift of the AFM cantilever in a liquid environment and the short lifetime of the cells.

#### 3.5.4 Collagen Degradation Study (OCT)

Previous sections have investigated the appearance and mechanical behaviour of the membranes after manufacture, and the response of fibroblasts to the membranes. The membranes have been found to be recognised, at some level by the cells of the body. However, the membranes are not designed to remain in situ forever. They must be degraded and resorbed into the body in a controlled manner, to allow for the growth of healthy tissue. One of the ways that the membranes are resorbed is using collagenases to enzymatically cleave them. As collagenases only recognise specific cleavage sites on collagen, it was not known whether enzymatic digestion would still occur, nor was the rate of digestion known <sup>408–410</sup>. Therefore, Objective 4 “*measure the degradation process of the membranes in vitro when exposed to collagenase*” was needed. Firstly, collagenase degradation needed to be confirmed, and if and once it was confirmed, measured and recorded.

In order to investigate this, OCT was used in semi-real-time to image the membranes with collagenase added. En-face images (top view) were used to observe

the surface changes while the B-scans images were used to look at the change in cross-sectional morphology of the membranes. Additionally, line profiles of the B-scans were plotted to measure the change in optical density (calculated as a gradient coefficient) of the membranes as a function of the digestion time points. The full dataset of the top, middle and bottom scans are presented in Appendix A.

### 3.5.4.1 Bio-Gide (BG)

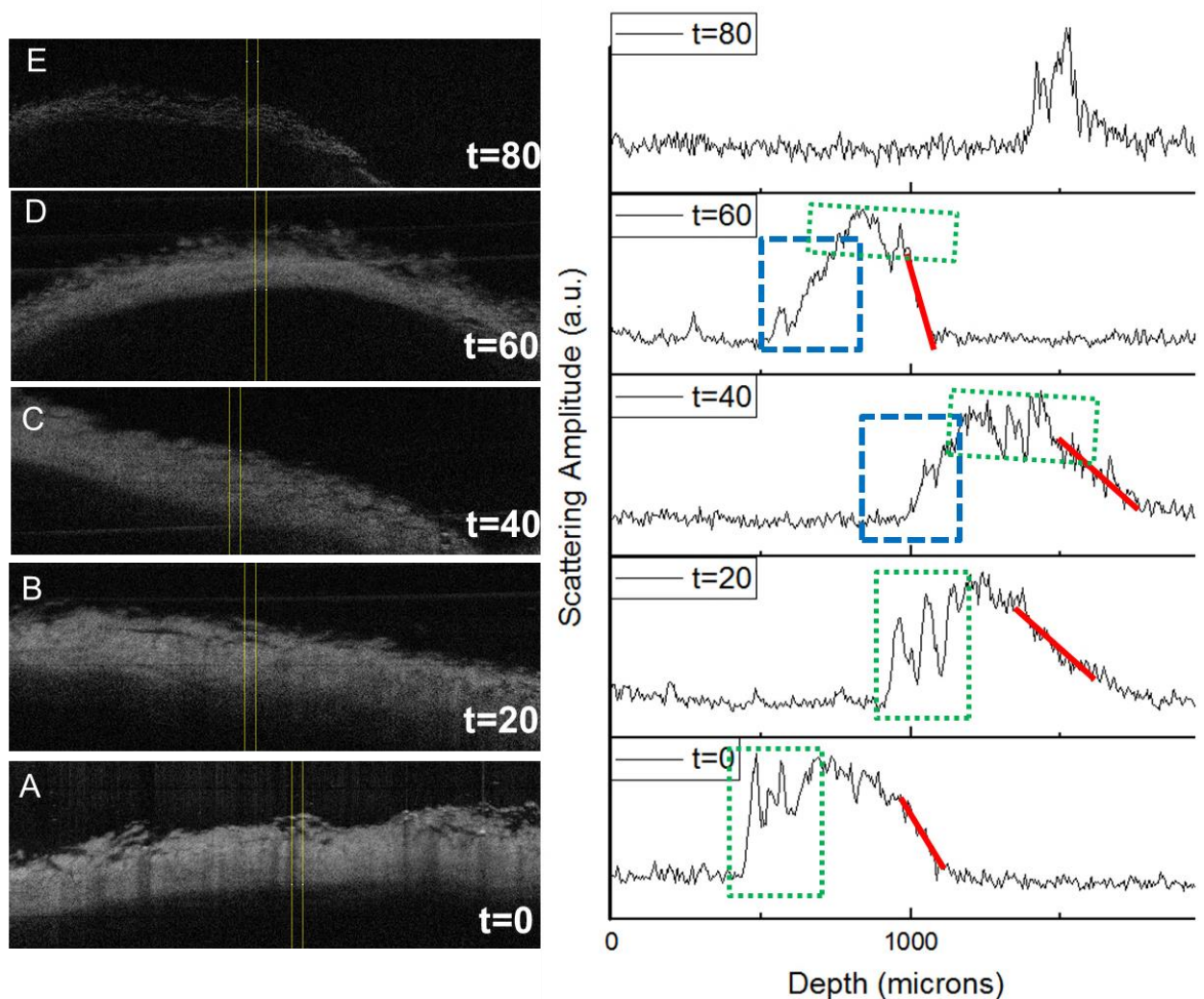


Figure 3-16 Left: B-scan images during degradation of BG, 0-80 minutes. Right: B-scans of the Density is measured by the red line, porosity on the green box and surface behaviour in blue

**Figure 3-16** shows the analysis of the B-scans during degradation. Image **A** shows 0 minutes when the collagenase was added. Here, large pores were seen on the frayed surface, with loose material readily visible. The membrane had a medium density (0.17), with a large swelling observed in response to the uptake of liquid. Image **B** shows BG after 20 minutes of collagenase exposure. No change was seen from 0 minutes, except a slight bowing in the membrane. Image **C** shows the membrane 40 minutes after collagenase exposure. The porosity became smaller and was seen throughout the membrane, without any change in the density or surface behaviour. Image **D** shows BG after 60 minutes of collagenase exposure. The top of the membrane was porous and frayed, with a highly dense bottom layer measured as 0.74. Image **E** shows 80 minutes after collagenase exposure, with only the residual non-specific undigested membrane remaining.

The top layer (towards the top of the image) of the membrane is smoother and more compact than the bottom layer (bottom layer). OCT is a coherent light based technique which works on the difference in optical properties and refractive indices between materials <sup>392,411</sup>. The lower surface appears darker due to the decrease in the amount of light which can be reflected from the membrane, decreasing the apparent resolution <sup>412,413</sup>. This makes the lower surface appear featureless, despite having more roughness than the top surface <sup>219,384,401</sup>.

Regarding the digestion process, immediately after the collagenase buffer is added, an amount of surface movement is seen. The top surface layers are digested, the number and depth of the pores increases and the surface becomes increasingly frayed<sup>414</sup>. The surface area of the collagen then increases, causing an increase in the



enzymatic rate of digestion<sup>356,415</sup>. When the exposed sections of the membrane are digested, only the compact layers are left, which are in turn exposed and degraded. This then bows significantly, increase the density of the bottom-most layer. As the structural support of the membrane is lost, the bowing increases. Eventually only parts of the membrane which are non-reactive to collagenase remain. Without any support, this residue material lacks structural integrity and is dispersed throughout the buffer solution. This pattern of degradation matches the private in-house studies performed by Geistlich, as well as clinical studies into BG resorption.

### 3.5.4.2 *Mucograft (MG)*

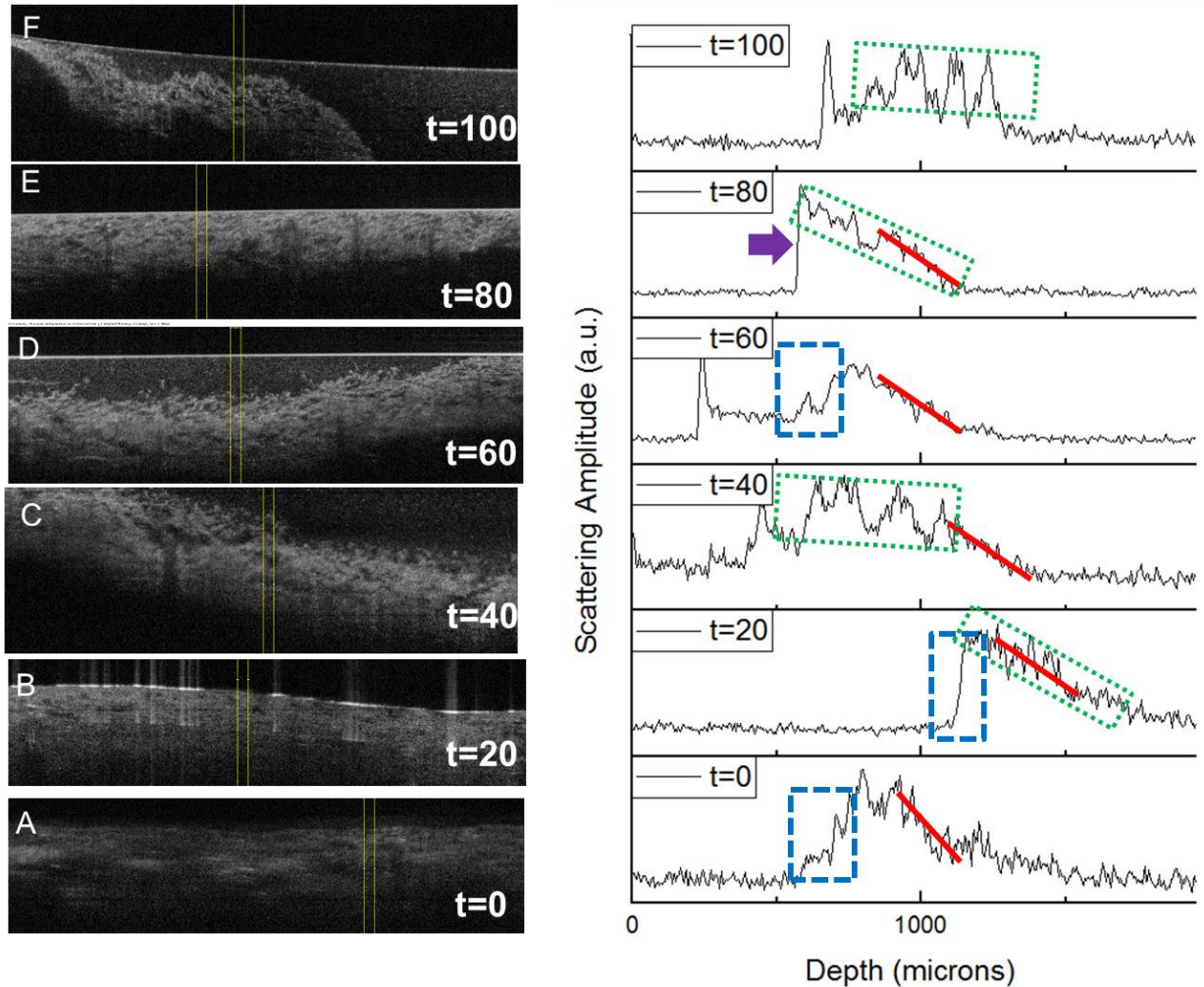


**Figure 3-17** B-scan images during degradation of MG, 0-100 minutes. Density in red, porosity in green, surface in blue and surface compliance in purple

**Figure 3-17** shows the analysis of the B-scans during degradation. Image **A** shows 0 minutes when collagenase was added. The surface was smooth, with porosity found through the membrane, which was found to be medium density (0.27). Image **B** shows 20 minutes, where the surface remained smooth with small porosity, but the density decreased to 0.13. Image **C** shows 40 minutes where the surface became frayed

with loose material seen on the surface. Small and large pores were seen throughout the surface which lost density again to 0.07. Image **D** shows the membrane after 60 minutes of collagenase degradation. The fraying of the surface increased again with only small porosity throughout the membrane. The density increased substantially to a medium value (0.3), returning to a similar value at T0. This was caused by the loss of large pores, with many smaller pores present. Image **E** shows 80 minutes after exposure, with the surface in compliance with the buffer solution. Some small porosity remained, causing a slight drop in density (0.2), but still giving a medium value. Image **F** shows 100 minutes after collagenase exposure, where only non-specific undigested membrane material remained.

In terms of rates of degradation, there are few published studies which have investigated the degradation of these membranes. From personal communication of unpublished internal data, Geistlich confirmed that timings reported here matched their findings. One publication sought to use bacteria found in the mouth to degrade a sample of BG. This suggested a degradation time in physiological conditions of under 4 hours for a complete cessation of enzymatic activity <sup>415</sup>. This is in keeping with the values from Figure 3-16, which stopped at two hours with the ending point being measured as the lack of visibility of the membrane under the OCT. At the other end of the scale, another publication investigated the presence of bony defects, confirming membrane degradation, after surgery to be found within 2-4 weeks <sup>378</sup>. This study was not concerning, however, as the measurement point was the visibility of the healing bone underneath the surgical site, prophylactic antibiotics were prescribed for 10 days, after which chlorhexidine mouthwash was used for 14 days. Chlorhexidine has been found

to kill bacteria, but also increase the adhesion of bacteria onto a surface, potentially shielding the membrane from degradation <sup>305</sup>. Therefore it can be concluded that the data obtained here matches what would be expected, and what is found clinically when the same conditions are met.

As a membrane, the collagenase digestion of MG was similar to BG in that exposed frayed collagen was digested first. However, the digestion route that each membrane took was different. BG is a composite of a majority of collagen and a smaller percentage of keratin, which swells initially on contact with liquid <sup>416</sup>. The collagenase added will only degrade the collagen component, leading to an increase in porosity <sup>379,416</sup>. The amount of visible porosity was linked to the fraying of the surface and increased over time. The initial amount of porosity is high and is essential *in vivo* for cell communication <sup>114,417</sup>. Eventually, however, it could be that the surface tension of the liquid (predominantly water) allowed for an increase in density once the majority of the collagen had been digested. The density of the membrane immediately decreased after T0 but increased over time to return to a similar level at T100. The residual material, likely to be predominantly keratin, could still be seen at T80 and T100. This material still gave some mechanical support to the membrane, keeping it intact until the complete disintegration before 120 minutes.

#### **3.5.4.3 Section Summary**

OCT has been successfully used to confirm that collagenases are still able to digest the membranes, and the rate at which the subsequent digestion occurred was recorded. OCT allowed for three separate answers to the challenge posed by Objective 4. Firstly, degradation was confirmed to be taking place. Secondly, the termination point

could be measured in twenty-minute intervals. Thirdly, the morphological pattern by which the degradation occurred could be visualised. Although the application of OCT in this protocol was not the most effective method of calculating the degradation rate, the visualisation of the degradation allowed for additional data to be collected.

Initially, BG exhibited large porosity which increased over time along with an increase in density. Digestion was complete by 80 minutes. MG exhibited small porosity throughout the thickness of the membrane and a variable density over time. Digestion took 100 minutes to complete. The pathway for digestion for each membrane differed, but both were successfully digested within 100 minutes.

### 3.6 Part B Ex-Vivo Animal Model

Throughout this chapter in Part A, it has been shown that the membranes BG and MG are collagen-based and have behaviours like collagen materials that have been partially digested. The final investigation into the BG membrane was to use it an *in vivo* experiment, where the membranes were implanted into bone defects in rats. After periods of healing, the defects were extracted and biopsied as *ex-vivo*. Investigations were performed using LM, SEM and AFM. By using the same techniques as used in Part A of this chapter, information was sought on the behaviour of the membranes as they would be used clinically. This was the purpose of Objective 5: “*apply knowledge learnt in Part A to characterise the morphology of ex-vivo membranes*”. Particular focus was placed on the morphology of the membranes as they degraded, and data on the interactions between the host and the membrane as this had been shown to be crucial in Part A. Due to external sample preparation, nanomechanical data using AFM could not be collected from these samples, so reliable measurements could not be obtained, and that data is not presented here.

### 3.6.1.1 Day 7 Ex-Vivo

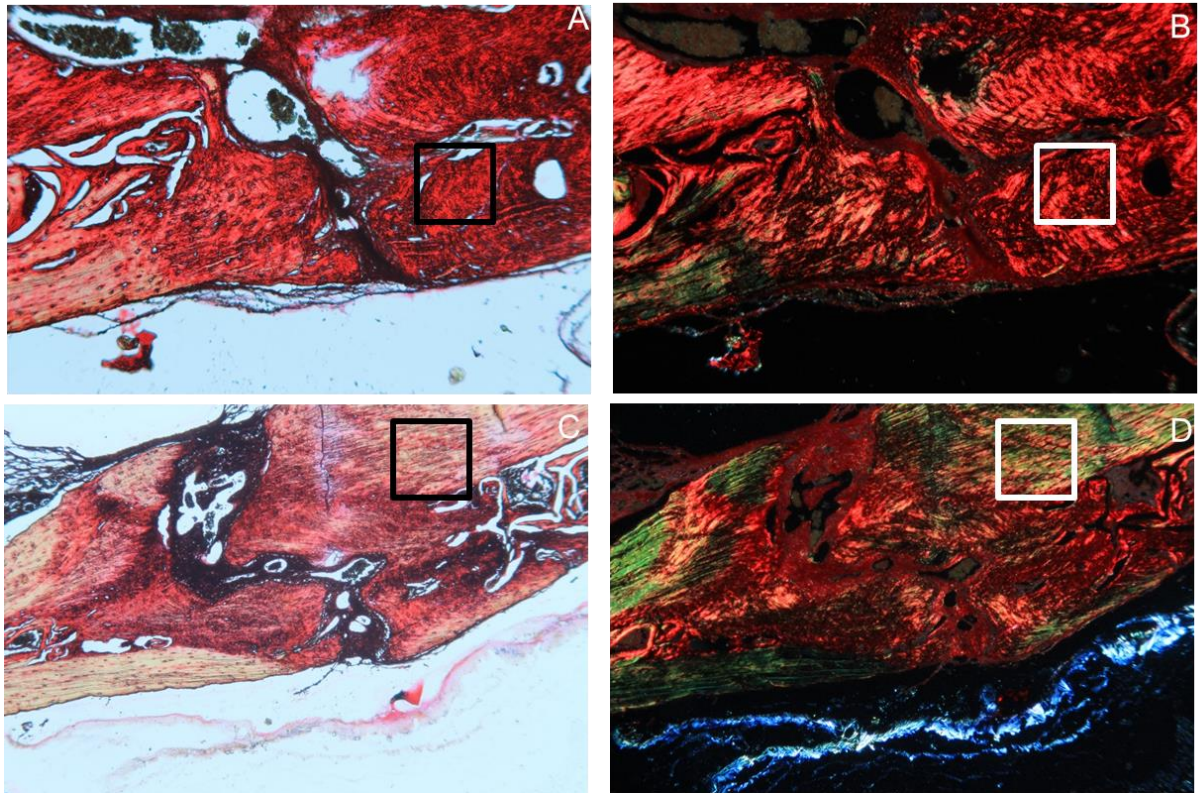
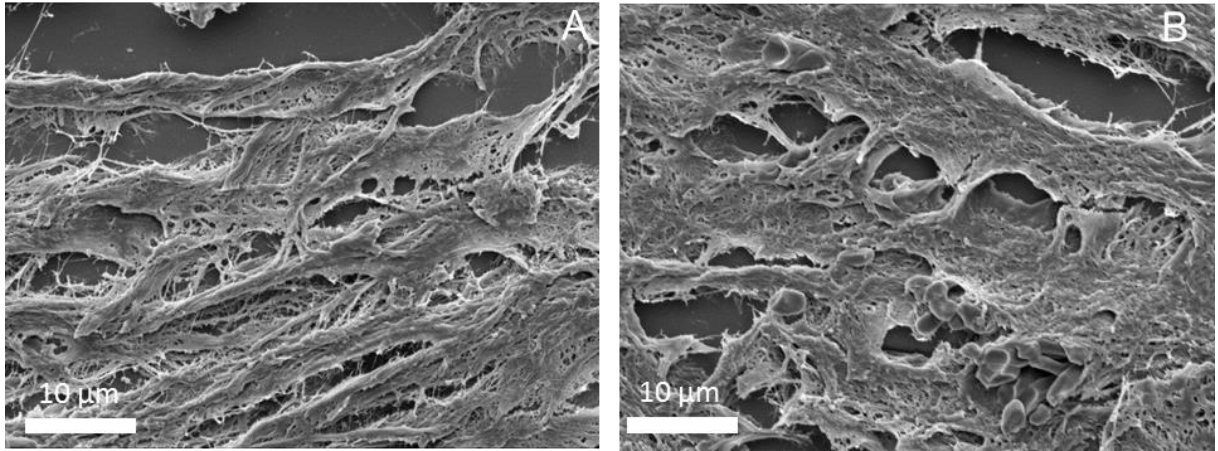


Figure 3-18 Light and dark field LM of the clavicular defect after 7 days of healing. A, B) red area C, D) yellow area. 10x magnification.

**Figure 3-18** shows the LM images of the membrane after 7 days of healing. Image **A** shows an area of the membrane close to the defect. The extensive coverage of red shows a high amount of collagen as stained by PS. Image **B** shows the polarised (dark field) corresponding image from A. The polarisation confirms that the majority of the collagen appears to be aligned and in register. Image **C** shows another location on the membrane far from the site of surgery but close to an exposed area. Image **D** is the corresponding polarised image from C. Green, yellow and red areas are present throughout the image, and the highlighted area has a broad coverage of green and yellow within the membrane.



**Figure 3-19** SEM images of the membrane after 7 days of healing. A) red area, B) yellow area.  
2000x magnification

**Figure 3-19** shows the SEM images of the membrane after 7 days of healing. Images were taken from the areas highlighted in the LM images (Figure 3-18). Image **A** is from the red area. This shows thick bundled fibres with strong directional orientation. Twisting of the bundles is seen, indicative of healthy collagen. Additionally, there are gaps and pores between the fibre bundles with a smaller fibre network connecting the larger bundles. Some collagen sheets are also present. Image **B** is from the yellow area. This shows an extensive covering of collagen sheets, without bundling. The sheets are smooth, without many fibres visible and appear to be compacted. Towards the bottom of the image, infiltration by white blood cells shows an immune response from the animal model.



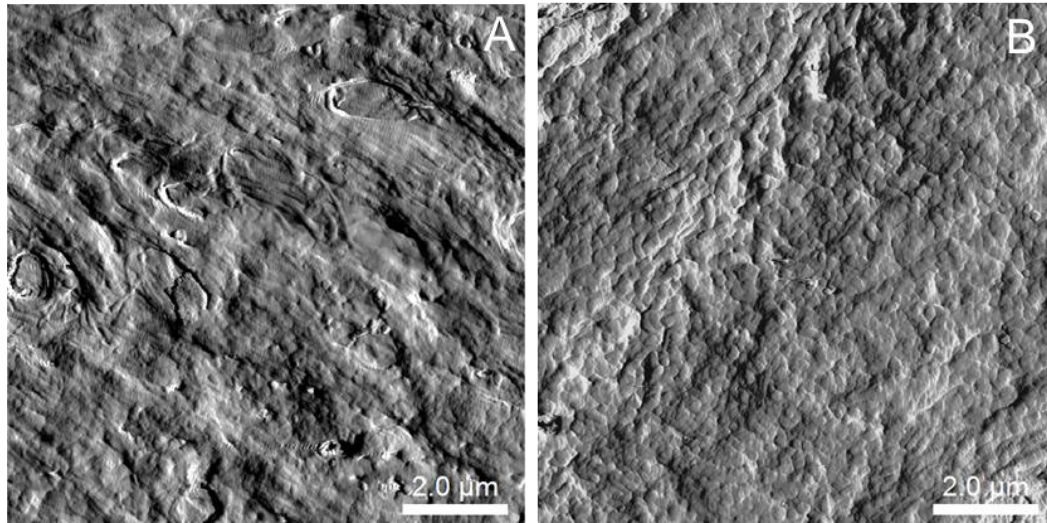


**Figure 3-20** AFM of the membrane after 7 days of healing A) red area, B) yellow area

**Figure 3-20** shows the AFM images of the membrane after 7 days of healing taken in intermittent contact mode. Images were taken from the areas highlighted in the LM images (Figure 3-18). Image A is from the red area. Small bundles of fibres are visible which have a strong directional orientation. There are also small loose fibres present. However, D-banding cannot be identified in this image. Some gaps and pores are also seen. Image B is from the yellow area. There are some fibre-like features seen, but these are indistinct. Some areas are smooth and featureless. There is a considerable amount of unidentifiable material present, which does not resemble collagen.

### 3.6.1.2 Day 14 Ex-Vivo

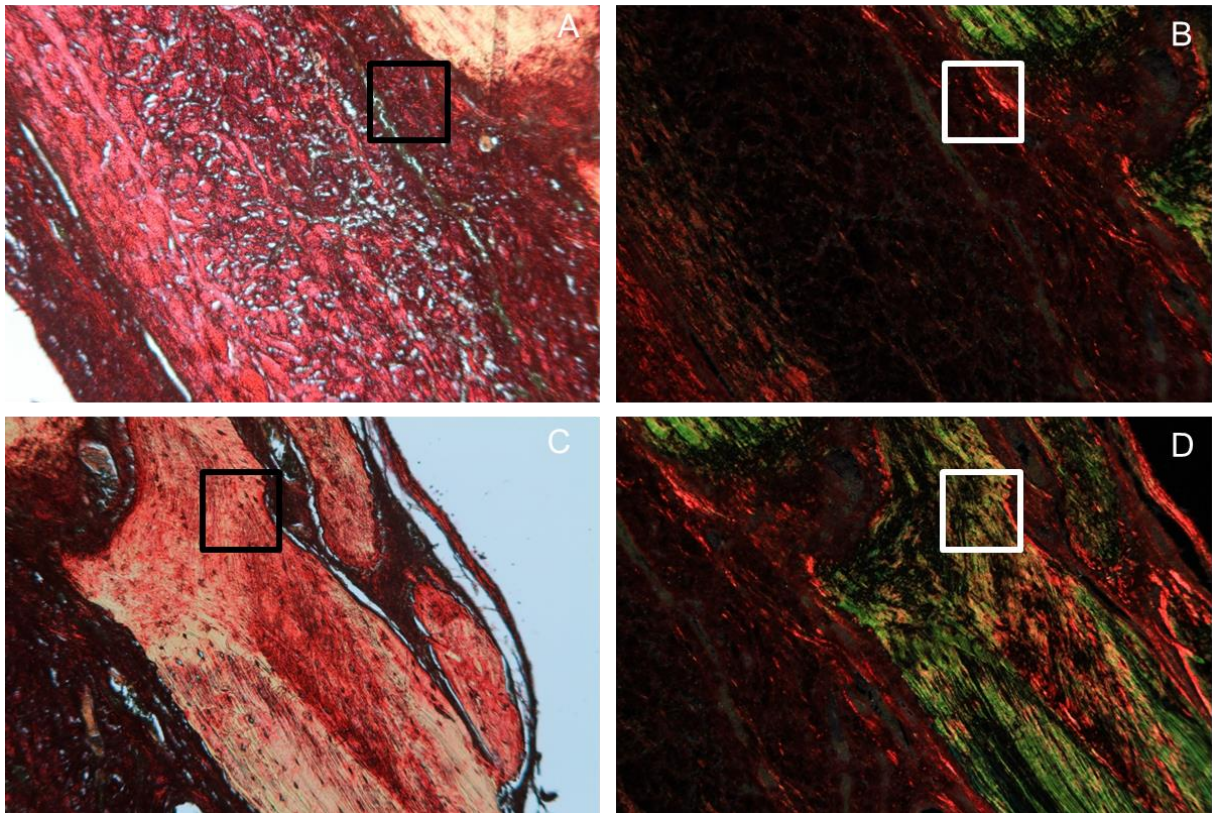


**Figure 3-21** Light and dark field LM of the clavicular defect after 14 days of healing. A, B) red area C, D) yellow area. 10x magnification.

**Figure 3-21** shows the LM images of the membrane after 14 days of healing. Image **A** shows a region of various density tissues, some heavily stained red by picrosirius red stain, confirming the presence of collagen. Porosity in the tissue appears to be regular. Image **B** shows the polarised (dark filed) image corresponding to A. Some small areas shown up as red for collagen, with musculature at the top of the image seen as green. The highlighted area is solidly red, suggesting ordered collagen in that region. Image **C** shows a dense region of collagen and muscle tissue, close to the edge of the membrane. A dense collagen sheet can be seen at the bottom-left of the image. Image **D** shows the polarised image corresponding to C. A mixture of green and yellow areas

can be seen in the highlighted area, suggesting a combination of disordered collagen and non-collagenous material such as muscle tissue.

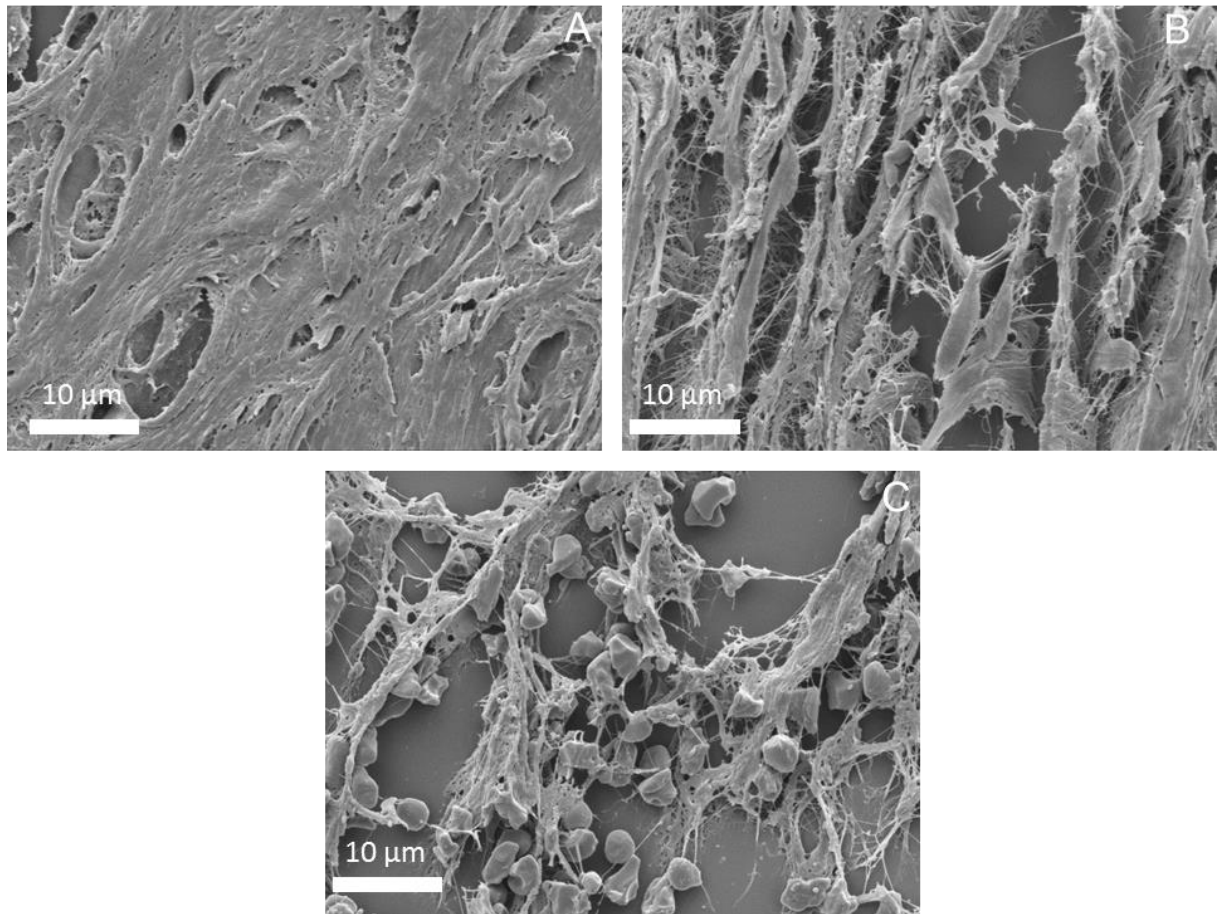


**Figure 3-22 SEM images of the membrane after 14 days of healing. A) red area, B & C) yellow area. 2000x magnification**

Figure 3-22 shows the SEM images of the membrane after 14 days of healing. Images were taken from the areas highlighted in the LM images (Figure 3-21). Image **A** is from the red area. Collagen can be seen through the image and is broadly well aligned and dense. The dense smoothed sheets of collagen means that individual fibres cannot

be observed. There are some gaps and swirls within the sheets, consistent with healthy collagen. Image **B** is from the yellow area. Immediately there is a substantial difference compared to image A, with long thin strands of collagen fibres present. There are large gaps between the fibre bundles, with a meshwork of smaller fibrils linking the larger bundles. There is some directional order amongst the larger bundles, interspersed with the smooth amorphous material. Image **C** shows another location in the yellow area. Here there are few collagen fibres present in bundles, but an extensive covering of smaller fibrils form a meshwork structure. There are noticeable gaps between the bundles and fibres, show the low density of the sample. Large numbers of white blood cells cover the sample, showing an immune response by the host.



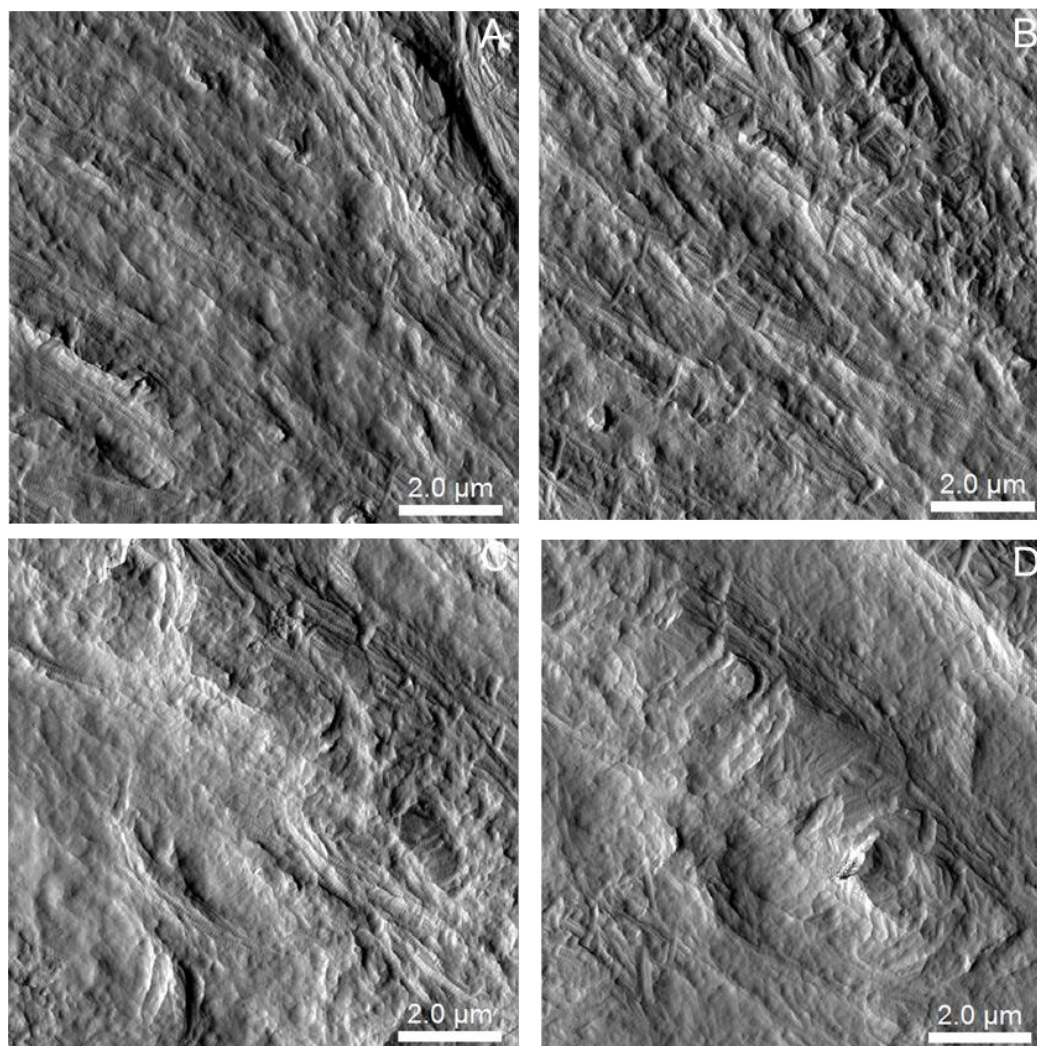


**Figure 3-23** AFM of the membrane after 14 days of healing A & B) red area, C & D) yellow area

**Figure 3-23** shows the AFM images of the membrane after 14 days of healing. Images were taken from the areas highlighted in the LM images (Figure 3-21). Image **A** is from a red area and shows bundles of collagen fibres well aligned but without identifiable D-banding. Some fibres appear to be degraded, as they are smooth, but fibres seen below the plane of the image are intact. Poor histology technique could cause surface damage to the fibres. Image **B** is also from the red area but shows different collagen behaviour than in image A. Here there are larger bundles of fibres,

with strong directional orientation. Fibres are seen in the gaps between the bundles, and D-banding is readily identifiable. This confirms that the collagen is intact, with porosity not being observed. Image **C** is from a yellow area and shows large smooth regions, suggesting collagen degradation. Between the smooth areas, some fibrils can be seen which have some directional orientation. However, the fibres appear to be swollen in areas which indicates collagen damage. Image **D** is also from the yellow area and shows some fibrils present. These fibrils do not appear to be healthy, with a number of them swollen and degraded. Additionally, there are two broad areas of degraded collagen in the image, consistent with image C. The swelling in the fibres has likely disrupted any D-banding that would have been seen.

### 3.6.1.3 Day 30 Ex-Vivo

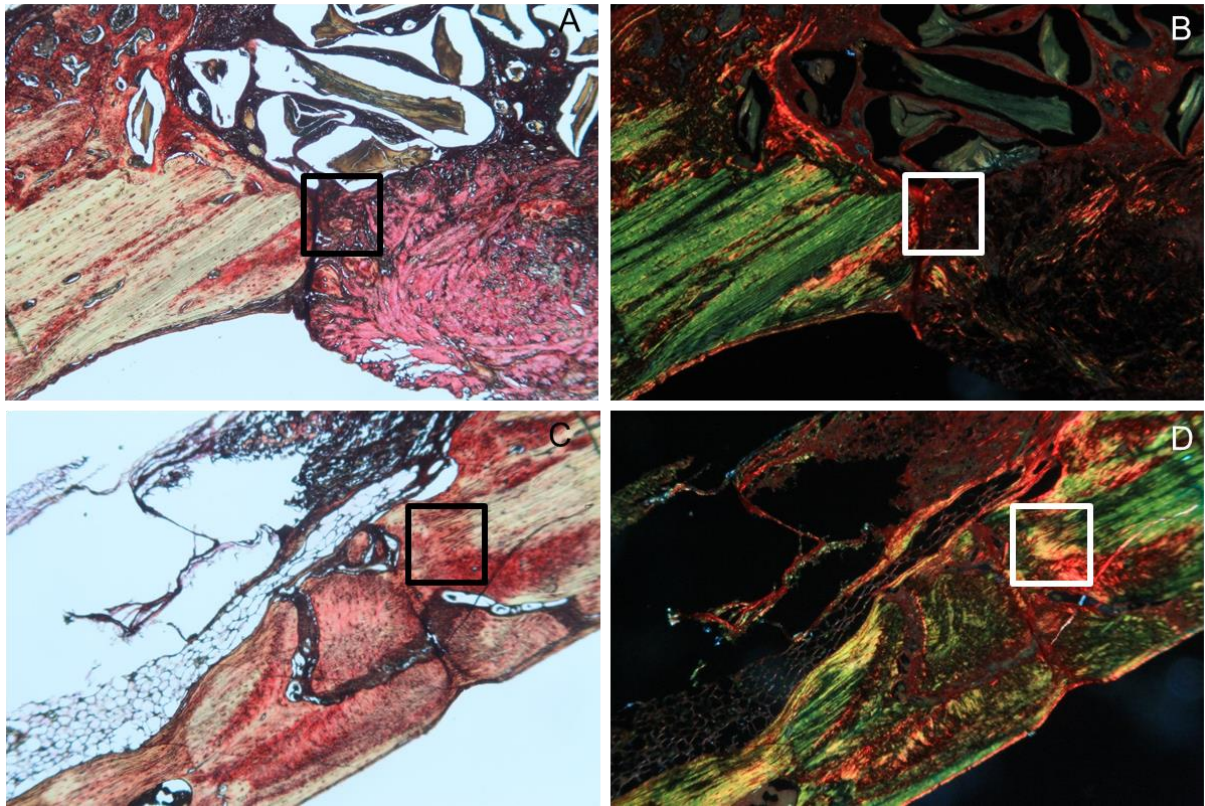


**Figure 3-24** Light and dark field LM of the clavicular defect after 30 days of healing. A, B) red area C, D) yellow area. 10x magnification.

**Figure 3-24** shows the LM images of the membrane after 30 days of healing. Image **A** shows a region on the border of the intact tissue and the wound healing site. The interface can be seen and appears to be a dense area. The tissues are heavily stained red suggesting a large amount of collagen is present. Image **B** shows the polarised image corresponding to image A. The highlighted area is confirmed to be rich in collagen as it is dark red, likely due to the density of the tissue. The surrounding areas also have collagen present, with the musculature of the wound appearing as bright green. Image **C** shows a region where the membrane and wound site have fused. Collagen-rich areas can be seen, with some of the degraded membrane still visible at

the top of the image. Image **D** shows the polarised image corresponding to C. The highlighted area is on the border of the red, yellow and green sections of the tissue. The multi-coloured areas seen in the image along with the apparent density of the areas are indications of the advanced wound healing that has likely occurred.

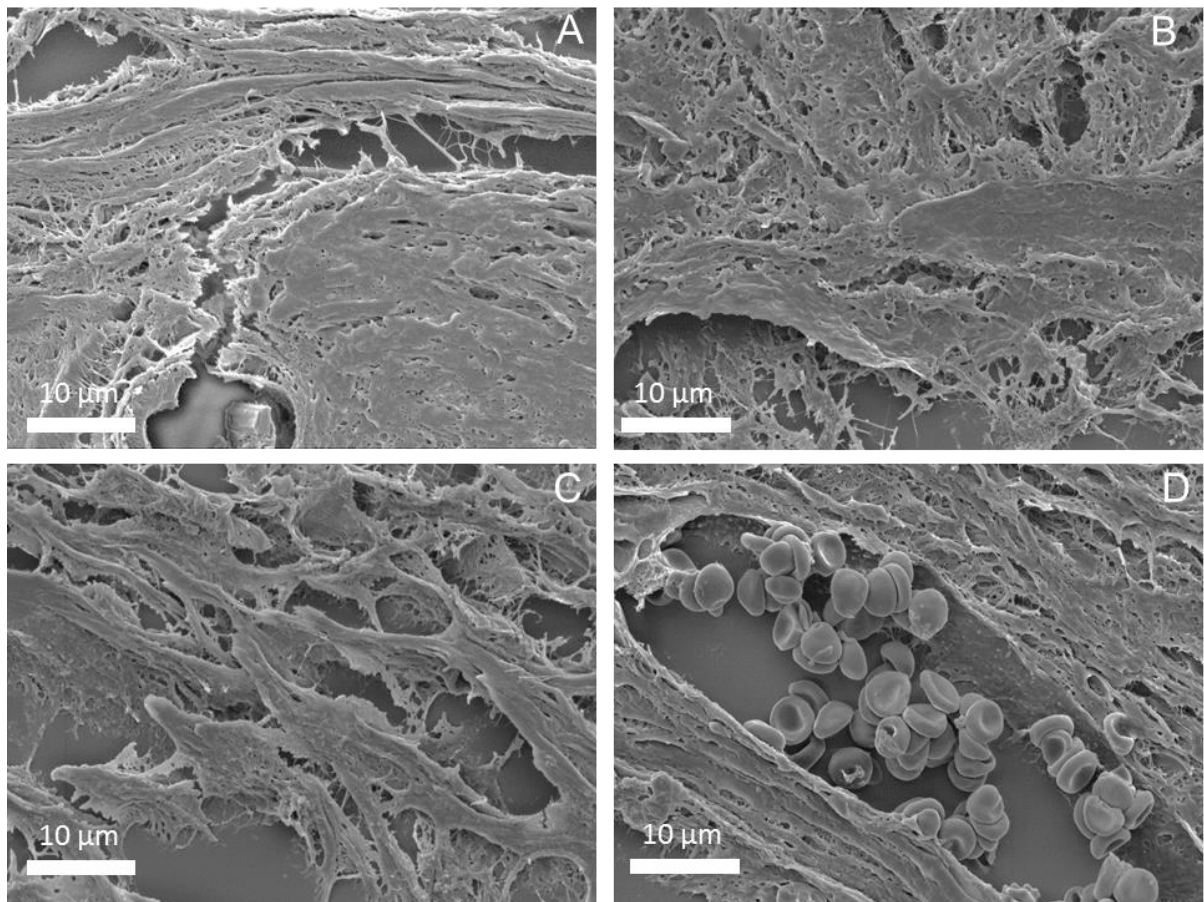


**Figure 3-25 SEM images of the membrane after 30 days of healing. A & B) red areas, C & D) yellow areas. 2000x magnification.**

**Figure 3-25** shows the SEM images of the membrane after 30 days of healing. Images were taken from the areas highlighted in the LM images (Figure 3-24). Image **A** is from the red area and shows thick bundling of collagen fibres with strong directional orientation. Amongst the thick bundles other smaller fibres can be seen, connecting the bundles. Other areas appeared flat and smooth, suggesting collagen degradation.



Image **B** was taken from another location in the red area. There are many smaller fibres, alongside sheets of collagen. There is minimal directional orientation. The smooth and glassy appearance of the fibres consistent with gelatinisation. Image **C** was taken from the yellow area. Here there are smooth glassy sheets, without visible bundling. There are also numerous smaller fibres connecting the sheets, which are highly porous. The glass surface underneath can be seen, showing the high levels of collagen digestion which had occurred. Image **D** shows more intact collagen, with bundling and fibre orientation seen. There is an abundant infiltration of red blood cells, showing that angiogenesis has occurred around the site of injury.

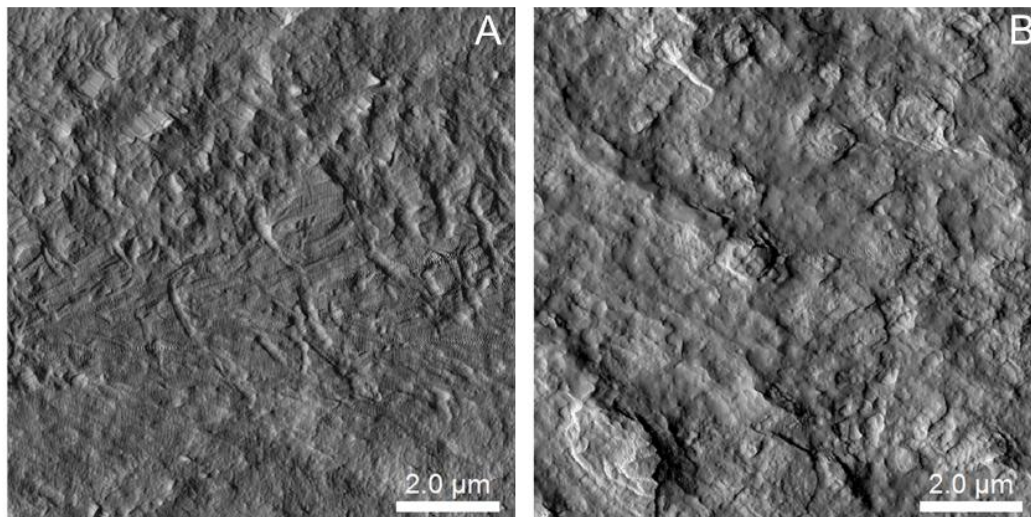


**Figure 3-26 AFM of the membrane after 30 days of healing in the red area**

**Figure 3-26** shows the AFM images of the membrane after 30 days of healing. Images were taken from the areas highlighted in the LM images (Figure 3-24). Image **A** is from the red area, which clearly shows intact collagen fibrils. These fibrils form a collagen sheet with some D-banding present. The D-banding appears to be regular, and line profile analysis confirmed the average D-banding length to be 69.2 nm. There is,

however, evidence of collagen degradation with flattened and sheared collagen fibrils towards the top of the image. Image **B** is from the yellow area. Some fibrils can be seen, but contrasting with image A, there is no D-banding present. The fibrils that are present do not look intact and appear to be degraded. There are holes on the surface, suggesting porosity.

This experiment showed the degradation over time of Bio-Gide when implanted into a rabbit model. From the early work in this chapter, a baseline has been established for the appearance of the membrane under SEM (Figure 3-3) and AFM (Figure 3-7). Regrettably, due to external preparation involving paraffin infiltration and fixation of the samples mechanics measurements using AFM could not be taken.

At 7 days under polarised LM, a large area shows as red, suggesting collagen aligned and in register according to the PS staining (Figure 3-18). This corresponds to a robust initial separation between collagen in register and disrupted non-collagenous regions. The interface between the induced injury and the muscle can be observed. At the other end of the injury, there is a considerable variety of colour, containing red, yellow and green regions. This variation in collagen under LM was seen again clearly under SEM (Figure 3-19), immediately showing the difference between the two areas. The red area showed thick bundled collagen following directional alignment, while the yellow area had collagen showing signs of degradation. This degradation was further visually confirmed using AFM (Figure 3-20). Collagen bundling was seen in the red area, with only evidence of initial degradation seen in the yellow area. Within the initial 7 days post-surgery, there is a clear demarcation between the various regions as seen under PS staining.

After 14 days under LM, the demarcation of the areas is lost with the mixing of the colour regions observed (Figure 3-21), indicating a heterogeneous collagen distribution. This is confirmed by SEM (Figure 3-22) when an infiltration of leukocyte and erythrocyte was observed. This immune response was only seen in the host tissue and not in the membrane area (yellow and red colours respectively). There is an initial inflammatory response at the site of the injury, during which time little wound healing occurs<sup>418</sup>. An excess of cytokines can hinder tissue regeneration<sup>419,420</sup>. As a wound healing device, BG has been used to limit the initial molecular response of the host that may impede healing<sup>421–423</sup>. At 14 days the presence of red and white blood cells suggest that vasculogenesis has occurred<sup>424</sup>. Throughout the membrane and wound there is evidence of at least some level of collagen digestion. This suggests that wound healing is occurring, mediated by fibroblasts<sup>425,426</sup>. After 30 days the SEM showed the presence of erythrocytes but few leukocytes (Figure 3-25), suggesting that the immune response is complete<sup>220</sup>. This also fits with the clinical observations of using BG for wound healing and guided bone regeneration<sup>379,415,416,427</sup>. AFM showed two patterns of collagen; either with fibrils seen in bundles or with glassy structures indicative of collagen degradation.

#### **3.6.1.4 Section Summary**

This study was the culmination of the knowledge obtained in Part A, to satisfy Objective 5. Investigating the properties of the BG membrane during *in vitro* experiments allowed for a benchmark set of data to be collected. However, it was not known whether the same markers of disorder would be detected during an *ex-vivo* study when conditions cannot be so easily controlled. This study showed that markers such as the potential loss of D-banding and fibril register were, in fact, still significant indicators of collagen disorder during membrane degradation. As the timepoints increased in the study, the collagen lost register and appeared to become glassy, with fibrils losing cohesion. All of these are indicators of disorder and point to the host digesting the membrane. It was also seen that increasing cell infiltration occurred as the time points increased, with significant numbers of leukocytes and erythrocytes seen by Day 30.

A key lesson was also learnt about sample preparation. The samples had been embedded in paraffin for histology by an external collaborator, and de-waxed using xylene. This was apparently insufficient for AFM measurements. While some collagen could be seen, the D-banding could not be resolved as is normal in collagen AFM imaging. All of the samples were prepared in the same manner, so can be compared to each other, but it is impossible to make firm conclusions as to the degradation of the membrane. The force curves that were taken for mechanical measurements did not correspond to any reasonable behaviour of collagen or its derivatives (data not shown). In future, only cryosectioning of samples that does not require paraffin would be used.

### 3.7 Chapter Summary

Throughout this chapter, LM, SEM, AFM and OCT have been used to measure the degradation behaviour of collagen medical devices, and the relationship between the membranes and the host. This was performed with both quantitative and qualitative data collection wherever possible. In Part A, the use of multimodal techniques has led to the comparison of morphological and mechanical markers of collagen, both in order and disorder. Taking this knowledge further into Part B, *ex-vivo* experiments showed that the morphological markers were still valid.

Outside of experimental results, the data collected in this chapter led to grants, publications and conference presentations.

All of the established objectives were met. In summary:

#### Part A

- Mesoscale imaging using SEM confirmed the morphology expected for each of the tested membranes but could not identify all the features of collagen. Imaging using AFM also confirmed the presence of highly disordered and degraded collagen. This gave information which suggested potential manufacturing methods of the membranes.
- Nanoindentation using AFM of the membranes in air and liquid with tips and beads was performed. The Young's modulus range of values were not comparable to human tissue and were significantly lower in both tested materials in air (25 – 280 MPa), and in liquid (3 – 15 kPa).

- MG-63 cells respond differently to each material at various time points. Significant differences between the behaviours of both materials were found. The adhesion energy for BG was much higher than that of MG, while the adhesion force was similar, suggesting different adhesion pathways for cells on each material.
- The digestion of two of the membranes using collagenase has been visually confirmed using OCT. The rate of digestion is comparable to published data and allows for a simultaneous visual and quantitative digestion assay.

### Part B

- An animal model was used to investigate the behaviour of the membrane as it is resorbed by the body, in conjunction with histological analysis. Clear evidence of collagen digestion was seen throughout the timepoints, reinforcing clinical data. The use of histological staining was invaluable in informing the locations for AFM imaging, but paraffin will not be used in future studies.

## 4 Collagen Disease Model in Mice

---

### 4.1 Introduction

Connective tissue diseases are a group of invasive conditions, generally characterised by systemic and quality of life symptoms. While some of these diseases such as scleroderma or Sjögren's syndrome are developed during a patient's lifetime, the majority such as osteogenesis imperfecta (OI), Ehlers-Danlos syndrome or Alport syndrome can be inherited<sup>12–14,49,100,158,192,428</sup>. These diseases are complex, multifactorial and systemic, which limits the possibility of creating *in vitro* lab models<sup>429</sup>. The use of animal models from the families of Muridae to Canidae have successfully modelled several of these diseases such as Alport syndrome or OI<sup>429–432</sup>. More recently, arthrogryposis renal dysfunction cholestasis (ARC) syndrome has been successfully modelled in juvenile mice<sup>402</sup>.

In the previous chapter, Chapter 3 it was seen that collagen membranes could be characterised using multimodal techniques (LM, AFM and SEM). Markers of ordered collagen such as fibrils aligned in register and the presence of D-banding were identified. Similarly identified were markers of disorder such as a loss of register or the presence of gelatinised areas. Through the use of nanoindentation, a range of Young's moduli in air and liquid were measured and compared.

Expanding on that work, the aim of this thesis chapter was to apply the same characterisation techniques to mice skin, tendons and bones. A multimodal approach

using imaging and mechanical measurements that was successfully implemented on collagen membranes was replicated on to *ex-vivo* mouse samples.

The work in this chapter has been published, and two further studies looking at control tendons and bones are found in Appendices C & D <sup>402</sup>.

## 4.2 Aim

This investigation aimed to identify markers of health, disease and disorder in collagen from *ex-vivo* mouse tissues with a particular focus on ARC syndrome.

## 4.3 Objectives

1. Compare mesoscale images of ARC syndrome tendons with WT to identify signs of disorder.
2. Identify further morphological disorder at the nanoscale and compare to known effects of collagen formation.
3. Confirm that identified disorder causes a change to mechanical structure of the collagen, and confirm if this is a strengthen or weakening effect.

## 4.4 Materials and Methods

### 4.4.1 Materials

ARC syndrome mice were reared by the group of Prof Paul Giessen (UCL LMCB & GOSH). 2 types of knockout (KO), vacuolar protein sorting-associated protein 33B (VPS33B) and VPS33B interacting protein, apical-basolateral polarity regular (VIPAR) were created using chimeric mice. The mice were bred with conditional VPS33B or VIPAR (KO), and combined with a tamoxifen-inducible Cre recombinase expression.



The KO exon was induced was induced by intraperitoneal injections of 100 mg/ kg per day tamoxifen for five consecutive days on 6–8-week-old mice.

Wild-type (WT) mice used were either VIPAR KO mice not induced with tamoxifen or VPS33B KO mice without Cre recombinase that had been treated with tamoxifen. This is due to complexity in rearing and breeding the recombinant KO mice. In all WT mice, the KO gene was either not present or not activated. All analyses were performed 5–6 weeks post-induction, adding some potential variability because of different mouse age and induction length. All mice were therefore 11-14 weeks old. All procedures were undertaken with Home Office approval (licence number PPL 70/7470) in accordance with the legal requirements of the Animals (Scientific Procedures) Act 1986. Tendons and skin were extracted from sacrificed mice, at least 5 mice per KO status. Skin samples were snap-frozen in methyl butane (iso-pentane) cooled with liquid nitrogen. These were later embedded in optimal controlled temperature (OCT) media at the Blizzard Institute (Queen Mary, University of London) for histological sectioning, into 10 µm sections. Samples were mounted on to glass slides and stored at 4°C until use.

#### 4.4.2 Methodology

##### **4.4.2.1 Mesoscale Imaging**

Type I collagen fibrils were dissected from mice tail tendon, and stored in PBS buffer at 4°C before further preparation. Extracts from the tendon (~5mm long) were sectioned with a scalpel and washed for 5 minutes in deionised water and left to dry before fixation for 24 hours 3% glutaraldehyde in 0.1M sodium cacodylate solution. The samples were then dehydrated using an ethanol series over 20 minutes, before critical

point drying with hexamethyldisilazane. Samples were mounted using carbon adhesive tabs to aluminium stubs (Agar Scientific, UK), and coated in Au/Pd. Imaging was performed using a Philips XL30 FEG-SEM (FEI, Eindhoven), with an accelerating voltage of 5 kV. Low, medium and high magnifications were chosen as appropriate for each sample. Images were taken in random locations (minimum of 3 per sample) or to display notable features.

#### **4.4.2.2 Nanoscale Imaging**

Extracts from the tendon (~5mm long) were sectioned with a scalpel and washed for 5 minutes in deionised (DI) water. These were placed on a glass microscopy slide, and separated with a hypodermic needle before being allowed to dry and physisorb to the surface.

A Nanowizard 1 AFM operated in contact mode in air was used to image most samples, equipped with MSNL cantilevers with  $k = 0.03\text{-}0.6\text{ N/m}$ . The setpoint, gains and scanning speed were optimised for each sample. Images were taken in random locations across the sample, processed using proprietary JPK software, and representative images presented.

#### **4.4.2.3 Nanoscale Indentation**

For mechanical indentation measurements the Nanowizard 1 AFM was used. Calibrated RFESPA (Bruker, Santa Barbara) cantilevers,  $k = 3\text{ N/m}$ , were employed to take 300 force-displacement measurements on the sample with an applied relative setpoint of 300 nN. The force-displacement curves were processed using proprietary

JPK software and fitted according to the Sneddon model to obtain the Young's modulus. This data was graphed, statistically analysed and presented using OriginPro.

## 4.5 Results and Discussion

### 4.5.1 Mesoscale Imaging

In Chapter 3, mesoscale imaging identified key features of disorder in collagen, such as the loss of fibre and fibril alignment. Here, mesoscale imaging was used again to attempt to identify these and other morphological markers of disorder that could arise from improper post-translational modification of the collagen as a result of ARC syndrome. This would fulfil the requirements of Objective 1: *“Compare mesoscale images of ARC syndrome tendons with WT to identify signs of disorder.”*

#### 4.5.1.1 WT

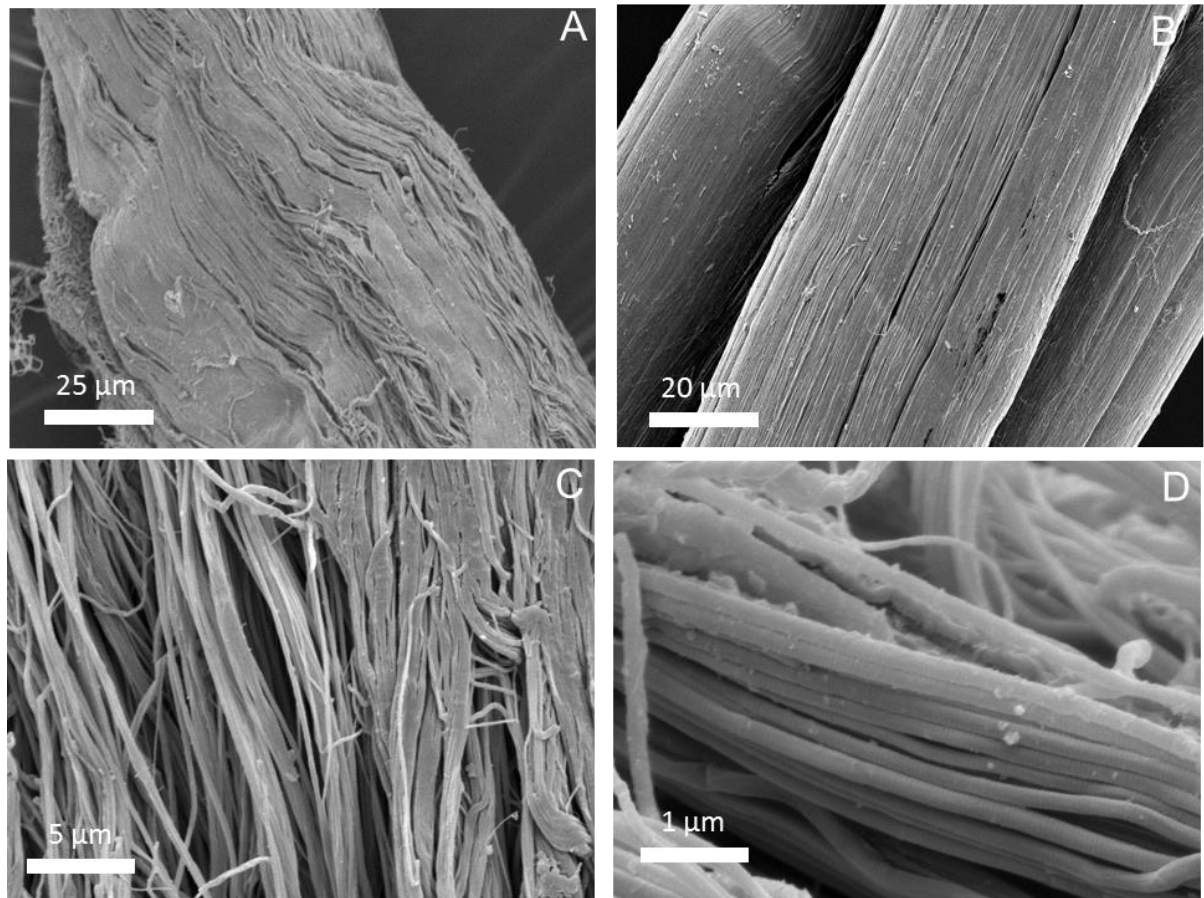


**Figure 4-1 SEM of WT mouse tendon showing fascicle alignment. A 650x, B 1000x, C 5000x, D 20000x magnification**

**Figure 4-1** show SEM images of WT tendons. Image **A** shows crimping in the tendon, suggestive of a relaxed tendon. Fascicles are visible, and these have a strong preferential alignment, and run up-to-down in the image. Areas at the junction of the crimps have created gaps in the tendon structure, where smaller fibre bundles can be observed. Some smaller bundles are coming out of the surface around the gaps. Image **B** shows a highly aligned and regular tendon. There is an almost perfect alignment of the fascicles running along the main core of the tendon. Some shrinkage, likely artefacts

of the SEM preparation process, is visible between the fascicles which could result in the formation of gaps. These gaps also have strong alignment between the fascicles. Image **C** is a magnification of an area in image A. Here the alignment of the fibres is replicated in the higher magnification image. Several fibres are unwinding into smaller fibrils, and a number of the smallest fibrils have lost their directional alignment. Image **D** is a higher magnification of an area of image B. In the foreground, highly aligned collagen fibrils can be seen, easily identified by the D-banding present. The fibrils all in register, with several kinks present in the structures towards the end and bottom of the image. In the background of the image, some fibres can be identified as tightly bundled together but are nevertheless out of alignment with the fibrils seen in the foreground.

#### 4.5.1.2 VIPAR

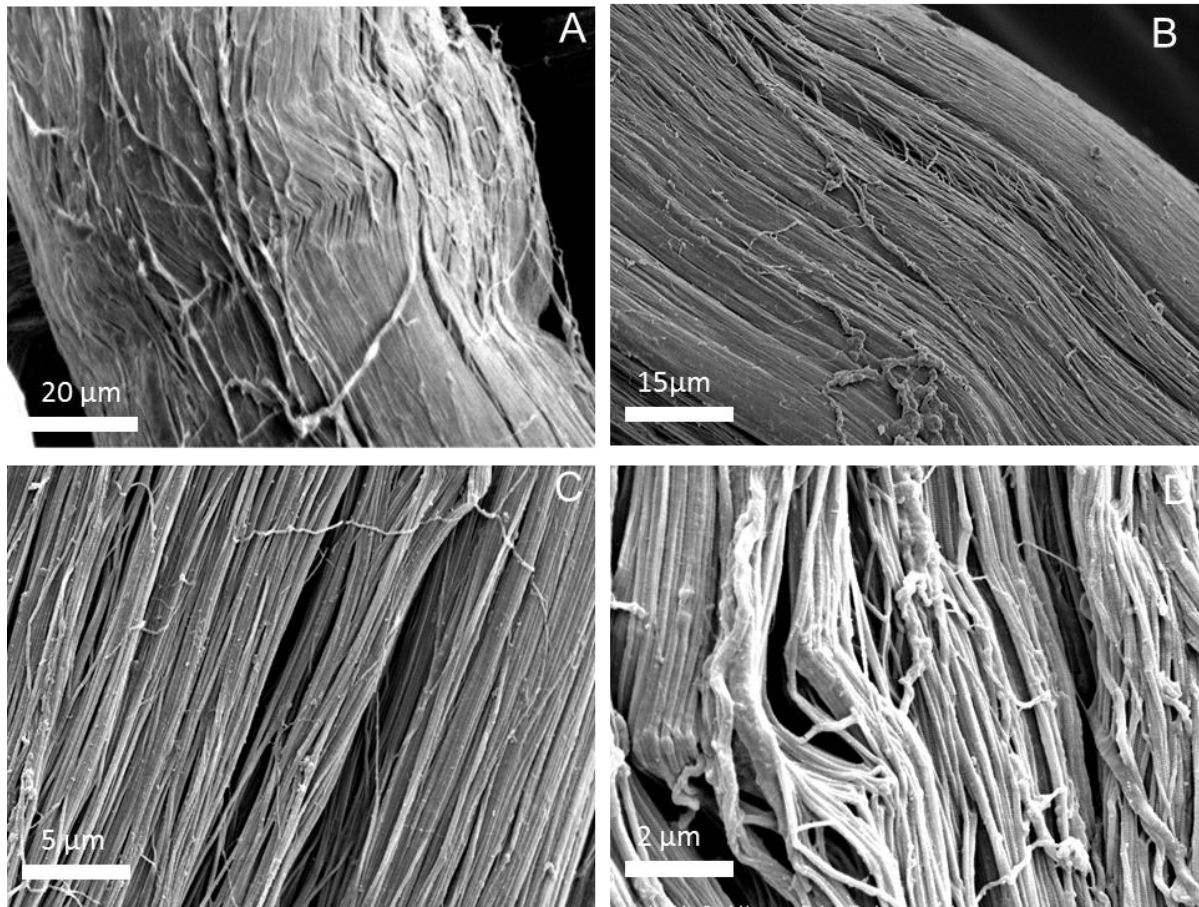


Figure 4-2 SEM of VIPAR mouse tendon showing some fascicle alignment. A 1000x, B 1500x, C 5000x, D 10000x magnification

**Figure 4-2** shows SEM images of VIPAR tendons. Image **A** shows a relaxed tendon, with crimping visible in the centre of the image. The majority of the fascicles are well aligned and follow the register of the core tendon. The fascicles are densely packed, with some small gaps visible. There is a notable meshwork of smaller fibres that cover the outside of the tendon. These are connected, follow the direction of the tendon, but also cross it laterally. Image **B** is more magnified and shows alternately dense and loose bundles of fibres. When they are at their densest, these bundles appear to act as a

conglomeration, and the individual fibrils cannot be distinguished. The meshwork of smaller fibrils is also present. Image **C** shows a magnified view of the fibrils. Here the register of fibrils is seen again, but there are much larger gaps between the bundles. These gaps show a low density of the fibrils, leading to a less packed tendon structure. D-banding can be faintly seen on some fibrils. Image **D** shows a magnification of the crimped areas. Although there is both bundling and alignment of the fibrils, they are not in register. The dense crimping has created a loose network of fibrils which do not bundle as tightly as seen in other images. The smaller meshwork of fibrils is seen, which appears to have formed from the unwinding of larger fibrils.

#### 4.5.1.3 VPS33B Tendon

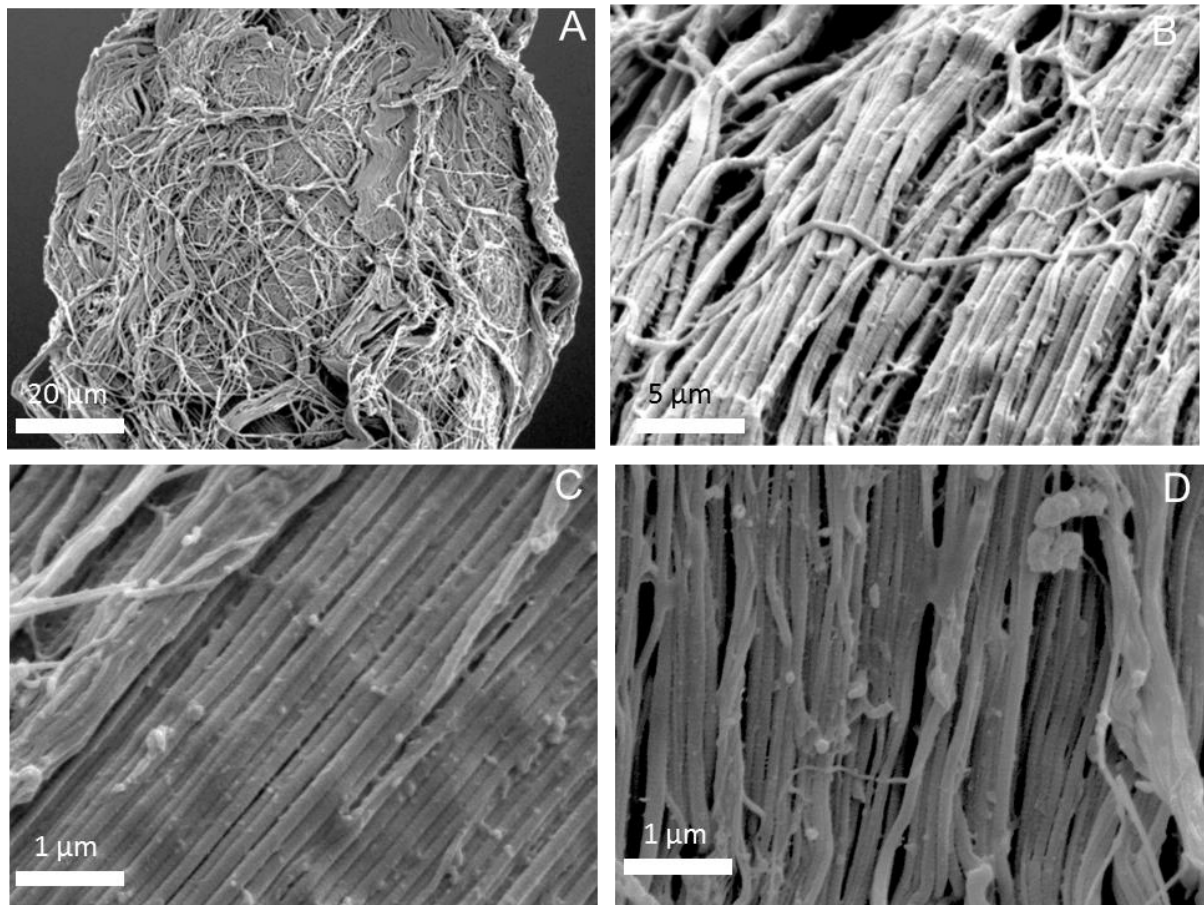


Figure 4-3 SEM of VPS33B mouse tendon showing disordered fascicles. A 1000x, B 5000x, C 20000x, D 20000x magnification

**Figure 4-3** shows SEM of VPS33B tendons. Image **A** shows a highly disordered tendon structure. While there is a general top-to-bottom majority alignment of the tendon core, there is a highly disorganised meshwork of smaller fibrils that do not have alignment. There are also fascicles that have extensive evidence of crimping and shrinkage. Other fascicles are misshapen and appear to be curling back on themselves. Image **B** shows well-aligned fibrils in register. These fibrils are not tightly packed, so there are large gaps between the bundles of fibrils. Some smaller fibrils are seen to run



perpendicular to the main alignment. There appears to be some localised swelling in some fibrils. D-banding, though faint, can be seen. Image **C** shows highly aligned fibrils in a densely packed arrangement, as would be expected in healthy tendons. Few gaps are visible in the foreground. There is evidence of bundling and twisting of the fibrils at one side of the image, where there is also less alignment. Image **D** shows fibrils in varying states of disorder. There are aligned fibrils in closely packed bundles, indicative of healthy collagen. Other fibrils have smooth glassy features, indicating that degradation from collagen to gelatine has occurred.

#### **4.5.1.4 Mesoscale Imaging Discussion**

The WT samples acted as controls for this study. The WT mice had the same genetic defect as either the VIPAR or VPS33B mice, but this defect was not activated as tamoxifen was not injected. The images show the tendons in two different healthy states. The first (Figure 4-1 A) shows visible crimping in the tendon, causing a change to the pattern of the collagen fascicles. This crimping is a well-known phenomenon in tendon behaviour and does not indicate disorder<sup>92,344,433,434</sup>. The fascicles' directional orientation is notable, and this is a recognisably healthy tendon. The other state is that of the tendon still under tension (Figure 4-1 B). This produces remarkably well-aligned fascicles, with an exceptionally clear register resulting in directional alignment. This alignment is recognised as being the preferred behaviour of the tendon *in vivo*, and would be the healthy and natural state of the tendon under strain<sup>433,435–437</sup>. After magnification, the two states are seen again, with one showing crimped but aligned fibrils (Figure 4-1 C), the other showing fibrils all in register (Figure 4-1 D). This gave a baseline to which appearance of the VIPAR and VPS33B KO mice could be compared.

Clinically, the phenotype that arises from a VIPAR disorder is considered less serious than the VPS33B disorder, though may still be fatal <sup>438,439</sup>. Additionally, the enzymatic role that the vipar protein has in cell transport is complementary to VPS33B and its homologs <sup>402</sup>. Thus, it was not unexpected that the SEM for the VIPAR showed indications of both disorder and order in the tendon. Similar to the WT sample, crimping was found (Figure 4-2 A & C), without significant alterations to the register of the fibrils (Figure 4-2 B & D). What was unique to the two KO samples was the meshwork of smaller fibrils, which was present in VIPAR, but more so in the VPS33B sample. This could have occurred as the intermolecular crosslinks formed by lysyl oxidase were not present due to the defect <sup>16,46,438,439</sup>.

VPS33B is the more serious of the two genetic defects investigated, and invariably causes mortality <sup>98,202,440</sup>. This disorder was most evident in the low magnification image (Figure 4-3 A). This was a fully disordered structure, with only some localised behaviour appearing to be consistent with tendons<sup>433</sup>. As a structural protein, collagen depends on its strong directional alignment, often referred to as register <sup>53,114,220</sup>. When this register is altered, causing a subsequent change in topography, this often results in a change in the physical behaviour of the collagen; a recurring theme in this thesis <sup>395,436</sup>. This is important for all structural behaviours of fibrillar collagen, but it is especially important in highly aligned tissues such as tendons or ligaments <sup>441,442</sup>. A loss of alignment and order as seen under the SEM would doubtless cause a loss of function in the host animal. The large gaps between the fibre bundles seen in VPS33B could be evidence of a lack of interfibrillar crosslinking.

However, the disorder was not seen throughout the entire data set, with both high magnification images (Figure 4-3 C & D) suggesting that in some areas that the alignment remains. Evidence of gelatinisation, the final stage in collagen degradation was seen <sup>356</sup>. In this case, SEM had allowed for an investigation of the microscale effects of the knockouts, and how these affect changes to the middle-level hierarchy of collagen. The level of disorder stretches across several hierarchical domains.

It was not unexpected that a significant percentage of the tendon would be unaffected. The induction of the KO did not occur until at least week 6, while the mice were still juveniles but crucially still growing. Until the induction of the KO, the mice did not have any abnormalities and would have been the same as the WT mice. The KO would not have taken effect until the final six weeks of development of the mice. Therefore, it is understandable that the outer layers of the tendon appear to be highly disordered, while deeper layers are regular in appearance like the WT. KO *in utero* had been previously attempted, which invariably lead to spontaneous termination. By comparing the WT to the two KO samples, a potentially pathological presence of smaller tendons has been found, which is likely the result of incorrect post-translational modification.

#### **4.5.1.5 Mesoscale Imaging Summary**

The primary objective of this section was to discover if markers of health and disease could be visually identified using mesoscale imaging in mouse tendons. Initial promising results from the collagen membranes study in Chapter 3 suggested that it would be possible to use SEM for this analysis. Baseline markers were found in the WT tendon when it was both relaxed and under tension. VIPAR tendons showed some

evidence of disease with fascicle gaps and a meshwork of disordered fibrils. VPS33B tendons showed increased levels of disorder. Both KO tendons had some areas that were healthy.

#### 4.5.2 Nanoscale Imaging

Mesoscale imaging with SEM in section 4.5.1 confirmed that evidence of disorder was seen in the KO tendons, following Objective 1. There was some evidence of gelatinisation, and not all tendons had identifiable D-banding. As ARC syndrome is a disorder that would affect collagen at the nanoscale due to incorrecion fibrillogenesis, Objective 2, *“identify further morphological disorder at the nanoscale and compare to known effects of collagen formation”*, was investigated using AFM. AFM was used to confirm whether any of the markers seen under SEM could be duplicated at the nanoscale, and if further evidence of collagen disorder could be identified, especially evidence that could be linked to incorrect fibrillogenesis.

#### 4.5.2.1 WT

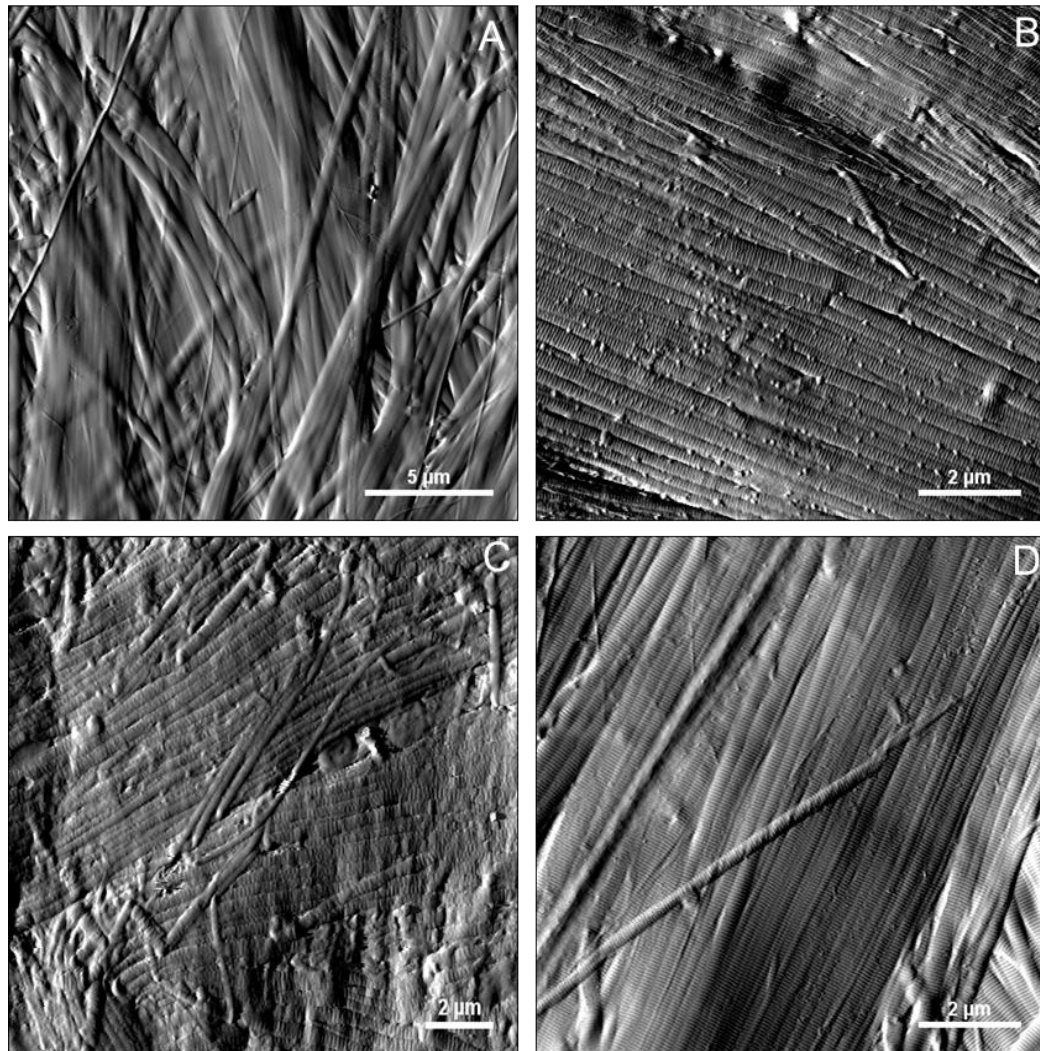


Figure 4-4 AFM of WT mouse tendon showing aligned fibrils in sheets

**Figure 4-4** shows AFM images of the WT tendon. Image **A** shows a large area with clear evidence of bundling of fibrils. Twisting is seen as well, and there is a considerable amount of topography present; fibrils are seen underneath the central plane of the image and crossing over each other. D-banding cannot be seen in this image. Image **B** shows fibrils in register, showing a high degree of directional orientation. Almost all of the fibres are following a single direction, with some small

swelling seen at the junction of two fibrils. Small dots visible on the surface are likely imaging artefacts and are not linked to the collagen structure. D-banding is readily visible. Image **C** shows several layers of tendons interacting. There are at least three distinct planes, all following their directional alignment. Some fibrils which are lying on the main bulk of collagen, are not aligned. Towards the edges of the image, there is some evidence of gelatinisation with a loss of D-banding. Otherwise, the D-banding is visible. Image **D** shows collagen in strict register being highly aligned. D-banding is visible, but the complex 3-D nature of tendon fascicles can again be seen towards the lower right corner of the image. Collagen fibrils are seen below the plane of the image, which appears to be larger than the main group of fibrils in register.

#### 4.5.2.2 VIPAR

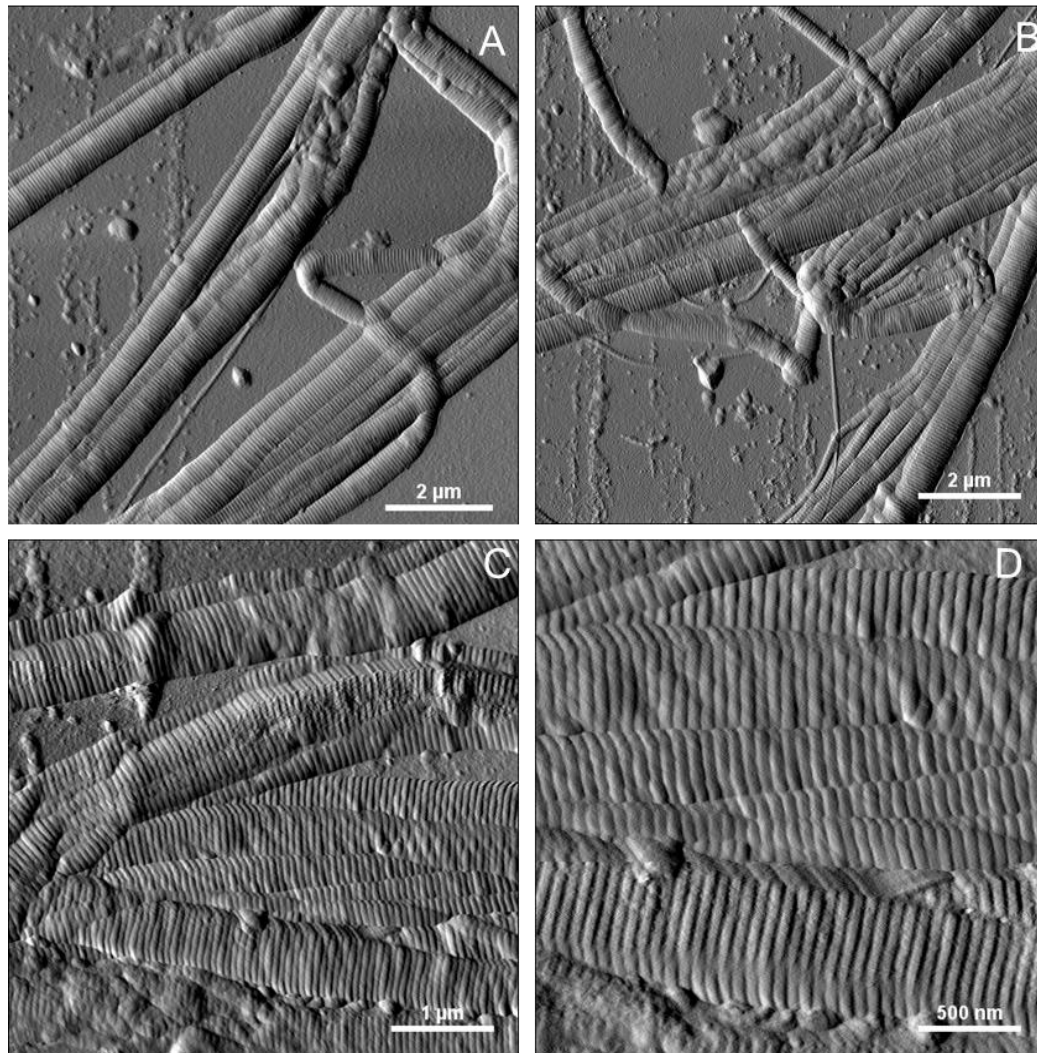


Figure 4-5 AFM of VIPAR mouse tendon on the glass surface

**Figure 4-5** shows the AFM images of the VIPAR tendon. Image **A** shows aligned collagen fibrils in distinct groups. The glass surface is visible as a background. Some sections of the fibrils appear to be swollen with a loss of fibril integrity suggestive of disorder. Image **B** is similar to image A and shows more tendon fibrils on a glass surface. Immediately visible in the centre of the image is a large mass of fibrils without register or orientation. D-banding is only present in some fibrils. Swelling is evident in many of

the fibrils, with some areas heavily distorted. Image **C** is taken at a lower length scale and focuses on a mass of fibrils. Some of these fibrils are in register with each other, but there is no overall directional orientation. Other fibrils appear to be in a state of severe disorder without any discernible shape to their structures. Even in aligned fibrils, there are areas where the fibrils have lost D-banding, giving evidence of local gelatinisation. Most notably D-banding is visible, but this banding is not regular. Areas of the D-band appear to be swollen, creating an uneven line profile in the affected the fibrils. Image **D** shows an increased focus on the central area of image C. This allows for a closer investigation of the swollen D-band areas. The swelling appears to have an alignment preference, being found mostly on the 'bottom' of the fibrils as they have been imaged. Additionally, only some areas of the fibrils appear to have been affected by the swelling. Individual fibrils have areas with swollen D-banding at one location, but then appear to be healthy and intact along different regions of the same fibril. For some of the fibrils visible in this image, there does not appear to be any D-bands with visible swelling.



#### 4.5.2.3 VPS33B

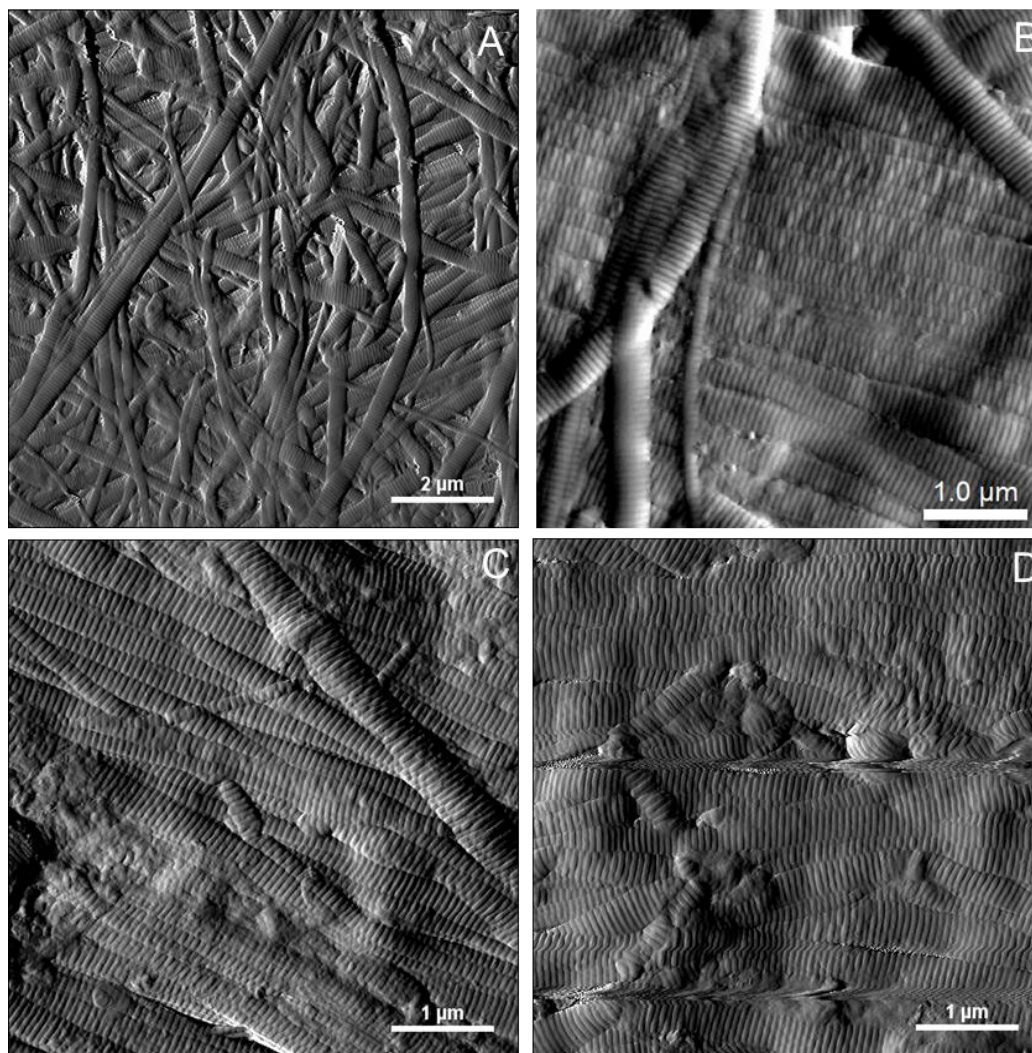
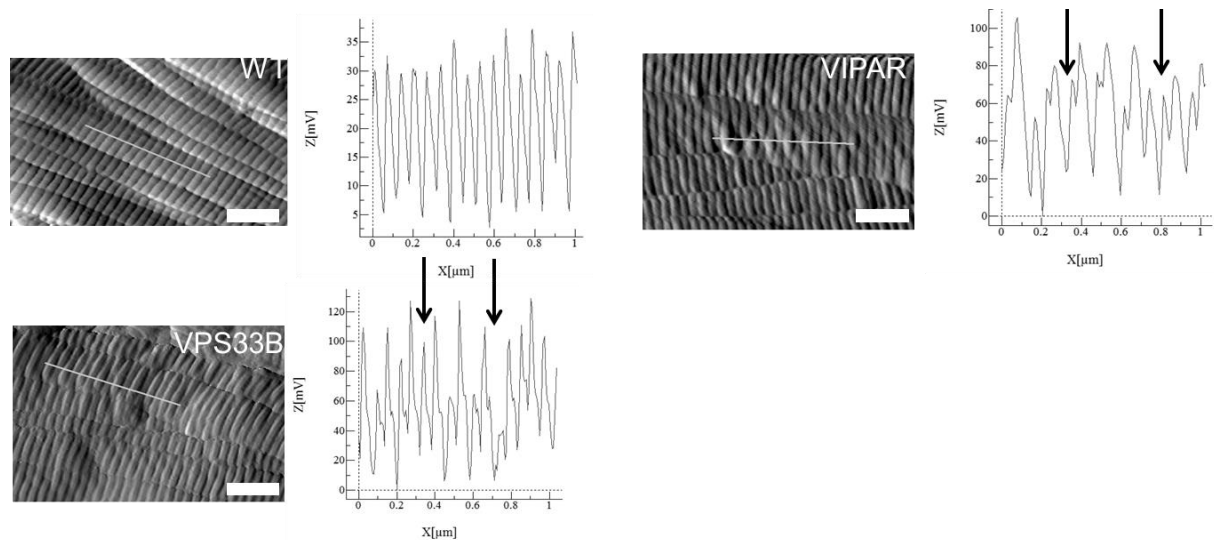


Figure 4-6 AFM of VPS33B mouse tendon on the glass surface

**Figure 4-6** shows AFM images of the VPS33B tendon. Image **A** shows a large mass of highly disordered fibrils. There is no directional orientation, and there is a lack of any semblance of alignment and register throughout the image. D-banding is only identifiable in a small number of fibrils, which is likely to indicate level of disorder in the tendon. Image **B** shows highly aligned and ordered fibrils. D-banding is identifiable. However, the majority of the fibrils have swollen areas on the D-band, without any

apparent preference for the location of the swollen area. There are several thicker fibrils which covered the main body of aligned fibrils. Image **C** is similar and contains well-aligned fibrils which are mostly in register. There is D-banding present, but some swelling is also seen. Image **D** shows swollen fibrils with some directional alignment. The swelling of the fibrils means that identifying the edges of each individual fibril is not always possible. There is D-banding present, but again this is swollen and suggestive of disordered collagen fibrils.



**Figure 4-7 shows the D-band line profile analysis. Arrows indicate profile distortion. Scale bar**  
**500 nm**

**Figure 4-7** shows the line profile analysis comparison between WT, VIPAR and VPS33B. The swelling in the D-banding seen in VIPAR and VPS33B was analysed using line profile analysis. Analysing the topography of the D-banding with reference to the measured height allows the fibrillar swelling to be quantitatively analysed. **WT** shows a smooth profile with repeated peaks and troughs on the height axis. The D-band repeat for the WT sample was calculated as being  $65.2 \pm 1.1$  nm, which compares favourably

to the literature reported value of 67nm. **VIPAR** KO profiles showed some irregularity, with jagged peaks seen highlighted. **VPS33B** shows the most irregularity, with considerable variations in height, as well as jagged line profiles showing the extent of the fibril distortion. The average major peak to peak distance, being the average D-band length, does not change significantly in the WT, VIPAR or VPS33B samples. However while the repeated raised areas of the fibrils are indicative of disordered collagen, the degree of the swelling of the fibril in the knockout samples could be more significant. The Z-axis range, showing the height difference in the sample, indicates consistent swelling for VPS33B of at least three times that of the WT (30-36 $\mu$ m versus 100-120 $\mu$ m). Fast Fourier transform (FFT) analysis of the collagen confirmed that when the swollen areas were discounted, the average D-band length was  $66.8 \pm 1.3$  nm for all tendons, without a significant difference between any of the samples.

#### **4.5.2.4 Nanoscale Imaging Discussion**

The challenge of Objective 2 was to *“identify further morphological disorder at the nanoscale and compare to known effects of collagen formation”*. This was first answered by comparing the AFM and SEM images.

For the WT tendons, the AFM (Figure 4-4) images are similar to the images seen during mesoscale imaging with SEM (Figure 4-1). The fibrils are mostly well aligned, and in register with each other. It is clear that ordered and well-aligned fibrils are expected in healthy tendons, without much variation in width <sup>71,74,433,443,444</sup>. VIPAR tendons vary greatly, (Figure 4-5) with some locations showing aligned and well-orientated fibrils, with some differences in size visible. Although tendons are expected

to be regular size for optimum use, a change in diameter is not necessarily linked to poor tendon health <sup>445,446</sup>.

The second challenge of Objective 2 was to identify morphological disorder at the nanoscale. It was, therefore, more important to note that D-banding swelling was observed. This D-band swelling has not been repeatedly reported in the literature, the closest images to the ones presented here are low-quality and do not allow for a direct comparison of the features. Other reports focus on the effects of water content on the collagen fibrils, with an increase in bound water linked to a decrease in transverse Young's modulus <sup>279,280,447</sup>. In VPS33B the D-banding swelling was severe and was seen in fibrils irrespective of their alignment or register. Further tests using line profile analysis confirmed that the swelling causes a tripling in the height of the D-band without altering the width of the band. Under AFM for the nanoscale imaging, only the WT tendons showed a preferential alignment of fibrils throughout the images taken, but D-banding was visible in all samples tested.

The D-banding swelling is a clear maker of disorder, but this suggests that the disorder appears and perhaps increases in severity over time. When the KO mice were first created, attempts to activate the VIPAR/VPS33B mutation *in utero* were useful and caused the spontaneous termination of the foetus. This is not due to the induction of the mutation, but due to the lethal effects of the mutation itself. The induction of the KO occurs after eight weeks, allowing for a healthy centre of the tendon to develop, free of disorder. As the protein alteration occurs, the collagen is malformed. This abnormal collagen is then added to the core of the tendon, as the juvenile mice continue to mature. The mice continue to ambulate in a reasonable and healthy way while causing the

diseased effect to increase. These defects in collagen crosslinking are observed across the range of hierarchical structures. If these defects were seen through the entirety of the collagen, then the ability of the tendon to act normally is likely to be compromised.

Due to the effects of VIPAR and VPS33B, it is suggested that this swelling is a result of a disruption of the quaternary structure of the collagen as the lysyl oxidase is not fully secreted, it would be unable to form aldehyde bonds in the lysine. These cross-links are known to pull the collagen into a head-to-tail arrangement during fibrillogenesis<sup>1,16</sup>. If this process was incomplete, this could cause conformational changes in the triple helix structure of collagen. One area of vulnerability to conformational changes is glycine in collagen. As its R-group consists only of a hydrogen atom, its small size allows for the tight winding of the triple helix<sup>1,13,19,448</sup>. It has been established that if a larger amino acid were to take the place of glycine, this could cause the swelling observed in the VIPAR and VPS33B KO. A similar pathway of glycine substitution causing a fatal disease has been reported for dwarfism and osteogenesis imperfecta<sup>43,134</sup>. It is also possible that the abnormal bundling seen under SEM is a result of this quaternary structure malformation. This could be the result of amino acids forming abnormal van der Waals interactions which then allows for crosslinking in an unusual manner.

#### **4.5.2.5 Nanoscale Imaging Summary**

Nanoscale imaging using AFM was successfully used to identify markers of disorder in the tendons. Incorrect collagen alignment in the tendon, first identified in the ultrascale using SEM, was confirmed using AFM. Biological variability could be seen between the samples, particularly within the WT tendons. An additional marker of disorder, not thought to have been identified previously, was seen in both KO tendons.

The pathological swelling of the D-band is theorised to be because of an incorrection amino acid packing.

#### 4.5.3 Nanoscale Indentation

In the previous two sections, it was noted that disorder in a tissue such as a tendon could cause significant locomotive issues for the mice in this experiment, but that these issues were not reported. It has also been established in Chapter 3 that differences in mechanical behaviour can be detected at the nanoscale using AFM. Visually, the differences between the WT and VIPAR and VPS33B samples are significant, so a further investigation to see if these differences are mechanical as well, was warranted. The conclusion of the previous section suggested that there was abnormal bundling of collagen, and the swelling of the D-band was suggested to be caused by the incorrect placement of amino acids.

This leads to two possible outcomes that are tested by Objective 3: *“confirm that identified disorder causes a change to mechanical structure of the collagen, and confirm if this is a strengthen or weakening effect”*. The swelling of the D-bands was possibly causing a weakening of the collagen. Similarly, the change in tendon structure under SEM was suggested to be linked to locomotive issues in the behaviour of the mice due to weakened tendons. The AFM can be used to test these theories though indentation.

#### 4.5.3.1 WT

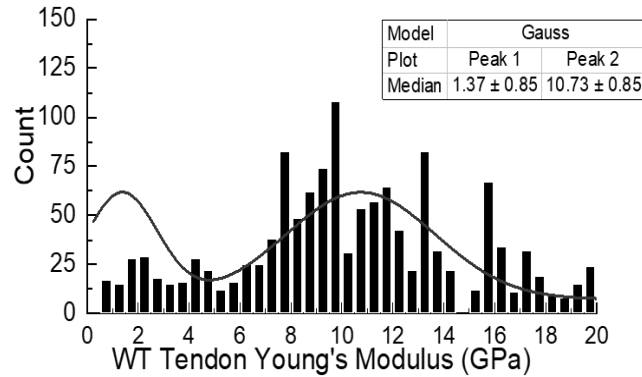


Figure 4-8 Young's modulus of WT tendon showing some bimodal distribution

**Figure 4-8** shows the Young's modulus of the WT tendon. The indentation gave a bimodal distribution, with lower peak of  $1.37 \pm 0.85$  GPa and a higher peak of  $10.73 \pm 0.85$  GPa. The fit of the graph on this sample was poor, suggesting limited bimodal distribution

#### 4.5.3.2 VIPAR

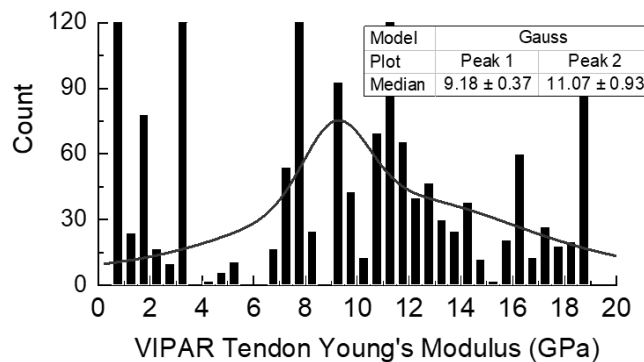
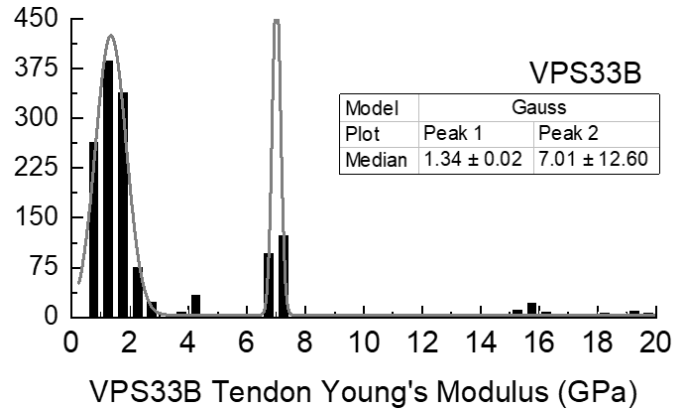


Figure 4-9 Young's modulus of VIPAR tendon showing bimodal distribution

**Figure 4-9** shows the Young's modulus of the VIPAR tendon. The indentation gave a variation of bimodal distribution, with a sharp peak at  $9.18 \pm 0.37$  GPa and a smaller more diffuse peak of  $11.07 \pm 0.93$  GPa.

#### 4.5.3.3 VPS33B



**Figure 4-10 Young's modulus of VPS33B tendon showing strong bimodal distribution**

Figure 4-10 shows the Young's modulus of the VPS33B tendon. Two distinct peaks are visible, with bimodal distribution evident. The lower peak is centred on  $1.34 \pm 1.2$  GPa with the higher peak calculated as  $7.01 \pm 0.2$  GPa. The distribution on this graph was very sharp, suggesting a very narrow variation of measurements.



#### 4.5.3.4 Overall Mechanics

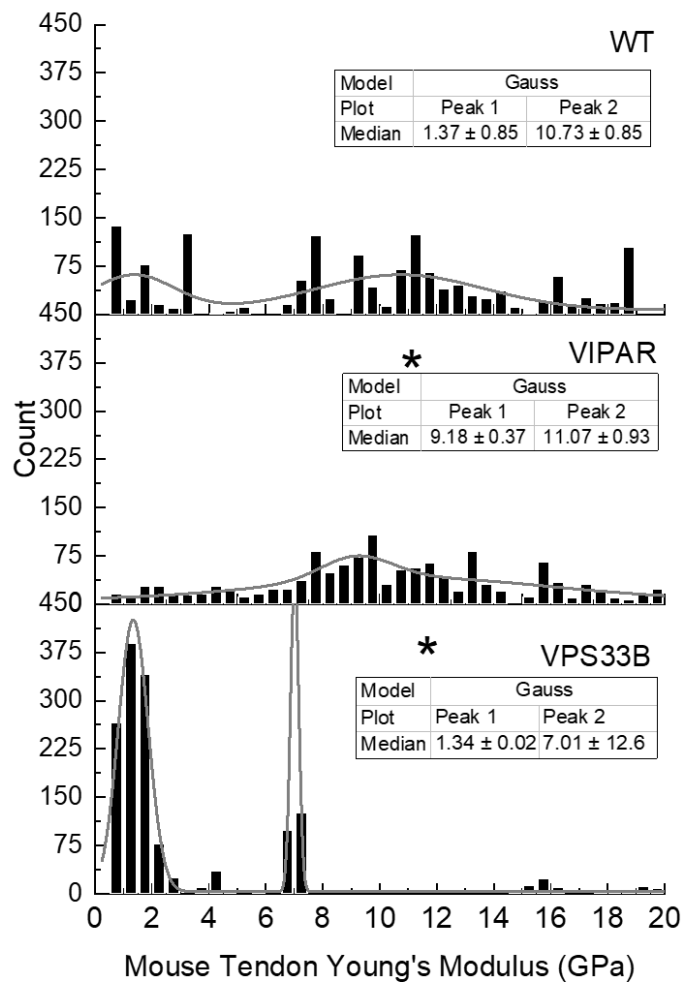


Figure 4-11 Young's modulus of all tendon samples showing comparisons

**Figure 4-11** shows the comparison between the indentation of the WT, VIPAR and VPS33B tendons. Although it was not clear from the graph, a statistically significant decrease in Young's modulus was confirmed between WT and VIPAR. Additionally, a significant decrease in Young's modulus was also found between both WT and VIPAR when compared to VPS33B. WT and VPS33B had significant differences in Young's modulus in both the higher and lower peaks, with  $p < 0.05$ , Kruskal-Wallis. A difference in Young's modulus WT and VIPAR was noted between the lower peaks, with both

VIPAR values in the 9-11 GPa, compared to the 1.37 GPa and 10.73 GPa range of the WT sample,  $p < 0.05$ , Kruskal-Wallis.

#### **4.5.3.5 Nanoscale Indentation Discussion**

The task of Objective 3 in this section was to identify if there were mechanical differences between the tendons. Firstly, measurements were taken from each sample. For the WT tendon (Figure 4-8), bimodal distribution was observed, similar to the pattern seen in the control mouse in Appendix C tendon previously tested. However, the medians for both peaks were considerably lower in the WT tendon.

The VIPAR knockout (Figure 4-9) gave a very weak bimodal distribution. The VPS33B tendon (Figure 4-10) had clear bimodal distribution. The lower median was the same in both the VPS33B and WT samples, but the upper median of VPS33B was significantly lower than all of the other medians recorded.

The behaviour of tendons has already been reported as being an ordered structure<sup>15,344,449</sup>. This directional orientation allows for the anisotropic stiffness of the tendons that are crucial to its biological function<sup>335,450,451</sup>. Disruptions to this alignment have already been shown to cause a morphological change in the collagen, especially in the VPS33B tendon (Figure 4-6). The swollen D-bands in those images are likely to have caused the decrease in Young's modulus of the tendons. The theoretical incorrect arrangement of the amino acids which caused the swelling are likely to leave voids instead of a tightly packed fibril structure. These weakened areas, along with incorrectly crosslinked fibrils, may explain why the higher median for VPS33B is so low. Fibrils that were not affected by the knockout, or not affected significantly, were not weakened. This

kept the lower median of Young's modulus the same for both the WT and VPS33B samples. While the bimodal distribution of Young's modulus is expected in tendon collagen, the significant decrease in Young's modulus must be pathological <sup>59,443,445,452</sup>. A decrease in Young's modulus of the tendon has been clinically reported as causing failure, rupture, and often requires surgical intervention <sup>442,453–455</sup>.

#### **4.5.3.6 Nanoscale Indentation Summary**

Indentation using AFM was successfully used to characterise a mechanical property of the tendons. Variation was seen between all of the samples, and none of the samples matched the Young's modulus of the control taken previously. Bimodal distribution was seen, and significant decreases in Young's modulus for the KO samples was measured. The decrease in values is consistent with the changes in morphology previously shown.

#### **4.5.4 Chapter Summary**

Throughout this chapter, SEM, AFM and a range of mechanical measurements were performed on tendons and bones as a model of ARC syndrome. This was a novel combination of the techniques and allows for multimodal analysis of the effects of the knockouts at different hierarchies. This work was showcased by different presenters at various conferences and has been published. In summary:

- The markers of collagen disorder first identified in Chapter 3.5 were reconfirmed and validated in tendons. AFM and SEM both yielded results in showing ordered tissues.

- Markers of collagen health were identified in the control samples. A bimodal distribution of Young's modulus (3, 14.5 GPa) and well-aligned collagen fibrils were seen.
- The evaluation of ARC syndrome models using SEM confirmed disordered fibril structure as a marker of VIPAR KO, which was even more disordered in VPS33B. AFM additionally showed the presence of D-band swelling in both KOs. A decrease in Young's modulus was measured in the KOs. A decrease in macroscale mechanical properties was measured in bones for both KO when collagen was the dominant factor (Appendix D).
- Genetic alterations to the mice resulted in severely altered collagen, which showed an increasing level of disordered and a decrease in measured mechanical properties. Therefore, these genetic alterations gave both a morphological and a mechanical effect to the fibrilised collagen.

## 5 Developing Quantitative Nanohistology in Skin & Case Studies of Scleroderma<sup>3</sup>

---

### 5.1 Introduction

The use of biopsies to diagnose skin conditions is extensive <sup>110,137</sup>. A punch biopsy, where a 2-6 mm<sup>2</sup> full thickness of skin is removed, is commonplace and allows for full histological analysis to be performed <sup>456,457</sup>. This is considered to be as minimally invasive as possible, leaving behind a small scar that can rapidly heal <sup>458,459</sup>. Many conditions, ranging from quality of life disorders such as uncombable hair syndrome to widespread malignancies such as melanoma benefit from an invasive removal of tissue for further analysis <sup>422,460–462</sup>. One condition that can benefit from rigorous analysis after a biopsy is taken is systemic scleroderma (SSc). SSc is an is a multi-systemic fibrotic collagen disorder of indeterminate aetiology. However, a change in the post-translational crosslinking of lysyl oxidase is noted as a possible cause <sup>184,189,192,463</sup>. Patients often report an initial onset of skin fibrosis, but fibrosis of the viscera, widespread vasculopathy and a spectrum of other features can arise <sup>101,179,184</sup>. SSc is a disorder that affects women primarily, although age and ethnicity as demographic details are also important factors in understanding collagen behaviour <sup>127,280,401,464,465</sup>.

---

<sup>3</sup> The work in this chapter formed part of a collaboration with Dr Herve Pagion (L'Oréal) who sponsored R&D related to this work, with some data collection and analysis performed with Anna Maeva (UCL).

A number of case studies of skin biopsies were analysed refining the quantitative nanohistology (QNH) protocol and introducing a novel image quantification process. The QNH protocol was then applied to two SSc patients with demographically matched controls.

The work in this chapter and in Appendix E in has been published as “Role of the prolyl 3-hydroxylase LEPREL1 in fibrosis” <sup>466</sup> and subsequent work been accepted pending final corrections as “Role of the prolyl 3-hydroxylase LEPREL1 in scleroderma and in experimental skin fibrosis”. The work in Part B has been published as “Quantitative nanohistological investigation of scleroderma: an atomic force microscopy-based approach to disease characterisation” <sup>395</sup>. Additionally, a further paper is being prepared for submission.

## 5.2 Aim

This chapter aimed to bring together the advances made in Chapter 4 by seeking to develop the QNH protocol for clinical samples, and to test the protocol on SSc, allowing for the use of AFM as an adjunct diagnostic tool.

## 5.3 Objectives

### Part A:

1. Measure the Young's modulus and topography of case studies of healthy skin donors.
2. Enumerate topographical images using an image quantification system.
3. Refine the QNH protocol by introducing histological and mesoscale imaging where appropriate.

### Part B:

4. Test the QNH protocol on case studies of SSc to allow for direct comparisons.

These objectives will be met in two parts. Initially, in part A, healthy skin samples will be examined to develop the QNH protocol. Once refined, QNH will be applied to case studies of SSc to test its effectiveness.

## 5.4 Materials and Methods

### 5.4.1 Materials

#### **5.4.1.1 Human Skin Case Studies**

All samples for the comparative SSc studies were obtained under ethical approval (Research Ethics Committee Cambridge, 06/6398) and patient consent was obtained following local guidelines by the team of Dr Richard Stratton, consultant rheumatologist, Royal Free Hospital and UCL . Volunteer patients had a 4 mm punch biopsy taken from the upper forearm in a non-load-bearing area, including the sclerotic lesion where appropriate for this study. All SSc patients were diagnosed in clinic as being at a severe stage of the disease, ensuring that any samples taken would have sclerotic lesions.

Similarly, the biopsies for case studies of healthy skin were obtained under consent by a collaborator and processed using the same histological protocol as described above.

### 5.4.2 Methodology

#### **5.4.2.1 Histological Staining**

After skin samples were obtained as above, biopsies were snap-frozen in methyl butane and liquid nitrogen. Samples were histologically cut into 10  $\mu$ m sections at a clinical laboratory (Blizard Institute – Queen Mary University London). The sections were subsequently stained with picrosirius red (PS) for collagen alignment after being

dried through physisorption onto a glass slide. The prepared sections were then stored at 4°C under Human Tissue Act guidelines until required for experiments.

#### **5.4.2.2 Histological Imaging**

A Leica (Wetzlar, Germany) light microscope (LM) with 4x, 10x and 20x magnification lenses was used for LM imaging. The LM was additionally equipped with two crossed-light polarisers (90°), to allow for polarisation (darkfield) LM. At least three images were taken in each location for each sample, with at least three biopsies per patient analysed. Images were captured using an 8-megapixel digital camera (EOS Rebel 100, Canon). Where applicable hundreds of individual LM images were combined using Autostitch into a single overview image as described <sup>467</sup>.

#### **5.4.2.3 Mesoscale Imaging**

Previously sectioned samples were fixed for 24 hours using 3% glutaraldehyde in 0.1M sodium cacodylate solution. The samples were then dehydrated using an ethanol series over 20 minutes, before critical point drying with hexamethyldisilazane. Samples were mounted using carbon adhesive tabs to aluminium stubs (Agar Scientific, UK), and coated in Au/Pd. Imaging was performed using a Philips XL30 FEG-SEM (FEI, Eindhoven), with an accelerating voltage of 5 kV. Low, medium and high magnifications were chosen as appropriate for each sample. Images were taken in random locations (minimum of 3 per sample) or to display notable features.

#### **5.4.2.4 Nanoscale Imaging**

Samples were not fixed or treated after histology. Both a Nanowizard 1 and Nanowizard 4 AFM operated in contact mode in air were used to image most samples,



equipped with MSNL cantilevers with  $k = 0.03\text{-}0.6\text{ N/m}$ . The setpoint, gains and scanning speed were optimised for each sample. Images were taken in random locations across the sample, processed using proprietary JPK software, and representative images presented.

#### **5.4.2.5 Nanoscale Mechanics**

For mechanical measurements (indentation) both AFMs were used. Two types of calibrated cantilevers were used. For some experiments, RFESPA (Bruker, Santa Barbara) cantilevers,  $k = 3\text{ N/m}$ , were employed, with more recent experiments using NSC-35 (Mikromasch, Tallinn) cantilevers,  $k = 5.4 - 8.9\text{ N/m}$ . In each case, a minimum of 500 force-displacement measurements were taken on the collagen with an applied relative setpoint of 300 nN.. The force-displacement curves were processed using proprietary JPK software and fitted according to the Sneddon model. This data was graphed, statistically analysed and presented using OriginPro (Origin Corp, Massachusetts).

#### **5.4.2.6 Image Quantification**

As the QNH protocol was developed, AFM images were analysed to determine the dominant features using a colour coding system according to the following criteria:

- Type 0 – invalid pixels due to contamination, glass surface visible, cross-section artefacts on fibrils, preparation artefacts, imaging artefacts.
- Type 1 – holes or gaps between fibrils that are intact, excluding gaps between collagen sheets.
- Type 2 – non-collagenous material, loss of fibril integrity with loss of D-banding.

- Type 3 – intact fibrils with D-banding periodicity but not aligned.
- Type 4 – intact fibrils with D-banding periodicity and fibril alignment.

Each image was split into 100  $1\ \mu\text{m}^2$  pixels, and the dominant feature type was recorded and graphed to give an overview of the principal features of that area, to give exactly 100 features per image. A minimum of 6 images per sample were analysed using this method, to give 600 markers per sample. Currently, all images were analysed by one individual, after consultation with other experienced individuals. Additionally, each set of images were viewed en masse to give a qualitative overview of the features. The results of the image quantification were graphed on OriginPro (OriginCorp, Massachusetts) as box plots and bar charts as appropriate.

These feature markers were chosen to indicate certain behaviours indicate of typical and atypical collagen. Type 0 indicates an invalid pixel, from which useful data cannot be extracted. This is required as the image analysis protocol requires one feature per pixel, so type 0 allows for this standardisation without biasing the results. Type 1 indicates an abnormal hole, gap or splitting between recognised collagen fibrils. These holes are considered to be a precursor to further disorder but show that collagen is still present in the pixel. Type 2 is non-collagenous material, which could be either collagen that has degraded into gelatine or one of the many other components of skin that could be present. As polarised light histology is introduced in Part B of this chapter, it was considered unlikely that there would be too much non-collagen present in the areas selected for imaging, so any type 2 is more likely to be degraded collagen. Type 3 is disordered collagen, which still shows D-banding. This is collagen that is out of alignment with its neighbouring fibrils and does not seem to follow a discreet register or

alignment. Type 4 collagen is well aligned and ordered, and is the generally accepted state of healthy human skin collagen. This would be the expected state of collagen in an otherwise healthy individual. The meaning of these damage markers and their significance in understanding collagen behaviour will be considered in the discussion sections. An example of two different images, the damage markers and the graphing is shown below:

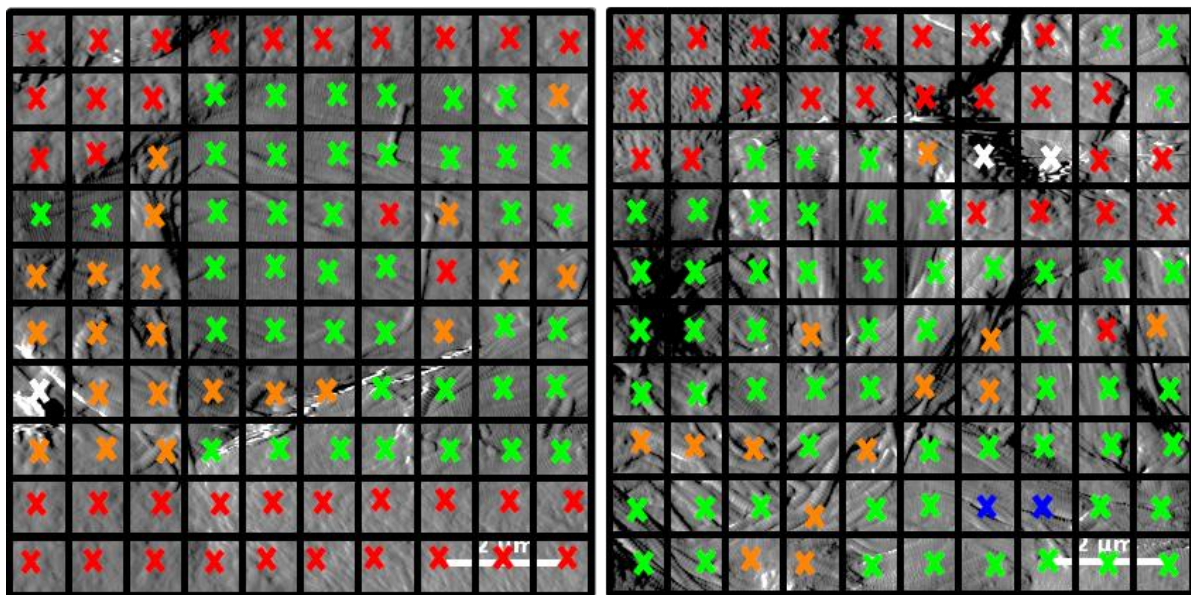
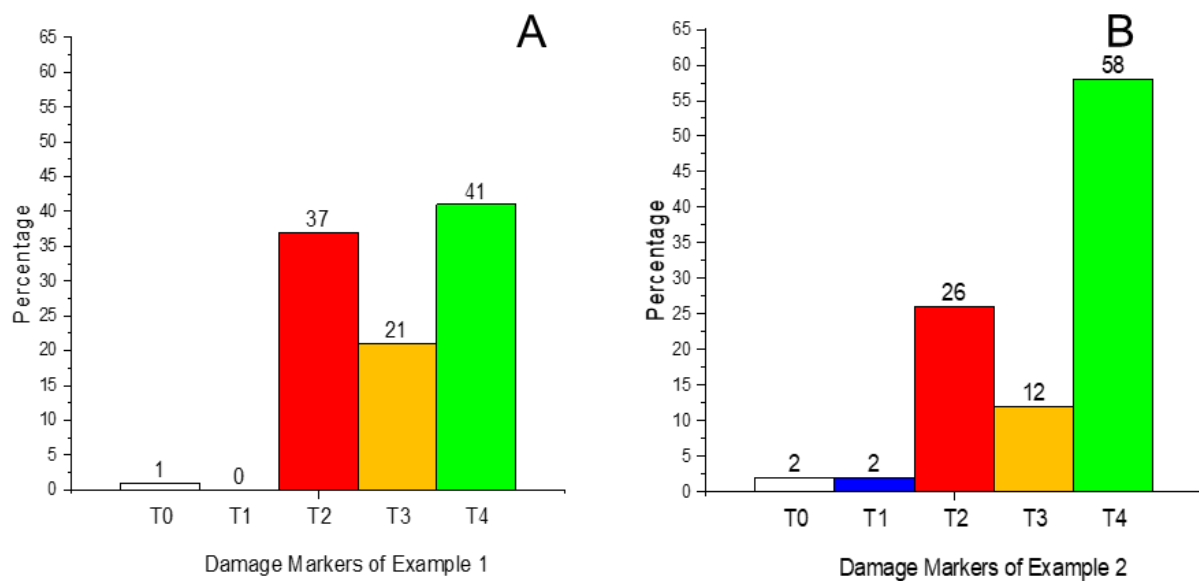


Figure 5-1 Image quantification examples

**Figure 5-1** shows two example images that have been analysed using the image quantification protocol. Each separate pixel had its dominant feature noted, according to the colour scheme as described above. This colour scheme is presented here for ease of explanation. They will not appear in the main results section, as the colours will be used differently to describe light microscopy images as a part of the overall protocol development. Repetition of colour levels could cause undue confusion.



**Figure 5-2 Image quantification graphs**

**Figure 5-2** shows the collated data obtained using the image quantification protocol. By normalising the image quantification data and presenting it as percentages, this allows for the easy scalability of the protocol.

## 5.5 Blind AFM Imaging and Mechanics

Having previously evaluated a mouse model for SSc in Appendix E, the first challenge of this chapter was to establish a baseline for the behaviour of human skin in healthy donors. By working towards the development of a conclusive protocol for collagen characterisation, the aim was to establish morphological and mechanical indicators of health which could later be applied to disease. Here, four donors are presented, and after development, the image analysis protocol was initially trialled, for Objective 1 of this chapter: *“measure the Young’s modulus and topography of case studies of healthy skin donors.”*

### 5.5.1 Patient 1

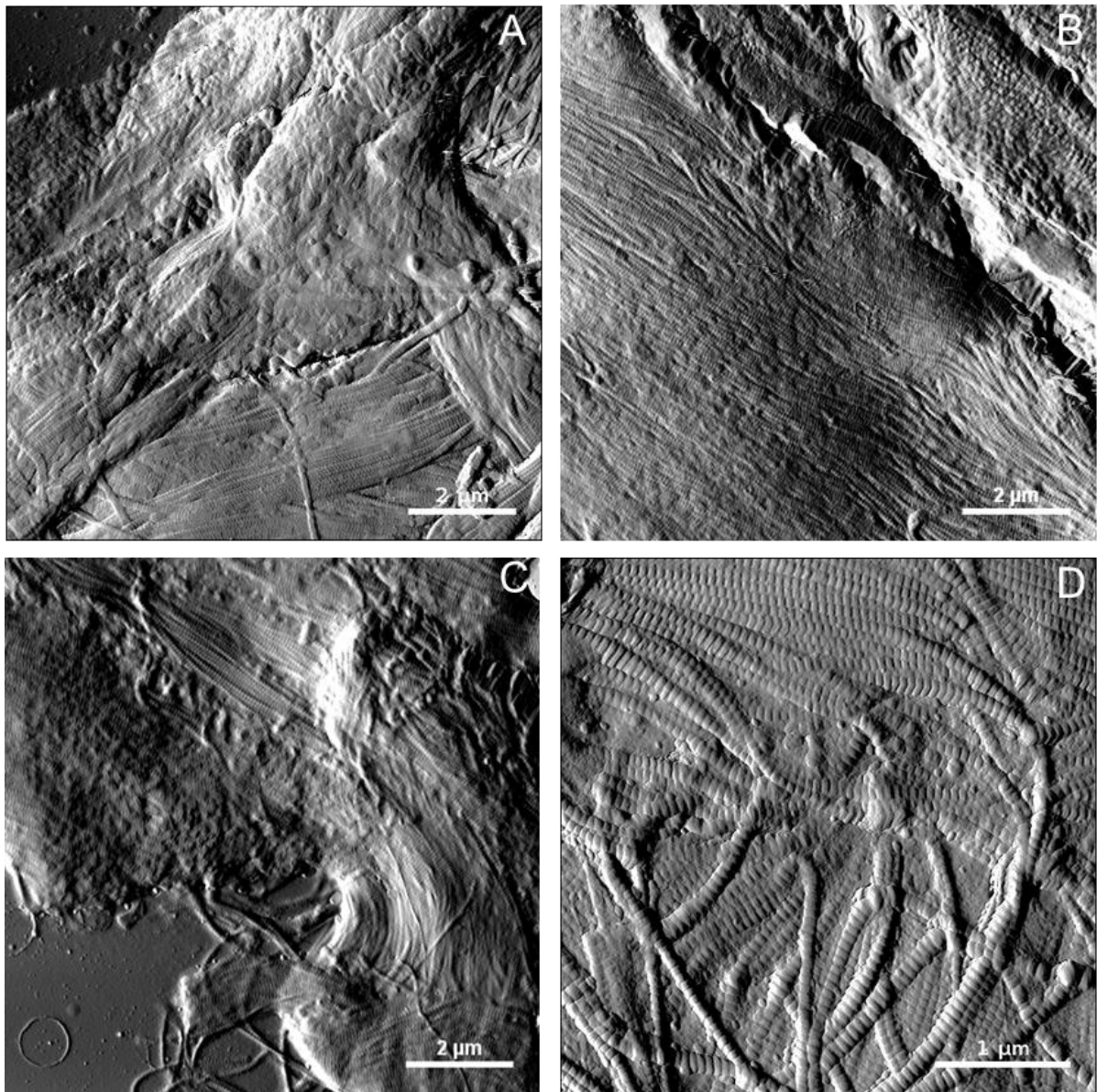


**Figure 5-3 Morphology of four locations of Patient 1**

**Figure 5-3** shows the AFM imaging of Patient 1. Image **A** shows a large mass of amorphous material, which covers bundles of fibres. Several distinct bundles are crossing each other, showing layers and directional alignment. D-banding is visible on the fibrils. Image **B** also shows a large amount of non-collagenous material. Collagen fibrils are present in the lower half of the image, with ends of fibrils exposed suggesting

that the histological sectioning has bisected a bundle of fibres. When the lengths of fibrils are visible, D-banding is present. Image **C** shows a range of morphologies, with bundles of fibrils crossing each other, indicating that sheets of collagen have been cut during preparation. Some fibrils are intact while others have been cut. The majority of the collagen imaged appears to be intact and well-aligned, and the glass slide is visible in the background. Image **D** shows a higher magnification image of collagen fibrils. D-banding is present on all fibrils, which is regular. It is important to note heterogeneity of alignment and organisation in the fibrils, even over the range of a 5  $\mu\text{m}^2$  image. The fibrils move from being aligned and in orientation at the top of the image to being disordered at the bottom of the image.

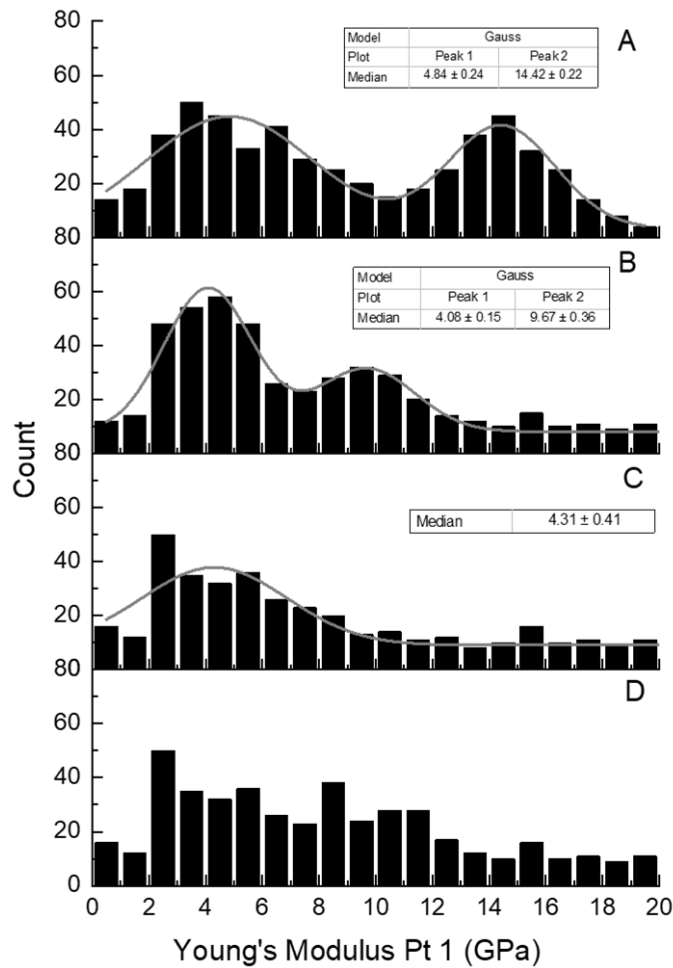


**Figure 5-4 Young's modulus of four locations of Patient 1**

**Figure 5-4** shows the Young's moduli of four locations of Patient 1 corresponding to the locations seen in Figure 5-3, with 3 of the graphs showing bimodal distribution. Graph **A** shows a bimodal distribution with a large range median of  $4.84 \pm 0.24$  GPa and a narrow median of  $14.42 \pm 0.22$  GPa. Graph **B** also has a bimodal distribution; two narrow medians of  $4.08 \pm 0.15$  GPa and  $9.67 \pm 0.36$  GPa. Graph **C** has a single distribution of  $4.31 \pm 0.141$  GPa but with a very wide range of data, similar to all of the other graphs shown in this figure. Graph **D** does not show any median distributions but contains a large range of values. All of the graphs with medians have a consistent low



median around 4 GPa, which were not significantly different from each other. Graphs A and C were both statistically different from each other and the other graphs, Kruskal-Wallis,  $p < 0.05$ .

#### 5.5.2 Patient 2

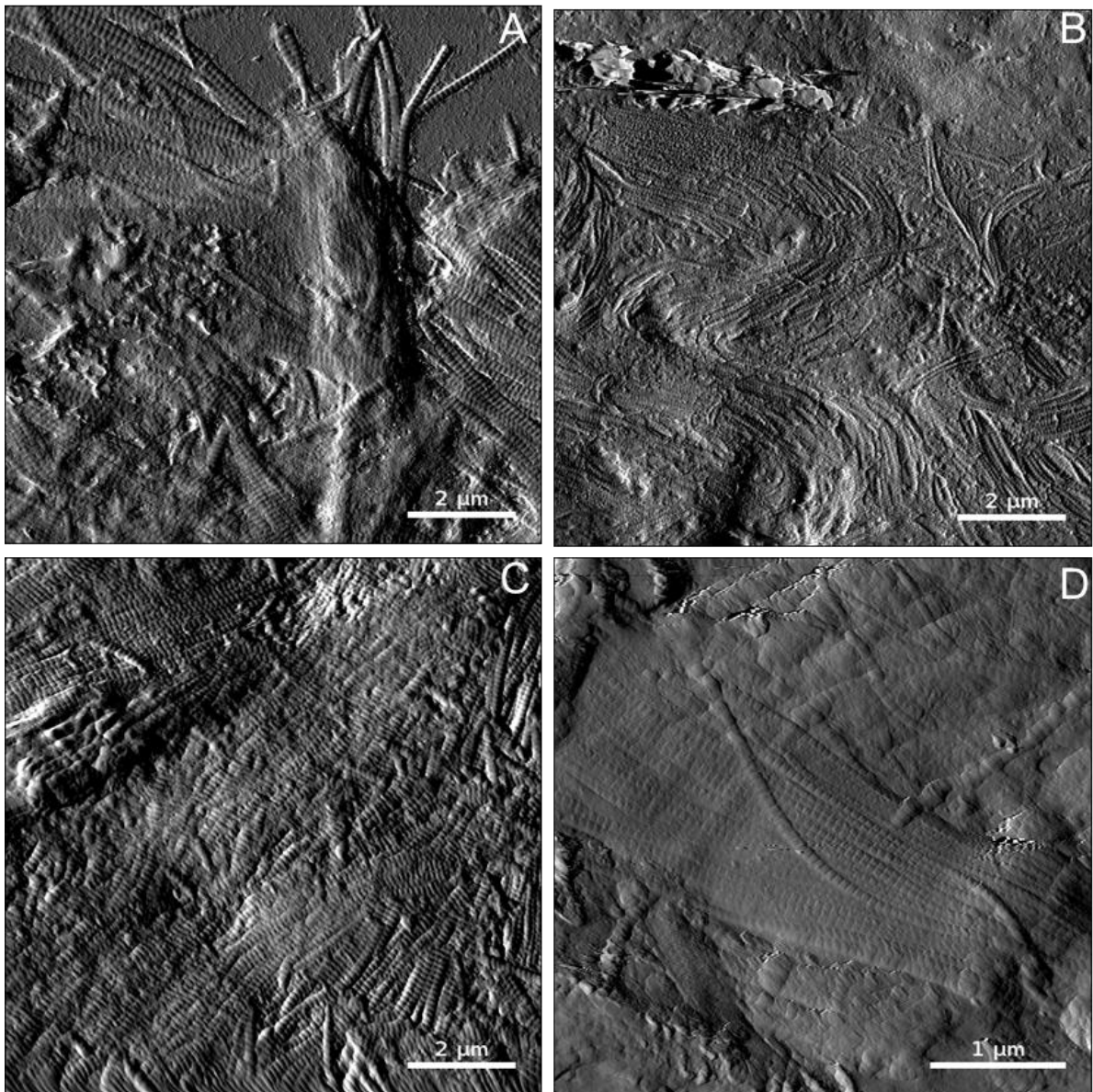


**Figure 5-5 Morphology of four locations of Patient 2**

**Figure 5-5** shows the morphology of Patient 2. Image **A** shows small bundles of fibrils with amorphous material present between the fibrils. There is alignment inside

fibril bundles but not between the bundles. Some of the fibrils have D-banding visible, but the close packing of some fibrils means that, if it is present on the other fibrils, it cannot be observed. Image **B** shows a large number of fibrils. These fibrils appear to be smaller than the other fibrils in image A, and have a distinctive wavy alignment to them, appearing in sheets. D-banding cannot be seen as, if it is present at all, it is either too small to be seen or the fibrils are too tightly packed to show it clearly. Image **C** shows sheets of collagen that have been cross-sectioned during sample preparation, showing the ends of the individual fibrils. There is an overall directional alignment, despite sectioning through the sheets and bundles. D-banding is present on all of the fibrils. Image **D** is a higher magnification image of collagen fibrils. While there are some fibrils in alignment towards the centre, the rest of the image shows amorphous material. D-banding is present, but it is irregular; appearing to be very faint. The fibrils embedded in the amorphous material also show D-banding despite lacking any register or alignment.

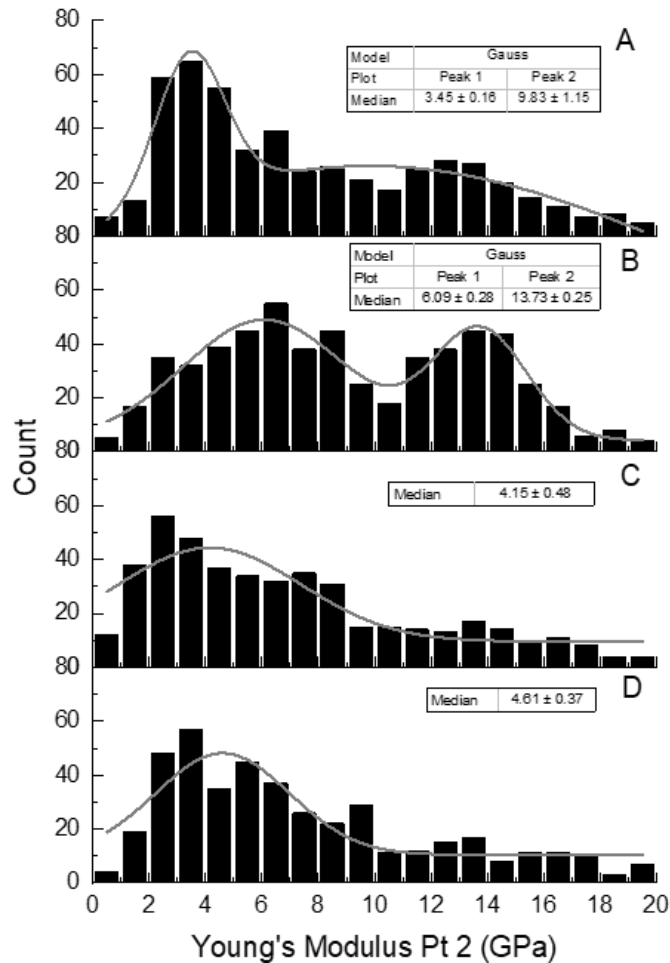


**Figure 5-6** Young's modulus of four locations of Patient 2

**Figure 5-6** shows the Young's moduli of four locations of Patient 2 corresponding to the locations seen in Figure 5-5. Graph **A** has a bimodal distribution with a lower narrow median of  $3.45 \pm 0.16$  GPa and a very wide upper median of  $9.83 \pm 1.15$  GPa. Graph **B** shows a bimodal distribution, with a wide median of  $6.09 \pm 0.28$  GPa and a narrow higher median of  $13.37 \pm 0.25$  GPa. Graph **C** has a long tail single wide median of  $4.15 \pm 0.48$  GPa. Graph **D** also shows a single wide median of  $4.61 \pm 0.37$  GPa with a long tail of data going to 20 GPa. Graphs C and D were extremely similar in their appearance, and their median averages, which were significantly different from

both graphs A and B. Graphs A and B were significantly different from each other and every other graph of Patient 2, Kruskal-Wallis,  $p < 0.05$ .

#### **5.5.2.1 Section Discussion**

Patients 1 and 2 both presented interesting case studies and, more importantly, allowed for the improvement of the QNH protocol. The appearance of Patient 1 (Figure 5-3) show the wide-ranging differences that were possible within in a single sample. In the four images presented there are: fibrils in and out of alignment, fibrils that have been cross-sectioned, non-collagenous material, a visible glass slide and imaging artefacts. In particular, Figure 5-3D show the changes in alignment that can occur over the space of one micron; fibrils change from being highly aligned to disordered to being aligned again. Patient 2 (Figure 5-5) also showed changes in alignment and collagen behaviour both in each individual image and between the image sets, causing intra-sample variation. Similar changes within a small location have been previously reported, with no particular solution presented<sup>26,468</sup>. While all of these images were described, it was obvious that a method of characterising the samples more fully and completely was needed. This has been described previously in the literature, with the intra-sample variation being noted as a significant barrier to image analysis<sup>115,457,461,469</sup>. One potential method of enhancing the image analysis is to use large data sets and neural networks to analyse repeating patterns present in the imaging data<sup>470</sup>. This would allow for both inter-sample and intra-sample variability to be considered during data analysis.

The mechanical measurements also identified the similarities and differences between the two case studies in Patient 1 (Figure 5-4) and Patient 2 (Figure 5-6). In each of the eight graphs, a low median value of around 4 GPa was calculated. However,

there was no apparent pattern within each sample regarding distribution. Both bimodal and single distributions were observed, with the upper modulus value varying from 9.5 GPa to 13.7 GPa. As described in Chapter 4.5, this value for collagen is consistent with data found in both this thesis, and reported in literature <sup>277,280,374</sup>.

Additionally, a bimodal distribution around 5 GPa and 12 GPa has been suggested as being the average behaviour for collagen in skin <sup>343,471,472</sup>. Differences between the two major dermal layers, the papillary and the reticular dermis, should also be considered when noting disparate mechanical measurements and changes in morphology <sup>107,108,473</sup>. Crucially, Objective 1 has been met as “*measure the Young’s modulus and topography of case studies of healthy skin donors*” was successfully performed.

## 5.6 LM-Guided QNH Protocol

In the above section, AFM was used to investigate two healthy donors. However, large intra-sample variation presented an immediate problem. While some salient features of the image were highlighted, it appeared that every image has a large amount of variation. Two potential improvements were trialled for the final two healthy case studies, Patients 3 and 4. Light microscopy (LM), which was used effectively in Chapter 3.6 to locate areas of interest, is used here to ensure that measurements are always taken in similar regions of the dermis. Additionally, the dominant features of the individual images, and especially markers of potential damage to the collagen were recorded according to the image quantification protocol as described in Section 5.4.

These experiments sought to answer the challenge of this chapter's Objective 2: *"enumerate topographical images using an image quantification system"*.

### 5.6.1 Patient 3

#### 5.6.1.1 Histology

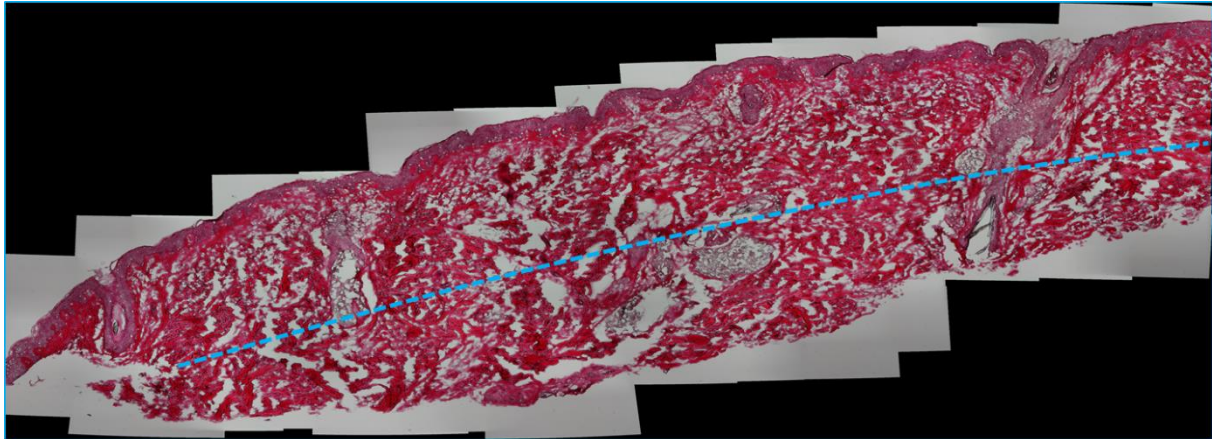
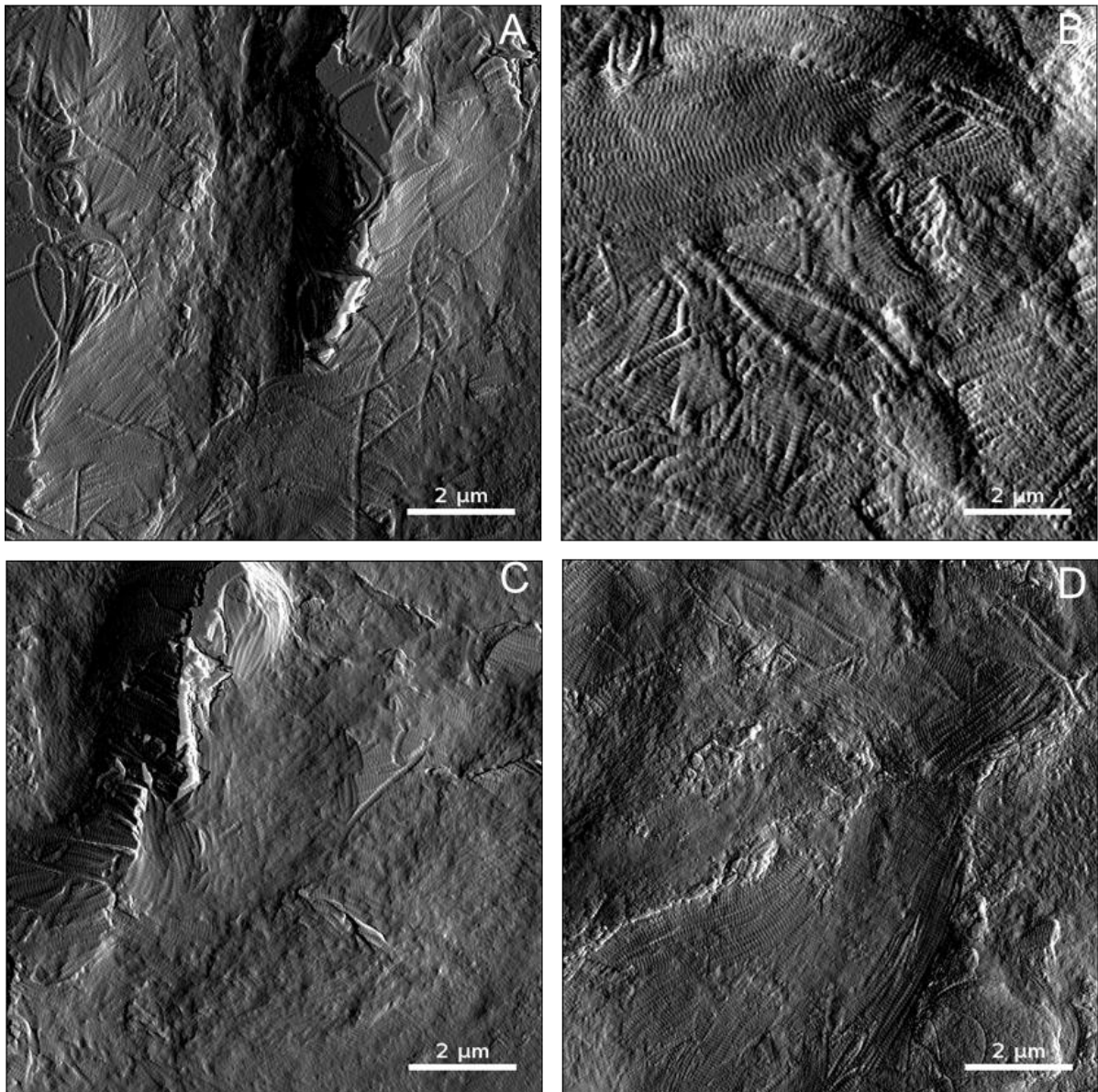


Figure 5-7 LM of the section of Pt 3, 20x magnification

Figure 5-7 shows a composite LM image of Patient 3, with the areas for investigation marked below the dotted line. The stratum corneum and epidermis are visible towards the top of the image. Below them are the papillary dermis and reticular dermis, which are collagen-rich areas. Further measurements with AFM were taken in the reticular dermis region.

### 5.6.1.2 Histology Guided Imaging



**Figure 5-8 Morphology of four locations of Patient 3**

**Figure 5-8** shows the morphology of Patient 3, taken from the reticular dermis region of the sample, as seen in Figure 5-7. Image **A** shows several intersecting collagen sheets. Large bundles of fibrils can be seen, but D-banding is not visible. While the fibrils are mostly in alignment, many have come out of the bundles and lost register.

The ends of some cross-sectioned fibrils and the glass slide are also present. Image **B** also shows the intersections of several collagen sheets. Here the fibrils show a large range of behaviours, but all of the bundles are well aligned. Some fibrils are lacking alignment but D-banding can be easily seen in all fibrils. Image **C** shows a large amount of amorphous material, where neither D-banding or fibrils can be seen on the surface. In some locations, especially towards the edges of the image, fibrils are seen, which appear to be well-aligned. Image **D** shows several bundles intersecting, with fibrils present. The fibrils and bundles are both well aligned. D-banding is seen, although some amorphous material is also present.

#### 5.6.1.3 Image Analysis

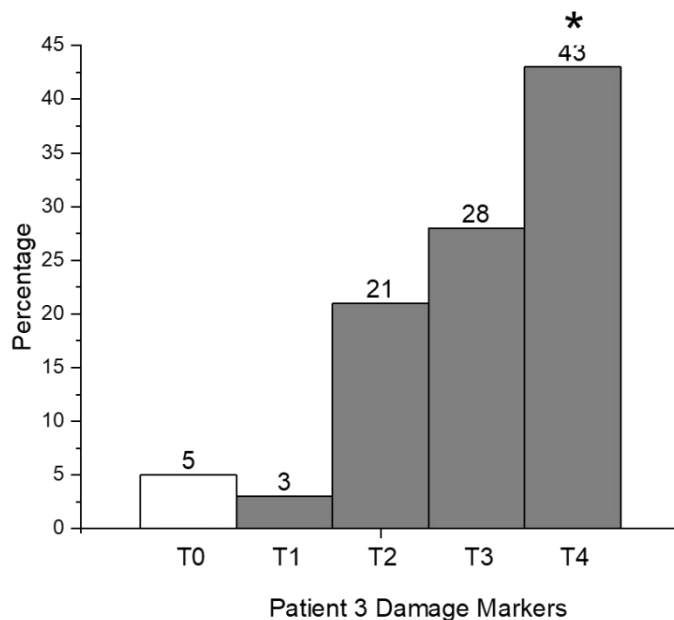


**Figure 5-9 Image quantification damage markers of Patient 3**

**Figure 5-9** shows the image quantification for Patient 3. The four images in Figure 5-8 were analysed in addition to two others not shown. The most frequent feature present was type 4, aligned fibrils. This was found to be significantly more numerous



than any of the other types tested. Despite not being easily observed when the entire image was viewed, there are large contributions from type 3, unaligned fibrils as well as a considerable amount of type 2, non-collagenous materials.

#### 5.6.1.4 Histology-Guided Nanomechanics

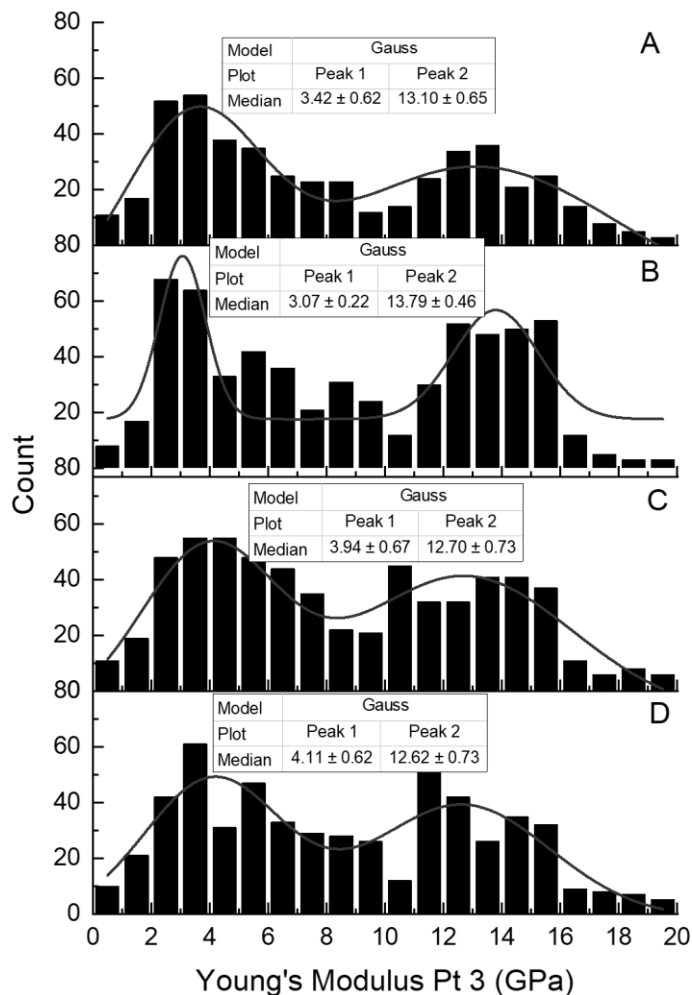


Figure 5-10 Young's modulus of four locations of Patient 3

**Figure 5-10** shows the Young's modulus for four locations seen in Figure 5-8. Graph **A** shows a bimodal distribution with wide medians of  $3.42 \pm 0.62$  GPa and  $13.10 \pm 0.65$  GPa. Graph **B** shows a bimodal distribution with a narrow lower median of  $3.07 \pm 0.22$  and a narrow upper median of  $13.79 \pm 0.46$  GPa. Graph **C** shows a bimodal

distribution with a wide lower median of  $3.94 \pm 0.67$  GPa and a wide upper median of  $12.7 \pm 0.73$  GPa. Graph **D** shows a bimodal distribution with a wide lower media of  $4.11 \pm 0.62$  GPa and a wide upper median of  $12.62 \pm 0.73$  GPa. None of the graphs were significantly different to each other, Kruskal-Wallis,  $p > 0.05$ .

#### 5.6.2 Patient 4

##### 5.6.2.1 Histology

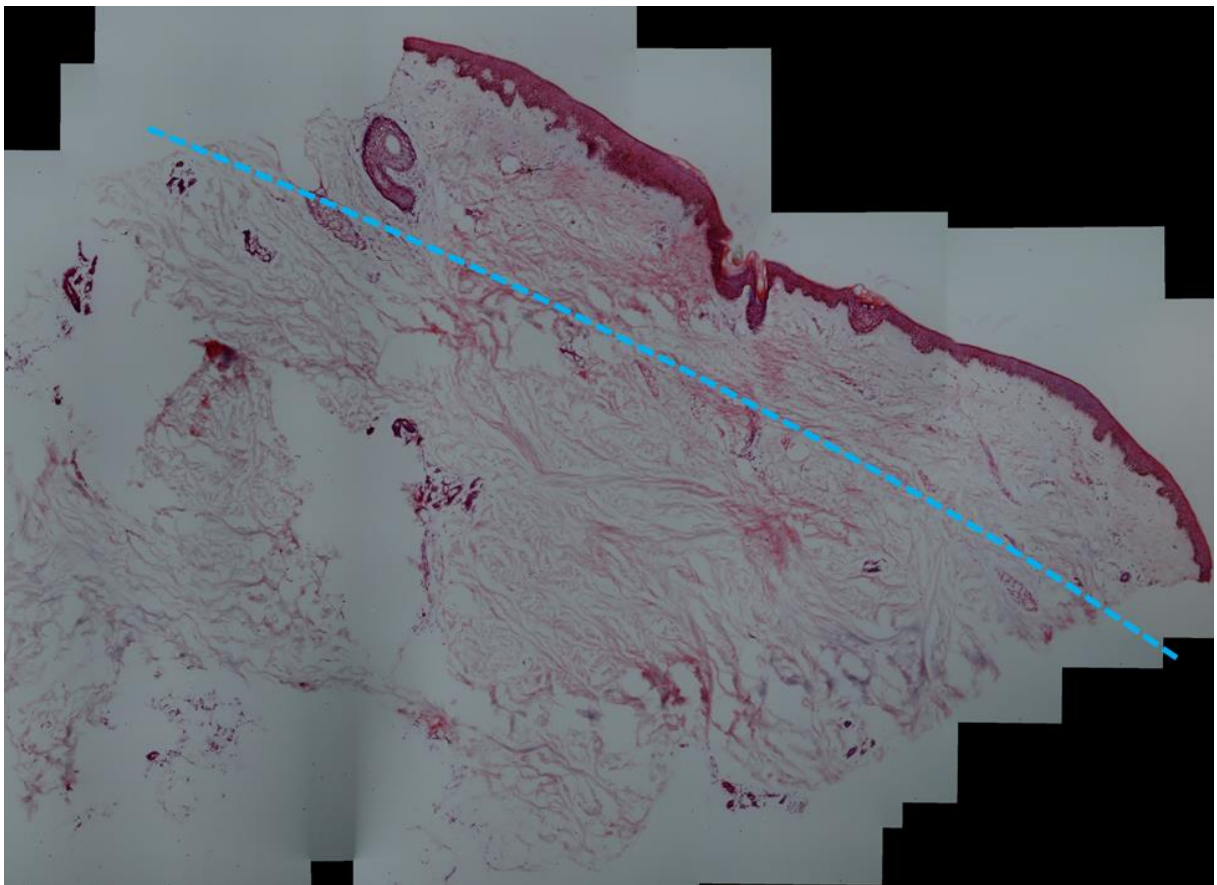


**Figure 5-11 LM of the section of Pt 4, 20x magnification**

Figure 5-11 shows a composite LM image of Patient 4, with the areas of investigation marked below the dotted line. The stratum corneum and epidermis are visible towards the top of the image. Below them are the papillary dermis and reticular

dermis, which are collagen-rich areas. Further measurements with AFM were taken in the reticular dermis region. This sample is highly porous, with large gaps visible between the tissue. Additionally, the sample appears to be lightly stained; likely a side-effect of the high porosity.

#### **5.6.2.2 Histology Guided Imaging**

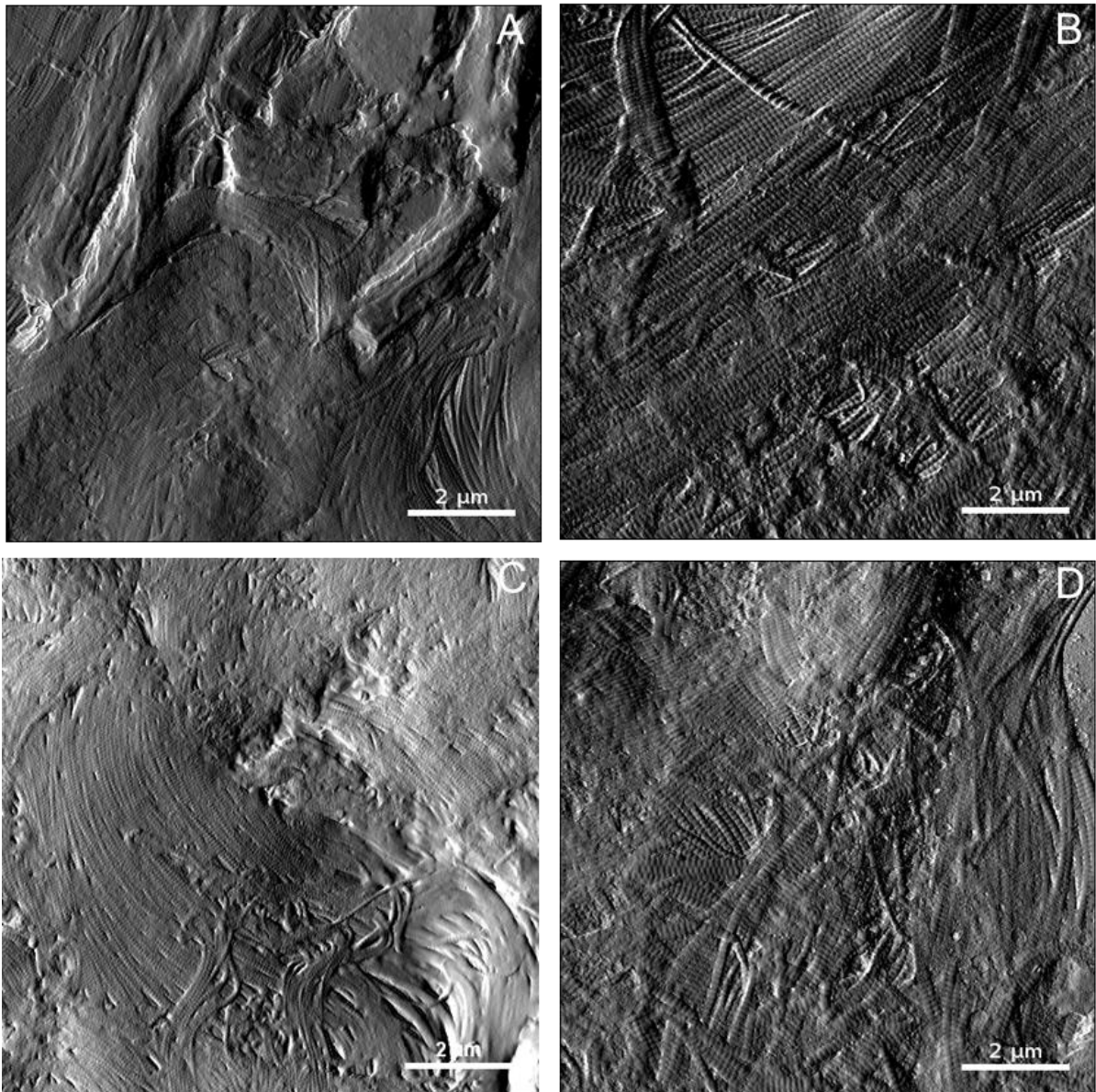


**Figure 5-12 Morphology of four locations of Patient 4**

**Figure 5-12** shows the morphology of Patient 4. Image **A** shows several bundles of collagen with varying appearances. Some fibrils are visible with D-banding evident; other fibrils are densely packed and form a thick sheet with some holes. There is minimal discernible orientation throughout the image. Some bundles do not show clear fibrils, and there is amorphous material present towards the top of the image. Image **B** shows a large number of fibrils which are visible. The fibrils are well aligned and show a high degree of directional orientation. Image **C** shows fibrils that are curved, and have a directional orientation as they pack into tight sheets. Some holes in the sheets can be seen as can D-banding. Image **D** shows a large number of fibrils without directional orientation but strong D-banding. Some amorphous material is present, as is the glass slide in the background. The ends of some fibrils are visible as a result of the cross-section.

### 5.6.2.3 Image Analysis

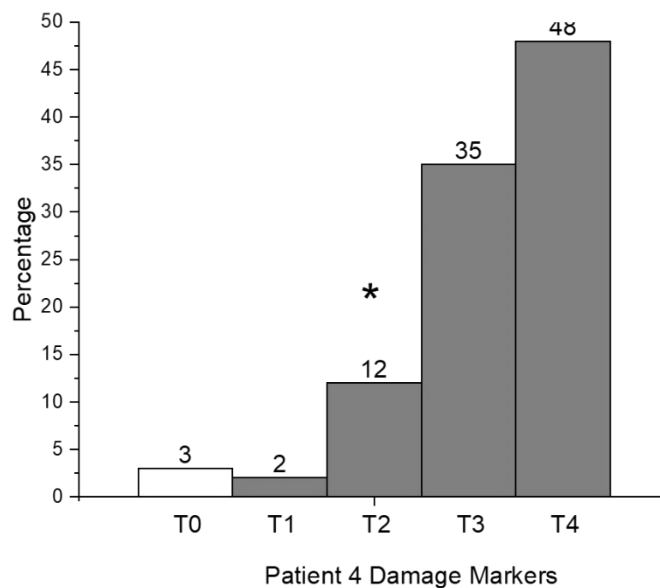


**Figure 5-13** Image quantification damage markers of Patient 4

**Figure 5-13** shows the image quantification for Patient 4. The four images in Figure 5-12 were analysed in addition to two others not shown. The most frequent feature present was type 4, aligned fibrils. Type 3, unaligned fibrils, was less prevalent but not significantly different from the amount of type 4 present. Both type 4 and type 3 markers were significantly more numerous than type 2, non-collagenous, which was only found in 12% of the pixels. Comparable numbers of type 1, holes, and type 0, invalid pixels, were also seen.

#### 5.6.2.4 Histology-Guided Nanomechanics

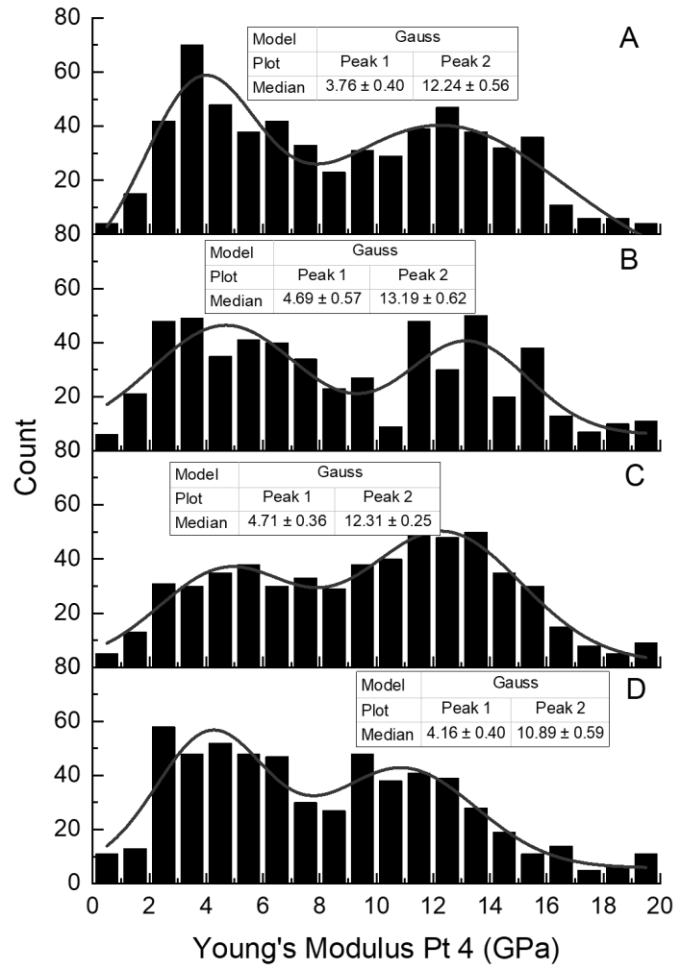


**Figure 5-14** Young's modulus of four locations of Patient 4

**Figure 5-14** shows the Young's modulus for four locations of Patient 4 seen in Figure 5-12. All graphs presented here show a bimodal distribution of Young's moduli. Graph **A** shows a low median of  $3.76 \pm 0.4$  GPa and an upper median of  $12.24 \pm 0.56$  GPa. Graph **B** shows a wide lower median of  $4.69 \pm 0.57$  GPa and a wide upper median of  $13.19 \pm 0.62$  GPa. Graph **C** shows a low median of  $4.71 \pm 0.36$  GPa and a high median of  $12.31 \pm 0.25$  GPa. Graph **D** shows a low median of  $4.16 \pm 0.4$  GPa and a high median of  $10.89 \pm 0.59$  GPa. No statistical differences were seen between any of the four graphs, Kruskal-Wallis,  $p > 0.05$ .

#### **5.6.2.5 Section Discussion**

This section differs from the work in Section 5.5 as it included the use of light microscopy and image quantification. Patients 3 and 4, which were investigated here, were shown to be more consistent regarding the features observed in the AFM images than Patients 1 and 2 (Figure 5-4 & Figure 5-6). The location chosen during LM for AFM imaging is the reticular dermis. The reticular dermis is the lower dermal layer and is comprised of dense irregular connective tissue, predominantly collagen<sup>32</sup>. This is contrasted with the upper dermal layer, the papillary dermis, which has a loose collagen meshwork<sup>32</sup>. Focusing on the reticular dermis for AFM analysis provides two advantages. Firstly, there is an obvious advantage to keeping the sampling site consistent across all samples, reducing experimental error and variability. Secondly, since the reticular dermis has a larger amount of ordered collagen present, there is a greater chance of finding consistent collagen in every scan which can be expected to be ordered and healthy. All experiments for Patients 3 and 4, along with the work in part B of this chapter, used LM to guide AFM data collection. The work in this section went

some way to answering Objective 3 *“add to the QNH protocol by introducing histological and mesoscale imaging.”*

The dominant features of Patient 3 (Figure 5-8) appeared to be intersecting sheets when observed solely as images without quantification. A large amount of non-collagenous material, probably gelatine, was present. Patient 4 (Figure 5-12) however, showed large numbers of bundles with both aligned and unaligned fibrils present. While this is the analysis for the image as it is presented, this approach of just looking at a group of single images as a whole allows for variation in interpretation. There is a risk of confirmation bias, and an inherent preference to focus on the major feature initially observed <sup>474–476</sup>. While imaging remains a key feature of this thesis, the use of image quantification allowed for the removal of some subjectivity in addition to allowing for statistical comparisons where appropriate. The image analysis of Patient 3 (Figure 5-9) showed that while the dominant features in the individual pixel were aligned fibrils, there was a minimal appreciable difference in number between gelatine and disorganised fibrils. The novel development of this system answered the requirement for Objective 2: *“enumerate topographical images using an image quantification system”*.

The damage marker types broadly follow the implication of the severity of the feature noted. Type 1, holes, between the fibrils, could be considered precursors to disorder as it suggests an unwinding of the collagen bundles, but it is not always linked directly to collagen damage <sup>477</sup>. The presence of large amounts of type 2 non-collagenous material, likely gelatine shows the greatest level of disorder in a sample. When collagen has degraded into gelatine, significant changes to its mechanical properties are noted, with the turnover of collagen under normal physiological conditions

regularly occurring<sup>356,399,478–480</sup>. Type 3, disorganised collagen fibrils, are not aligned to each other in register. As a biomaterial, collagen derives its mechanical properties from its isotropic nature, and often form sheets and bundles in hierarchy<sup>9,12,280</sup>. Disordered collagen disrupts that structure, often leading to a loss of ideal tissue properties<sup>12,59,74,158</sup>. Some levels of disorder are to be expected even in healthy individuals due to the turnover of collagen *in vivo*. Type 4, aligned collagen, is the preferred state of collagen regarding orientation and alignment. Here the fibrils, whether in a sheet or bundle, are well-aligned to their neighbours. This allows for the large range of interfibrillar crosslinking to occur, leading to an increase in stability of the larger hierarchical tissue<sup>27,57,434</sup>. Type 0, invalid pixels, is not an actual data point so appears white on the graphs; no particular patterns are expected to be seen between different samples as this is dependent on the AFM user's choice of imaging location. However, it can be supposed that by using light microscopy for Patients 3 and 4 to help inform the site choice for AFM imaging, fewer artefacts were observed than in Patients 1 and 2.

It has been well established that disorder in collagen alignment is suggestive of a weakened and possibly pathological collagen structure<sup>410,452,481</sup>. This was also observed in the ARC syndrome model mice in Chapter 3. This did not translate to a decrease in Young's modulus (Figure 5-10) for Patient 3. The nanoindentation protocol used throughout this thesis requires the identification of collagen fibrils through obvious morphological features such as the presence of D-banding. This ensures that only collagen is tested for Young's modulus where applicable; the quantity of collagen in a tested area has no bearing on the mechanical measurements. The nanoindentation tests individual collagen fibrils; the interaction of the collagen as an ultrascale feature is



not examined. The Young's modulus of both Patient 3 and Patient 4 (Figure 5-14) were mostly consistent with each other. Again, a lower modulus of 3-4 GPa with an upper value of 10-14 GPa was seen. Unlike in Patients 1 and 2, each graph had a bimodal distribution of values. It was already discussed that not being consistent in analysing the reticular or papillary dermis could lead to intrasample variation.

## 5.7 Part B - SSc Case Studies

Part A of this chapter established a baseline range of behaviour of skin from healthy donors as case studies, as well as developed the QNH protocol. In this section, a direct comparison will be drawn between other healthy donors to matched patients with diagnosed SSc. Following on from the findings in the previous sections, the use of mesoscale imaging using SEM will be included initially. Light microscopy, used to effect previously, will be greatly enhanced through the use of picrosirius red (PS) staining following its use in Chapter 3.6. Image quantification using dominant feature markers was initially trailed in part A for Patients 3 and 4. This will be more widely used, comparing between patients and between groups of samples with added delineation between different areas seen under LM. The work in part B, and especially in Patients NK and NR will seek to expand on the requirements for Objective 3 *“add to the QNH protocol by introducing histological and mesoscale imaging.”* Additionally, part B will answer Objectives 4, *“Test the QNH protocol on case studies of SSc”* and Objective 5 *“evaluate the performance of AFM and the QNH protocol for adjunct diagnostics.”*

### 5.7.1 Patient NK (healthy)

#### 5.7.1.1 Histological Polarised LM

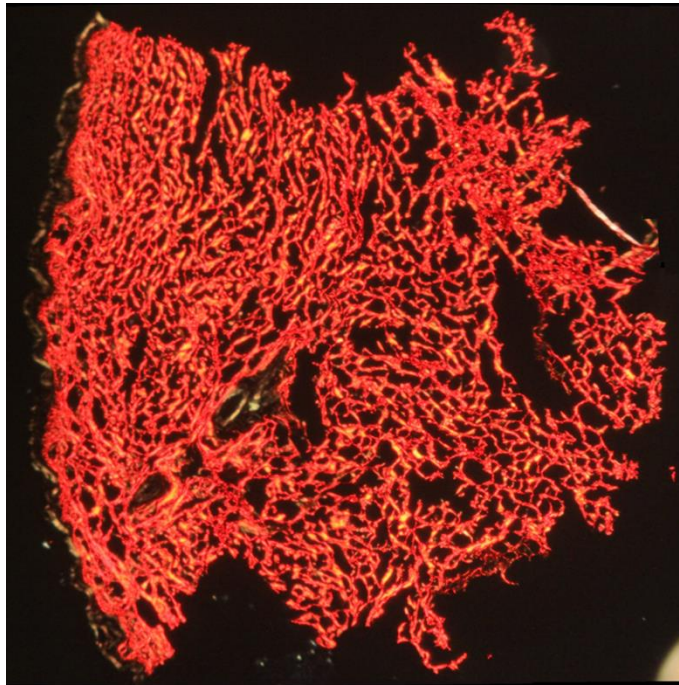


**Figure 5-15** LM of reticular dermis of NK (healthy), 20x magnification

**Figure 5-15** shows the composite LM of the reticular dermis of patient NK in preparation for AFM analysis. The sample has been stained with PS and is imaged using polarised (dark field) light microscopy. The image shows a section of healthy skin that can be considered to be dense in aligned collagen due to the almost total coverage of red regions in the image, with some yellow regions. Green regions were only seen on higher magnification images (not shown). The skin appears to be porous, with gaps between the tissue mostly regular in size. The background is readily identifiable.

### 5.7.1.2 Mesoscale Imaging

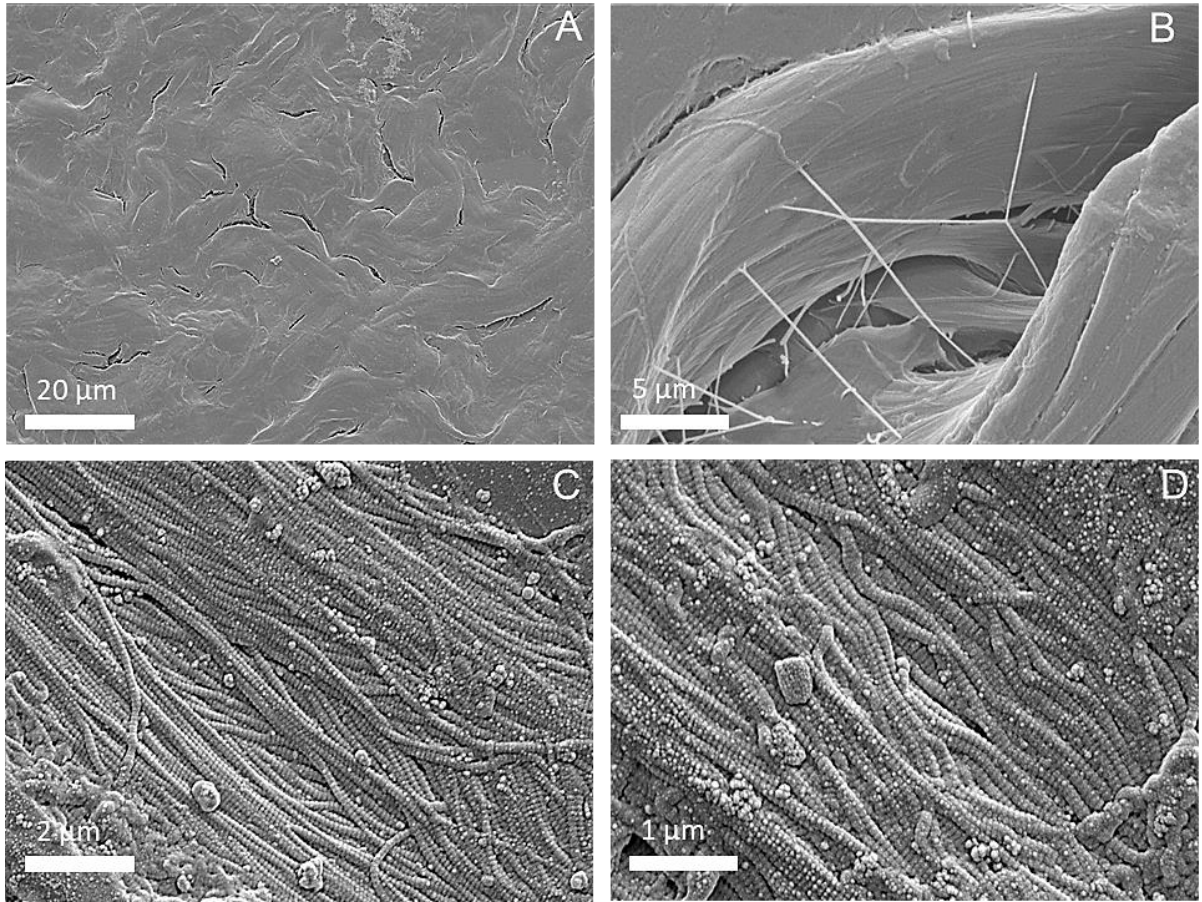
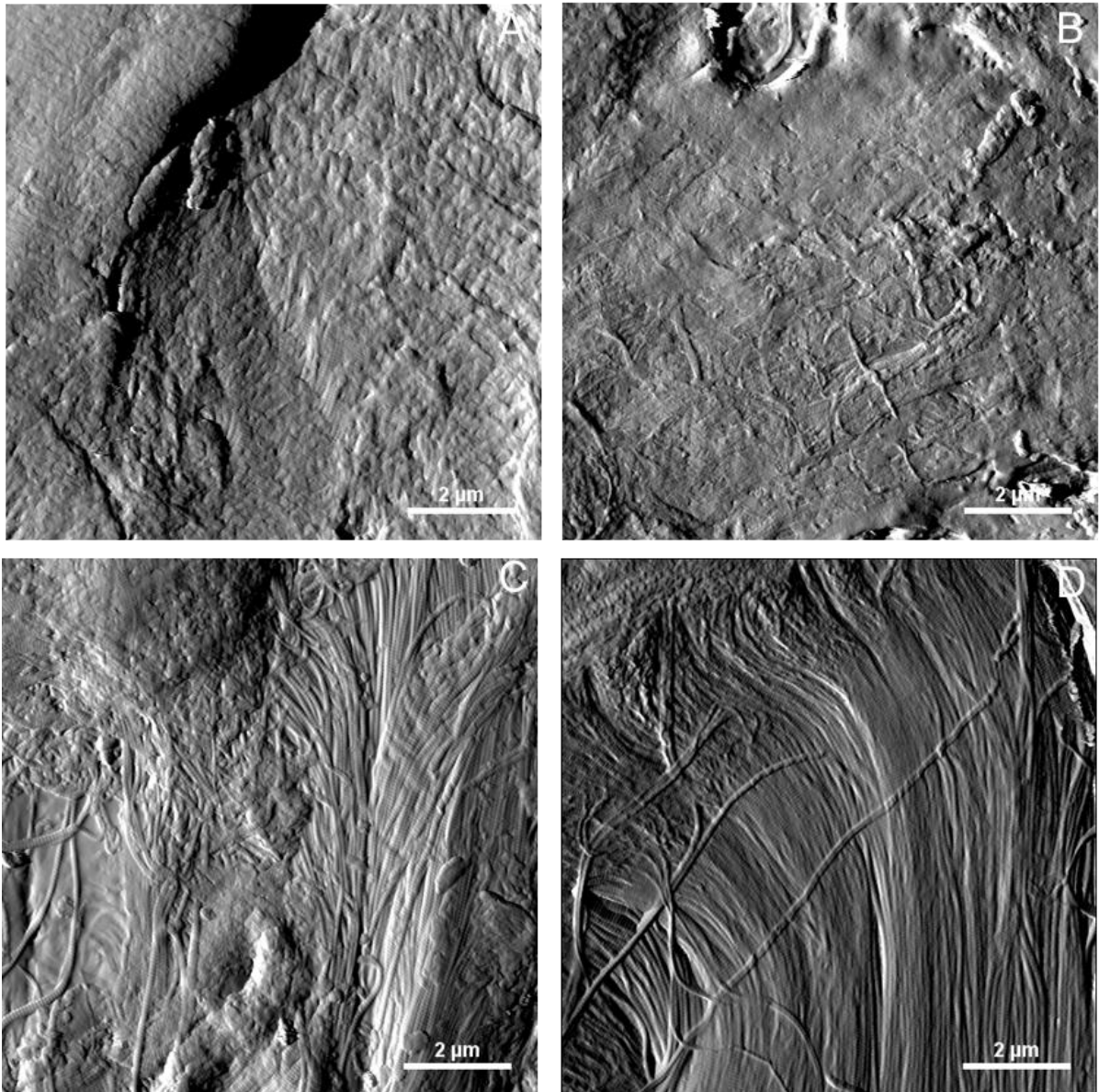


Figure 5-16 SEM of NK. A) 1000x, B) 8000x, C) 15000x, D) 20000x magnification

**Figure 5-16** shows the mesoscale imaging of NK using SEM. Image **A** shows a low-resolution scan. Thick bundles of tissue have formed swirling patterns, consistent with older skin. Cracks between the swirls are likely caused by desiccation in sample preparation. Image **B** shows several bundles. These are interconnected, possibly by collagen fibres. Faint outlines of bundle structure can be seen throughout the image. Image **C** shows a higher resolution image on collagen from bundles. The collagen is mostly aligned and in register, and D-banding can be seen. Image **D** is a higher magnification of collagen. Small kinks in the collagen are seen, likely caused by

dehydration during sample preparation. Some salt crystals remain on the surface, but otherwise the collagen is aligned.

### **5.7.1.3 Polarised LM Guided Imaging Analysis**



**Figure 5-17** AFM of NK. LM identified areas: A) red, B) yellow, C) red/yellow, D) red

**Figure 5-17** show nanoscale AFM imaging on NK from locations identified in Figure 5-15 under polarised light microscopy. Image **A** shows a green region, where

little collagen is seen. Instead, the surface is covered with amorphous material with some small areas that could be collagen, although conclusive identification is impossible. An area at the top of the image was too adhesive for successful imaging, suggesting gelatine. Image **B** shows a yellow region. Here, fibrils can be identified, some in bundles. The fibrils are present within a large mass of amorphous material, which appears to dominate areas of the image. Image **C** shows a boundary region, red/yellow, between the two areas. More fibrils can be seen in comparison with the yellow region, although large areas of gelatine are still present. Image **D** shows a red region. Collagen fibrils are present throughout the image. They are highly aligned and have a strong directional orientation.

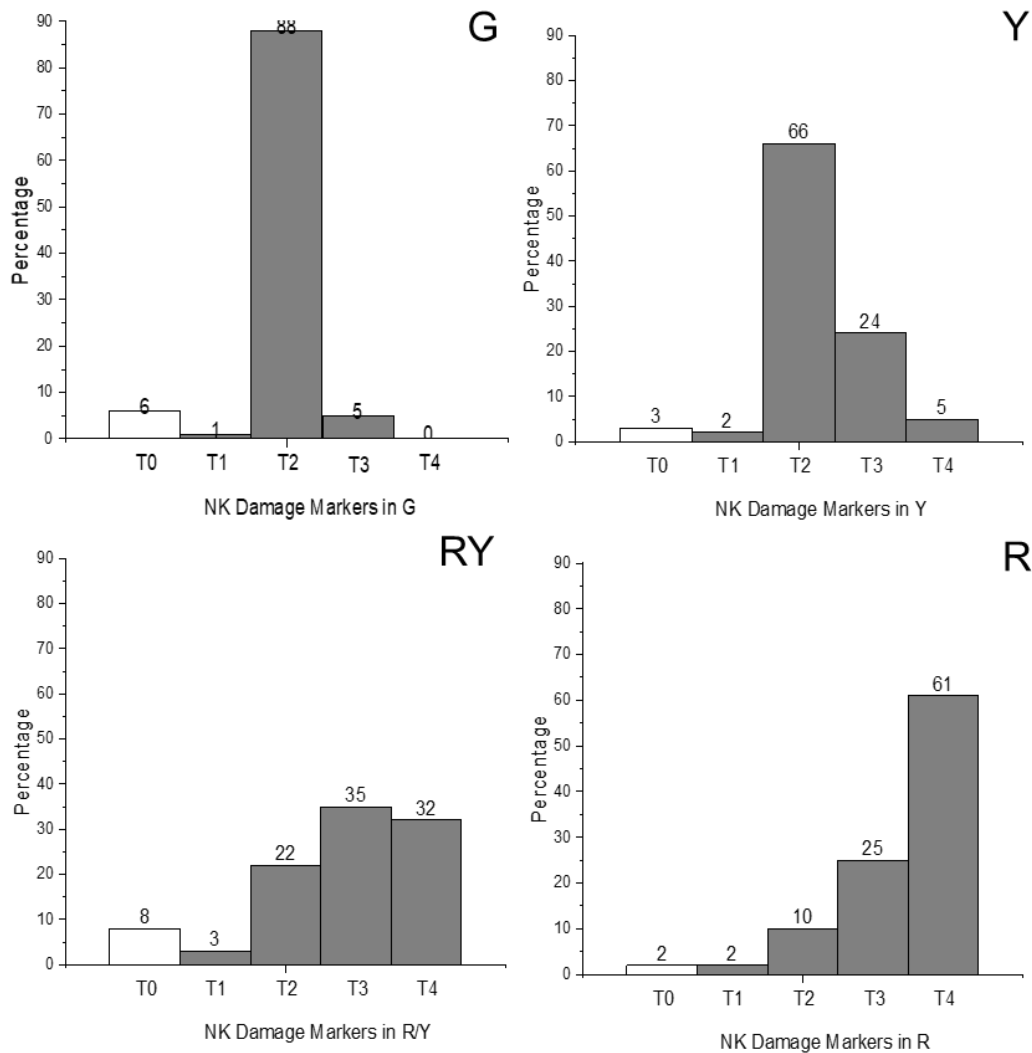


**Figure 5-18 Image quantification damage markers of NK, G) green, Y) yellow, RY) red/yellow, R) red areas**

**Figure 5-18** shows the image analysis of NK per identified area. As per the methodology, the representative image shown in Figure 5-17 was added to at least five other AFM images before analysis. Graph **G** shows an extreme preference for non-collagenous material, statistically greater than all other markers. However, some collagen was still present. Graph **Y** also shows a preference for non-collagenous material which was still significantly higher than other markers. Graph **RY** shows a balanced distribution of types 2-4, with none of them being present more than another.

Graph **R** shows a high preference for type 4, aligned collagen. Overall, the percentage of type 2 decreases throughout the graphs, in proportion to a rise in type 4. Type 1 remains constant with type 3 found mostly in yellow regions.

#### 5.7.1.4 Polarised LM Guided Nanomechanics

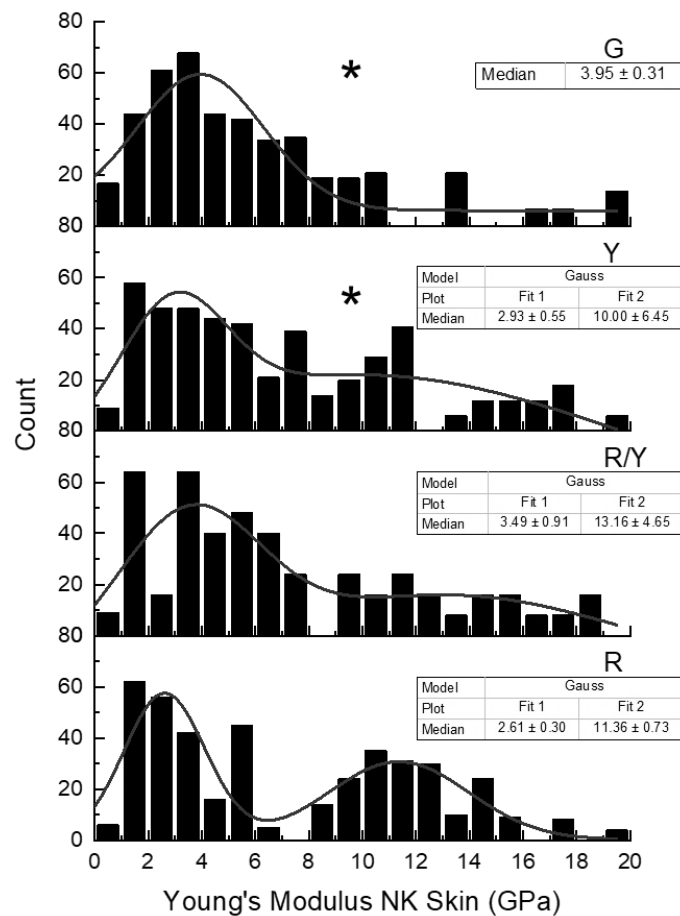


**Figure 5-19 Young's modulus of NK**

**Figure 5-19** shows the Young's modulus of NK per region. Graph **G** shows a median of  $3.95 \pm 0.31$  GPa. Graph **Y** shows a bimodal distribution with a low median of  $2.93 \pm 0.55$  GPa and a very wide upper median of  $10 \pm 6.45$  GPa. Graph **RY** shows a low median of  $3.49 \pm 0.91$  GPa and also has a very wide upper median of  $13.16 \pm 4.65$  GPa.



Graph **R** shows bimodal distribution with a narrow lower median of  $2.61 \pm 0.3$  GPa and a wider upper median of  $11.36 \pm 0.73$  GPa. A trend towards bimodal distribution towards red regions can be observed, with the smallest standard deviations seen in the lower medians and the red upper median. Significant differences were not seen between the red yellow and red regions.

#### 5.7.2 Patient NR (SSc)

##### 5.7.2.1 Histological Polarised LM

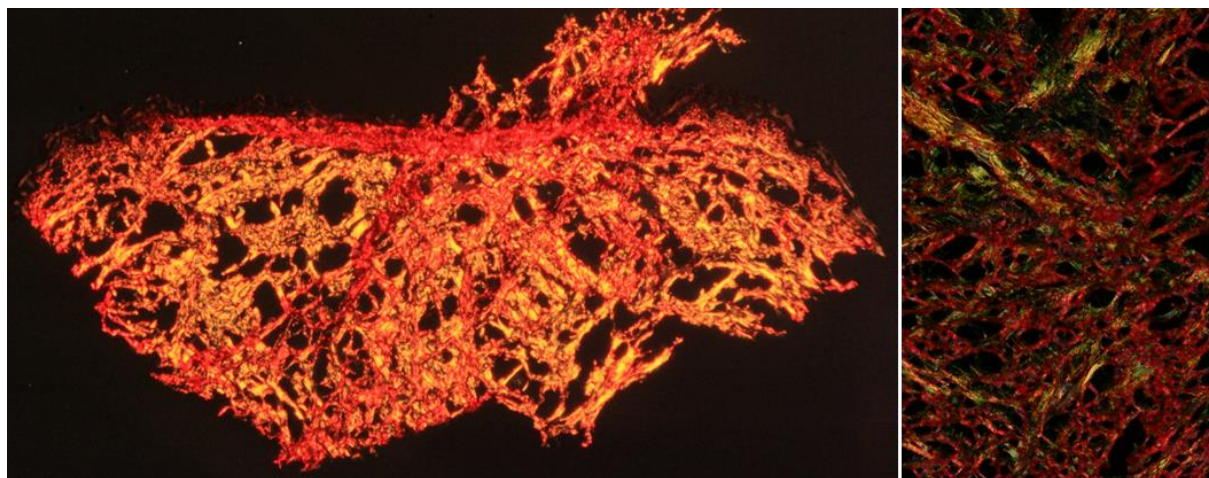


Figure 5-20 LM of reticular dermis of NR (SSc), 20x magnification

**Figure 5-20** shows the composite LM of the reticular dermis of patient NR in preparation for AFM analysis and an inset image. There are large amounts of both red and yellow stained tissue. Under higher magnification (inset) green, yellow and red stained tissue. The sample appears to be highly porous, with large irregular gaps between the tissue. The bottom of the section has folded across the top, obscuring the stratum corneum.

### 5.7.2.2 Mesoscale Imaging

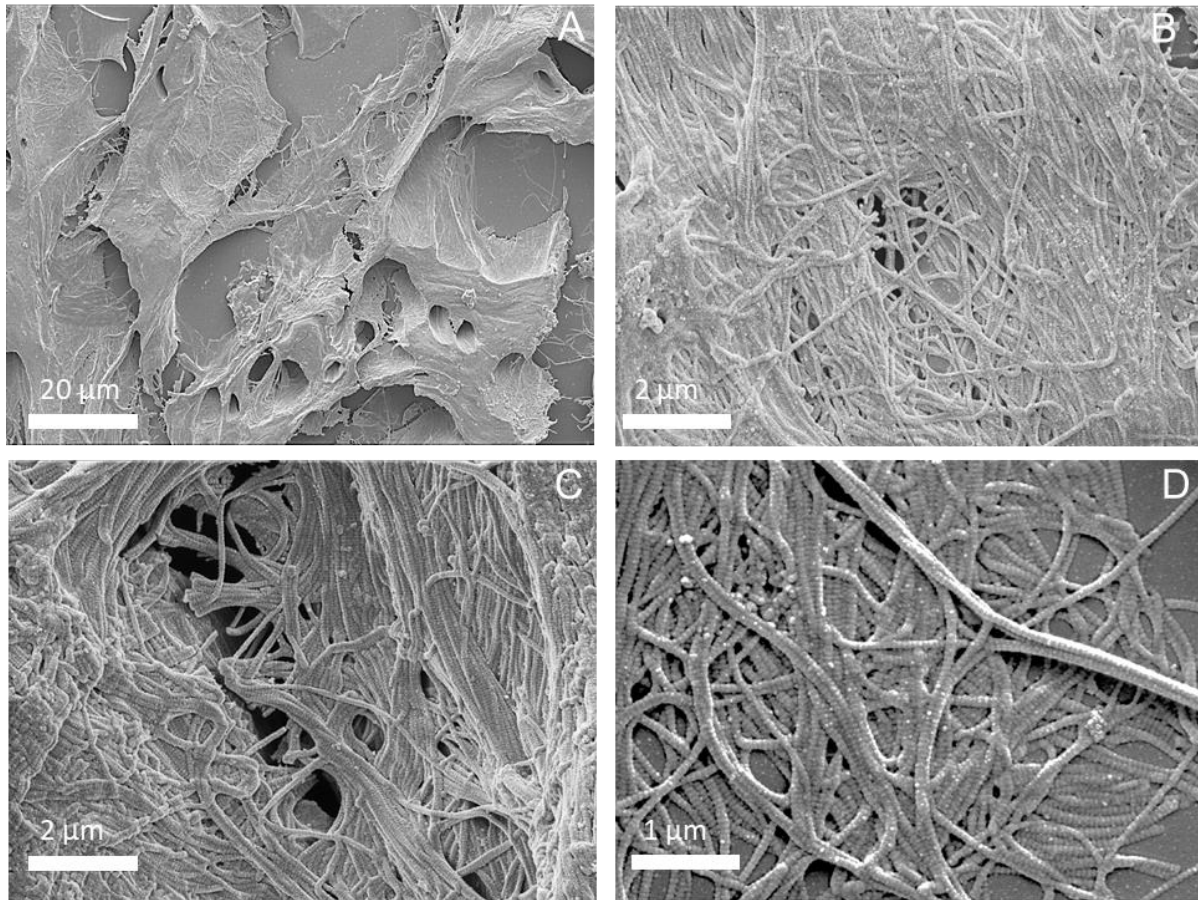


Figure 5-21 SEM of NR. A) 1000x, B) 8000x, C) 15000x, D) 20000x magnification

**Figure 5-21** shows the mesoscale imaging of NR using SEM. Image **A** shows a low-resolution image. Large holes are present across the surface of the tissue, and the background is clearly visible. Some smaller holes are also present, with the fibre bundles identifiable. Images **B** and **C** show fibrils and bundles of fibres without any alignment. There are many gaps between the individual fibrils and some amorphous material present. Some large cracks may be due to desiccation. Image **D** shows a high magnification image. Highly disorganised fibrils with D-banding are visible on the glass slide background. Some salt crystals are visible from preparation.

### 5.7.2.3 Polarised LM Guided Imaging Analysis

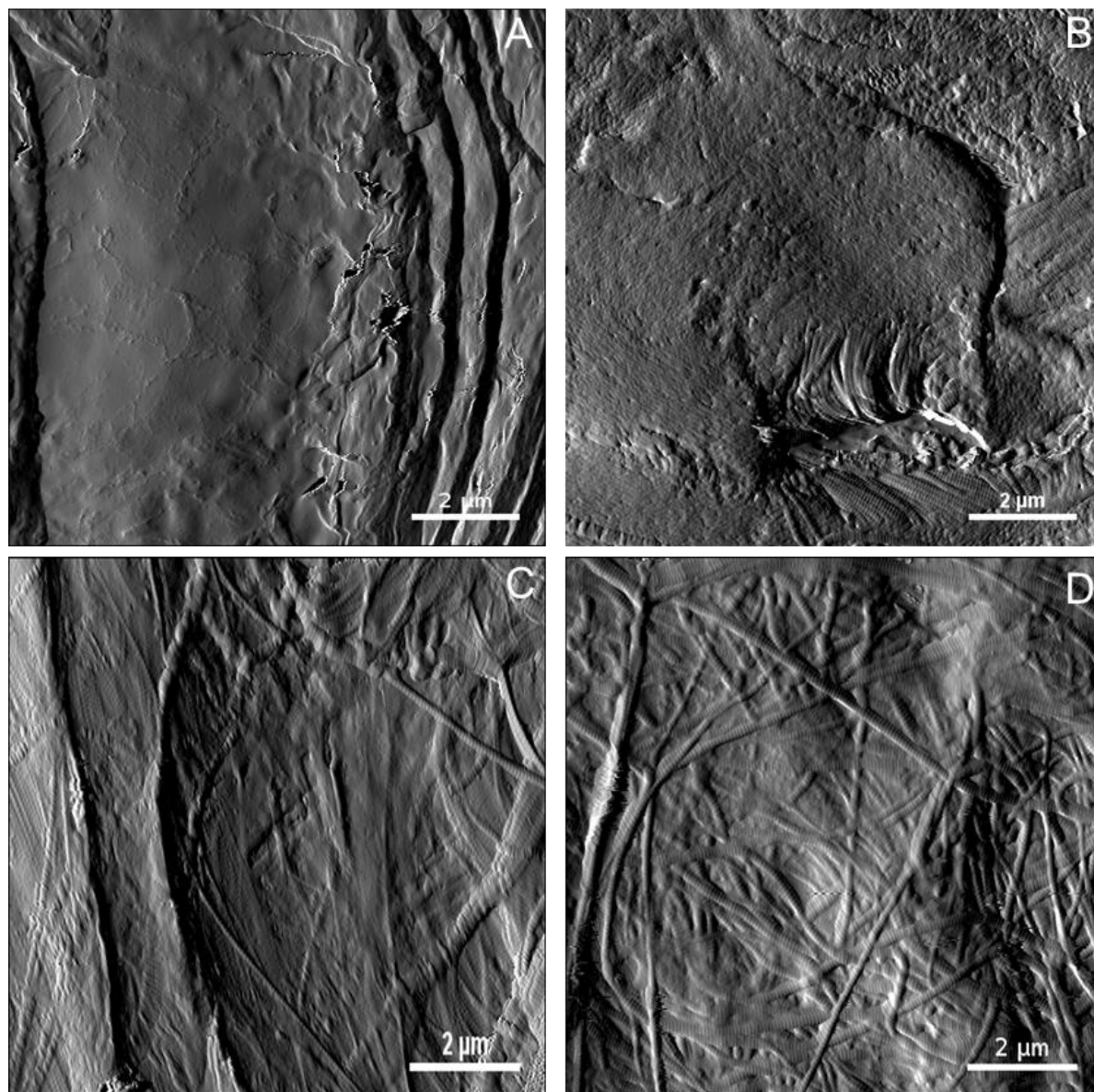
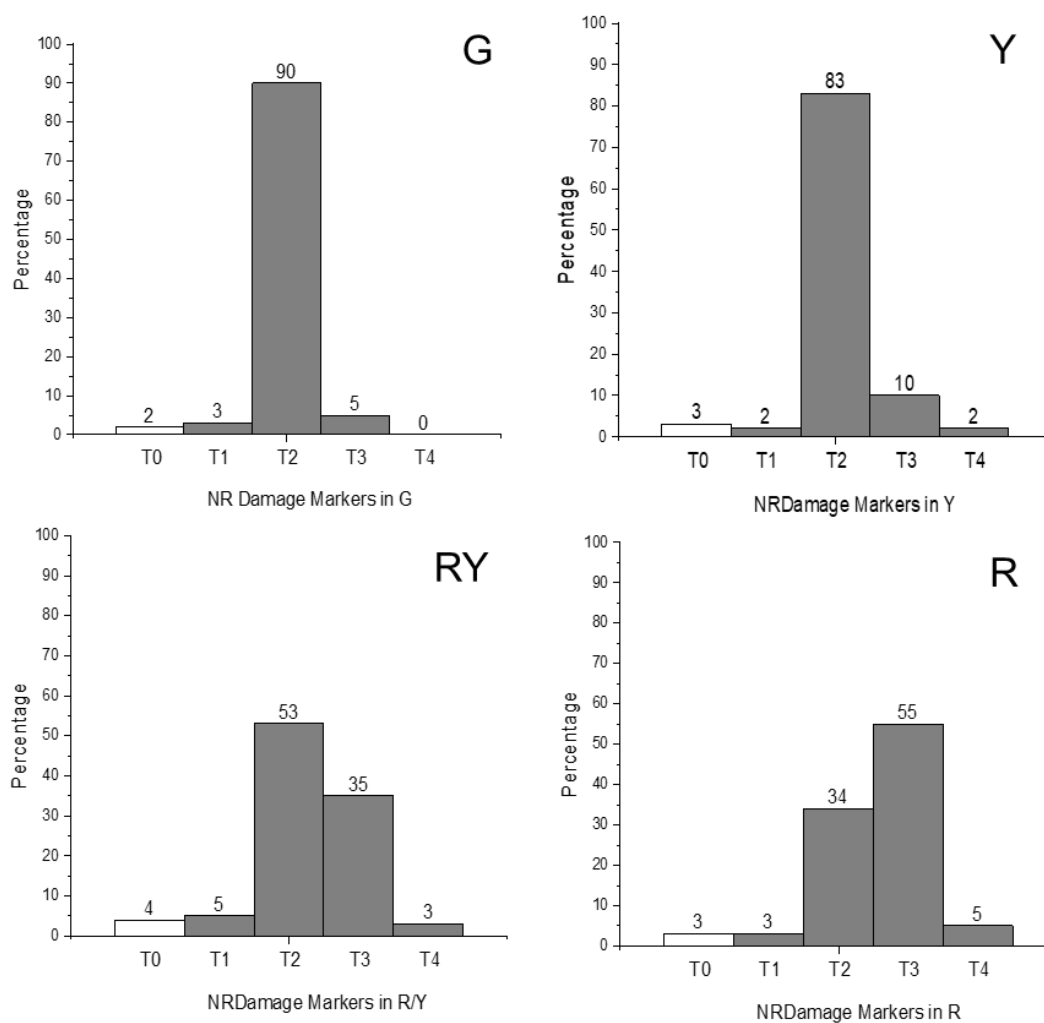


Figure 5-22 AFM of NR. LM identified areas: A) green, B) yellow, C) red/yellow, D) red

**Figure 5-22** show nanoscale AFM imaging on NR from locations identified in Figure 5-20 under polarised light microscopy. Image **A** shows a green region where only gelatine and other amorphous material appears to be present. Image **B** shows a yellow region. Some fibrils are visible in bundles, which appear to be ordered. The cross-

sectioned ends of fibrils are also present, but there is a large amount of gelatine present. Image **C** shows the red/yellow region. Here, bundles of fibrils are indistinct but have some directional orientation. D-banding is not visible, and gelatine is present. Image **D** shows the red region. Collagen fibrils are seen but without D-banding. The fibrils are highly disorganised without orientation.



**Figure 5-23 Image quantification damage markers of NR**

**Figure 5-23** shows the image analysis of NR per identified area. Graphs **G** and **Y** are dominated by type 2 non-collagenous material. Graph **RY** shows a preference for type 2 which was statistically higher than the other marker types, however, type 3 disorganised collagen as also present in large amounts. Graph **R** has mostly type 3 collagen, which was statistically higher than other makers present, although type 2 was still present. Overall, the percentage of type 2 decreases throughout the graphs, in proportion to a rise in type 3. RY and R swapped their amounts for types 2 and 3. Type 4 aligned collagen and type 1 holes were rarely seen in the images; the values remained consistent throughout the image analysis.

### 5.7.2.4 Polarised LM Guided Nanomechanics

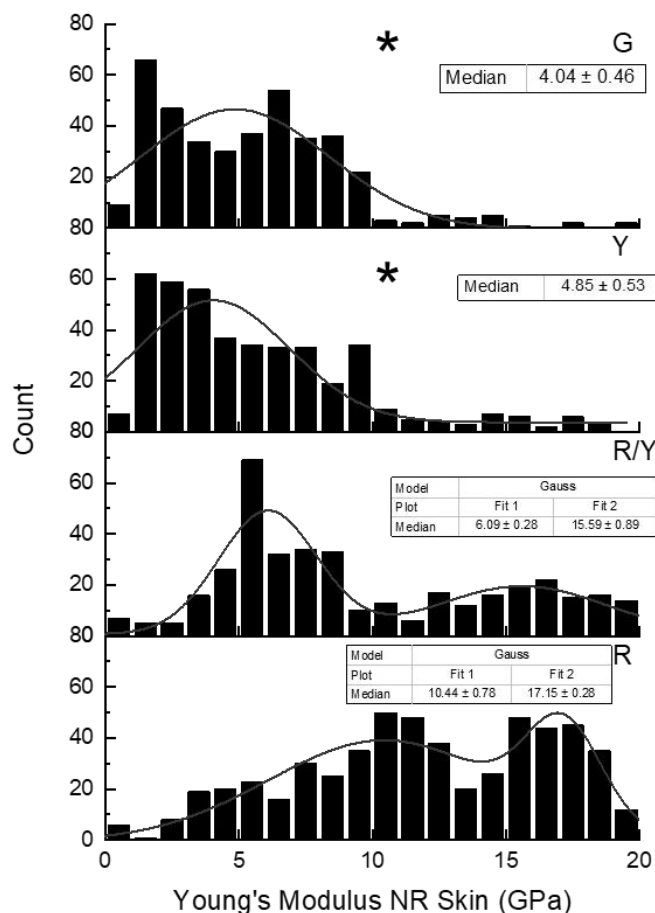


Figure 5-24 Young's modulus of NR, G) green, Y) yellow, RY) red/yellow, R) red areas

**Figure 5-24** shows the Young's modulus of NR regions. Graph **G** shows a median of  $4.04 \pm 0.46$  GPa. Graph **Y** shows a median of  $4.85 \pm 0.53$  GPa. Graph **RY** shows a bimodal distribution with a wide lower median of  $6.09 \pm 0.28$  GPa and an upper median  $15.59 \pm 0.89$  GPa. Graph **R** has a bimodal distribution median of  $10.44 \pm 0.78$  GPa  $17.15 \pm 0.28$  GPa. The Young's moduli values for the yellow and green regions were significantly lower than the values for the red yellow and red regions.

### 5.7.3 Data Collection Discussion

The discussion concerning the comparative findings of these patients will be dealt with below in section 5.7.9. However, some conclusions could easily be drawn from the metanalysis between the data sets after reviewing the data collecting protocol. Mesoscale imaging using SEM provided an overview of the surface of the sections. However, the preparation for SEM caused the irregular appearance of desiccation cracks which could have biased any conclusions that were drawn, and SEM preparation irrevocably damages the samples. Additionally, the higher magnification SEM images gave similar findings to the AFM imaging. As the AFM was required in the QNH protocol for nanoindentation, it was decided to forgo the use of SEM for the remainder of the case study patients.

Secondly, the differences between the four regions identified by PS for AFM were examined. The healthy sample NK had very little green and only some yellow regions that could be readily identified. Meanwhile, there was an abundance of yellow and green areas in NR. In order to improve consistency, future conclusions would be based primarily on the measurements made in the red region. As the three primary colours for PS are reported in the literature, data would still be reordered and reported for the green and yellow regions however<sup>382,482–484</sup>. It was also decided that the use of a red/yellow boundary region was inconsistent, so was excluded. By eliminating extraneous data and focusing on a smaller set of data collection markers, it was possible to go some way to answering Objective 5 “evaluate *the performance of AFM and the QNH protocol for adjunct diagnostics.*” From the data collected in part B so far, QNH could not currently act as an adjunct diagnostic tool. However, by streamlining the process and removing mesoscale SEM imaging, the QNH protocol became more refined and targeted towards

a scalable clinical use. It was not possible to make conclusions on the effects of SSc as a disease from the single comparative case study. Two further sets of patients were comparatively analysed with the modified protocol as discussed.

#### 5.7.4 Patient LG (healthy)

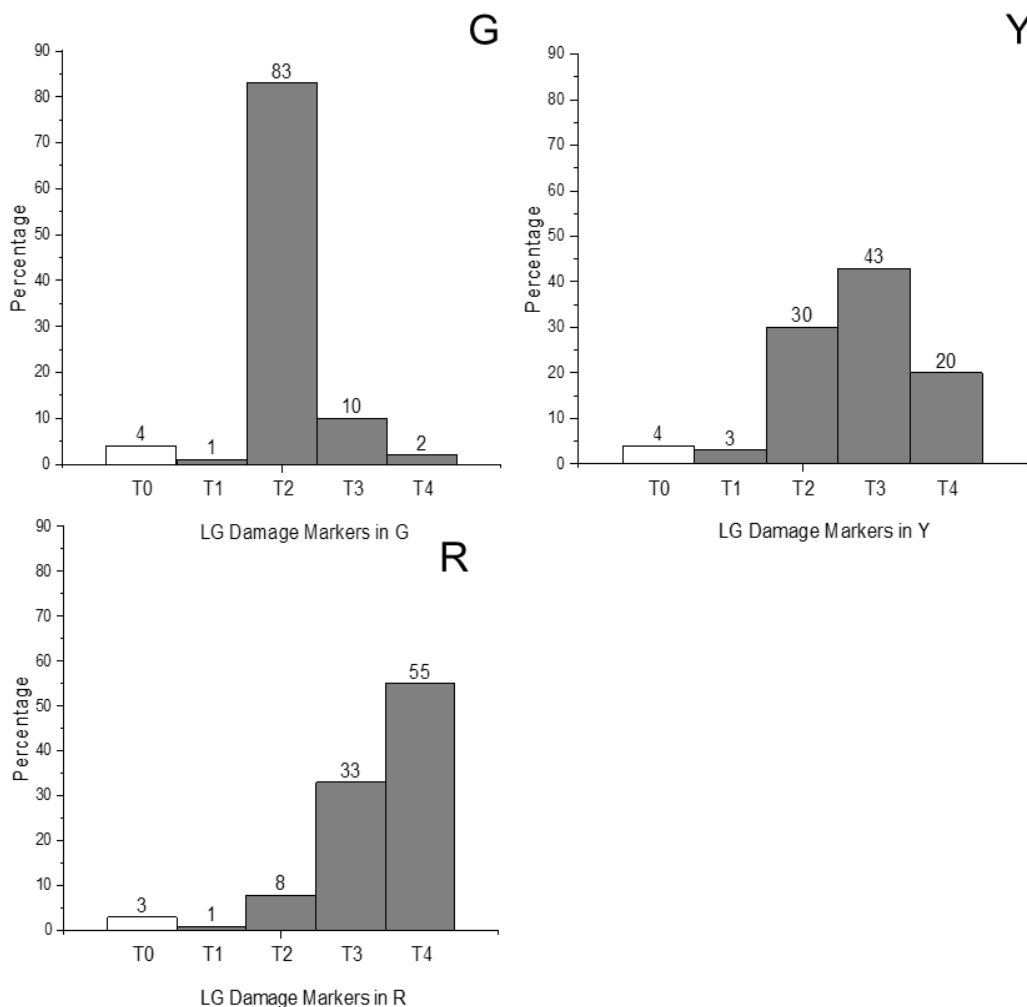


**Figure 5-25 Image quantification damage markers of LG**

**Figure 5-25** shows the image analysis of LG per identified area from LM with PS staining. Graph **G** shows an immediate dominance of type 2, non-collagenous material which is significantly higher than all other types. Some type 3 disordered collagen and a marginal amount of type 4 ordered collagen are also present. Graph **Y** shows an



overall trend of balance between the three major image analysis types, without any type being significantly more present than another. Graph **R** shows a preference for ordered collagen, which was significantly higher than all other types. Non-collagenous material was still present even in the red region. Additionally, disordered collagen was present significantly more than types 1 and 2.

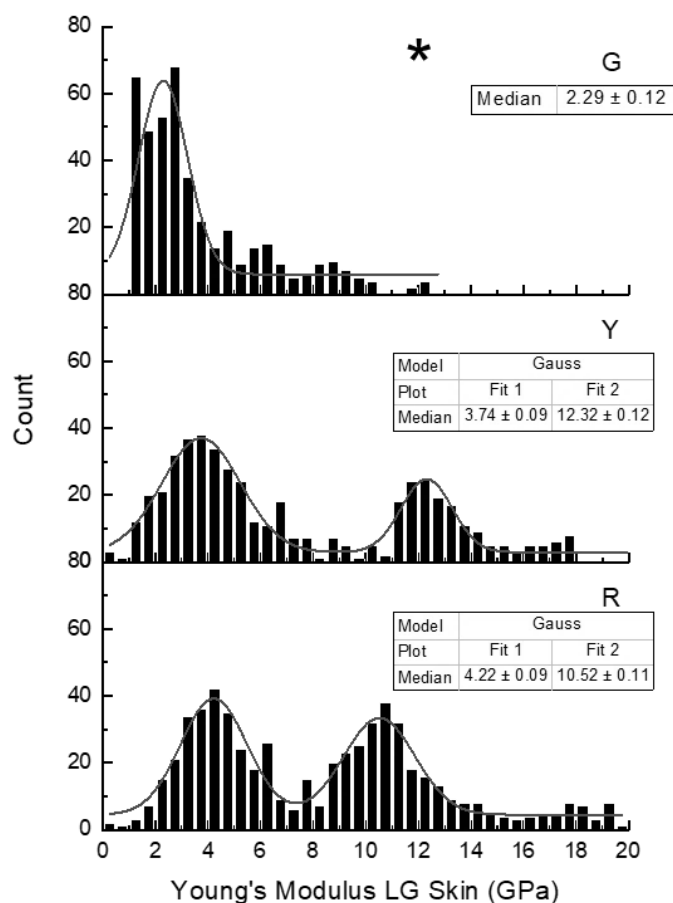


**Figure 5-26 Young's modulus of LG**

**Figure 5-26** shows the Young's modulus of LG regions. Graph **G** shows a unimodal distribution with a long tail of  $2.29 \pm 0.12$  GPa. Graph **Y** shows a bimodal distribution with a low peak of  $3.74 \pm 0.09$  GPa and  $12.32 \pm 0.12$  GPa. Graph **R** also shows a bimodal distribution with a lower median  $4.22 \pm 0.09$  GPa and an upper median of

10.52±0.11 GPa. The median Young's modulus of the green region was significantly lower than that of the yellow or red regions. No significant difference was reported between the yellow and red regions.

#### 5.7.5 Patient MA (SSc)

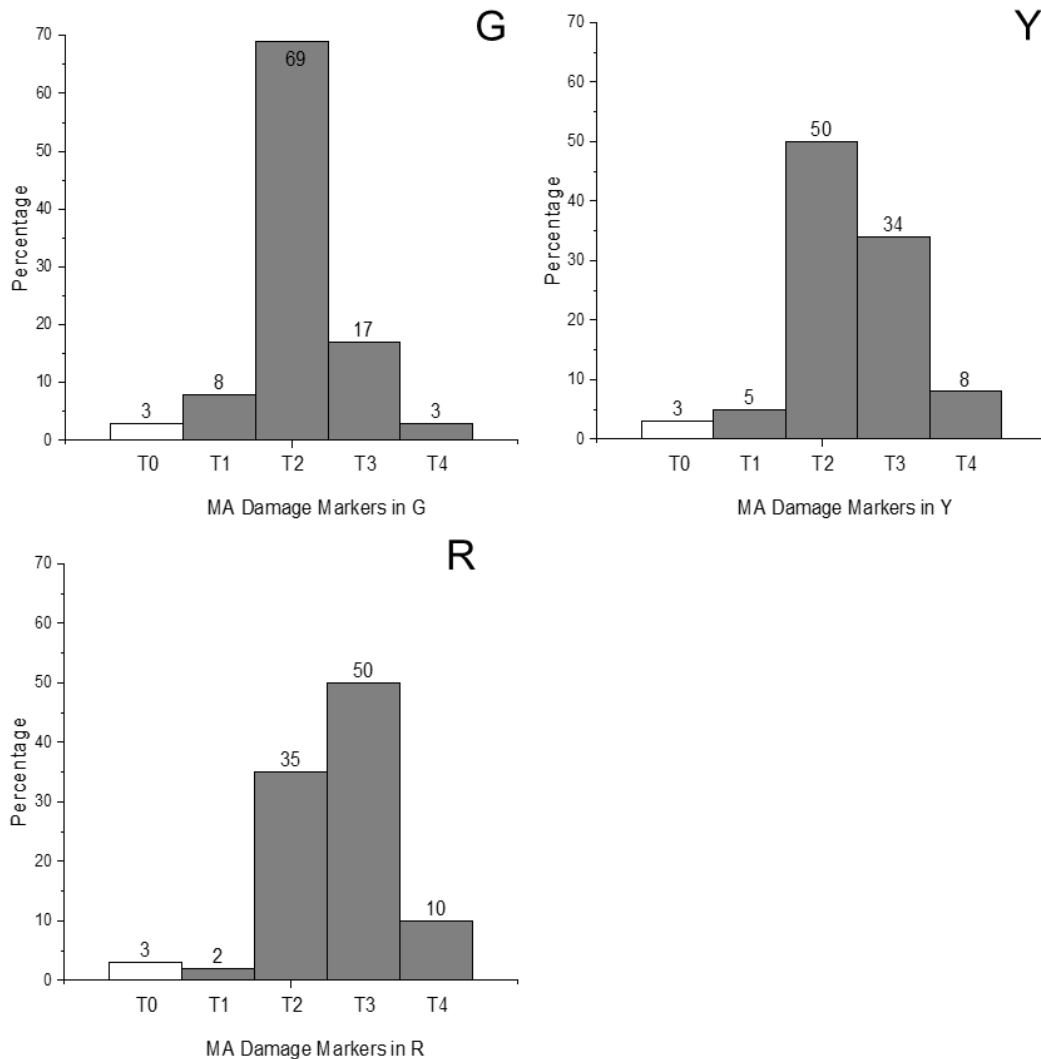


**Figure 5-27 Image quantification damage markers of MA**

**Figure 5-27** shows the image analysis of MA per identified area from LM with PS staining. Graph **G** shows an immediate dominance of type 2, non-collagenous material which is significantly higher than all other types. There was still a large presence of other

types of feature present. Graph **Y** continues to show a preference for the yellow region to show non-collagenous material, however, type 3 disordered collagen was present in over a third of all tested pixels. Graph **R** shows that disordered collagen was found most often, with still a large amount of non-collagenous material. Throughout all three regions, there was a low amount of type 4 ordered collagen present.

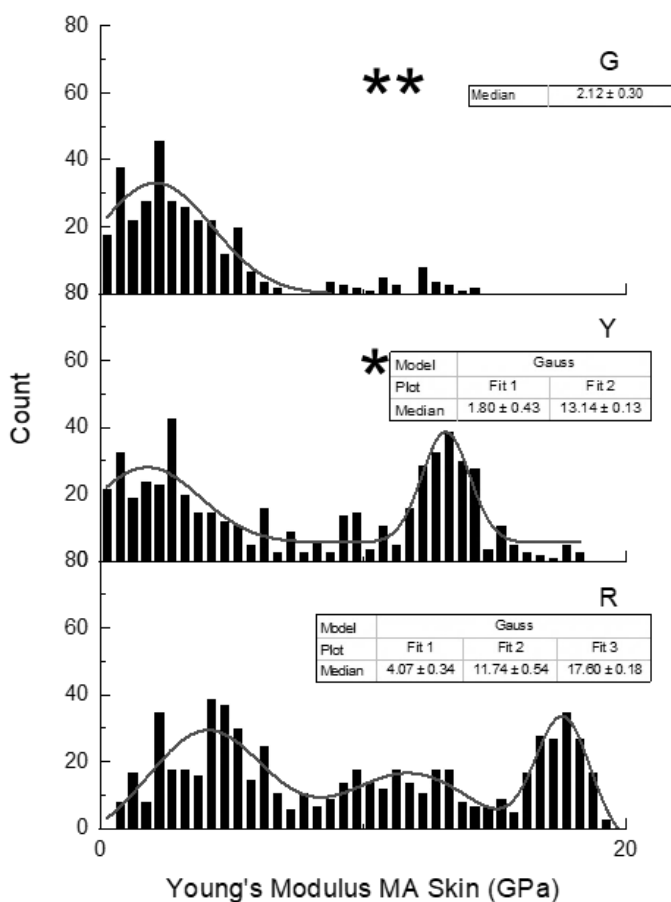


**Figure 5-28** Young's modulus of MA

**Figure 5-28** shows the Young's modulus of MA regions. Graph **G** shows a unimodal distribution of  $2.12 \pm 0.3$  GPa with a long tail. Several data points can be seen between 9 – 12 GPa. Graph **Y** has a bimodal distribution with a low median of  $1.8 \pm 0.43$  GPa and a narrow upper median of  $13.14 \pm 0.13$  GPa. Graph **R** has a trimodal distribution

with a wide lower median of  $4.07 \pm 0.34$  a narrow median of  $11.74 \pm 0.54$  and a narrow upper median of  $17.6 \pm 0.18$  GPa. Significant differences were seen between the red and yellow regions. Additionally, there was a significant difference in Young's modulus between the green region and both the red and yellow regions.

#### 5.7.6 Patient FM (Healthy)

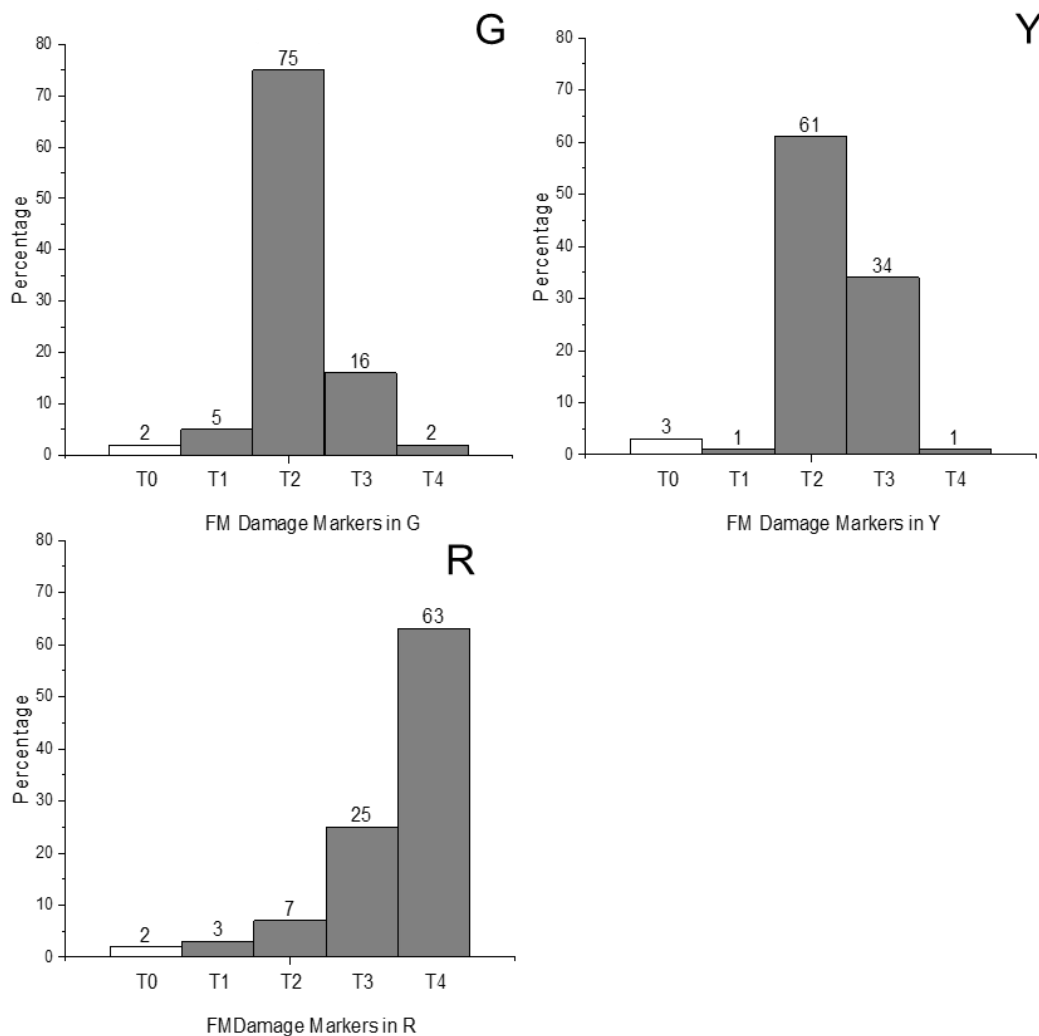


**Figure 5-29 Image quantification damage markers of FM**

**Figure 5-29** shows the image analysis of FM per identified area from LM with PS staining. Graph **G** shows the highest percentage of non-collagenous material, statistically greater than any other types, but some disordered collagen is also present.

Graph **Y** still shows a reduced preference for non-collagenous material, but the amount of disordered collagen has doubled in the yellow region compared to the green region. Graph **R** shows a significant preference for aligned collagen, with a decrease in disorganised collagen from the analysis of the yellow region. The amount of non-collagenous material is negligible, as was the number of holes seen.

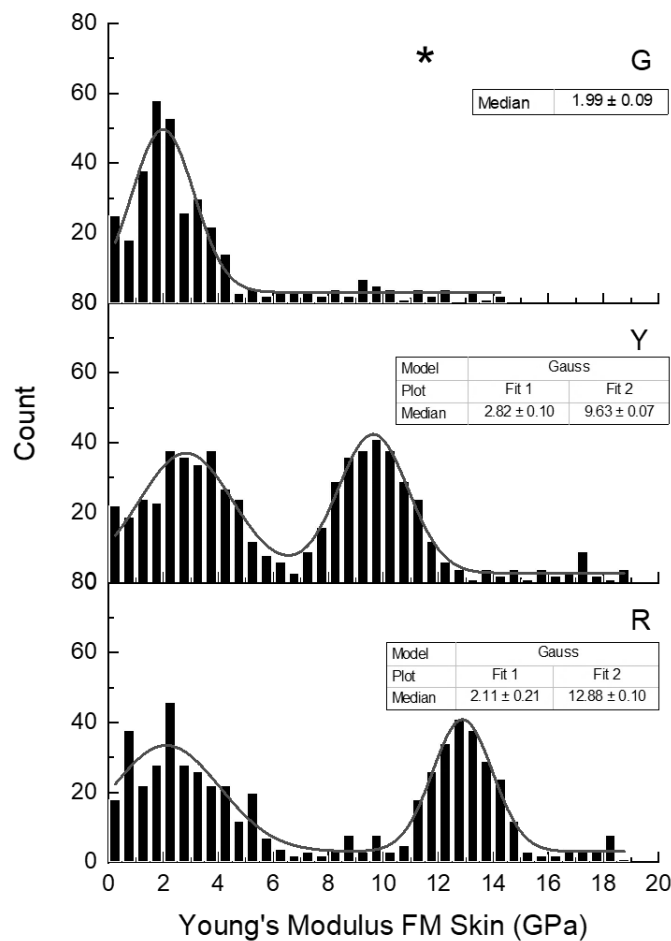


**Figure 5-30** Young's modulus of FM

**Figure 5-30** shows the Young's modulus of FM regions. Graph **G** shows a unimodal distribution of  $1.99 \pm 0.09$  GPa with a long tail. Graph **Y** shows two equal bimodal distributions of  $2.82 \pm 0.1$  GPa and  $9.63 \pm 0.07$  GPa. Graph **R** also has a bimodal distribution, with a low median of  $2.11 \pm 0.21$  GPa and an upper median of  $12.88 \pm 0.1$

GPa. Significant differences in Young's modulus were observed between the green region and both the yellow and red regions.

#### 5.7.7 Patient RT (SSc)

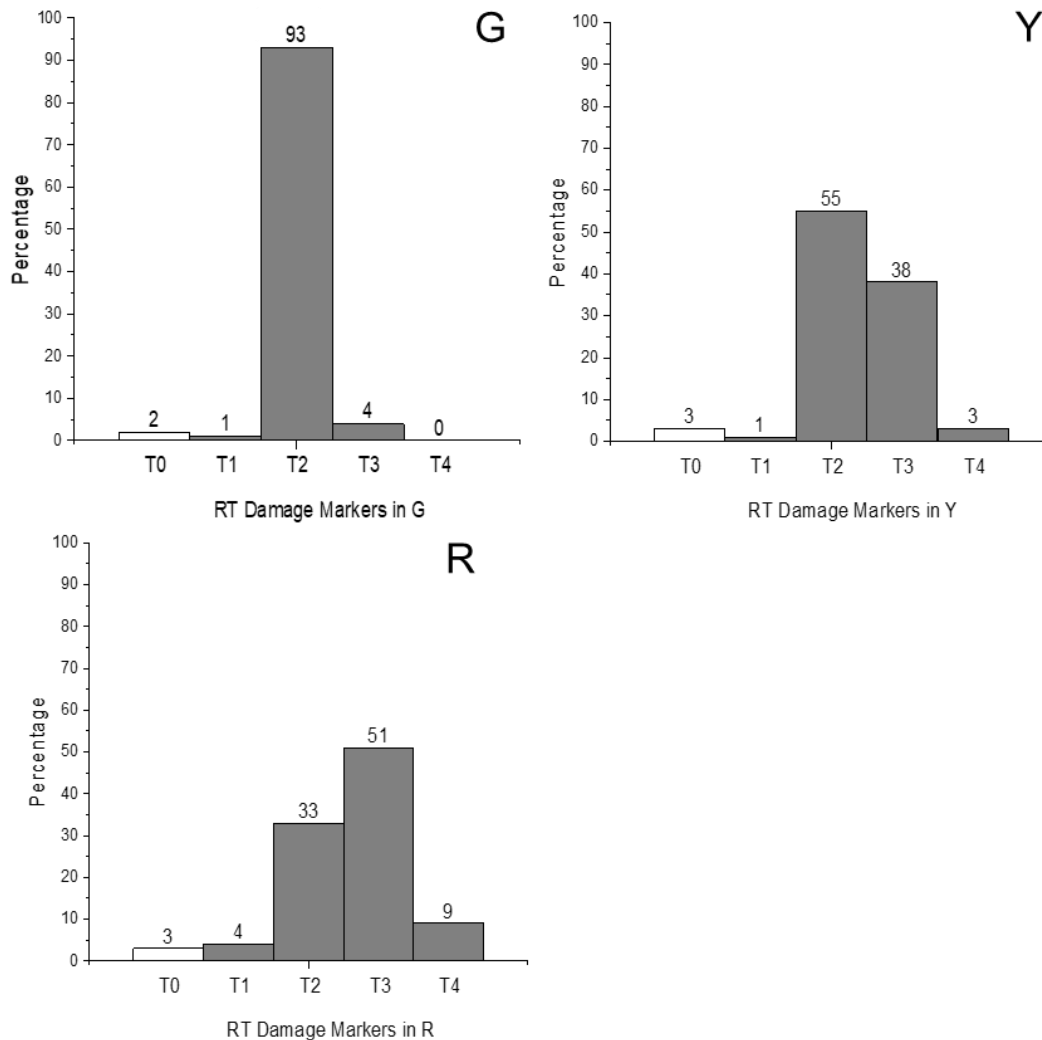


**Figure 5-31 Image quantification damage markers of RT**

**Figure 5-31** shows the image analysis of RT per identified area from LM with PS staining. Graph **G** shows an exceptionally high preference for non-collagenous material, at 93% although a very small minority of disordered collagen and holes are present. No ordered collagen was reported. Graph **Y** shows an increase in disordered collagen alongside a decrease in non-collagenous material which is still the dominant feature.

Graph **R** has reversed the values for the yellow region, with the majority (51%) of the pixels containing disordered collagen. Some ordered collagen was also present, but one-third of the pixels still contained non-collagenous material.

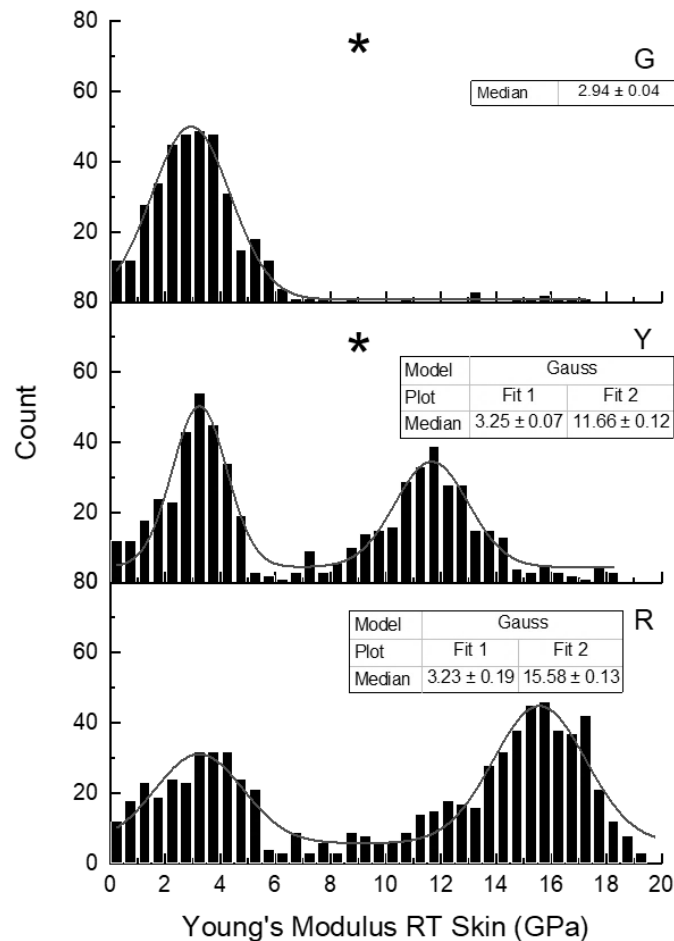


**Figure 5-32 Young's modulus of RT**

**Figure 5-32** shows the Young's modulus of the RT regions. Graph **G** shows a unimodal distribution of  $1.99 \pm 0.09$  GPa with a long tail. Graph **Y** shows a bimodal distribution, with a narrow lower median of  $3.25 \pm 0.07$  GPa and a wide upper median of  $11.66 \pm 0.12$  GPa. Graph **R** also has a bimodal distribution with a wide lower median of  $3.23 \pm 0.19$  GPa and an upper median of  $15.58 \pm 0.13$  GPa. There were significant differences between the red, yellow and green regions.

#### 5.7.8 Image Analysis Grouping Summary

Previously, comparisons were made between two individual patients with matched demographics. In this final section, the results of all the image analyses will be grouped and compared as a factor of each region. Lastly, the image analysis groups themselves will be combined to draw further conclusions as to the topographical effects of SSc at the nanoscale.

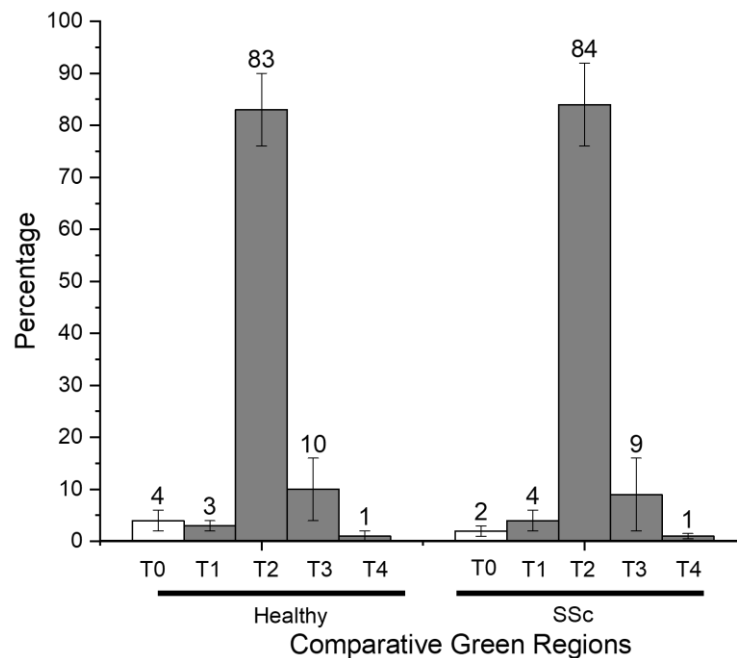


**Figure 5-33 Comparative green regions of healthy and SSc patients. Error bars show calculated standard deviation**

**Figure 5-33** shows the average image analysis of the green region of the healthy and SSc patients. There were no significant differences between any of the groups regarding damage marker types. Type 2 non-collagenous material was the dominant feature, with almost equal numbers of marker types also seen.



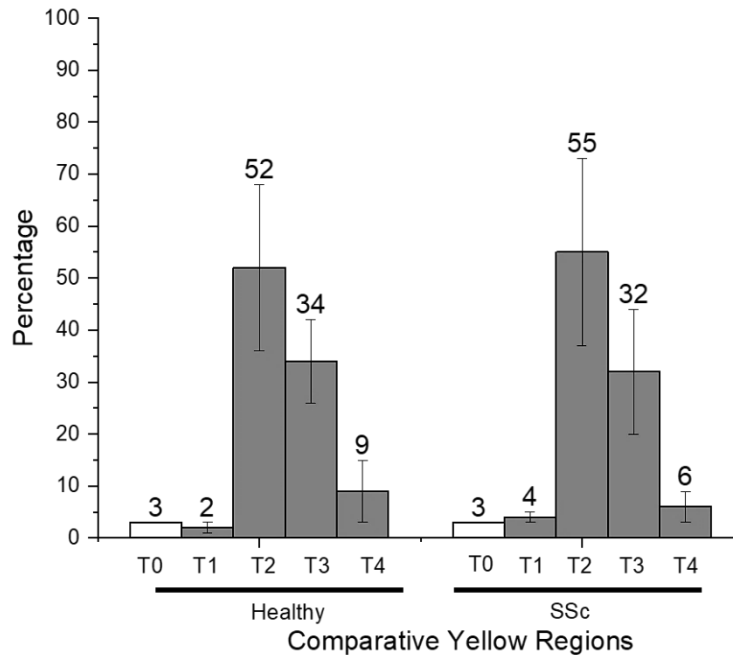


**Figure 5-34 Comparative yellow regions of healthy and SSc patients. Error bars show calculated standard deviation**

**Figure 5-34** shows the average image analysis of the yellow region of the healthy and SSc patients. Again, there were no significant differences between the two groups. Similar values for each damage marker types were reported, with non-collagenous material being the largest and lower values for disorganised collagen. The range of values for the error markers (calculated as the standard deviation) was much larger in the SSc group than the healthy group.

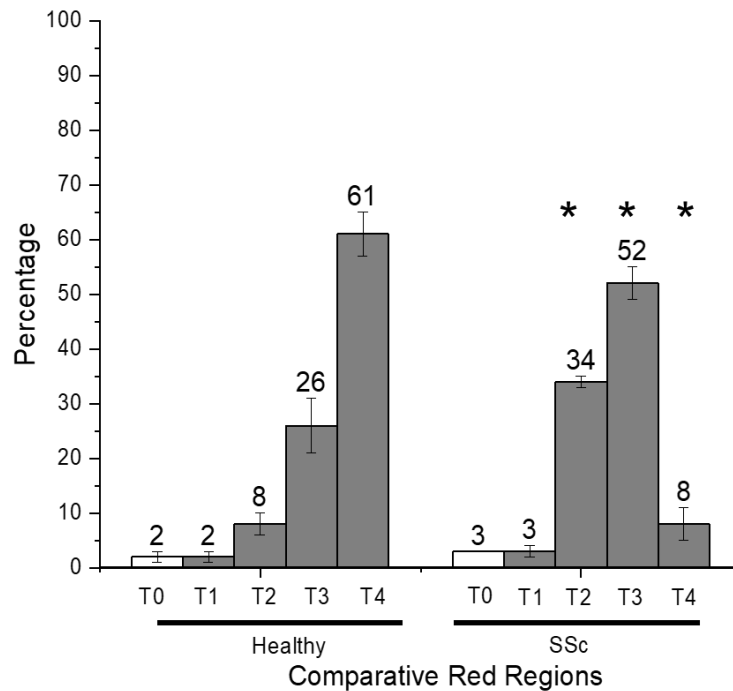


**Figure 5-35 Comparative red regions of healthy and SSc patients. Error bars show calculated standard deviation**

**Figure 5-35** shows the average image analysis of the red region of the healthy and SSc patients. Significant differences were seen on this graph between the two groups. The healthy group had significantly more organised collagen, and significantly less disorganised collagen and non-collagenous material than the SSc group.

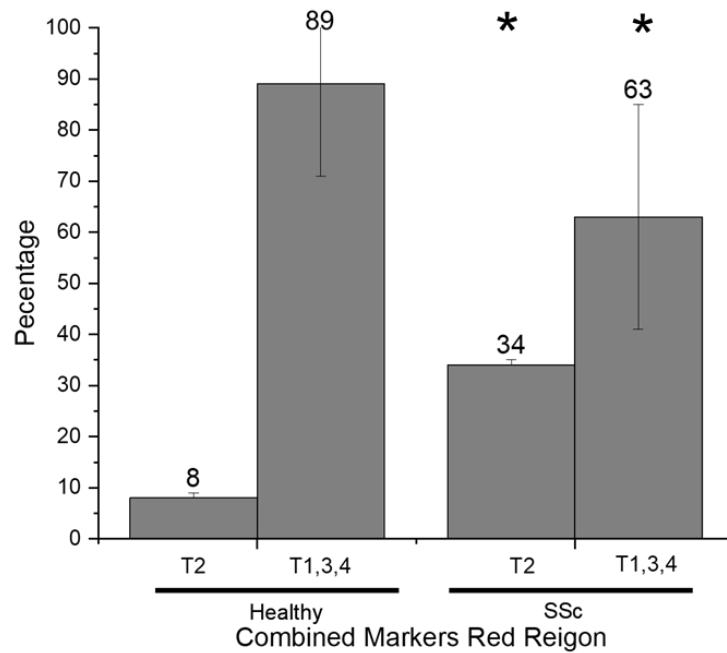


**Figure 5-36 Combined damage markers of the red region**

**Figure 5-36** shows the combined damage markers for collagen and non-collagen in the red region. There is a significant decrease in the presence of all collagen types in the SSc group, with a significant increase in the amount of non-collagenous material seen.

#### 5.7.9 SSc Patients Discussion

The methodology presented in this section shows the most detailed analysis of the collagen so far in this thesis. By combining LM, SEM, AFM imaging and mechanics with the novel image quantification system, comparisons can now be made between a healthy individual and a patient with SSc. Additionally, refinement of the protocol developed here allowed for quantitative comparisons between SSc and healthy skin tissue.

##### ***5.7.9.1 Histological Imaging***

Initially, the LM images provided crucial details of the skin biopsy, which were also used later on in the analysis. Only one set of LM of a pair of patients is compared in this chapter.

There is an immediately noticeable difference between NR and NK. The NK sample (Figure 5-15) shows a clear dominance of red regions. It is known that staining with PS does not show just collagen, but the register of the collagen <sup>382</sup>.

Sirius red, the crucial staining component of PS, is a strong anionic dye. The sulfonic acid groups react with basic groups present in the collagen molecule. Sirius red and collagen align so that their long axes are parallel, which corresponds to the long axis of the fibrils. This enhances the natural birefringence of collagen <sup>485</sup>. As PS aligns with the register of collagen fibrils, any changes from red to another colour in the polarised image is indicative that the collagen fibrils are not in register and that the collagen may be structurally disordered, in comparison to a well-ordered collagen sheet in healthy dermis <sup>395</sup>.

In NR (Figure 5-20), the similar amounts of red and yellow present, without a dominant colour suggests a non-localised disorder. The insert image shows a magnified area, with green as well as red and yellow regions. This shows an even greater level of the disorder may be present, which would not always be visible in a composite image. The top of the image shows the epidermal layer, with bulging from the dermal layers of the section, a pattern described as “cookie cutter;” suggestive of SSc<sup>184</sup>. The use of LM provides direct microscopic analysis of the ordering of the collagen in the sample, but there is no direct comparison by quantification provided by this method. This could be expanded upon in further work through the use of colour quantification based on an RGB scale

#### **5.7.9.2 Mesoscale Imaging**

Mesoscale imaging provided by SEM allows for a greater variety of imaging that can be provided by LM or AFM. The images of NK (Figure 5-16) showed dense and aligned collagen, while NR (Figure 5-21) showed large gaps between groups of fibrils which were disorganised. Using LM, it was established that colour changes in NR implied a loss of collagen register which was confirmed here using SEM.

Similarly, NR was implied to be regular and ordered from using LM, and this was also confirmed here. This helps to validate that microscale imaging with the PS stain can indicate a change of collagen ultrastructural register<sup>477,486</sup>. When both the healthy and SSc images are compared, it becomes evident that the main structural change relates to the lack of interfibrillar registration.

### **5.7.9.3 Nanoscale Imaging and Analysis**

Locations for nanoscale imaging using AFM were, for the first time, determined by polarised LM. NK (Figure 5-17) and NR (Figure 5-22) were imaged for green, yellow, red/yellow, and red regions. Visually, it is clear that green areas on both samples were severely devoid of collagen, and it can easily be surmised that the amount of collagen increases throughout the figures. NK demonstrates aligned collagen with clear directional orientation in the red region, with a similar, if more disordered appearance, in the red/yellow region. NR is far less ordered though the collagen can be seen in the red and red/yellow region. Both NK and NR AFM imaging has confirmed what was previously identified using SEM. NK had previously shown a dense and aligned fibril structure, with evidence of swirling. NR had distinct but highly disorganised fibrils. At this stage, it theorised that the lack of alignment could be caused by an increase in stiffness of the fibrils as a result of fibrosis, but that could not yet be proven.

Following on from the earlier successes using image analysis on healthy donors, it was used again to verify some of the observations made above, that arose from AFM imaging. NK (Figure 5-18) and NR (Figure 5-23) both had significant percentages of non-collagenous material in the green region, which was expected. All regions in both samples contained some identifiable collagen. This, however, was not unexpected, as the PS stain is a way of indicating at the microscale the majority collagen alignment at the ultrascale; many PS molecules are needed to effect a colour change. Progressive increases in the amount of collagen was seen in the yellow and red/yellow regions for both samples. However, the samples diverged in terms of alignment; NK had an increase first in disordered, and the ordered collagen, whilst the amount of ordered

collagen in NR remained negligible in all regions. NK had very high percentages of non-collagen in the red and yellow regions, with the amount of non-collagen in the yellow region being significantly higher than that of the yellow region of NK. There was significantly more non-collagen in NR red/yellow region compared to NK. There were clear differences in the red regions between both samples, which is consistent with what was observed during a qualitative overview of the images and SEM. Highly disorganised collagen has again been identified as a hallmark of SSc at the nanoscale.

The use of image quantification through the dominant damage marker system did not, however, give universally repeatable results. The yellow region in healthy samples LG (Figure 5-25) and FM (Figure 5-29), for example, has a large contrast between the two samples. There is twice as much non-collagenous material in FM compared with LG, and whereas LG has a notable amount of organised collagen (20%), the value for FM is negligible at 1%. In that region, FM is far more similar to the values of NK than LG. Whilst there is a substantial amount of intersample variation in certain regions, the values in the red region remain consistent, with similar distributions for all marker types across the three samples. These differences were expected, and are known to occur with variations in age, gender and ethnicity <sup>471,472,487</sup>. While this chapter has sought to provide a wide overview of a range of patients and demographics, the work presented here still only represents comparative and combined case studies, not an overarching conclusion for skin in healthy or SSc-diseased skin. Indeed, it is reasonable to theorise that there would be a larger variation in healthy patients, who would represent a full spectrum of behaviours, compared to a disease like SSc which has a narrow pattern of symptoms. This theory was immediately put to the test with the

SSc image quantification. By adding MA (Figure 5-27) and RT (Figure 5-31) to the data collected from NK, there are clear similarities in the red and green region.

#### **5.7.9.4 Combining Image Analysis Data**

After comparing the samples pair-wise previously, and by observing the similarities, these comparisons were formalised by averaging the damage marker summaries in the green, yellow and red regions. The green comparisons (Figure 5-33) confirmed the analysis of the individual samples; no significant differences were found between the two groups as the green region is dominated by non-collagenous material unaffected by SSc<sup>101,184,488,489</sup>. The yellow region (Figure 5-34) also did not show any significant differences, although the range of data was far larger in the healthy group than the SSc group. This reconfirms the theory that the behaviours of healthy individuals will be more varied than those of a set of patients with discrete symptoms<sup>490–492</sup>.

The significant differences between the groups were finally seen in the red region (Figure 5-35). Here, differences could clearly be observed in the amount of non-collagenous material, with there being a greater amount in the SSc samples than the healthy samples. In the red region, where a high degree of collagen is expected, then non-collagenous material is more likely to be degraded collagen as gelatine than it is to be lipids, vasculature or other tissue<sup>356,493,494</sup>. A greater tendency for the SSc samples to have disordered collagen was also seen, and this has already been theorised to be caused by a fibrotic stiffening of the collagen and will be explored in more detail in section 5.7.9.5 below.



The red region is again suggested to be the region of most interest for comparative studies. This was already suggested by the AFM imaging and LM performed above showing this region to be collagen-rich, and the image analysis suggests three complementary reasons. Firstly, this was reconfirmed as a collagen-rich region; secondly, the individual samples had the most similarities inside their groups in this region; thirdly, the most differences were seen between the two groups in that region.

Collagen is the focus of this thesis, and all of the data collected in this chapter aims to determine the presence, nature or quality of it. To that end, it was decided to combine all of the damage markers related to collagen (holes, disorder collagen and ordered collagen) into one super-type, and compared against the non-collagenous/gelatine in images taken from the red region. The graph (Figure 5-36) acted primarily as the final stage in simplifying the protocol, in fulfilment of Objective 4: *“streamline the QNH protocol to obtain large data sets efficiently which could act as an adjunct diagnostic method.”* This showed that, irrespective of its alignment or orientation, collagen is found far more frequently in the healthy skin samples than in the SSc biopsies.

#### **5.7.9.5 Nanomechanics**

The final analytical technique that was applied was AFM to determine the nanomechanics of the separate regions. NK (Figure 5-19) displayed trends like those previously observed by the healthy donors. The green region showed a distribution around 4 GPa, which was also seen throughout the other regions. Bimodal distributions, similar to those seen in Patients 3 and 4 (Figure 5-10 and Figure 5-14), were observed

for the yellow, red/yellow and red regions. All the values reported are consistent with previously established in this chapter. A shift towards a bimodal distribution was seen relative to the amount of collagen identified from the image analysis; red/yellow and red regions were found to have significantly higher amounts of collagen present. NR (Figure 5-23) had a similar Young's modulus median for the green region as NK. However, the yellow and green regions of NR were not significantly different. This could be linked to the lack of difference in the image quantification for these two regions; the amount of non-collagen remains very high even in the yellow region. Bimodal distributions were seen in both red/yellow and red regions. The Young's modulus of the red region in NR was significantly higher than that of the corresponding region in NK. The lower median in NR was higher than the upper median in NK in the red region, whilst the upper NR median was significantly larger than the NR values.

Using the newer, streamlined protocol, mechanical measurements for LG, MA, FM and RT were also acquired. Healthy samples LG (Figure 5-26) and FM (Figure 5-30) both show similar behaviour in the three colour regions in terms of distributions. However, there are differences in terms of the absolute values recorded for each distribution. SSc samples MA (Figure 5-28) and RT (Figure 5-32) had differences in behaviour between them, which was different from the behaviour of LG and FM. Differences were not found, however, in the green regions of all of the samples measured. The changes in the red region were significant, especially with the presence of a trimodal distribution in MA compared with a bimodal distribution in RT.

The differences between the three healthy samples in the same identified regions was not unexpected, as this had already been reported in the discussion of the image

analysis in sections 5.7.9.3-4. Due to these innate variations, it was decided that it would not be relevant or scientifically reasonable to group the healthy and SSc mechanics data as was done for the image quantification in section 5.7.8.

The lack of statistically significant differences between the green and, to some extent, the yellow regions was expected. As SSc is only known to affect collagen, it is reasonable to assume that the non-collagenous regions would be comparable between healthy and diseased tissues. However, it is hypothesised that the disorder seen in SSc patients can be directly linked to the increase in Young's modulus measured for SSc at the nanoscale in large bundles of collagen. The result of this high stiffness is that fibrils are incapable of forming the correct bundling structure; instead, they are not in register and are poorly aligned. This was repeatably observed during the image analysis and originally suggested as a potential mechanism. The severe difference in stiffness seen in the SSc sample could be linked to the severity of the disease in the patient when the sample was obtained.

In healthy tissue, collagen fibrils are stabilised by a series of crosslinks that can be classified as intramolecular, intrafibrillar and interfibrillar. It is also theorised that two mechanisms could explain the lack of register between collagen fibrils within an SSc lesion. Firstly, sclerotic fibrils might be unable to adjust their register due to an increase in interfibrillar collagen crosslinking. This crosslinking would act with a similar effect as a fixative, for example, glutaraldehyde in SEM preparation; indeed glutaraldehyde and other methods have been used previously as mimics for *in vitro* manufactured collagen crosslinking<sup>46,57,123,161,495–497</sup>. This pathological crosslinking would keep collagen in a disordered state of register. The second hypothesis is the antithesis of this; the

interfibrillar crosslinks may have become deficient. This could have led to a loosening of the collagen organisation within the reticular dermis, the area that was analysed. Clinically, SSc is known to cause stiffening in patients, primarily in the skin. Patients often report this abnormal stiffening of a lesion as the initial reason for seeking further specialist care <sup>101,186,187,498</sup>. As an abnormal stiffening has been reported at the macroscale, and in this chapter at the nanoscale, it is therefore unlikely that the organisation of the collagen fibrils has loosened due to a lack of interfibrillar crosslinking. It can, therefore, be surmised that in a similar manner to diabetes, SSc arises due to a pathological increase in collagen crosslinking which is detected across the hierarchy of collagen; from the skin of a patient to the fibrils of a biopsy <sup>55,57,499</sup>.

## 5.8 Chapter Summary

This chapter is the two-fold pinnacle of the work presented in this thesis; part A, the development of a repeatable, scalable and multimodal analytical protocol, QNH. In part B the QNH protocol of LM, qualitative and quantitative AFM imaging and nanomechanics generated data suitable for clinical comparisons between healthy and diseased tissue. This protocol has shown its potential as a diagnostic tool; the later experiments in this chapter could be easily replicated on biopsies from undiagnosed clinical cases.

The QNH protocol underwent development in this chapter, following five key objectives:

#### Part A

1. From the skills developed in Chapter 4 AFM was successfully applied to healthy skin biopsies, giving a baseline for the Young's modulus and topography of case studies of healthy skin
2. An image quantification system was designed and refined throughout the chapter, allowing for both detailed pixel-by-pixel analysis, or an immediate overview of the images
3. The QNH protocol was enhanced by the addition of the histological staining, without which the previous objective could not have been met. While SEM imaging was used to some effect, it was not found to add to the protocol significantly and was therefore excluded from the protocol in later studies.

#### Part B

4. As a result of the success of the previous objective, the QNH protocol was streamlined to allow for the most efficient generation of data possible. Through metanalysis of the image quantification protocol, the development of an overview system, and the Young's modulus data, the QNH protocol can be successfully used to obtain large data as an adjunct diagnostic tool.

## 6 Conclusions and Future Developments

---

As developed throughout this thesis, an AFM-based protocol has been presented that can quantitatively and qualitatively characterise collagen at the nanoscale. The core of the approach did not change from Chapters 3-5. AFM was used in imaging and mechanical modes to collect data from collagen samples. However, the complementary techniques were developed throughout the thesis, as were the methods of data interpretation. At all times, the protocol underwent a development cycle – it was itself tested and refined. This ensured that only the most relevant measurements were taken throughout the thesis. Eventually, the refined protocol, quantitative nanohistology, finally tested on human skin, culminating in answering the question: “*Can an AFM-based protocol be developed to characterise collagen in health and disease in connective tissues?*”.

### 6.1 Multimodal Approach

Initially, a wide range of techniques was applied to commercial collagen products in Chapter 3. The two membranes that were the focus of that chapter, BG and MG, could be imaged with AFM and SEM. The first challenge was to identify what were the imaging markers that should be selected for comparison. Porosity, collagen fibre and the presence of D-banding were chosen, as SEM and AFM could be used in a complementary way. The results showed that the collagen membranes were likely subjected to heat and acid treatment during the manufacturing process. These treatments clearly had an effect on the mechanics of the collagen, with a Young's

modulus far below what would be expected of healthy collagen in a dry state. In a liquid environment, again the indentation measurements showed a severe decrease in expected mechanical properties. The conclusion to this was clear; the manufacturing process had damaged the collagen beyond recognition in some areas.

These membranes are practical devices and need to be used clinically. Two approaches were chosen to test whether the membranes were still functioning practically as collagen. The adhesion experiments with the fibroblasts examined time-dependent interactions. Cells responded differently to each membrane. BG did not see a change in adhesion energy over time, but the adhesion forces increased after one second. For MG, the adhesion force grew over time although the adhesion energy did not change. Despite there being limited published data with which to correlate this, there was an apparent difference in behaviour between the membranes. The collagenase study also showed a difference in response of the membranes as they degraded. This was found to be consistent with some published studies, but the large interval between OCT scans and the use of line profile analysis did not give accurate timings of the digestion rate. The OCT approach did, however, confirm the digestion pathways differed due to differences in the membrane compositions.

The *ex-vivo* mouse experiment served to help narrow down the relevant techniques for collagen. SEM and AFM were again found to be complementary, and the two major imaging markers used previously, collagen fibril structure and D-banding presence, were still used. Degradation of the membrane was found to occur over time, and in keeping with other published clinical studies. Sample preparation using paraffin wax precluded mechanical measurements, and PS staining was initially used.

## 6.2 Tendon Hierarchy Affected by Interfibrillar Crosslinks

When an animal model of ARC syndrome was tested, the developments made to the analysis protocol allowed for more concise data collection in Chapter 4. This was the smallest chapter of the thesis and showed the importance of mechanical measurements on collagen. ARC syndrome is genetic, so the collagen was supposedly made incorrectly; this contrasted with the membranes and SSc samples where the collagen was formed correctly and altered later. The change in the tendon structure between the samples was most notable at the lower SEM magnifications. The lack of order and structure in the VP33B tendon was particularly evident and immediately suggested that there could be a deficiency in crosslinking throughout the SEM images. It was difficult to judge the fibril distribution and alignment from an oblique imaging angle under SEM, and D-banding was still not visible. To confirm whether that was a function of disease or an imaging artefact, AFM was used. Changes in the fibril orientation were reported, but crucially the swelling in the D-band region of the VPS33B and VIPAR samples was indicative of the disorder. Line profile analysis confirmed the swelling was not a visual artefact. The crosslinking defects of lysyl oxidase were suggested to be limiting the ability of the collagen to form a correct triple helix structure.

The lack of alignment seen under SEM and the swelling seen under AFM pointed to a pathological change in structure. With a lack of crosslinking suspected, it was assumed that an equivalent weakening of the mechanical properties of the collagen would be found. Indentation showed a significant decrease in Young's modulus for



VIPAR compared to the WT sample and an even greater one in the VPS33B tendon. The effects of the lack of interfibrillar crosslinking were evident in the tendon.

The approach taken here appeared to work well. In all of the measurements made, there was evidence of a pathological weakening of the collagen structure. AFM has shown how cellular enzyme changes can be measured, and that when collagen is formed incorrectly, the effect that can have throughout the hierarchy of a tissue.

### 6.3 Towards Quantitative Nanohistology

Without any change to the AFM protocol used on mice tendons, two healthy human skin samples were initially tested in Chapter 5. This was termed a ‘blind’ approach, with random areas on the skin being imaged and mechanically measured. Morphologically, there was a lot of variation between the different regions of each sample. Some areas had collagen that was well aligned, and in order, in other areas, there was little evidence of collagen. Mechanically, the results were also similar. The range of the data was consistent with healthy skin as were the median values where calculated. The lack of consistency in the blind approach limited the conclusions that could be drawn.

On reflection, the approach that was used on mice tendons should not have been directly applied to the skin. While tendons have a distinct hierarchy, that hierarchy is comprised solely of collagen which behaves similarly. Skin is a far more varied tissue, which has a large number of non-collagenous components and different structures. Histologically, it is split into three distinct regions that can be identified by the use of LM. LM was used to inform the location of the AFM, ensuring that the images and mechanics were taken in several different areas of the same histological regions for all samples.

Once the variation in sample location had been accounted for, similar results were found in both image analysis and in the mechanical data. The mechanical data was found to have bimodal distribution as previously expected.

Once reliable data had been obtained, this was taken forward into a comparison between healthy individuals and SSc patients. SEM was initially used for the first matched pair, but the data obtained did not add to anything not already found with AFM or LM, so SEM was not used for the other SSc comparisons. Staining with PS allowed the samples to be split into the main colours, (red, yellow and green) with a red/yellow overlap region. Significant differences were found in terms of the image analysis and mechanics in each region between the healthy and SSc samples. This was the first full iteration of the QNH protocol

However, after reviewing this approach, there were two salient issues. Firstly, the healthy sample did not have many green or yellow regions, so there was a risk of over-sampling the data. Secondly, identifying the red/yellow overlap region was considered to be too subjective. The first issue could not be mitigated; when the regions were present, data should be collected. However, the second issue was easily avoided; the next two sets of samples were only characterised in the red, yellow and green regions without any overlap.

The result of the continuing development cycle of the QNH protocol was one that was streamlined. For the next two samples, the main colour regions were characterised with the image analysis system. This showed a non-collagenous material in the green regions, and trended towards collagen becoming more ordered in the yellow and red regions. Mechanically, significant differences were observed in all regions, clearly

showing the nanoscale effects of the fibrotic SSc disorder. Further alterations to the image analysis protocol combined image markers into collagen versus non-collagen. Although these too showed significant differences between healthy and SSc skin, this only served to reiterate to conclusions made previously.

## 6.4 Future Developments

Mouse tendons were found to have changes that were detectable using AFM in an ARC syndrome model. However, in light of the developments made in the QNH protocol, a study could be undertaken into the mouse skin to see if the cross-linking deficiencies were present. It is likely that the collagen would be found to be significantly weaker in the diseased skin.

The cross-linking deficiencies in ARC syndrome could also be tested with AFM more directly. Single-molecular pulling, which was seen to some extent with the fibroblasts in Chapter 3.5.3, could be applied to the collagen to measure changes in adhesion of the diseased collagen fibrils

In human skin, staining using PS was found to correlate LM colour changes with nanoscale morphological features as seen using the image analysis system. However, a study was not performed to try to link the damage markers of the image analysis to mechanical changes that were calculated; this is a distinct area for development.

The QNH protocol should also be tested on other diseases apart from SSc. Ethical approval has already been obtained to testing on Ehlers-Danlos syndrome while testing on teeth with Osteogenesis Imperfecta has already been successfully completed and is

pending publication. Diseases with a secondary collagen effect could also be tested. Breast cancer is known to cause both an elastic and fibrotic response in collagen depending on proximity, metastatic potential, and hormone sensitivity of the malignancy. This could be examined using QNH, as could skin cancers such as malignant melanoma and basal cell carcinoma.

Currently, colleagues are investigating the use of the QNH protocol on the ageing of skin, both naturally and artificially. An early iteration of the protocol was used to characterise damage in historical parchment. Finally, variations of this approach have resulted in publications alongside colleagues (Appendices F-J), working in materials science, microbiology, dentistry and medicine, with several publications pending. Patient engagement events and awareness literature have been written as a result of this work, with the hope that the benefits of this research can soon be translated into clinical results.

## 6.5 Summary

Throughout this thesis, there was an aspect of duality to the purpose of each chapter. Every chapter sought to systematically describe the collagen samples using nanoscale and mesoscale techniques. Collagen was seen in membranes that were believed to be denatured, but the mechanics data did not show evidence of collagen. AFM mechanics proved that ARC syndrome mice produced significantly weaker collagen than usual, but expected visual differences were also found. SSc skin was shown to be fibrotic at the nanoscale, but those changes could also be quantified using

an image analysis protocol. Not only was each sample successfully characterised, but the lessons learnt from each sample helped to develop the QNH protocol further.

Overall, a protocol was successfully developed and tested. QNH has been shown in this thesis to be a scalable system that can readily identify markers of disorder in human skin. It can be used to identify mechanically and morphological signs of disease and is now ready to be expanded into clinical studies.

## 7 Bibliography

1. Brinckmann J. Collagens at a glance. *Top Curr Chem.* 2005;247(Pt 12):1-6. doi:10.1007/b103817
2. Shoulders MD, Raines RT. Collagen Structure and Stability. *Annu Rev Biochem.* 2009;78(1):929-958. doi:10.1146/annurev.biochem.77.032207.120833
3. Zhuang S, Linhananta A, Li H. Phenotypic effects of Ehlers-Danlos syndrome-associated mutation on the FnIII domain of tenascin-X. *Protein Sci.* 2010;19(11):2231-2239. doi:10.1002/pro.503
4. Yang L, van der Werf KO, Dijkstra PJ, Feijen J, Bennink ML. Micromechanical analysis of native and cross-linked collagen type I fibrils supports the existence of microfibrils. *J Mech Behav Biomed Mater.* 2012;6:148-158. doi:10.1016/j.jmbbm.2011.11.008
5. Bayer ML, Yeung CYC, Kadler KE, et al. The initiation of embryonic-like collagen fibrillogenesis by adult human tendon fibroblasts when cultured under tension. *Biomaterials.* 2010;31(18):4889-4897. doi:10.1016/j.biomaterials.2010.02.062
6. Marque V, Kieffer P, Atkinson J, Lartaud-Idjouadiene I. Elastic properties and composition of the aortic wall in old spontaneously hypertensive rats. *Hypertension.* 1999;34(3):415-422. doi:10.1161/01.HYP.34.3.415
7. van der Rest M, Garrone R. Collagen family of proteins. *FASEB J.* 1991;5(13):2814-2823. doi:10.1096/fasebj.5.13.1916105
8. Smith H, Galmes R, Gogolina E, et al. Associations among genotype, clinical phenotype, and intracellular localization of trafficking proteins in ARC syndrome. *Hum Mutat.* 2012;33(12):1656-1664. doi:10.1002/humu.22155
9. Prockop DJ. Collagens: Molecular Biology, Diseases, and Potentials for Therapy. *Annu Rev Biochem.* 1995;64(1):403-434. doi:10.1146/annurev.biochem.64.1.403
10. Pinnell SR, Krane SM, Kenzora JE, Glimcher MJ. A Heritable Disorder of Connective Tissue. *N Engl J Med.* 1972;286(19):1013-1020. doi:10.1056/NEJM197205112861901
11. Vassileva S, Drenovska K, Manuelyan K. Autoimmune blistering dermatoses as systemic diseases. *Clin Dermatol.* 2014;32(3):364-375. doi:10.1016/j.clindermatol.2013.11.003
12. Myllyharju J, Kivirikko KI. Collagens and collagen-related diseases. *Ann Med.* 2001;33(1):7-21. doi:10.3109/07853890109002055
13. Rauch F, Lalic L, Roughley P, Glorieux FH. Genotype-phenotype correlations in nonlethal osteogenesis imperfecta caused by mutations in the helical domain of collagen type I. *Eur J Hum Genet.* 2010;18(6):642-647. doi:10.1038/ejhg.2009.242
14. Majorana A, Bardellini E, Brunelli PC, Lacaita M, Cazzolla AP, Favia G. Dentinogenesis imperfecta in children with osteogenesis imperfecta: A clinical and ultrastructural study. *Int J Paediatr Dent.* 2010;20(2):112-118. doi:10.1111/j.1365-263X.2010.01033.x
15. Herchenhan A, Uhlenbrock F, Eliasson P, et al. Lysyl oxidase activity is required for ordered collagen fibrillogenesis by tendon cells. *J Biol Chem.* 2015;290(26):16440-16450. doi:10.1074/jbc.M115.641670
16. Diegelmann R. Collagen metabolism. *Wounds.* 2001;13(5):4-9.
17. Ricard-Blum S. The Collagen Family. *Cold Spring Harb Perspect Biol.*

- 2011;3(1):1-19. doi:10.1101/cshperspect.a004978
18. Brodsky B, Persikov A V, David ADP, John MS. Molecular Structure of the Collagen Triple Helix. *Adv Protein Chem.* 2005;Volume 70:301-339.
  19. Kadler KE, Holmes DF, Trotter JA, Chapman JA. Collagen fibril formation. *Biochem J.* 1996;316(1):1-11. doi:10.1042/bj3160001
  20. Karsenty G, Park RW. Regulation of type I collagen genes expression. *Int Rev Immunol.* 1995;12(2-4):177-185. doi:10.3109/08830189509056711
  21. Assaraf-Weill N, Gasse B, Silvent J, Bardet C, Sire JY, Davit-Béal T. Ameloblasts express type I collagen during amelogenesis. *J Dent Res.* 2014;93(5):502-507. doi:10.1177/0022034514526236
  22. Myllyharju J. Prolyl 4-hydroxylases, the key enzymes of collagen biosynthesis. *Matrix Biol.* 2003;22(1):15-24. doi:10.1016/S0945-053X(03)00006-4
  23. Prockop DJ. How Does a Skin Fibroblast Make Type I Collagen Fibers? *J Invest Dermatol.* 1982;79(1):3-6. doi:10.1038/jid.1982.2
  24. Schmidts TM, Linsenmayer TF. A Short Chain ( Pro ) collagen from Aged Endochondral Chondrocytes. *Pharmacol.* 1983;258(15):9504-9509.
  25. Myllyharju J, Kivirikko KI. Collagens, modifying enzymes and their mutations in humans, flies and worms. *Trends Genet.* 2004;20(1):33-43. doi:10.1016/j.tig.2003.11.004
  26. Dias J, Diakonis VF, Kankariya VP, Yoo SH, Ziebarth NM. Anterior and posterior corneal stroma elasticity after corneal collagen crosslinking treatment. *Exp Eye Res.* 2013;116:58-62. doi:10.1016/j.exer.2013.07.028
  27. Fawzy A, Nitisusanta L, Iqbal K, Daoud U, Beng LT, Neo J. Characterization of riboflavin-modified dentin collagen matrix. *J Dent Res.* 2012;91(11):1049-1054. doi:10.1177/0022034512459053
  28. Oldberg Å, Antonsson P, Lindblom K, Heinegård D. A collagen-binding 59-kd protein (fibromodulin) is structurally related to the small interstitial proteoglycans PG-S1 and PG-S2 (decorin). *Embo J.* 1989;8(9):2601-2604. doi:10.1016/B978-0-12-385999-0.00001-1
  29. Berg RA, Prockop DJ. The thermal transition of a non-hydroxylated form of collagen. Evidence for a role for hydroxyproline in stabilizing the triple-helix of collagen. *Biochem Biophys Res Commun.* 1973;52(1):115-120. doi:https://doi.org/10.1016/0006-291X(73)90961-3
  30. Risteli J, Niemi S, Kauppila S, Melkko J, Risteli L. Collagen propeptides as indicators of collagen assembly. *Acta Orthop.* 1995;66(S266):183-188. doi:10.3109/17453679509157688
  31. Jacob RA, Sotoudeh G. Vitamin C function and status in chronic disease. *Nutr Clin Care.* 2002;5(2):66-74. doi:10.1046/j.1523-5408.2002.00005.x
  32. Meigel WN, Gay S, Weber L. Dermal architecture and collagen type distribution. *Arch Dermatological Res.* 1977;259(1):1-10. doi:10.1007/BF00562732
  33. Tiainen PI, Pasanen A, Sormunen R, Myllyharju J. Characterization of recombinant human prolyl 3-hydroxylase isoenzyme 2, an enzyme modifying the basement membrane collagen IV. *J Biol Chem.* 2008;283(28):19432-19439. doi:10.1074/jbc.M802973200
  34. Paulson J, Colley K. Glycosyltransferases. *J Biol Chem.* 1989;264(30):17615-1761.

35. Lairson LL, Henrissat B, Davies GJ, Withers SG. Glycosyltransferases: Structures, Functions, and Mechanisms. *Annu Rev Biochem.* 2008;77(1):521-555. doi:10.1146/annurev.biochem.76.061005.092322
36. Bornstein P, Sage H. Structurally Distinct Collagen Types. *Annu Rev Biochem.* 1980;49(1):957-1003. doi:10.1146/annurev.bi.49.070180.004521
37. Ramachandran GN, Kartha G. Structure of collagen. *Nature.* 1955;176(4482):593-595.
38. Pepin MG, Byers PH. Ehlers-Danlos Syndrome Type IV. *Ncib.*
39. Yathindra N. The Madras Group and the structure of collagen. 1999;111(1):5-12.
40. Azim NH, Subki A, Yusof ZNB. *Abiotic Stresses Induce Total Phenolic, Total Flavonoid and Antioxidant Properties in Malaysian Indigenous Microalgae and Cyanobacterium.* Vol 14. New York: Garland Science; 2018. doi:10.1017/CBO9781107415324.004
41. Canty EG. Procollagen trafficking, processing and fibrillogenesis. *J Cell Sci.* 2005;118(7):1341-1353. doi:10.1242/jcs.01731
42. Koivunen P, Hirsilä M, Remes AM, Hassinen IE, Kivirikko KI, Myllyharju J. Inhibition of hypoxia-inducible factor (HIF) hydroxylases by citric acid cycle intermediates: Possible links between cell metabolism and stabilization of HIF. *J Biol Chem.* 2007;282(7):4524-4532. doi:10.1074/jbc.M610415200
43. Vissing H, D'Alessio M, Lee B, Ramirez F, Godfrey M, Hollister DW. Glycine to serine substitution in the triple helical domain of pro- $\alpha$ 1(II) collagen results in a lethal perinatal form of short-limbed dwarfism. *J Biol Chem.* 1989;264(31):18265-18267.
44. Uzman A. Fundamentals of Molecular Biology. In: Lodish H, Berk A, Zipersky S, Baltimore D, eds. *Biochemistry and Molecular Biology Education.* Vol 29. 4th ed. New York: W H Freeman; 2001:126-128. doi:10.1016/S1470-8175(01)00023-6
45. Meinhardt A, Cramer P. Recognition of RNA polymerase II carboxy-terminal domain by 3'-RNA-processing factors. *Nature.* 2004;430(6996):223-226. doi:10.1038/nature02679
46. Eyre D. Cross-Linking in Collagen and Elastin. *Annu Rev Biochem.* 1984;53(1):717-748. doi:10.1146/annurev.biochem.53.1.717
47. Gara SK, Grumati P, Urciuolo A, et al. Three novel collagen VI chains with high homology to the  $\alpha$ 3 chain. *J Biol Chem.* 2008;283(16):10658-10670. doi:10.1074/jbc.M709540200
48. Tucker N, Stanger J, Staiger M, Razzaq H, Hofman K. The History of the Science and Technology of Electrospinning from 1600 to 1995. *J Eng Fiber Fabr.* 2012;7:63-73.
49. Hudson BG, Tryggvason K, Sundaramoorthy M, Neilson EG. Alport's Syndrome, Goodpasture's Syndrome, and Type IV Collagen. *N Engl J Med.* 2003;348(25):2543-2556. doi:10.1056/NEJMra022296
50. Lehmann MS, Koetzle TF, Hamilton WC. Precision Neutron Diffraction Structure Determination of Protein and Nucleic Acid Components. I. The Crystal and Molecular Structure of the Amino Acid L-Alanine. *J Am Chem Soc.* 1972;94(8):2657-2660. doi:10.1021/ja00763a016
51. Veis A, Anesey J, Mussell S. A limiting microfibril model for the three-dimensional arrangement within collagen fibres. *Nature.* 1967;215(5104):931-934.



- doi:10.1038/215931a0
52. Bailey AJ, Light ND, Atkins EDT. Chemical Cross-Linking Restrictions on Models for the Molecular-Organization of the Collagen Fiber. *Nature*. 1980;288(5789):408-410. doi:10.1038/288408a0
  53. Abou Neel EA, Bozec L, Knowles JC, et al. Collagen - Emerging collagen based therapies hit the patient. *Adv Drug Deliv Rev*. 2013;65(4):429-456. doi:10.1016/j.addr.2012.08.010
  54. Valeyre D, Prasse A, Nunes H, Uzunhan Y, Brillet PY, Müller-Quernheim J. Sarcoidosis. *Lancet*. 2014;383(9923):1155-1167. doi:10.1016/S0140-6736(13)60680-7
  55. Singh R, Barden A, Mori T, Beilin L. Advanced glycation end-products : a review. 2001.
  56. Kosmopoulos M, Drekolias D, Zavras PD, Piperi C, Papavassiliou AG. Impact of advanced glycation end products (AGEs) signaling in coronary artery disease. *Biochim Biophys Acta Mol Basis Dis*. 2019;1865(3):611-619. doi:10.1016/j.bbadis.2019.01.006
  57. Saito M, Marumo K. Collagen cross-links as a determinant of bone quality: A possible explanation for bone fragility in aging, osteoporosis, and diabetes mellitus. *Osteoporos Int*. 2010;21(2):195-214. doi:10.1007/s00198-009-1066-z
  58. Baynes JW, Thorpe SR. Role of oxidative stress in diabetic complications: A new perspective on an old paradigm. *Diabetes*. 1999;48(1):1-9. doi:10.2337/diabetes.48.1.1
  59. Ahmed T, Nash A, Clark KEN, et al. Combining nano-physical and computational investigations to understand the nature of “aging” in dermal collagen. *Int J Nanomedicine*. 2017;12:3303-3314. doi:10.2147/IJN.S121400
  60. Koska J, Saremi A, Howell S, et al. Advanced glycation end products, oxidation products, and incident cardiovascular events in patients with type 2 diabetes. *Diabetes Care*. 2018;41(3):570-576. doi:10.2337/dc17-1740
  61. Petruska JA, Hodge AJ. A Subunit Model for the Tropocollagen Macromolecule. *Proc Natl Acad Sci*. 1964;51(5):871-876. doi:10.1073/pnas.51.5.871
  62. Hodge AJ, Petruska JA. Recent studies with the electron microscope on ordered aggregates of the tropocollagen macromolecule. In: Ramachandran G, ed. *Aspects of Protein Structure*. New York; 1963:289-300.
  63. Miller A. Molecular packing in collagen fibrils. *Trends Biochem Sci*. 1982;7(5294):13-18.
  64. Bozec L, Van Der Heijden G, Horton M. Collagen fibrils: Nanoscale ropes. *Biophys J*. 2007;92(1):70-75. doi:10.1529/biophysj.106.085704
  65. Baldwin SJ, Quigley AS, Clegg C, Kreplak L. Nanomechanical mapping of hydrated rat tail tendon collagen i fibrils. *Biophys J*. 2014;107(8):1794-1801. doi:10.1016/j.bpj.2014.09.003
  66. Piez KA, Trus BL. A new model for packing of type-I collagen molecules in the native fibril. *Biosci Rep*. 1981;1(10):801-810. doi:10.1007/BF01114803
  67. Orgel JPRO, Irving TC, Miller A, Wess TJ. Microfibrillar structure of type I collagen in situ. *Proc Natl Acad Sci*. 2006;103(24):9001-9005. doi:10.1073/pnas.0502718103
  68. Ortolani F, Giordano M, Marchini M. A model for type II collagen fibrils: Distinctive

- D-band patterns in native and reconstituted fibrils compared with sequence data for helix and telopeptide domains. *Biopolymers*. 2000;54(6):448-463. doi:10.1002/1097-0282(200011)54:6<448::AID-BIP80>3.0.CO;2-Q
69. Holmes DF, Gilpin CJ, Baldock C, Ziese U, Koster AJ, Kadler KE. Corneal collagen fibril structure in three dimensions: Structural insights into fibril assembly, mechanical properties, and tissue organization. *Proc Natl Acad Sci*. 2001;98(13):7307-7312. doi:10.1073/pnas.111150598
  70. Jastrzebska M, Mróz I, Barwiński B, Zalewska-Rejdak J, Turek A, Cwalina B. Supramolecular structure of human aortic valve and pericardial xenograft material: Atomic force microscopy study. *J Mater Sci Mater Med*. 2008;19(1):249-256. doi:10.1007/s10856-006-0049-2
  71. Silver FH, Freeman JW, Seehra GP. Collagen self-assembly and the development of tendon mechanical properties. *J Biomech*. 2003;36(10):1529-1553. doi:10.1016/S0021-9290(03)00135-0
  72. Subbiah T, Bhat GS, Tock RW, Parameswaran S, Ramkumar SS. Electrospinning of nanofibers. *J Appl Polym Sci*. 2005;96(2):557-569. doi:10.1002/app.21481
  73. Hirata E, Sakaguchi N, Uo M, et al. Transmission electron microscopic observation of cells cultured on multiwalled carbon nanotube-coated sponges. *J Electron Microscop (Tokyo)*. 2010;59(5):447-450. doi:10.1093/jmicro/dfq051
  74. Fang M, Goldstein EL, Turner AS, et al. Type I collagen D-spacing in fibril bundles of dermis, tendon, and bone: Bridging between nano- and micro-level tissue hierarchy. *ACS Nano*. 2012;6(11):9503-9514. doi:10.1021/nn302483x
  75. Hynes RO, Yamada KM. Fibronectins: Multifunctional modular glycoproteins. *J Cell Biol*. 1982;95(2):369-377. doi:10.1083/jcb.95.2.369
  76. Smith JW. Molecular pattern in native collagen [13]. *Nature*. 1968;219(5150):157-158. doi:10.1038/219157a0
  77. Trus BL, Piez K. Molecular Packing of Collagen: Three-dimensional Analysis of Electrostatic Interactions. *J Mol Biol*. 1976;108(4):705-732.
  78. Hulmes DJS, Miller A. Quasi-hexagonal molecular packing in collagen fibrils [34]. *Nature*. 1979;282(5741):878-880. doi:10.1038/282878a0
  79. Fraser RDB, MacRae TP, Miller A. Molecular packing in type I collagen fibrils. *J Mol Biol*. 1987;193(1):115-125. doi:10.1016/0022-2836(87)90631-0
  80. Yadavalli VK, Svintradze D V., Pidaparti RM. Nanoscale measurements of the assembly of collagen to fibrils. *Int J Biol Macromol*. 2010;46(4):458-464. doi:10.1016/j.ijbiomac.2010.02.012
  81. Bertassoni LE, Marshall GW, Swain M V. Mechanical heterogeneity of dentin at different length scales as determined by AFM phase contrast. *Micron*. 2012;43(12):1364-1371. doi:10.1016/j.micron.2012.03.021
  82. Andriotis OG, Desissaire S, Thurner PJ. Collagen Fibrils: Nature's Highly Tunable Nonlinear Springs. *ACS Nano*. 2018;12(4):3671-3680. doi:10.1021/acsnano.8b00837
  83. Joshi J, Mahajan G, Kothapalli CR. Three-dimensional collagenous niche and azacytidine selectively promote time-dependent cardiomyogenesis from human bone marrow-derived MSC spheroids. *Biotechnol Bioeng*. 2018;115(8):2013-2026. doi:10.1002/bit.26714
  84. Daghma DES, Malhan D, Simon P, et al. Computational segmentation of collagen

- fibers in bone matrix indicates bone quality in ovariectomized rat spine. *J Bone Miner Metab.* 2018;36(3):297-306. doi:10.1007/s00774-017-0844-5
85. Bürck J, Aras O, Bertinetti L, et al. Observation of triple helix motif on electrospun collagen nanofibers and its effect on the physical and structural properties. *J Mol Struct.* 2018;1151:73-80. doi:10.1016/j.molstruc.2017.09.030
  86. Lausch AJ, Chong LC, Uludag H, Sone ED. Multiphasic Collagen Scaffolds for Engineered Tissue Interfaces. *Adv Funct Mater.* 2018;1804730:1-9. doi:10.1002/adfm.201804730
  87. Aziz J, Ahmad MF, Rahman MT, Yahya NA, Czernuszka J, Radzi Z. AFM analysis of collagen fibrils in expanded scalp tissue after anisotropic tissue expansion. *Int J Biol Macromol.* 2018;107(PartA):1030-1038. doi:10.1016/j.ijbiomac.2017.09.066
  88. Grässel S, Bauer RJ. Collagen XVI in health and disease. *Matrix Biol.* 2013;32(2):64-73. doi:10.1016/j.matbio.2012.11.001
  89. Bella J, Hulmes DJS. Fibrillar collagens. *Subcell Biochem.* 2017;82:457-490. doi:10.1007/978-3-319-49674-0\_14
  90. Gautieri A, Vesentini S, Redaelli A, Buehler MJ. Hierarchical structure and nanomechanics of collagen microfibrils from the atomistic scale up. *Nano Lett.* 2011;11(2):757-766. doi:10.1021/nl103943u
  91. Vaz CM, van Tuijl S, Bouten CVC, Baaijens FPT. Design of scaffolds for blood vessel tissue engineering using a multi-layering electrospinning technique. *Acta Biomater.* 2005;1(5):575-582. doi:10.1016/j.actbio.2005.06.006
  92. Grytz R, Meschke G. Constitutive modeling of crimped collagen fibrils in soft tissues. *J Mech Behav Biomed Mater.* 2009;2(5):522-533. doi:10.1016/j.jmbbm.2008.12.009
  93. Strasser S, Zink A, Janko M, Heckl WM, Thalhammer S. Structural investigations on native collagen type I fibrils using AFM. *Biochem Biophys Res Commun.* 2007;354(1):27-32. doi:10.1016/j.bbrc.2006.12.114
  94. Grover NB. Three-dimensional structure of collagen bands. *J Ultrastructure Res.* 1965;12(5-6):574-578. doi:10.1016/S0022-5320(65)80048-X
  95. Stylianou A, Gkretsi V, Stylianopoulos T. Atomic force microscopy nano-characterization of 3D collagen gels with tunable stiffness. *MethodsX.* 2018;5:503-513. doi:https://doi.org/10.1016/j.mex.2018.05.009
  96. Yang B, Adelung R, Ludwig K, Bößmann K, Pashley DH, Kern M. Effect of structural change of collagen fibrils on the durability of dentin bonding. *Biomaterials.* 2005;26(24):5021-5031. doi:10.1016/j.biomaterials.2005.01.024
  97. Lingham-Soliar T, Wesley-Smith J. First investigation of the collagen D-band ultrastructure in fossilized vertebrate integument. *Proc R Soc B Biol Sci.* 2008;275(1648):2207-2212. doi:10.1098/rspb.2008.0489
  98. Gissen P, Johnson CA, Gentle D, et al. Comparative evolutionary analysis of VPS33 homologues: Genetic and functional insights. *Hum Mol Genet.* 2005;14(10):1261-1270. doi:10.1093/hmg/ddi137
  99. Glorieux FH. Osteogenesis imperfecta. *Best Pract Res Clin Rheumatol.* 2008;22(1):85-100. doi:10.1016/j.berh.2007.12.012
  100. Grahame R. Joint hypermobility and genetic collagen disorders: Are they related? *Arch Dis Child.* 1999;80(2):188-191. doi:10.1136/ad.80.2.188

101. LeRoy EC, Medsger J. Criteria for the classification of early systemic sclerosis. *J Rheumatol*. 2001;28(7):1573-1576. doi:10.1002/cpa.3160150207
102. Wysocki AB. Skin anatomy, physiology, and pathophysiology. *Nurs Clin North Am*. 1999;34(4):777-797, v. <http://www.ncbi.nlm.nih.gov/pubmed/10523436>.
103. Janson D, Rietveld M, Mahé C, Saintigny G, El Ghalbzouri A. Differential effect of extracellular matrix derived from papillary and reticular fibroblasts on epidermal development in vitro. *Eur J Dermatology*. 2017;27(3):237-246. doi:10.1684/ejd.2017.2984
104. Imokawa G, Abe A, Jin K, Higaki Y, Kawashima M, Hidano A. Decreased level of ceramides in stratum corneum of atopic dermatitis: an etiologic factor in atopic dry skin? *J Invest Dermatol*. 1991;96(4):523-526. doi:10.1111/1523-1747.ep12470233
105. Harding CR. The stratum corneum: structure and function in health and disease. *Dermatol Ther*. 2004;17(s1):6-15. doi:10.12892/ejgo3153.2016
106. Baker H, Kligman AM. Technique for Estimating Turnover Time of Human Stratum Corneum. *Arch Dermatol*. 1967;95(4):408-411. doi:10.1001/archderm.1967.01600340068016
107. Woodley DT. Distinct Fibroblasts in the Papillary and Reticular Dermis: Implications for Wound Healing. *Dermatol Clin*. 2017;35(1):95-100. doi:10.1016/j.det.2016.07.004
108. Driskell RR, Watt FM. Understanding fibroblast heterogeneity in the skin. *Trends Cell Biol*. 2015;25(2):92-99. doi:10.1016/j.tcb.2014.10.001
109. Kleinman HK, Klebe RJ, Martin GR. Role of collagenous matrices in the adhesion and growth of cells. *J Cell Biol*. 1981;88(3):473-485. doi:10.1083/jcb.88.3.473
110. Ring HC, Mogensen M, Hussain AA, et al. Imaging of collagen deposition disorders using optical coherence tomography. *J Eur Acad Dermatol Venereol*. 2015;29(5):890-898. doi:10.1111/jdv.12708
111. Carmichael SW. The tangled web of Langer's lines. *Clin Anat*. 2014;27(2):162-168. doi:10.1002/ca.22278
112. Cao Y, Vacanti JP, Paige KT, Upton J, Vacanti CA. Transplantation of chondrocytes utilizing a polymer-cell construct to produce tissue-engineered cartilage in the shape of a human ear. *Plast Reconstr Surg*. 1997;100(2):297-304. doi:10.1097/00006534-199708000-00001
113. Israelsen NM, Maria M, Mogensen M, et al. The value of ultrahigh resolution OCT in dermatology - delineating the dermo-epidermal junction, capillaries in the dermal papillae and vellus hairs. *Biomed Opt Express*. 2018;9(5):2240. doi:10.1364/BOE.9.002240
114. Wolf K, Alexander S, Schacht V, et al. Collagen-based cell migration models in vitro and in vivo. *Semin Cell Dev Biol*. 2009;20(8):931-941. doi:10.1016/j.semcdb.2009.08.005
115. Arau T, Aguiar P, Eloy C. Classification of breast cancer histology images using Convolutional Neural Networks. *PLoS One*. 2017;12(6):1-14. doi:10.1371/journal.pone.0177544
116. Goodpaster BH, Thaete FL, Simoneau JA, Kelley DE. Subcutaneous abdominal fat and thigh muscle composition predict insulin sensitivity independently of visceral fat. *Diabetes*. 1997;46(10):1579-1585.

doi:10.1109/ICINDMA.2010.5538095

117. Mallal SA, John M, Moore CB, James IR, McKinnon EJ. Contribution of nucleoside analogue reverse transcriptase inhibitors to subcutaneous fat wasting in patients with HIV infection. *Aids*. 2000;14(10):1309-1316. doi:10.1097/00002030-200007070-00002
118. Delgado-Gonzalo R, Parak J, Tarniceriu A, Renevey P, Bertschi M, Korhonen I. Evaluation of accuracy and reliability of PulseOn optical heart rate monitoring device. *Proc Annu Int Conf IEEE Eng Med Biol Soc EMBS*. 2015;2015-Novem:430-433. doi:10.1109/EMBC.2015.7318391
119. Padayatty SJ, Levine M. Vitamin C: the known and the unknown and Goldilocks. *Oral Dis*. 2016;22(6):463-493. doi:10.1111/odi.12446
120. Amrein K, Oudemans-van Straaten HM, Berger MM. Vitamin therapy in critically ill patients: focus on thiamine, vitamin C, and vitamin D. *Intensive Care Med*. 2018. doi:10.1007/s00134-018-5107-y
121. Cimmino L, Neel BG, Aifantis I. Vitamin C in Stem Cell Reprogramming and Cancer. *Trends Cell Biol*. 2018;28(9):698-708. doi:10.1016/j.tcb.2018.04.001
122. Jiang AW, Vijayaraghavan M, Mills EG, Prisco AR, Thurn JR. Scurvy, a Not-So-Ancient Disease. *Am J Med*. 2018;131(5):e185-e186. doi:10.1016/j.amjmed.2017.12.007
123. Svensson RB, Smith ST, Moyer PJ, Magnusson SP. Effects of maturation and advanced glycation on tensile mechanics of collagen fibrils from rat tail and Achilles tendons. *Acta Biomater*. 2018;70:270-280. doi:10.1016/j.actbio.2018.02.005
124. Fisher GJ, Wang Z, Datta SC, Varani J, Kang S, Voorhees JJ. Pathophysiology of Premature Skin Aging Induced by Ultraviolet Light. *N Engl J Med*. 1997;337(20):1419-1429. doi:10.1056/NEJM199711133372003
125. Fisher GJ, Kang S, Varani J, et al. Mechanisms of photoaging and chronological skin aging. *Arch Dermatol*. 2002;138(11):1462-1470. doi:10.1001/archderm.138.11.1462
126. Wilhelm K-P, Cua AB, Maibach HI. Skin Aging. *Arch Dermatol*. 1991;127(12):1806. doi:10.1001/archderm.1991.04520010052006
127. Heckman CJ, Darlow SD, Ritterband LM, Handorf EA, Manne SL. Efficacy of an intervention to alter skin cancer risk behaviors in young adults. *Am J Prev Med*. 2016;51(1):1-11. doi:10.1016/j.amepre.2015.11.008
128. Al-Hadithy H, Isenberg DA, Addison IE, Goldstone AH, Snaith ML. Neutrophil function in systemic lupus erythematosus and other collagen diseases. *Ann Rheum Dis*. 1982;41(1):33-38. doi:10.1136/ard.41.1.33
129. Nomura S, Nozaki S, Hamazaki T, et al. PET Imaging Analysis with <sup>64</sup>Cu in Disulfiram Treatment for Aberrant Copper Biodistribution in Menkes Disease Mouse Model. *J Nucl Med*. 2014;55(5):845-851. doi:10.2967/jnumed.113.131797
130. Slack JL, Liska DJ, Bornstein P. Regulation of expression of the type I collagen genes. *Am J Med Genet*. 1993;45(2):140-151. doi:10.1002/ajmg.1320450203
131. Van Dijk FS, Pals G, Van Rijn RR, Nikkels PGJ, Cobben JM. Classification of Osteogenesis Imperfecta revisited. *Eur J Med Genet*. 2010;53(1):1-5. doi:10.1016/j.ejmg.2009.10.007
132. Burkitt Wright EMM, Porter LF, Spencer HL, et al. Brittle cornea syndrome:

- Recognition, molecular diagnosis and management. *Orphanet J Rare Dis.* 2013;8(1):68. doi:10.1186/1750-1172-8-68
133. Sillence DO, Senn A, Danks DM. Genetic heterogeneity in osteogenesis imperfecta. *J Med Genet.* 1979;16(2):101-116. doi:10.1136/jmg.16.2.101
  134. Beck K, Chan VC, Shenoy N, Kirkpatrick A, Ramshaw JAM, Brodsky B. Destabilization of osteogenesis imperfecta collagen-like model peptides correlates with the identity of the residue replacing glycine. *Proc Natl Acad Sci.* 2000;97(8):4273-4278. doi:10.1073/pnas.070050097
  135. Asanbaeva A, Masuda K, Thonar EJMA, Klisch SM, Sah RL. Cartilage growth and remodeling: modulation of balance between proteoglycan and collagen network in vitro with  $\beta$ -aminopropionitrile. *Osteoarthr Cartil.* 2008;16(1):1-11. doi:10.1016/j.joca.2007.05.019
  136. Siegel RC, Pinnell SR, Martin GR. Cross-Linking of Collagen and Elastin. Properties of Lysyl Oxidase. *Biochemistry.* 1970;9(23):4486-4492. doi:10.1021/bi00825a004
  137. Fratzl-Zelman N, Schmidt I, Roschger P, et al. Unique micro- and nano-scale mineralization pattern of human osteogenesis imperfecta type VI bone. *Bone.* 2015;73:233-241. doi:10.1016/j.bone.2014.12.023
  138. Galicka A, Wolczynski S, Gindzienski A. Comparative studies of osteoblast and fibroblast type I collagen in a patient with osteogenesis imperfecta type IV. *J Pathol.* 2002;196(2):235-237. doi:10.1002/path.1030
  139. Hudson DM, Eyre DR. Collagen prolyl 3-hydroxylation: A major role for a minor post-translational modification? *Connect Tissue Res.* 2013;54(4-5):245-251. doi:10.3109/03008207.2013.800867
  140. Roughley PJ, Rauch F, Glorieux FH, Hofstetter W, Alini M. Osteogenesis imperfecta - Clinical and molecular diversity. *Eur Cells Mater.* 2003;5:41-47. doi:10.22203/eCM.v005a04
  141. Willing MC, Deschenes SP, Slayton RL, Roberts1 ' EJ. Premature Chain Termination Is a Unifying Mechanism for COL1A1 Null Alleles in Osteogenesis Imperfecta Type I Cell Strains. *Am J Hum Genet.* 1996;59(4):799-809. <https://www.ncbi.nlm.nih.gov/pubmed/8808594>.
  142. Byers PH. Osteogenesis imperfecta: Perspectives and opportunities. *Curr Opin Pediatr.* 2000;12(6):603-609.
  143. Boyde A, Travers R, Glorieux FH, Jones SJ. The mineralization density of iliac crest bone from children with osteogenesis imperfecta. *Calcif Tissue Int.* 1999;64(3):185-190. doi:10.1007/s002239900600
  144. Barron MJ, McDonnell ST, MacKie I, Dixon MJ. Hereditary dentine disorders: Dentinogenesis imperfecta and dentine dysplasia. *Orphanet J Rare Dis.* 2008;3(1):31. doi:10.1186/1750-1172-3-31
  145. Malmgren B, Norgren S. Dental aberrations in children and adolescents with osteogenesis imperfecta. *Acta Odontol Scand.* 2002;60(2):65-71. doi:10.1080/000163502753509446
  146. Tsai C-L, Lin Y-T, Lin Y-T. Dentinogenesis imperfecta associated with osteogenesis imperfecta: report of two cases. *Chang Gung Med J.* 2003;26:138-143. <http://www.ncbi.nlm.nih.gov/pubmed/12718392>.
  147. Thotakura SRR, Mah T, Srinivasan R, Takagi Y, Veis A, George A. The non-

- collagenous dentin matrix proteins are involved in Dentinogenesis Imperfecta type II (DGI-II). *J Dent Res.* 2000;79(3):835-839. doi:10.1177/00220345000790030901
148. Elkayam O, Ben Itzhak S, Avrahami E, et al. Multidisciplinary approach to chronic back pain: Prognostic elements of the outcome. *Clin Exp Rheumatol.* 1996;14(3):281-288. doi:10.1016/0029-7844(94)00457-O
  149. Niño-Barrera JL, Gutiérrez ML, Garzón-Alvarado DA. A theoretical model of dentinogenesis: Dentin and dentinal tubule formation. *Comput Methods Programs Biomed.* 2013;112(1):219-227. doi:10.1016/j.cmpb.2013.06.010
  150. Linde A, Goldberg M. Dentinogenesis. *Crit Rev Oral Biol Med.* 1993;4(5):679-728. doi:10.1177/10454411930040050301
  151. Youravong N, Teanpaisan R, Norén JG, et al. Chemical composition of enamel and dentine in primary teeth in children from Thailand exposed to lead. *Sci Total Environ.* 2008;389(2-3):253-258. doi:10.1016/j.scitotenv.2007.08.053
  152. Wiczorek A, Loster J. Dentinogenesis imperfecta type II: Ultrastructure of teeth in sagittal sections. *Folia Histochem Cytobiol.* 2013;51(3):244-247. doi:10.5603/FHC.2013.0035
  153. Clayton HA, Cressman EK, Henriques DYP. Proprioceptive sensitivity in Ehlers-Danlos syndrome patients. *Exp Brain Res.* 2013;230(3):311-321. doi:10.1007/s00221-013-3656-4
  154. Guilleminault C, Primeau M, Chiu HY, Yuen KM, Leger D, Metlaine A. Sleep-disordered breathing in Ehlers-Danlos syndrome: A genetic model of OSA. *Chest.* 2013;144(5):1503-1511. doi:10.1378/chest.13-0174
  155. Rahman N, Dunstan M, Teare MD, et al. Ehlers-Danlos Syndrome with Severe Early-Onset Periodontal Disease (EDS-VIII) Is a Distinct, Heterogeneous Disorder with One Predisposition Gene at Chromosome 12p13. *Am J Hum Genet.* 2003;73(1):198-204. doi:10.1086/376416
  156. Wenstrup RJ, Florer JB, Willing MC, et al. COL5A1 Haploinsufficiency Is a Common Molecular Mechanism Underlying the Classical Form of EDS. *Am J Hum Genet.* 2000;66(6):1766-1776. doi:10.1086/302930
  157. Pau M, Galli M, Celletti C, et al. Plantar pressure patterns in women affected by Ehlers-Danlos syndrome while standing and walking. *Res Dev Disabil.* 2013;34(11):3720-3726. doi:10.1016/j.ridd.2013.07.040
  158. Lawrence EJ. The clinical presentation of Ehlers-Danlos syndrome. *Adv Neonatal Care.* 2005;5(6):301-314. doi:10.1016/j.adnc.2005.09.006
  159. Beighton P, De Paepe A, Steinmann B, Tsipouras P, Wenstrup RJ. Ehlers-danlos syndromes: Revised nosology, Villefranche, 1997. *Am J Med Genet.* 1998;77(1):31-37.
  160. Steinmann B, Royce PM, Superti-furga A. *Chapter 9 The Ehlers-Danlos Syndrome.* William Heinemann Medical Books; 1993.
  161. Steinmann B, Eyre D, Shao P. Urinary pyridinoline cross-links in Ehlers-Danlos syndrome type VI. *Am J Hum Genet.* 1995;57(1982):1505-1508.
  162. Mataix J, Bañuls J, Muñoz C, Bermejo A, Climent JM. Periodontal Ehlers-Danlos syndrome associated with type III and I collagen deficiencies. *Br J Dermatol.* 2008;158(4):825-830. doi:10.1111/j.1365-2133.2008.08434.x
  163. Malfait F, Francomano C, Byers P, et al. The 2017 international classification of

- the Ehlers–Danlos syndromes. *Am J Med Genet Part C Semin Med Genet*. 2017;175(1):8-26. doi:10.1002/ajmg.c.31552
164. Adikaram SGS, Chathurangana PW, Perera TMR. Classic Ehlers-Danlos syndrome. *Sri Lanka Journal of Child Health*. doi:10.4038/slch.v43i1.6667
  165. De Paepe A, Malfait F. Bleeding and bruising in patients with Ehlers-Danlos syndrome and other collagen vascular disorders. *Br J Haematol*. 2004;127(5):491-500. doi:10.1111/j.1365-2141.2004.05220.x
  166. Fernandes NF, Schwartz RA. A “hyperextensive” review of Ehlers-Danlos syndrome. *Cutis*. 2008;82(4):242-248. <http://www.ncbi.nlm.nih.gov/pubmed/19055167>.
  167. Poppe H, Hamm H. Piezogenic papules in ehlers-danlos syndrome. *J Pediatr*. 2013;163(6):1788. doi:10.1016/j.jpeds.2013.07.035
  168. De Coster PJ, Martens LC, De Paepe A. Oral health in prevalent types of Ehlers-Danlos syndromes. *J Oral Pathol Med*. 2005;34(5):298-307. doi:10.1111/j.1600-0714.2004.00300.x
  169. Moore MM, Votava JM, Orlow SJ, Schaffer J V. Ehlers-Danlos syndrome type VIII: Periodontitis, easy bruising, marfanoid habitus, and distinctive facies. *J Am Acad Dermatol*. 2006;55(2 SUPPL.):S41-5. doi:10.1016/j.jaad.2006.02.024
  170. Lum YW, Brooke BS, Black JH. Contemporary management of vascular Ehlers-Danlos syndrome. *Curr Opin Cardiol*. 2011;26(6):494-501. doi:10.1097/HCO.0b013e32834ad55a
  171. Wendorff H, Pelisek J, Zimmermann A, et al. Early venous manifestation of Ehlers-Danlos syndrome Type IV through a novel mutation in COL3A1. *Cardiovasc Pathol*. 2013;22(6):488-492. doi:10.1016/j.carpath.2013.04.003
  172. Muller GA, Hansen U, Xu Z, et al. Allele-specific siRNA knockdown as a personalized treatment strategy for vascular Ehlers-Danlos syndrome in human fibroblasts. *FASEB J*. 2012;26(2):668-677. doi:10.1096/fj.11-182162
  173. Dame C, Hausser I, Geukens J, Brenner RE. Diagnosis and Discussion: Ehlers-Danlos Syndrome Classic Type. *Arch Pediatr Adolesc Med*. 2001;155:1275-1276.
  174. Bolton-Maggs PHB, Perry DJ, Chalmers EA, et al. The rare coagulation disorders - Review with guidelines for management from the United Kingdom Haemophilia Centre Doctors' Organisation. *Haemophilia*. 2004;10(5):593-628. doi:10.1111/j.1365-2516.2004.00944.x
  175. Levy HP. Ehlers-Danlos Syndrome, Hypermobility Type. GeneReviews(®). doi:NBK1279 [bookaccession]
  176. Yeowell H, Steinmann B. Ehlers-Danlos Syndrome , Kyphoscoliotic Form. Ncib.
  177. Baumann M, Giunta C, Krabichler B, et al. Mutations in FKBP14 cause a variant of Ehlers-Danlos syndrome with progressive kyphoscoliosis, myopathy, and hearing loss. *Am J Hum Genet*. 2012;90(2):201-216. doi:10.1016/j.ajhg.2011.12.004
  178. LeRoy E, Medsger T. Criteria for the classification of early systemic sclerosis. *J Rheumatol*. 2001;28(7). <http://www.jrheum.org/content/28/7/1573.short>. Accessed May 26, 2015.
  179. D'Angelo WA, Fries JF, Masi AT, Shulman LE. Pathologic observations in systemic sclerosis (scleroderma). *Am J Med*. 1969;46(3):428-440. doi:10.1016/0002-9343(69)90044-8



180. Warden SJ, Mantila Roosa SM. Physical activity completed when young has residual bone benefits at 94 years of age: A within-subject controlled case study. *J Musculoskelet Neuronal Interact.* 2014;14(2):239-243. doi:10.1038/nature13314.A
181. Englert H, Brennan P, McNeil D, Black C, Silman AJ. Reproductive function prior to disease onset in women with scleroderma. *J Rheumatol.* 1992;19(10):1575-1579. <http://europepmc.org/abstract/MED/1464871>.
182. Nietert PJ, Silver RM. Systemic sclerosis: Environmental and occupational risk factors. *Curr Opin Rheumatol.* 2000;12(6):520-526. doi:10.1097/00002281-200011000-00008
183. Pelletier JP, Martel-Pelletier J AS. Osteoarthritis, an inflammatory disease: potential implication for the selection of new therapeutic targets. *Arthritis Rheum.* 2001;44(6):1237-1247. doi:10.1002/1529-0131(200106)44
184. Katsumoto TR, Whitfield ML, Connolly MK. The Pathogenesis of Systemic Sclerosis. *Annu Rev Pathol Mech Dis.* 2011;6(1):509-537. doi:10.1146/annurev-pathol-011110-130312
185. Rosenbloom J, Feldman G, Freundlich B, Jimenez SA. Inhibition of excessive scleroderma fibroblast collagen production by recombinant  $\gamma$ -interferon: Association with a coordinate decrease in types I and III procollagen messenger RNA levels. *Arthritis Rheum.* 1986;29(7):851-856. doi:10.1002/art.1780290706
186. Kreuter A. Localized scleroderma. *Dermatol Ther.* 2012;25(2):135-147. doi:10.1111/j.1529-8019.2012.01479.x
187. Peterson LS, Nelson AM, Su WPD. Classification of Morphea (Localized Scleroderma). *Mayo Clin Proc.* 1995;70(11):1068-1076. doi:10.4065/70.11.1068
188. Simeón-Aznar CP, Tolosa-Vilella C, Gabarró-Juliá L, et al. Systemic sclerosis sine scleroderma and limited cutaneous systemic sclerosis: similarities and differences. *Clin Exp Rheumatol.* 2014;32(6). <http://europepmc.org/abstract/med/24776173>. Accessed May 26, 2015.
189. Mayes MD, Lacey J V., Beebe-Dimmer J, et al. Prevalence, incidence, survival, and disease characteristics of systemic sclerosis in a large US population. *Arthritis Rheum.* 2003;48(8):2246-2255. doi:10.1002/art.11073
190. Goulabchand R, Khellaf L, Forestier A, et al. Acute and regressive scleroderma concomitant to an acute CMV primary infection. *J Clin Virol.* 2014;61(4):604-607. doi:10.1016/j.jcv.2014.10.003
191. Abignano G, Aydin SZ, Castillo-Gallego C, et al. Virtual skin biopsy by optical coherence tomography: The first quantitative imaging biomarker for scleroderma. *Ann Rheum Dis.* 2013;72(11):1845-1851. doi:10.1136/annrheumdis-2012-202682
192. Jimenez SA, Hitraya E, Varga J. Pathogenesis of scleroderma. Collagen. *Rheum Dis Clin North Am.* 1996;22(4):647-674. doi:10.1016/S0889-857X(05)70294-5
193. Minier T, Guiducci S, Bellando-Randone S, et al. Preliminary analysis of the Very Early Diagnosis of Systemic Sclerosis (VEDOSS) EUSTAR multicentre study: Evidence for puffy fingers as a pivotal sign for suspicion of systemic sclerosis. *Ann Rheum Dis.* 2014;73(12):2087-2093. doi:10.1136/annrheumdis-2013-203716
194. Pavlov-Dolijanovic S, Damjanov NS, Stojanovic RM, Vujasinovic Stupar NZ,

- Stanisavljevic DM. Scleroderma pattern of nailfold capillary changes as predictive value for the development of a connective tissue disease: A follow-up study of 3,029 patients with primary Raynaud's phenomenon. *Rheumatol Int.* 2012;32(10):3039-3045. doi:10.1007/s00296-011-2109-2
195. Brinckmann J, Neess CM, Gaber Y, et al. Different pattern of collagen cross-links in two sclerotic skin diseases: Lipodermatosclerosis and circumscribed scleroderma. *J Invest Dermatol.* 2001;117(2):269-273. doi:10.1046/j.0022-202X.2001.01414.x
  196. Smith-Mungo LI, Kagan HM. Lysyl oxidase: properties, regulation and multiple forms in biology. *Matrix Biol.* 1998;16(7):387-398. doi:http://dx.doi.org/10.1016/S0945-053X(98)90012-9
  197. Orban JM, Wilson LB, Kofroth JA, El-Kurdi MS, Maul TM, Vorp DA. Crosslinking of collagen gels by transglutaminase. *J Biomed Mater Res - Part A.* 2004;68(4):756-762. doi:10.1002/jbm.a.20110
  198. Rich H, Odlyha M, Cheema U, Mudera V, Bozec L. Effects of photochemical riboflavin-mediated crosslinks on the physical properties of collagen constructs and fibrils. *J Mater Sci Mater Med.* 2014;25(1):11-21. doi:10.1007/s10856-013-5038-7
  199. Bashey RI, Jimenez SA. Increased sensitivity of scleroderma fibroblasts in culture to stimulation of protein and collagen synthesis by serum. *Biochem Biophys Res Commun.* 1977;76(4):1214-1222. doi:10.1016/0006-291X(77)90985-8
  200. Bernstein EJ, Peterson ER, Sell JL, et al. Survival of Adults With Systemic Sclerosis Following Lung Transplantation: A Nationwide Cohort Study. *Arthritis Rheumatol.* 2015;67(5):1314-1322. doi:10.1002/art.39021
  201. Li LT, Zhao J, Chen R, Wang JS. Two novel VPS33B mutations in a patient with arthrogryposis, renal dysfunction and cholestasis syndrome in mainland China. *World J Gastroenterol.* 2014;20(1):326-329. doi:10.3748/wjg.v20.i1.326
  202. Gissen P, Johnson CA, Morgan N V., et al. Mutations in VPS33B, encoding a regulator of SNARE-dependent membrane fusion, cause arthrogryposis-renal dysfunction-cholestasis (ARC) syndrome. *Nat Genet.* 2004;36(4):400-404. doi:10.1038/ng1325
  203. Gissen P, Tee L, Johnson CA, et al. Clinical and molecular genetic features of ARC syndrome. *Hum Genet.* 2006;120(3):396-409. doi:10.1007/s00439-006-0232-z
  204. Stenberg PE, McEver RP, Shuman MA, Jacques Y V., Bainton DF. A platelet alpha-granule membrane protein (GMP-140) is expressed on the plasma membrane after activation. *J Cell Biol.* 1985;101(3):880-886. doi:10.1083/jcb.101.3.880
  205. Senior RM, Griffin GL, Huang JS, Walz DA, Deuel TF. Chemotactic activity of platelet alpha granule proteins for fibroblasts. *J Cell Biol.* 1983;96(2):382-385. doi:10.1083/jcb.96.2.382
  206. Wang JS, Zhao J, Li LT. Arc syndrome with high GGT cholestasis caused by VPS33B mutations. *World J Gastroenterol.* 2014;20(16):4830-4834. doi:10.3748/wjg.v20.i16.4830
  207. Bhat S, Kumar A. Biomaterials and bioengineering tomorrow's healthcare. *Biomatter.* 2013;3(3). doi:10.4161/biom.24717

208. Nair LS, Laurencin CT. Biodegradable polymers as biomaterials. *Prog Polym Sci*. 2007;32(8-9):762-798. doi:10.1016/j.progpolymsci.2007.05.017
209. Arciola CR, Campoccia D, Montanaro L. Implant infections: Adhesion, biofilm formation and immune evasion. *Nat Rev Microbiol*. 2018;16(7):397-409. doi:10.1038/s41579-018-0019-y
210. Liu J, Kerns DG. Mechanisms of Guided Bone Regeneration: A Review. *Open Dent J*. 2014;8:56-65. doi:10.2174/1874210601408010056
211. Wang HL, Boyapati L. "PASS" principles for predictable bone regeneration. *Implant Dent*. 2006;15(1):8-17. doi:10.1097/01.id.0000204762.39826.0f
212. Schenk RK, Buser D, Hardwick WR, Dahlin C. Healing pattern of bone regeneration in membrane-protected defects: a histologic study in the canine mandible. *Int J Oral Maxillofac Implants*. 1997;9(1):13-29.
213. Nowzari H, Slots J. Microbiologic and clinical study of polytetrafluoroethylene membranes for guided bone regeneration around implants. *Int J Oral Maxillofac Implants*. 1997;10(1):67-73.
214. Tempro PJ, Nalbandian J. Colonization of Retrieved Polytetrafluoroethylene Membranes: Morphological and Microbiological Observations. *J Periodontol*. 1993;64(3):162-168. doi:10.1902/jop.1993.64.3.162
215. Rasmusson L, Sennerby L, Lundgren D, Nyman S. Morphological and dimensional changes after barrier removal in bone formed beyond the skeletal borders at titanium implants: A kinetic study in the rabbit tibia. *Clin Oral Implants Res*. 1997;8(2):103-116. doi:10.1034/j.1600-0501.1997.080205.x
216. Bunyaratavej P, Wang H-L. Collagen Membranes: A Review. *J Periodontol*. 2001;72(2):215-229. doi:10.1902/jop.2001.72.2.215
217. Xu C, Lei C, Meng L, Wang C, Song Y. Chitosan as a barrier membrane material in periodontal tissue regeneration. *J Biomed Mater Res - Part B Appl Biomater*. 2012;100(5):1435-1443. doi:10.1002/jbm.b.32662
218. Ueyama Y, Koyama T, Ishikawa K, et al. Comparison of ready-made and self-setting alginate membranes used as a barrier membrane for guided bone regeneration. *J Mater Sci Mater Med*. 2006. doi:10.1007/s10856-006-7315-1
219. Jung RE, Fenner N, Hämmerle CHF, Zitzmann NU. Long-term outcome of implants placed with guided bone regeneration (GBR) using resorbable and non-resorbable membranes after 12-14 years. *Clin Oral Implants Res*. 2013;24(10):1065-1073. doi:10.1111/j.1600-0501.2012.02522.x
220. Calciolari E, Ravanetti F, Strange A, et al. Degradation pattern of a porcine collagen membrane in an in vivo model of guided bone regeneration. *J Periodontol Res*. 2018;53(3):430-439. doi:10.1111/jre.12530
221. Ashworth JC, Mehr M, Buxton PG, Best SM, Cameron RE. Parameterizing the Transport Pathways for Cell Invasion in Complex Scaffold Architectures. *Tissue Eng Part C Methods*. 2016;22(5):409-417. doi:10.1089/ten.tec.2015.0483
222. Henriksen K, Karsdal MA. Type I Collagen. *Biochem Collagens, Laminins Elastin*. January 2016:1-11. doi:10.1016/B978-0-12-809847-9.00001-5
223. Rothamel D, Schwarz F, Sculean A, Hertel M, Scherbaum W, Becker J. Biocompatibility of various collagen membranes in cultures of human PDL fibroblasts and human osteoblast-like cells. *Clin Oral Implants Res*. 2004;15(4):443-449. doi:10.1111/j.1600-0501.2004.01039.x

224. Behring J, Junker R, Walboomers XF, Chessnut B, Jansen JA. Toward guided tissue and bone regeneration: Morphology, attachment, proliferation, and migration of cells cultured on collagen barrier membranes. A systematic review. *Odontology*. 2008;96(1):1-11. doi:10.1007/s10266-008-0087-y
225. Nagase H, Visse R, Murphy G. Structure and function of matrix metalloproteinases and TIMPs. *Cardiovasc Res*. 2006;69(3):562-573. doi:10.1016/j.cardiores.2005.12.002
226. Owens KW, Yukna RA. Collagen membrane resorption in dogs: A comparative study. *Implant Dent*. 2001;10(1):49-58. doi:10.1097/00008505-200101000-00016
227. Lee SH, Shin H. Matrices and scaffolds for delivery of bioactive molecules in bone and cartilage tissue engineering. *Adv Drug Deliv Rev*. 2007;59(4-5):339-359. doi:10.1016/j.addr.2007.03.016
228. Buermans HPJ, den Dunnen JT. Next generation sequencing technology: Advances and applications. *Biochim Biophys Acta - Mol Basis Dis*. 2014;1842(10):1932-1941. doi:10.1016/j.bbadis.2014.06.015
229. Boisseau P, Loubaton B. Nanomedicine, nanotechnology in medicine. *Comptes Rendus Phys*. 2011;12(7):620-636. doi:10.1016/j.crhy.2011.06.001
230. Burr DB. Anatomy and physiology of the mineralized tissues: Role in the pathogenesis of osteoarthritis. *Osteoarthr Cartil*. 2004;12(SUPPL.):20-30. doi:10.1016/j.joca.2003.09.016
231. Iwase H, Greenman JM, Barnes DM, Hodgson S, Bobrow L, Mathew CG. Sequence variants of the estrogen receptor (ER) gene found in breast cancer patients with ER negative and progesterone receptor positive tumors. *Cancer Lett*. 1996;108(2):179-184. doi:10.1016/S0304-3835(96)04406-0
232. Moghimi SM, Hunter AC, Murray JC. Nanomedicine: current status and future prospects. *FASEB J*. 2005;19(3):311-330. doi:10.1096/fj.04-2747rev
233. Riehemann K, Schneider SW, Luger TA, Godin B, Ferrari M, Fuchs H. Nanomedicine - Challenge and perspectives. *Angew Chemie - Int Ed*. 2009;48(5):872-897. doi:10.1002/anie.200802585
234. Marchesan S, Prato M. Nanomaterials for (Nano)medicine. *ACS Med Chem Lett*. 2013;4(2):147-149. doi:10.1021/ml3003742
235. Farokhzad OC, Jon S, Khademhosseini A, Tran TNT, LaVan DA, Langer R. Nanoparticle-aptamer bioconjugates: A new approach for targeting prostate cancer cells. *Cancer Res*. 2004;64(21):7668-7672. doi:10.1158/0008-5472.CAN-04-2550
236. Hanahan D, Weinberg RA. The Hallmarks of Cancer. *Cell*. 2000;100(1):57-70. doi:https://doi.org/10.1016/S0092-8674(00)81683-9
237. Sweedler J V., Arriaga EA. Single cell analysis. *Anal Bioanal Chem*. 2007;387(1):1-2. doi:10.1007/s00216-006-0921-4
238. Engelberg S, Modrejewski J, Walter JG, Livney YD, Assaraf YG. Cancer cell-selective, clathrin-mediated endocytosis of aptamerdecorated nanoparticles. *Oncotarget*. 2018;9(30):20993-21006. doi:10.18632/oncotarget.24772
239. Benson RS. Use of radiation in biomaterials science. *Nucl Instruments Methods Phys Res Sect B Beam Interact with Mater Atoms*. 2002;191(1-4):752-757. doi:10.1016/S0168-583X(02)00647-X
240. DePaola DP. The revitalization of U.S. dental education. *J Dent Educ*. 2008;72(2

- Suppl):28-42. <http://www.ncbi.nlm.nih.gov/pubmed/18250376>.
241. Neel EAA, Bozec L, Perez RA, Kim HW, Knowles JC. Nanotechnology in dentistry: Prevention, diagnosis, and therapy. *Int J Nanomedicine*. 2015;10:6371-6394. doi:10.2147/IJN.S86033
  242. Li Y, Denny P, Ho CM, et al. The Oral Fluid MEMS/NEMS Chip (OFMNC): diagnostic and translational applications. *Adv Dent Res*. 2005;18(1):3-5. doi:10.1177/154407370501800102
  243. Lui C, Cady NC, Batt CA. Nucleic acid-based detection of bacterial pathogens using integrated microfluidic platform systems. *Sensors*. 2009;9(5):3713-3744. doi:10.3390/s90503713
  244. Lu N, Hu Y, Zhu L, et al. DNA microarray analysis reveals that antibiotic resistance-gene diversity in human gut microbiota is age related. *Sci Rep*. 2014;4:4302. doi:10.1038/srep04302
  245. Perreten V, Vorlet-Fawer L, Slickers P, Ehricht R, Kuhnert P, Frey J. Microarray-based detection of 90 antibiotic resistance genes of gram-positive bacteria. *J Clin Microbiol*. 2005;43(5):2291-2302. doi:10.1128/JCM.43.5.2291-2302.2005
  246. Pelaz B, Alexiou C, Alvarez-Puebla RA, et al. Diverse Applications of Nanomedicine. *ACS Nano*. 2017;11(3):2313-2381. doi:10.1021/acsnano.6b06040
  247. Herr AE, Hatch A V., Throckmorton DJ, et al. Microfluidic immunoassays as rapid saliva-based clinical diagnostics. *Proc Natl Acad Sci*. 2007;104(13):5268-5273. doi:10.1073/pnas.0607254104
  248. Segal A, Wong DT. Salivary diagnostics: Enhancing disease detection and making medicine better. *Eur J Dent Educ*. 2008;12(SUPPL. 1):22-29. doi:10.1111/j.1600-0579.2007.00477.x
  249. Yager P, Edwards T, Fu E, et al. Microfluidic diagnostic technologies for global public health. *Nature*. 2006;442(7101):412-418. doi:10.1038/nature05064
  250. Fuentes L, Yakob M, Wong DTW. Emerging horizons of salivary diagnostics for periodontal disease. *Br Dent J*. 2014;217(10):567-573. doi:10.1038/sj.bdj.2014.1005
  251. Kwon J, Hong J, Kim YS, et al. Atomic force microscope with improved scan accuracy, scan speed, and optical vision. *Rev Sci Instrum*. 2003;74(10):4378-4383. doi:10.1063/1.1610782
  252. Binning G, Rohrer H, Gerber C, Weibel E. Surface studies by scanning tunneling microscopy. *Phys Rev Lett*. 1982;49(1):57-61. doi:10.1103/PhysRevLett.49.57
  253. Sasagawa I. Fine structure of the cap enameloid and of the dental epithelial cells during enameloid mineralisation and early maturation stages in the tilapia, a teleost. *J Anat*. 1997;190(4):589-600. doi:10.1017/S002187829700201X
  254. Olbrich M, Punshon G, Frischauf I, et al. UV surface modification of a new nanocomposite polymer to improve cytocompatibility. *J Biomater Sci Polym Ed*. 2007;18(4):453-468. doi:10.1163/156856207780425059
  255. Pyne ALB, Hoogenboom BW. Imaging DNA structure by atomic force microscopy. *Methods Mol Biol*. 2016;1431:47-60. doi:10.1007/978-1-4939-3631-1\_5
  256. Pyne A, Thompson R, Leung C, Roy D, Hoogenboom BW. Single-molecule reconstruction of oligonucleotide secondary structure by atomic force microscopy. *Small*. 2014;10(16):3257-3261. doi:10.1002/smll.201400265

257. Wei Q, Luo W, Chiang S, et al. Imaging and sizing of single DNA molecules on a mobile phone. *ACS Nano*. 2014;8(12):12725-12733. doi:10.1021/nn505821y
258. Rief M, Gautel M, Oesterhelt F, Fernandez JM, Gaub HE. Reversible unfolding of individual titin immunoglobulin domains by AFM. *Science* (80- ). 1997;276(5315):1109-1112. doi:10.1126/science.276.5315.1109
259. Wang D, Ye J, Hudson SD, Scott KCK, Lin-Gibson S. Effects of nanoparticle size and charge on interactions with self-assembled collagen. *J Colloid Interface Sci*. 2014;417:244-249. doi:10.1016/j.jcis.2013.11.019
260. Gosal W, Myers S, Radford S, Thomson N. Amyloid Under the Atomic Force Microscope. *Protein Pept Lett*. 2006;13(3):261-270. doi:10.2174/092986606775338498
261. Rekhater MD. Collagen synthesis in atherosclerosis: Too much and not enough. *Cardiovasc Res*. 1999;41(2):376-384. doi:10.1016/S0008-6363(98)00321-6
262. Canale C, Oropesa-Nuñez R, Diaspro A, Dante S. Amyloid and membrane complexity: The toxic interplay revealed by AFM. *Semin Cell Dev Biol*. 2018;73:82-94. doi:10.1016/j.semcdb.2017.08.046
263. Marzec KM, Wrobel TP, Rygula A, et al. Visualization of the biochemical markers of atherosclerotic plaque with the use of Raman, IR and AFM. *J Biophotonics*. 2014;7(9):744-756. doi:10.1002/jbio.201400014
264. Hayashi K, Iwata M. Stiffness of cancer cells measured with an AFM indentation method. *J Mech Behav Biomed Mater*. 2015;49:105-111. doi:10.1016/j.jmbbm.2015.04.030
265. Sundar Rajan V, Laurent VM, Verdier C, Duperray A. Unraveling the Receptor-Ligand Interactions between Bladder Cancer Cells and the Endothelium Using AFM. *Biophys J*. 2017;112(6):1246-1257. doi:10.1016/j.bpj.2017.01.033
266. Calzado-Martín A, Encinar M, Tamayo J, Calleja M, San Paulo A. Effect of Actin Organization on the Stiffness of Living Breast Cancer Cells Revealed by Peak-Force Modulation Atomic Force Microscopy. *ACS Nano*. 2016;10(3):3365-3374. doi:10.1021/acsnano.5b07162
267. Fang HHP, Chan KY, Xu LC. Quantification of bacterial adhesion forces using atomic force microscopy (AFM). *J Microbiol Methods*. 2000;40(1):89-97. doi:10.1016/S0167-7012(99)00137-2
268. Alsteens D, Garcia MC, Lipke PN, Dufrene YF. Force-induced formation and propagation of adhesion nanodomains in living fungal cells. *Proc Natl Acad Sci*. 2010;107(48):20744-20749. doi:10.1073/pnas.1013893107
269. Doktycz MJ, Sullivan CJ, Hoyt PR, Pelletier DA, Wu S, Allison DP. AFM imaging of bacteria in liquid media immobilized on gelatin coated mica surfaces. *Ultramicroscopy*. 2003;97(1-4):209-216. doi:10.1016/S0304-3991(03)00045-7
270. Hyonchol K, Arakawa H, Osada T, Ikai A. Quantification of fibronectin and cell surface interactions by AFM. *Colloids Surfaces B Biointerfaces*. 2002;25(1):33-43. doi:10.1016/S0927-7765(01)00299-5
271. Aguayo S, Donos N, Spratt D, Bozec L. Single-bacterium nanomechanics in biomedicine: Unravelling the dynamics of bacterial cells. *Nanotechnology*. 2015;26(6):62001. doi:10.1088/0957-4484/26/6/062001
272. Van Helvert S, Friedl P. Strain Stiffening of Fibrillar Collagen during Individual and Collective Cell Migration Identified by AFM Nanoindentation. *ACS Appl Mater*

- Interfaces*. 2016;8(34):21946-21955. doi:10.1021/acsami.6b01755
273. Parbhu AN, Bryson WG, Lal R. Disulfide bonds in the outer layer of keratin fibers confer higher mechanical rigidity: Correlative nano-indentation and elasticity measurement with an AFM. *Biochemistry*. 1999;38(36):11755-11761. doi:10.1021/bi990746d
  274. Oh YJ, Hinterdorfer P. Sensing the ultrastructure of bacterial surfaces and their molecular binding forces using AFM. In: Lyubchenko YL, ed. *Methods in Molecular Biology*. Vol 1814. New York, NY: Springer New York; 2018:363-372. doi:10.1007/978-1-4939-8591-3\_21
  275. Mitsi M, Handschin S, Gerber I, et al. The ultrastructure of fibronectin fibers pulled from a protein monolayer at the air-liquid interface and the mechanism of the sheet-to-fiber transition. *Biomaterials*. 2015;36:66-79. doi:10.1016/j.biomaterials.2014.08.012
  276. Khademhosseini A, Chan WWC, Chhowalla M, et al. Nanoscience and Nanotechnology Cross Borders. *ACS Nano*. 2017;11(2):1123-1126. doi:10.1021/acsnano.7b00953
  277. Bozec L, Horton M. Topography and mechanical properties of single molecules of type I collagen using atomic force microscopy. *Biophys J*. 2005;88(6):4223-4231. doi:10.1529/biophysj.104.055228
  278. Jackson DS, Cleary EG. The determination of collagen and elastin. *Methods Biochem Anal*. 1967;15(186):25-76. doi:10.1002/9780470110331.ch2
  279. Grant CA, Brockwell DJ, Radford SE, Thomson NH. Tuning the elastic modulus of hydrated collagen fibrils. *Biophys J*. 2009;97(11):2985-2992. doi:10.1016/j.bpj.2009.09.010
  280. Ahmed T, Nash A, Clark KENN, et al. Combining nano-physical and computational investigations to understand the nature of “aging” in dermal collagen. *Int J Nanomedicine*. 2017;12:3303-3314. doi:10.2147/IJN.S121400
  281. Craig JA, Rexeisen EL, Mardilovich A, Shroff K, Kokkoli E. Effect of linker and spacer on the design of a fibronectin-mimetic peptide evaluated via cell studies and AFM adhesion forces. *Langmuir*. 2008;24(18):10282-10292. doi:10.1021/la702434p
  282. Hsueh YJ, Huang SF, Lai JY, et al. Preservation of epithelial progenitor cells from collagenase-digested oral mucosa during ex vivo cultivation. *Sci Rep*. 2016;6. doi:10.1038/srep36266
  283. Kim SJ, Jang DH, Park WH, Min BM. Fabrication and characterization of 3-dimensional PLGA nanofiber/microfiber composite scaffolds. *Polymer (Guildf)*. 2010;51(6):1320-1327. doi:10.1016/j.polymer.2010.01.025
  284. Melling M, Karimian-Teherani D, Behnam M, Mostler S. Morphological study of the healthy human oculomotor nerve by atomic force microscopy. *Neuroimage*. 2003;20(2):795-801. doi:10.1016/S1053-8119(03)00359-8
  285. Aktas O, Wattjes MP, Stangel M, Hartung HP. Diagnosis of multiple sclerosis: revision of the McDonald criteria 2017. *Nervenarzt*. 2018;17(2):1-10. doi:10.1007/s00115-018-0550-0
  286. Heredia A, Bui CC, Suter U, Young P, Schäffer TE. AFM combines functional and morphological analysis of peripheral myelinated and demyelinated nerve fibers. *Neuroimage*. 2007;37(4):1218-1226. doi:10.1016/j.neuroimage.2007.06.007

287. Sealy C. Scaffold shape gets nerve cells into the groove. *Mater Today*. 2016;19(3):136-137. doi:10.1016/j.mattod.2016.02.005
288. Nune M, Manchineella S, Govindaraju T, Narayan KS. Melanin incorporated electroactive and antioxidant silk fibroin nanofibrous scaffolds for nerve tissue engineering. *Mater Sci Eng C*. 2019;94:17-25. doi:10.1016/j.msec.2018.09.014
289. Dirisamer M, Ham L, Dapena I, et al. Efficacy of descemet membrane endothelial keratoplasty: Clinical outcome of 200 consecutive cases after a learning curve of 25 cases. *Arch Ophthalmol*. 2011;129(11):1435-1443. doi:10.1001/archophthalmol.2011.195
290. McKee CT, Last JA, Russell P, Murphy CJ. Indentation Versus Tensile Measurements of Young's Modulus for Soft Biological Tissues. *Tissue Eng Part B Rev*. 2011;17(3):155-164. doi:10.1089/ten.teb.2010.0520
291. Di Mundo R, Recchia G, Parekh M, Ruzza A, Ferrari S, Carbone G. Sensing inhomogeneous mechanical properties of human corneal Descemet's membrane with AFM nano-indentation. *J Mech Behav Biomed Mater*. 2017;74(January):21-27. doi:10.1016/j.jmbbm.2017.05.019
292. Kaufman HE, Clower JW. Irregularities of Bowman's membrane. *Am J Ophthalmol*. 1966;61(2):227-230. doi:10.1016/0002-9394(66)90275-3
293. Țălu Ș, Stach S, Sueiras V, Ziebarth NM. Fractal Analysis of AFM Images of the Surface of Bowman's Membrane of the Human Cornea. *Ann Biomed Eng*. 2015;43(4):906-916. doi:10.1007/s10439-014-1140-3
294. Chakrabarti A, Halder S, Karmakar S. Erythrocyte and platelet proteomics in hematological disorders. *Proteomics - Clin Appl*. 2016;10(4):403-414. doi:10.1002/prca.201500080
295. Chien S. Red Cell Deformability and its Relevance to Blood Flow. *Annu Rev Physiol*. 1987;49(1):177-192. doi:10.1146/annurev.ph.49.030187.001141
296. Barns S, Balanant MA, Sauret E, Flower R, Saha S, Gu YT. Investigation of red blood cell mechanical properties using AFM indentation and coarse-grained particle method. *Biomed Eng Online*. 2017;16(1):1-21. doi:10.1186/s12938-017-0429-5
297. Maiellaro K, Taylor WR. The role of the adventitia in vascular inflammation. *Cardiovasc Res*. 2007;75(4):640-648. doi:10.1016/j.cardiores.2007.06.023
298. Han X, Li H, Hua W, et al. Fluid in the tissue channels of vascular adventitia investigated by AFM and TEM. *Clin Hemorheol Microcirc*. 2017;67(2):173-182. doi:10.3233/CH-170284
299. Hassanizadeh SM, Gray WG. Mechanics and thermodynamics of multiphase flow in porous media including interphase boundaries. *Adv Water Resour*. 1990;13(4):169-186. doi:https://doi.org/10.1016/0309-1708(90)90040-B
300. Ovchinnikova E, Hoes M, Ustyantsev K, et al. Modeling Human Cardiac Hypertrophy in Stem Cell-Derived Cardiomyocytes. *Stem Cell Reports*. 2018;10(3):794-807. doi:https://doi.org/10.1016/j.stemcr.2018.01.016
301. Chtcheglova LA, Waschke J, Wildling L, Drenckhahn D, Hinterdorfer P. Nano-scale dynamic recognition imaging on vascular endothelial cells. *Biophys J*. 2007;93(2):L11-L13. doi:10.1529/biophysj.107.109751
302. Chtcheglova LA, Wildling L, Waschke J, Drenckhahn D, Hinterdorfer P. AFM functional imaging on vascular endothelial cells. *J Mol Recognit*. 2010;23(6):589-



596. doi:10.1002/jmr.1052
303. Sicard D, Fredenburgh LE, Tschumperlin DJ. Measured pulmonary arterial tissue stiffness is highly sensitive to AFM indenter dimensions. *J Mech Behav Biomed Mater.* 2017;74(February):118-127. doi:10.1016/j.jmbbm.2017.05.039
  304. Esposito M, Ardebili Y, Worthington H V. Interventions for replacing missing teeth: Different types of dental implants. *Cochrane Database Syst Rev.* 2014;2014(7). doi:10.1002/14651858.CD003815.pub4
  305. Aguayo S, Donos N, Spratt D, Bozec L. Nanoadhesion of Staphylococcus aureus onto titanium implant surfaces. *J Dent Res.* 2015;94(8):1078-1084. doi:10.1177/0022034515591485
  306. Müller DJ, Helenius J, Alsteens D, Dufrêne YF. Force probing surfaces of living cells to molecular resolution. *Nat Chem Biol.* 2009;5(6):383-390. doi:10.1038/nchembio.181
  307. Hinterdorfer P, Dufrêne YF. Detection and localization of single molecular recognition events using atomic force microscopy. *Nat Methods.* 2006;3(5):347-355. doi:10.1038/nmeth871
  308. Moynihan P, Lussi A, Jaeggi T, Schaffner M. Diet and dental erosion. *Nutrition.* 2002;18(9):780-781. doi:10.1016/S0899-9007(02)00836-5
  309. Neel EAA, Aljabo A, Strange AP, et al. Demineralization–remineralization dynamics in teeth and bone. *Int J Nanomedicine.* 2016;11:4743-4763. doi:10.2147/IJN.S107624
  310. Meurman JH, Gate JM. Pathogenesis and modifying factors of dental erosion. *Eur J Oral Sci.* 1996;104(2):199-206. doi:10.1111/j.1600-0722.1996.tb00068.x
  311. Barbour ME, Finke M, Parker DM, Hughes JA, Allen GC, Addy M. The relationship between enamel softening and erosion caused by soft drinks at a range of temperatures. *J Dent.* 2006;34(3):207-213. doi:10.1016/j.jdent.2005.06.002
  312. Barbour ME, Shellis RP. An investigation using atomic force microscopy nanoindentation of dental enamel demineralization as a function of undissociated acid concentration and differential buffer capacity. *Phys Med Biol.* 2007;52(4):899-910. doi:10.1088/0031-9155/52/4/003
  313. Aguayo S, Strange A, Gadegaard N, Dalby MJ, Bozec L. Influence of biomaterial nanotopography on the adhesive and elastic properties of Staphylococcus aureus cells. *RSC Adv.* 2016;6(92):89347-89355. doi:10.1039/c6ra12504b
  314. Wang C, Zhao Y, Zheng S, et al. Effect of enamel morphology on nanoscale adhesion forces of streptococcal bacteria: An AFM study. *Scanning.* 2015;37(5):313-321. doi:10.1002/sca.21218
  315. Ceci M, Mirando M, Beltrami R, Chiesa M, Colombo M, Poggio C. Effect of self-assembling peptide P11-4 on enamel erosion: AFM and SEM studies. *Scanning.* 2016;38(4):344-351. doi:10.1002/sca.21276
  316. Rianna C, Radmacher M. Cell mechanics as a marker for diseases: Biomedical applications of AFM. *AIP Conf Proc.* 2016;1760. doi:10.1063/1.4960276
  317. Taichman DB, Sahni P, Pinborg A, et al. Data Sharing Statements for Clinical Trials: A Requirement of the International Committee of Medical Journal Editors. *PLoS Med.* 2017;14(6):63-65. doi:10.1371/journal.pmed.1002315
  318. Happonen SM, Halkoaho A, Lehto SM, Keränen T. The effect of study type on research ethics committees' queries in medical studies. *Res Ethics.* 2016;13(3-

- 4):115-127. doi:10.1177/1747016116656912
319. Smajdor A, Sydes MR, Gelling L, Wilkinson M. Practice Pointer: Applying for ethical approval for research in the United Kingdom. *BMJ*. 2009;339(7727):968-971. doi:10.1136/bmj.b4013
  320. Kurland NE, Drira Z, Yadavalli VK. Measurement of nanomechanical properties of biomolecules using atomic force microscopy. *Micron*. 2012;43(2-3):116-128. doi:10.1016/j.micron.2011.07.017
  321. Wu JW, Huang KC, Chiang ML, Chen MY, Fu LC. Modeling and controller design of a precision hybrid scanner for application in large measurement-range atomic force microscopy. *IEEE Trans Ind Electron*. 2014;61(7):3704-3712. doi:10.1109/TIE.2013.2279352
  322. Schillers H. Measuring the elastic properties of living cells. In: Santos NC, Carvalho FA, eds. *Methods in Molecular Biology*. Vol 1886. New York, NY: Springer New York; 2019:291-313. doi:10.1007/978-1-4939-8894-5\_17
  323. Schillers H, Rianna C, Schäpe J, et al. Standardized Nanomechanical Atomic Force Microscopy Procedure (SNAP) for Measuring Soft and Biological Samples. *Sci Rep*. 2017;7(1):1-9. doi:10.1038/s41598-017-05383-0
  324. Zhou M, Smith AM, Das AK, et al. Self-assembled peptide-based hydrogels as scaffolds for anchorage-dependent cells. *Biomaterials*. 2009;30(13):2523-2530. doi:10.1016/j.biomaterials.2009.01.010
  325. Rajabinejad H, Patrucco A, Caringella R, Montarsolo A, Zoccola M, Pozzo PD. Preparation of keratin-based microcapsules for encapsulation of hydrophilic molecules. *Ultrason Sonochem*. 2018;40:527-532. doi:10.1016/j.ultsonch.2017.07.039
  326. Casdorff K, Keplinger T, Burgert I. Nano-mechanical characterization of the wood cell wall by AFM studies: Comparison between AC- and QI™ mode. *Plant Methods*. 2017;13(1):60. doi:10.1186/s13007-017-0211-5
  327. Smolyakov G, Pruvost S, Cardoso L, Alonso B, Belamie E, Duchet-Rumeau J. AFM PeakForce QNM mode: Evidencing nanometre-scale mechanical properties of chitin-silica hybrid nanocomposites. *Carbohydr Polym*. 2016;151:373-380. doi:https://doi.org/10.1016/j.carbpol.2016.05.042
  328. Roberts WE. Skin Type Classification Systems Old and New. *Dermatol Clin*. 2009;27(4):529-533. doi:10.1016/j.det.2009.08.006
  329. Wilkes M, Wright CY, Du Plessis JL, Reeder A. Fitzpatrick skin type, individual typology angle, and melanin index in an African population: Steps toward universally applicable skin photosensitivity assessments. *JAMA Dermatology*. 2015;151(8):902-903. doi:10.1001/jamadermatol.2015.0351
  330. Yang J, Guo X, Tong X, Tao J. Treatment of venous lake with multiwavelength 595 and 1064 nm lasers in Asian Fitzpatrick skin type IV patients. *Photodermatol Photoimmunol Photomed*. 2017;33(5):267-270. doi:10.1111/phpp.12317
  331. Hulshof L, Hack DP, Hasnoe QCJ, et al. A minimally invasive tool to study immune response and skin barrier in children with atopic dermatitis. *Br J Dermatol*. 2018;0-3. doi:10.1111/bjd.16994
  332. Estanqueiro M, Conceição J, Amaral MH, Lobo JMS. Chapter 12 - The role of liposomes and lipid nanoparticles in the skin hydration. In: Grumezescu AM, ed. *Nanobiomaterials in Galenic Formulations and Cosmetics*. William Andrew

- Publishing; 2016:297-326. doi:<https://doi.org/10.1016/B978-0-323-42868-2.00012-7>
333. Grant CA, Twigg PC, Baker R, Tobin DJ. Tattoo ink nanoparticles in skin tissue and fibroblasts. *Beilstein J Nanotechnol.* 2015;6(1):1183-1191. doi:10.3762/bjnano.6.120
  334. Kluger N, Koljonen V. Tattoos, inks, and cancer. *Lancet Oncol.* 2012;13(4):e161-e168. doi:10.1016/S1470-2045(11)70340-0
  335. Katz EP, Li ST. Structure and function of bone collagen fibrils. *J Mol Biol.* 1973;80(1):1-15. doi:10.1016/0022-2836(73)90230-1
  336. Grant CA, Twigg PC, Tobin DJ. Nano-scale observations of tattoo pigments in skin by atomic force microscopy. *Curr Probl Dermatology.* 2015;48:97-102. doi:10.1159/000369187
  337. Argyropoulos AJ, Robichaud P, Balimunkwe RM, et al. Alterations of dermal connective tissue collagen in diabetes: Molecular basis of aged-appearing skin. *PLoS One.* 2016;11(4):1-17. doi:10.1371/journal.pone.0153806
  338. Shao Y, He T, Fisher GJ, Voorhees JJ, Quan T. Molecular basis of retinol anti-ageing properties in naturally aged human skin in vivo. *Int J Cosmet Sci.* 2017;39(1):56-65. doi:10.1111/ics.12348
  339. Shao Y, Qin Z, Alexander Wilks J, et al. Physical properties of the photodamaged human skin dermis: Rougher collagen surface and stiffer/harder mechanical properties. *Exp Dermatol.* 2018;(June):1-8. doi:10.1111/exd.13728
  340. Pilkington S, Griffiths CEM, Watson REB, et al. Structural and compositional diversity of fibrillin microfibrils in human tissues. *J Biol Chem.* 2018;293(14):5117-5133. doi:10.1074/jbc.ra117.001483
  341. Hibbert SA, Costello P, O'Connor C, et al. A new in vitro assay to test UVR protection of dermal extracellular matrix components by a flat spectrum sunscreen. *J Photochem Photobiol B Biol.* 2017;175:58-64. doi:10.1016/j.jphotobiol.2017.08.020
  342. Kontomaris S V., Yova D, Sambani K, Stylianou A. AFM investigation of the influence of red light irradiation on collagen. In: Kyriacou E, Christofides S, Pattichis CS, eds. *IFMBE Proceedings*. Vol 57. Cham: Springer International Publishing; 2016:269-274. doi:10.1007/978-3-319-32703-7\_54
  343. Kontomaris S V., Yova D, Stylianou A, Balogiannis G. The effects of UV irradiation on collagen D-band revealed by atomic force microscopy. *Scanning.* 2015;37(2):101-111. doi:10.1002/sca.21185
  344. Kastelic J, Galeski A, Baer E. The multicomposite ultrastructure of tendon. *Connect Tissue Res.* 1978;6(1):11-23. doi:10.3109/03008207809152283
  345. Hansen P, Bojsen-Moller J, Aagaard P, Kjaer M, Magnusson SP. Mechanical properties of the human patellar tendon, in vivo. *Clin Biomech.* 2006;21(1):54-58. doi:<https://doi.org/10.1016/j.clinbiomech.2005.07.008>
  346. Pennisi E. Tending tender tendons. *Science (80- ).* 2002;295(5557):1011. doi:10.1126/science.295.5557.1011
  347. Benjamin M, Ralphs JR. Tendons and ligaments - An overview. *Histol Histopathol.* 1997;12(4):1135-1144. doi:10.1111/j.1741-3737.2000.00792.x
  348. Dex S, Alberton P, Willkomm L, et al. Tenomodulin is Required for Tendon Endurance Running and Collagen I Fibril Adaptation to Mechanical Load.

- EBioMedicine*. 2017;20:240-254. doi:10.1016/j.ebiom.2017.05.003
349. Holmes DF, Lu Y, Starborg T, Kadler KE. *Collagen Fibril Assembly and Function*. Vol 130. 1st ed. Elsevier Inc.; 2018. doi:10.1016/bs.ctdb.2018.02.004
  350. Veres SP, Harrison JM, Lee JM. Mechanically overloading collagen fibrils uncoils collagen molecules, placing them in a stable, denatured state. *Matrix Biol*. 2014;33:54-59. doi:10.1016/j.matbio.2013.07.003
  351. Elliot D. Structure and Function of Mammalian Tendon. *Biol Rev Camb Philos Soc*. 1965;40(3):392-421. doi:10.1111/j.1469-185X.1965.tb00808.x
  352. Veres SP, Deska-Gauthier D, Légaré F, Kreplak L, Quigley AS, Bancelin S. In tendons, differing physiological requirements lead to functionally distinct nanostructures. *Sci Rep*. 2018;8(1):1-14. doi:10.1038/s41598-018-22741-8
  353. Orgel JPRO, San Antonio JD, Antipova O. Molecular and structural mapping of collagen fibril interactions. *Connect Tissue Res*. 2011;52(1):2-17. doi:10.3109/03008207.2010.511353
  354. Szczesny SE, Aeppli C, David A, Mauck RL. Fatigue loading of tendon results in collagen kinking and denaturation but does not change local tissue mechanics. *J Biomech*. 2018;71:251-256. doi:10.1016/j.jbiomech.2018.02.014
  355. Kidoaki S, Kwon IK, Matsuda T. Mesoscopic spatial designs of nano- and microfiber meshes for tissue-engineering matrix and scaffold based on newly devised multilayering and mixing electrospinning techniques. *Biomaterials*. 2005;26(1):37-46. doi:10.1016/j.biomaterials.2004.01.063
  356. Ma M, Ma L, Yu W, Zhang X, Shen Y, Zhang Y. Research on rapid gelatinization of rabbit skin collagen as effect of acid treatment. *Food Hydrocoll*. 2018;77:945-951. doi:10.1016/j.foodhyd.2017.11.042
  357. Reichling M, Barth C. No Title. In: Morita S, Wiesendanger R, Meyer E, eds. *Noncontact Atomic Force Microscopy*. 1st ed. Berlin: Springer Verlag; 2002.
  358. Brand U, Gao S, Engl W, et al. Comparing AFM cantilever stiffness measured using the thermal vibration and the improved thermal vibration methods with that of an SI traceable method based on MEMS. *Meas Sci Technol*. 2017;28(3). doi:10.1088/1361-6501/28/3/034010
  359. Butt HJ, Cappella B, Kappl M. Force measurements with the atomic force microscope: Technique, interpretation and applications. *Surf Sci Rep*. 2005;59(1-6):1-152. doi:10.1016/j.surfrep.2005.08.003
  360. Gibson CT, Watson GS, Myhra S. analysis cantilevers Determination of the spring constants of probes for force microscopy / spectroscopy. *Nanotechnology*. 1996;7:259-262. doi:129.234.0.68
  361. Mascaro A, Miyahara Y, Dagdeviren OE, Grütter P. Eliminating the effect of acoustic noise on cantilever spring constant calibration. *Appl Phys Lett*. 2018;113(23):233105. doi:10.1063/1.5063992
  362. Kinnear C, Moore TL, Rodriguez-Lorenzo L, Rothen-Rutishauser B, Petri-Fink A. Form Follows Function: Nanoparticle Shape and Its Implications for Nanomedicine. *Chem Rev*. 2017;117(17):11476-11521. doi:10.1021/acs.chemrev.7b00194
  363. Cheng X, Putz KW, Wood CD, Brinson LC. Characterization of local elastic modulus in confined polymer films via AFM indentation. *Macromol Rapid Commun*. 2015;36(4):391-397. doi:10.1002/marc.201400487

364. Bouchonville N, Nicolas A. Quantification of the elastic properties of soft and sticky materials using AFM. In: Santos NC, Carvalho FA, eds. *Methods in Molecular Biology*. Vol 1886. Lisbon: Springer; 2019:281-290. doi:10.1007/978-1-4939-8894-5\_16
365. Dong XN, Guo XE. The dependence of transversely isotropic elasticity of human femoral cortical bone on porosity. *J Biomech*. 2004;37(8):1281-1287. doi:10.1016/j.jbiomech.2003.12.011
366. Lin DC, Horkay F. Nanomechanics of polymer gels and biological tissues: A critical review of analytical approaches in the Hertzian regime and beyond. *Soft Matter*. 2008;4(4):669-682. doi:10.1039/b714637j
367. H. Korayem M, Rastegar Z, Taheri M. Sensitivity Analysis of Nano-contact Mechanics Models in Manipulation of Biological Cell. *Nanosci Nanotechnol*. 2012;2(3):49-56. doi:10.5923/j.nn.20120203.02
368. Grierson DS, Flater EE, Carpick RW. Accounting for the JKR-DMT transition in adhesion and friction measurements with atomic force microscopy. *J Adhes Sci Technol*. 2005;19(3-5):291-311. doi:10.1163/1568561054352685
369. Sirghi L, Ponti J, Broggi F, Rossi F. Probing elasticity and adhesion of live cells by atomic force microscopy indentation. *Eur Biophys J*. 2008;37(6):935-945. doi:10.1007/s00249-008-0311-2
370. Pharr GM. An improved technique for determining hardness and elastic modulus using load and displacement sensing indentation experiments. *J Mater Res*. 1992;7(6):1564-1583. doi:10.1557/JMR.1992.1564
371. Oliver WC, Pharr GM. Measurement of hardness and elastic modulus by instrumented indentation: Advances in understanding and refinements to methodology. *J Mater Res*. 2004;19(01):3-20. doi:10.1557/jmr.2004.19.1.3
372. Kan Q, Yan W, Kang G, Sun Q. Oliver-Pharr indentation method in determining elastic moduli of shape memory alloys - A phase transformable material. *J Mech Phys Solids*. 2013;61(10):2015-2033. doi:10.1016/j.jmps.2013.05.007
373. Palumbo M, Teklu A, Flagg J, Kuthirummal N, Barry C, Weiwadel C. Mechanical Characterization of Reduced Graphene Oxide Using AFM. *Adv Condens Matter Phys*. 2019;2019:1-13. doi:10.1155/2019/8713965
374. Wenger MPE, Bozec L, Horton MA, Mesquidaz P. Mechanical properties of collagen fibrils. *Biophys J*. 2007;93(4):1255-1263. doi:10.1529/biophysj.106.103192
375. Heim AJ, Matthews WG, Koob TJ. Determination of the elastic modulus of native collagen fibrils via radial indentation. *Appl Phys Lett*. 2006;89(18). doi:10.1063/1.2367660
376. Carini F, Longoni S, Pisapia V, Francesconi M, Saggese V, Porcaro G. Immediate loading of implants in the aesthetic zone: comparison between two placement timings. *Ann Stomatol (Roma)*. 2014;5(Suppl 2 to No 2):15-26.
377. iData Research Inc. US Dental Bone Graft Substitutes and other Biomaterials Market. 2011.
378. Tal H, Kozlovsky A, Artzi Z, Nemcovsky CE, Moses O. Long-term bio-degradation of cross-linked and non-cross-linked collagen barriers in human guided bone regeneration. *Clin Oral Implants Res*. 2008;19(3):295-302. doi:10.1111/j.1600-0501.2007.01424.x

379. Sanz M, Lorenzo R, Aranda JJ, Martin C, Orsini M. Clinical evaluation of a new collagen matrix (Mucograft® prototype) to enhance the width of keratinized tissue in patients with fixed prosthetic restorations: A randomized prospective clinical trial. *J Clin Periodontol.* 2009;36(10):868-876. doi:10.1111/j.1600-051X.2009.01460.x
380. Kilkenny C, Browne WJ, Cuthill IC, Emerson M, Altman DG. Improving bioscience research reporting: The arrive guidelines for reporting animal research. *Animals.* 2013;4(1):35-44. doi:10.3390/ani4010035
381. Calciolari E, Mardas N, Dereka X, Kostomitsopoulos N, Petrie A, Donos N. The effect of experimental osteoporosis on bone regeneration: Part 1, histology findings. *Clin Oral Implants Res.* 2017;28(9):e101-e110. doi:10.1111/clr.12936
382. Junqueira LCU, Bignolas G, Brentani RRR. Picrosirius staining plus polarization microscopy, a specific method for collagen detection in tissue sections. *Histochem J.* 1979;11(4):447-455. doi:10.1007/BF01002772
383. Datar UV, Mohan BC, Hallikerimath S, Angadi P, Kale A, Mane D. Clinicopathologic study of a series of giant cell fibroma using picrosirius red polarizing microscopy technique. *Arch Iran Med.* 2014;17(11):746-749.
384. Geutjes PJ, Van Der Vliet JA, Faraj KA, et al. Preparation and characterization of injectable fibrillar type I collagen and evaluation for pseudoaneurysm treatment in a pig model. *J Vasc Surg.* 2010;52(5):1330-1338. doi:10.1016/j.jvs.2010.05.118
385. Herdegen V, Felix A, Haseneder R, et al. Sterilization of medical products from collagen by means of supercritical CO<sub>2</sub>. *Chem Eng Technol.* 2014;37(11):1891-1895. doi:10.1002/ceat.201300679
386. Nataraj C, Ritter G, Dumas S, Helfer FD, Brunelle J, Sander TW. Extracellular Wound Matrices: Novel Stabilization and Sterilization Method for Collagen-based Biologic Wound Dressings. *Wounds a Compend Clin Res Pract.* 2007;19(6):148-156.
387. Ekaputra AK, Prestwich GD, Cool SM, Hutmacher DW. The three-dimensional vascularization of growth factor-releasing hybrid scaffold of poly (ε-caprolactone)/collagen fibers and hyaluronic acid hydrogel. *Biomaterials.* 2011;32(32):8108-8117. doi:10.1016/j.biomaterials.2011.07.022
388. Strange A. An Investigation into the Effects of Sterilisation on Poly(caprolactone) for In Vitro and In Vivo Medical Use. 2013.
389. Tyan YC, Liao J Der, Lin SP, Chen CC. The study of the sterilization effect of gamma ray irradiation of immobilized collagen polypropylene nonwoven fabric surfaces. *J Biomed Mater Res - Part A.* 2003;67(3):1033-1043. doi:10.1002/jbm.a.10024
390. Huang X qing, Camba J, Gu L sha, et al. Mechanism of bioactive molecular extraction from mineralized dentin by calcium hydroxide and tricalcium silicate cement. *Dent Mater.* 2017;34(2):317-330. doi:10.1016/j.dental.2017.11.010
391. Sahoo N, Narasimhan A, Dhar P, Das SK. Non-Fourier thermal transport induced structural hierarchy and damage to collagen ultrastructure subjected to laser irradiation. *Int J Hyperth.* 2018;34(3):229-242. doi:10.1080/02656736.2017.1342873
392. Latour G, Robinet L, Dazzi A, Portier F, Deniset-Besseau A, Schanne-Klein MC. Correlative nonlinear optical microscopy and infrared nanoscopy reveals collagen

- degradation in altered parchments. *Sci Rep.* 2016;6. doi:10.1038/srep26344
393. Burton B, Gaspar A, Josey D, Tupy J, Grynpas MD, Willett TL. Bone embrittlement and collagen modifications due to high-dose gamma-irradiation sterilization. *Bone.* 2014;61:71-81. doi:10.1016/j.bone.2014.01.006
  394. Maslennikova A, Kochueva M, Ignatieva N, et al. Effects of gamma irradiation on collagen damage and remodeling. *Int J Radiat Biol.* 2015;91(3):240-247. doi:10.3109/09553002.2014.969848
  395. Strange AP, Aguayo S, Ahmed T, et al. Quantitative nanohistological investigation of scleroderma: An atomic force microscopy-based approach to disease characterization. *Int J Nanomedicine.* 2017;12:411-420. doi:10.2147/IJN.S118690
  396. Sanches CP, Vianna AGD, Barreto F de C. The impact of type 2 diabetes on bone metabolism. *Diabetol Metab Syndr.* 2017;9(1):85. doi:10.1186/s13098-017-0278-1
  397. Jost T, Zipprich A, Glomb MA. Analysis of Advanced Glycation Endproducts in Rat Tail Collagen and Correlation to Tendon Stiffening. *J Agric Food Chem.* 2018;66(15):3957-3965. doi:10.1021/acs.jafc.8b00937
  398. Widdowson JP, Picton AJ, Vince V, Wright CJ, Mearns-Spragg A. In vivo comparison of jellyfish and bovine collagen sponges as prototype medical devices. *J Biomed Mater Res - Part B Appl Biomater.* 2018;106(4):1524-1533. doi:10.1002/jbm.b.33959
  399. Bozec L, Odlyha M. Thermal denaturation studies of collagen by microthermal analysis and atomic force microscopy. *Biophys J.* 2011;101(1):228-236. doi:10.1016/j.bpj.2011.04.033
  400. Tomasek JJ, Gabbiani G, Hinz B, Chaponnier C, Brown RA. Myofibroblasts and mechano: Regulation of connective tissue remodelling. *Nat Rev Mol Cell Biol.* 2002;3(5):349-363. doi:10.1038/nrm809
  401. Achterberg VF, Buscemi L, Diekmann H, et al. The nano-scale mechanical properties of the extracellular matrix regulate dermal fibroblast function. *J Invest Dermatol.* 2014;134(7):1862-1872. doi:10.1038/jid.2014.90
  402. Banushi B, Forneris F, Straatman-Iwanowska A, et al. Regulation of post-Golgi LH3 trafficking is essential for collagen homeostasis. *Nat Commun.* 2016;7:12111. doi:10.1038/ncomms12111
  403. Formosa-Dague C, Fu ZH, Feuillie C, et al. Forces between: Staphylococcus aureus and human skin. *Nanoscale Horizons.* 2016;1(4):298-303. doi:10.1039/c6nh00057f
  404. Franz CM. Analyzing focal adhesion structure by atomic force microscopy. *J Cell Sci.* 2005;118(22):5315-5323. doi:10.1242/jcs.02653
  405. Matsuura S, Kondo S, Suga K, Kinoshita Y, Urushihara M, Kagami S. Expression of focal adhesion proteins in the developing rat kidney. *J Histochem Cytochem.* 2011;59(9):864-874. doi:10.1369/0022155411413929
  406. Sigaut L, Von Bilderling C, Bianchi M, Burdisso JE, Gastaldi L, Pietrasanta LI. Live cell imaging reveals focal adhesions mechanoresponses in mammary epithelial cells under sustained equibiaxial stress. *Sci Rep.* 2018;8(1):1-15. doi:10.1038/s41598-018-27948-3
  407. Marszalek PE, Dufrêne YF. Stretching single polysaccharides and proteins using

- atomic force microscopy. *Chem Soc Rev.* 2012;41(9):3523-3534. doi:10.1039/c2cs15329g
408. Ellerbroek SM, Wu YI, Overall CM, Stack MS. Functional Interplay between Type I Collagen and Cell Surface Matrix Metalloproteinase Activity. *J Biol Chem.* 2001;276(27):24833-24842. doi:10.1074/jbc.M005631200
  409. Zheng X, Hu J, Chen Y, Zhu Y, Chen H. AFM study of the effects of collagenase and its inhibitors on dentine collagen fibrils. *J Dent.* 2012;40(2):163-171. doi:10.1016/j.jdent.2011.12.009
  410. Bastiaansen-Jenniskens YM, Koevoet W, de Bart ACW, et al. Contribution of collagen network features to functional properties of engineered cartilage. *Osteoarthr Cartil.* 2008;16(3):359-366. doi:10.1016/j.joca.2007.07.003
  411. Cuenca N, Ortuño-Lizarán I, Pinilla I. Cellular Characterization of OCT and Outer Retinal Bands Using Specific Immunohistochemistry Markers and Clinical Implications. *Ophthalmology.* 2018;125(3):407-422. doi:10.1016/j.ophtha.2017.09.016
  412. Fercher AF, Mengedoh K, Werner W. Eye-length measurement by interferometry with partially coherent light. *Opt Lett.* 1988;13(3):186. doi:10.1364/OL.13.000186
  413. Al-Azri K, Melita LN, Strange AP, et al. Optical coherence tomography use in the diagnosis of enamel defects. *J Biomed Opt.* 2016;21(3):036004. doi:10.1117/1.JBO.21.3.036004
  414. Chambers TJ, Darby JA, Fuller K. Mammalian collagenase predisposes bone surfaces to osteoclastic resorption. *Cell Tissue Res.* 1985;241(3):671-675. doi:10.1007/BF00214590
  415. Sela MN, Kohavi D, Krausz E, Steinberg D, Rosen G. Enzymatic degradation of collagen-guided tissue regeneration membranes by periodontal bacteria. *Clin Oral Implants Res.* 2003;14(3):263-268. doi:10.1034/j.1600-0501.2003.140302.x
  416. Schmitt CM, Moest T, Lutz R, Wehrhan F, Neukam FW, Schlegel KA. Long-term outcomes after vestibuloplasty with a porcine collagen matrix (Mucograft®) versus the free gingival graft: a comparative prospective clinical trial. *Clin Oral Implants Res.* 2016;27(11):e125-e133. doi:10.1111/clr.12575
  417. Ramachandra SS, Rana R, Reetika S, Jithendra KD. Options to avoid the second surgical site: A review of literature. *Cell Tissue Bank.* 2014;15(3):297-305. doi:10.1007/s10561-013-9395-8
  418. Guo S, DiPietro LA. Critical review in oral biology & medicine: Factors affecting wound healing. *J Dent Res.* 2010;89(3):219-229. doi:10.1177/0022034509359125
  419. Eming SA, Krieg T, Davidson JM. Inflammation in wound repair: Molecular and cellular mechanisms. *J Invest Dermatol.* 2007;127(3):514-525. doi:10.1038/sj.jid.5700701
  420. Badiavas E V., Abedi M, Butmarc J, Falanga V, Quesenberry P. Participation of bone marrow derived cells in cutaneous wound healing. *J Cell Physiol.* 2003;196(2):245-250. doi:10.1002/jcp.10260
  421. Fickl S, Kauffmann F, Stappert C, Kauffmann A, Schlagenhauf U. Scar Tissue Formation Following Alveolar Ridge Preservation: A Case Control Study. *Int J Periodontics Restorative Dent.* 2018;38(1):e1-e7. doi:10.11607/prd.3347
  422. Stanford CM. Surface modification of biomedical and dental implants and the



- processes of inflammation, wound healing and bone formation. *Int J Mol Sci*. 2010;11(1):354-369. doi:10.3390/ijms11010354
423. Calciolari E, Mardas N, Dereka X, Anagnostopoulos AK, Tsangaris GT, Donos N. Protein expression during early stages of bone regeneration under hydrophobic and hydrophilic titanium domes. A pilot study. *J Periodontal Res*. 2018;53(2):174-187. doi:10.1111/jre.12498
  424. Shakirova F V, Galimzyanov IG, Valeeva AN, et al. The Efficacy of the Drug “Angiogen” in the Treatment of Wounds in Rats. *Res J Pharm Biol Chem Sci*. 2018;9(2):402-410.
  425. Martin P. Wound healing - Aiming for perfect skin regeneration. *Science (80- )*. 1997;276(5309):75-81. doi:10.1126/science.276.5309.75
  426. Montesano R, Orci L. Transforming growth factor beta stimulates collagen-matrix contraction by fibroblasts: implications for wound healing. *Proc Natl Acad Sci*. 1988;85(13):4894-4897. doi:10.1073/pnas.85.13.4894
  427. Caballé-Serrano J, Munar-Frau A, Ortiz-Puigpelat O, Soto-Penaloza D, Peñarrocha M, Hernández-Alfaro F. On the search of the ideal barrier membrane for guided bone regeneration. *J Clin Exp Dent*. 2018;10(5):e477-e483. doi:10.4317/jced.54767
  428. Ratiu I, Virden TB, Baylow H, Flint M, Esfandiarei M. Executive function and quality of life in individuals with Marfan syndrome. *Qual Life Res*. 2018;27(8):2057-2065. doi:10.1007/s11136-018-1859-7
  429. Jansen B, Tryphonas L, Wong J, et al. Mode of inheritance of Samoyed hereditary glomerulopathy: an animal model for hereditary nephritis in humans. *J Lab Clin Med*. 1986;107(6):551-555.
  430. Misof K, Landis WJ, Klaushofer K, Fratzl P. Collagen from the osteogenesis imperfecta mouse model (oim) shows reduced resistance against tensile stress. *J Clin Invest*. 1997;100(1):40-45. doi:10.1172/JCI119519
  431. Omosule CL, Jeong Y, Phillips C, Pfeiffer F. Soluble Activin Type IIB Receptor Decoy changes Gene Expression Profiles of Bone Cells in the OIM and not the G610C Mouse Model of Osteogenesis Imperfecta. *Faseb J*. 2018;32(1, S).
  432. Jeong Y, Daghlis SA, Kahveci AS, et al. Soluble activin receptor type IIB decoy receptor differentially impacts murine osteogenesis imperfecta muscle function. *Muscle and Nerve*. 2018;57(2):294-304. doi:10.1002/mus.25706
  433. Hansen KA, Weiss JA, Barton JK. Recruitment of Tendon Crimp With Applied Tensile Strain. *J Biomech Eng*. 2002;124(1):72. doi:10.1115/1.1427698
  434. Herod TW, Chambers NC, Veres SP. Collagen fibrils in functionally distinct tendons have differing structural responses to tendon rupture and fatigue loading. *Acta Biomater*. 2016;42:296-307. doi:10.1016/j.actbio.2016.06.017
  435. Ning LJ, Zhang YJ, Zhang Y, et al. The utilization of decellularized tendon slices to provide an inductive microenvironment for the proliferation and tenogenic differentiation of stem cells. *Biomaterials*. 2015;52(1):539-550. doi:10.1016/j.biomaterials.2015.02.061
  436. Panwar P, Du X, Sharma V, et al. Effects of cysteine proteases on the structural and mechanical properties of collagen fibers. *J Biol Chem*. 2013;288(8):5940-5950. doi:10.1074/jbc.M112.419689
  437. Martín-Alguacil JL, Arroyo-Morales M, Martín-Gómez JL, et al. Strength recovery

- after anterior cruciate ligament reconstruction with quadriceps tendon versus hamstring tendon autografts in soccer players: A randomized controlled trial. *Knee*. 2018;25(4):704-714. doi:10.1016/j.knee.2018.03.011
438. Cullinane AR, Straatman-Iwanowska A, Zaucker A, et al. Mutations in VIPAR cause an arthrogryposis, renal dysfunction and cholestasis syndrome phenotype with defects in epithelial polarization. *Nat Genet*. 2010;42(4):303-312. doi:10.1038/ng.538
  439. Hanley J, Dhar DK, Mazzacuva F, et al. Vps33b is crucial for structural and functional hepatocyte polarity. *J Hepatol*. 2017;66(5):1001-1011. doi:10.1016/j.jhep.2017.01.001
  440. Aflatoonian M, Smith H, Farahani F, et al. Novel VIPAS39 mutation in a syndromic patient with arthrogryposis, renal tubular dysfunction and intrahepatic cholestasis. *Eur J Med Genet*. 2016;59(4):237-239. doi:10.1016/j.ejmg.2016.01.005
  441. Thayer PS, Verbridge SS, Dahlgren LA, Kakar S, Guelcher SA, Goldstein AS. Fiber/collagen composites for ligament tissue engineering: influence of elastic moduli of sparse aligned fibers on mesenchymal stem cells. *J Biomed Mater Res - Part A*. 2016;104(8):1894-1901. doi:10.1002/jbm.a.35716
  442. Yunoki S, Hatayama H, Ebisawa M, Kondo E, Yasuda K. A novel fabrication method to create a thick collagen bundle composed of uniaxially aligned fibrils: An essential technology for the development of artificial tendon/ligament matrices. *J Biomed Mater Res - Part A*. 2015;103(9):3054-3065. doi:10.1002/jbm.a.35440
  443. Liu J-F, He J-H. Hierarchical structure and fractal dimensions of tendon. *Mater Sci Technol*. 2010;26(11):1317-1319. doi:10.1179/026708310X12798718274232
  444. Dahlin RL, Kasper FK, Mikos AG. Polymeric Nanofibers in Tissue Engineering. *Tissue Eng Part B Rev*. 2011;17(5):349-364. doi:10.1089/ten.teb.2011.0238
  445. Lavagnino M, Arnoczky SP, Frank K, Tian T. Collagen fibril diameter distribution does not reflect changes in the mechanical properties of in vitro stress-deprived tendons. *J Biomech*. 2005;38(1):69-75. doi:10.1016/j.jbiomech.2004.03.035
  446. Ishikawa M, Komi P V. Muscle fascicle and tendon behavior during human locomotion revisited. *Exerc Sport Sci Rev*. 2008;36(4):193-199. doi:10.1097/JES.0b013e3181878417
  447. Spitzner EC, Röper S, Zerson M, Bernstein A, Magerle R. Nanoscale Swelling Heterogeneities in Type I Collagen Fibrils. *ACS Nano*. 2015;9(6):5683-5694. doi:10.1021/nn503637q
  448. In 't Veld PJ, Stevens MJ. Simulation of the mechanical strength of a single collagen molecule. *Biophys J*. 2008;95(1):33-39. doi:10.1529/biophysj.107.120659
  449. Rigby BJ. The Mechanical Properties of Rat Tail Tendon. *J Gen Physiol*. 1959;43(2):265-283. doi:10.1085/jgp.43.2.265
  450. Wang JH-C, Guo Q, Li B. Tendon Biomechanics and Mechanobiology—A Minireview of Basic Concepts and Recent Advancements. *J Hand Ther*. 2012;25(2):133-141. doi:https://doi.org/10.1016/j.jht.2011.07.004
  451. Turner CH, Rho J, Takano Y, Tsui TY, Pharr GM. The elastic properties of trabecular and cortical bone tissues are similar: Results from two microscopic measurement techniques. *J Biomech*. 1999;32(4):437-441. doi:10.1016/S0021-9290(98)00177-8

452. Goh KL, Holmes DF, Lu Y, et al. Bimodal collagen fibril diameter distributions direct age-related variations in tendon resilience and resistance to rupture. *J Appl Physiol*. 2012;113(6):878-888. doi:10.1152/japplphysiol.00258.2012
453. Hara H, Mihara M. Comparison of Two Methods, the Sponge Method and Young's Modulus, for Evaluating Stiffness of Skin or Subcutaneous Tissues in the Extremities of Patients with Lymphedema: A Pilot Study. *Lymphat Res Biol*. 2018;16(5):464-470. doi:10.1089/lrb.2017.0071
454. James H-C. Wang, Qianping Guo, Bin Li. Tendon Biomechanics and Mechanobiology—A Minireview of Basic Concepts and Recent Advancements. *J Hand Ther*. 2012;25(2):133-141. doi:10.1016/j.jht.2011.07.004
455. Witthaut J, Jones G, Skrepnik N, Kushner H, Houston A, Lindau TR. Efficacy and safety of collagenase clostridium histolyticum injection for dupuytren contracture: Short-term results from 2 open-label studies. *J Hand Surg Am*. 2013;38(1):2-11. doi:10.1016/j.jhsa.2012.10.008
456. Levine TD, Saperstein DS. Routine use of punch biopsy to diagnose small fiber neuropathy in fibromyalgia patients. *Clin Rheumatol*. 2015;34(3):413-417. doi:10.1007/s10067-014-2850-5
457. Kadouch DJ, Van Haersma de With A, Limpens J, et al. Is a punch biopsy reliable in subtyping basal cell carcinoma? A systematic review. *Br J Dermatol*. 2016;175(2):401-403. doi:10.1111/bjd.14458
458. Proß S, Bachmann B. A Petri Net Library for Modeling Hybrid Systems in OpenModelica. *Brain Behav Immun*. 2009;61:454-462. doi:10.3384/ecp09430014
459. Christensen E, Mjølnes P, Grimstad Ø, Rørdam OM, Foss OA. Diagnostic accuracy in Subtyping basal cell carcinoma by clinical diagnosis compared with punch biopsy. *Acta Derm Venereol*. 2016;96(6):862-863. doi:10.2340/00015555-2448
460. Cobb H, Tiu A. A case of uncombable hair syndrome and global developmental delays. *J Am Acad Dermatol*. 2017;76(6, 1):AB9.
461. Nault A, Zhang C, Kim KM, Saha S, Bennett DD, Xu YG. Biopsy use in skin cancer diagnosis: Comparing dermatology physicians and advanced practice professionals. *JAMA Dermatology*. 2015;151(8):899-902. doi:10.1001/jamadermatol.2015.0173
462. Ü. Basmanav FB, Cau L, Tafazzoli A, et al. Mutations in Three Genes Encoding Proteins Involved in Hair Shaft Formation Cause Uncombable Hair Syndrome. *Am J Hum Genet*. 2016;99(6):1292-1304. doi:10.1016/j.ajhg.2016.10.004
463. Van der Slot AJ, Zuurmond AM, Bardoel AFJ, et al. Identification of PLOD2 as Telopeptide Lysyl Hydroxylase, an Important Enzyme in Fibrosis. *J Biol Chem*. 2003;278(42):40967-40972. doi:10.1074/jbc.M307380200
464. Farage MA, Miller KW, Elsner P, Maibach HI. Characteristics of the Aging Skin. *Adv Wound Care*. 2013;2(1):5-10. doi:10.1089/wound.2011.0356
465. Farage MA, Miller KW, Maibach HI. Determinants in the rate of skin aging: Ethnicity, gender, and lifestyle influences. In: *Textbook of Aging Skin*. ; 2010:983-997. doi:10.1007/978-3-540-89656-2\_92
466. Lopez H, Abdi Ahmed B, Abraham D, et al. Role of the prolyl 3-hydroxylase leprel1 in fibrosis. *Ann Rheum Dis*. 2018;77(2).

467. Brown M, Lowe D. Automatic Panoramic Image Stitching Automatic 2D Stitching. *Int J Comput Vis.* 2007;74(1):59-73.
468. Wallace JM, Orr BG, Marini JC, Holl MMB. Nanoscale morphology of Type I collagen is altered in the Brl mouse model of Osteogenesis Imperfecta. *J Struct Biol.* 2011;173(1):146-152. doi:10.1016/j.jsb.2010.08.003
469. Esteva A, Kuprel B, Novoa RA, et al. Dermatologist-level classification of skin cancer with deep neural networks. *Nature.* 2017;542(7639):115-118. doi:10.1038/nature21056
470. De Fauw J, Ledsam JR, Romera-Paredes B, et al. Clinically applicable deep learning for diagnosis and referral in retinal disease. *Nat Med.* 2018;24(9):1342-1350. doi:10.1038/s41591-018-0107-6
471. Agache PG, Monneur C, Leveque JL, De Rigo J. Mechanical properties and Young's modulus of human skin in vivo. *Arch Dermatol Res.* 1980;269(3):221-232. doi:10.1007/BF00406415
472. Fratzl P. Collagen: Structure and mechanics, an introduction. In: Fratzl P, ed. *Collagen: Structure and Mechanics.* Boston, MA, MA: Springer US; 2008:1-13. doi:10.1007/978-0-387-73906-9\_1
473. Breslow A. Thickness, cross-sectional areas and depth of invasion in the prognosis of cutaneous melanoma. *Ann Surg.* 1970;172(5):902-908. doi:10.1097/0000658-197011000-00017
474. Barten PGJ. Evaluation of subjective image quality with the square-root integral method. *J Opt Soc Am A.* 1990;7(10):2024-2031. doi:10.1364/JOSAA.7.002024
475. Nickerson RS. Confirmation bias: A ubiquitous phenomenon in many guises. *Rev Gen Psychol.* 1998;2(2):175.
476. Ormerod AD, Dwyer CM, Weller R, Cox DH, Price R. A comparison of subjective and objective measures of reduction of psoriasis with the use of ultrasound, reflectance colorimetry, computerized video image analysis, and nitric oxide production. *J Am Acad Dermatol.* 1997;37(1):51-57. doi:https://doi.org/10.1016/S0190-9622(97)70211-1
477. Vogel B, Siebert H, Hofmann U, Frantz S. Determination of collagen content within picosirius red stained paraffin-embedded tissue sections using fluorescence microscopy. *MethodsX.* 2015;2:124-134. doi:10.1016/j.mex.2015.02.007
478. Pfretzschner H-U. Collagen gelatinization: the key to understand early bone-diagenesis. *Palaeontogr Abteilung A.* 2006;278(1-6):135-148. doi:10.1127/pala/278/2006/135
479. Dynamic GJ. Dynamic state of collagen : pathways of collagen degradation in vivo and their possible role in regulation of collagen mass. *Cell Physiol.* 1987;252(1):C1-C9. doi:10.1152/ajpcell.1987.252.1.C1
480. Klein L, ChandraRajan J. Collagen degradation in rat skin but not in intestine during rapid growth: effect on collagen types I and III from skin. *Proc Natl Acad Sci U S A.* 1977;74(4):1436-1439. doi:cep3523 [pii]
481. Paepe A De, Nuytinck L, Hausser I, Anton-Lamprecht I, Naeyaert JM. Mutations in the COL5A1 gene are causal in the Ehlers-Danlos syndromes I and II. *Am J Hum Genet.* 1997;60(3):547-554. [http://www.ncbi.nlm.nih.gov/sites/entrez?Db=pubmed&Cmd=Retrieve&list\\_uids=9042913&dopt=abstractplus](http://www.ncbi.nlm.nih.gov/sites/entrez?Db=pubmed&Cmd=Retrieve&list_uids=9042913&dopt=abstractplus).

482. MONTES G, JUNQUEIRA L. the Use of the Picrosirius-Polarization Method for the Study of the Biopathology of Collagen. *Mem Inst Oswaldo Cruz*. 1991;86(III):1-11.  
[http://apps.webofknowledge.com/full\\_record.do?product=UA&search\\_mode=GeneralSearch&qid=16&SID=Z1u3qpo9KrbETt52IRt&page=1&doc=3](http://apps.webofknowledge.com/full_record.do?product=UA&search_mode=GeneralSearch&qid=16&SID=Z1u3qpo9KrbETt52IRt&page=1&doc=3).
483. Velidandla S, Gaikwad P, Ealla KKR, Bhorgonde KD, Hunsingi P, Kumar A. Histochemical analysis of polarizing colors of collagen using Picrosirius Red staining in oral submucous fibrosis. *J Int oral Heal JIOH*. 2014;6(1):33-38.  
<http://www.pubmedcentral.nih.gov/articlerender.fcgi?artid=3959134&tool=pmcentrez&rendertype=abstract>. Accessed September 11, 2015.
484. Rich L, Whittaker P. Collagen and Picrosirius Red Staining: a Polarized Light Assessment of Fibrillar Hue and Spatial Distribution. *Braz J Morphol Sci*. 2005;22(2):97-104. <http://jms.org.br/PDF/v22n2a06.pdf>. Accessed March 27, 2015.
485. Coelho PGB, Souza MV de, Conceicao LG, Vitoria MIV, Bedoya SAO. Evaluation of dermal collagen stained with picrosirius red and examined under polarized light microscopy. *An Bras Dermatol*. 2018;93:415-418.  
[http://www.scielo.br/scielo.php?script=sci\\_arttext&pid=S0365-05962018000300415&nrm=iso](http://www.scielo.br/scielo.php?script=sci_arttext&pid=S0365-05962018000300415&nrm=iso).
486. Hashimoto M, Tay FR, Ohno H, et al. SEM and TEM Analysis of Water Degradation of Human Dentinal Collagen. *J Biomed Mater Res - Part B Appl Biomater*. 2003;66(1):287-298. doi:10.1002/jbm.b.10560
487. Daly CH, Odland G. Age-related changes in the mechanical properties of human skin. *J Invest Dermatol*. 1979;73(1):84-87.
488. Balbir-Gurman A, Denton CP, Nichols B, et al. Non-invasive measurement of biomechanical skin properties in systemic sclerosis. *Ann Rheum Dis*. 2002;61(3):237-241. doi:10.1136/ard.61.3.237
489. Varga J, Abraham D. Systemic sclerosis: A prototypic multisystem fibrotic disorder. *J Clin Invest*. 2007;117(3):557-567. doi:10.1172/JCI31139
490. Clements PJ, Lachenbruch PA, Seibold JR, Zee B, Steen VD BP et al. (1993) Skin thickness score in systemic sclerosis: an assessment of interobserver variability in 3 independent studies. *J Rheumatol* 20:1892–1896. *J Rheumatol*. 1993;20(11):1892—1896. <http://europepmc.org/abstract/MED/8308774>.
491. Crary MA, Carnaby (Mann) GD, Groher ME. Biomechanical Correlates of Surface Electromyography Signals Obtained During Swallowing by Healthy Adults. *J Speech Lang Hear Res*. 2006;49(1):186. doi:10.1044/1092-4388(2006/015)
492. Palou J, Carcas A, Segarra J, et al. Phase I pharmacokinetic study of a single intravesical instillation of gemcitabine administered immediately after transurethral resection plus multiple random biopsies in patients with superficial bladder cancer. *J Urol*. 2004;172(2):485-488. doi:10.1097/01.ju.0000131770.14409.7f
493. Berardesca E, Barbareschi M, Veraldi S, Pimpinelli N. Evaluation of efficacy of a skin lipid mixture in patients with irritant contact dermatitis, allergic contact dermatitis or atopic dermatitis: A multicenter study. *Contact Dermatitis*. 2001;45(5):280-285. doi:10.1034/j.1600-0536.2001.450505.x
494. Hurbain I, Romao M, Sextius P, et al. Melanosome Distribution in Keratinocytes

- in Different Skin Types: Melanosome Clusters Are Not Degradative Organelles. *J Invest Dermatol.* 2018;138(3):647-656. doi:10.1016/j.jid.2017.09.039
495. Olde Damink LHH, Dijkstra PJ, Van Luyn MJA, Van Wachem PB, Nieuwenhuis P, Feijen J. Glutaraldehyde as a crosslinking agent for collagen-based biomaterials. *J Mater Sci Mater Med.* 1995;6(8):460-472. doi:10.1007/BF00123371
  496. Ruijgrok JM, de Wijn JR, Boon ME. Glutaraldehyde crosslinking of collagen: Effects of time, temperature, concentration and presoaking as measured by shrinkage temperature. *Clin Mater.* 1994;17(1):23-27. doi:10.1016/0267-6605(94)90044-2
  497. Erbersdobler HF, Faist V. Metabolic transit of Amadori products. *Nahrung - Food.* 2001;45(3):177-181. doi:10.1002/1521-3803(20010601)45:3<177::AID-FOOD177>3.0.CO;2-A
  498. Leduc C, Young ID, Joneja MG, Parker CM. Unexpected post-mortem diagnosis of systemic sclerosis presenting as pneumatosis intestinalis: Revised diagnostic criteria and medicolegal implications. *Leg Med.* 2015;17(1):29-33. doi:10.1016/j.legalmed.2014.08.005
  499. Monnier VM, Glomb M, Elgawish A, Sell DR. The mechanism of collagen cross-linking in diabetes: A puzzle nearing resolution. *Diabetes.* 1996;45(3 SUPPL.):S67-S72. doi:10.2337/diab.45.3.S67
  500. Wilson R, Cohen JM, Reglinski M, et al. Naturally Acquired Human Immunity to Pneumococcus Is Dependent on Antibody to Protein Antigens. *PLoS Pathog.* 2017;13(1). doi:10.1371/journal.ppat.1006137
  501. Braly A, Darnell LA, Mann AB, Teaforde MF, Weihs TP. The effect of prism orientation on the indentation testing of human molar enamel. *Arch Oral Biol.* 2007;52(9):856-860. doi:10.1016/j.archoralbio.2007.03.005
  502. Hill RG, Gillam DG, Chen X. The ability of a nano hydroxyapatite toothpaste and oral rinse containing fluoride to protect enamel during an acid challenge using <sup>19</sup>F solid state NMR spectroscopy. *Mater Lett.* 2015;156:69-71. doi:10.1016/j.matlet.2015.04.140
  503. Posner AS. The mineral of bone. *Clin Orthop Relat Res.* 1985;200(200):87-99. doi:10.1097/00003086-198511000-00018
  504. Yasukawa A, Ouchi S, Kandori K, Ishikawa T. Preparation and characterization of magnesium–calcium hydroxyapatites. *J Mater Chem.* 1996;6(8):1401-1405.
  505. Rho JY, Roy ME, Tsui TY, Pharr GM. Elastic properties of microstructural components of human bone tissue as measured by nanoindentation. *J Biomed Mater Res.* 1999;45(1):48-54. doi:10.1002/(SICI)1097-4636(199904)45:1<48::AID-JBM7>3.0.CO;2-5
  506. Sabir MI, Xu X, Li L. A review on biodegradable polymeric materials for bone tissue engineering applications. *J Mater Sci.* 2009;44(21):5713-5724. doi:10.1007/s10853-009-3770-7
  507. BAILEY LK, J A. Collagen Cross-Links in Mineralizing Tissues: A Review of Their Chemistry, Function, and Clinical Relevance. *Bone.* 1998;22(3):181-187.
  508. Nudelman F, Pieterse K, George A, et al. The role of collagen in bone apatite formation in the presence of hydroxyapatite nucleation inhibitors. *Nat Mater.* 2010;9(12):1004-1009. doi:10.1038/nmat2875

509. Anderson BG, Wolfinbarger Jr L. Composite bone graft, method of making and using same. March 2001.
510. Liu GR. A step-by-step method of rule-of-mixture of fiber- and particle-reinforced composite materials. *Compos Struct*. 1997;40(3-4):313-322. doi:10.1016/S0263-8223(98)00033-6
511. Yamashita J, Li X, Furman BR, Ralph Rawls H, Wang X, Mauli Agrawal C. Collagen and bone viscoelasticity: A dynamic mechanical analysis. *J Biomed Mater Res*. 2002;63(1):31-36. doi:10.1002/jbm.10086
512. Pathak S, Gregory Swadener J, Kalidindi SR, Courtland HW, Jepsen KJ, Goldman HM. Measuring the dynamic mechanical response of hydrated mouse bone by nanoindentation. *J Mech Behav Biomed Mater*. 2011;4(1):34-43. doi:10.1016/j.jmbbm.2010.09.002
513. Vranka JA, Sakai LY, Bächinger HP. Prolyl 3-hydroxylase 1, enzyme characterization and identification of a novel family of enzymes. *J Biol Chem*. 2004;279(22):23615-23621. doi:10.1074/jbc.M312807200
514. Cheema U, Brown RA. Rapid Fabrication of Living Tissue Models by Collagen Plastic Compression: Understanding Three-Dimensional Cell Matrix Repair *In Vitro*. *Adv Wound Care*. 2013;2(4):176-184. doi:10.1089/wound.2012.0392
515. Davidenko N, Schuster CF, Bax D V., et al. Control of crosslinking for tailoring collagen-based scaffolds stability and mechanics. *Acta Biomater*. 2015;25:131-142. doi:10.1016/j.actbio.2015.07.034
516. Mordechai S, Gradstein L, Pasanen A, et al. High myopia caused by a mutation in LEPREL1, encoding prolyl 3-hydroxylase 2. *Am J Hum Genet*. 2011;89(3):438-445. doi:10.1016/j.ajhg.2011.08.003
517. Barnes AM, Kozma C, Tifft CJ, et al. Prolyl 3-hydroxylase 1 deficiency causes a recessive metabolic bone disorder resembling lethal/severe osteogenesis imperfecta. *Nat Genet*. 2007;39(3):359-365. doi:10.1038/ng1968

## Appendices

### A. Optical Coherence Tomography

The data presented here follows on from Chapter 3.5.4 and shows further Optical Coherence Tomography (OCT) images of the two major membranes.

#### Bio-Gide (BG)

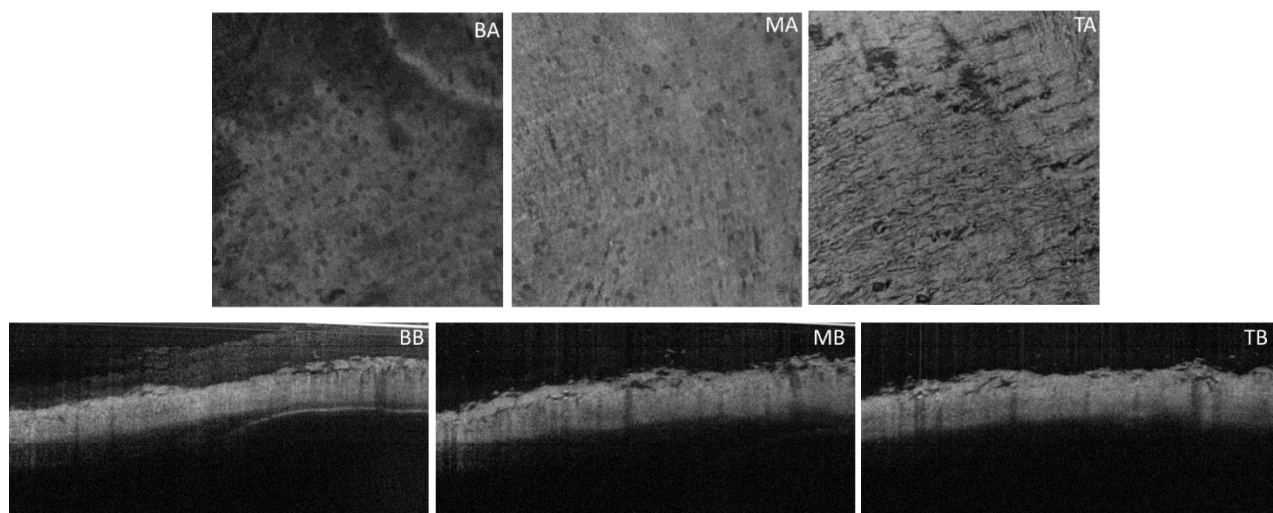


Figure A-1 en-face (top row) and B-scan (bottom row) during collagen degradation at T0 on BG

**Figure A-1** shows the OCT scans for T0. This shows the initial response of the membrane when collagenase and buffer is added. The en-face images show different layering throughout the depth of the material. **TA** shows striations in the membrane similar to those seen under SEM. **BA** shows a higher number of pores, with fibres not seen, but there are some lower surface features visible. **MA** is an intermediary stage in terms of visible fibres. Both **TB** and **MB** show initial swelling, with full thickness pores seen, as confirmed in **BB**. All three B-scans show loose surface material and some large gaps at the top of the membrane.



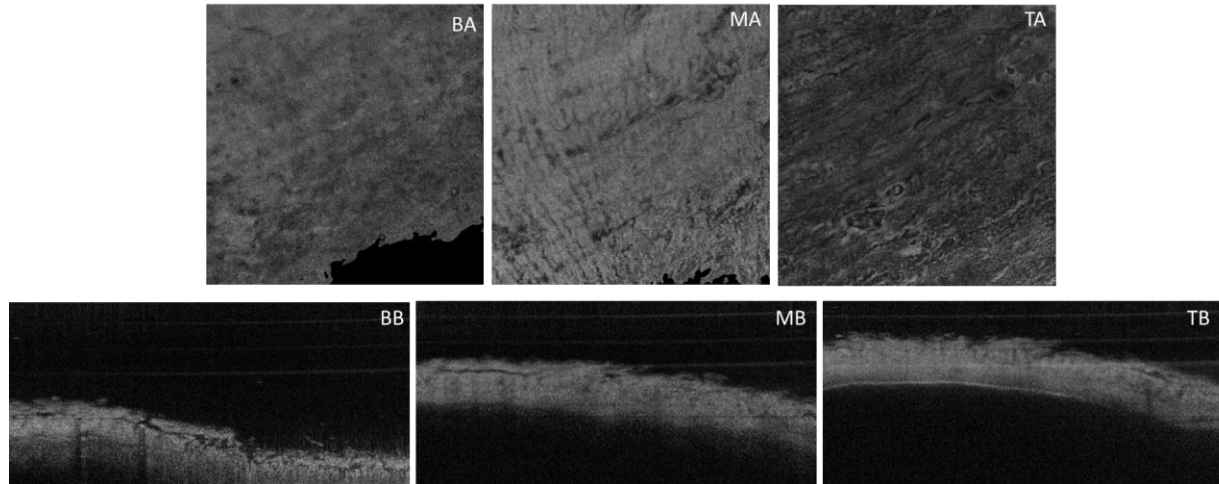


Figure A-2 en-face (top row) and B-scan (bottom row) during collagen degradation at T20 on BG

**Figure A-2** shows the OCT scans for T20. **TA** shows some large features, but the details are difficult to distinguish. Some pores can be seen. **MA** shows a large number of visible fibres, without orientation. This closely resembles the initial top membrane seen in T0, and shows the process of the digestion (Figure A-1 TA). Few features are visible in **BA**. **TB** and **MB** show that the small collagen fragments initially seen have been digested, and larger frayed surfaces are forming. **BB** shows the membrane movement and that some membrane areas have fully detached from the larger surface.

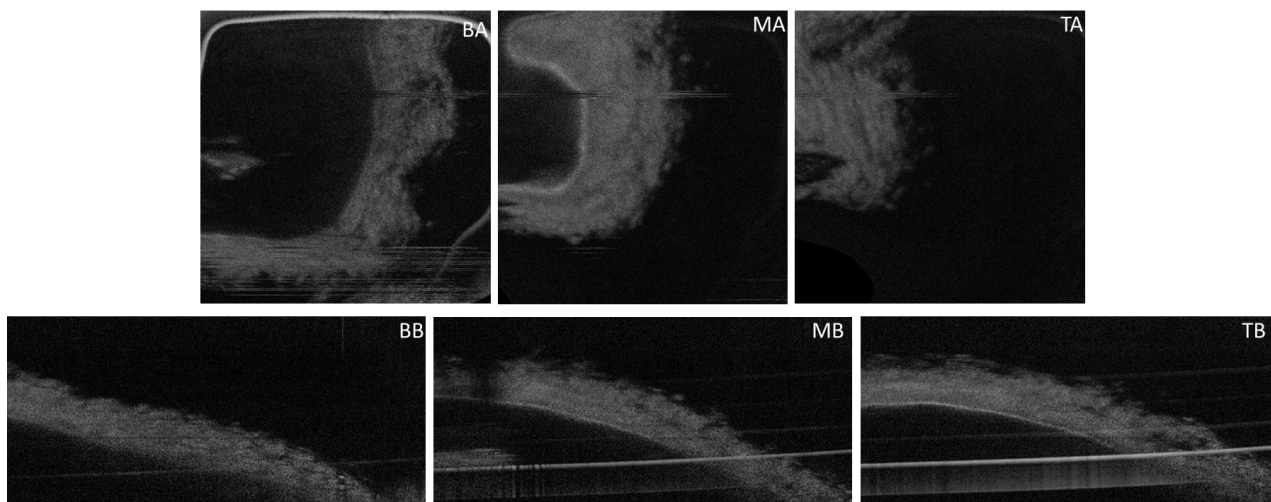


Figure A-3 en-face (top row) and B-scan (bottom row) during collagen degradation at T40 on BG

**Figure A-3** shows the OCT scans for T40. **TA**, **MA** and **BA** all show the curvature of the membrane. Only small amounts of the membrane were found at the surface, and the digestion is progressing. **TB** and **MB** show the bowing of the membrane and the frayed surface. They also show that the depth of the membrane appears to be intact, and reflections from the buffer are visible. **BB** shows some porosity and fraying.

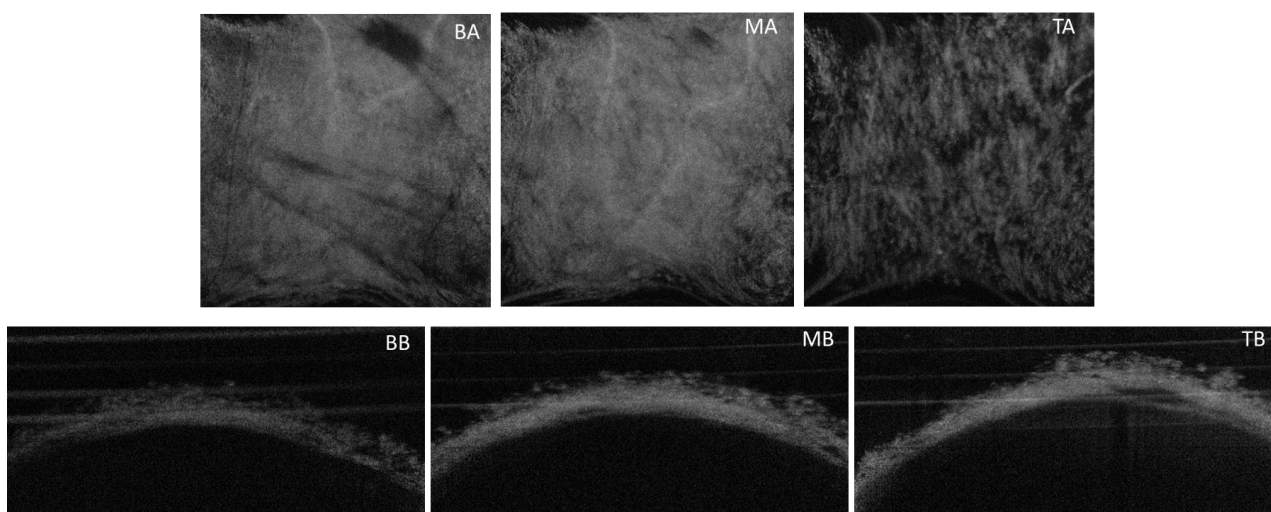
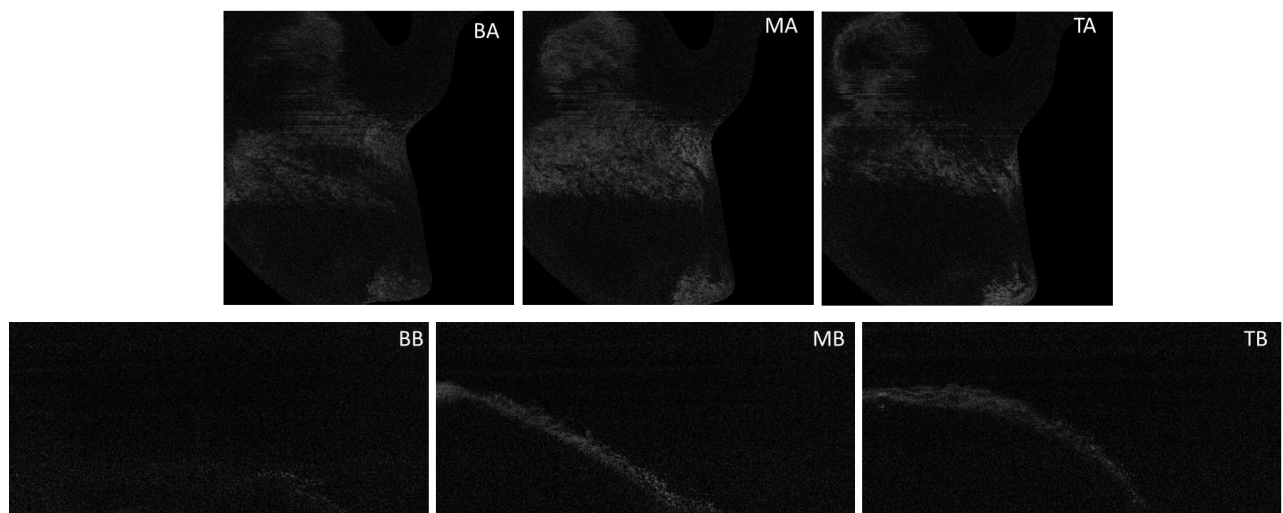


Figure A-4 en-face (top row) and B-scan (bottom row) during collagen degradation at T60 on BG

**Figure A-4** shows the OCT scans for T60. **TA** shows the amount of digestion that has occurred since T0 (Figure A-1); the fibres are now much smaller, and large gaps are frequently seen. **MA** and **BA** are very similar, and show an amorphous membrane, without any visible fibres. Some gaps or folds are present. **TB** and **MB** both show large amounts of fraying, with loose collagen present. **BB** shows large holes throughout the thickness of the remaining membrane. This is suggestive of a significant weakening of the integrity of the membrane. At the bottom of the image, where the membrane initially was rough, the membrane now appears to be smooth and featureless (Figure A-1). This could suggest that the loose collagen parts of the membrane have been fully digested before the top of surface.



**Figure A-5 en-face (top row) and B-scan (bottom row) during collagen degradation at T80 on BG**

**Figure A-5** shows the OCT scans for T80. **TA**, **MA** and **BA** only show small areas of the membrane which have remained intact. **TB** and **MB** show a long thin strand, which is likely to be the remaining non-digested part of the membrane. The sample was not visible in **BB**.

## Mucograft (MG)

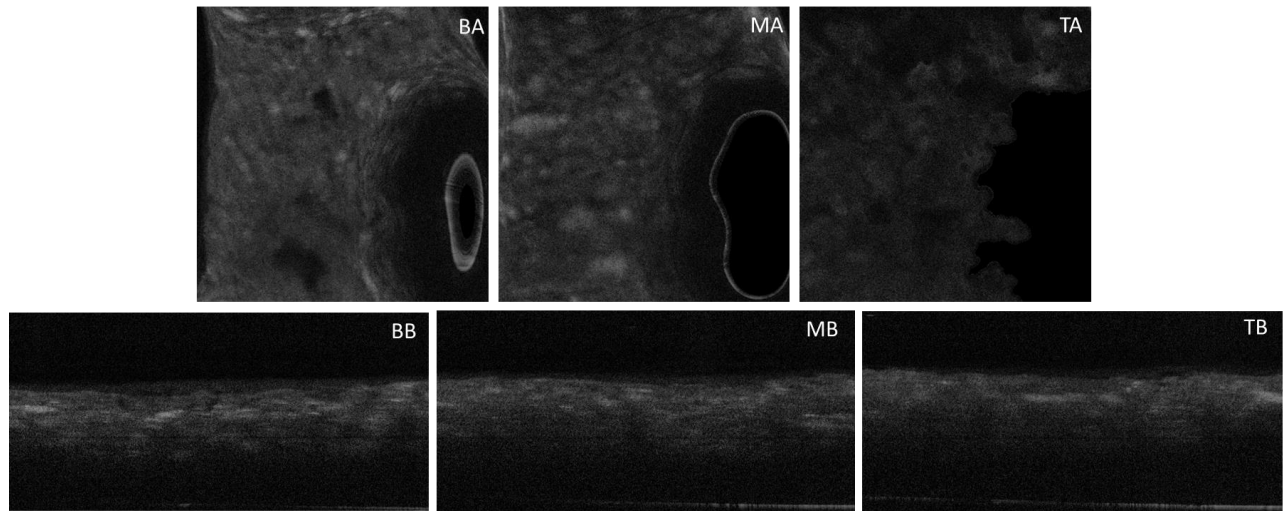


**Figure A-6 en-face (top row) and B-scan (bottom row) during collagen degradation at T0 on MG**

**Figure A-6** shows the OCT scans for T0. This shows the initial response of the membrane when collagenase and buffer is added. **TA** has few noticeable features on the en-face scan, and is swollen due to liquid uptake. **MA** and **BA** are similar to TA but show more features. BA specifically has discernible groups with some orientation and porosity. **TB**, **MB** and **BB** are all similar. Surface features on either side are not visible due to the membrane's swelling response.

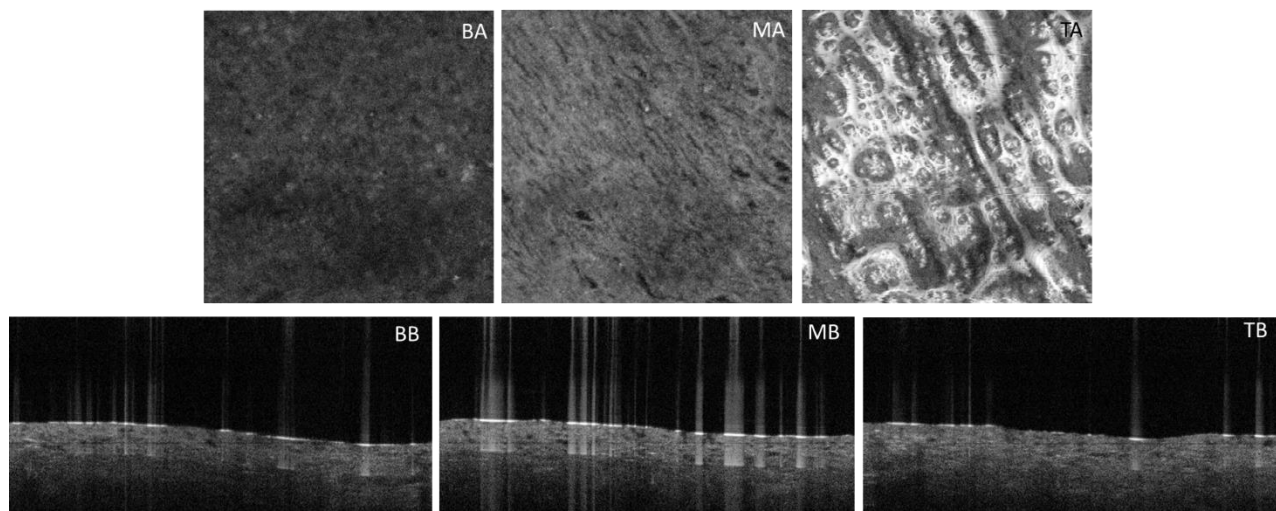


**Figure A-7 en-face (top row) and B-scan (bottom row) during collagen degradation at T20 on MG**

**Figure A-7** shows the OCT scans for T20. **TA** shows the very top of the membrane, with pores and holes visible. The topography of the sample is also visible, with some areas shown to be raised from the surface. The distinct features seen here are unique to this time point, and likely show the early stage degradation. **MA** is more familiar and shows the middle of the membrane. The fibres seen have a strong directional orientation, with a range of pore sizes which are between the fibre bundles. **BA** has a large number of small pores, without any fibre bundles visible. **TB** and **MB** both show sub-surface porosity and dips, which are causing surface reflections. The membrane appears to be intact and compact. **BB** shows some pores, but features are not visible on the bottom of membrane.

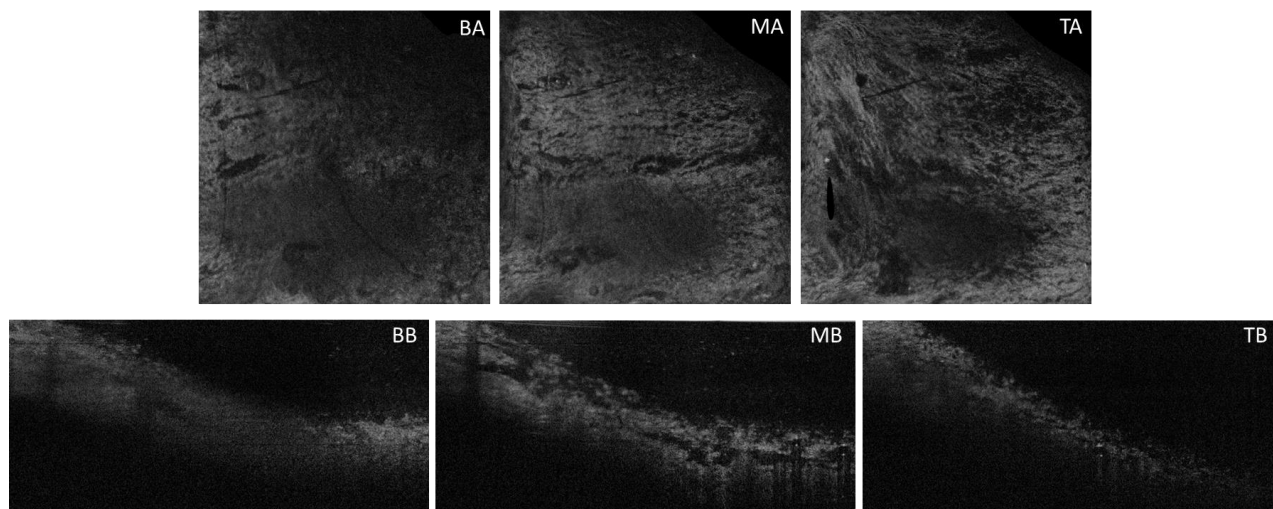


Figure A-8 en-face (top row) and B-scan (bottom row) during collagen degradation at T40 on MG

**Figure A-8** shows the OCT scans for T40. **TA** shows the membrane has degraded significantly since T20 (Figure A-7). There are large pores with only fragments seen in some locations. One location towards the bottom of the scan has degraded significantly. **MA** shows large fragments separated by crevices in the membrane. Some fibre orientation is visible, but there are large pores interspaced between the fibres. **BA** shows similar large pores as seen in MA, but without large crevices separating the membranes, suggesting that the membrane is intact. **TB** shows the steep angle of the membrane and how it has moved over time. Some small fraying of the surface is visible. **MB** also shows a frayed surface, with porosity and gaps also visible. **BB** shows some fraying, but also larger gaps in the structure, suggesting that any breakup of the membrane would start from the bottom surface.

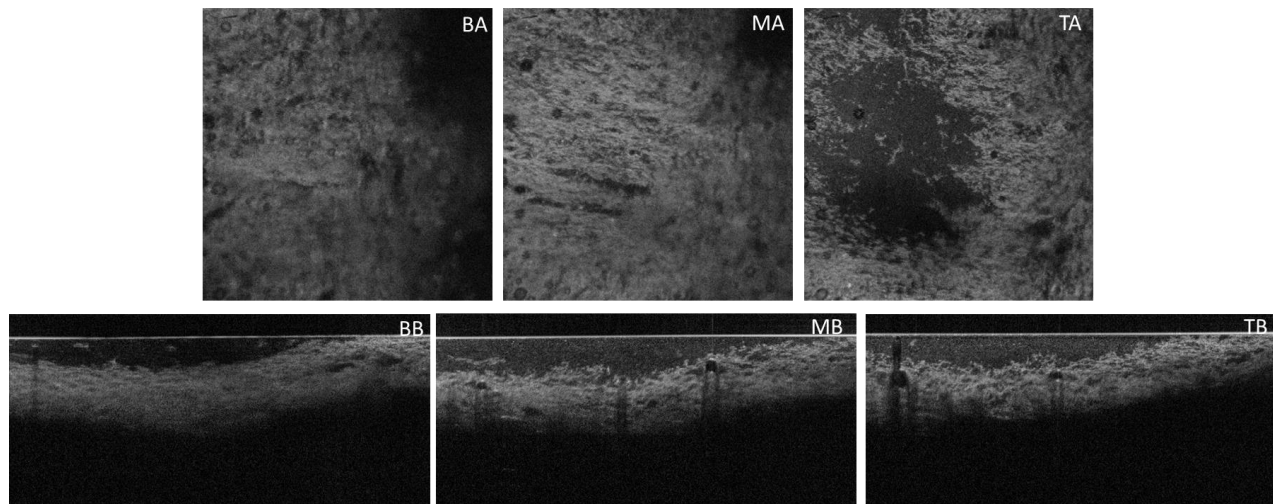
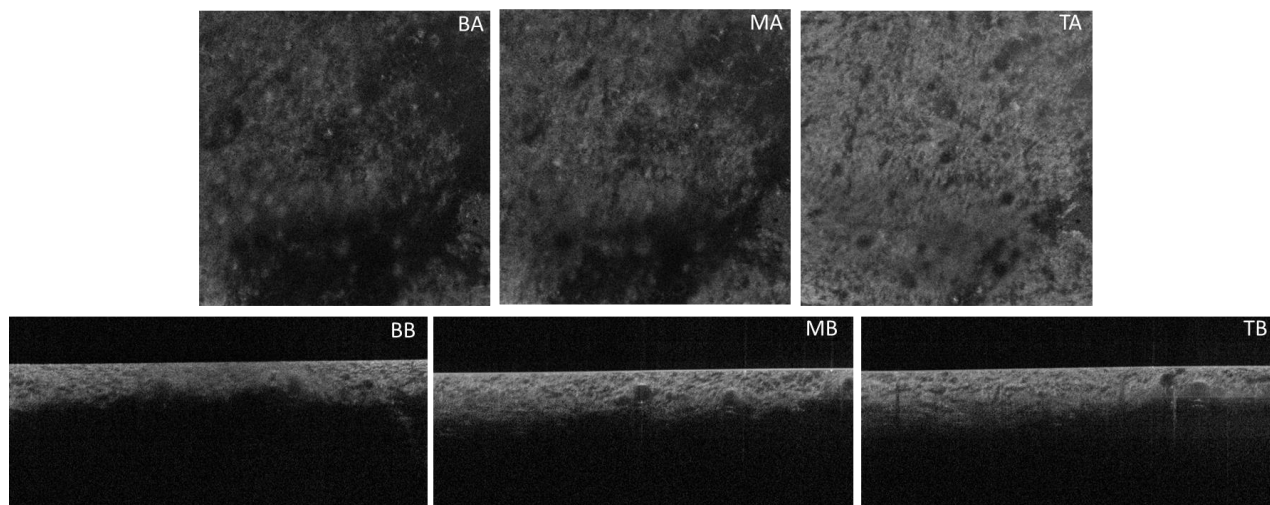


Figure A-9 en-face (top row) and B-scan (bottom row) during collagen degradation at T60 on MG

**Figure A-9** shows the OCT scans for T60. **TA** shows large areas with gaps and pores present. Some structural features remain intact, but these are separated from each other and are floating. **MA** and **BA** have similar features, showing that most of the membrane remains intact, although large gaps are forming. This suggests that the middle and bottom layers of the membrane remained intact for longer than the top of the membrane at this time point. **TB** and **MB** show the liquid surface, and that the membrane has sunk beneath it whilst still remaining intact. There, the surface of the membrane is frayed, and loose material can be seen at the top. Gaps in between the frayed surface and full thickness pores are also present, suggesting that the membrane is beginning to lose its integrity. **BB** does not show the details of the fraying of the top surface membrane, but does show some indistinct features on the bottom surface. These are also consistent with collagenase degradation as seen on the top surface. Porosity is varied and readily identified.



**Figure A-10 en-face (top) and B-scan (bottom) during collagen degradation at T80 on MG**

**Figure A-10** shows the OCT scans for T80. **TA** shows a larger covering of fibres than that seen in T60 (Figure A-9) but the range of porosity appears to be larger. Large areas of the surface are isolated due to digestion. **MA** and **BA** show similar features. The fibres are not readily identified, with large gaps present, showing that the bottom and middle sections of the membrane are heavily digested. **TB** and **MB** confirm that the membrane is now fully compliant with the liquid surface. This had the effect of decreasing the thickness of the membrane while increasing its density; the large gaps seen previously are no longer present and have been replaced with numerous smaller pores (Figure A-9). **BB** shows some fraying on the bottom surface, but this is difficult to distinguish.



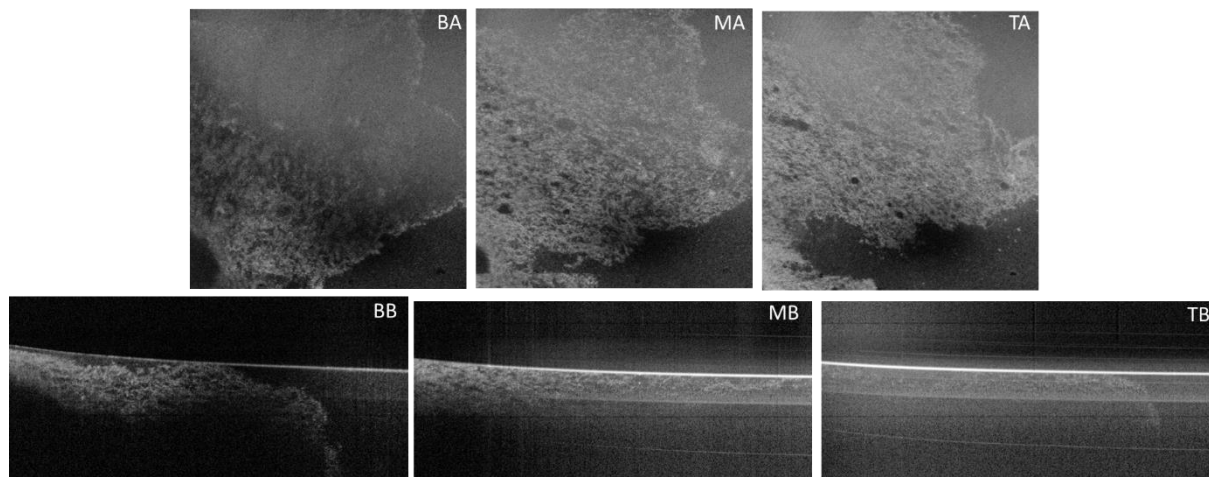


Figure A-11 en-face (top) and B-scan (bottom) during collagen degradation at T100 on MG

**Figure A-11** shows the OCT scans for T100. **TA** and **MA** show similar features, with a very thin porous membrane seen. Few distinct features are visible, and most of the membrane has been digested. **BA** shows a similar amount of degradation, but the membrane is difficult to image due to movement. **TB** shows the membrane fully compliant with the liquid surface, and it is difficult to identify. **MB** shows the compacted surface has porosity but is still very faint. **BB** indicates that the membrane has lost compliance below the surface of the liquid. This appears extremely frayed with large gaps present at both the top and bottom surfaces of the membrane. Little if any membrane integrity remained after T100; scans were not taken at T120.

## C. Morphology and Mechanics of Mice Tendons

---

### Materials

Control mice were donated by Dr Helina Marshall (UCL) and the group of Prof Jeremy Brown, (UCL & UCLH) after inoculation with *Streptococcus pneumoniae*<sup>500</sup>. At least 3 were sacrificed as juveniles, and their tails were collected. This animal study was conducted according to Home Office guidance (licence PPL70/6510). The fur was removed, exposing four tendons on the tail, each containing type I and III collagen. The tendons were removed and the collagen collected and stored in phosphate buffered saline (PBS) solution. Samples were washed in deionised water (DI), and tendon extracts (~5mm long) were taken and prepared for AFM and SEM.

### Data

#### **Mesoscale Skin Imaging**

Following the same principle that baseline measurements were sought for the collagen membranes in Chapter 3.5; a mesoscale imaging approach was initially used. This approach was successful previously in identify ordered and disordered collagen. A further challenge was presented in this chapter, however, as there is also wildtype and two sets of diseased mice that were analysed. In order to correctly identify healthy and ordered collagen, a separate set of healthy mice, the control samples, were obtained and analysed.

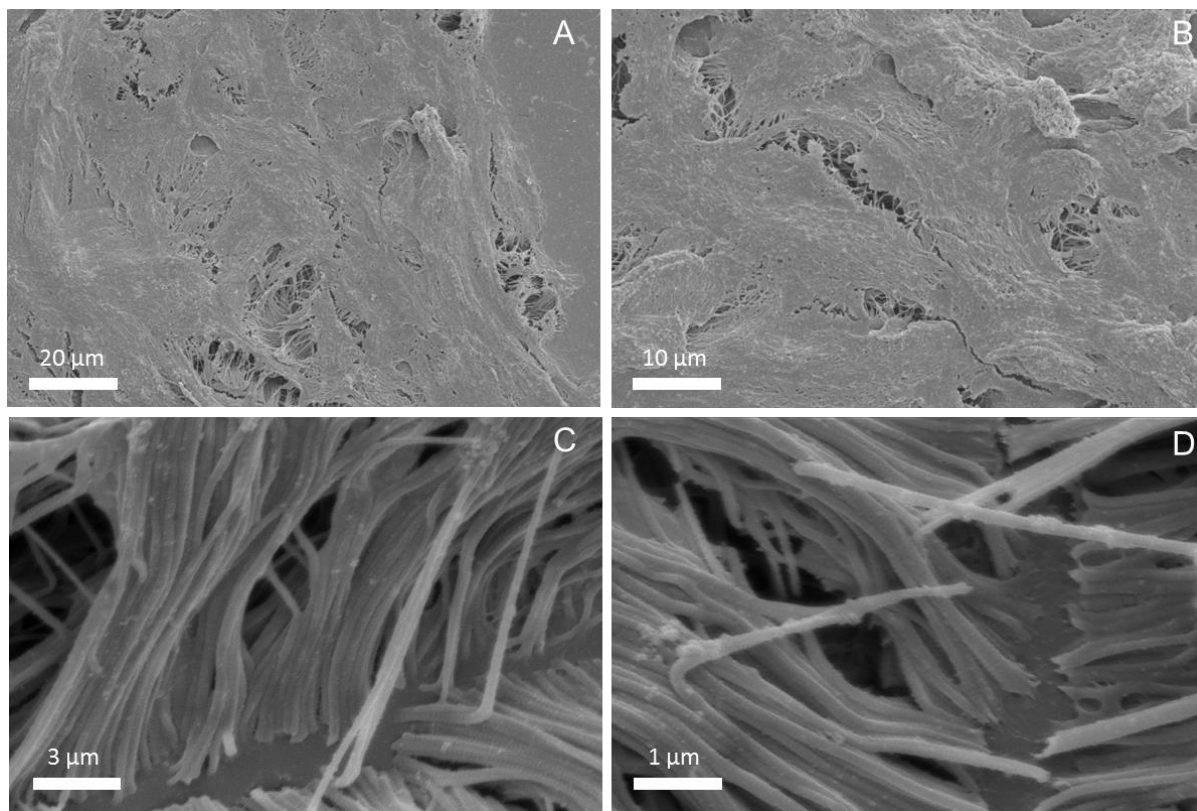


**Figure C-1 SEM of control mouse skin showing surface features and fibrils within surface cracks.**

**A 1200x, B 2000x, C 12000x, D 20000x magnification**

**Figure C-1** shows control skin mesoscale imaging using SEM. Image **A** shows a low magnification image of the skin. The surface is dense, with swirling visible. Fibres can be seen between gaps. Desiccation cracks due to sample preparation are present. The glass surface can be seen in the background. Image **B** shows a higher magnification of the skin surface. Here, fibres are readily visible inside the desiccation cracks that follow the swirling of the collagen sheets. The surface has some porosity, but otherwise appears dense outside of the cracks. Image **C** is at a much higher magnification and shows fibrils from inside a swirl. The ends of the fibrils are touching the glass surface. The fibrils are reasonably well aligned and in register, with bundling of 3-8 fibrils appearing to be common. D-banding can be seen on some fibrils, although

this appears to be quite faint. Image **D** is taken at the highest magnification and shows similar features to image C. Fibrils are present and aligned in bundles. Evidence of some swirling in the fibrils can be seen towards the top of the image. Again D-banding can be found, but this is faint.

### **Nanoscale Imaging**

Mesoscale imaging confirmed markers of alignment and D-banding were present in the control mouse skin. Subsequently, nanoscale imaging, with a particular focus on the localised alignment and the periodicity of the D-band was performed.

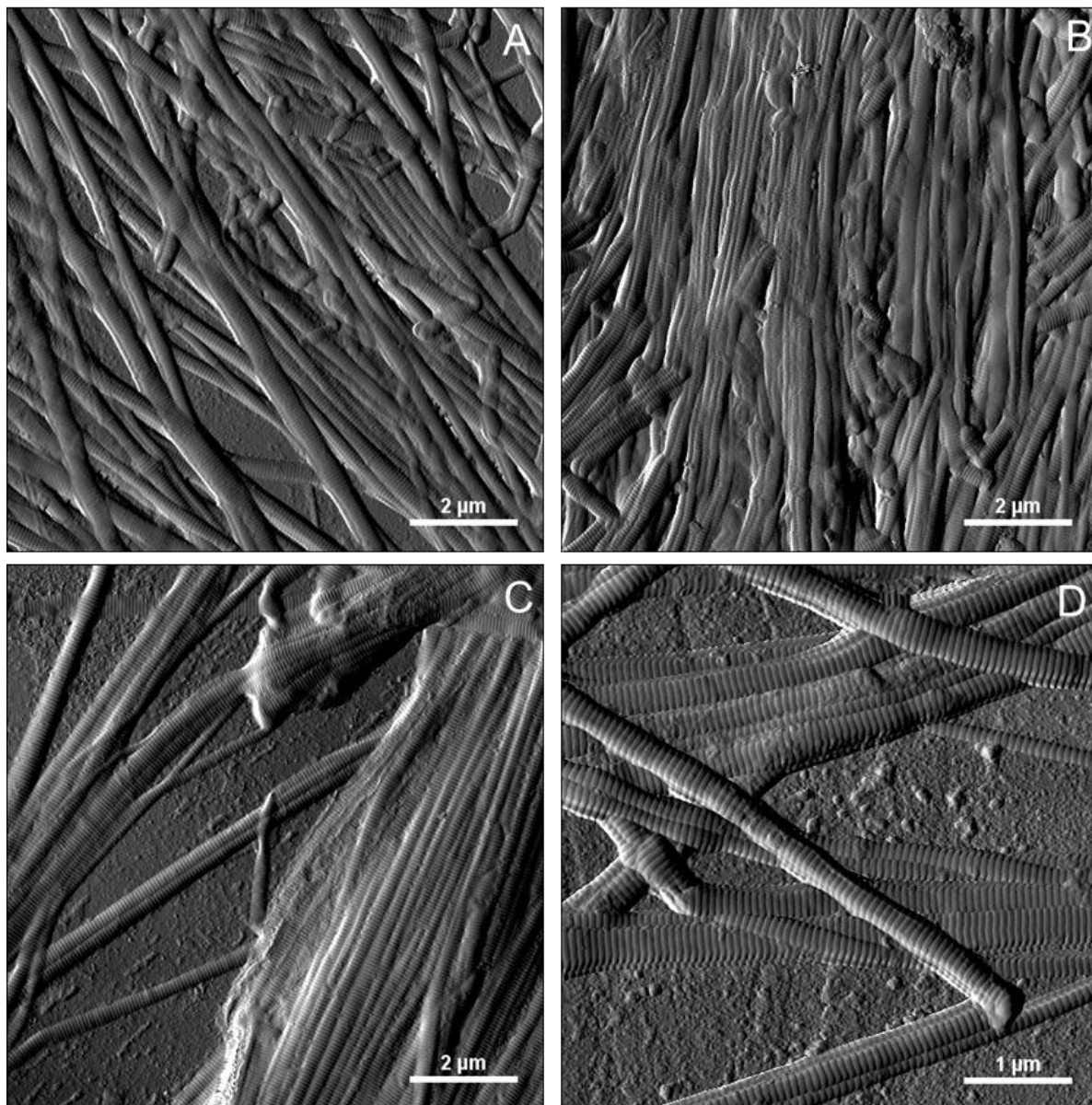


**Figure C-2 AFM of control mouse tendon. A) & B) aligned bundles of tendon fibres C) & D)**

**tendons opened**

**Figure C-2** shows the collagen fibrils in tendons taken from control mice. Two separate types of location were chosen for imaging. In image **A**, a large bundle of fibres was imaged, giving rise to large variations in topography. The fibrils are mostly aligned and in register, with some glass surface visible underneath. The D-banding is faint but

present. The cross-over of fibrils running against the main direction of the fibrils gives rise to the appearance of swelling. There is some evidence of degradation, with areas appearing to be gelatinised. Image **B** is also from a large bundle and shows well-aligned fibrils in a top-to-bottom orientation. Some swelling is also seen between the bundles of fibrils. The dense packing means that D-banding is not obvious apart from on fibrils towards the edge of the top of the image, which is out of alignment with the core fibres. Image **C** shows collagen fibrils from fibres that have been manually extracted and opened. Some inherent disorder in alignment is expected when the sample has been prepared in this way. Bundles of fibrils are shown to have register, but there is a lack of fibril alignment throughout the whole image. D-banding is visible on the fibrils. Most of the fibrils appear to be homogenous in size, with three smaller fibrils seen on the left of the image. Image **D** shows a smaller scale image of extracted and opened tendons. Similar to image C and in places in image A, there is a local register of fibrils without an overall directional alignment in the image. The D-banding is strikingly clear and was found to be regular in its periodicity (66.4 nm).

This gave rise to two different types of location. The first, as seen in images A and B came from disordered regions of bundled tendon. This showed a large number of fibrils, but without any discernable orientation to them. The second type was from open and splayed tendons, which gave a much more ordered appearance. Individual fibrils were visible, and the contrast with the glass surface allowed for easy identification of D-banding which was then quantified. However, in order to image these fibrils, the tendon fascicles must be manually separated using forceps and scalpels. This could potentially cause damage to the fibrils and certainly does not represent a realistic appearance of

the fascicle. Each location has distinct advantages regarding representing the tendon as either a tissue or a composite of individual fibrils.

### **Nanoindentation**

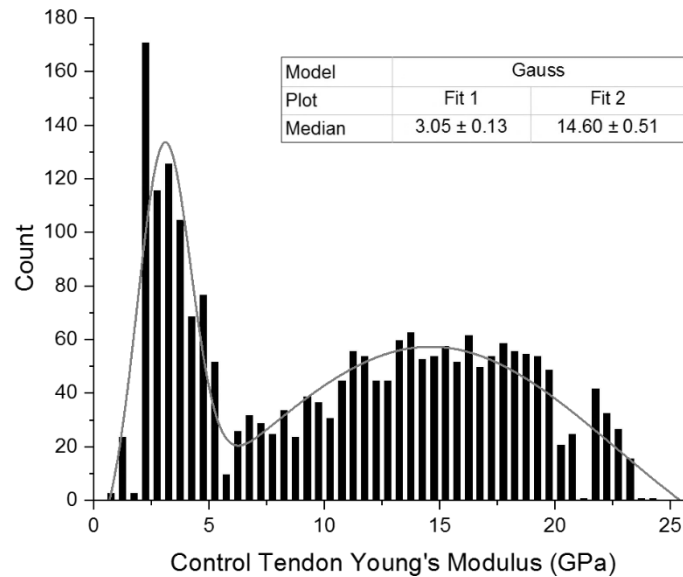


**Figure C-3 AFM mechanics of control mouse tendon showing bimodal distribution**

**Figure C-3** shows the nanoindentation for the control mouse tail tendon as taken by the AFM. After processing, a bimodal distribution was found, with a narrow peak at  $3.05 \pm 0.13$  GPa and a much broader distribution with a median value of  $14.6 \pm 0.5$  GPa.

## **D. Bone Fragility of ARC Syndrome Mice**

In addition to the tendons collected from ARC model mice in Chapter 4 ,bones were also collected and analysed. This data is presented here.

### **Methodology**

#### **Dynamic Mechanical Analysis**

Testing for Young's modulus and yield stress was performed on a DMA 7e (Perkin-Elmer Instruments, UK) with the data analysed on Pyris TA Software, v6 (Perkin-Elmer Instruments, UK). The data was exported as a stress-strain curve. The values of Young's modulus could be obtained (Equation D-1) from the linear section of the graph, along with maximum (yield) stress, and maximum strain. Results were graphed on OriginPro v9.1 (OriginCorp, Massachusetts) as a box-plot graph. This shows the minimum and maximum range of the data, and the mean average for the whole range at the range within a 95% confidence interval.

$$E = \frac{FL_0}{A_0\Delta L}$$

Equation D-1 Young's modulus (E), where F tensile force,  $l_0$  original length,  $A_0$  original area,  $\Delta l$  change in length

#### **Indentation and Hardness**

The indentation was performed on a Wallace micro-indentation tester (Wallace & Co, UK) with a load weight cell of 300g. The long axis of the bone was indented for 30 seconds with a diamond tip, and the results obtained as an indentation count. This



was converted to a Vickers' Hardness Number (VHN) value (Equation D-2) and converted again into SI units. Results were graphed on OriginPro v9.1 (OriginCorp, Massachusetts).

$$HV = \frac{F}{A} \quad \text{Where } A: A = \frac{d^2}{2\sin(\frac{136^\circ}{2})}$$

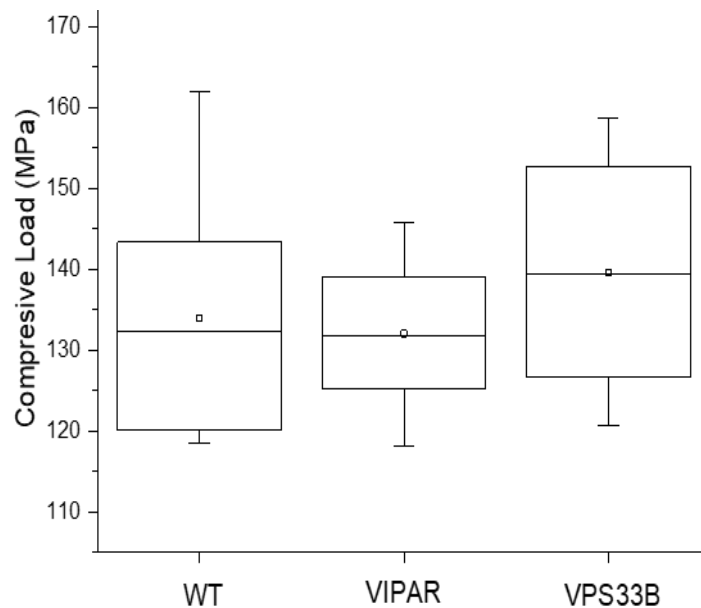
**Equation D-2 Equation for the calculation of the VHN, independent of diamond size, where HV**  
**VHN, F load applied**

$$\text{Diamond dimension, } A: A \approx \frac{d^2}{1.8544} \quad \text{So HV: } HV \cong \frac{(1.8544 \times 300g)}{d^2}$$

**Equation D-3 Equation for the VHN based on diamond dimensions and conversion on SI units,**  
**where HV Vickers' hardness number, d average diagonal length left by the indenter.**

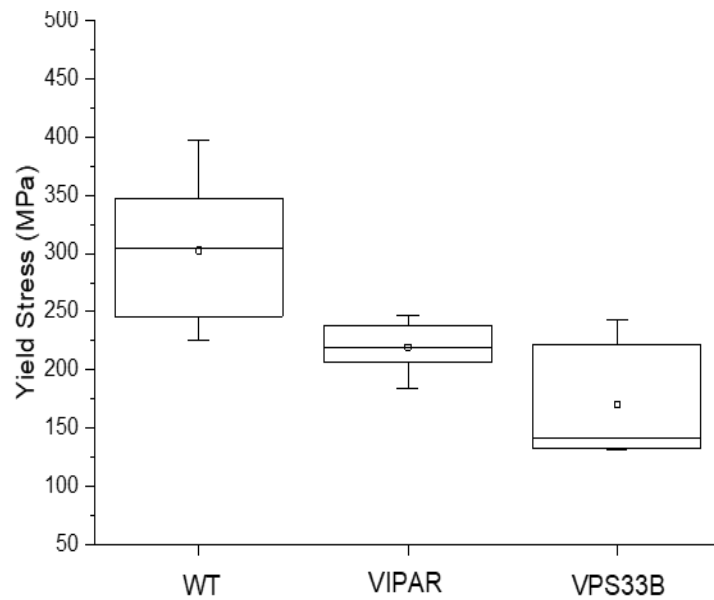
## Bone Fragility Results

It has become clear from the investigations into mice tendons so far that VPS33B and VIPAR knockouts have a significant effect on the fibrillar structure of collagen. Until this point, all investigations have focused on the nanoscale and mesoscale without any investigation into the macroscale. Any alteration in tissue properties is expected to be seen when collagen is the major constituent of the tissue. It was unclear how collagen defects would affect the overall tissue behaviour in areas where collagen, not the dominant tissue type. Indentation as performed using a Wallace hardness tester on mouse bones. Forelimbs of the mice were chosen due to sample availability and were indented to measure compressive load, yield stress and Young's modulus.



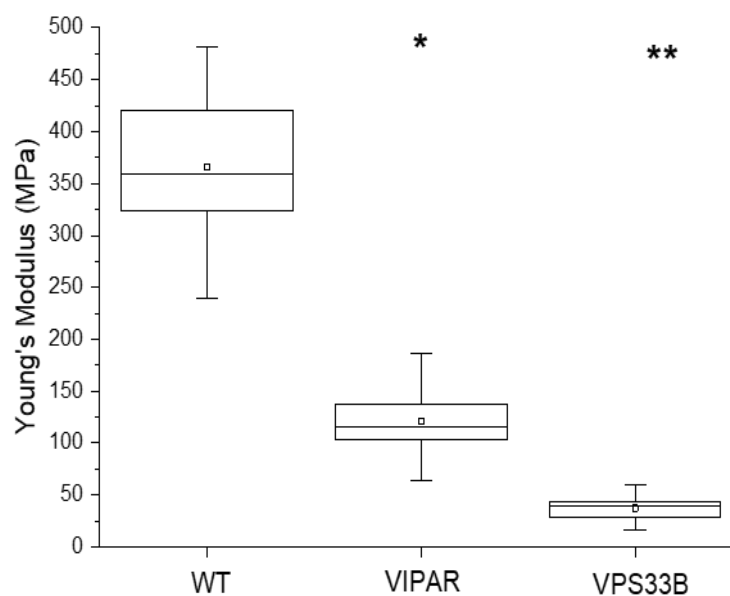
**Figure D-1 Graph showing compressive load through indentation, N = 8. P < 0.05**

Figure D-1 shows the compressive load of the mouse bones. The WT had a median of 133.2 MPa, the VIPAR KO had a median of 132.1 MPa, and the VPS33B KO had a median of 137.4 MPa. No significant differences were found after statistical analysis with the Kruskal-Wallace test with a P value of 0.05.



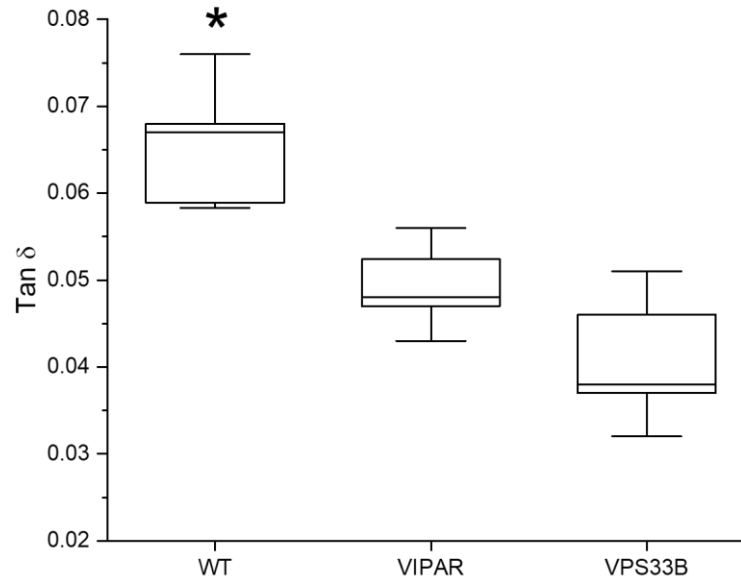
**Figure D-2 Graph showing the yield stress through indentation, N = 8. P < 0.05**

Figure D-2 shows the yield stress of the mouse bones. The WT had a median value of 307.4 MPa, the VIPAR KO had a median of 248.21 MPa, and the VPS33B had a median of 136.69 MPa. Despite appearances in the graph, no statistical difference was found after analysis with the Kruskal-Wallace test with a P value of 0.05.



**Figure D-3 Graph showing Young's modulus through indentation, N = 8. P <0.05**

Figure D-3 shows Young's modulus of the bones. This was calculated from the indentation at the linear section of the stress/strain graph. There is a significant difference (at  $p < 0.05$ ) between the modulus of the WT and that of the VIPAR, with a further significant difference ( $p < 0.005$ ) between the WT and the VPS33B KO. The mean average of the WT samples was  $366 \pm 75$  MPa, VIPAR  $130 \pm 36$  MPa, and VPS33B  $37.4 \pm 13$  MPa, one order of magnitude lower than the WT values.



**Figure D-4 shows tan  $\delta$  of mouse bones, N = 6. P < 0.05**

Figure D-4 shows the tan  $\delta$  measurements of the bones derived from DMA analysis. The WT sample had a mean average of 0.066, compared with VIPAR average of 0.049, and the VPS33B average of 0.041. This result was statistically significant ( $p > 0.5$ , Kruskal-Wallis.) No significant changes were seen between the two KO groups.

### Bone Fragility Discussion

In bones, indentation is a property controlled by the hardest materials, in this case, primarily hydroxyapatite and other mineralised components<sup>501–504</sup>. The genetic KO in the mice is known to affect only the extracellular transport of collagen at the juvenile stage. As such, it was not expected for there to be any change in the mineralisation of bone at the macroscale. The experiment involved the application of a 300g weight on the long axis of the bone, as a uniaxial compressive load. The resultant force was sufficient to indent the bone, without destroying it. Uniaxial compressive load seeks to shorten the axis under stress (in this case, stressing a cross-section of bone);

softer materials are more likely to compress, whilst harder materials will resist compression. Additionally, it is important to note that under general physiological conditions, the bone will be stressed in a transverse direction <sup>451</sup>.

Further investigations analysed the mechanical properties of yield stress and Young's modulus of the bones in tension. Bone samples were stretched under uniaxial tension along the long axis of the bone. The yield stress of a material is the point at which the material deforms plastically (irreversible or inelastically). This is calculated from a stress-strain graph. A set strain rate was applied, and the results (Figure D-2) show that there was no statistical significance between the three tested samples. However, the WT samples did show a more extensive data spread within the 95% confidence interval (CI) than the KOs. Some values for the VIPAR and VPS33B samples had comparable yield stresses. As cortical bone is mostly inelastic, there is little to no elastic deformation occurring during tensile testing <sup>365,451</sup>. Hydroxyapatite deforms to failure before the collagen, meaning that the yield stress value is also a mineral-controlled property <sup>452,505</sup>. It can be assumed that the yield stress is very close or equal to that of the failure stress of the bone, which is another mineral-controlled property <sup>57</sup>. Following that there was no significance found in the yield stress, there was also no significance in the failure stress.

Two distinct types of measurements were generated from the tensile testing; yield stress and Young's modulus. Bone can be considered to be a composite material with the collagen fibres acting as a scaffold within the hydroxyapatite<sup>506–509</sup>. In an engineered composite, the rule of mixtures is often applied, with the volume fraction and independent Young's modulus of the fibres and matrix calculated separately<sup>510</sup>. Given

that these experiments were performed on samples which were difficult to obtain and test, an experiment could not be performed to determine the ratio of matrix to fibre. To that end, the Young's modulus was calculated directly from the stress/strain graph of the bones under tensile stress. The Young's modulus data (Figure D-3) showed a broad range of data, likely because of biological heterogeneity. However, the VIPAR and VPS33B samples were consistently weaker than the WT samples. The  $\tan \delta$  measurements were also used to confirm this variation.  $\tan \delta$  is defined as the ratio between loss modulus and storage modulus, and is a measure of viscoelasticity, and is an ancillary measure of bone strength<sup>511,512</sup>. As the largest elastic component of the bone, the  $\tan \delta$  value could be interpreted as a measurement of the quality of the collagen, which makes up the largest elastic component of bone<sup>511</sup>. A significant lowering in  $\tan \delta$  was seen in both KO samples. Data is consistent with the data for Young's modulus which showed a consistent decrease in values for the KO bones. The decrease in the mechanical properties can be linked to the collagen defects induced by *vipar* and *vps33b* and has been observed in both transverse and longitudinal measurements, affecting collagen in both connective and mineralised tissues.

As previously described, the VPS33B knockout affects the ability of collagen to form lysyl oxidase crosslinks after secretion to the extracellular matrix. It could be argued that the lack of crosslinks causes both the fibril swelling seen under AFM and SEM as shown in previous sections, as well as these changes in mechanical behaviour. Therefore, changes made to molecular crosslinks are conserved and propagated throughout the organisational hierarchy of collagen, resulting in disorganised fibrils, tendons and more fragile bones. Similarly, to the SEM and AFM data obtained, the

change in the mechanical behaviour of the VIPAR KO was less severe than that of the VBS33B KO. This is consistent with the clinical literature, which reports patients with VIPAR mutations as having similar but reduced symptoms than those with VPS33B mutations in ARC syndrome <sup>438</sup>.

### **Bone Fragility Summary**

Mechanical testing was performed on the bones in macroscale. Parameters where the mineral content is dominant, such as the compressive load and the yield stress, did not give significant differences between the samples. The range of the data was also consistent between the samples. The  $\tan \delta$ , measuring the elastic change in the bone, showed a significant decrease in the VIPAR and VPS33B samples. Most importantly, the Young's modulus significantly decreased in the VIPAR and VPS33B samples. This showed a severe weakening of the collagen and is consistent with the nanoscale and ultrascale measurements taken previously.



## **E. Mouse Model of Scleroderma**

---

This appendix shows LM, SEM, AFM imaging and mechanics on a mouse model of SSc, and formed a prelude to the QNH protocol development on SSc featured in Chapter 5.

### **Materials**

Two mice models of SSc have been developed with a single knock out (SKO) or double knock out (DKO) of the gene *LEPREL1*. Additionally, wild type (WT) controls were reared. KO mice were provided by Dr Hans Peter Bachinger (Shriner Hospital, Portland Oregon) and reared by the team of Dr Richard Stratton (UCL). Ten-week-old female mice were studied in three groups (6-12 mice per group). These were all given daily subcutaneous injections of bleomycin 0.09 units in 100  $\mu$ L of sterile saline per injection site, per mouse, for 21 days, before euthanasia on day 30 for analysis. Additionally, WT, SKO and DKO dermal fibroblasts were cultured from explanted skin biopsy material and seeded at the same density in serum-free media. Conditioned media from dermal fibroblasts were left overnight with saturated ammonium sulphate (20%) in order to precipitate out of solution any proteins. These proteins were then treated with collagenase, removing any non-collagenous material. The collagen onto glass cover-slips for nanoscale indentation and topographical imaging.

In Chapter 4 it was clearly shown that nanoscale imaging and indentation could successfully differentiate between mouse models of the disease ARC syndrome. Differences were seen in the appearance of the collagen and in their Young's moduli. This approach has been replicated on to a mouse model of SSc, knockouts of the gene *LEPREL1*. This gene is known to influence the triple helix formation of collagen and is suspected of having a role in SSc aetiology<sup>33,513</sup>. Here, LM and SEM of the cells were taken, along with AFM images and mechanical analysis of any residual proteins.

## Results and Discussion

### Microscale Fibroblast Imaging

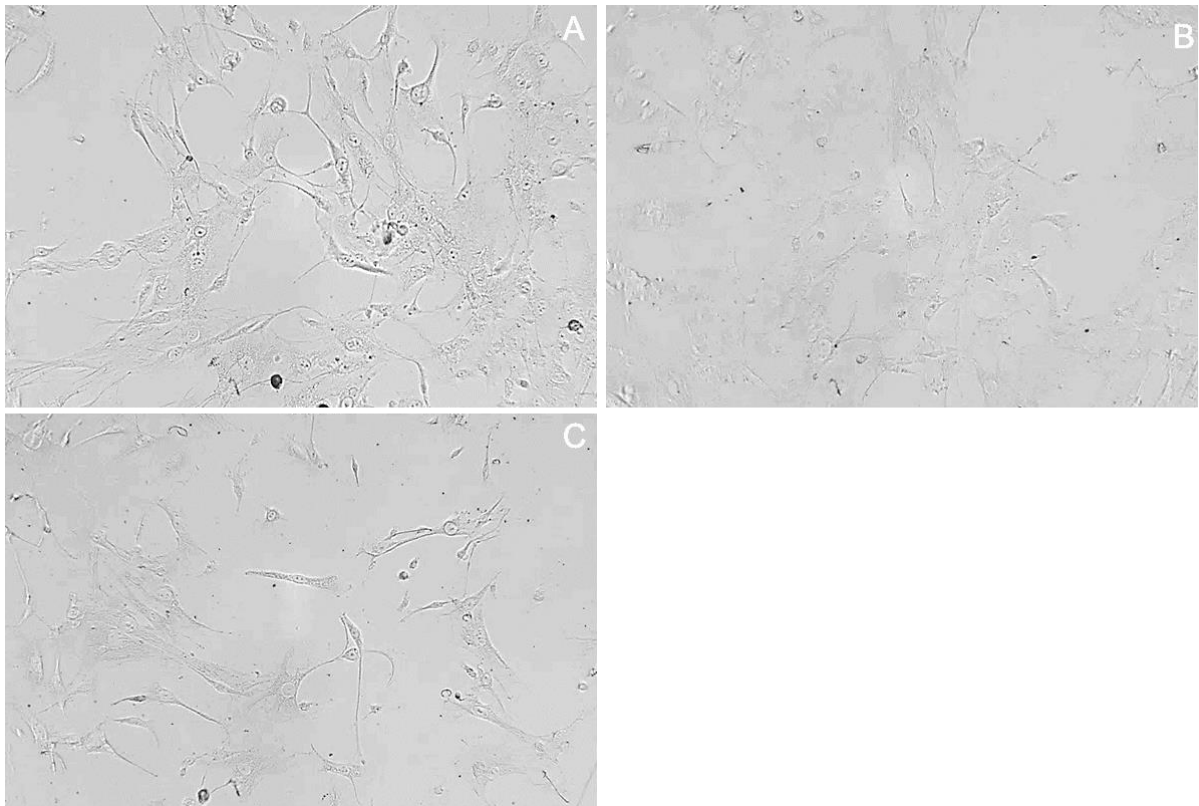


**Figure E-1** Light field LM of the fibroblast KO's after purification. A) WT, B) SKO, C) DKO. 10x magnification

**Figure E-1** shows fibroblast cells purified from the mouse biopsies before animal sacrifice. Image **A** show the WT cells, with regular morphology. Cell processes are

visible without evidence of cellular necrosis or apoptosis. Image **B** shows the SKO cells, which are similarly regular in appearance, with the nuclei visible. Image **C** shows the DKO cells, which are not as tightly packed as the cells in image A or B. Material that could be cellular fragments are also present.

#### Mesoscale Fibroblast Imaging

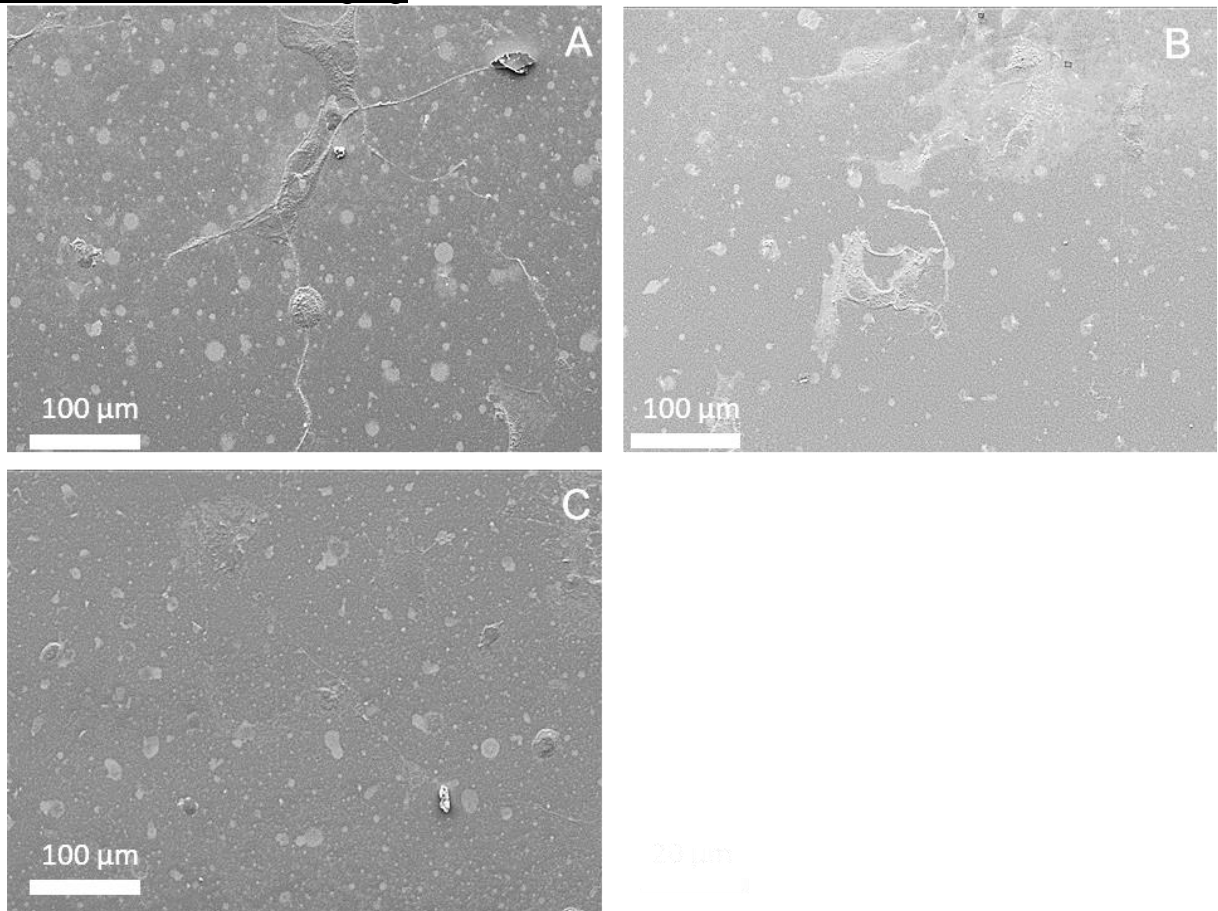


**Figure E-2 SEM of fibroblast cells on glass slides. A) WT, B) SKO, C) DKO. 200x magnification**

**Figure E-2** shows the SEM fibroblast cells after purification. Image **A** shows the WT sample, with a large fibroblast clearly visible in the centre of the image. Cellular processes and other cells are discernible towards the edges of the image. Image **B** shows the SKO sample, and several cells can be seen in the middle of the

image. The cells appear to be smaller in the SKO image than those seen in the WT sample. Image **C** shows the DKO sample, although only faint traces of cells were seen in any of the DKO images taken. Evidence of residue and other material forms the background of all of the images.

#### Nanoscale Protein Imaging

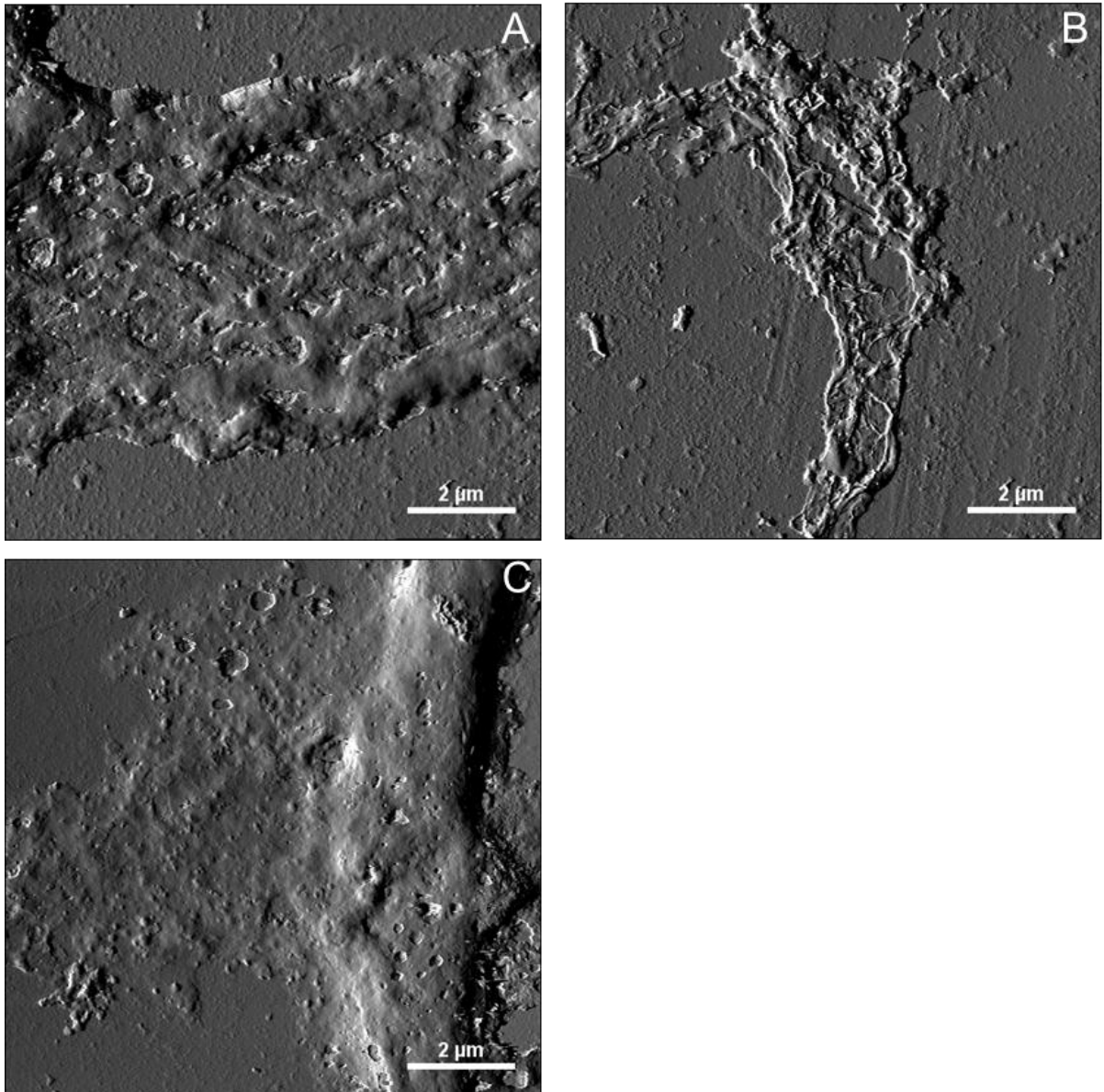


**Figure E-3** AFM of proteins after precipitation, glass is visible as the background. A) WT, B) SKO, C) DKO.

**Figure E-3** shows the AFM of precipitated media from knockout fibroblasts after treatment with collagenase. Image **A** shows the WT media. There are numerous distinct structures present in the centre of the mass, which have a degree of directional alignment. Surrounding those is amorphous material. Image **B** shows the SKO samples. Long fibrils are seen, which have a clear directional orientation. Some thinner fibres are connecting the larger bundles. Image **C** shows the DKO media. There is coverage of amorphous material with a large agglomeration present. No fibres or ordered structures are visible. Small dots visible in the mass are likely to be residual ammonium sulphate crystals.

#### Nanoscale Collagen Indentation

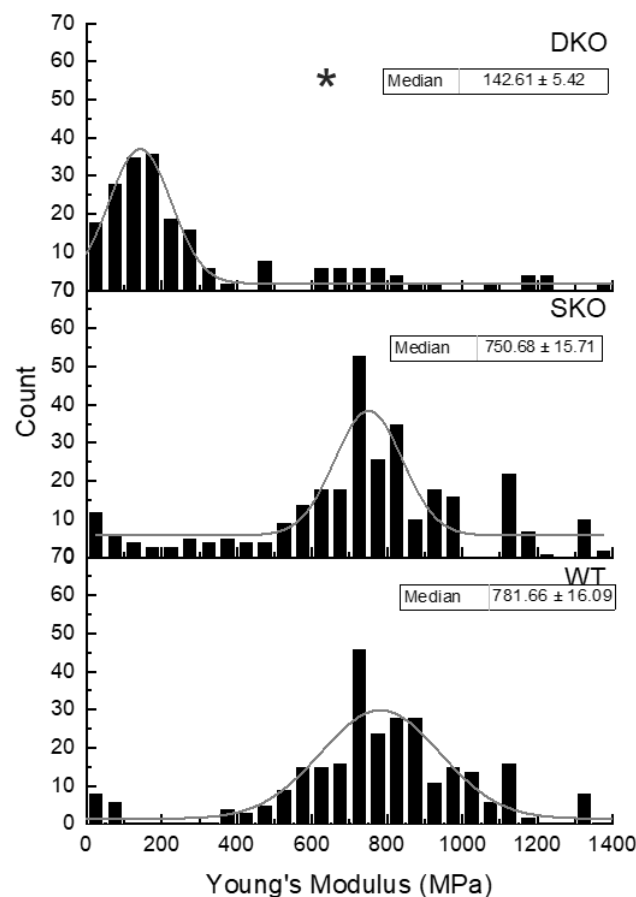


**Figure E-4** Young's modulus of WT, SKO and DKO showing unimodal distribution

**Figure E-4** shows the comparison in Young's modulus between WT, SKO and DKO samples. WT has a unimodal distribution of  $781.66 \pm 16.06$  MPa, with a broad range between 400-1200 MPa. SKO has a similar unimodal distribution of  $750.68 \pm 15.71$  MPa, which was not found to be statistically different to WT. DKO has a unimodal distribution of  $142.61 \pm 5.42$  MPa, which was statistically lower than either the WT or SKO moduli,  $p < 0.05$ , Kruskal-Wallis.

#### Mouse Model Discussion

*In vivo*, *LEPREL1* forms a part of the prolyl 3-hydroxylases, essential in aligning nascent procollagen in the endoplasmic reticulum before the formation of the collagen triple helix, which is eventually stabilised by prolyl 4-hydroxylases<sup>33,139,513</sup>. Previous to this study, prolyl 3-hydroxylases had not been studied for their effects on fibrosis, but it was theorised that these enzymes could be rate limiting the production of collagen.

Starting with the LM images (Figure E-10) there were initial indications that similarities exist between the WT and SKO sample, which the DKO sample was showing a decreased number of cells. This was again found in SEM (Figure E-2) with the morphology of the cells appearing similar for WT and SKO, but without large numbers of cells present in the DKO sample. After a random sampling of locations, the majority of DKO areas did not have cells present. The amount of background material appears to be similar in all of the images. This prompted further investigation, leading to the analysis of the proteins present in the cells. Having purified the collagen, the AFM images showed that WT and SKO were able to form identifiable structures (Figure E-3) while the DKO collagen appeared as an amorphous mass. Comparisons can easily be made to collagen gels when made *in vitro*<sup>514</sup>. When made correctly and pH stabilised,

these gels will naturally form fibrils similar to *in vivo* collagen but without any alignment or directional orientation, lacking crosslinks<sup>197,515</sup>. The mechanical properties of the gels are also weakened<sup>515</sup>. The mass seen in DKO is similar to unpolymerised collagen gels, which are often formless. However the lack of D-banding in the WT or SKO samples show that fibrillar collagen was not made.

Indentation using AFM on the structures or masses seen in the samples (Figure E-4) showed that WT and SKO are again similar, this time without any statistical differences between the results. SKO had the largest range of data out of the three conditions tested, supporting its theorised role as an intermediate knockout that would not be as atypical as DKO. The DKO Young's modulus was significantly lower than that of the WT or SKO. The range of the Young's moduli values are lower than expected for *in vivo* collagen, which is between 0.5-20 GPa<sup>59,374,395</sup>. The values of WT and SKO are consistent with that range, as well as the values for uncompressed and uncrosslinked collagen gels<sup>343</sup>. An initial concern was ensuring the purification of the collagen alone, as other proteins could be present in the culture media. Salting out the proteins using ammonium sulphate is an established technique, which combined with the addition of collagenase (previously used in Chapter 3.4.2.5) allowed for confidence that only collagen was present in the tested samples<sup>408</sup>.

The mechanical measurements are counterintuitive when considering the effects of SSc. As a disease, the fibrosis of collagen causing a visible hardening of the skin, and a measurable increase in the Young's modulus of the collagen<sup>189,395,489</sup>. However, the model of SSc caused a decrease in the Young's modulus when measured in this study. Mutations in LEPREL1 have been linked to OI and high myopia, both collagen

weakening disorders which support the Young's modulus findings here <sup>516,517</sup>. Along with other findings, it was proposed that the encoded LEPREL1 enzyme might be an important rate-limiting factor in the SSc fibrotic responses or otherwise critically involved in the disease process, which could be targeted by therapeutics<sup>466</sup>. Furthermore, it was suggested that there is a greater requirement for increased levels of prolyl 3-hydroxylase enzymes during the formation of collagen-rich tissues, such as the cornea, skin and tendons. Therefore, while any adverse effects of prolyl 3-hydroxylase inhibitors on health would need to be carefully evaluated, the effects of *LEPREL1* on the SSc fibrosis pathway need further investigation.

#### Mouse Model Summary

The work in Chapter 4 provided an outline for the work in this section. Here, a model of SSc based on knockouts of *LEPREL1* was found to behave as predicted, with the DKO acting significantly different from that of WT and SKO in all measurements. SEM and LM showed the behaviour of fibroblasts with the knockouts, while AFM was used on purified collagen. WT and SKO formed identifiable structures, while DKO remained amorphous. Differences in Young's modulus showed that DKO was less stiff than WT and SKO, suggesting that in SSc patients, LEPREL1 could act as a rate-limiting factor to limit the spread of the disease.



# F. An Engineered, Quantifiable In Vitro Model for Analysing the Effect of Proteostasis-Targeting Drugs on Tissue Physical Properties

Biomaterials 183 (2018) 102–113



Contents lists available at ScienceDirect

Biomaterials

journal homepage: [www.elsevier.com/locate/biomaterials](http://www.elsevier.com/locate/biomaterials)



## An engineered, quantifiable *in vitro* model for analysing the effect of proteostasis-targeting drugs on tissue physical properties



Sandra Loaiza<sup>a,1</sup>, Silvia A. Ferreira<sup>b,1</sup>, Tamara M. Chinn<sup>a,b</sup>, Alex Kirby<sup>c</sup>, Elena Tsolaki<sup>c</sup>, Camilla Dondi<sup>b</sup>, Katarzyna Parzych<sup>a</sup>, Adam P. Strange<sup>d</sup>, Laurent Bozec<sup>d,f</sup>, Sergio Bertazzo<sup>c</sup>, Martin A.B. Hedegaard<sup>c</sup>, Eileen Gentleman<sup>b,\*</sup>, Holger W. Auner<sup>a,\*</sup>

<sup>a</sup> Cancer Cell Protein Metabolism Group, Department of Medicine, Imperial College London, London W12 0NN, UK

<sup>b</sup> Centre for Craniofacial and Regenerative Biology, King's College London, London SE1 9RT, UK

<sup>c</sup> Department of Medical Physics and Biomedical Engineering, University College London, London WC1E 6BT, UK

<sup>d</sup> Biomaterials and Tissue Engineering, Eastman Dental Institute, University College London, London WC1X 8LD, UK

<sup>e</sup> Department of Chemical Engineering, Biotechnology and Environmental Technology, University of Southern Denmark, 5230 Odense M, Denmark

<sup>f</sup> Faculty of Dentistry, University of Toronto, 124 Edward Street, Toronto, ON M5G 1G6, Canada

### ARTICLE INFO

#### Keywords:

Proteostasis  
VCP/p97  
Raman spectroscopy  
Cancer diagnosis and therapy  
Atomic force microscopy  
Proteasome

### ABSTRACT

Cellular function depends on the maintenance of protein homeostasis (proteostasis) by regulated protein degradation. Chronic dysregulation of proteostasis is associated with neurodegenerative and age-related diseases, and drugs targeting components of the protein degradation apparatus are increasingly used in cancer therapies. However, as chronic imbalances rather than loss of function mediate their pathogenesis, research models that allow for the study of the complex effects of drugs on tissue properties in proteostasis-associated diseases are almost completely lacking. Here, to determine the functional effects of impaired proteostatic fine-tuning, we applied a combination of materials science characterisation techniques to a cell-derived, *in vitro* model of bone-like tissue formation in which we pharmacologically perturbed protein degradation. We show that low-level inhibition of VCP/p97 and the proteasome, two major components of the degradation machinery, have remarkably different effects on the bone-like material that human bone-marrow derived mesenchymal stromal cells (hMSC) form *in vitro*. Specifically, whilst proteasome inhibition mildly enhances tissue formation, Raman spectroscopic, atomic force microscopy-based indentation, and electron microscopy imaging reveal that VCP/p97 inhibition induces the formation of bone-like tissue that is softer, contains less protein, appears to have more crystalline mineral, and may involve aberrant micro- and ultra-structural tissue organisation. These observations contrast with findings from conventional osteogenic assays that failed to identify any effect on mineralisation. Taken together, these data suggest that mild proteostatic impairment in hMSC alters the bone-like material they form in ways that could explain some pathologies associated with VCP/p97-related diseases. They also demonstrate the utility of quantitative materials science approaches for tackling long-standing questions in biology and medicine, and could form the basis for preclinical drug testing platforms to develop therapies for diseases stemming from perturbed proteostasis or for cancer therapies targeting protein degradation. Our findings may also have important implications for the field of tissue engineering, as the manufacture of cell-derived biomaterial scaffolds may need to consider proteostasis to effectively replicate native tissues.

### 1. Introduction

Accurate and stable maintenance of cellular protein homeostasis (proteostasis) is critical for tissue integrity and has been linked to longevity [1–4]. Perturbed proteostasis contributes to the pathogenesis

of a myriad of predominantly age-related diseases ranging from neurodegenerative disorders to diabetes and cancer [5–7]. An elaborate network of mechanisms constantly monitors and fine-tunes the intracellular proteome [8,9]. The controlled degradation of proteins that are dysfunctional, damaged, or no longer needed is central to this

\* Corresponding authors.

E-mail addresses: [eileen.gentleman@kcl.ac.uk](mailto:eileen.gentleman@kcl.ac.uk) (E. Gentleman), [holger.auner04@imperial.ac.uk](mailto:holger.auner04@imperial.ac.uk) (H.W. Auner).

<sup>1</sup> These authors contributed equally to this work.

<sup>2</sup> These authors provided equal joint supervision.

<https://doi.org/10.1016/j.biomaterials.2018.08.041>

Received 10 August 2018; Accepted 20 August 2018

Available online 21 August 2018

0142-9612/ © 2018 The Authors. Published by Elsevier Ltd. This is an open access article under the CC BY license

(<http://creativecommons.org/licenses/by/4.0/>).

process and is primarily executed by the ubiquitin-proteasome system (UPS). The UPS recognises proteins that have been earmarked for degradation by the addition of polyubiquitin chains, and degrades them in the 26S proteasome, thereby regulating multiple cellular functions, including stem cell fate [10–13]. Small molecule inhibitors of the proteasome are widely used in the treatment of multiple myeloma, and pharmacological targeting of other UPS components is a major area of anti-cancer research [14].

The ATPase VCP/p97 plays a central role in the UPS by extracting ubiquitinated proteins from cellular structures and delivering them to the proteasome [15–19]. Drugs targeting VCP/p97 have therapeutic potential as anti-cancer agents and for the treatment of epilepsy linked to GABAA receptor mutations [20–22]. VCP/p97 mutations have been associated with a multisystem degenerative disease that comprises Paget's disease of bone, inclusion body myopathy, and fronto-temporal dementia (IBMPFD), and with several other diseases of the nervous and muscular system [23–28]. In short, VCP/p97 is essential for cellular proteostasis and maintains skeletal and neurological health [29].

Although the pathogenesis of VCP/p97-related diseases remains to be established, their associated cellular dysfunction has been linked to defective proteostatic fine-tuning [29–31]. This putative mechanism is compatible with the notion that relatively minor but chronic or intermittent imbalances in proteostasis contribute to many age-related diseases [4,29]. However, perturbations in fine-tuning that result in chronic or intermittent imbalances in intracellular proteostasis are extremely challenging to replicate in *in vitro* and particularly in *in vivo* models. Indeed, the relative difficulty of establishing a research model when impairment rather than loss of function mediates complex tissue pathologies has hampered research efforts to identify the pathogenesis of VCP/p97-related diseases. Moreover, there are currently no robust experimental paradigms to study the functional effects of intracellular proteostasis imbalance or test potential therapeutic compounds that modulate proteostasis. In short, a research platform that could mimic the functional tissue effects of chronic or intermittent proteostasis imbalances could be invaluable in both exploring disease mechanisms and screening for drug effects.

The bone-like material that can be formed by osteogenic cells *in vitro* constitutes a highly informative model system to study how impaired intracellular proteostasis might impact functional tissue properties. As mesenchymal stromal/stem cells (MSC) differentiate down the osteogenic lineage and synthesise large amounts of extracellular matrix (ECM), they become highly dependent on mechanisms which control proteostasis [32–34]. This secreted proteinaceous matrix is then progressively mineralised by poorly crystalline carbonated apatite, producing a bone-like nano-composite structure in a highly controlled process such that even small perturbations to the composition of either the proteinaceous or mineral phases can significantly impact bone quality [35–37], providing a read-out of proteostasis imbalance. This model is also of direct clinical relevance because the pathogenesis of VCP/p97-related bone disease is incompletely understood; and whilst proteasome inhibitors purportedly stimulate bone regeneration in myeloma patients, the effects of drugs targeting VCP/p97 on bone have not been established [38–40]. Moreover, cell-derived, ECM-based materials have been proposed as promising scaffolds to direct SC differentiation in tissue engineering applications [41,42]. Therefore, insight into how proteostasis imbalances may impact these biomaterials' functional properties may be important for creating scaffolds that appropriately mimic native tissues.

To understand how impaired proteostatic fine-tuning functionally affected tissue, we created an *in vitro* model using intermittent low-level proteasome or VCP/p97 inhibition in human MSC (hMSC) as they differentiated into osteoblasts and formed a cell-derived, bone-like material (Supplementary Fig. 1). We show that low-level inhibition of VCP/p97 and the proteasome differentially affect the bone-like material that hMSC form *in vitro*. Indeed, whilst proteasome inhibition subtly promotes the formation of a material akin to native bone, Raman

spectroscopic, atomic force microscopy (AFM)-based indentation, and electron microscopy imaging suggest that VCP/p97 inhibition results in a material that is softer and less proteinaceous, but whose mineral appears to be more crystalline and morphologically aberrant. These observations suggest that mild VCP/p97 impairment in hMSC undergoing osteogenic differentiation may alter tissue physical properties in a way that could explain some of the pathologies associated VCP/p97-related diseases, including changes in bone mechanical properties [43]. Our results highlight the utility of applying materials science approaches to challenges that biological techniques cannot yet address. They may also provide the basis for *in vitro* platforms that would allow for the functional effects of proteostasis imbalances to be evaluated quantitatively in a model that could be particularly relevant for high-throughput pre-clinical drug screening purposes. Finally, our findings suggest that the fabrication of biomaterial scaffolds that utilise cell-derived matrices may need to consider the effects of proteostasis in order to properly match scaffold properties to those of the native tissue.

## 2. Results

### 2.1. DBeQ and bortezomib induce a mild proteotoxic stress response in differentiating hMSC

To develop an *in vitro* model of proteostasis imbalance, we first aimed to determine if we could mildly perturb proteostasis in hMSC undergoing osteogenic differentiation. Genetic approaches to deplete VCP/p97 or the proteasome are not suitable to study the effects of mild functional impairments [20,44]. Therefore, we took a pharmacological approach and treated hMSC with either the well-characterised and highly selective VCP/p97 inhibitor, DBeQ [45–48], or the first-in-class clinical proteasome inhibitor, bortezomib [49]. To define inhibitor concentrations that would induce mild functional impairment without overt toxic effects, we initially determined IC<sub>50</sub> values for viability. We found that osteogenic differentiation increased the IC<sub>50</sub> for DBeQ (as determined by cellular metabolic activity) from 7.5 μM in undifferentiated hMSC to 22 μM in their differentiated progeny (Fig. 1a). For comparison, bortezomib, which effectively kills multiple myeloma cells *in vitro* at concentrations of 10–20 nM [47] (Supplementary Fig. 2), did not reduce viability of differentiating hMSC at concentrations up to 1000 nM (Fig. 1a). Next, we aimed to determine the degree of proteotoxic stress caused by a concentration of DBeQ that did not affect viability (5 μM) at any stage of *in vitro* differentiation compared to a clinically relevant concentration of bortezomib (20 nM) by quantifying the expression of a panel of genes encoding proteins with key roles in proteostasis. DBeQ and bortezomib both induced a very mild proteotoxic stress response, as determined by low-level changes in proteostasis gene mRNA levels that were largely non-significant (Fig. 1b and Supplementary Table 1). For comparison, the protein glycosylation inhibitor tunicamycin, which causes protein misfolding in the endoplasmic reticulum, resulted in more pronounced changes in proteostasis gene mRNAs when given at a nonlethal dose (Fig. 1b and Supplementary Table 1). However, immunoblotting for ubiquitinated proteins confirmed that bortezomib and DBeQ perturbed the UPS, with a clear increase in the level of ubiquitinated proteins in cells treated with bortezomib, while DBeQ had a minor effect (Fig. 1c and Supplementary Fig. 3). These observations demonstrate that by fine-tuning an appropriate dose in differentiating hMSC, DBeQ and bortezomib can impair intracellular proteostasis and trigger mild proteotoxic stress that is not acutely toxic to cells.

### 2.2. Neither VCP/p97 nor proteasome inhibition affect gross measures of hMSC osteogenic differentiation

Like primary osteoblasts, hMSC form bone-like mineralised nodules *in vitro* in response to chemical induction. To study the effects of VCP/p97 and proteasome inhibition on this process, we first used

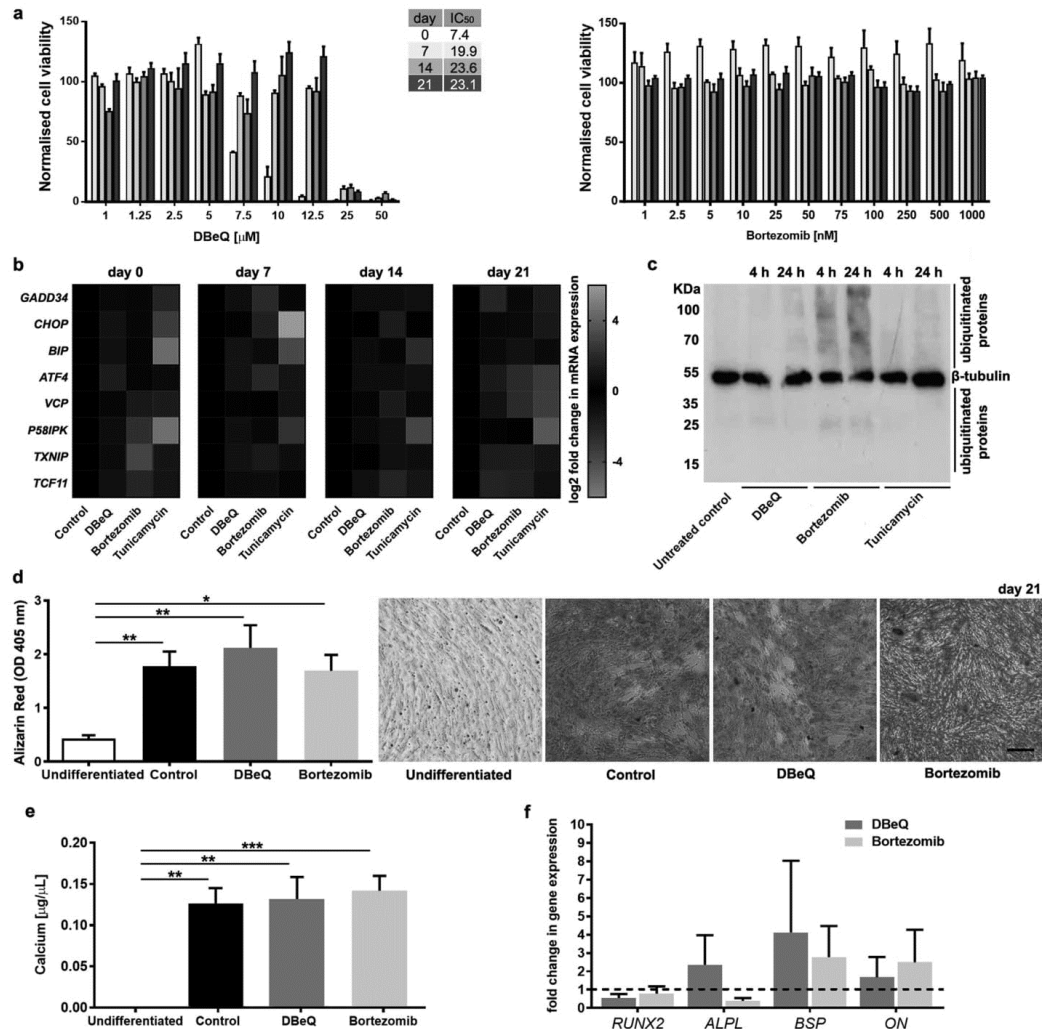


**Fig. 1.** Mild proteostasis perturbations do not grossly affect the osteogenic differentiation of hMSC. **a**, Normalised viability of hMSC undergoing osteogenic differentiation treated on days 0, 7, 14, and 21 with the indicated concentrations of DBEq or bortezomib for 48 h ( $n = 3$ ). **b**, Heatmaps showing relative mRNA expression levels (normalised to undifferentiated controls) for *GADD34*, *CHOP*, *BIP*, *ATF4*, *VCP*, *P58IPK*, *TXNIP* and *TCF11* in differentiating hMSC on days 0, 7, 14, and 21 after treatment for 24 h with DBEq (5  $\mu$ M), bortezomib (20 nM), or tunicamycin (5  $\mu$ g/mL). **c**, Immunoblotting for  $\beta$ -tubulin and ubiquitinated proteins on whole cell extracts from undifferentiated hMSC untreated (control) or treated for 4 h or 24 h with 5  $\mu$ M DBEq, 20 nM bortezomib, or 5  $\mu$ g/mL tunicamycin. **d**, Quantification and representative micrographs showing Alizarin Red S staining (Scale bar = 200  $\mu$ m) and **e**, colorimetric calcium content quantitation of differentiated hMSC cultures. **f**, Relative mRNA expression levels for markers of osteogenic differentiation compared to undifferentiated controls, which are set to 1 (dotted horizontal line). In **a**, **d**–**f**, plots show mean + SEM and in **b**, heat maps show mean of log<sub>2</sub> fold changes in gene expression (normalised to undifferentiated controls) for hMSC from 3 different donors. In **d**–**f**, a Kruskal–Wallis non-parametric test followed by Dunn's Multiple Comparison test was used to detect statistical significance, \* $p < 0.05$ , \*\* $p < 0.01$  and \*\*\* $p < 0.001$ . For detailed  $n$  and  $p$  values see Supplementary Tables 1–4. (For interpretation of the references to colour in this figure legend, the reader is referred to the Web version of this article.)

conventional Alizarin Red S staining (Fig. 1d and Supplementary Table 2) and colorimetric calcium content quantitation (Fig. 1e and Supplementary Table 3), and although subtle qualitative changes in staining patterns were sometimes evident, we found that neither DBEq nor bortezomib treatment resulted in significant gross changes in the

formation of mineralised nodules. We also quantified the expression of genes associated with osteogenic differentiation and found that mRNA levels of *RUNX2*, *ALPL*, *BSP*, and *ON* were not significantly affected by treatment with DBEq or bortezomib (Fig. 1f, Supplementary Table 4 and Supplementary Fig. 4). Taken together, these data suggest that mild

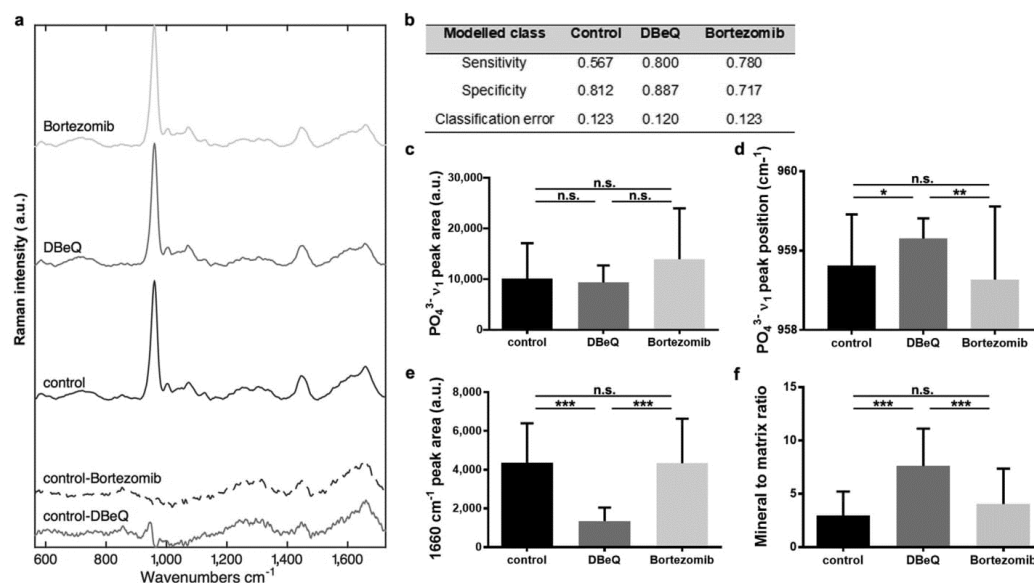


**Fig. 2.** VCP/p97 inhibition alters mineralised nodule composition as determined by Raman spectroscopy. **a**, Mean Raman spectra collected from mineralised nodules formed in control, DBeQ- and bortezomib-treated hMSC cultures. Difference spectra of DBeQ- and bortezomib-treated cultures compared to controls are shown in the bottom of the panel. Spectra are offset on the y-axis for clarity. **b**, Table showing the fraction of spectra in DBeQ- and bortezomib-treated groups and the control that could be classified by sensitivity, specificity and classification error using a cross-validated 6-component Partial Least Squares-Discriminant Analysis model. **c**, Univariate analyses of the mean  $PO_4^{3-} \nu_1$  peak area at  $\sim 960 \text{ cm}^{-1}$  in control, DBeQ- and bortezomib-treated cultures, **d**, mean  $PO_4^{3-} \nu_1$  peak position, and **e**,  $1660 \text{ cm}^{-1}$  peak area. **f**, Mean mineral to matrix ratio in control, DBeQ- and bortezomib-treated cultures. In **c**, **d**, **e**, **f**, data are means + SD and a Kruskal-Wallis non-parametric test followed by Dunn's Multiple Comparison test was used to detect statistical significance. \* $p < 0.05$ , \*\* $p < 0.01$  and \*\*\* $p < 0.001$ . For detailed  $n$  and  $p$  values see Supplementary Table 5.

VCP/p97 or proteasome inhibition did not grossly affect the formation of bone-like mineralised nodules nor the expression of genes known to be key drivers of osteogenic differentiation *in vitro*.

### 2.3. Proteasome, but not VCP/p97 inhibition, subtly promotes mineralised matrix formation

Simple, gross observations of osteogenesis are qualitative and can fail to take into account more subtle aspects of bone formation and structure [50]. Therefore, to generate quantitative measures of the effects of proteostasis imbalances on tissue function, we next applied materials characterisation techniques to analyse the impact of VCP/p97 and proteasome inhibition on differentiating hMSC's ability to form a bone-like material *in vitro*. Raman spectroscopy detects vibrational chemical bonds, capturing the 'biochemical signature' of a substance. Raman spectroscopy has been used to characterise both the composition of native ECM [51] and that secreted by cultured cells [50,52,53]. Raman spectra collected from mineralised nodules formed under all conditions revealed a sharp peak at  $\sim 960 \text{ cm}^{-1}$  indicative of mineral phosphate ion vibrations ( $PO_4^{3-} \nu_1$ ) and other spectral features typical of native bone (Fig. 2a) [54]. This observation confirmed that all groups broadly formed a bone-like material, as previously described [50,52,53]. We then examined the integrated area of the  $PO_4^{3-} \nu_1$  peak, a relative measure of the amount of bone-like apatite [51]. Using standard univariate peak analysis, we observed an increase (although not statistically significant,  $p = 0.085$ ) in the  $\nu_1$   $PO_4^{3-}$  peak area in bortezomib-treated cultures compared to controls (Fig. 2c and Supplementary Table 5). VCP/p97 inhibition, on the other hand, did not alter the intensity of the  $PO_4^{3-} \nu_1$  peak. This suggests that whilst

VCP/p97 inhibition did not affect the amount of mineral produced by hMSC, proteasome inhibition subtly enhanced it, a finding compatible with reports of the anabolic effects of proteasome inhibitors on bone [39,55–57], particularly in multiple myeloma [58–60].

### 2.4. VCP/p97, but not proteasome inhibition, impacts spectroscopic measures of mineral crystallinity and decreases proteinaceous matrix deposition

Raman spectral analyses not only provide information about the relative quantity of a substance, but also its structure. Therefore, we next analysed  $PO_4^{3-} \nu_1$  peak position as an indicator of mineral crystallinity. A downward shift is associated with a more amorphous, disorganised apatite whereas an upward shift suggests that the mineral is more crystalline [51]. Mean  $\nu_1$   $PO_4^{3-}$  peak position for bortezomib-treated hMSC was similar to that of controls. However, in the DBeQ-treated group, it was significantly higher (Fig. 2d and Supplementary Table 5). A shift in  $PO_4^{3-} \nu_1$  peak position was also evident in difference spectra generated by comparing mean DBeQ- and bortezomib-treated conditions to controls (Fig. 2a, bottom-most spectra). The 'control-DBeQ' spectrum produced a shift at  $\sim 960 \text{ cm}^{-1}$ , whilst no shift was evident in the 'control-bortezomib' difference spectrum.

As VCP/p97 inhibition appeared to impact nodules' mineral crystallinity, we next asked if the proteinaceous component had also been affected. The Raman peak centred at  $\sim 1660 \text{ cm}^{-1}$  has been attributed to Amide I and is an indication of protein content [51]. Bortezomib treatment did not affect the integrated area of the Amide I peak, however, it was significantly lower in DBeQ-treated nodules compared to controls (Fig. 2e and Supplementary Table 5), suggesting that VCP/

p97 inhibition decreased the amount of Amide I-containing protein secreted by hMSC. This was reflected in mineral to matrix ratio, a measure of the relative amount of apatite to protein in nodules. Whilst bortezomib-treated nodules were no different, DBE-Q treatment produced nodules with significantly higher mineral to matrix ratios compared to controls (Fig. 2f and Supplementary Table 5).

We next aimed to confirm the Raman spectroscopic distinctiveness of nodules formed when hMSC were subjected to VCP/p97 as opposed to proteasome inhibition by multi-variate analysis techniques. Using a 6-component Partial Least Squares-Discriminant Analysis model, we found that whilst all groups showed similar classification error, we were able to classify a larger fraction of DBE-Q-treated spectra with better sensitivity and specificity than either control or bortezomib-treated groups (Fig. 2b). This suggests that whilst control and bortezomib-treated mineralised nodules were similar spectroscopically, DBE-Q treatment produced spectra that were more unique and so amenable to classification in the model. Taken together, these observations suggest not only that VCP/p97 inhibition affected the composition of the cell-derived mineralised material created by differentiating hMSC, but also highlights that these effects were quantifiable using a relatively simple interdisciplinary technique.

#### 2.5. VCP/p97, but not proteasome inhibition, decreases mineralised nodule stiffness

As VCP/p97 inhibition affected the biochemical composition of mineralised nodules, we next aimed to expand our *in vitro* model and determine its effect on nodules' nano-scale mechanical properties by measuring their stiffness. AFM is known for its high-resolution imaging capabilities; however, it is also a powerful tool for carrying out force-indentation measurements (Fig. 3a/b), producing quantitative insight into the mechanical properties of a material at the nano-scale [61]. We found that Young's modulus (*E*) was significantly lower in nodules treated with DBE-Q compared to controls or those treated with bortezomib (Fig. 3c and Supplementary Table 6). As indentation was carried out with a probe whose tip radius was 8 nm (manufacturer's specification), this observation suggests that VCP/p97 inhibition significantly reduced the stiffness of the cell-derived material created by differentiating hMSC at the scale of the nano-composite structure of native bone.

#### 2.6. Proteasome inhibition reduces the strength of adhesion interactions, but VCP/p97 inhibition enhances the total energy dissipated

In addition to probing their stiffness, AFM-based indentation measurements also reveal information regarding the cell-derived materials' proteinaceous content. This is because upon indentation, the AFM probe forms non-specific adhesion interactions with the surface of the nodule (likely with proteins). During unloading of the indentation measurement, the deflection of the cantilever can reveal the strength of the adhesion interactions between the probe and the sample, as well as measure the distance over which those adhesion interactions take place. We first found that adhesion force (Fig. 3d, Supplementary Fig. 5, and Supplementary Table 6) was not different in DBE-Q-treated samples compared to controls; however, in bortezomib-treated samples, it was significantly lower. This suggests that bortezomib-treated nodules interacted with the AFM probe less strongly, likely because the protein composition was different and/or was tightly bound to the more highly mineralised nodules and thus less available to interact with the AFM probe.

We next examined the length of the adhesion interactions, a measure of the distance over which adhesion interactions take place between the sample and the AFM probe during the unloading phase (Fig. 3e and Supplementary Table 6). DBE-Q treatment produced interactions at significantly larger adhesion interactions lengths than those observed in either control or bortezomib-treated nodules. Analyses of

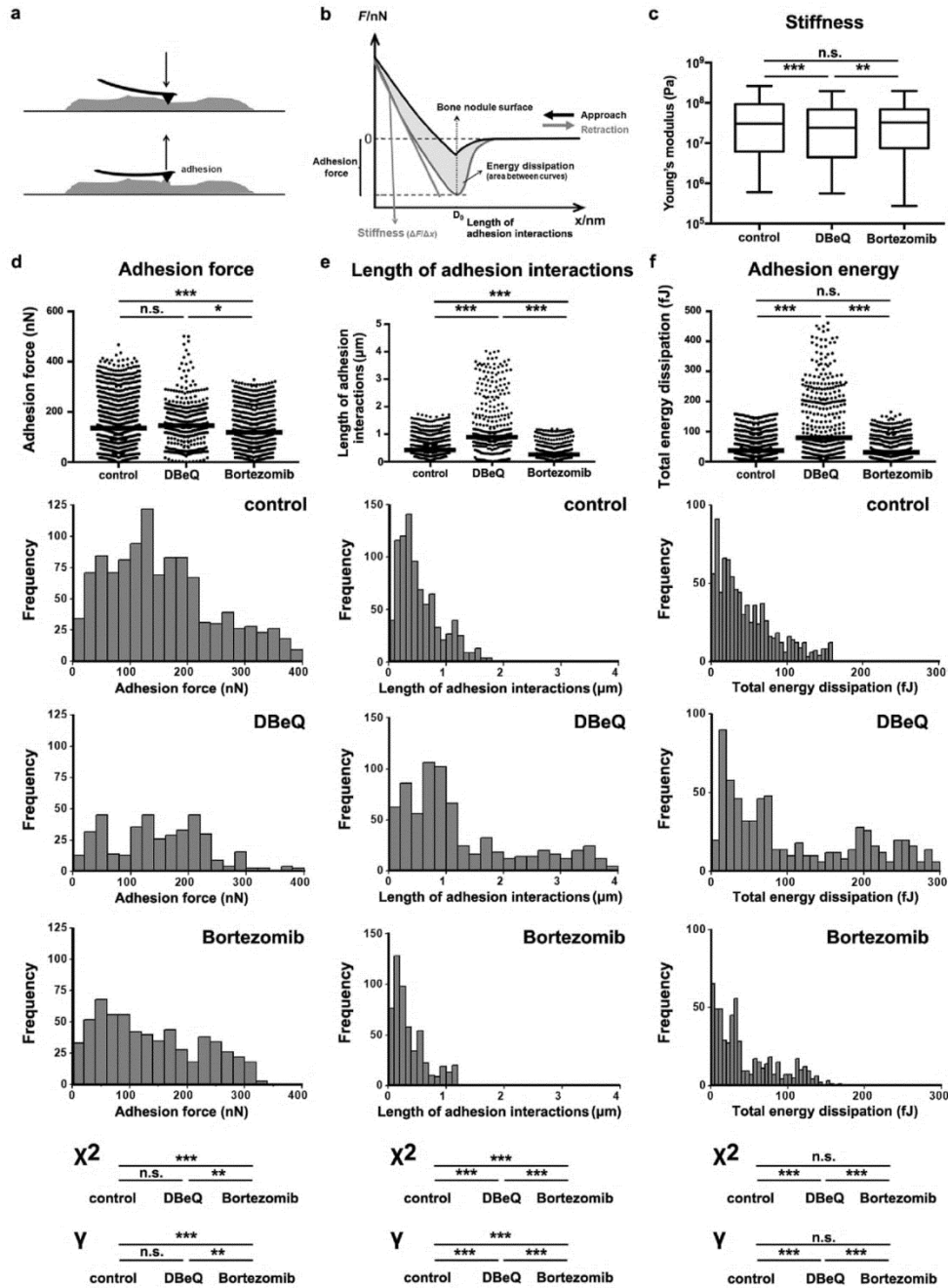
the distributions showed that in DBE-Q-treated nodules, interactions often took place as the probe retracted several microns from the contact point (2–4 µm), as confirmed by statistical analyses for trend (Fig. 3e and Supplementary Table 6). This contrasts with measurements on control and bortezomib-treated cultures, where most interactions took place within a few hundred nanometers of the contact point. This was also evident in measurements of total adhesion energy, which accounts for both adhesion strength and the distance over which it acts (Fig. 3f and Supplementary Table 6). All groups showed interactions with the probe at low values for total energy (first peak in histograms at < 20 fJ), likely reflecting interactions between the AFM probe and protein that was strongly bound to mineral. However, median adhesion energy was significantly higher in DBE-Q-treated groups and was concomitant with many individual measurements at high values of energy dissipation. These observations suggest that VCP/p97 inhibition produced nodules that were highly compliant mechanically and whose protein may have been less tightly bound to the mineral (or the protein had different charge/adhesive properties), and thus could be extended away from the nodules and dissipate energy via interactions with the AFM probe. On the other hand, protein in control and bortezomib-treated nodules may have been more strongly bound to mineral, as in native bone. Moreover, these observations demonstrate that AFM, a widely-available technique, can identify quantifiable changes in tissue properties in response to mild VCP/p97 impairment.

#### 2.7. VCP/p97, but not proteasome inhibition impacts the ultra- and micro-structure of mineralised nodules

As VCP/p97 inhibition affected the biochemical composition, as well as the mechanical and adhesive properties of the bone-like material formed by hMSC, we next aimed to visualise its effects on this matrix using a combination of transmission (TEM) and scanning electron microscopy (SEM). TEM micrographs of control and bortezomib-treated cultures had similar ultrastructures to those previously described for bone-like nodules [50,62], and were notable for aligned fibrous protein between cells (Fig. 4). However, in DBE-Q-treated cultures, we often observed more disorganised matrix in the intercellular space, and aligned fibrous protein was less common. We also examined nodules by SEM using both backscatter and secondary electron modes. Combining the two to create density-dependent colour SEM (DDC-SEM) images allowed us to visualise dense mineralised and less dense proteinaceous areas [63]. hMSC cultured under basal conditions did not form mineralised nodules (Supplementary Fig. 6). Images of the material formed under control conditions and those treated with bortezomib contained dense, mineralised areas that appeared to closely associate with less dense matrix, with morphologies similar to those previously described [64]. However, in DBE-Q-treated cultures, although some dense material localised with matrix, we also observed highly dense areas with little to no associated less dense matrix. Moreover, the structure of the dense mineral in DBE-Q-treated cultures appeared different morphologically. Whilst dense mineralised areas of control cultures appeared smooth, mineral in DBE-Q-treated cultures appeared rougher, with needle-like crystals characteristic of non-physiological precipitation (Supplementary Fig. 7).

### 3. Discussion

Here, we used a combination of materials science-based characterisation approaches to show that very mild impairment of intracellular proteostasis can modify tissue physical properties in a cell-derived *in vitro* model that mimics the formation of native bone tissue. Alizarin Red S staining and calcium quantification showed that DBE-Q- and bortezomib-treated as well as control cultures all produced a similar amount of mineralised material. However, by quantifying the  $PO_4^{3-} \nu_1$  peak intensity of Raman spectra, we determined that bortezomib-treated samples produced numerically (but not statistically significant)



(caption on next page)

**Fig. 3. Proteasome and VCP/p97 inhibition have differing effects on mineralised nodules' stiffness and adhesion interactions.** a, Schematic showing how mineralised nodules were probed by AFM in force-indentation mode using a cantilever with a pyramidal tip. b, Typical force-indentation curve generated from indenting a mineralised nodule. Schematic shows how nodule stiffness and adhesion interactions were calculated from the retraction curve. c, Measurements of Young's Modulus (Pa) of mineralised nodules. Plots show medians, 1st and 3rd quartiles and highest and lowest values. d, Measurements of adhesion force, e, length of adhesion interactions and f, adhesion energy generated from force-indentation curves on control, DBBeQ- and bortezomib-treated cultures. Plots show medians. Histograms with their associated statistical analyses show how the distributions of values differed between the groups. In c–f, a non-parametric Kruskal-Wallis test followed by Dunn's multiple comparison was used to determine statistical significance. Significant differences in the distributions of adhesion values were evaluated using a Mantel-Haenszel linear-by-linear association Chi-squared ( $\chi^2$ ) test for trend. Power was evaluated by determining Goodman and Kruskal's gamma ( $\gamma$ ). \* $p < 0.05$ , \*\* $p < 0.01$  and \*\*\* $p < 0.001$ . For detailed  $n$  and  $p$  values see Supplementary Table 6.

more apatite than other groups. Alizarin red S staining is a crude estimate of bone formation and whilst it detects the presence of calcium-containing compounds [41], bone mineral is more complex. Here, Raman spectral measurements were able to provide more specific information regarding bone-like tissue formation.

In our *in vitro* model, Raman spectroscopy identified quantitative effects of VCP/p97 inhibition, which contrasted with those of proteasome inhibition. Specifically, whilst DBBeQ appeared to increase mineral crystallinity, bortezomib had no significant effect on spectroscopic measures of apatite structure. Mineral crystallinity increases with age [35] and has been associated with decreased bone ductility [36] and increased fracture risk [65], suggesting spectroscopic measurements may provide informative functional measurements of bone quality. VCP/p97 inhibition also significantly decreased nodule protein content, producing a higher mineral to matrix ratio when compared to controls. Although bortezomib treatment subtly promoted mineral formation, this was accompanied by appropriate formation of proteinaceous matrix, as mineral to matrix ratio was not different than that of controls. As bone formation is a highly controlled process in which mineral templates on a proteinaceous matrix, this observation suggests that whilst bortezomib increased mineralisation (in line with previous observations [39,57,58]), proteasome inhibition did not fundamentally interfere with this process. DBBeQ treatment, on the other hand, induced the formation of mineral in the absence of appropriate proteinaceous matrix deposition, suggesting that the mineral may have been aberrant. As Raman spectral measurements are relatively straightforward and can be performed on almost any biological sample under any condition (wet/dry/fixed/unfixed/etc.) in the absence of labelling or staining, these observations highlight the technique's utility as a quantitative means to identify functional tissue effects of VCP/p97 perturbations.

One of bone's primary roles is to resist applied load. Therefore, its mechanical properties, including stiffness, are central to its function.

Indeed, pathological changes in mechanical properties are associated with diseases including osteogenesis imperfecta, osteopetrosis, osteoporosis and rickets [66]. Our AFM-based indentation measurements showed that whilst bortezomib had no effect on the cell-derived materials' stiffness, DBBeQ significantly decreased their Young's modulus. Differences in stiffness are likely not attributable to cultures forming less mineral, as both histochemical staining and spectroscopic analyses showed that VCP/p97 inhibition did not reduce the amount of mineral compared to control cultures. Instead, our observations suggest that DBBeQ altered either the composition or structure of mineralised nodules. In bone, the protein-mineral nano-composite provides toughness via pre-stress within its structure. This is mediated by cross-linked collagen fibres, which impart compressive stress on mineral crystals as they form, whilst the growing mineral crystals tense the collagen structure [67]. Our observations that DBBeQ-treated nodules were less stiff suggests that these composite interactions may have been limited.

Our AFM-based indentation measurements also produced highly informative observations with regards to adhesion interactions. Adhesion interactions with the AFM probe can be mediated by non-specific interactions, likely with protein via hydrophobic, ionic, steric, and/or Van der Waals forces [68]. We observed that DBBeQ, but not bortezomib treatment, led to striking changes in key measures of adhesion, including energy dissipation, suggesting that protein within DBBeQ-treated nodules was either less tightly bound to mineral or the proteome of DBBeQ-treated nodules differed from that in control or bortezomib-treated groups. Bone mineralisation is thought to occur when negatively charged proteins stabilise disordered mineral precursors, which later become more crystalline and grow [69], creating a nano-composite structure. This structure requires a precise protein composition to allow for correct formation. Our observations suggest that in DBBeQ-treated cultures, this balance may have been disrupted, precluding the formation of bone-like mineral with appropriate

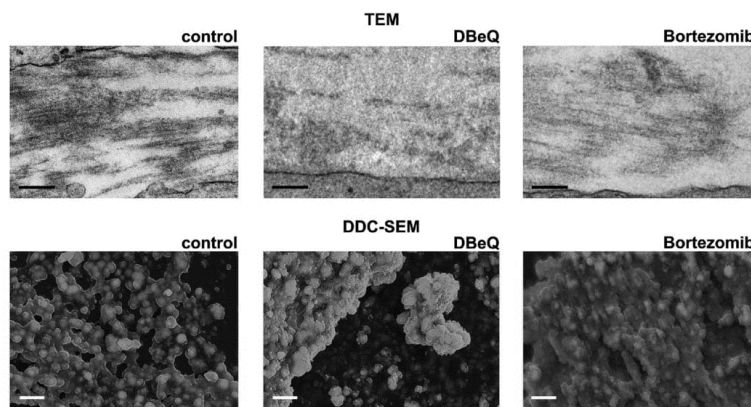


**Fig. 4. VCP/p97 inhibition impacts the ultra- and micro-structure of mineralised nodules.** Transmission electron microscopy (TEM) and density-dependent colour scanning electron microscopy (DDC-SEM) micrographs of mineralised nodules formed from hMSC under standard osteogenic conditions or treated with DBBeQ or bortezomib. In TEM images, proteinaceous fibrils are evident in the intercellular space in control and bortezomib-treated cultures. In DBBeQ-treated samples, the proteinaceous matrix between cells appeared amorphous and clear fibrils were often not evident. Scale bar = 250 nm. In DDC-SEM micrographs, images were coloured in post-processing by combining images from secondary and backscatter electron detectors to identify dense mineral (red) and less dense matrix (green). In control and bortezomib-treated groups, there appears to be an association between the organic matrix and the mineral.

neral. In DBBeQ-treated groups, dense mineral was often detected without the associated presence of less-dense matrix. Images are representative from experiments carried out on cultures grown from 3 independent donors. Scale bar = 2  $\mu$ m. (For interpretation of the references to colour in this figure legend, the reader is referred to the Web version of this article.)



nanostructure. However, despite our quantitative insights, the effects of mild VCP/p97 impairment were subtle and not all adhesion interactions in DBeQ-treated groups displayed long-range, energy dissipative behaviours. Indeed, distributions revealed many measurements with short-range behaviour, similar to that in control and bortezomib-treated groups. Indeed, our observations suggest that either a subset of cells secreted protein that produced aberrant interactions, or a subset of the secreted proteome was aberrant.

TEM and SEM imaging suggested that DBeQ differentially affected the ultra- and micro-structure of the bone-like material created by hMSC compared to bortezomib treatment. Indeed, in DBeQ-treated samples, we observed amorphous rather than fibrillar proteinaceous matrix in the intercellular spaces. As apatite templates on fibrillar collagen in native bone, this observation lends further support to our AFM-based findings that mineral failed to strongly interact with appropriate protein to create a bone-like nano-structure. DDC-SEM images similarly suggested a lack of close association between less dense matrix and denser mineral in DBeQ-treated cultures. Moreover, high magnification secondary electron SEM images of DBeQ-treated cultures revealed needle-like mineral, akin to that observed in non-physiological precipitation reactions [70]. These observations suggest that in addition to an aberrant cell-mediated mineralisation process, the more crystalline mineral in DBeQ-treated cultures could have been formed in a pure physicochemical process, similar to that in pathological calcifications [63].

Here, we describe a cell-derived, biomaterial-based *in vitro* model of bone formation whereby we used pharmacological inhibition of two key components of the intracellular protein degradation apparatus to induce mild cellular stress. We then identified a series of relatively straightforward, widely available techniques from materials science that allowed us to quantitatively characterise changes to tissue biochemical composition, mechanical and adhesive properties, as well as observe morphological changes to their micro- and ultra-structure. This combination of materials science characterisation techniques is particularly amenable for analysing changes in bone-like tissue formation because neither AFM-based indentation, Raman spectroscopy nor the imaging techniques requires specific staining/labeling, which would require *a priori* knowledge of specific targets of the inhibition. The limitation of this approach, of course, is that specific targets are not identified; however, as VCP/p97 and the proteasome inhibitors affect the proteome broadly, this approach may be superior. Moreover, as the techniques analyse the physical material created by cells, they can also detect potential post-translational changes in proteins, which may impact on cell/tissue function. These changes may be missed by standard proteomic techniques, for example. In time, techniques such as single cell proteomics that can analyse post-translation modifications to proteins may become widely available; however, until then, physical science-based characterisations may remain the gold standard.

As our *in vitro* experimental platform allows for the functional effects of proteostasis imbalances to be evaluated quantitatively, it may find use in high-throughput pre-clinical drug screening purposes [71], particularly to evaluate the functional effects on tissues of therapies designed to treat diseases stemming from perturbed proteostasis or for cancer therapies targeting protein degradation. Given that multiple components of protein degradation pathways are being investigated as anti-cancer drug targets, our findings both highlight potential unwanted skeletal effects such approaches might bring, and also offer an early preclinical screening tool. Finally, cell-derived, ECM-based biomaterials akin to the mineralised nodules formed by our hMSC cultures are highly promising as potential scaffolds for tissue engineering [41,42]. As these materials are secreted/arranged by tissue-specific cells, they are both composed of appropriate ECM and contain tethered growth and other regulatory factors to direct seeded SC. However, tissue engineering approaches such as culture on 3D scaffolds can expose cells to reactive oxygen species, acidosis and hypoxia, all of which are known to perturb proteostasis and activate the unfolded protein

response [72]. Our finding that mildly perturbing proteostasis significantly impacts tissue properties suggests that maintaining proteostasis may be essential in forming ECM-based biomaterial scaffolds that replicate the native tissue.

#### 4. Conclusions

Using a cell-derived model of bone formation in which we mildly perturb proteostasis, we have shown that a combination of techniques from materials science can quantitatively detect tissue effects that may explain some of the pathologies associated with VCP/p97-related diseases. This model may have important implications for studying VCP/p97-related diseases. This is because there are no existing *in vivo* models that can replicate the subtle/intermittent proteostasis imbalances that characterise these diseases. Moreover, this is the first *in vitro* model we are aware of that examines the effects of proteostasis imbalances on the mechanical, morphological and biochemical characteristics of tissues, as previous *in vitro* studies using pharmacological agents to perturb proteostasis have only carried out limited molecular analyses, which provide little insight into the tissue pathologies observed in patients. Furthermore, whilst Raman spectroscopy, AFM and electron microscopy have been used to analyse tissues [51,63], including the material formed by cells *in vitro* [50,52,53]; to our knowledge this is the first report using these techniques to analyse tissue changes mediated by VCP/p97 and/or proteasome inhibition.

#### 5. Methods

##### 5.1. hMSC expansion

Human samples used in this research project were obtained from the Imperial College Healthcare Tissue Bank (ICHTB, HTA license 12275). ICHTB is supported by the National Institute for Health Research Biomedical Research Centre based at Imperial College Healthcare NHS Trust and Imperial College London. ICHTB is approved by the UK National Research Ethics Service to release human material for research (12/WA/0196), and the samples for this project were issued from sub-collection R16052. Bone marrow aspirates were obtained at St. Mary's Hospital Imperial College Healthcare NHS Trust (IHCNT) from healthy paediatric stem cell donors. hMSC were expanded for clinical use for the treatment of Graft-versus-Host-Disease. Written informed consent for the use of hMSC for research was obtained from the donors' parents.

Primary cultures were established using CellSTACK® culture chambers, filling caps (Corning Incorporated, Life Sciences) and Macopharma seeding sets (Macopharma) with a grade A cleanroom environment under good manufacturing practice (GMP) conditions. We targeted a seed rate of  $25 \times 10^6$  total nucleated cells per level. Cells were cultured in Minimum Essential Medium  $\alpha$  with GlutaMAX™ (αMEM, Gibco) supplemented with 5% in-house made platelet lysate. Platelets obtained by apheresis from 10 donors by the National Blood Service were pooled, centrifuged at 3000 rpm for 10 min to eliminate platelet bodies, and frozen at  $-80^\circ\text{C}$ . Platelet lysate pools were batch-tested for their ability to support hMSC growth. Cells were cultured in a humidified incubator in 5%  $\text{CO}_2$  at  $37^\circ\text{C}$  until confluent. When confluent (usually after 14 days) cells were harvested and cryopreserved using a controlled rate freezer in 5% human albumin solution (Biotest) containing 10% DMSO (CryoPur™, OriGen) in a 1:1 ratio. Prior to cryopreservation, hMSC were immunophenotyped by staining with a panel of labelled mouse anti-human antibodies (CD105-APC, CD73-PE, CD90-APC, CD45-FITC, CD34-PE, CD3<sup>+</sup>, CD19-PE, HLA-DR-FITC and CD14-PE; BD Biosciences) using a FACSCalibur™ analyser (BD Biosciences) and CELLQUEST software. hMSC expressed CD90, CD105, and CD73 and were negative for hematopoietic markers CD34 and CD45 [73] (data not shown).



## 5.2. Cellular metabolic activity

Cellular metabolic activity as a read-out of cellular viability was measured using the Alamar Blue<sup>®</sup> (Life Technologies) assay according to the manufacturer's instructions. The assay is based on the reduction of resazurin, a non-fluorescent dye, to highly fluorescent red resorufin in healthy cells. The Alamar Blue<sup>®</sup> cell viability reagent was incubated at 10% of sample volume for 1–4 h at 37 °C, and the fluorescence (590 nm) of the sample measured using a FLUOstar Omega BMG Labtech plate reader. Viability was determined relative to untreated cells or cells treated with vehicle only.

## 5.3. Osteogenic differentiation of hMSC and inhibitors

hMSC were seeded at  $5 \times 10^3$  cells/cm<sup>2</sup> in  $\alpha$ -MEM. After 24 h, cells were approximately 80% confluent and osteogenic differentiation was initiated by switching to commercially available Stempro<sup>®</sup> Osteogenesis Differentiation kit medium (Invitrogen) or osteogenic differentiation medium consisting of  $\alpha$ -MEM, 15% FBS, 100  $\mu$ M ascorbic acid (Scientific Lab Supplies, UK), 2.5 mM  $\beta$ -glycerophosphate (Calbiochem) and 100 nM dexamethasone (Sigma). For experiments on undifferentiated hMSC, cells were grown in  $\alpha$ -MEM supplemented with 10% heat-inactivated foetal bovine serum (FBS, Sigma), 1000 U/mL penicillin, and 10 mg/mL streptomycin (Sigma). Medium was changed every 3–4 days, and cells were used until passage 8 only. VCP/p97 and the proteasome were inhibited with DBE-Q (Biovision) or bortezomib (Calbiochem). Tunicamycin was purchased from Sigma.

## 5.4. Myeloma cell line

Human OPM-2 multiple myeloma cells (obtained from the Deutsche Sammlung von Mikroorganismen und Zellkulturen DSMZ; identity confirmed using short tandem repeat profiling of 10 loci (Core Genomic Facility, Medical School, University of Sheffield)) were cultured in RPMI-1640 (Invitrogen) supplemented with 10% FBS.

## 5.5. RNA extraction and reverse transcription

Cells were harvested and snap frozen using liquid nitrogen. RNA was extracted using the GeneJET RNA Purification kit (Thermo Scientific) followed by removal of genomic DNA according to the manufacturer's instructions. Remaining traces of DNA were removed using DNase I treatment (Invitrogen). cDNA synthesis was performed using the RevertAid First Strand cDNA Synthesis kit (Thermo Scientific) according to the manufacturer's instructions using an Applied Biosystems 2720 Thermal Cycler (Life Technologies).

## 5.6. Quantitation of gene expression by real-time PCR

PCR reactions were performed on an Applied Biosystems StepOnePlus<sup>™</sup> PCR machine using 10  $\mu$ L SYBR Green JumpStart<sup>™</sup> Taq ready Mix<sup>™</sup> PCR (Sigma), 0.48  $\mu$ L sequence-specific primers at 300 nM (Supplementary Table 7) and 5  $\mu$ L cDNA. A three-step cycle was employed: (1) denaturation at 94 °C for 2 min; (2) annealing/extension at 60 °C for 1 min; and (3) melting from 60 °C to 94 °C for 2.5 min. The  $\Delta\Delta$ CT method was used to quantify fold changes in expression ( $2^{-\Delta\Delta C_T}$ ) of each gene of interest and normalised to the expression of GAPDH in undifferentiated control cells.

## 5.7. Immunoblotting

Whole-cell protein extracts were prepared on ice using a lysis buffer (Cell Signalling) supplemented with Complete EDTA-free Protease Inhibitor Cocktail (Roche). Then, after 10 min on ice and centrifugation at 4 °C (14,000 rpm) for 10 min, the supernatant was collected. Protein concentration was measured using Bradford reagent (Bio-RAD)

according to the manufacturer's instructions. Proteins were denatured at 100 °C for 5 min with standard SDS-PAGE Loading Buffer (200 mM Tris-Cl, pH 6.8), 400 mM DTT, 8% SDS, 0.4% bromophenol blue, 40% glycerol). Proteins were separated on a 10% SDS polyacrylamide gel using electrophoresis and transferred to PVDF membranes (GE Healthcare). Membranes were blocked with 0.1% TBST (Tris-Buffered Saline, Tween20) containing 5% non-fat milk for 1 h at room temperature, incubated with primary antibodies against ubiquitin (Cell Signalling Technology, cat. no. 39335) and beta-tubulin (Cell Signalling Technology, cat. no. 21465) and then with a secondary anti-rabbit IgG labelled with horseradish peroxidase (Cell Signalling Technology, cat. no. 70745). Finally, an electrochemiluminescence (ECL<sup>™</sup> Western Blotting Reagents, GE Healthcare) system was used to detect proteins.

## 5.8. Alizarin Red S staining

Mineralisation was measured by staining with Alizarin Red S (ARS), a Ca<sup>2+</sup>-binding dye. Cells were washed with phosphate-buffered saline (PBS; Sigma) and fixed in 10% formalin in PBS for 20 min. Cells were washed twice in PBS followed by staining with 2% (w/v) Alizarin Red S (Sigma) solution in dH<sub>2</sub>O (after adjusting the pH to 4.2 using 10% NH<sub>4</sub>OH) for 10 min at room temperature. The dye solution was drained and the cells washed with running water for 30 min. Cultures were visualised using an EVOS  $\times$ 1 Core digital inverted cell imaging microscope system.

## 5.9. Calcium quantification

Differentiated cell cultures were rinsed with PBS and then incubated at 4 °C on an orbital shaker overnight in 0.5 M HCl. Calcium quantification was then performed on lysates using the Calcium Colorimetric Assay kit (BioVision) according to the manufacturer's instructions. Briefly, 10  $\mu$ L of sample (HCl with dissolved nodules) or known standards were incubated with 90  $\mu$ L of chromogenic reagent that binds to the complex formed between calcium ions and O-cresolphthalein, and 60  $\mu$ L of assay buffer. The absorbance was then measured at 575 nm using a FLUOstar Omega BMG Labtech plate reader. The calcium concentration in the samples was then calculated using a standard curve generated using serial dilutions (0–2  $\mu$ g).

## 5.10. Raman spectroscopy measurements and analyses

For Raman spectroscopy measurements, hMSC were cultured as described above, but were seeded on MgF<sub>2</sub> coverslips (Crystran, UK) instead of tissue culture plastic to facilitate Raman spectral analyses. MgF<sub>2</sub> is a weak Raman scatterer, whilst tissue culture plastic produces an intense Raman signal [74]. After 21 days in culture, MgF<sub>2</sub> coverslips were briefly rinsed with deionised H<sub>2</sub>O and dried in a bell jar desiccator [50]. Raman measurements were performed using a custom build Raman system consisting of a Laser Quantum Ventus 532 nm Laser (Stockport, UK). The laser was coupled via free space optics into an Olympus BX60 microscope (Hamburg, DE). Raman scattered light was collected through a 50 $\times$ /NA 0.8 objective and fibre coupled into an Acton SpectraPro 2500i f/6.5 spectrograph, using a 1200 lines/mm grating with a Princeton Instruments PIXIS 400F 1340  $\times$  400 pixel CCD camera (Trenton, NJ) operating at  $-75$  °C. Integration time was 10 s, averaged 3 times for each spectrum, using 30 mW at the sample. We have previously shown that these conditions do not cause spectral changes due to sample heating/burning [52]. For univariate peak analyses, between 295 and 315 spectra were examined per group.

Data were smoothed using a 5 point Savitzky-Golay filter and background corrected by a 5th order polynomial using an automated weighted least squares fitting method [75]. To determine the position of the  $PO_4^{3-} \nu_1$  peak at  $\sim 960$  cm<sup>-1</sup>, a single Gaussian was fit to the data, as previously described [76,77]. Gaussian fits were used to calculate the 960 cm<sup>-1</sup> ( $PO_4^{3-} \nu_1$ ) and 1660 cm<sup>-1</sup> (Amide I) peak areas.

The mineral to matrix ratio was calculated by determining the ratio of the area of the  $960\text{ cm}^{-1}$  peak to that of the  $1660\text{ cm}^{-1}$  peak [50,51] after normalization using Multiplicative Scatter Correction. Spectra with a  $\text{PO}_4^{3-}$   $\nu_1$  peak area of less than 500 were excluded from multivariate analyses and in total, spectra collected from 29 control-, 38 DBE- and 42 bortezomib-treated cultures were analysed. For classification analyses, a 6-component Partial Least Squares-Discriminant Analysis model was fitted and cross validated using venetian blinds and 10 splits.

#### 5.11. Atomic force microscopy (AFM) measurements of nodule stiffness and adhesion

22 mm glass coverslips were prepared by soaking in FBS overnight and allowing to air dry. hMSC were seeded at 190,000 cells/coverslip. The next day, basal medium was replaced with osteogenic medium and cells were differentiated as described above. After 21 days, coverslips were frozen slowly [50]. Briefly, medium was aspirated from plates and replaced with a 1:1 solution of 20% DMSO in FBS:basal medium. Plates were then sealed with parafilm and placed within 2 nesting polystyrene boxes at  $-80^\circ\text{C}$ . Samples were defrosted at room temperature immediately prior to measurements. Coverslips were immobilised on 60 mm diameter tissue culture dishes (TPP, CH) by gluing small coverslips to the plate at the sample edges. Coverslips were immersed in PBS (without calcium and magnesium, pH 7.4, Gibco) and measurements were made at room temperature. Mineralised nodules were identified from bright field images as dense, opaque patches on the culture surface that varied in diameter between  $\sim 35$  and  $125\text{ }\mu\text{m}$ . Indentation measurements were carried out on a JPK Nanowizard<sup>®</sup> I AFM equipped with a cantilever (cantilever B, spring constant,  $K \sim 16\text{ N/m}$ ) with a pyramidal, silicon AFM probe (HQ:NSC35/Hard/AL BS, Mikro-Masch<sup>®</sup>, DE). Cantilevers were calibrated using the thermal method [78]. Analysis was performed using J Unicam and JPK SPM software 2.3 01/2006 (JPK Instruments AG, DE). Indentations were carried out at 1 Hz under a constant loading rate with a relative setpoint force set as 3650 nN and no dwelling time. The effect of the hard underlying substrate was assumed to be negligible as the indenter penetration was less than 10% of the nodule thickness [79,80]. Nanoindentations were made at between 1 and 5 locations on each nodule's surface. 20 individual force indentation curves were made at each location ( $1 \times 1\text{ }\mu\text{m}^2$ ). Measurements were performed on at least 12 nodules per donor per treatment. Young's modulus ( $E$ ), maximum adhesion force, maximum length of adhesion interactions, and adhesion energy were determined in JPK SPM software using the Hertz model. The Poisson's ratio of both the sample and tip were assumed to be 0.3 [81].

#### 5.12. Transmission electron microscope (TEM) imaging

Differentiated hMSC cultures were scraped from plates and pelleted in PBS. Pellets were fixed with 1% (w/v) glutaraldehyde for 15 min, then washed in cacodylate buffer three times, followed by incubation in 1% (w/v) osmium tetroxide and 1.5% (w/v) potassium ferrocyanide in  $\text{H}_2\text{O}$  for 1 h. Pellets were then washed in  $\text{H}_2\text{O}$  three times and dehydrated in an ethanol/distilled water series at concentrations from 20 to 100% ethanol for 15 min in each. Samples were then infiltrated with Epon 812 (EMS) epoxy resin in absolute ethanol at ratios of 3:1, 2:1, 1:1, 1:2, 1:3 (ethanol:resin) and then 100% epoxy resin for 6 h each. Samples were then cured at  $60^\circ\text{C}$  for 48 h. Resin blocks were sectioned on a Leica Ultracut EM FC7 ultramicrotome on an ultracut UC7 chassis into 80 nm sections, placed on grids, stained with Reynold's lead citrate for 15 min and 1% (w/v) uranyl acetate for 15 min, then imaged on a Jeol 1010 TEM at 80 KV.

#### 5.13. Scanning electron microscope (SEM) imaging

Cultures in well plates were dehydrated using increasing

concentrations of ethanol (20%, 30%, 40%, 50%, 60%, 70%, 80%, 90%, 100%, 100% and 100% for 10 min each) and mounted on SEM stubs using carbon tape. Silver painting and carbon coating was carried out using a Quorum K975X Carbon coater. Samples were imaged on either a Hitachi S-3499N or a Zeiss Sigma. For DDC-SEM images, secondary electron (SE) mode was used to obtain topographic information, whilst the backscattered electron detector (BSE) was applied to differentiate between organic and inorganic material. DDC-SEM images were produced by assigning different colours to the BSE and SE modes using Image J.

#### 5.14. Statistical analyses

Statistical analyses for all measurements were carried out using a non-parametric Kruskal-Wallis test followed by Dunn's multiple comparison test unless stated otherwise. All analyses were carried out using GraphPad Prism version 7 for Windows (GraphPad Software, USA). Significant differences in the distributions of adhesion values between treatments were evaluated using a Mantel-Haenszel linear-by-linear association Chi-squared ( $\chi^2$ ) test for trend. Power was evaluated by determining Goodman and Kruskal's gamma ( $\gamma$ ) and standardised residuals (SR) were used to identify the most significant intervals that contributed to differences between histograms, all three using IBM<sup>®</sup> SPSS<sup>®</sup> statistics version V23.  $p$  values are indicated in figure captions,  $*p < 0.05$ ,  $**p < 0.01$  and  $***p < 0.001$  and showed in detail in supplementary tables.

#### Author contributions

EG and HWA conceived the study, supervised the project, analysed data, and wrote the manuscript. SL, SAF, TMC, AK, ET, CD, KP, APS, SB, LB and MABH conducted experiments, analysed data, and contributed to writing the manuscript.

#### Conflicts of interest

HWA has received research support unrelated to this project from Amgen, and honoraria from Novartis, Amgen, and Karyopharm.

#### Data availability

The raw/processed data required to reproduce these findings cannot be shared at this time due to technical or time limitations.

#### Acknowledgements

HWA and SL acknowledge the support of the Imperial College London NIHR BRC, the Cancer Research UK Imperial Centre, the Imperial Experimental Cancer Medicine Centre, and the Imperial College Healthcare Tissue Biobank. HWA was supported by a Cancer Research UK Clinician Scientist Fellowship. EG was supported by a Research Career Development Fellowship from the Wellcome Trust and a Philip Leverhulme Prize from the Leverhulme Trust. MABH was supported by a STSM Grant from the COST Action BM1401. TMC was supported by a Whitaker International Program Fellowship.

#### Appendix A. Supplementary data

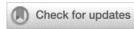
Supplementary data related to this article can be found at <https://doi.org/10.1016/j.biomaterials.2018.08.041>.

#### References

- [1] V.I. Perez, R. Buffenstein, V. Masamsetti, S. Leonard, A.B. Salmon, J. Mele, et al., Protein stability and resistance to oxidative stress are determinants of longevity in the longest-living rodent, the naked mole-rat, *Proc. Natl. Acad. Sci. U.S.A.* 106

# G. Impact of Carbamide Peroxide Whitening Agent on Dentinal Collagen

---



*Research Reports: Biological*

---

## Impact of Carbamide Peroxide Whitening Agent on Dentinal Collagen

O. Redha<sup>1</sup>, A. Strange<sup>2</sup>, A. Maeva<sup>2</sup>, R. Sambrook<sup>1</sup>, N. Mordan<sup>2</sup>,  
A. McDonald<sup>1</sup>, and L. Bozec<sup>2,3</sup>

Journal of Dental Research  
1–7  
© International & American Associations  
for Dental Research 2019  
Article reuse guidelines:  
sagepub.com/journals-permissions  
DOI: 10.1177/0022034518822826  
journals.sagepub.com/home/jdr













# H. Influence of Biomaterial Nanotopography on Adhesive and Elastic Properties Of *Staphylococcus aureus* Cells

RSC Advances



PAPER

[View Article Online](#)  
[View Journal](#) | [View Issue](#)



Cite this: *RSC Adv.*, 2016, 6, 89347

## Influence of biomaterial nanotopography on the adhesive and elastic properties of *Staphylococcus aureus* cells†

S. Aguayo,<sup>\*a</sup> A. Strange,<sup>a</sup> N. Gadegaard,<sup>b</sup> M. J. Dalby<sup>c</sup> and L. Bozec<sup>a</sup>

















# I. Optical Coherence Tomography Use in the Diagnosis of Enamel Defects

Journal of Biomedical Optics 21(3), 036004 (March 2016)

## Optical coherence tomography use in the diagnosis of enamel defects

Khalifa Al-Azri,<sup>a</sup> Lucia N. Melita,<sup>b</sup> Adam P. Strange,<sup>b</sup> Frederic Festy,<sup>c</sup> Maisoon Al-Jawad,<sup>d</sup> Richard Cook,<sup>c</sup> Susan Parekh,<sup>a</sup> and Laurent Bozec<sup>b,\*</sup>

<sup>a</sup>University College London, Eastman Dental Institute, Paediatric Department, WC1X 8LD, London, United Kingdom

<sup>b</sup>University College London, Eastman Dental Institute, Biomaterials and Tissue Engineering, 308 Sussex Wing, WC1X 8LD, London, United Kingdom

<sup>c</sup>King's College London Dental Institute, Tissue Engineering and Biophotonics, Floor 17, Tower Wing, Guy's Hospital Campus, Great Maze Pond, London Bridge SE1 9RT, United Kingdom

<sup>d</sup>Queen Mary University of London, Barts and The London School of Medicine and Dentistry, London E1 4NS, United Kingdom

**Abstract.** Molar incisor hypomineralization (MIH) affects the permanent incisors and molars, whose undermineralized matrix is evidenced by lesions ranging from white to yellow/brown opacities to crumbling enamel lesions incapable of withstanding normal occlusal forces and function. Diagnosing the condition involves clinical and radiographic examination of these teeth, with known limitations in determining the depth extent of the enamel defects in particular. Optical coherence tomography (OCT) is an emerging hard and soft tissue imaging technique, which was investigated as a new potential diagnostic method in dentistry. A comparison between the diagnostic potential of the conventional methods and OCT was conducted. Compared to conventional imaging methods, OCT gave more information on the structure of the enamel defects as well as the depth extent of the defects into the enamel structure. Different types of enamel defects were compared, each type presenting a unique identifiable pattern when imaged using OCT. Additionally, advanced methods of OCT image analysis including backscattered light intensity profile analysis and enamel reconstruction were performed. Both methods confirmed the potential of OCT in enamel defects diagnosis. In conclusion, OCT imaging enabled the identification of the type of enamel defect and the determination of the extent of the enamel defects in MIH with the advantage of being a radiation free diagnostic technique. © The Authors. Published by SPIE under a Creative Commons Attribution 3.0 Unported License. Distribution or reproduction of this work in whole or in part requires full attribution of the original publication, including its DOI. [DOI: 10.1117/JBO.21.3.036004]

**Keywords:** optical coherence tomography; hypomineralization; diagnosis; enamel.

Paper 150694R received Oct. 15, 2015; accepted for publication Feb. 9, 2016; published online Mar. 10, 2016.

### 1 Introduction

Molar incisor hypomineralization (MIH) is defined as “hypomineralization of systemic origin affecting at least one first permanent molar (FPM), which is frequently associated with affected incisors.”<sup>1</sup> The prevalence of MIH was reported to range from 2.8% to 25% in pediatric patients.<sup>2</sup> The significant variation in prevalence data can be related to the weakness of diagnostic criteria as MIH may often be confused with fluorosis or early carious (white spot) lesions. MIH can occur at any stage during the enamel formation and mineralization of FPMs and permanent incisors, which takes around 1000 days and continues for several years (~5 years). It has been suggested that the most critical period is the first year of life when early enamel maturation starts, particularly on first permanent incisors and FPMs.<sup>3</sup>

The etiology of MIH is still not completely understood and there is disagreement as to the criteria and factors that contribute to the correct diagnosis of this enamel defect.<sup>4</sup> Systematic reviews investigating the causative factors of MIH concluded that the best levels of evidence are either weak or moderate.<sup>3,5</sup> Enamel hypomineralization can occur in different clinical forms, ranging from mild to severe involvement. While less dramatic forms are characterized by porous and soft subsurface enamel, severe MIH can lead to post-eruptive breakdown (PEB)

of the affected enamel.<sup>6</sup> Once the FPMs come into occlusion, they start to break down as the enamel—even if bearing an intact surface—is substantially undermined within its depths and thus fundamentally weakened.<sup>3</sup> However, incisors do not generally show PEB, as they are not subjected to such substantial occlusal loads.<sup>7,8</sup>

Clinical features of MIH include opacities of large well-defined areas, ranging in color from white/creamy blemishes to yellow brown opacities. FPMs affected by MIH can be hypersensitive to hot and cold stimuli<sup>9</sup> and local anesthetic may not always be effective,<sup>8</sup> supposedly due to the porous enamel resulting in chronic clinically inflamed pulps.<sup>9</sup> Porous enamel may also facilitate the access of bacterial products causing inflammation of the pulp. Caries can progress rapidly in MIH teeth, making diagnosis difficult, especially if the tooth is badly broken down. It has been postulated that that children with very sensitive teeth might face difficulties during brushing, leading to poor oral hygiene and eventually caries.<sup>8,10</sup>

Currently, the main diagnostic method for MIH is clinical visual examination of the teeth. This can be performed with the aid of indices used to describe enamel defects, such as the modified developmental defects of enamel index (mDDE index)<sup>11</sup> or the European Association of Pediatric Dentistry (EAPD) MIH index, the latter requiring the examination of 12 permanent teeth (8 permanent incisors and 4 FPMs) at the age of eight.<sup>4</sup> Diagnosis at an early stage is key in the

\*Address all correspondence to: Laurent Bozec, E-mail: l.bozec@ucl.ac.uk

management of MIH teeth, in order to reinforce oral hygiene, to maximize opportunities for teeth remineralization, and to reduce hypersensitivity. The available treatment options for MIH teeth are complex, ranging from prevention and restoration to extraction, depending on the patient's dental age, the severity of the condition, the child/parent's expectations, and background.<sup>12</sup> One major challenge is the assessment of the depth of the involved tissue, which has major impacts upon the specific design of the treatment plan to mask, remove, or cover the affected regions. Therefore, the determination of the extent of an MIH lesion into the enamel depths is crucial to determine the prognosis and treatment plan for affected teeth. However, this can be difficult to evaluate accurately solely from clinical examination, and as the lesions are superimposed on the bulk of the tooth structure. Similarly, such imaging modalities offer poor spatial resolution. Ultrahigh resolution clinical three-dimensional (3-D) techniques, such as cone beam computed tomography, necessitates significant radiological doses and are probably not justified in these scenarios, when no other radiological alternatives are possible.

The investigation of a more accurate diagnostic tool is important to enable us to determine the prognosis of affected teeth and, at the same time, gives an opportunity to move away from techniques, which expose patients to ionizing radiation. Optical coherence tomography (OCT) is a nondestructive imaging system, using a near-infrared (NIR) laser<sup>13</sup> to investigate the internal biological structures to a depth of up to 2 to 3 mm, depending on the light source and the scattering properties of the material of interest.<sup>14,15</sup> The image grayscale contrast obtained by OCT is the result of an interferometric correlation between the incident beam scattered by the sample and an equal length reference beam. In essence, OCT enables imaging the sample's structure at 2 to 3 mm depth, using partial time-coherence interferograms. This imaging depth is ideally suited to assessing full thickness of human enamel mantles, including the enamel-dentine junction (EDJ). The resulting image, also known as a B-scan, is two-dimensional (2-D) ( $X-Z$ ) and is a direct measurement of the scattering and absorption properties of the underlying sample. Multiple B-scan images can be recorded in sequence in the  $Y$ -plane direction, resulting in the creation of a lateral tack of images that can be recomputed to form a 3-D image of the underlying sample—in this case, the enamel.

In dentistry, OCT has been used to investigate caries, artificial demineralization, and remineralization of enamel and dentine.<sup>15–21</sup> Jones et al.<sup>15</sup> used polarization-sensitive OCT (PS-OCT) to image artificial occlusal caries by investigating the magnitude of backscattered light with variations in the enamel volume.<sup>15</sup> They also used transverse sections from digital microradiography to obtain the quantitative mineral content

profile and relative mineral loss. It was concluded that PS-OCT could be used to measure artificial occlusal caries by observing the changes in backscattering and depolarization of NIR light. The technique demonstrated its potential in detecting and monitoring early enamel caries.<sup>15</sup> A study conducted by Fried et al.<sup>16</sup> demonstrated that PS-OCT is an invaluable tool for imaging interproximal, occlusal, and early root caries and caries underneath composite fillings. Manesh et al.<sup>19</sup> also showed that PS-OCT can be used to detect remineralization of dentine. The aim of the present study was to prove that OCT could be used as a diagnostic tool in clinical practice for the noninvasive and noncontact cross-sectional investigation of enamel defects in a common enamel anomaly such as MIH.

## 2 Experimental Method

### 2.1 Sample Collection

Ethical approval for this study was obtained from the National Health Services Research Ethics Committee (NHS REC), United Kingdom (R & D reference number 11/LO/0777, Project ID: 11/0223), and 19 teeth were collected ( $n = 19$ ) at the pediatric department at the Eastman Dental Hospital. Thirteen of them were MIH-affected FPMs ( $n = 13$ ) and six were control teeth ( $n = 6$ ). Following local hard tissue management protocols, the extracted teeth were collected and stored in 70% ethanol for 48 h at room temperature, before being debrided and stored in 0.1% aqueous thymol solution at 4°C (to maintain enamel hydration) until imaging.

### 2.2 Photographic Imaging and Modified Developmental Defects of Enamel Index

Photographs of the samples were taken using a Canon EOS Digital Rebel DS6041 equipped with a Canon Macro Ring Lite MR-14EX flash. Each sample was photographed against a dark background to enhance the contrast between the sample and the background (buccal, distal, lingual/palatal, and mesial surfaces were imaged). At this stage, the mDDE index was used to characterize the enamel lesions of the teeth, and each tooth surface was coded according to its location (L), demarcation (D), extent (E), and type of lesion (T).<sup>11</sup> Each code was graded according to severity of the lesion and was given grade 1 to 3, with 3 being most severe. This is summarized in Table 1.

### 2.3 Radiographic Assessment

Samples were imaged radiographically, immediately after the photographic investigation. Clinically relevant radiographic images for the control and the MIH-affected FPMs were performed on intraoral size 2 radiographic films—D speed

**Table 1** Summary of the scoring indices and weighting used for the clinical diagnostics of MIH. Note that PEB refers to posteruptive breakdown.

	Location (L)	Demarcation (D)	Extent (E)	Type (T)
1	Occlusal half	Diffuse	<1/3 of surface involved	White creamy
2	Gingival half	Demarcated	1/3 to 2/3 of surface involved	Yellow brown
3	Whole surface	Both	<2/3 of surface involved	N/A
8	N/A	N/A	N/A	PEB

(Insight, Carestream Health, Inc., Rochester, New York, United States). For each tooth sample, two images were recorded: the first view was taken with the x-ray beam directed toward the buccolingual axis of the x-ray direction in order to image the mesial and distal surfaces, whereas the second view being taken with a perpendicular mesiodistal imaging axis was taken with the x-ray beam directed towards the mesiodistal direction in order to image the buccal and lingual surfaces.

## 2.4 Histology and Polarization Microscopy

A diamond-edged Accutom 5 rotary saw (Struers, Denmark) was used to cut the sample in cross-section near the MIH lesion of interest. Samples were cut into 2-mm-thick disks. Samples were then polished smooth by hand to  $\sim 300\ \mu\text{m}$  thickness, using silicon carbide grinding paper grit 1200 (Struers, Denmark). The polished disks were washed in deionized water in an ultrasonic bath for 2 min.

For histological imaging, the disks were imaged using a Leica (Wetzlar, Germany) light microscope. This was equipped with a  $5\times$  magnification lens and two crossed light polarizers (90 deg) for optical polarization imaging. Images were captured using an 8-megapixel EOS Rebel t3i camera (Canon, Tokyo). Individual images were analyzed and stitched together to form a composite image using Photoshop processing software (Adobe, San Jose, California).

## 2.5 Optical Coherence Tomography Scanning Instrument

A VivoSight OCT scanner (Michelson Diagnostics, Kent, United Kingdom), based on a multibeam swept-source (SS) frequency domain was used during this research. It is equipped with a class I eye safe laser ( $\lambda = 1305\ \text{nm}$ ) and features an optical resolution in tissue of less than  $7.5\ \mu\text{m}$  laterally and less than  $5\ \mu\text{m}$  axially. The depth of focus of each of the four SSs is 1 mm and each is set 0.5 mm in advance of the previous one to enhance tissue penetration at higher resolution. The area scanned can be up to  $6\ \text{mm} \times 6\ \text{mm}$  (length  $\times$  width), with an image depth of 1.2 to 2.0 mm depending on the tissue. The scan rate is 10 kHz and the frame rate can be up to 35 frames per second. The images are presented as stacks of vertical B-scans for a total of 600 frames, acquired at a distance of  $10\ \mu\text{m}$  between each frame. As such, each frames measured 6 mm width and about 1.84 mm depth (in the XZ or B scan dimensions). The images were then exported from OCT software as 16-bit TIFF images.

Each tooth sample was taken from the storage medium and the excess moisture removed before being mounted on the instrument imaging stage. For reproducibility and image stability, the handheld OCT probe was mounted onto a movable arm. All scans started at or close to the cemento-enamel junction (CEJ) cervically and ended at the cusps occlusally. Each of the tooth surfaces (buccal, distal, lingual/palatal, and mesial) were imaged regardless of the presence of MIH lesion. Occlusal surfaces were not scanned due to their complex morphology and the presence of restorations in some of the samples.

## 2.6 Image Processing

All OCT images, either as single frames or as a full stack of images, were processed using Image J software (Image J

1.47 with 64-bit Java, 2013, Bethesda, Maryland, United States). For conciseness of the report, the single frames presented were randomly selected from a stack of interest (either control or MIH) and found to be representative of the overall scattering pattern observed within the image stacks. Additionally, the scattering profiles were extracted from each frame and plotted as a function of sample's depth, using Origin Pro 9.0 (Origin Lab Corporation, Northampton, Massachusetts, United States). The regions selected to obtain the scattering profiles from the randomly selected single frame were also chosen at random to ensure that the analysis avoided sampling bias. All distances presented on the X-axis of the scattering profiles plotted are defined as optical rather than absolute distances as they have not been corrected for the indices of refraction.

## 3 Results and Discussion

### 3.1 Clinical Photographs

The photographic images of MIH teeth were examined and the mDDE index was used to characterize the MIH lesions. An example of the phenotypic characterization in Fig. 1 shows the buccal surface of an upper-right FPM with an MIH lesion. The whole of the tooth surface is involved, consequently code L3 is assigned. Additionally, the lesion is both demarcated and diffuse resulting in a code of D3 for demarcation. At least two-thirds of the tooth is affected; therefore, E3 is given for the extent of the lesion. Three types of MIH enamel defects are detected: type 1, white creamy lesion (T1); type 2, yellow-brown lesion (T2); and type 8, PEB (T8). Table 2 summarizes the mDDE index score for the enamel defects present in all MIH-affected FPMs.

This index is used routinely in clinics and forms part of the clinical assessment. However, this index describes only the external features of each lesion and does not give any indication of the impact of the lesion on the internal structure of each tooth surface. For example, there are no means to evaluate whether the MIH lesion is affecting the entire enamel thickness or whether the lesion is affected subsurface by cracks, which may lead to PEB. However, a study by Farah et al.<sup>23</sup> showed that such visual

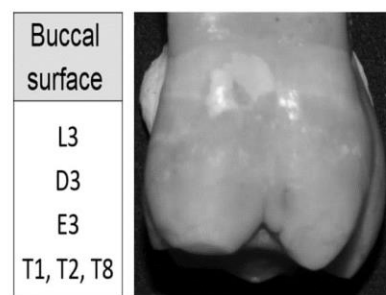


**Fig. 1** Example of the phenotypic characterization of the buccal surface of an upper-right FPM with a MIH lesion. The whole of the tooth surface is involved, consequently code L3 is assigned. Additionally, the lesion is both demarcated and diffuse, resulting in a code of D3 for demarcation. At least two-thirds of the tooth is affected; therefore, E3 is given for the extent of the lesion.

**Table 2** Summary of the mDDE index scores of the enamel defects present in all MIH-affected FPM teeth used as part of this study.

Tooth sample	Location (L)	Demarcation (D)	Extent of defect (E)	Type of defect (T)
MIH 1	L3	D3	E3	T2
MIH 2	L3	D3	E3	T1 and T8
MIH 3	L3	D3	E3	T2 and T8
MIH 4	L3	D3	E3	T1
MIH 5	L3	D2	E3	T1 and T8
MIH 6	L1	D1	E1	T2 and T8
MIH 7	L3	D3	E3	T1 and T8
MIH 8	L3	D3	E3	T1 and T8
MIH 9	L3	D3	E3	T1 and T8
MIH 10	L3	D3	E3	T1 and T8
MIH 11	L3	D2	E3	T1
MIH 12	L3	D3	E3	T2
MIH 13	L1	D2	E2	T1 and T8

assessment of the degree of staining of MIH-affected teeth may be used to clinically reflect the severity of the defect but should be used in combination with other diagnostics approaches. An alternative index, the molar hypomineralization severity index (MHSI), was investigated by Oliver et al.<sup>23</sup> in 2014, to determine treatment of defects in MIH based on their clinical characteristics. Their study showed that treatment modalities are dependent on color and location of defects, and the amount of PEB affecting FPMs.

This index was not available when the current study was started in 2012, but the mDDE index used to cover the same characteristics of location, color, and PEB. While the MHSI is useful for clinical management, it does not aid in diagnosis of defects, as many children present in the early mixed dentition before all the FPMs and permanent incisors have erupted. Therefore, the mDDE index, which can be used to record all enamel defects, irrespective of clinical diagnosis, is more useful.

### 3.2 Radiographic Examination

Radiographic imaging is one of the most common diagnostic tools used in the field of dentistry. Although efforts are made to reduce the ionizing radiation exposure to patients and practitioners, by principles of justification and optimization of radiographic imaging, the versatile use of x-ray imaging is still a cause for concern for individual safety. From a diagnostics point of view, radiographic imaging produces 2-D images of 3-D teeth. In the context of MIH diagnostics, it is used to demonstrate the extent of the lesion and determine mainly if the lesion is severe. Figure 2 shows a comparison between clinical photographs and radiographs for both control tooth [Figs. 2(a) and 2(b)] and MIH-affected tooth [Figs. 2(c) and 2(d)].

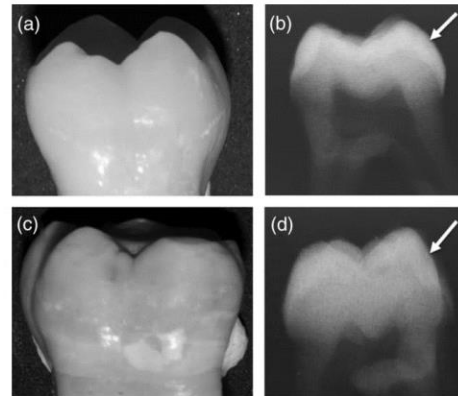


**Fig. 2** Clinical photographs and radiographic images of (a and b) a control tooth and (c and d) an MIH-affected tooth. The mesiodistal view of the tooth is presented in the clinical photograph (a–c), whereas it is the buccolingual view that is presented in the radiographic image (b–d) in an effort to observe the depth of penetration of the MIH lesion. The arrows point to the same area for both teeth, highlighting the area affected with MIH (d) and its corresponding healthy control area (b).

On the radiographic images of both control and MIH-affected teeth, the different surfaces are superimposed, making it difficult to discern specific features, besides the EDJ, the CEJ, and pulp chamber. However, the occlusal, mesial, and distal surfaces can be examined in detail without shading as a result of the 3-D projection. From a diagnostic point of view, these images are of low resolution and even though the whole dental crown (enamel, EDJ, dentine, and the dental pulp) can be seen clearly, radiographic images cannot show fine details of these structures, such as disorganized enamel, change in mineralization, or cracks within the enamel formation. This lack of ability to resolve finer enamel structures or defects may enhance diagnostic errors, particularly with regards to lesion depth extent, although they can be visually identified at the surface of the enamel. This effectively reduces the pertinence of the diagnostics.

### 3.3 Optical Coherence Tomography Imaging of Healthy and Molar Incisor Hypomineralization Affected Tooth

#### 3.3.1 Control teeth

An example of a single-frame OCT image of a healthy enamel layer from a control tooth is shown in Fig. 3(b). In this example, a palatal surface of an upper-right FPM was imaged, as shown in the clinical photograph in Fig. 3(a). The dotted square area drawn on the tooth surface is representative of the 6 mm × 6 mm scanning window preset by the instrument. Figure 3(b) is a representative single-frame OCT image (B-scan) of healthy enamel. The enamel and dentine layers are labeled 1 and 2, respectively, and the EDJ is labeled as 3 in Fig. 3(b). The interface between the air (dark area above the enamel) and the enamel appears particularly bright due to the high scattering of the incident photons as they encounter a

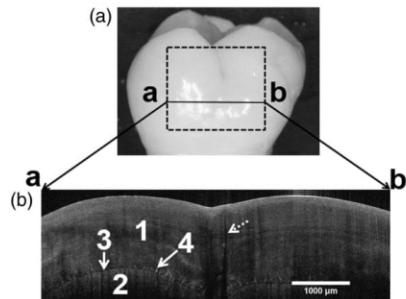


**Fig. 3** (a) Clinical photograph of a palatal surface of an upper-right control FPM and a representative single-frame OCT image (B-scan) taken from the OCT stacks recorded with the dotted square area drawn on the tooth surface. (b) The enamel and dentine layers are labeled 1 and 2, respectively, and the EDJ is labeled as 3. Needle-like structures associated with the EDJ, labeled 4, may correspond to enamel spindles. An enamel crack can also be observed (dotted arrow).

region with a high refractive index and with an uneven surface topography.

The transmitted photons penetrate the enamel layer and were reflected by the internal enamel features. Although intensity was reduced from greater depths by increased scattering, any structural changes in the enamel layer induced a new scattering front, which was demonstrated as a brighter line or region in the grayscale image. Subtle variations in the grayscale contrast of the image could also be indicative of small variations in the enamel mineral contents. It is also possible to distinguish small needle-like structures associated with the EDJ [labeled 4 on Fig. 3(b)], which possibly correspond to either enamel spindles as seen histologically, or alternatively, small cracks across the EDJ.

Another type of feature frequently seen in OCT images is enamel crack lines, which may run from the enamel surface toward the EDJ or from the EDJ toward the enamel surface as demonstrated by the dotted arrow [Fig. 3(b)]. OCT is particularly efficient at detecting these fine crack lines, as their presence is usually amplified by an increase of scattering light, as demonstrated by Imai et al.<sup>24</sup> and a resulting shadowing effect presented as a darker region immediately below the crack on

the B-scan. The shadowing effect can be considered as an imaging artifact, but in practice, it allows the rapid detection of crack lines that are sometimes barely visible.

### 3.3.2 Correlation between histology and optical coherence tomography imaging on a molar incisor hypomineralization affected tooth

Previous studies have tried to correlate *in vivo* OCT with *ex vivo* histology.<sup>25</sup> Although the current study only investigates *ex vivo* teeth, a similar approach was used. Figure 4(a) shows the clinical photograph of an MIH tooth with a diffuse T2 MIH lesion as an example for the correlation between these techniques. OCT imaging [Fig. 4(d)] was performed on the tooth along the marked line, as shown in Fig. 4(a), prior to any further histology preparation. Histology sectioning was then performed on the tooth before polishing the section down to a thickness of 250  $\mu\text{m}$  to allow for histology imaging. During the cutting procedure, a portion of the T2 lesions broke off, as highlighted by the arrow in Fig. 4(b). This occurred frequently, as the MIH-affected area of the tooth is mechanically weaker when compared to its surrounding healthy enamel. It is also likely that there may have been underlying undetected PEB present at that location. Nonetheless, the separate regions, healthy and MIH affected, are evident in Fig. 4(b). The presence of the MIH lesion near the occlusal surface becomes more apparent while imaging the section under polarization microscopy. Under this mode of imaging, the healthy enamel appears opalescent, whereas the MIH-affected enamel is more opaque. Although this T2 lesion near the occlusal part of the tooth was damaged during the histological process, it is still possible to correlate the OCT scan with the histology sectioning. The star shows the location of the healthy enamel on both imaging mode (polarization microscopy and OCT) lesion, whereas the triangle shows the MIH-affected area. The correlation between the two areas matches accurately and the interface between healthy and affected enamel becomes clearer in the case of OCT imaging. In 2008, Hirasuna et al.<sup>26</sup> used PS-OCT and NIR to monitor early carious lesions. In their approach, they also used a digital micro-radiography system to quantify the enamel defect severity by measurement of the relative mineral loss for comparison with optical scattering measurements. Developmental defects were clearly visible in the polarization-resolved OCT images, demonstrating that PS-OCT could be utilized to nondestructively

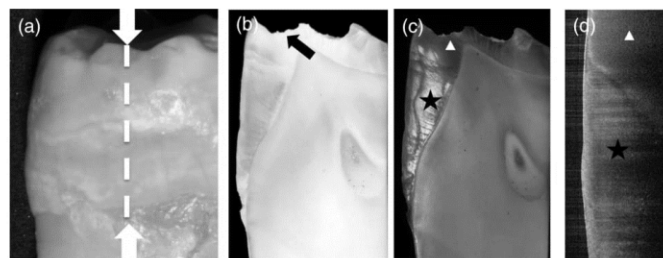


**Fig. 4** (a) Clinical photograph of a buccal surface of an MIH diffuse T2 (top) defects, the dotted lines show the OCT scan area. (b) Histology image of tooth at 5x magnification with the arrow indicating loss of enamel due to PEB. (c) Polarized histology image of tooth, with T1 defect starred at 5x magnification. (d) OCT image of the MIH diffuse T2 area.

measure the depth and possible severity of the defects. With the recent improvements made in OCT resolution and speed, combined with the vulnerability of the MIH teeth to damage, the nondestructive *in vivo* OCT technique should be preferred over the *ex vivo* destructive histological analysis.

### 3.4 Qualitative Diagnostics of Molar Incisor Hypomineralization Types Using Optical Coherence Tomography Imaging

#### 3.4.1 Type 1 (white/creamy) molar incisor hypomineralization defect

Figure 5(b) shows the image of diffuse type 1 defect, a white creamy MIH defect present on the palatal surface of the affected tooth. According to the mDDE index in Fig. 5(a), the defect is located on the whole surface of the tooth (L3), diffuse (D2), and extending at least two-thirds of the surface (E3). Three representative OCT scans were chosen in Fig. 5(c) to demonstrate the appearance of this type of MIH defect (diffuse type 1 defect). The dotted lines highlight where the OCT scans were taken. The defect is mainly affecting the distal half of the tooth surface while part of the mesial half is spared especially in Figs. 5(c1) and 5(c2). In Fig. 5(c3), the enamel is broken in the mesial side, as observed in the clinical picture in Fig. 5(b).

It can be seen that there is an increase in the scattering of the photons just below the enamel surface, as shown by the solid white arrow. Because of the high level of scattering present in that region, there is a significant amount of shadowing occurring, meaning that it proves difficult to evaluate the intactness of the enamel layer below that critical region. However, the OCT image clearly demonstrates that the region adjacent to that critically scattering region is healthy.

An example of demarcated type 1 defect is found in the buccal surface of the affected tooth shown in Fig. 6(b). The tooth presents two types of defects: the demarcated type 1 white creamy defect and the diffuse (D2) type 2 yellow brown defect, which is shown in Fig. 7. According to the mDDE index MIH, it involves the whole surface of the tooth (L3) and extends to more

than two-thirds of the surface (E3) in Fig. 6(a). However, the description of this defect using mDDE index does not give us enough information on the extent of the lesion deep into enamel. It superficially describes the defect extent across the surface.

The OCT scans are located at the occlusal and cervical ends of the defect, respectively. In a similar manner to Fig. 5(c), the OCT images of demarcated type 1 defect in Fig. 6(c) show an irregular crack line about 2 mm long below the surface of the enamel. On the right-hand side of the scans, it is possible to see that the crack line has erupted at the enamel surface. From a diagnostic point of view, it is likely that this tooth may lose over time the entire enamel section sitting above the crack line, effectively creating a PEB.

#### 3.4.2 Type 2 (yellow/brown) molar incisor hypomineralization defect

Figures 7 and 8 show OCT images obtained, respectively, from diffuse and demarcated type 2 defects. In Fig. 7(a), according to the mDDE index, the yellow brown defect involves the buccal half of the surface (L3), diffuse (D3), and it extended across the whole surface of the tooth (E3). The OCT scan in Fig. 7(c) shows the appearance of the diffuse type 2 defect present on the surface. The white arrows in Figs. 7(b1), 7(b2), and 7(b3) indicate the defect extension into enamel. The image contrast at the surface appears gradually brighter than the surrounding enamel, especially near the enamel surface. The area below this bright band of subsurface enamel has significant shadowing, rendering the enamel below dark, with difficulties in assessing the quality of the enamel structure.

In the case of the demarcated type 2 (Fig. 8), the defect is localized in the occlusal half of the surface (L1), demarcated (D1), and extends to about a third of the surface (E1). The palatal defect (white arrow) is visible in all the corresponding OCT sequence [Fig. 8(c)], initiating close to the EDJ [Fig. 8(c5)] and progressing to the surface of the enamel [Fig. 8(c1)]. As it spreads across the palatal side of the distal surface, it exhibits featureless appearance with loss of normal scattering of light,

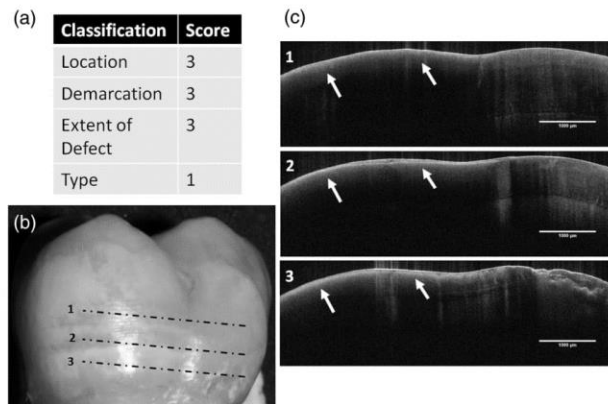
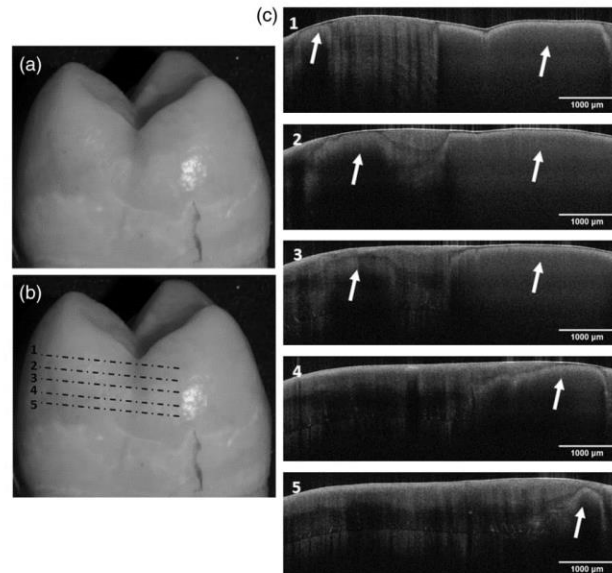


Fig. 5 (a) MIH-affected tooth showing a diffuse T1 defect. (b) Clinical photograph of a palatal surface with the locations labeled as 1, 2, 3 corresponding to the (c) OCT cross-sectional images.





**Fig. 8** (a) MIH-affected tooth showing a demarcated T2 defect. (b) Clinical photograph of a distal surface (b) with the locations labeled 1, 2, 3, 4, and 5 corresponding to the (c) OCT cross-sectional images.

normally expected in healthy enamel. The image contrast is very homogeneous with a featureless appearance of enamel in the deeper region below the surface. It is worth noting the narrow bright band just below the enamel surface.

### 3.4.3 Type 8 (with posteruptive breakdown) molar incisor hypomineralization defect

Figure 9 shows a tooth affected by a type 8 defect on the occlusal surface. The defect is confined occlusally to the buccal cusps with a yellow brown halo around it. According to the mDDE index in Fig. 9(a), the defect is localized in the occlusal half of the tooth (L1), demarcated (D1), and its extent is less than a third of the tooth (E1). Previously, Fig. 6(c1) indicated the position of the OCT frames selected close to the PEB region occlusally. The OCT images [Fig. 9(c)] show the appearance of the defect in enamel, as indicated by the arrow. The images were taken from the buccal surface close to the PEB. The white arrows indicate a fracture line extending into the enamel surface, which could have propagated from the area close to the PEB [Fig. 9(c1)] down to into the cervical area [Fig. 9(c5)], suggesting that the surface is weakened by the breakdown, which occurred occlusally.

A second example is shown in Fig. 10. The occlusal surface is affected by a type 2 defect in Fig. 10(b), but it is closely situated to a type 8 PEB from Fig. 9(b). According to the mDDE index in Fig. 10(a), the MIH defect is located on the occlusal half (L1), demarcated (D1), and it extends to less than a third of the surface (E1). The corresponding OCT images [Fig. 10(c)] show the extent of the defect deep into enamel. Although the region from which these images were taken

was classified clinically as unaffected, the enamel seemed severely affected on the OCT. The breakdown in enamel appears to begin from the EDJ, indicated by the white arrows and becomes more evident dividing the thickness of enamel into two layers, leading to PEB. The blue arrows in the OCT scans highlight the presence of a crack extending from the enamel surface to the EDJ. The diagnosis of this feature is important as it helps clinicians to determine the prognosis of the tooth as it weakens.

### 3.4.4 Merits of qualitative diagnostics using optical coherence tomography imaging

One key outcome of this qualitative diagnostics study using OCT imaging is to appreciate the complexity of the scattering images recorded by OCT. To make the most of these images, clinicians need some knowledge regarding how the instrument produces these images in order to refine their understanding of the variation in image contrast. The use of OCT as a diagnostic method has some advantages when characterizing MIH-affected teeth compared to clinical and radiographic methods. It is possible to visualize the subsurface structure of enamel with a high spatial resolution ( $5\ \mu\text{m}$ ) and the details obtained from these images can only be obtained microscopically. This is consistent with the result obtained by a previous study.<sup>27</sup> By using OCT for the diagnosis of MIH lesions, one key element is to be able to assess the depth of each of these lesions once they have been clearly identified, allowing the clinician to plan their approaches to masking the lesions by informing the depth of the defects and whether external adhesive or coronal encircling restorations are more appropriate.

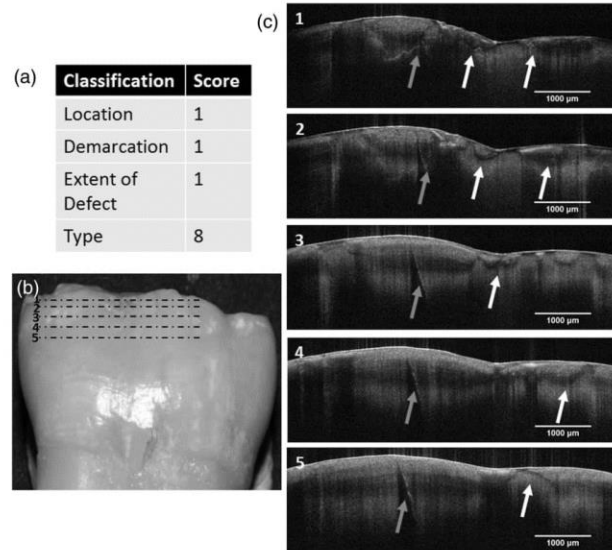


**Fig. 9** (a) MIH-affected tooth showing a T8 defect with PEB. (b) Clinical photograph of a buccal surface with the locations labeled 1, 2, 3, 4 and 5 corresponding to the (c) OCT cross-sectional images.

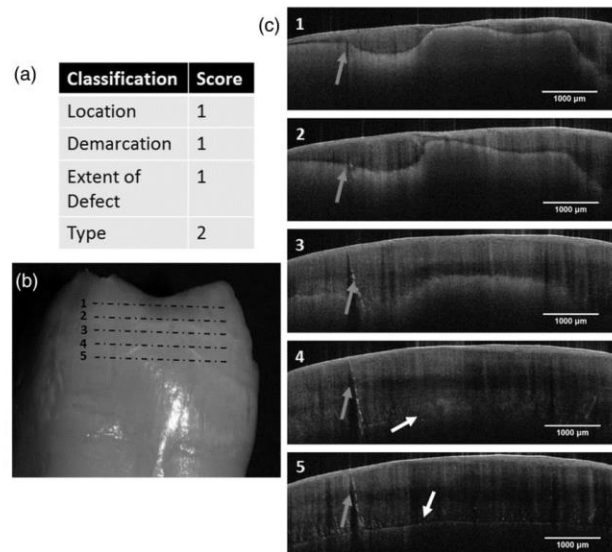


**Fig. 10** (a) MIH-affected tooth showing a T2 defect. (b) Clinical photograph of an occlusal surface with the locations labeled as 1, 2, 3, 4, and 5 corresponding to the (c) OCT cross-sectional images.



The plurality of scattering behaviors represented in the different types of MIH enamel defect is also indicative that MIH as a condition is poorly understood in terms of enamel structure versus MIH type and that more research is required to understand these correlations. One of the most encouraging early publications, presenting OCT as possible clinical diagnostics tool, was performed by Louie et al.<sup>25</sup> They tested the hypothesis that PS-OCT may be used to nondestructively measure and quantify the severity of the early demineralization of enamel on buccal and occlusal surfaces and assess the inhibitory effect of fluoride varnish *in vivo*. In their study, high-contrast PS-OCT images were acquired of both occlusal and buccal surfaces *in vivo*. Both occlusal and buccal surfaces showed a significant difference ( $P < 0.05$ ) in the integrated reflectivity ( $\Delta R$ ) between the “sound” and “carious” enamel groups.

Like the work present by Louie et al.,<sup>25</sup> our analysis from a nonpolarizing OCT system presented single frames for each of the key MIH lesion, but in fact, each of the scans collected 600 frames. This is a significant amount of data for any clinical team to process and use in their diagnostics. The current method of qualitative diagnostics is informative, but more work is required to establish specific databases where clinicians could compare their scan with defined cases. The main disadvantage of this approach is that the maximum depth of imaging is about 2 mm and ~1.8 mm of enamel could be successfully imaged. Though it is a sufficient depth for scanning enamel in some regions, the EDJ may be beyond resolution in the region of the cusps of the teeth, where the thickness is often above 2 mm. More complex enamel structures here would need more interpretation—smooth surfaces affording clearer understanding of enamel derangements and allow chronological interpretation of the likely occlusal and cuspal depths of involvement.

## 4 Advanced Diagnostics Using Optical Coherence Tomography

### 4.1 Scattering Profiles

In order to assess the merit of using OCT for a more systematic diagnostic dental application, OCT images were further analyzed. To do so, scattering profiles as a function of the enamel depth were measured in selected B-scans of both control and MIH teeth. These profiles provide a direct representation of the scattering of photons as they travel through the enamel layer and any disruption in the enamel structure may result in scattering that can be measured in the profile. Figure 11 shows the results of such an approach on a control sample. For consistency, each scattering profile is the average of a 10-pixel (40.5  $\mu\text{m}$ ) width area in the X-axis.

The subsequent profiles were then plotted as function of depth before being normalized to the enamel/air scattering peak. Figure 11(b) shows a series of profiles that have been obtained within the same B-scan, as shown in Fig. 11(a). These profiles were usually characterized by an initial nonscattering phase when the photons are travelling through the air before they encounter the enamel surface. At this stage, the profile exhibits a very strong scattering peak as the photons encounter a medium with a greater refraction index ( $n \sim 1.63$ )<sup>28,29</sup> compared to air ( $n = 1$ ). Following this strong scattering peak, the profile presents a decay profile as the photons become progressively more scattered as their bidirectional journey includes greater depths of the scattering sample of enamel, as shown in Fig. 11(c). It is worth noting that the decay of the scattering profiles in healthy enamel may present some small variations, which are due to localized interruptions in the enamel structural and chemical homogeneity. These could relate to normal variations of structure, including enamel spindles or small

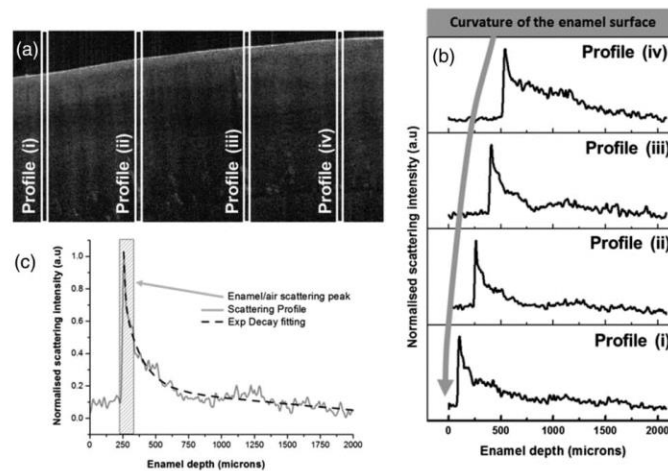


**Fig. 11** (a) OCT image of healthy enamel used for scattering profiles analysis selected randomly from a full stack (600 images). (b) The scattering profiles (average of 10 individual pixel columns) plotted as a function of enamel depth from random location in (a). The large arrow in (b) indicates the surface curvature of the enamel. (c) The scattering profile observed for healthy enamel is summarized.

cracks in the proximity of the EDJ. It is also necessary to consider that the nonscattering phase prior to the enamel/air scattering peak will vary from profile to profile because of the curvature of the enamel surface while recording the profiles.

The same approach was performed on B-scans obtained from an MIH-affected tooth. Again, several profiles were recorded at

different locations within B-scan as shown, respectively, in Fig. 12(a). A similar enamel–air scattering peak was recorded as the control healthy enamel. However, the overall shape of the profiles dramatically changed while penetrating deeper in the enamel layer. In all profiles presented in Fig. 12(b), it is possible to observe one or more strong scattering peaks at various

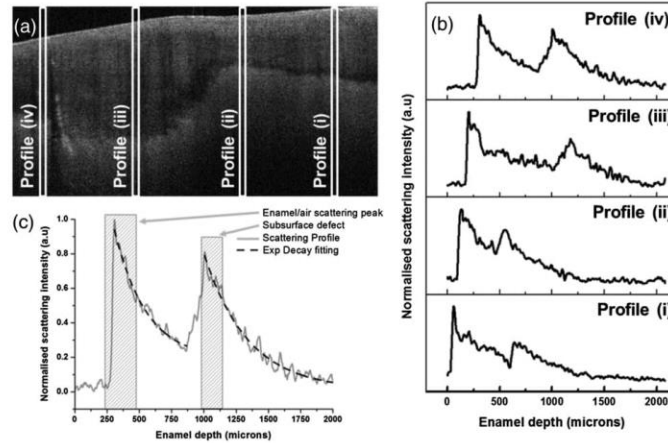


**Fig. 12** (a) OCT image of MIH-affected enamel used for scattering profiles analysis selected randomly from a full stack (600 images). (b) The scattering profiles plotted at a function of enamel depth from a random location in (a) are shown. (c) A representative scattering profile observed for MIH-affected enamel is shown in greater details. This is the same tooth as in Fig. 10.

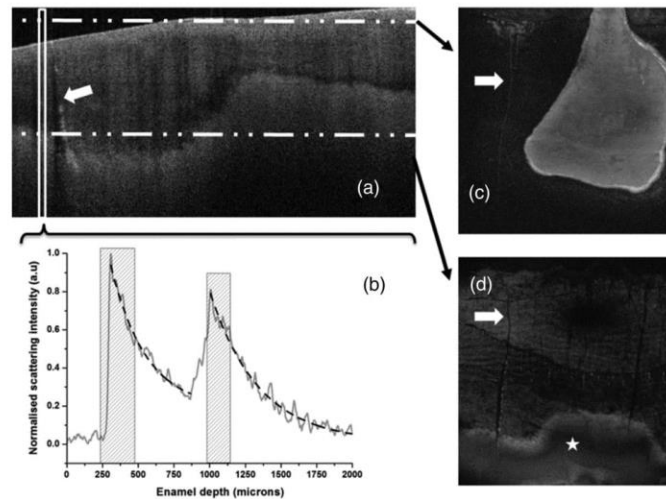


**Fig. 13** Enface reconstruction of the entire OCT images stack. Frames (c) and (d) are reconstructed frames and the dot-dash-dot lines in (a) indicate the corresponding depth of both the reconstructed frames in (c) and (d). (b) The scattering profile recorded at that location in (a) and is representative of a MIH lesion. The white arrow in (a) highlights an enamel crack that is also found in (c) and (d) after the reconstruction.

distances from the enamel/air interface. The presence of these scattering peaks is indicative of a considerable local disruption of the enamel structure. From a diagnostic point of view, these scattering peaks may be used as an indicator of the depths of the enamel defect components and boundaries. For example, from the signal intensity profile in Fig. 12(b), (i) the depth to which the defect extends can be found to be 1000  $\mu\text{m}$ . The ability to detect the depth below the air/enamel layer of each defect is informative, as this will inform clinicians about the depth extent of the lesion. Serial adjacent scans will inform the lateral extent of the same lesion. In Fig. 12(c), a decay that is reminiscent to that of healthy enamel can be observed between each of the two strong scattering peaks. A further approach, not presented in this paper, may be the investigation of the characteristic nature of that decay and the link with structural changes in enamel layers, healthy or not.

#### 4.2 Enface Reconstruction

In order to evaluate the extent of the MIH lesions at a given depth within the tooth, the entire stack of B-scans was recomputed to create an enface reconstruction (C-scan). In this reconstruction, a frame is no longer a vertical B-scan but in fact is now a horizontal plane made of stacked rows of pixels each coming from the same Z-axis depth of the original B-scans. The full reconstruction creates a frontal section. During the reconstruction, corrective factors for the aspect ratio of individual frame are introduced so that the final dimension of each frame respects the original scanning area of 6 mm  $\times$  6 mm. Figure 13 presents an area affected by MIH discussed previously. Enface reconstruction was performed on the original dataset to evaluate the extent of the subsurface lesion. Both Figs. 13(c) and 13(d) are reconstructed frames and the dot-dash-dot lines in Fig. 13(a) indicate the corresponding depth of both the reconstructed frames in Figs. 13(c) and 13(d), respectively. Figure 13(c) shows how the surface enamel is not flat in the mesial part of the tooth where the scan was recorded. The brighter area is indicative of the enamel, whereas the darker area is the air. As we consider the frame taken deeper within the enamel, as shown in Fig. 13(d), the lesion becomes apparent (highlighted by the star symbol). It is clearly possible to measure the extent of the lesion of interest in all three dimensions: X, Y, and Z. A significant crack is also visible in all the frames (B-scan and the two C-scans) as indicated by the arrows. This crack was used as a reference in this study to confirm the correlation between the B-scan and frames presented.

This mode of imaging represents a significant advance in both immediate diagnostics and following lesions longitudinally to ensure the management strategies chosen remain appropriate, as it enables subsurface imaging on nonprepared teeth. Provided that the full depth of the enamel can be imaged to include the EDG then, enface OCT imaging will permit its volumetric assessment. However, current data processing techniques are not yet versatile enough to allow this technology to be routinely used in a clinical setting, but it is not inconceivable to forecast that OCT (pending developments) could become a routine diagnostic tool for the assessing and treatment planning of enamel defects.

#### Acknowledgments

The authors would like to thank Peter Pilecki from the King's College London Dental Institute, Tissue Engineering and

Biophotonics; Ministry of Higher Education and Armed Forces Medical Services, the Royal Army of Oman, Sultanate of Oman.

#### References

1. K. L. Weerheijm, B. Jalevik, and S. Alaluusua, "Molar-incisor hypomineralisation," *Caries Res.* **35**(5), 390–391 (2001).
2. N. S. Willmott, R. A. E. Bryan, and M. S. Duggal, "Molar-incisor hypomineralisation: a literature review," *Eur. Arch. Paediatr. Dent.* **9**(4), 172–179 (2008).
3. S. Alaluusua, "Aetiology of molar-incisor hypomineralisation: a systematic review," *Eur. Arch. Paediatr. Dent.* **11**(2), 53–58 (2010).
4. K. L. Weerheijm et al., "Judgement criteria for molar incisor hypomineralisation (MIH) in epidemiologic studies: a summary of the European meeting on MIH held in Athens, 2003," *Eur. Arch. Paediatr. Dent.* **4**(3), 110–133 (2003).
5. F. Crombie, D. Manton, and N. Kilpatrick, "Aetiology of molar-incisor hypomineralization: a critical review," *Int. J. Paediatr. Dent.* **19**(2), 73–83 (2009).
6. D. Daly and J. M. Waldron, "Molar incisor hypomineralisation: clinical management of the young patient," *J. Ir. Dent. Assoc.* **55**(2), 83–86 (2009).
7. S. A. Fayle, "Molar incisor hypomineralisation: restorative management," *Eur. J. Paediatr. Dent.* **4**(3), 121–126 (2003).
8. K. L. Weerheijm, "Molar incisor hypomineralisation (MIH)," *Eur. J. Paediatr. Dent.* **4**(3), 114–120 (2003).
9. B. Jalevik and G. A. Klingberg, "Dental treatment, dental fear and behaviour management problems in children with severe enamel hypomineralization of their permanent first molars," *Int. J. Paediatr. Dent.* **12**(1), 24–32 (2002).
10. V. E. V. M. Beentjes, K. L. Weerheijm, and H. J. Groen, "Factors involved in the etiology of hypomineralized first permanent molars," *Ned. Tijdschr Tandheelkd.* **109**(10), 387–390 (2002).
11. FDI, Commission on Oral Health, Research and Epidemiology, "A review of the developmental defects of dental enamel index (D.D.E index)," *Int. Dent. J.* **42**(6), 411–426 (1992).
12. N. A. Lygidakis et al., "Best clinical practice guidance for clinicians dealing with children presenting with molar-incisor-hypomineralisation (MIH): an EAPD policy document," *Eur. Arch. Paediatr. Dent.* **11**(2), 75–81 (2010).
13. A. Fercher and C. Hitzenberger, "Optical coherence tomography," in *Progress in Optics*, E. Wolf, Ed., pp. 215–302, Elsevier Science B. V., Amsterdam (2002).
14. D. Huang et al., "Optical coherence tomography," *Science* **254**(5035), 1178–1181 (1991).
15. R. S. Jones et al., "Imaging artificial caries on the occlusal surfaces with polarization-sensitive optical coherence tomography," *Caries Res.* **40**(2), 81–89 (2006).
16. D. Fried et al., "Imaging caries lesions and lesion progression with polarization sensitive optical coherence tomography," *J. Biomed. Opt.* **7**(4), 618–627 (2002).
17. B. T. Amaechi et al., "Quantification of root caries using optical coherence tomography and microradiography: a correlational study," *Oral Health Prev. Dent.* **2**(4), 377–382 (2004).
18. R. S. Jones and D. Fried, "Remineralization of enamel caries can decrease optical reflectivity," *J. Dent. Res.* **85**(9), 804–808 (2006).
19. S. K. Manesh, C. L. Darling, and D. Fried, "Polarization-sensitive optical coherence tomography for the nondestructive assessment of the remineralization of dentin," *J. Biomed. Opt.* **14**(4), 044002 (2009).
20. A. M. A. Maia et al., "Characterization of enamel in primary teeth by optical coherence tomography for assessment of dental caries," *Int. J. Paediatr. Dent.* **20**(2), 158–164 (2010).
21. C. S. D. Azevedo et al., "Evaluation of caries-affected dentin with optical coherence tomography," *Braz. Oral Res.* **25**(5), 407–413 (2011).
22. R. Farah et al., "Linking the clinical presentation of molar-incisor hypomineralisation to its mineral density," *Int. J. Paediatr. Dent.* **20**(5), 353–360 (2010).
23. K. Oliver et al., "Distribution and severity of molar hypomineralisation: trial of a new severity index," *Int. J. Paediatr. Dent.* **24**(2), 131–151 (2014).

# J. Demineralisation-Remineralisation Dynamics in Teeth and Bone

International Journal of Nanomedicine

Dovepress

open access to scientific and medical research

 Open Access Full Text Article

REVIEW

## Demineralization–remineralization dynamics in teeth and bone

This article was published in the following Dove Press journal:  
International Journal of Nanomedicine  
19 September 2016  
Number of times this article has been viewed

Ensanya Ali Abou Neel<sup>1–3</sup>  
Anas Aljabo<sup>3</sup>  
Adam Strange<sup>3</sup>  
Salwa Ibrahim<sup>3</sup>  
Melanie Coathup<sup>4</sup>  
Anne M Young<sup>3</sup>  
Laurent Bozec<sup>3</sup>  
Vivek Mudera<sup>4</sup>

<sup>1</sup>Division of Biomaterials, Operative Dentistry Department, Faculty of Dentistry, King Abdulaziz University, Jeddah, Saudi Arabia; <sup>2</sup>Biomaterials Department, Faculty of Dentistry, Tanta University, Tanta, Egypt; <sup>3</sup>Department of Biomaterials and Tissue Engineering, UCL Eastman Dental Institute, London, UK; <sup>4</sup>UCL Institute of Orthopaedics and Musculoskeletal Sciences, Royal National Orthopaedic Hospital, Stanmore, London, UK

**Abstract:** Biomineralization is a dynamic, complex, lifelong process by which living organisms control precipitations of inorganic nanocrystals within organic matrices to form unique hybrid biological tissues, for example, enamel, dentin, cementum, and bone. Understanding the process of mineral deposition is important for the development of treatments for mineralization-related diseases and also for the innovation and development of scaffolds. This review provides a thorough overview of the up-to-date information on the theories describing the possible mechanisms and the factors implicated as agonists and antagonists of mineralization. Then, the role of calcium and phosphate ions in the maintenance of teeth and bone health is described. Throughout the life, teeth and bone are at risk of demineralization, with particular emphasis on teeth, due to their anatomical arrangement and location. Teeth are exposed to food, drink, and the microbiota of the mouth; therefore, they have developed a high resistance to localized demineralization that is unmatched by bone. The mechanisms by which demineralization–remineralization process occurs in both teeth and bone and the new therapies/technologies that reverse demineralization or boost remineralization are also scrupulously discussed. Technologies discussed include composites with nano- and micron-sized inorganic minerals that can mimic mechanical properties of the tooth and bone in addition to promoting more natural repair of surrounding tissues. Turning these new technologies to products and practices would improve health care worldwide.

**Keywords:** demineralization, remineralization, teeth, bone and calcium phosphates

### Introduction

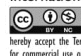
Enamel, dentin, cementum, and bone are natural composites of both organic and inorganic components. Bone, cementum, and dentin are specialized connective tissues, while enamel has an ectodermal origin. For the specialized connective tissues (bone, cementum, and dentin), collagen type I constitutes ~90% of their organic component;<sup>1,2</sup> noncollagenous proteins form the remaining. On the other hand, enamel has little or no collagen, and its organic matrix is made up of noncollagenous protein, which is 90% amelogenin.<sup>3</sup> The inorganic component of these hard tissues consists of biological apatite,  $\text{Ca}_{10}(\text{PO}_4)_6(\text{OH})_2$ . Enamel has more inorganic content (~90% prismatic crystals) than dentin and bone (~70%) and cementum (45%). The unit cell of biological apatite is hexagonal in shape; repetitions of the unit cells produce crystals of various sizes. In dentin, the crystals are plate like of 50 nm length, 20 nm width, and 2–5 nm thickness.<sup>4</sup> In bone, the crystals are known to be ~2–6 nm thick, 30–50 nm wide, and 60–100 nm long.<sup>5</sup> However, they are bigger and highly oriented in enamel than in bone and dentin, making it the hardest tissue in the body. Due to the presence of a variety of substitutions and vacancies within the biological apatite, its calcium–phosphate ratio is different from that of stoichiometric hydroxyapatite (HA, 1.67). Enamel apatite,

Correspondence: Ensanya Ali Abou Neel  
Division of Biomaterials, Operative Dentistry Department, Faculty of Dentistry, King Abdulaziz University, PO Box 80209, Jeddah 21589, Saudi Arabia  
Tel +966 596820208  
Email eabouneel@kau.edu.sa

submit your manuscript | [www.dovepress.com](http://www.dovepress.com)  
Dovepress  
<http://dx.doi.org/10.2147/IJN.S107624>

International Journal of Nanomedicine 2016:11 4743–4763

4743

 © 2014 Abou Neel et al. This work is published and licensed by Dove Medical Press Limited. The full terms of this license are available at <http://www.dovepress.com/terms.php> and incorporate the Creative Commons Attribution – Non Commercial (unported, v3.0) License (<http://creativecommons.org/licenses/by-nc/3.0/>). By accessing the work you hereby accept the Terms. Non-commercial uses of the work are permitted without any further permission from Dove Medical Press Limited, provided the work is properly attributed. For permission for commercial use of this work, please see paragraphs 4.2 and 5 of our Terms (<http://www.dovepress.com/terms.php>).

resembling the stoichiometric HA, has fewer substitutions than bone and dentin mineral.<sup>6</sup> Examples of ion substitution that could occur in biological apatite include substitution of calcium ions with magnesium and sodium, substitution of hydroxyl sites with fluoride and chloride, and substitution of both phosphate and hydroxyl sites with carbonate. With ion substitutions, a considerable variation in apatite properties could occur, for example, magnesium substitution inhibits crystal growth, carbonate substitution increases solubility, and fluoride substitution decreases the solubility.<sup>3</sup> The carbonate content of bone and teeth HA is 4%–8%; with age, the carbonate content increases but the hydrogen phosphate decreases.<sup>3,4</sup> The ratio of inorganic-to-organic contents varies according to the tissue; such variation reflects the properties of each tissue. For example, with high inorganic content, enamel is tougher and more highly resistant to force than any other hard tissues in the body. With high organic content, however, dentin is more resilient than enamel and therefore provides a resilient layer under enamel and cementum.

Furthermore, these hard tissues have different regenerative capacity. Unlike ameloblasts and odontoblasts, which leave no cellular bodies in their secreted products during the later stage of apposition, many cementoblasts and osteoblasts become entrapped by the formed cementum and bone they produce, becoming cementocytes and osteocytes, respectively. Although bone is a highly adaptive tissue (ie, continually undergoing remodeling), cementum has a very slow regenerative capacity<sup>7</sup> and is not resorbed under normal conditions. Dentin and enamel develop their definitive structure during odontogenesis. Dentin has the capacity to regenerate by the formation of secondary and tertiary dentin, but enamel does not have the regenerative capacity. Unlike skeletal bones, facial bones are derived from both neural crest and paraxial mesoderm and they respond differently to growth factors and mechanical stimuli.<sup>8</sup>

### Mineralization of teeth and bone

Mineralization is a lifelong process, in which an inorganic substance precipitates onto an organic matrix. Normal biological processes include the formation of hard connective tissues, such as bone, dentin, and cementum, in which collagen fibrils form a scaffold for a highly organized arrangement of uniaxially organized calcium phosphate crystals.<sup>9</sup> Pathological processes of mineralization result in calcification within blood vessels or in, for example, the kidney or formation of gallstones.<sup>10</sup> Understanding the process of mineral deposition is important for the development of treatments for mineralization-related diseases and also for the

innovation and development of scaffolds. However, there are still critical gaps in understanding the process. While the structure of mineralized collagen is now well understood, how mineral precipitates with the spatial and hierarchical order found in tissues is still largely unknown. Cells control the mineralization process of crystal morphology, growth, composition, and location. The molecules of the extracellular matrix (ECM) and a series of enzymes, however, direct the entry and fixation of mineral salts (calcium and phosphate ions) in bone, dentin, and enamel.

### Teeth

Teeth are composed of enamel, pulp–dentine complex, and cementum. Dentine forms the largest portion of a tooth. It is 70% mineralized by weight, with the organic content accounting for 20% of the matrix, and the remaining 10% being water. Type I collagen is the primary component of the organic portion of dentine, accounting for >85%, with the remaining amounts being collagen types III and V. The non-collagenous part of the organic matrix is composed mainly of dentine phosphoprotein, accounting for ~50% of the noncollagenous part. The remaining inorganic matrix is composed primarily of HA.<sup>11</sup> Several studies have suggested that collagen in enamel matrix is completely removed with all other organic components during the course of its mineralization and maturation.<sup>12–14</sup> These studies refuted the earlier theories that proposed that a small percentage of collagen is retained after enamel maturation.<sup>15,16</sup> A more recent study concluded that there is minimal collagen content, mostly types I and V, found in mineralized and mature enamel in comparison with dentine.<sup>17,18</sup> It is commonly believed that HAs are generally encompassed within and coated by the organic material present in the tooth structure. While the physical properties of teeth are largely attributed to the presence of enamel, it is also hypothesized that collagen acts as an active protective protein sheath of the underlying HA crystallite lattice.

Type I collagen, a heterotrimer of two  $\alpha 1(I)$  chains and one  $\alpha 2(I)$  chain folded in a triple helix structure, has a rod-like structure of 1.5 nm diameter and >300 nm long. The triple helix domain is flanked by nonhelical N- and C-propeptides. This form of collagen, known as procollagen, is secreted from cells, for example, fibroblasts, odontoblasts, and osteoblasts into the extracellular spaces where it is converted into tropocollagen by the removal of N- and C-propeptides. Tropocollagen can then spontaneously self-assemble into fibrils (ie, the fibril is built from the staggered packing of the individual collagen molecules such that there are periodic gaps along the fibril surface and

channels extending through the fibril<sup>19</sup>). Each collagen unit is ~300 nm long and overlaps neighboring units by ~67 nm.<sup>19</sup> Fibrils contain gap regions of 40 nm between end-to-end collagen units. Packing of collagen is stabilized by weak dispersive and hydrogen interactions as well as by strong intermolecular cross-links. This stabilization is essential for the structural stability and insolubility of collagen in water.<sup>20</sup> End-to-end elongation and lateral aggregation of collagen fibrils are responsible for increasing its diameter and migration<sup>21</sup> toward the place where they undergo mineralization, for example, movement of collagen fibrils from the proximal to the distal predentin where the mineralization occurs.<sup>3</sup> In dentin, collagen type I accommodates ~56% of mineral in its holes and pores of fibrils. The noncollagenous proteins act as inhibitors, promoters, and/or stabilizers of mineral deposition. For example, glycoproteins prevent premature mineralization until the collagen fibrils become mature and attain their correct dimensions. Dentin matrix protein-1, an acidic phosphoprotein, plays an important role in initiation of nucleation and modulation of the morphology of mineral phase.<sup>22</sup> During dentinogenesis, three types of mineralization usually occur; they include matrix vesicle-derived mineralization (in mantle dentin), ECM molecule-derived mineralization (in majority of dentin), and blood–serum-derived mineralization (in peritubular dentin).<sup>23</sup> Odontoblasts secrete an acid mucopolysaccharide, for example, chondroitin sulfate, which is a prerequisite for start of mineralization. This mucopolysaccharide is transported to the site of mineralization in dentin matrix; it attracts calcium and serves to transport minerals from cells to the ECM.<sup>24</sup>

In enamel, immediately after initial dentin mineralization at the dentinoenamel junction, ameloblast cells secrete enamel matrix proteins (eg, amelogenin, ameloblastin, and enamelin) and proteinases (matrix metalloproteinase-20 and kallikrein-related peptidase-4) at the dentin surface. These proteins and proteinases are responsible for immediate mineralization of ~30% of enamel. The first formed enamel crystals (ribbons) grow between the existing dentin crystals by mineralizing around dentin proteins. These crystal ribbons then elongate at the mineralization front where enamel proteins are secreted. While they are moving away from the dentin surface, the ameloblast start secreting large amounts of enamel matrix proteins. When the entire thickness of enamel is formed, the ameloblasts become protein-resorbing cells (ie, remove enamel matrix proteins); and therefore, additional mineral is required to coincide with the bulk removal of enamel proteins and water to produce enamel

with >95% mineral content. The formed crystals are long, thin, and parallel ribbons of 26×368 nm<sup>2</sup>; ~10,000–40,000 ribbons at packing density of 550 crystallites/μm<sup>2</sup><sup>25</sup> form a rod (prism) with ~5 μm diameter.<sup>26</sup> Each ameloblast produces one rod; all rods are organized in a three-dimensional structure. The mineral crystals formed within the enamel rods grow in *c*-axis length parallel to each other all the way from dentinoenamel junction to the tooth surface, while those developed between the rods (ie, interrod) have limited lengths and always ordered at angles relative to the rod crystals. Since this process of enamel formation and maturation is a cell-mediated process, completion of mineralization is associated with several morphological changes in ameloblasts; hence, the matrix removal and crystal growth occur efficiently. For calcification, the influx of calcium from the blood to the enamel matrix involves intercellular and transcellular routes. Unlike collagen-based mineralized tissues, no matrix vesicles are associated with mineralization of enamel. The mineral content is reduced from the enamel surface toward the dentinoenamel junction. The position of HA is located between the nanospheres of amelogenin.<sup>3,27</sup> Therefore, ameloblasts are not only responsible for secreting the enamel matrix proteins and proteinases but also induce mineral formation and finally organize these minerals into rod and interrod patterns.

## Bone

During the formation of mineralized bone matrix, osteoblasts first deposit unmineralized osteoid and release mineral-nucleating proteins that catalyze the process where osteoid starts to calcify. Mineralization occurs after ~15 days. The primary phase of mineralization to ~70% of full mineralization is a rapid process, whereas the secondary phase to full mineralization is slower and can last for several months to years. This process of mineral accumulation within each site of newly formed bone together with the activation frequency of remodeling sites causes a specific mineralization pattern in the bone material. As mentioned above, type I collagen is known to be the predominant component of the ECM of bone, calcifying tendon, dentin, and cementum. Crystals may be formed within the individual type I collagen fibrils, with the same periodicity displayed by the collagen, and along the fibril surfaces in the extrafibrillar spaces between packed collagen fibrils of the bone and dentin fibers.<sup>28</sup> In 1952, Robinson and Watson<sup>29</sup> showed that carbonated HA crystals exist within collagen (intrafibrillar deposition) with their *c*-axis nearly parallel with the long axis of the collagen fibril. The crystals are known to be ~2–6 nm thick, 30–50 nm wide, and 60–100 nm

long.<sup>5</sup> Several studies have shown that the matrix nucleates preferentially form within the gap regions of collagen fibrils, where most crystals are well organized into parallel arrays, in almost continuous dark bands.<sup>5,19</sup> While the mineral precipitates preferentially in the gaps between the collagen fibrils, the crystals have been shown to grow and eventually exceed the size of the gap.<sup>19</sup> Furthermore, mineral exists both within and external to the collagen fibrils (interfibrillar deposition); however, it is generally accepted that the majority of the mineral exists within the fibrils.<sup>30</sup> Interfibrillar mineralization of collagen is directed by the collagen matrix,<sup>31</sup> which leads to nanostructured architecture consisting of uniaxially orientated nanocrystals of HA embedded within and roughly aligned parallel to the long collagen fibril axis. Previous studies have suggested that type I collagen polypeptide stereochemistry and other factors are fundamental in the initial events of mineral deposition with the intrafibrillar spaces of the molecule.<sup>32,33</sup> The side chains of polypeptide-charged amino acids are thought to contribute binding sites for calcium and phosphate ions found in the circulating supersaturated fluid of the tissues.<sup>32</sup> The configurations would conceptually bring these ions into close association and lead to their nucleation. Apatite growth and development would follow initial nucleation events to result in platelet-shaped crystals growing preferentially along collagen assemblies.<sup>32,34</sup> It is clear that not all collagenous tissues mineralize and investigating the process *in vivo* is difficult. Therefore, many of the studies that have investigated the possible physicochemical mechanisms of mineralization used *in vitro* models.

The control of bone biomineralization is dynamic and complex with many theories, describing the responsible mechanisms, and many factors have been implicated as agonists and antagonists of mineralization; the deregulation of which can lead to pathological extraskelatal mineralization. The crystallization process can be considered from several different perspectives: 1) the development of crystallinity in a mineral phase developed directly from a supersaturated solution of the mineral ions, 2) the presence of polymeric (protein) polyions in the mineralizing system and how they might interact *in vitro* with the free ions or with nanoclusters of Ca and PO<sub>4</sub> ions to modulate the mineralization process, 3) small integrin-binding ligand, N-linked glycoproteins (SIBLINGS) and how they might be delivered *in vivo* to regulate mineralization at specific sites, including the processes of nucleation, crystal growth, crystal morphology, and size regulation, and 4) the delivery of sequestered, vesicular nanoclusters of Ca and P directly from the cell or the mitochondria to the mineralization front.<sup>35</sup> Veis and Dorvee<sup>35</sup>

speculated that it is likely that some common mechanisms may be applicable in all cases.

Mineralization was initially viewed as a classical precipitation and growth of apatite crystals directly from interstitial fluid supersaturated with calcium and phosphate phases. Studies have shown that serum is a metastable solution from which calcium phosphate precipitates in the presence of calcifiable templates such as collagen, elastin, and cell debris.<sup>36,37</sup> Recently, it was demonstrated that apatite formation in bone and teeth does not occur directly by the association of ions from solution but is preceded by an amorphous calcium phosphate (ACP) precursor phase that may later transform into octacalcium phosphate before becoming HA,<sup>38</sup> although the mechanism of this pathway is under debate.<sup>39,40</sup> It has been suggested that calcium phosphate precipitation *in vitro* is kinetically driven, meaning that the mineral does not crystallize directly into the most thermodynamically stable product but instead precipitates first into the kinetically most accessible form, ACP, which is subsequently transformed into the most thermodynamically stable phase. ACP formation is thought to proceed through subnanometer-sized prenucleation clusters with a chemical composition Ca<sub>9</sub>(PO<sub>4</sub>)<sub>6</sub>, which are stable clusters present in solution before nucleation as was recently demonstrated for CaCO<sub>3</sub>.<sup>41</sup> However, the role of these nanometer-sized clusters as building blocks for ACP formation has been debated for many years.<sup>40</sup> The origin of the mineral and how it infiltrates the collagen fibrils are still unknown.

ECM noncollagenous proteins (NCPs, now known as SIBLING) are believed to control several aspects of the mineralization process, specifically through the mechanisms of inhibition and promotion by phosphoproteins, glycoproteins, Gla-containing proteins, and proteoglycans.<sup>31</sup> It has been shown that protein concentration and whether the protein is free or immobilized can profoundly affect function in precipitation models. Presently, there is no clear role of these SIBLINGs, although it has been suggested that SIBLINGs regulate solution crystal growth by an epitaxial relationship between specific crystallographic faces and specific protein conformers.<sup>31</sup> Osteocalcin and osteopontin are two of the most abundant noncollagenous proteins, and both have been shown to influence the deposition of mineral within the collagen fibril-rich bone ECM. *In vitro* studies have shown osteocalcin and osteopontin control HA nucleation, size, shape, and orientation.<sup>42,43</sup>

Regulation of the mineralization process is also known to rely largely on inorganic pyrophosphate (PPi), a potent inhibitor of mineralization. Osteoblast and osteocyte-derived



matrix vesicles control extracellular PPi levels with a host of factors, at least three other molecules: nucleotide pyrophosphatase phosphodiesterase 1, ankylosis protein (ANK), and tissue-nonspecific alkaline phosphatase (TNAP). TNAP is an enzyme that hydrolyses and inactivates PPi and is normally expressed at sites of mineralization during development. Loss of TNAP function results in hypomineralized bone.<sup>44–46</sup> Conversely, ANK is expressed in nonmineralizing tissues, where it transports PPi to the extracellular space to antagonize mineralization. Loss of functional mutations in ANK causes hypermineralization and the formation of bone spurs or bone-like hardening of tendons and ligaments of the spine.<sup>47</sup> Much of the *in vivo* evidence regarding the role of specific proteins comes from their distribution and genetic knockout studies. However, proteins such as osteopontin have multiple roles, complicating interpretation. Tissue localization can give clues to a role but does not provide any functional information.<sup>30</sup>

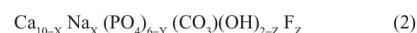
How Ca and PO<sub>4</sub> ions are delivered to the mineralization front is still a matter of debate. Pioneering studies have suggested the role of mitochondria in taking in large amounts of Ca and PO<sub>4</sub> ions, accumulating them, and delivering calcium phosphate in membrane bound vesicles to the extracellular spaces of mineralizing cartilage and bone.<sup>35,48,49</sup> Matrix vesicles are extracellular, membrane-invested vesicles 50–200 nm in diameter and are formed by polarized budding from the surface membrane of chondrocytes, osteoblasts, and odontoblasts. The signals that release matrix vesicles are not well understood, although the concentrations of intracellular calcium and extracellular phosphate may be important.<sup>50</sup> Mineralization begins with the formation of HA crystals within matrix vesicles, followed by propagation of HA through the membrane into the ECM. The origin of calcium and phosphate within the vesicles has not been elucidated. When the accumulation of calcium and phosphate exceed the solubility point for calcium phosphate, deposition of HA occurs within the matrix vesicles.<sup>50</sup> In the second step, HA crystals penetrate the matrix vesicle membrane and are elongated into the extracellular space. The ratio of phosphate ions to PPi is crucial in the second step of mineralization. PPi, which inhibits the formation of HA,<sup>51</sup> is formed by nucleotide pyrophosphatase phosphodiesterase 1. Alkaline phosphatase hydrolyses PPi to generate phosphate ions. The mechanisms by which vesicles may be broken open and their mineral contents transferred and localized to the collagen are still a subject of current study and debate.<sup>35</sup> There is abundant evidence that the mineral-containing intracellular vesicles do exist, and their contents in different situations contain ACP

or apatite needle-like crystals. Mahamid et al<sup>52</sup> showed that mineral is released in globules (presumably ACP) from cells at the growth zone. Further questions that remain unsolved are those surrounding the mechanisms by which the mineral is transformed from the mitochondria to the mineralizing matrix, then reordered, in essence dissolved, and recrystallized on the collagen fibril matrix on the fibril surfaces, or within the fibrils themselves.<sup>35</sup>

## Role of calcium and phosphate ions in teeth and bone

Calcium phosphate is fundamental for the formation of bone and teeth and is essential for achieving optimal peak bone mass in the first 2–3 decades of life and for the maintenance of bone in later life.<sup>53</sup> Mineral concentration is a major determinant of the elastic modulus of the bone matrix. As the mineral fraction of the bone ECM increases, hence does the elastic modulus.<sup>54</sup> Therefore, different tissues in the body can provide either rigidity (high mineral content) or flexibility (low mineral content).

The HA in teeth varies from empirically derived HA, and HA found in bones, as the dental version, is often calcium deficient due to fluorine substitutions – Equations 1 and 2 – that shows the stoichiometric formula of HA (Equation 1). The formula of HA shows the sites for atomic substitution (Equation 2). This HA is calcium deficient and carbonated. X, calcium substitution with metal cation; Y, phosphate substitution with carbonate; and Z, hydroxide substitution with fluoride.<sup>55–57</sup>



Calcium-deficient carbonated HA comprises the major substitution activity that takes place. Other much smaller number of substitutions occur where calcium ions, ~1%, is replaced by other metal ions, including potassium, sodium, and magnesium.<sup>58</sup> The presence of carbonates and other ionic substitutions significantly disrupts the crystal lattice in HA. This weakens the HA, increasing its susceptibility to acid attack and solubility.<sup>59</sup> The carbonate content of dentine is 5%–6%, while in enamel it is 3%, and the HA crystal size in dentine is much smaller than those in enamel, thus making dentinal matrix much more vulnerable to acidic attack.<sup>60</sup>

With age, the crystallinity of dental HA decreased but the carbonate content increased. The  $\alpha$ -lattice constant,



associated with the carbonate content, decreased while the c-lattice, associated with hydroxyl sites, does not change significantly with age. Increased crystal structure disorder and reduction in crystallinity are expected with higher number of planar carbonate ions substituting for tetrahedral phosphate ions in the apatite structure.<sup>61</sup> Both A- and B-type of carbonate substitutions are present but the B-type (carbonate for phosphate) is greater than the A-type (carbonate for hydroxyl).<sup>61</sup> Since c-lattice parameter is nearly age independent; this indicates that the phosphate tetrahedron represents the main site of carbonate substitution in the apatite lattice.<sup>61</sup> A decrease in crystallinity and increase in carbonate content favor the dissolution of dental apatite. This is a change in material phase and the composition of dental mineral, while also reducing crystal size.<sup>61</sup> The carbonate content has a significant effect on the reactivity and solubility of physiological HA.

Calcium, phosphate, and fluoride ions play an important role in the battle between demineralization and remineralization processes and accordingly modify the susceptibility of tooth to caries progression.<sup>62</sup> During demineralization, calcium release precedes phosphate release from enamel, dentin, and cementum. Therefore, using calcium rather than phosphate to suppress the demineralization process would be effective.<sup>63</sup>

## Demineralization–remineralization dynamics in teeth

Demineralization is the process of removing mineral ions from HA crystals of hard tissues, for example, enamel, dentin, cementum, and bone. Restoring these mineral ions again to the HA crystals is called remineralization. Both processes occur on the tooth surface, and a substantial number of mineral ions can be lost from HA without destroying its integrity but high sensitivity to hot, cold, pressure, and pain would be expected. Lacking of the integrity of HA latticework, however, produces cavities. Demineralization is a reversible process; hence, the partially demineralized HA crystals in teeth can grow to their original size if they are exposed to oral environments that favor remineralization.<sup>64</sup>

## Demineralization

Similar to bone, teeth are composites comprised of the phosphate-based mineral HA in the enamel, collagen in the dentine, and living tissues.<sup>65–67</sup> However, it is the anatomical arrangement and location of teeth that sets them apart from bones.<sup>68</sup> Exposed to food, drink, and the microbiota of the mouth, teeth have developed a high resistance to localized

demineralization unmatched by other mineralized tissues.<sup>59,69</sup> This resistance is chiefly due to the enamel layer that covers the crown of the teeth.<sup>70,71</sup>

Chemical demineralization of teeth is caused by acidic attack through two primary means: dietary acid consumed through food or drink and microbial attack from bacteria present in the mouth.<sup>69,72,73</sup> Published literature in this area seeks to apply chemical theory to the erosion of dental hard tissues, chiefly enamel.<sup>59,74,75</sup>

During an acidic attack, or a typical demineralization regime, chemical dissolution of both the organic and inorganic matrix components takes place. This is brought about by the water content of enamel and dentine, which facilitate acid diffusion in and mineral content out of tooth.<sup>60</sup>

## Etiology and risk factors: a multifactorial process

Demineralization and the subsequent erosion and/or loss of tooth surface versus remineralization are dynamic processes that are dependent on several modifying factors, as shown in Table 1. These factors are split into two main groups, extrinsic and intrinsic, which can be altered by the last group, the modifying factors. Extrinsic factors include diet and medication. Intrinsic factors are mostly diseases that can sometimes be treated with medications that are themselves extrinsic factors of erosion. Modifying factors can be variations in the biochemical characteristics of an intrinsic or extrinsic factor, behavioral patterns such as regular tooth brushing, some of which can also be classed as socioeconomic factors.

Erosion and carious lesions are the two main consequences of demineralization. Public awareness of dental erosion is still not widespread, and its differential diagnosis among dental professionals has proven to be a challenge.<sup>76</sup> The dietary consumption of soft or fruit-based drinks in the developed world is thought to be over half of all of the liquids consumed.<sup>77</sup> The spread of the commercialization of the soft drinks market has increased by 56% over the past 10 years and is growing by a rate of 2%–3% yearly.<sup>78</sup> In 2002, the consumption of these high acid drinks was

**Table 1** Interaction of different factors in relation to tooth surface loss

Biological	Chemical	Health and education	Behavioral
Saliva flow	pH type	Current health	Eating habits
Soft tissue anatomy	Acid type	Socioeconomic status	Drinking habits
Tooth anatomy	Chelation potential	Medication and drugs	Brushing frequency

predicted to show an increase in dental issues over the following 5 years.<sup>74,79</sup> This has been shown to be the case, as repeated studies have shown erosion throughout different demographic groups.<sup>55,77,78,80,81</sup>

Erosion and its extrinsic causative factors have been included in the UK Children's Health Survey since 1993, and a trend toward higher prevalence of erosion in those who often consumed carbonated drinks was shown.<sup>82</sup> In the UK in 2003, >50% of 5–6 years old had exhibited significant enamel erosion, linked to the consumption of acidic drinks. Furthermore, 25% of 11- to 14-year olds had significant erosion, rising to 77% in 20- to 25-year olds.<sup>83,84</sup> A recent study in 2015 showed an increase in pediatric dental hospital admissions, with cases strongly linked to sugar erosion.<sup>85</sup> There is a widespread misunderstanding by patients that the extraction of primary teeth is not a matter of concern, since these will be replaced by permanent teeth. This has been repeatedly shown to be false, and the damage done by the primary teeth issues may be affecting the future health of the permanent teeth.<sup>66,80,86,87</sup> Previous in vitro models were made on the belief that the tooth–acid interactions last for several minutes. However, more recent in vivo studies suggest that the in vitro tooth–acid models should focus on the acid interaction for 30 seconds. This would better represent in vivo conditions.<sup>78,86,88</sup>

The most recent study in the US has shown that 79% of adults have at least moderate evidence of tooth decay; regardless of demographic, the key feature was the excessive daily consumption of fruit juices and soft drinks.<sup>89</sup> The most recent study in the Peoples' Republic of China showed 89% tooth wear among 15 years old, with 7% showing dentine exposure; a mark of the severity of the erosion.<sup>90</sup> Other studies from Japan and India also showed comparable data for early-stage tooth erosion.<sup>91,92</sup> Modifying behavioral factors that affect dietary consumption include types of drinks consumed, method by which a drink is consumed, and frequency of drinking. For example, an increase in agitation when a drink is swished around the mouth will enhance the dissolution process.<sup>93</sup> Moreover, several medication and asthmatic inhalers were shown to induce xerostomia by reducing salivary flow, in addition to decreasing its pH; thus, weakening its overall buffering effect against intrinsic and extrinsic acids.<sup>94,95</sup> Saliva is considered one of the most important biological factors in dictating the intraoral neutralizing effects of acid exposure. Pathogenesis of dental erosion is directly related to the buffering capacity and rate of secretion of saliva.<sup>96</sup>

The mineralization percentage of permanent teeth is higher than that of primary teeth;<sup>68</sup> nevertheless, adults frequently

experience the effects of acid damage on teeth. Mechanically, the teeth are softer and weakened, although there is no change in the brittleness. Intrinsic factors that may lead to erosion include gastroesophageal reflux, often seen in diabetic and obese individuals, bulimia nervosa, and dental rumination. Diseases such as bulimia nervosa have the symptom of self-induced vomiting, which can be a leading cause in dental erosion if occurring often enough. For gastroesophageal reflux, it is defined as a normal physiologic retrograde flow of gastric contents and acid regurgitation into the esophagus and sometimes mouth, which occurs mostly postprandial, after meals, for ~1 hour.<sup>97</sup> Irrespective of the cause, excessive stomach acid has a deleterious effect on dental health. Endogenous acids has a pH of 1.2, that is well below the critical pH for fluoroapatite (FAP) and HA dissolution,<sup>66,98,99</sup> thus leading to rapid demineralization of tooth surfaces. Regardless of the type of causative factors, teeth eroded by acid are more likely to crack or chip if damaged and are harder to repair.<sup>100,101</sup> The areas of structural weakness that have been demineralized are also targets for caries formation.<sup>74,102,103</sup> Bacteria can easily colonize the demineralized areas of the tooth and, with a combination of their own acid formation, are able to penetrate into the dentine.<sup>81,104</sup> The dentinal contribution of the demineralization-assisted caries is higher than when acid drinks are not involved and is a marker of the severity of the caries.

## Bacteria

Dental caries is the most common childhood chronic infectious disease. It is caused by the interaction of bacteria, mostly *Streptococcus mutans*, and sugar on tooth enamel surface. Bacteria breakdown fermentable carbohydrate such as glucose, sucrose, and fructose and cause an acidic environment that leads to demineralization and resultant carious lesions.<sup>98,99</sup> There are several theories proposed as to how oral bacteria are actually acquired. At birth, the oral cavity is known to be effectively sterile; however, acquisition is achieved via transmission from food/milk/water, from parents, or from oral mucosa shedding surface during eruption of primary dentition. The most widely accepted hypothesis with regard to the role of bacteria in acid production and caries formation is the “ecological hypothesis”, where dental plaque is defined as a dynamic microbial ecosystem in which nonmutans bacteria are key players for maintaining dynamic stability.<sup>93</sup> *S. mutans*, *Streptococcus sobrinus*, and lactobacilli are the main oral cariogenic pathogens due to their ability to produce high levels of lactic acid following sugar fermentation and their resistance to the adverse effects of low

pH.<sup>105,106</sup> In some studies, *S. mutans* were seen to be >30% of oral microflora in children with early childhood caries.<sup>107</sup> Higher frequency of sugar intake leads to increased risk and susceptibility to caries due to prolonged exposure to acidic conditions, regardless of the amount ingested.

#### Acid erosion mechanisms

Dental erosion can be defined as being the loss of hard tissues though dissolution by acids of nonbacterial origin or mechanical damage. When exposed to acid, teeth become softer as the HA is solubilized, and therefore, more susceptible to mechanical wear. The two chemical methods by which this can occur are either direct acid attack or chelation.<sup>57,74,90</sup>

When hydronium ions are formed from an acid in solution, they bind with carbonate or phosphate in HA, releasing the anions into solution in a form of chemical etching. Carbonate is more reactive than phosphate, and requires a lower concentration of hydronium to react with, and is therefore why HA is weaker with excess carbonate.<sup>57</sup>

Three phases of attack have been identified, based on the pH of the acid.<sup>108</sup> Acids with pH <1 can cause surface etching when exposed to teeth for very short time periods. Nanoscale surface softening occurs with short exposure at pH 2–4, but this does not extend to the macroscale.<sup>70,109</sup> The third and most common form of acid attack is through weak acid (pH 4.5–6.9) subsurface dissolution. This along with bacteria can lead to the formation of carious lesions and as a result has been well studied.

Exposure to acids with pH >4 is not a common biological occurrence. Emesis is the normal mechanism, whereby stomach acids can come into contact with the teeth. Some patients with the most severe and prolonged hyperemesis episodes, such as those with alcoholism, may subject their teeth to acids with a pH of 1.<sup>55</sup> This is well below the demineralization pH and can cause surface etching, which is highly dangerous for teeth. Dentition in patients with intrinsic disease factors such as hyperemesis gravidarum or bulimia may be exposed to low pH acids regularly enough to cause nanoscale surface softening.<sup>70,109,110</sup> However, the weak acid dissolution pathway has many possible causes. Fruits commonly have carboxylic or citric acids.<sup>87,109</sup> The hydronium ion formed by carboxylic acids readily binds with phosphate, forming phosphate cations.<sup>55,111</sup> These cations can form a calcium acid chelation complex, debonding mineral ions in the surrounding lattice causing widespread demineralization.<sup>74</sup> Alternatively and more rarely, these can remain in proximity to the HA layer, with minimal demineralization.

Carboxylic acids can also allow for attacks through chelation. Fruit acids such as citric acid ( $C_6H_8O_7$ ) are commonly found examples of this. In citric acid, the COOH group is dissociated, forming  $H^+$  for  $H_3O^+$  and allowing a  $COO^-$  anion to cause calcium chelation.<sup>87</sup> The direct acid attack, using hydronium ions, has already been described above. Two anions, however, are able to form a soluble chelate complex with three calcium ions. This is dependent on the dissolution strength of the anion relative to the bound calcium in HA and results in the formation of a chelate at pH 3.8–4, the pH of fruit and fruit drinks.<sup>93</sup> As the chelate is soluble, this can then be carried from the enamel surface, resulting in a net loss of mineral for the teeth. Although commonly found in fruits and soft drinks, citric acid is particularly damaging teeth, and it can act through two mechanisms to remove both phosphate and calcium from the HA.<sup>77,88</sup> Carbonic acid behaves similarly to citric acid; however, the dissolution constant is lower (pKa 3.6) compared with citric acid (pKa 6.4). Carbonic acid can disassociate to form both bicarbonate anions  $HCO_3^-$  and orthocarbonic acid  $C(OH)_4$ , which increases the risk of acid attack on teeth.<sup>57,112</sup> The amount of carbonic acid added to carbonated (“fizzy”) drinks is often too low to have significant effects.

Although the carbonic acid content may be low, the presence of phosphoric acid in soft drinks, especially cola products, is damaging to teeth. Phosphoric acid ( $H_3PO_4$ ) does not contain a carboxylic group but still attacks teeth through both the direct pathway and chelation.<sup>112,113</sup> Two hydrogens disassociate from phosphoric acid, allowing two hydronium ions to be formed for direct acid attack.<sup>18,77</sup> The remaining phosphate ion ( $PO_4^{3-}$ ) can chelate with calcium cations at ratio of 2:3, forming soluble calcium phosphate. Some hydrogen phosphate ( $HPO_4^{2-}$ ) is also formed that chelates with calcium cations in a 1:1 ratio. Both pathways occur at low pH ranges and contribute to demineralization with acidic and sparkling drinks; the effect of which is seen in Figure 1.<sup>108,113</sup>

#### Chemical erosion mechanisms

When discussing tooth erosion, pH is important, but it is not necessarily the crucial factor.<sup>114,115</sup> The routes of direct acidic attack have been seen at length and are well documented. Irrespective of the exact type of acid in a drink, a lower pH dissolves HA in enamel at a faster rate and more severely than would a higher pH acid drink. Chelation causes a destabilization of the HA surface at low pH, weakening the phosphate coordination bonds.<sup>60</sup> Acid concentration in molarity should also be taken into consideration. Titratable acidity, the amount of alkali required to titrate the subject to

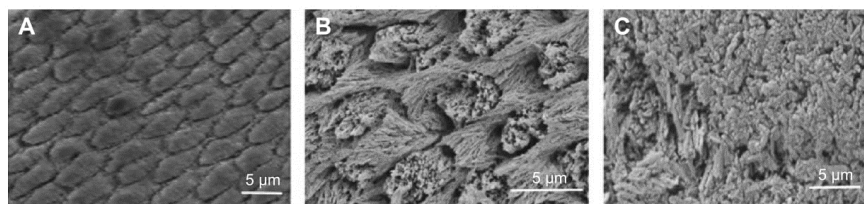


**Figure 1** Scanning electron microscopic images showing (A) normal enamel, (B) enamel etched with phosphoric acid at the same concentration as found in drinks, and (C) the recrystallized HA after solubilization (edges of the image) compared to unetched HA (center of the image).  
**Abbreviation:** HA, hydroxyapatite.

its natural value, has been used to measure the concentration of acids present in drinks.<sup>116</sup> Although the pH ranges that can be tested using this method are often not found in commercial products, nor is the length of exposure relevant to drinking, titratable acidity remains a commonly tested value.<sup>117</sup> While pH measures just the dissociated ions in a solution, which could form acids or alkalis, titratable acidity also measures the bound compounds giving a larger overview of the potential acidity of a solution.<sup>60,114,117</sup> Although titratable acidity experiments often have experimental drawbacks, an increase in titratable acidity has been shown to be linked to an increase in enamel loss in model studies.<sup>80,118</sup>

Linked to titratable acidity is the undissociated acid concentration, a measure of the inactive acidity of a solution. This describes solute that does not contribute to the pH of a solution.<sup>115</sup> These molecules are also uncharged, which allows for a localized increase in hydrogen ions once diffused into the HA. Acids that have a low pKa have an increased concentration of molecules in a disassociated form.<sup>93</sup> These hydrogen ions react with water to form hydronium ions, which are delivered to enamel. This high concentration of hydrogen ions favors dissolution of the enamel, at a layer known as the mineralization front.<sup>93</sup> Short-term erosion sides have shown significant reduction in hydrogen when the disassociated value of acids was changed to favor higher pH levels.<sup>117</sup> The pH remains the value that is most quoted for expositors to dietary acid over normal eating or drinking timescales.

The equilibrium constant for acid dissociation (Ka) and its logarithmic value (pKa) indicate the ratio of ionized-to-nonionized acid groups in aqueous solution.<sup>119</sup> A solution with equal pKa and pH values will have 50% chelator anions and 50% disassociated acid in solution.<sup>60</sup> pKa values alter with environment, solvent, and structural changes. The pathway by which an acid is likely to attack HA in teeth can be predicted from the pKa value. A carboxylic acid with a low pKa

value in water is likely to produce a high number of chelating ions, while a higher pKa value suggests direct hydrogen ion attack.<sup>60</sup> Although citric acid has a low pKa value (3.1) in water compared with hydrochloric acid (−6.1), it does not mean that the carboxylic acids are not damaging.<sup>120</sup> Ka or pKa values cannot be used to directly measure the severity of an acid but is crucial in modeling other values.<sup>118</sup>

Although chemical and mechanical methods of erosion are often considered separately, models such as the differential buffering capacity (DBC) of an acid can predict the mechanical effects of acid demineralization.<sup>117,121</sup> DBC is measured as the gradient of a titration curve at a certain pH value and gives the concentration of acid required to lower the pH by 1.<sup>122</sup> Acids with lower DBC values have been shown to have more severe effects on enamel for short-term exposure than higher DBC values.<sup>117,121</sup> The DBC value of an acid is made up of the pKa and pH values and is therefore considered to be a more reliable marker of erosion properties over long-term exposure, when the pH range is relevant for dietary exposure.<sup>122</sup>

Temperature has a significant impact on the kinetics of dissolution. In the mouth, the ambient temperature is higher than room temperature, increasing the kinetic rate of reaction.<sup>68,110</sup> The ions in solution, which impact the enamel causing dissolution, exceed the total energy required for the dissolution of the calcium. The results in a greater level of demineralization would occur at room temperature but is unavoidable due to physiological conditions.<sup>123</sup>

All these descriptors factor into the erosion of enamel by dietary acids. However, there is no conclusive study indicating which is more important or representative for dietary conditions.

## Remineralization

This section covers both prevention and cure of demineralization that can be arrested or reversed particularly in its

early stage. Saliva, fluoride therapy, diet control, and probiotic bacteria are described as preventive regimes for tooth demineralization. Dental composites containing different forms of calcium phosphates (CaPs) are discussed as potentially curative regime for tooth demineralization. The use of nanotechnology in preventive dentistry, as antibacterial nanotherapy and biomimetic remineralization for reversing an incipient caries or recurrent decay, was explained in details in the literature.<sup>124</sup>

### Saliva

As mentioned above, saliva is considered one of the most important biological factors in dictating the intraoral neutralizing effects of acid exposure. Pathogenesis of dental erosion is directly related to the buffering capacity and rate of secretion of saliva.<sup>96</sup> In addition to its cleansing and antibacterial action,<sup>125</sup> saliva acts as a constant source for calcium and phosphate that helps in maintaining supersaturation with respect to tooth minerals, therefore inhibiting tooth demineralization during periods of low pH, and they promote tooth remineralization when the pH returns to neutral state. Furthermore, when saliva secretion is stimulated, a rapid rise in pH to above neutrality occurs. As a result a complex of calcium phosphate and glycoprotein called salivary precipitin is formed. This complex is readily incorporated into dental plaque. Due to its high solubility of calcium phosphate in salivary proteins (eight to ten times higher than calcium phosphate in tooth), it serves as a sacrificial mineral that dissolves preferentially before tooth mineral, ie, reducing demineralization. It also acts as a source of calcium and phosphate ions that are required for remineralization of decalcified tooth.<sup>63,126</sup>

Saliva constantly delivers fluoride to the tooth surface; salivary fluoride is a key player in preventing tooth demineralization and enhancing remineralization<sup>125</sup> as described in the “Fluoride therapy” section.

### Fluoride therapy

Fluorination of teeth is encouraged;<sup>127</sup> the most effective method of caries prevention is through the use of topical fluoride, such as toothpaste and varnish. The calcium in HA is displaced by fluorine, forming FAP, which has a much lower solubility than either the original or calcium-deficient HA. FAP forms a solid-state solution with the phosphate-rich HA, with a hydroxide being displaced.<sup>55,77</sup> FAP has two main advantages over HA, and fluorine is often added to drinking water to encourage the conversion.<sup>127</sup> First, fluoride acts as a catalyst, assisting in the remineralization enamel

with phosphate ions dissolved in saliva.<sup>103,128</sup> This can help to counteract any demineralization which has occurred.<sup>111</sup> Second, the displacement of hydroxide with fluoride removes a weakness in HA to lactic acid; FAP  $[\text{Ca}_{10}(\text{PO}_4)_6\text{F}_2]$  is not dissolved by this in the mouth.<sup>74,129,130</sup> For the formation of FAP, for every two fluoride ions, ten calcium ions and six phosphate ions are required. Accordingly, the presence of inadequate calcium and phosphate can limit the remineralization process. Casein phosphopeptide-ACP (CPP-ACP) has been developed for this purpose. Aggregation of CPP with calcium phosphate forms clusters of ACP. This aggregation prevents the precipitation of calcium phosphate and hence results in a state of supersaturation with respect to enamel, thus preventing demineralization and enhancing remineralization.<sup>131</sup> Some commercially available dental products contain both CPP-ACP and fluoride, and they are very effective remineralizing agents.<sup>132–134</sup> Regardless of the significant effect of fluoride in preventing tooth demineralization, care as to not exceed the maximum recommended dose of fluoride is highly advised. Overconsumption of fluoride through fluoridated water/foods and/or supplements may lead to dental and/or skeletal fluorosis. Dental fluorosis is defined as mineralization defects of enamel, resulting from subsurface porosity below a well-mineralized surface zone.<sup>14</sup>

Since the recovery of plaque pH to a higher level than the critical pH plays a key role in remineralization process, addition of 1.5% arginine (insoluble calcium compound) to fluoride in tooth dentifrices was more effective in reducing tooth demineralization and progression of caries to cavitation than those containing fluoride alone. The arginine is broken down into ammonia by nonpathogenic arginolytic bacteria; ammonia helps in neutralizing plaque acid and maintaining the plaque biofilm on tooth surface in a healthy state.<sup>63,135,136</sup>

### Diet control and oral hygiene instructions

Additionally, dietary advice, oral hygiene instruction, and application of fissure sealants are still used as further preventive regime to dental caries in both high- and low-risk individuals. In most recent studies, it was shown that the use of nonfermentable sugars in chewing gum, such as xylitol, was seen to inhibit the effect of *S. mutans*; however, more conclusive evidence is yet to be achieved.

### Probiotic bacteria

Probiotic bacteria, defined as “live microorganisms which, when administered in adequate amounts, confer a health benefit on the host” (WHO), are commonly suggested candidates

for bacteriotherapy.<sup>137</sup> The word probiotics means “for life”, and this is either naturally occurring or genetically engineered bacterial strains that can be used for intervention.<sup>137</sup> Examples of probiotics that have the ability to confer oral health benefits for the host include *Lactobacillus* (eg, *salvarius*,<sup>138</sup> *reuteri*,<sup>139</sup> and *rhamnosus*<sup>140</sup>) and *Bifidobacterium* that are part of normal oral flora.<sup>140–142</sup> They can be used as biotherapy for prevention or treatment of dental caries and periodontal diseases<sup>143</sup> by reducing the number of pathogenic bacteria (*S. mutans*)<sup>143,144</sup> or inhibiting the expression of *S. mutans* virulence genes, for example, *GtfB* and *LuxS*<sup>140,145</sup> and therefore alter or reduce biofilm formation.<sup>138</sup>

For administration of probiotic strains, several appropriate vehicles are available; they vary from dairy products, ice cream and curds,<sup>146</sup> oral thin film,<sup>147</sup> tablets,<sup>139,148</sup> and lozenges (eg, PerioBalance).<sup>149</sup> The use of probiotic products found a potential use as alternative strategy for displacing pathogenic bacteria with probiotic microorganism and can therefore be exploited for the prevention of enamel demineralization.<sup>146</sup>

Another avenue to reduce the cariogenicity of *S. mutans* is the generation of strains without the open reading frame of lactate hydrogenase.<sup>150</sup>

#### Electrically assisted enhanced remineralization

A new technology that has been developed by Reminova Ltd<sup>151</sup> relies on the use of an electric current to reverse tooth decay by boosting remineralization. The use of tiny electric current of few microamperes that cannot be felt by the patient pushes the minerals into the tooth to repair the clean defect. This process requires no injection, no drilling of tooth, and no filling materials and triggers the remineralization from the deeper portion of the lesion. The development of a model ready to use by dentists from the prototype device developed by Reminova Ltd is currently under investigation.<sup>151</sup>

#### Dental composites with remineralizing action

Resin-based composites have been used as dental filling materials for >50 years.<sup>152</sup> These materials have evolved throughout the years. The most important changes have involved the reinforcing fillers to improve the mechanical properties, polishability, and wear resistance. Recently, the focus has shifted to equipping composite systems with remineralizing and antibacterial properties. Various forms of calcium phosphates (CaP) have been incorporated into resin-based composites to provide mineral release that could potentially remineralize the tooth structure. This section provides an overview on the development of potentially

remineralizing composites for tooth repair that have recently been introduced.

Calcium phosphates in different forms have been studied as fillers to make mineral releasing dental composites. This includes ACP, HA, tetracalcium phosphate (TTCP), dicalcium phosphate (DCP) anhydrous, and mono-, di-, and TCPs. These calcium phosphate fillers partially replaced the reinforcing fillers. Unfortunately, this can compromise composite mechanical properties.

#### Composites containing ACP

ACP has been evaluated as filler for dental composites and adhesives. Skrtic et al<sup>153–155</sup> has introduced composite materials containing ACP, which release significant amount of calcium and phosphate ions. It was demonstrated that the remineralizing potential of ACP was enhanced through its hybridization with silicon or zirconium elements. Adding these elements to ACP increased the time of mineral ion release through their ability to slow down the intracomposite ACP to HA conversion.<sup>156,157</sup> Mineral ion release from ACP composites was shown to efficiently restore the mineral lost from enamel surfaces following acid attack.<sup>158,159</sup> Another study has incorporated ACP into a composite adhesive system. The ACP was shown to infiltrate the dentinal tubules without causing negative effect to bond strength.<sup>160</sup>

Compared with glass or ceramic-only filled composites, the ACP-filled composites are more hydrophilic and biodegradable. In addition, they exhibit inferior mechanical properties and durability.<sup>161</sup> ACP particles aggregation, poor interfacial interaction with matrix, and excessive water sorption contribute to compromising the mechanical properties.<sup>155,162,163</sup> Mechanical milling reduced the particles size of ACP-zirconium fillers to ~20 µm, providing more homogeneous filler distribution and a reduction in voids formation was obtained. Biaxial flexural strength was, therefore, increased from 50 to 75 MPa.<sup>161,164–166</sup> This is, however, still lower than the strength of commercial dental composites (100–180 MPa), restricting the use of ACP-filled composites as potential direct dental-filling materials.<sup>167</sup> A recent study showed that 120 MPa flexural strength could be obtained if the mass fraction of ACP was kept at 10 wt%. However, this significantly reduced the amount of calcium and phosphate ions that could be released.<sup>168</sup>

#### Composites containing HA

Coupling agent treatment of calcium phosphate fillers with citric acid, acrylic acid, or methacrylic acid improved the flexural strength of composites containing HA.<sup>169,170</sup> However, γ-methacryloxypropyltrimethoxysilane coupling agent

had no effect on strength.<sup>171</sup> Microscopic HA fillers provided higher strength than nanoscopic fillers.<sup>169,170,172</sup> It was also reported that HA fillers in the form of whiskers further enhanced flexural strength.<sup>173,174</sup>

Water sorption of resin-based composites containing silane coupling agent-treated and -untreated HA fillers was consistent with a diffusion-controlled process. Incorporation of HA reduced the water uptake, and this decreased further upon silane treating of HA fillers,<sup>175</sup> which subsequently led to deterioration in CaP release.

In an attempt to improve the mechanical properties, small fraction (3 wt%) of HA filler were impregnated into composites. This low mass fraction of HA was well dispersed, leading to increase in the flexural strength up to 120 MPa. Raising mass fraction of HA to 10 wt% caused to decrease strength to 95 MPa due to the formation of aggregates of HA that served as a defect site.<sup>176</sup>

#### Composites containing TTCPs

Recently, TTCP particles were investigated as potentially remineralizing fillers for dental composites. Upon addition of TTCP, the mechanical properties of the composites decreased dramatically. Replacing 50% of TTCP by silicon nitride whiskers increased the strength of the composites from 50 to 100 MPa. Calcium and phosphate ion release, however, was decreased by an order of magnitude.<sup>177</sup> Another study showed that flexural strength can reach 80 MPa for composites filled with 40 wt% TTCP. This has increased further upon addition of an antibacterial agent.<sup>178</sup>

#### Composites containing mono-, di-, and tricalcium phosphates

Calcium phosphates in the form of monocalcium phosphate (MCPM), DCP, and TCP were also incorporated into dental composites materials. The solubility of these forms of calcium phosphate differs significantly. The mineral ion release from MCPM composite was shown to be dependent on the amount of MCPM added to the formulation. Replacing the MCPM with reinforcing whiskers was shown again to improve mechanical properties but dramatically decrease calcium and phosphate release.<sup>179</sup> Replacing MCPM with less soluble DCP enhanced the strength but significantly reduced mineral ions release.<sup>180</sup> A study showed that by decreasing the particle size of DCP fillers to ~110 nm, the amount of mineral ions release can be significantly increased.<sup>181</sup> It has also confirmed that replacing DCP with silicon nitride whiskers enhanced the strength but at the expense of the mineral ion

release. In addition, incorporating whiskers in the composite formulations compromised the optical properties preventing light cure feasibility.

TCP has been added together with MCPM to enable more control on the latter dissolution and composite water sorption.<sup>182–185</sup> Highly soluble MCPM on the surface of the composite dissolved but at the core it reacted with  $\beta$ -TCP to form less soluble brushite (DCP dihydrate). Partial replacement of calcium and phosphate with reinforcing opaque fillers improved the strength but these again compromised the mineral ion release and optical properties.<sup>182</sup> A recent study has introduced light-cured composites containing both MCPM and TCP with strength within the range expected for commercial composites.<sup>183,184</sup> HA precipitation at the surfaces of these composites was used to evaluate the remineralization potential of these materials. These HA layers were formed of calcium and phosphate ions released from within the composite samples.<sup>184</sup> Although these results are promising, the ability of these composites to remineralize the demineralized dentine has yet to be demonstrated.

### Demineralization–remineralization dynamics in bone

Bone remodeling is a physiologic process that continues within discrete sites following cessation of skeletal growth. During remodeling, packets of bone are laid down and turned over in order to facilitate the repair of damaged older bone. Osteoclasts resorb bone, and these resorption lacunae are subsequently filled with new bone matrix deposited by osteoblasts. As newly formed bone accumulates mineral with time, the most recently deposited bone will generally be less mineralized than bone deposited months or years earlier. Regions with high turnover, containing many newly formed osteons, generally display lower average mineralization than areas of low turnover. During secondary mineralization, the mineral content of an individual unit continuously increases with time (referred to as the mineralization law), with a steep slope in the beginning and a significant reduction in the slope afterward.<sup>186</sup> The weight or volume fraction of mineral in the bone matrix is measured spatially by methods such as plain radiography, dual-energy X-ray absorptiometry, Faxitron X-ray microradiography, synchrotron, microcomputed tomography, and quantitative backscattered electron microscopy.

Bone remodeling is essential for the required tooth movement during orthodontic treatment. The interaction between the receptor activator of nuclear factor  $\kappa$ B (RANK) that is expressed on osteoclast precursor cells, its ligand (RANKL)

that is expressed on osteoblast cells, and osteoprotegerin is responsible for the regulation of bone remodeling process. Binding of RANKL to RANK results in differentiation of precursor osteoclast cells to mature osteoclasts. Osteoprotegerin competes with RANK for RANKL binding and inhibits osteoclast differentiation. The balance of these trimolecular control factors maintains physiologic bone remodeling.<sup>187</sup>

Any imbalance between bone formation and resorption has undesirable consequences.

### Demineralization (hyper- and hypomineralization)

The mineralization density at the tissue level reflects the contribution of all osteons with different degrees of mineralization and disruptions in the physiological and biochemical processes that regulate the deposition and removal of calcium apatite in a tissue may be caused by age,<sup>188</sup> disease, and drug treatment.<sup>189</sup> Small increases in mineralization lead to relatively large increases in the strength of bone, although levels  $>66\%$  mineralization have been shown to lead to brittleness and a reduction in bone strength.<sup>190</sup>

Hypermineralization and hypomineralization are deviations that occur within the mineral content of fully mineralized bone. Only a pathologically altered organic matrix and/or abnormalities in crystal size and shape can lead to a hypermineralization, a mineralization density exceeding that of fully mineralized normal bone matrix. In contrast, hypomineralization results when the organic matrix is not fully mineralized due to a lack of time for secondary mineralization and/or by a pathologically altered bone matrix, affecting normal mineralization kinetics.<sup>189</sup> Bone diseases such as rickets and osteoporosis cause a significant reduction in bone mineralization and bone mineral density, which lead to functional consequences in terms of increased fracture risk and skeletal deformity, respectively.<sup>188</sup> Mild primary hyperthyroidism is characterized by abnormally elevated parathyroid hormone serum levels accompanied by hypercalcemia, which also results in a low bone mineralization density that is thought to be due to an increased bone turnover and bone formation rate.<sup>186</sup>

Osteogenesis imperfecta is a genetic disorder associated with increased bone fragility. Studies indicate a shift toward a higher mineralization density of bone tissue, only marginally exceeding that of normal adults.<sup>191</sup> Weber et al<sup>192</sup> suggested that the higher mineral content was not exclusively due to an altered collagen structure but may also be caused by an accelerated mineralization

process. Alterations in bone mineral density have also been measured in male osteoporosis, idiopathic osteoporosis, patients with collagen I polymorphisms,<sup>193</sup> osteomalacia,<sup>194</sup> hypophosphatemia, Paget's disease, Bruck's syndrome, myopathy, renal osteodystrophy,<sup>195</sup> and liver transplantation.<sup>196</sup> All showed a shift to lower mineralization density, while pycnodysostosis,<sup>197</sup> hypoparathyroidism, osteopetrosis, and osteonecrosis all led to an increased mineralization density.<sup>189</sup>

### Remineralization

Some drugs have been developed to either reduce bone resorption (eg, bisphosphonates<sup>198</sup>) or promote bone formation (hormonal replacement,<sup>199</sup> calcium, and vitamin D supplements). Combination and sequential treatment using both bone formation stimulator and bone resorption inhibitors have been attempted. Combination treatment using both bone resorption inhibitors and bone-formation stimulators has not showed any additional benefit over the use of each medication alone. The use of bone-formation stimulators is independent on the previous use of bone resorption inhibitor. The use of bone resorption inhibitors; however, maintains the benefit of the former bone formation stimulator.<sup>199</sup> Generally, serious side effects, however, have now been associated with the extensive use of these drugs.<sup>198,200,201</sup> This, however, is not the main focus of this review. Only the materials with remineralizing action will be covered in details.

### Bone cements/composites with remineralizing action

Poly(methylmethacrylate) (PMMA) has been widely used in orthopedic surgeries as anchoring agent in hip and knee replacement to repair vertebral fractures and skull defects.<sup>202</sup> To overcome the disadvantages of conventional PMMA cements such as lack of adhesion to bone and heat generation during polymerization, calcium phosphate cements and polymeric cements with mineralizing fillers have been investigated as alternatives.

Various forms of calcium phosphates have been studied as bone cements due to their excellent biocompatibility.<sup>203</sup> The main shortcomings of these materials, however, are the mechanical properties. These properties were improved through formation of polymer composites containing calcium phosphate. The polymer matrix reinforced with glass or ceramic fillers and contain CaP fillers can potentially provide remineralizing materials with good mechanical properties. This includes calcium phosphates in the forms of HA,  $\beta$ -TCP, and biphasic calcium phosphate.



### Nondegradable cements/composites

Cements/composites containing HA. HA was used as filler in self-curing two paste bone cements. Upon immersion in simulated body fluid, the materials were shown to form an apatite layer. This feature has been associated with bone bonding ability.<sup>202</sup> Bioactive glass, HA, and  $\beta$ -TCP have also been used to develop bone cements that have been reported to exhibit bone-bonding properties.<sup>204,205</sup> Enhanced cellular activity has been associated with increased levels of HA fillers in the composite materials.<sup>206</sup> Ultimate tensile strength, however, decreased with increased HA content.

A combination of strontium and HA containing bone cement was reported to provide superior bone-bonding strength to that with conventional PMMA cement.<sup>207</sup> Addition of HA to PMMA also enhanced the biocompatibility and osteoconductivity of the cement.<sup>208</sup>

Cements/composites containing  $\beta$ -TCP. Composite bone cements containing  $\beta$ -TCP were also reported to be biocompatible, and osteoconduction was attained within 4 weeks of direct contact with bone.<sup>209</sup> A study showed that resin composite bone cements contain either bioactive glass ceramics or  $\beta$ -TCP that induces bone formation at the interface.<sup>210</sup> However, the mechanical properties of the former were higher than the latter.

### Biodegradable calcium and phosphate cements

Calcium and phosphate cements have been investigated as synthetic materials to fill bone defects and cavities due to their excellent biocompatibility and osteoconductivity.<sup>203,211</sup> The formation of these materials is activated by mixing various calcium phosphate phases with a liquid phase at a specific pH. The pH of the chemical reaction dictates the type of final product; HA forms at pH >4.2 or brushite at pH <4.2.<sup>211,212</sup> Unlike brushite ( $\text{CaHPO}_4 \cdot 2\text{H}_2\text{O}$ ), HA-based cements were shown to have poor solubility at a physiological pH.<sup>213</sup> Calcium and phosphate cements are brittle with low strength and can only be used in nonload-bearing applications.<sup>211</sup>

### Apatite cements

Commercially available apatite cements were developed using different chemical formulations containing more than one type of calcium phosphates such as  $\alpha$ -TCP, MCPM, and TTCP. Precipitated HA or calcium-deficient HA can be formed by hydrolyzing calcium phosphate or by mixing two calcium phosphate powders with Ca:P ratio lower than the stoichiometric ratio for HA (Ca:P = 1.67).<sup>214</sup> These materials were shown to have poor solubility and subsequently reduced chances of replacement with natural bone tissues.

### Brushite cement

These cements have been developed to take advantage of their high solubility in order to increase the amount of regenerated tissues.<sup>211</sup> In a physiological condition, brushite dissolves providing calcium and phosphates ions, in addition, to their high biocompatibility and osteoconductivity.<sup>215</sup> Mechanical properties of brushite cements, however, are lower than apatite cements. Today, research is focused on improving the overall performance of brushite by balancing resorbability and mechanical properties.

Throughout this review, the mechanisms of demineralization–remineralization in both teeth and bone as well as therapies that boost remineralization have been thoroughly discussed. Understanding these processes is also important for the innovation and development of scaffolds or implant surfaces that are able to stimulate mineralization or osseointegration. The interaction of biomaterials with host tissues is an important issue that has to be addressed during designing scaffolds or implants for biomedical use. The topography, chemical, and mechanical properties of the materials from which scaffolds or implants has been made have fundamental influence on the host response. Some innovative approaches seem to be promising in designing scaffolds or implants with topographical features that favor osteogenic differentiation. Electrospinning, rapid prototyping,<sup>216</sup> and two-photon polymerization<sup>217</sup> could be promising in designing scaffolds with biomimetic architecture, required for nutrient supply and diffusion, as well as with instructive surface properties required for directing cells into the proper lineage. Osteoprints, bioinspired two-photon polymerized 3D trabecular-like structures, deeply influenced cellular behavior, enhanced osteogenic differentiation, and increased HA production.<sup>217</sup> Direct laser writing/atomic layer deposition,<sup>218</sup> lithography, ionic implantation, anodization,<sup>219</sup> radio frequency plasma treatments,<sup>220–223</sup> and surface treatment (eg, glow discharge, acid etching, or UV irradiation)<sup>224</sup> have been used to tailor implants' surface topography in favor of osseointegration.<sup>225,226</sup> Controlling the surface topography at nanoscale level or chemistry of scaffolds or implants could influence cells spreading<sup>222</sup> and differentiation.<sup>220,221</sup> Modification of chitosan scaffolds with barium titanate nanoparticles or strontium phosphate favored the osteogenic differentiation of mesenchymal stem cells.<sup>227,228</sup> Nanoarrays from tantalum improved adhesion, proliferation, and differentiation of osteoblast cells on implant surface.<sup>229</sup> Biofunctionalization, that is, immobilization of specific active biomolecules known with their effective role on osteogenesis on the surface of scaffolds or implants, has also been attempted to improve their long-term acceptance.<sup>230</sup> Examples include ECM proteins,<sup>231</sup> adhesion

molecule (arginyl-glycyl-aspartic),<sup>232</sup> and bone morphogenic protein.<sup>233</sup>

## Concluding remarks and future prospects

Demineralization–remineralization is a dynamic process, and there is always a battle between them. Both processes can occur on the hard tissues surface to some extent. They therefore have an impact on the health of hard tissues, and the surrounding environment plays a key role in determining which process wins the battle. Therefore, the main aim would be maintaining the environment that prevents demineralization but encourages remineralization.

The understanding of the process of demineralization and remineralization in teeth is very well understood. However, despite efforts by researchers and clinicians, maintaining a good oral and dental health throughout patients' life remained a big challenge. The constant change in diet associated with the more and more widespread accessibility of fizzing sugary drinks is putting pressure on the whole dental profession to safeguard good oral and dental health, even in wealthy country. A University College London survey at the London 2012 Olympic Games found that 18% of athletes said that their oral health had a negative impact on their performance and 46.5% had not been to the dentist in the past year. In terms of dentistry, the challenge in the next decade is to either promote a change in the habits of population or for scientists to develop new products that may counter the demineralization process that results from the consumption of these fizzing sugary drinks. The more and more widespread prevalence of dental caries is a direct consequence of this growing population behavior, and it will become ever more important to involve the public and patients to devise strategies to overcome this growing health burden. The wider use of gums that promote salivary release or neutralized the mouth pH is also explored and would help toward building sufficient sacrificial amorphous enamel layer. The development of smart restorative materials has made tremendous progress in the field of dentistry, but their translation to market is slower than in medicine, maybe due to the reticence of dental practitioners to adopt these novel materials. It is likely that in the next few years, new generation of restorative materials will become accessible that will make traditional mechanical drilling redundant. The challenge for bone remains to find long-term solution to conditions associated with persistent bone loss such as osteoporosis. Research in this area is still very active, but it has yet to find a sustainable approach to reverse the slow

resorption of bone, which consequently may fracture and impact greatly upon the patients' quality of life. Similarly, the development of smart materials in dentistry, a similar approach exists for bone with the genesis of bone cements that are becoming available for repairing spinal cord injuries, for example. Unlike dentistry, the causative effects of bone demineralization are not patients' behavior driven except for reduced physical activity. Coupling these strategies for earlier diagnostics of bone fragility or dental demineralization would greatly enhance patients' recovery. Thus, research is currently being carried out across the world to offer new diagnostic tools for clinical use to help with the early detection. Few of these tools, such as Bio-Dent and dental optical coherence tomography, are currently on the market, and it will take a few more years for their acceptance by clinical colleagues. Ultimately, although scientists and/or clinicians may discover new understanding, develop new technologies, and products, it is still the responsibility of the patients to adapt their personal behaviors to minimize the risk factors associated with bone or dental surface loss.

## Disclosure

The authors report no conflicts of interest in this work.

## References

1. Gelse K, Poschl E, Aigner T. Collagens-structure, function, and biosynthesis. *Adv Drug Deliv Rev*. 2003;55(12):1531–1546.
2. Lin C, Douglas WH, Erlandsen SL. Scanning electron microscopy of type I collagen at the dentin-enamel junction of human teeth. *J Histochem Cytochem*. 1993;41(3):381–388.
3. Nanci A. *Ten Cate's Oral Histology: Development, Structure, and Function*. Maryland Heights, MO: Mosby; 2008.
4. Vallet-Regi M, González-Calbet JM. Calcium phosphates as substitution of bone tissues. *Prog Solid State Chem*. 2004;32(1–2):1–31.
5. Beniash E. Biomaterials-hierarchical nanocomposites: the example of bone wires. *Nanomed Nanobiotechnol*. 2011;3(1):47–69.
6. Boskey A, Young M, Kilts T, Verdelis K. Variation in mineral properties in normal and mutant bones and teeth. *Cells Tissues Organs*. 2005;181(3–4):144–153.
7. Duailibi MT, Duailibi SE, Young CS, Bartlett JD, Vacanti JP, Yelick PC. Bioengineered teeth from cultured rat tooth bud cells. *J Dent Res*. 2004;83(7):523–528.
8. Herring SW, Ochareon P. Bone – special problems of the craniofacial region. *Orthod Craniofac Res*. 2005;8(3):174–182.
9. Nudelman F, Pieterse K, George A, et al. The role of collagen in bone apatite formation in the presence of hydroxyapatite nucleation inhibitors. *Nat Mater*. 2010;9(12):1004–1009.
10. Dorozhkin S, Epple M. Biological and medical significance of calcium phosphates. *Angew Chem Int Ed Engl*. 2002;41(17):3130–3146.
11. Hart S, Hart T. Disorders of human dentin. *Cells Tissues Organs*. 2007;186(1):70–77.
12. Sasagawa I. Fine structure of the cap enameloid and of the dental epithelial cells during enameloid mineralisation and early maturation stages in the tilapia, a teleost. *J Anat*. 1997;190(Pt 4):589–600.
13. Felszeghy S, Holló K, Módos L, Lammi M. Type X collagen in human enamel development: a possible role in mineralization. *Acta Odontol Scand*. 2000;58(4):171–176.